UNIVERSITY OF CALIFORNIA, SAN DIEGO

Star Formation in Damped Lyman-alpha systems and the Outskirts of Lyman Break Galaxies

A dissertation submitted in partial satisfaction of the
requirements for the degree
Doctor of Philosophy

in

Physics

by

Marc Alexander Rafelski

Committee in charge:

Professor Arthur Wolfe, Chair
Professor Alison Coil
Professor Kim Griest
Professor Kevin Quest
Professor Barney Rickett

2011

The dissertation of Marc Alexander Rafelski is approved, and it is acceptable in quality and form for publication on microfilm and electronically:

_____

_____

_____

_____

_____

Chair

University of California, San Diego

2011

DEDICATION

To my mother
Helga

For her love and inspiration,
in both life and science.

EPIGRAPH

A theory is something nobody believes,
except the person who made it.
An experiment is something everybody believes,
except the person who made it.
—Albert Einstein

TABLE OF CONTENTS

Signature Page iii

Dedication iv

Epigraph iv

Table of Contents vi

List of Figures ix

List of Tables xi

Acknowledgements xiv

Vita and Publications xvii

Abstract of the Dissertation xix

Chapter 1 Introduction 1
1.1 The Formation and Evolution of Galaxies 1
1.2 Star Formation 5
1.3 Lyman Break Galaxies 7
1.4 Quasar Absorption Line Systems 9
1.5 Damped Lyman-α Systems 11
1.6 Massive Stars at the Galactic Center 13
1.7 Overview of Thesis 14
References 17

Chapter 2 Deep Keck u-band imaging of the Hubble Ultra Deep Field: A catalog of $z \sim 3$ Lyman Break Galaxies 24
2.1 Introduction 24
2.2 Observations 28
2.3 Data Reduction and Analysis 31
2.3.1 Image processing 31
2.3.2 Photometric Calibration 32
2.3.3 Depth of the u-band Image 33
2.3.4 Photometry through Template Fitting 34
2.3.5 Sample Selection 40
2.4 Photometric Selection of $z \sim 3$ Galaxies 41
2.4.1 Photometric Redshifts 43
2.4.2 Color Selection 57
2.5 Sample of z $\sim$ 3 Galaxies 62

2.5.1 Redshift Distribution . . . 63
2.5.2 Cosmic Variance . . . 66
2.5.3 LBG Number Counts . . . 68
2.6 Summary . . . 70
2.7 Acknowledgments . . . 73
References . . . 73

Chapter 3 Star Formation from DLA Gas in the Outskirts of Lyman Break Galaxies at z∼3 . . . 81
3.1 Introduction . . . 81
3.2 Observations . . . 86
3.3 Sample Selection . . . 87
3.3.1 Number Counts . . . 88
3.3.2 Catalogs of LBGs and Stars . . . 90
3.3.3 Comparison of the Subset and Full LBG Samples 92
3.4 Analysis of UDF Images . . . 94
3.4.1 Image Stacks . . . 94
3.4.2 Sky Subtraction Uncertainty . . . 96
3.4.3 Radial Surface Brightness Profile . . . 97
3.4.4 Effects of the Ly-α Line on the Image Stack . . . 99
3.5 Direct Inferences from the Data . . . 100
3.5.1 Connecting the Observed Intensity to the SFR Surface Density . . . 101
3.5.2 Covering Fraction of LBGs Compared to the Underlying Gas . . . 102
3.5.3 Measurements of the SFR and $\dot{\rho}_*$ in the Outskirts of LBGs . . . 110
3.5.4 Metal Production in the Outskirts of LBGs . . . 114
3.6 Star Formation Rate Efficiency in Neutral Atomic-dominated Gas . . . 115
3.6.1 Theoretical Framework . . . 116
3.6.2 Stacking Randomly Inclined Disks . . . 122
3.6.3 The Kennicutt Schmidt Relation for Atomic-dominated Gas at High Redshift . . . 127
3.7 Discussion of Results . . . 130
3.7.1 Models of the Kennicutt Schmidt Relation in High Redshift Galaxies . . . 131
3.7.2 The Roles of Molecular and Atomic-dominated Gas in the Kennicutt Schmidt Relation . . . 133
3.7.3 Is There a Variation of the Kennicutt Schmidt Relation with Redshift? . . . 137
3.7.4 Bimodality of DLAs . . . 142
3.7.5 Effects of Different DLA Sizes . . . 143

3.7.6 The 'Missing Metals' Problem . . . 144
3.8 Summary and Concluding Remarks . . . 146
3.9 Acknowledgments . . . 149
References . . . 150

Chapter 4 Metallicity Evolution of Damped Lyman Alpha Systems out to $z \sim 5$ . . . 162
4.1 Introduction . . . 162
4.2 Observations and Data Reduction . . . 165
4.3 Analysis and Results . . . 172
4.3.1 Voigt Profile Fitting . . . 172
4.3.2 Element Abundances . . . 173
4.3.3 Evolution of Cosmic Metallicity . . . 177
4.3.4 Comparison of DLA Metallicities with those of Halo Stars . . . 182
4.4 Discussion . . . 185
4.5 Summary . . . 190
4.6 Acknowledgements . . . 192
References . . . 192

Chapter 5 Photometric Stellar Variability in the Galactic Center . . . 198
5.1 Introduction . . . 198
5.2 Observations . . . 201
5.3 Data Analysis and Results . . . 201
5.3.1 Image Processing . . . 201
5.3.2 Variability . . . 206
5.4 Discussion . . . 213
5.4.1 Ofpe/WN9 Stars . . . 217
5.4.2 Late-type WC Wolf-Rayet Stars: Variations Associated with a Wind Colliding Binary . . . 221
5.4.3 Comments on Other Stars . . . 221
5.4.4 Interstellar Material . . . 223
5.5 Summary . . . 231
5.6 Acknowledgements . . . 232
References . . . 232

Appendix A Completeness Corrections . . . 239
A.1 Covering Fraction Completeness Correction . . . 239
A.2 $\dot{\rho}_*$ Completeness Correction . . . 242
A.3 $\Delta\dot{\rho}_*$ Completeness Corrections . . . 242

Appendix B Comparison of the Subset and Full LBG Stacks . . . 244

Appendix C Full Tables . . . 247

LIST OF FIGURES

Figure 2.1: u-band transmission for different air masses 29
Figure 2.2: Filter transmission curves 30
Figure 2.3: Detection efficiency of the u-band image 35
Figure 2.4: Quality of TFIT photometric fits 39
Figure 2.5: Comparison of spectroscopic and photometric redshifts 50
Figure 2.6: Example galaxy SED with a catastrophic redshift error 53
Figure 2.7: Example galaxy SED where the u-band changes the photometric redshift 54
Figure 2.8: Comparison of photo-z's with and without u-band data 56
Figure 2.9: Model $(u - V)$ versus $(V - z')$ color–color diagram 59
Figure 2.10: Comparison of color selection criteria with reliable spec-z's . . . 61
Figure 2.11: Photo-z results on a color-color diagram 64
Figure 2.12: Histogram of color selected photometric redshifts 66
Figure 2.13: Number counts of $z \sim 3$ LBGs 71

Figure 3.1: Comparison of the number counts of $z \sim 3$ LBGs 89
Figure 3.2: Thumbnail images in the V-band of the 48 $z \sim 3$ LBGs 91
Figure 3.3: Composite image in the V-band of the 48 $z \sim 3$ LBGs 95
Figure 3.4: Surface brightness profile of stacked LBG image 98
Figure 3.5: Cumulative covering fraction of DLA systems with columns greater than some column density N 106
Figure 3.6: Cumulative covering fraction of gas with columns greater than some column density N 109
Figure 3.7: Surface brightness (μ_V) vs. the differential comoving SFR density per intensity ($\Delta\dot{\rho}_*/\Delta\langle I^{obs}_{\nu_0}\rangle$) predicted for the Kennicutt-Schmidt relation 121
Figure 3.8: Predicted μ_V vs. $\Delta\dot{\rho}_*/\Delta\langle I^{obs}_{\nu_0}\rangle$ compared to the emission in the outskirts of LBGs 124
Figure 3.9: Predicted μ_V vs. $\Delta\dot{\rho}_*/\Delta\langle I^{obs}_{\nu_0}\rangle$ compared to the emission in the outskirts of LBGs corrected for completeness 126
Figure 3.10: Star formation rate per unit area ($\Sigma_{\rm SFR}$) versus gas density ($\Sigma_{\rm gas}$) 129
Figure 3.11: $\Sigma_{\rm SFR}$ versus $\Sigma_{\rm gas}$ compared to simulations 134
Figure 3.12: $\Sigma_{\rm SFR}$ versus $\Sigma_{\rm gas}$ compared to outskirts of spiral galaxies 140

Figure 4.1: ESI spectra of quasars with DLAs at $z > 4$ 169
Figure 4.2: Voigt profile fits to confirmed DLAs 170
Figure 4.3: Voigt profile fits to confirmed DLAs 171
Figure 4.4: Example velocity profiles of metal-line transitions 175
Figure 4.5: New metal abundances versus redshift 178
Figure 4.6: Metal abundance evolution versus redshift 179
Figure 4.7: Metal abundance evolution versus time 181

Figure 4.8: Histograms comparing abundances for DLAs and think, thick, and halo stars . . . 184
Figure 4.9: Histogram comparing α/Fe ratios for DLAs and halo stars . . . 186
Figure 4.10: Comparison of Si and Zn abundances . . . 189

Figure 5.1: Identification of sources . . . 205
Figure 5.2: Histogram of 131 stars in sample . . . 206
Figure 5.3: The average normalized flux densities vs. time . . . 207
Figure 5.4: Median measurement uncertainty vs. K magnitude . . . 207
Figure 5.5: KS test probabilities of all the stars . . . 209
Figure 5.6: Determination of IRS 16SW's period using Dworetsky's string length method . . . 214
Figure 5.7: The phased light curve of IRS 16SW . . . 215
Figure 5.8: Apparent K magnitudes versus spectral type . . . 216
Figure 5.9: Light curves of candidate LBVs . . . 218
Figure 5.10: Light curves of Wolf-Rayet stars of type WC . . . 222
Figure 5.11: Light curves of variable OB stars . . . 224
Figure 5.12: Light curves of early-type variable stars . . . 225
Figure 5.13: Light curves of a late-type star, and two unknown type stars . . . 227
Figure 5.14: Location of the source S2-11 . . . 228
Figure 5.15: Light curves of 7 central arcsecond sources that have known 3-dimensional orbits . . . 230

LIST OF TABLES

Table 2.1: Catalog of u-band Objects 42
Table 2.2: Catalog of Bayesian Photometric Redshifts 45
Table 2.3: Catalog of Galaxies with Reliable Spectroscopic Redshifts in the UDF 51
Table 2.4: Catalog of Candidate z∼3 LBGs in the UDF 65

Table 3.1: Properties of LBGs included in image stack 92
Table 3.2: SFR, $\dot{\rho}_*$, and Metallicity 113

Table 4.1: Journal of Observations 167
Table 4.2: New DLA metallicities 176

Table 5.1: List of Observations 202
Table 5.2: List of Variable Stars 210
Table 5.3: List of Non-variable Stars 212

Table C.1: Catalog of u-band Objects 248
Table C.2: Catalog of Bayesian Photometric Redshifts 289
Table C.3: Catalog of Galaxies with Reliable Spectroscopic Redshifts in the UDF 330
Table C.4: Catalog of Candidate z∼3 LBGs in the UDF 333
Table C.5: Properties of LBGs included in image stack 341
Table C.6: Journal of Observations 342
Table C.7: New DLA metallicities 344
Table C.8: List of Observations 345
Table C.9: List of Variable Stars 346
Table C.10: List of Non-variable Stars 347

ACKNOWLEDGEMENTS

First, I thank my advisor Arthur Wolfe, without whom this dissertation would not be possible. I appreciate all the support he has given me, both personal and scientifically. His help in solving my two body problem is invaluable. He has inspired me as a researcher, and has been supportive of both my research and my non-research based academic development. Moreover, he has helped me develop my research skills, facilitated my becoming a better scientific writer, and taught me how to observe, write grants, and many other such vital skills. I also appreciate the many opportunities he has provided me, such as ensuring my continued funding, helping me build collaborations, and getting me invited to conferences. He has been all a mentor should be, and much more.

I would like to thank my entire family, who have led me to where I am today. I especially thank my wife Lauren, for her love and unrelenting support. She was always there for me, providing encouragement throughout the trials of graduate school. She was very understanding of everything I had to do, from staying up all night observing, to being away at conferences. She is the best part of my life, the best friend anyone could ask for, and I am so fortunate to have her in my life. I thank my sister, for her lifelong friendship and love. She is the most caring person I know, always trying to make everyone around her happy, and has dependably made me so. I thank my parents, Johann and Helga, for inspiring me to be the scientist I am today. They taught me to be curious about the world around me, and to ask questions about everything. Thanks for an amazing childhood and providing me with many unique experiences throughout the world. I thank my new mother Vicky making my father so happy, and making sure that our far-flung family makes time for each other in our busy lives. She has provided me a new perspective of life outside academia, and a sounding board for life's challenges. I thank my grandparents, Opa and Oma, for their unconditional support, best wishes, and encouragement throughout my life. Although they live in a very different world, they always strive to understand my life and be a part of it. I also thank my family-in-law, Bruce, Debbie, and Scott, for their amazing support, inspiration, and making me feel part of the family.

There are many colleagues that have helped me throughout the years to become the scientist I am today. I thank Hsiao-Wen Chen and Jeff Cooke for their mentoring, many helpful discussions, careful editing of manuscripts, and instruction in practical astrophysics. I thank J. Xavier Prochaska for his advice, mentoring, stimulating conversations, and financial support. I thank Kim Griest, Tom Murphy, and George Fuller for the lively intellectual discussions on uncountable subjects. I thank my colleagues at UCLA for so many things. Andrea Ghez was a great first graduate advisor, who inspired me, mentored me, and helped me solve my two body problem. She taught me that every scientific field has interesting questions that need investigating. Jessica Lu and Seth Hornstein helped me transition to graduate school, and showed me how to work in a group. I also thank Dennis Zaritsky for teaching me how to conduct research, how to write scientific papers, and his mentorship and advice throughout the years. Lastly, I thank all the amazing people working at the Keck Telescopes for providing such an amazing telescope and helping me obtain amazing data that enabled this Thesis.

I am grateful for many supportive friends who make my life so enjoyable. I especially want to thank my best friend Jacob Pitts, for being an amazing friend, always being there, and staying in touch over the years. I also thank Gergerly Kota, Gary Yee, Andrew Crites, Kevin Wampler, Alyssa Sarid, and Kris Brown for helping to take my mind of work and giving me excuses for trips around the country. I thank Chad Kishimoto, Wendell Misch, Jonathan Whitmore, Slawomir Suchy, Liz Rivers, David Boettger, Eric Michelsen, Nathan Johnson, Nathan Miller, JJ Cherry, Alex Mendez, James Aird, and many others for all the good times at tea time, BASH, grilling, and beyond. I also want to thank my Scripps friends Anais Orsi, Dian Putrasahan, Robbert Tood, Sylvia Cole, Marcel Croon, Rose Anderson, Lauren Franck, Simon Freeman, Laura Brooks, and many more. I thank my friends from my time at UCLA, Damien Ramunno-Johnson, Tuan Do, Chun Ly, Matt Wood, Erin Smith, Mike Mammarella, and Christina Oran for all their friendship, companionship, helping me study for my comprehensive exam, and support in solving my two body problem. I also thank my friends and colleagues at the Center for Adaptive Optics and the Center for Astronomy Education for

their role in teaching me about science education and how to become a better teacher.

Lastly, I thank my thesis committee, Kim Griest, Alison Coil, Kevin Quest, and Barney Rickett for agreeing to be on my committee, reading this thesis, and providing feedback and support over the years.

OFFICIAL ACKNOWLEDGEMENTS

Chapter 2, in full (with minor exceptions to conform to this thesis), is a reprint of material previously published as "Deep Keck u-band imaging of the Hubble Ultra Deep Field: A catalog of $z \sim 3$ Lyman Break Galaxies", by Marc Rafelski, Arthur M. Wolfe, Jeff Cooke, Hsiao-Wen Chen, Greg Wirth, & Taft E. Armandroff, published in the The Astrophysical Journal, 2009, Vol. 703, p. 2033. I was the primary investigator and author of this paper.

Chapter 3, in full (with minor exceptions to conform to this thesis), is a reprint of material previously submitted as "Star Formation from DLA Gas in the Outskirts of Lyman Break Galaxies at z$\sim$3", by Marc Rafelski, Arthur M. Wolfe, &, Hsiao-Wen Chen, to the The Astrophysical Journal, 2010. I was the primary investigator and author of this paper.

Chapter 4 is a draft of material that will be submitted as "Metallicity Evolution of Damped Lyman Alpha Systems out to $z \sim 5$" by Marc Rafelski, Arthur M. Wolfe, J. Xavier Prochaska, & Alexander Mendez, to the The Astrophysical Journal. I am the primary investigator and author of this paper.

Chapter 5, in full (with minor exceptions to conform to this thesis), is a reprint of "Photometric Stellar Variability in the Galactic Center", by Marc Rafelski, Andrea. M. Ghez, Seth D. Hornstein, Jessica R. Lu, & Mark Morris, published in the The Astrophysical Journal, 2007, Vol. 659, p. 1241. I was the primary investigator and author of this paper.

VITA

2004	B. S. in Physics and Astronomy, *magna cum laude*, University of Arizona
2006	M. S in Astronomy, University of California, Los Angeles
2011	Ph. D. in Physics, University of California, San Diego

PUBLICATIONS

Rafelski, Marc, Wolfe, Arthur M., Prochaska, Jason X., Mendez, Alexander, "Metallicity Evolution of Damped Lyman Alpha Systems out to $z \sim 5$", 2011 in prep

Rafelski, Marc, Wolfe, Arthur M., Chen, Hsiao-Wen "Star Formation from DLA Gas in the Outskirts of Lyman Break Galaxies at $z \sim 3$", 2010, to appear in the Astrophysical Journal, in press (arXiv:1011.6390)

Chornock, R., Filippenko, A. V., Li, W., Marion, G. H., Foley, R. J., Modjaz, M., **Rafelski, M.**, Becker, G. D., de Vries, W. H., Garnavich, P., Jorgenson, R. A., Lynch, D. K., Malec, A. L., Moran, E. C., Murphy, M. T., Rudy, R. J., Russell, R. W., Silverman, J. M., Steele, T. N., Stockton, A., Wolfe, A. M., Woodward, C. E., 2010, "The Transitional Stripped-Envelope SN 2008ax: Spectral Evolution and Evidence for Large Asphericity", 2011, to appear in Astrophysical Journal, in press (arXiv:1001.2775)

Chornock, R., Bloom, J. S., Cenko, S. B., Filippenko, A. V., Silverman, J. M., Hicks, M. D., Lawrence, K. J., Mendez, A. J., **Rafelski, M.**, Wolfe, A. M., 2010, "The Quasar SDSS J1536+0441: An Unusual Double-peaked Emitter", 2010, *Astrophysical Journal Letters*, 709L, 39

Rafelski, Marc, Wolfe, Arthur M., Cooke, Jeff, Chen, Hsiao-Wen, Armandroff, Taft E., Wirth, Gregory D.., "Deep Keck u-band Imaging of the Hubble Ultra Deep Field: A Catalog of $z \sim 3$ Lyman Break Galaxies", 2009, *Astrophysical Journal*, 703, 2050

Wolfe, Arthur M., Prochaska, Jason X., Jorgenson, Regina A., **Rafelski, Marc**, "Bimodality in Damped Lyman Alpha Systems", 2008, *Astrophysical Journal* 681, 881

Rafelski, M., Ghez, A. M., Hornstein, S. D., Lu, J. R., Morris, M., "Photometric Stellar Variability in the Galactic Center", 2007, *Astrophysical Journal*, 659, 1241

Hornstein, S. D., Matthews, K., Ghez, A. M., Lu, J. R., Morris, M., Becklin, E. E., **Rafelski, M.**, Baganoff, F. K., "A Constant Spectral Index for Sagittarius A* During Infrared/X-Ray Intensity Variations", 2007, *Astrophysical Journal*, 667, 900

Hughes, John P., **Rafelski, Marc**, Warren, Jessica S., Rakowski, Cara, Slane, Patrick, Burrows, David, Nousek, John, "The Chandra View of the Supernova Remnant 0506-68.0 in the Large Magellanic Cloud", 2006, *Astrophysical Journal*, 645, L117

Rafelski, Marc & Zaritsky, Dennis, "The Star Clusters of the Small Magellanic Cloud: Age Distribution", 2005, *Astronomical Journal* 129, 2701

B.B.Back et al., "Energy Dependence of Particle Multiplicities in Central Au+Au Collisions", 2002, *Physical Review Letters*, 88, 022302

B.B.Back et al., "Centrality dependence of the charged particle multiplicity near mid-rapidity in Au+Au collisions at sqrt(sNN)= 130 and 200 GeV", 2002, *Physical Review C*, C65, 061901R

A. Olszewski et al., "Overview of Results from Phobos Experiment at RHIC", 2002, *Journal of Physics G: Nuclear Partical Physics*, G28, 1801

NON-REFEREED PUBLICATIONS

Marc Rafelski, Michael Foley, Genevieve J. Graves, Katherine A. Kretke, Elisabeth Mills, Michael Nassir, and Shannon Patel, "Teaching Astronomy with an Inquiry Activity on Stellar Populations", 2010, *ASP Conference Series 436, Learning from Inquiry in Practice*, eds. L. Hunter & A. J. Metevier (San Francisco, CA: ASP)

Emily L. Rice, Michael McElwain, Sarah Sonnett, and **Marc Rafelski**, 2010, "The Evolution of Inquiry Activities in the Akamai Observatory Short Course", *ASP Conference Series 436, Learning from Inquiry in Practice*, eds. L. Hunter & A. J. Metevier (San Francisco, CA: ASP)

Rafelski, M., Ghez, A. M., Hornstein, S. D., Lu, J. R., Morris, M., 2006, "Photometric Stellar Variability in the Galactic Center", *Journal of Physics Conference Series*, 54, 316

Hornstein, S. D., Matthews, K., Ghez, A. M., Lu, J. R., Morris, M., Becklin, E. E., Baganoff, F. K., **Rafelski, M.**, "Infrared/X-ray intensity variations and the color of Sgr A*", 2006, *Journal of Physics Conference Series*, 54, 399

ABSTRACT OF THE DISSERTATION

Star Formation in Damped Lyman-alpha systems and the Outskirts of Lyman Break Galaxies

by

Marc Alexander Rafelski

Doctor of Philosophy in Physics

University of California, San Diego, 2011

Professor Arthur Wolfe, Chair

In this thesis we begin to unify two pictures of the high redshift universe: absorption line systems such as damped Lyman alpha systems (DLAs) that provide the fuel for star formation, and compact star forming regions such as Lyman break galaxies (LBGs) which form the majority of stars. Wolfe & Chen (2006) find that the *in situ* star formation in DLAs is less than 5% of what is expected from the Kennicutt-Schmidt (KS) relation, but they do not constrain DLAs associated with bright star-forming regions such as LBGs. In this work we search for spatially-extended star formation in the outskirts of LBGs at $z \sim 3$. To this end, we create a sample of $z \sim 3$ LBGs in the Hubble Ultra Deep Field (UDF) by using photometric redshifts enabled by the introduction of an extremely deep u-band image. By

stacking these galaxies, we find spatially extended low surface brightness emission around LBGs in the V-band image of the UDF, corresponding to the $z \sim 3$ rest-frame far-ultraviolet light, which is a sensitive measure of star formation rates (SFRs). We connect this emission around LBGs to the expected emission from DLAs, and the results suggest that the SFR efficiency in such gas at $z \sim 3$ is between factors of 10 and 50 lower than predictions based on the KS relation. This decreased efficiency is likely due to the lower metallicity of DLA gas. In addition, we measure the metallicity evolution of DLAs out to $z \sim 5$, and find a continued decrease of metallicity with increasing redshift and a metallicity "floor" around one thousandth of the solar value. We also compare the metallicity distribution and chemistry of DLAs and halo stars, and find that they are not inconsistent. Lastly, we study the photometric variability of stars in the Galactic center in order to further our understanding of the massive young stars forming in the presence of a super massive black hole. All together, these results improve our understanding of star formation and provide constraints for models and simulations of galaxy formation and evolution that will yield a more complete understanding of star formation across cosmic time.

Chapter 1

Introduction

Observational astronomy is different from most sciences because scientists lack the ability to create laboratory experiments to test how the universe works. Two primary impediments to such experiments are that the objects of study are too massive to create or fit in a laboratory, and that they often change over time-scales of millions of years. Instead, we observe what occurs in nature, and interpret it in terms of our prior astrophysical knowledge and hypotheses. Most of what we learn comes in the form of photons collected via large telescopes on the ground or in outer space. Since the majority of the observed objects vary over time scales much larger than the human lifetime, we instead must observe individual objects at specific stages of their evolution. However, since the observed photons travel at the speed of light, we have the unique ability to look back in time and therewith select and observe different cosmological epochs to gain a picture of the evolution of the Universe. For example, we cannot watch one specific galaxy form and evolve. However, we can observe different galaxies at different epochs, in order to put together a sequence of events responsible for galaxy formation and evolution.

1.1 The Formation and Evolution of Galaxies

Understanding the formation and evolution of galaxies as a function of cosmic time is one of the major goals of current research in astrophysics. In the current paradigm of galaxy formation, galaxies build up via mergers between

two or more galaxies and via cold flow accretion of primarily hydrogen gas. The standard model, known as Hierarchical Cold Dark Matter (ΛCDM), provides a rough guide to a possible sequence of events and consists of multiple components. First, the model depends on the existence of dark matter, which is necessary to explain the rotation curves of galaxies (circular velocity as a function of radius) which remain flat out to large radii as opposed to falling off (e.g. Rubin et al., 1980), and to explain the gravitational lensing of light by galaxy clusters (e.g. Wu et al., 1998). The rotation curves match what would be expected if the galaxies reside in significantly larger and more massive dark matter halos than the observed baryons. The dark matter is generally believed to be 'cold', which means that it consists of non-baryons, has non-relativistic velocities, and is dissipationless and collisionless.

The Λ in ΛCDM represents the cosmological constant which is associated with dark energy, and is necessary to explain the accelerating expansion of the universe against the attractive force of gravity (e.g. Riess et al., 1998; Perlmutter et al., 1999). Measurements of the cosmic microwave background (CMB) radiation, type Ia supernovae, and baryon acoustic oscillations find that the fraction of the energy density of the Universe associated with dark energy is 0.74, with dark matter is 0.21, and with baryons is 0.04 (Hinshaw et al., 2009). In other words, only 4% of the energy density of the Universe is made of baryonic matter such as stars, galaxies, and the gas in-between.

The hierarchical part of ΛCDM is the prediction that galaxies are spatially clustered and increase in mass via galaxy merging and gas accretion. In this scenario, structures first formed after the Big Bang from tiny primordial quantum fluctuations. As the Universe cooled, these fluctuations grew due to the gravitational attraction of matter. The dark matter halos condensed from the background, and grew via mergers with other dark matter halos. Later, the baryons decoupled and fell into the potential wells of the dark matter halos, forming proto-galaxies that consisted of dark matter and clouds of primarily hydrogen gas. In this paradigm, galaxies evolved in a hierarchical buildup often called the "Bottom-Up" scenario, in which the galaxies start out smaller and build up mass via a series of mergers.

During the merger process, the dark matter did not fall into the potential well of the merging galaxies, while the baryons, made up mostly of hydrogen gas, contracted and collapsed to form rotating disks, and then condensed to form stars. In addition to galaxy mergers, recent models suggest another possible mechanism where the galaxies are primarily supplied with baryons via cold mode accretion, where gas is accreted through filamentary streams of gas (e.g. Kereš et al., 2005, 2009).

These models are generally well supported by observations of large scale structure (which refer to the spatial clustering of mass) of relatively nearby galaxies (at low redshift, see §1.2). Large surveys of galaxies such as the Sloan Digital Sky Survey (SDSS) (York et al., 2000) and the 2dF Galaxy Redshift Survey (Colless et al., 2001) have mapped out the large scale structure of the Universe, have measured the matter power spectrum (e.g. Percival et al., 2007; Cole et al., 2005), and have measured many physical properties of low redshift galaxies. These observations are in general agreement with large N-body simulations such as the Millennium simulations (Springel et al., 2005; Boylan-Kolchin et al., 2009). However, a major limitation of these N-body simulations is that they are generally dark matter only simulations, not including gas, stars, star formation, dust, and other such galaxy components and processes.

There are two different solutions being used to address the limitations of N-body simulations. The first is to use semi-analytical models (for a review, see Baugh, 2006), which artificially populate the dark matter halos with galaxies and gas. The models are based on analytical equations to model the physics of observed galactic phenomena, such as active galactic nuclei (AGN) feedback, the cooling and heating of gas, and star formation. Often, these simulations are grafted onto N-body simulations to get the large scale structure and dark matter components right. The resultant simulations predict specific properties that galaxies should exhibit, such as the luminosity function, color, star formation history, feedback processes, galaxy sizes, and many others (e.g. Cole et al., 2000; Hatton et al., 2003; Nagashima et al., 2005). While these simulations increase our physical understanding of the processes they are testing, they rely on prior observations to tune their many

parameters, and therefore generally do not predict new phenomena.

An alternative method to address N-body simulation limitations is to use smoothed particle hydrodynamical (SPH) modeling of the gas within dark matter halos based on N-body simulations. (e.g. Springel & Hernquist, 2003; Springel, 2005; Brooks et al., 2007, 2009; Dekel et al., 2009b; Nagamine et al., 2006; Kereš et al., 2005, 2009) or adaptive mesh refinement (AMR) codes, which are grid-based hybrid hydrodynamical and N-body simulations(e.g. Kravtsov et al., 1997, 2004). There are many advantages to SPH simulations, as they include some radiative transfer for the cooling of the gas, supernovae and AGN feedback, and much else. Most importantly, the gas is treated hydrodynamically and therefore the results are more realistic than N-body simulations and semi-analytical models. However, SPH simulations are significantly more complex, and therefore can only probe significantly smaller cosmological volumes.

While our current models are successful in explaining many observations, our understanding of galaxy formation and evolution is far from complete. There are many knobs to turn to get the models to agree with the observations, such as parameters that describe feedback from AGNs and star formation. One of the models' most significant predictions is the presence of substantial gas inflows, while generally only outflows are observed. Recent simulations suggest that the spatial covering fraction of the inflows is small, and so would not be frequently observed (Faucher-Giguère & Kereš, 2011). Nonetheless, there are still many discrepancies between the models and the data, such as our understanding of the physical mechanism that stops the infall of gas in elliptical galaxies, and what occurs when the infalling gas interacts with the interstellar medium or the surrounding gas, as well as the missing satellite problem, in which simulations predict substantially more small sized halos around the Milky Way than observed. The models also do not reproduce the rotation speed and size of disk galaxies, and the timescales of the collapse and formation of galaxies is not well understood. Moreover, because star formation is such an important part of galaxy formation and evolution, it is crucial that this part of the models is correctly prescribed. However, there is a problem with the general assumptions used for the star formation prescription in many of

the simulations (see §1.2).

1.2 Star Formation

Stars are observed to form in molecular hydrogen clouds, although our knowledge of the physics of star formation is incomplete. In general, interstellar clouds are in hydrostatic equilibrium, such that the outward gas pressure gradient is balanced by the inward gravitational force. If the cloud gains sufficient mass such that the gas pressure can no longer support the cloud, then the cloud collapses. The minimum mass for such a collapse is called the Jeans mass, and it depends on the density and temperature of the gas ($\propto T^{3/2}\rho^{-1/2}$). In a closed system, the collapse of the cloud would adiabatically increase the temperature of the gas, increasing the gas pressure. Therefore, in order for the cloud to continue to collapse, the gravitational potential energy must be radiated away.

This energy is radiated away primarily by the molecular hydrogen emission lines, which is effective at cooling gas down to 200K via the vibrational excited transitions that absorb far-ultraviolet (FUV) photons and emit infrared (IR) photons. After this, the primary cooling is due to atomic fine structure emission, dominated by C^+, which can cool the gas down to 20-60K (via the [C II] 158μm line). It is believed that to cool the gas to even lower temperatures typical of pre-stellar cores ($\sim$ 10K), molecules such as CO are required. CO generally only forms efficiently in the presence of molecular hydrogen, resulting in stars forming in molecular clouds. However, recent models by Low & Glover (2010) suggest that molecular hydrogen may not be the cause, but rather a consequence of star formation. In this scenario, molecular hydrogen and CO trace dense gas that is already gravitationally unstable and would probably form stars regardless of their presence. Therefore, more investigations are needed to better understand what is fundamentally required for star formation, so that we can improve the assumptions going into star formation prescriptions. For example, currently simulations use observational prescriptions of star formation measured at low redshift even when simulating the high-redshift universe.

The term redshift (z) refers to the increase in the wavelength of light due to the Doppler effect and the expansion of the Universe. Galaxies that are further away have larger redshifts and formed at earlier times since it takes light longer to reach us. For example, the Ly-α line, is observed on earth at $\lambda = 1216$Å. However, at $z = 3$, it would be redshifted to appear at $\lambda = 4863$Å ($\lambda_{\rm observed} = \lambda_{\rm intrinsic}(1+z)$). Objects can be identified to be at high redshift with the identification of multiple lines that occur at the expected redshifted wavelengths.

The prescription of star formation generally used in simulations is the Kennicutt-Schmidt (KS) relation (Kennicutt, 1998; Schmidt, 1959), which relates the star formation rate (SFR) per unit area ($\Sigma_{\rm SFR}$) and the total gas surface density of atomic and molecular gas ($\Sigma_{\rm gas}$) via a power law ($\Sigma_{\rm SFR} \propto \Sigma_{\rm gas}^{1.4}$). The SFR is a measure of how much gas mass is converted into stars per time interval. The KS relation is established in nearby local ($z = 0$) galaxies based on observational measurements of these parameters, and we discuss it in more detail in §3.7.2 and 3.7.3. While it is reasonable to use this relationship at low redshift in normal star forming galaxies, many simulations use it at all redshifts without distinguishing between atomic and molecular gas, which could result in an too many stars being formed (e.g. Nagamine et al., 2004, 2007, 2010; Razoumov et al., 2006; Brooks et al., 2007, 2009; Pontzen et al., 2008; Razoumov et al., 2008; Razoumov, 2009; Tescari et al., 2009; Dekel et al., 2009a,b; Kereš et al., 2009; Barnes & Haehnelt, 2010).

At $z \sim 3$, the SFR per unit comoving volume, $\dot{\rho}_*$, of neutral atomic hydrogen (H I) gas was found to be less than 5% of what is expected from the KS relation (Wolfe & Chen, 2006). This means that a substantial lower level of *in situ* star formation occurs in H I gas at $z \sim 3$ than in modern galaxies, with one caveat: the search algorithm excluded star formation in H I gas containing compact bright regions, such as high redshift galaxies. This thesis addresses this caveat in Chapters 2 and 3 by determining if star formation occurs at the KS rate in gas around high redshift galaxies, and investigates what this means for the physics of H I gas and theories of galaxy formation and evolution. The most numerous and well understood population of galaxies at high redshift are Lyman break galaxies, and

we therefore focus our study around these galaxies.

1.3 Lyman Break Galaxies

Lyman break galaxies (LBGs) are star-forming galaxies at high redshift ($z > 2$) that are selected based on a break in their spectral energy distribution (SED) at wavelengths shortward of the rest-frame 912 Å Lyman limit. This break is caused by absorption by hydrogen gas both intrinsic to the galaxy, and due to intervening intergalactic systems. FUV photons emitted by the LBG at bluer wavelengths than 912 Å have energies sufficient to ionize neutral hydrogen, which results in virtually complete attenuation of any flux (energy per area per second). In addition, photons shortward of Ly-α 1216 Å are absorbed by the Lyman series of multiple intervening systems. This second effect grows stronger with increasing redshift, and becomes very significant at redshifts $z \gtrsim 4$. In general, longward of Ly-α 1216 Å, the spectral energy distribution (SED) continuum of the LBGs are relatively flat, making the break relatively obvious and easy to observe at high redshift.

While the spectral features are difficult to observe in their rest-frame FUV wavelengths, they are redshifted to optical wavelengths at high redshift. The ability to observe the Lyman break optically allows large samples of high-redshift galaxies to be identified based on multicolor photometry, where LBGs are selected by a strong flux decrement shortward of the Lyman limit, and a continuum of flux longward of rest frame Lyα (1215 Å). In essence, observations of galaxies with multiple filters act as a poor-man's spectrograph, with very coarse resolution. If a galaxy is observed in one or more broadband filters, but not in others, the galaxy is identified as a "dropout" galaxy and is a candidate high redshift galaxy. For example, for a galaxy with a redshift of ~ 2.5, the Lyman break occurs at $\sim$3500 Å, which is observable in the u-band from the ground.

This technique enables large surveys of high redshift galaxies by selecting them based on their colors, and was extensively used to build large samples of LBG candidates (e.g., Steidel & Hamilton, 1992; Steidel et al., 1995, 1996a,b). This

method for finding LBGs by their photometric colors was confirmed by thousands of low resolution spectra (e.g. Steidel et al., 2003; Shapley et al., 2003; Cooke et al., 2005; Reddy & Steidel, 2009). In addition to color selection techniques, photometric redshift determination algorithms can estimate object redshifts using galaxy SED templates. These include additional information other than the Lyman break, such as the slope of the SED, the Balmer break at 3646 Å, and the more pronounced 4000 Å break, which is due to the sudden onset of stellar photospheric opacity by ionized metals and the CaII HK doublet (Hamilton, 1985). These photometric selection techniques have been extended to both low and high redshifts, and we have samples of LBGs spanning the redshift range $1 \lesssim z \lesssim 10$ (e.g. Bouwens et al., 2010).

Using both imaging and spectroscopy, we have learned a lot about LBGs. We know that LBGs have a wide range of morphologies, with $z \sim 3$ LBGs having half-light radii of about $\sim 2-3$ kpc in the optical at ~ 25 mag (Giavalisco et al., 1996; Law et al., 2007). They also have very high star formation rates (SFRs), with typical values of $\sim$80 $M_\odot$ yr^{-1} after correcting for extinction (Shapley et al., 2003), and form the majority of stars in the Universe. These rates are significantly larger than that of the Milky Way, which has a SFR of $\sim$1 $M_\odot$ yr^{-1} (Robitaille & Whitney, 2010). In addition, LBGs have large stellar masses of $\sim 10^{10} M_\odot$, dark matter halo masses of $\sim 10^{12} M_\odot$, and are highly clustered at both large and small scales (Giavalisco et al., 1998; Ouchi et al., 2004; Shapley et al., 2005). The LBGs typically have metallicities of about half to a fourth of the solar value, have strong outflows of gas, and have significant extinction from dust (Pettini et al., 2001; Shapley et al., 2001, 2003).

Most of what we know about these high redshift galaxies in the early Universe comes from the light that they emit while forming stars. Star formation can be probed directly in emission by measuring the FUV light from short-lived high mass stars, dust reprocessed infrared light, and by using various emission line indicators. Using these techniques, astronomers have traced the history of cosmic star formation in emission starting from redshifts $z = 8$, when the age of the Universe $t_{\rm age} \approx 0.6$ Gyr, to the current epoch when $t_{\rm age}$=13.7 Gyr. We know

that the comoving SFR density, $\dot{\rho}_*(z)$, increased more than an order of magnitude between $z > 6$ and $z \sim 2$ (e.g. Madau et al., 1996, 1998; Bouwens et al., 2010), and sharply declined with time thereafter. Moreover, about half of the stellar content of current galaxies formed at $z > 2$ (Reddy et al., 2008).

Although these results have greatly advanced the field of galaxy evolution, the emerging picture remains incomplete: most of the baryons in high-z galaxies are gas rather than stars, but we do not know how galaxies get their gas nor how that gas condenses into stars. The cold gas from which stars form does not emit much light, and therefore is generally studied in absorption. Absorption line spectroscopy allows us to probe the distribution and properties of the gas and provides us with powerful tools to investigate how galaxies accrete, process, and return gas into the intergalactic medium over a large range of redshift. Studies of neutral H I gas at high redshift (i.e. Damped Lyman-α Systems) provide insights into the evolution of gas associated with star-forming galaxies, which is accomplished with studies of Quasar absorption line systems (QALs).

1.4 Quasar Absorption Line Systems

Quasar absorption line systems are gas clouds detected in absorption against the light emitted by background quasars. Quasars are generally used as background sources as they are the most luminous objects in the universe, powered by accretion of material onto a supermassive black hole at the center of galaxies. In addition, they exist at high redshifts and the continuum SED of quasars is easily modeled, making them ideal targets for measuring absorption lines. The absorption lines occur when the light emitted by the quasar is absorbed by intervening gas in the interstellar medium (ISM) and the intergalactic medium (IGM). The QALs are classified according to the absorption transition of a given element, and depth and width of the corresponding lines.

The line depth is related to the column density, N, and the oscillator strength, f (also called the f-value). The column density is a measure of the integrated number density along a line of sight, or N$= \int n \mathrm{d}s$, where n is the number

density and s is the path length. While neither n nor s is directly observable, N can be measured from the line depth. The oscillator strength is based on the probability of an electron making a transition from a specific orbital. Therefore, for the same oscillator strength, a line with a larger column density results in a deeper line, until the line is saturated. In the optically thin case (weak lines), the column density can be determined by measuring the equivalent width, EW, of a line, which is the width that a rectangle would have for the same area as the spectral line. One nice property of the EW is that it is insensitive to the instrument resolution. As the optical depth increases (strong lines) and the lines saturate, the EW also depends on the line width.

The line width is related to the Doppler parameter, b, and is caused by two main effects; Doppler broadening and natural broadening. The Doppler broadening is from the thermal, turbulent, and collisional motions of the atoms yielding a velocity distribution with atoms moving toward and away from the observer. These velocities are then Doppler shifted, resulting in a gaussian line profile. Natural broadening is a quantum mechanical effect due to the Heisenberg uncertainty principle, which states that the energy spread varies with the duration of the transition ($\Delta E \Delta t = \hbar$). This results in an uncertainty in the wavelength of the absorbed photon, resulting in a Lorentzian profile (often called damping profile). The combination of these two profiles is called a Voigt profile, where the Gaussian profile dominates the core and the damping profile dominates the wings.

There are many types of Lyman-α absorption line systems, which are at rest-frame 1216 Å for photons with energies of 10.2 eV, and occur due to the excitation of neutral hydrogen atoms from the 1s to the 2p state. The most numerous lines are the Lyman-α forest absorbers, which are defined to have column densities of $N_{\rm HI} < 1 \times 10^{17} {\rm cm}^{-2}$. These absorbers are filaments of hydrogen gas in the sight lines of the quasars, and are optically thin at the Lyman limit and therefore are fully ionized by background radiation. Systems with $1 \times 10^{17} {\rm cm}^{-2} < N_{\rm HI} < 2 \times 10^{20} {\rm cm}^{-2}$ are called Lyman limit systems (LLS), and are optically thick at the Lyman limit and therefore only partially ionized. At larger column densities, we enter into the regime of Damped Lyman-α systems, which are important for understanding

galaxy formation and evolution.

1.5 Damped Lyman-α Systems

Damped Lyman-α systems (DLAs) are absorption line systems selected for their neutral hydrogen column densities of $N_{\rm HI} \geq 2 \times 10^{20} {\rm cm}^{-2}$ (Wolfe et al., 1995). At these high column densities, the damping wings in the line profile appear, resulting in a Voigt profile, which is the origin of the name Damped Lyman-α systems. DLAs are optically thick, and the column densities are sufficiently high that the gas is self shielding from the background radiation field, and therefore most of the gas is neutral. This neutrality is an important characteristic of DLAs, which is different from all other absorption line systems that are either fully or partially ionized. The neutrality of the gas is vital, because neutral cold gas is a necessary component of star formation, as it is needed to form molecular clouds (the birthplace of stars) and to replenish their gas supply. In addition, neutral gas reservoirs are needed to form the first galaxies, and DLAs are widely believed to be gas clouds that are the progenitors of galaxies.

DLAs are also important for understanding galaxy formation because they dominate the neutral-gas content of the Universe in the redshift interval $0 < z < 5$. In the redshift range $2.5 \lesssim z \lesssim 3.5$, they cover one third of the sky and contain enough gas to account for 50% of the mass content of visible matter in modern galaxies (for a review, see Wolfe et al., 2005). This latter property has led to the widely accepted idea that DLAs act as neutral gas reservoirs for star formation at high redshifts (e.g. Nagamine et al., 2004), providing the fuel for star forming galaxies. In addition, the neutrality of the gas allows us to calculate metal abundances without the large uncertainties introduced by ionization corrections, and to calculate the SFR per area.

The metal abundance is characterized by the metallicity, [M/H], which is the proportion that the gas is made up of ions other than hydrogen and helium. The definition of a metal, M, here is different than the standard definition, and refers to any element other than hydrogen or helium, such as O, Si, S,

Fe, Ni, and etc. The metallicity is usually obtained by comparing column densities of undepleted low-ions such as S^+ and Si^+ to $N_{\rm HI}$ for each individual DLA, (i.e. $[M/H] = \log_{10}(N_M/N_H)_{\rm DLA} - \log_{10}(N_M/N_H)_{\odot}$). Without the need for ionization corrections, these measurements yield the most accurate absolute metallicities measured in the high redshift universe. DLAs generally have metallicities of a tenth to a hundredth of the solar metallicity. The basic statistic used to explore the evolution of metallicity is the column-density weighted mean metallicity, which is equivalent to the cosmic metallicity, $\langle {\rm Z/H} \rangle$. The cosmic metallicity is defined as $\langle {\rm Z} \rangle \equiv \log_{10}(\Omega_{\rm metals}\ /\ \Omega_{\rm gas}) - \log_{10}{\rm Z}_{\odot}$, where $\Omega_{\rm metals}$ is the mass per unit comoving volume of metals at redshift z, and $\Omega_{\rm gas}$ is the comoving density of neutral gas. This statistic describes the mean metallicity of neutral gas *independently* of the mass, morphology, etc. of the galaxies that host DLAs. Studies of DLA gas at high redshift have found that the cosmic metallicity of the H I gas is observed to increase by a factor of 6 from $z \approx 4$ to $z \approx 1$ (Prochaska et al., 2003). This evolution of the metallicity is consistent with the gas being metal enriched by star formation, and is investigated out to $z \sim 5$ in Chapter 4. These observations of the metallicity evolution tightly constrain the star formation history of $z \sim 5$ galaxies and the processes that transport metals from star-forming regions to the ambient ISM.

The SFR of DLA gas is obtained by measuring the [C II] 158 μm cooling rate of cold neutral gas , which is the primary coolant of the Galactic ISM (Wright et al., 1991). This measurement is enabled by the CII* 1335.7 Å transition, which arises from the same excited $^2P_{3/2}$ fine-structure state of C^+ that produces [C II] 158 μm emission through spontaneous photon decay to the $^2P_{1/2}$ ground state (Wolfe et al., 2003b). The cooling rate per atom is then calculated with the CII* column density in conjunction with $N_{\rm HI}$. Assuming thermal balance, the cooling rate equals the heating rate, and the primary heating mechanism is the grain photoelectric effect. In this effect, FUV photons penetrate dust grains and eject photoelectrons that migrate to the surface and escape from the grains. These photoelectrons then heat the gas via Coulomb interactions with ambient electrons. There are two primary sources of FUV radiation in DLAs: 1) the FUV background

due to galaxies and quasars along the past light cone of the DLA, and 2) FUV radiation emitted by stars in the DLA, in which case the intensity is proportional to the SFR per unit area (Wolfe et al., 2003a,b).

The cooling rates of DLAs are bimodal, which suggests that there are two populations of DLAs (high cool and low cool; Wolfe et al., 2008). These two populations have significant differences in their cooling rates (and therefore SFRs), velocity widths, metallicity, dust-to-gas ratio, and Si II equivalent widths. The gas in the high cool population cannot be heated by background and/or *in situ* star formation alone, and so Wolfe et al. (2008) suggest that the high cool population is associated with LBGs. If DLAs and LBGs are associated, then the lack of detected *in situ* star formation in DLAs at high redshift may be due to the nature of the search algorithm used in Wolfe & Chen (2006), which avoided known LBGs. Therefore, in Chapter 3 of this thesis, we search for spatially regions of low surface-brightness emission surrounding the LBGs at $z \sim 3$. Using these measurements, we determine whether star formation occurs in the outskirts of LBGs, whether that star formation occurs in atomic-dominated gas, and at what SFR efficiency the stars form.

1.6 Massive Stars at the Galactic Center

Another approach to learn about star formation is to study it in extreme environments, and thereby test our theories in new situations. Ideally, we would study massive stars because they have relatively short lifetimes, which yields a constraint on their age. In order to study individual stars in sufficient detail, they would need to reside locally in our galaxy. We therefore study the star formation occurring at the Galactic center, where massive possibly form in the presence of a $3-4\times10^6 M_\odot$ supermassive black hole (SMBH), Sgr A*, (Ghez et al., 2003; Schödel et al., 2003). It is unclear how a population of young (∼10-100 Myr) massive (∼10-120 $M_\odot$) stars exist near Sgr A* because the observed gas densities are too low to overcome the tidal forces of the SMBH to collapse and form stars. Yet, over 100 of such stars are observed, and the stars at the galactic center provide a unique

opportunity to study star formation in a very different environment (Ghez et al., 2003; Paumard et al., 2006; Lu et al., 2009). There are multiple theories on the origin of these young stars, and the three primary ones are 1) *in situ* formation in disks to overcome the low gas densities, 2) rejuvenation of older stars to make them look young, and 3) migration from larger radii where the conditions are more favorable for star formation (Ghez et al., 2003; Paumard et al., 2006; Lu et al., 2009).

One method to get a handle on this unusual population of stars is by investigating their photometric variability, which is studied in Chapter 5. Variable light curves can be used to find and study close binary stars, which could provide a mechanism for capturing young stars from larger radii. They can also be used to find very massive stars (M $>$ 60-85 $M_{\odot}$) such as luminous blue variables (LBVs), which are very young by definition as such massive stars live only a few million years. The light curves of the stars closest to Sgr A* can also probe the possibility of a cold, geometrically thin, inactive accretion disk, as nearby stars would be eclipsed or reddened when the stars pass behind the disk. In short, the variations of the stars' photometry yields insights into the nature of the stars residing at the Galactic center, by identifying characteristics of the stars to classify the type of star that they are, and thereby constrain the theories on the origin of the young stars at the Galactic center.

1.7 Overview of Thesis

The aim of this thesis is to begin to unify two pictures of the high redshift universe: absorption line systems such as DLAs that provide the fuel for star formation, and compact star forming regions such as LBGs which form the majority of stars. Each population provides valuable and independent information about the early Universe (for reviews, see Giavalisco, 2002; Wolfe et al., 2005). Connecting these two populations helps us to form a more complete understanding of star formation in different gas phases and varying redshifts. This thereby yields insights into how stars form from gas, which is an important part in understanding

galaxy formation and evolution. Wolfe & Chen (2006) start to bridge two separate but complementary fields in astrophysics by setting sensitive upper limits on star formation in DLAs measured in emission. They find that the *in situ* star formation in DLAs is less than 5% of what is expected from the KS relation. However, they do not include DLAs associated with bright star-forming regions such as LBGs. In this Thesis we address this caveat by searching for star formation in the outskirts of LBGs at $z \sim 3$. Together, the constraints on the SFR efficiency of DLA gas from Wolfe & Chen (2006) and those from this Thesis constrain all possibilities for star formation from H I gas at high redshift.

In order to connect the outskirts of LBGs with DLA gas, we first require a large sample of $z \sim 3$ LBGs in the Hubble Ultra Deep Field (UDF), as it is the only field with sufficient rest-frame FUV sensitivity and resolution to measure the SFR in the outskirts of LBGs. The LBGs in the UDF are too faint for us to obtain spectroscopic redshifts, and therefore they must be selected using color selection and photometric redshifts, which require sampling the Lyman break. At $z \sim 3$, the Lyman break falls into the u-band, and since no such data previously existed, we obtained and analyzed one of the deepest u-band images, and create a reliable sample of $z \sim 3$ LBGs in Chapter 2. This sample of LBGs provides an unprecedented view of $z \sim 3$ LBGs via the high resolution and super-sensitive multiband imaging from the Hubble Space Telescope (HST) available in this field. This sample can therefore be used for a myriad of scientific investigations, such as improving our understanding of their highly irregular rest-frame UV morphologies down to unprecedented depths, or studying tadpole galaxies at $z \sim 3$ (as was done by Elmegreen & Elmegreen, 2010). Here, we use the sample to search for star formation in the outskirts of LBGs.

We measure spatially extended low surface brightness emission around LBGs in the V-band image of the UDF, corresponding to the $z \sim 3$ rest-frame FUV light, which is a sensitive measure of SFRs. We show that the covering fraction of molecular gas at $z \sim 3$ is not adequate to explain the emission in the outskirts of LBGs, while the covering fraction of neutral atomic-dominated hydrogen gas at high redshift is sufficient, and thus the emission is likely due to star formation in

atomic-dominated hydrogen gas. We therefore develop a theoretical framework to connect this emission around LBGs to the expected emission from neutral H I gas i.e., DLAs, using the KS relation. The results suggest that the SFR efficiency in such gas at $z \sim 3$ is between factors of 10 and 50 lower than predictions based on the local KS relation, similar to the results by Wolfe & Chen (2006). This confirms that the SFR efficiency of atomic-dominated gas at high redshift is significantly lower than predicted by the KS relation for nearby galaxies. The reduced SFR efficiency is either due to the properties of the gas such as its composition or metallicity, or due to suppression of gravitational collapse at high redshift, and the results and interpretation are presented in Chapter 3. We find that the most likely cause for the decreased SFR efficiency is the low metallicities of DLAs, which is itself a function of redshift.

We investigate the metallicity evolution of DLAs out to $z \sim 5$ in Chapter 4. We obtain new high resolution spectroscopy for quasar sight-lines for a large number of $z > 4$ DLAs, quadrupling the number of $z > 4$ DLA metallicity measurements. We measure the metallicities using undepleted low-ions such as S^+ and Si^+ where possible, and from depleted low-ions such as Fe^+ and Ni^+ with corrections for depletion for a small fraction. We find that there is a continued decrease of cosmic metallicity with increasing redshift. Although the observations have sufficient sensitivity and resolution to measure much lower metallicities, there is a floor in metallicity around one thousandth solar, which represents the minimum metallicity of DLA gas. In addition, we find that the metallicity distribution and the α/Fe ratios of $z > 2$ DLAs are not inconsistent with those for halo stars. This is the first time that any known population of stars have been shown to not have inconsistent metallicity distributions with that of DLAs. This result constrains the processes that transport metals from star-forming regions to the ambient ISM. In addition, it constrains future models and simulations of the star formation history of galaxies.

Lastly, we study the photometric variability of massive stars in the Galactic center in order to further our understanding of the stars forming in the presence of a SMBH. Using 10 years of speckle imaging, we find 15 variable stars. Among

them, we find an eclipsing binary star with an asymmetric phased light curve which is likely due to tidal deformations of two very massive young stars. We also find a wind colliding binary, which is an eccentric binary star system consisting of massive young stars that produce dust episodically. We also constrain the possibility of a geometrically thin, inactive accretion disk around Sgr A*. These variability measurements are presented in Chapter 5 and yield insights into the formation of stars in extreme environments and the nature of stars residing at the galactic center.

In summary, the work presented in this Thesis provide us with a sample of of $z \sim 3$ LBGs in the UDF, and high resolution spectroscopy of a large sample of DLAs, which are suitable for a wide range of scientific study. More importantly, the results obtained from an extensive analysis of this sample improve our understanding of star formation occurring in atomic-dominated gas at high redshift, and the metallicity evolution of DLAs out to $z \sim 5$. In addition, these results provide constraints for models and simulations of galaxy formation and evolution that will yield a more complete understanding of star formation across cosmic time.

References

Barnes, L. A. & Haehnelt, M. G. 2010, Monthly Notices of the Royal Astronomical Society, 403, 870

Baugh, C. M. 2006, Reports on Progress in Physics, 69, 3101

Bouwens, R. J., Illingworth, G. D., Oesch, P. A., Stiavelli, M., van Dokkum, P., Trenti, M., Magee, D., Labbé, I., Franx, M., Carollo, C. M., & Gonzalez, V. 2010, The Astrophysical Journal Letters, 709, L133

Boylan-Kolchin, M., Springel, V., White, S. D. M., Jenkins, A., & Lemson, G. 2009, Monthly Notices of the Royal Astronomical Society, 398, 1150

Brooks, A. M., Governato, F., Booth, C. M., Willman, B., Gardner, J. P., Wadsley, J., Stinson, G., & Quinn, T. 2007, The Astrophysical Journal, 655, L17

Brooks, A. M., Governato, F., Quinn, T., Brook, C. B., & Wadsley, J. 2009, The Astrophysical Journal, 694, 396

Cole, S., Lacey, C. G., Baugh, C. M., & Frenk, C. S. 2000, Monthly Notices of the Royal Astronomical Society, 319, 168

Cole, S., Percival, W. J., Peacock, J. A., Norberg, P., Baugh, C. M., Frenk, C. S., Baldry, I., Bland-Hawthorn, J., Bridges, T., Cannon, R., Colless, M., Collins, C., Couch, W., Cross, N. J. G., Dalton, G., Eke, V. R., Propris, R. D., Driver, S. P., Efstathiou, G., Ellis, R. S., Glazebrook, K., Jackson, C., Jenkins, A., Lahav, O., Lewis, I., Lumsden, S., Maddox, S., Madgwick, D., Peterson, B. A., Sutherland, W., & Taylor, K. 2005, Monthly Notices of the Royal Astronomical Society, 362, 505

Colless, M., Dalton, G., Maddox, S., Sutherland, W., Norberg, P., Cole, S., Bland-Hawthorn, J., Bridges, T., Cannon, R., Collins, C., Couch, W., Cross, N., Deeley, K., Propris, R. D., Driver, S. P., Efstathiou, G., Ellis, R. S., Frenk, C. S., Glazebrook, K., Jackson, C., Lahav, O., Lewis, I., Lumsden, S., Madgwick, D., Peacock, J. A., Peterson, B. A., Price, I., Seaborne, M., & Taylor, K. 2001, Monthly Notices of the Royal Astronomical Society, 328, 1039

Cooke, J., Wolfe, A. M., Prochaska, J. X., & Gawiser, E. 2005, The Astrophysical Journal, 621, 596

Dekel, A., Birnboim, Y., Engel, G., Freundlich, J., Goerdt, T., Mumcuoglu, M., Neistein, E., Pichon, C., Teyssier, R., & Zinger, E. 2009a, Nature, 457, 451

Dekel, A., Sari, R., & Ceverino, D. 2009b, The Astrophysical Journal, 703, 785

Elmegreen, B. G. & Elmegreen, D. M. 2010, The Astrophysical Journal, 722, 1895

Faucher-Giguère, C.-A. & Kereš, D. 2011, Monthly Notices of the Royal Astronomical Society: Letters, L208

Ghez, A. M., Duchêne, G., Matthews, K., Hornstein, S. D., Tanner, A., Larkin, J., Morris, M., Becklin, E. E., Salim, S., Kremenek, T., Thompson, D., Soifer, B. T., Neugebauer, G., & McLean, I. 2003, The Astrophysical Journal, 586, L127

Giavalisco, M. 2002, Annual Review of Astronomy and Astrophysics, 40, 579

Giavalisco, M., Steidel, C. C., Adelberger, K. L., Dickinson, M. E., Pettini, M., & Kellogg, M. 1998, Astrophysical Journal, 503, 543

Giavalisco, M., Steidel, C. C., & Macchetto, F. D. 1996, The Astrophysical Journal, 470, 189

Hamilton, D. 1985, The Astrophysical Journal, 297, 371

Hatton, S., Devriendt, J. E. G., Ninin, S., Bouchet, F. R., Guiderdoni, B., & Vibert, D. 2003, Monthly Notice of the Royal Astronomical Society, 343, 75

Hinshaw, G., Weiland, J. L., Hill, R. S., Odegard, N., Larson, D., Bennett, C. L., Dunkley, J., Gold, B., Greason, M. R., Jarosik, N., Komatsu, E., Nolta, M. R., Page, L., Spergel, D. N., Wollack, E., Halpern, M., Kogut, A., Limon, M., Meyer, S. S., Tucker, G. S., & Wright, E. L. 2009, The Astrophysical Journal Supplement, 180, 225

Kennicutt, R. C. 1998, The Astrophysical Journal, 498, 541

Kereš, D., Katz, N., Fardal, M., Davé, R., & Weinberg, D. H. 2009, Monthly Notices of the Royal Astronomical Society, 395, 160

Kereš, D., Katz, N., Weinberg, D. H., & Davé, R. 2005, Monthly Notices of the Royal Astronomical Society, 363, 2

Kravtsov, A. V., Gnedin, O. Y., & Klypin, A. A. 2004, The Astrophysical Journal, 609, 482

Kravtsov, A. V., Klypin, A. A., & Khokhlov, A. M. 1997, Astrophysical Journal Supplement v.111, 111, 73

Law, D. R., Steidel, C. C., Erb, D. K., Pettini, M., Reddy, N. A., Shapley, A. E., Adelberger, K. L., & Simenc, D. J. 2007, The Astrophysical Journal, 656, 1

Low, M.-M. M. & Glover, S. C. O. 2010, arXiv, astro-ph.GA

Lu, J. R., Ghez, A. M., Hornstein, S. D., Morris, M. R., Becklin, E. E., & Matthews, K. 2009, The Astrophysical Journal, 690, 1463

Madau, P., Ferguson, H. C., Dickinson, M. E., Giavalisco, M., Steidel, C. C., & Fruchter, A. 1996, Monthly Notices of the Royal Astronomical Society, 283, 1388

Madau, P., Pozzetti, L., & Dickinson, M. 1998, The Astrophysical Journal, 498, 106

Nagamine, K., Choi, J.-H., & Yajima, H. 2010, The Astrophysical Journal Letters, 725, L219

Nagamine, K., Springel, V., & Hernquist, L. 2004, Monthly Notices of the Royal Astronomical Society, 348, 435

Nagamine, K., Wolfe, A. M., & Hernquist, L. 2006, The Astrophysical Journal, 647, 60

Nagamine, K., Wolfe, A. M., Hernquist, L., & Springel, V. 2007, The Astrophysical Journal, 660, 945

Nagashima, M., Lacey, C. G., Baugh, C. M., Frenk, C. S., & Cole, S. 2005, Monthly Notices of the Royal Astronomical Society, 358, 1247

Ouchi, M., Shimasaku, K., Okamura, S., Furusawa, H., Kashikawa, N., Ota, K., Doi, M., Hamabe, M., Kimura, M., Komiyama, Y., Miyazaki, M., Miyazaki, S., Nakata, F., Sekiguchi, M., Yagi, M., & Yasuda, N. 2004, The Astrophysical Journal, 611, 685

Paumard, T., Genzel, R., Martins, F., Nayakshin, S., Beloborodov, A. M., Levin, Y., Trippe, S., Eisenhauer, F., Ott, T., Gillessen, S., Abuter, R., Cuadra, J., Alexander, T., & Sternberg, A. 2006, The Astrophysical Journal, 643, 1011

Percival, W. J., Nichol, R. C., Eisenstein, D. J., Frieman, J. A., Fukugita, M., Loveday, J., Pope, A. C., Schneider, D. P., Szalay, A. S., Tegmark, M., Vogeley, M. S., Weinberg, D. H., Zehavi, I., Bahcall, N. A., Brinkmann, J., Connolly, A. J., & Meiksin, A. 2007, The Astrophysical Journal, 657, 645

Perlmutter, S., Aldering, G., Goldhaber, G., Knop, R. A., Nugent, P., Castro, P. G., Deustua, S., Fabbro, S., Goobar, A., Groom, D. E., Hook, I. M., Kim, A. G., Kim, M. Y., Lee, J. C., Nunes, N. J., Pain, R., Pennypacker, C. R., Quimby, R., Lidman, C., Ellis, R. S., Irwin, M., McMahon, R. G., Ruiz-Lapuente, P., Walton, N., Schaefer, B., Boyle, B. J., Filippenko, A. V., Matheson, T., Fruchter, A. S., Panagia, N., Newberg, H. J. M., Couch, W. J., & Project, T. S. C. 1999, The Astrophysical Journal, 517, 565

Pettini, M., Shapley, A. E., Steidel, C. C., Cuby, J.-G., Dickinson, M., Moorwood, A. F. M., Adelberger, K. L., & Giavalisco, M. 2001, The Astrophysical Journal, 554, 981

Pontzen, A., Governato, F., Pettini, M., Booth, C. M., Stinson, G., Wadsley, J., Brooks, A., Quinn, T., & Haehnelt, M. 2008, Monthly Notices of the Royal Astronomical Society, 390, 1349

Prochaska, J. X., Gawiser, E., Wolfe, A. M., Castro, S., & Djorgovski, S. G. 2003, The Astrophysical Journal, 595, L9

Razoumov, A. O. 2009, The Astrophysical Journal, 707, 738

Razoumov, A. O., Norman, M. L., Prochaska, J. X., Sommer-Larsen, J., Wolfe, A. M., & Yang, Y.-J. 2008, The Astrophysical Journal, 683, 149

Razoumov, A. O., Norman, M. L., Prochaska, J. X., & Wolfe, A. M. 2006, The Astrophysical Journal, 645, 55

Reddy, N. A. & Steidel, C. C. 2009, The Astrophysical Journal, 692, 778

Reddy, N. A., Steidel, C. C., Pettini, M., Adelberger, K. L., Shapley, A. E., Erb, D. K., & Dickinson, M. 2008, The Astrophysical Journal Supplement Series, 175, 48

Riess, A. G., Filippenko, A. V., Challis, P., Clocchiatti, A., Diercks, A., Garnavich, P. M., Gilliland, R. L., Hogan, C. J., Jha, S., Kirshner, R. P., Leibundgut, B., Phillips, M. M., Reiss, D., Schmidt, B. P., Schommer, R. A., Smith, R. C., Spyromilio, J., Stubbs, C., Suntzeff, N. B., & Tonry, J. 1998, The Astronomical Journal, 116, 1009

Robitaille, T. P. & Whitney, B. A. 2010, The Astrophysical Journal Letters, 710, L11

Rubin, V. C., Ford, W. K. J., & Thonnard, N. . 1980, The Astrophysical Journal, 238, 471

Schmidt, M. 1959, The Astrophysical Journal, 129, 243

Schödel, R., Ott, T., Genzel, R., Eckart, A., Mouawad, N., & Alexander, T. 2003, The Astrophysical Journal, 596, 1015

Shapley, A. E., Steidel, C. C., Adelberger, K. L., Dickinson, M., Giavalisco, M., & Pettini, M. 2001, The Astrophysical Journal, 562, 95

Shapley, A. E., Steidel, C. C., Erb, D. K., Reddy, N. A., Adelberger, K. L., Pettini, M., Barmby, P., & Huang, J. 2005, The Astrophysical Journal, 626, 698

Shapley, A. E., Steidel, C. C., Pettini, M., & Adelberger, K. L. 2003, The Astrophysical Journal, 588, 65

Springel, V. 2005, Monthly Notices of the Royal Astronomical Society, 364, 1105

Springel, V. & Hernquist, L. 2003, Monthly Notice of the Royal Astronomical Society, 339, 289

Springel, V., White, S. D. M., Jenkins, A., Frenk, C. S., Yoshida, N., Gao, L., Navarro, J., Thacker, R., Croton, D., Helly, J., Peacock, J. A., Cole, S., Thomas, P., Couchman, H., Evrard, A., Colberg, J., & Pearce, F. 2005, Nature, 435, 629

Steidel, C. C., Adelberger, K. L., Shapley, A. E., Pettini, M., Dickinson, M., & Giavalisco, M. 2003, The Astrophysical Journal, 592, 728

Steidel, C. C., Giavalisco, M., Dickinson, M., & Adelberger, K. L. 1996a, The Astronomical Journal, 112, 352

Steidel, C. C., Giavalisco, M., Pettini, M., Dickinson, M., & Adelberger, K. L. 1996b, The Astrophysical Journal, 462, L17

Steidel, C. C. & Hamilton, D. 1992, The Astronomical Journal, 104, 941

Steidel, C. C., Pettini, M., & Hamilton, D. 1995, The Astronomical Journal, 110, 2519

Tescari, E., Viel, M., Tornatore, L., & Borgani, S. 2009, Monthly Notices of the Royal Astronomical Society, 1

Wolfe, A. M. & Chen, H.-W. 2006, The Astrophysical Journal, 652, 981

Wolfe, A. M., Gawiser, E., & Prochaska, J. X. 2003a, The Astrophysical Journal, 593, 235

—. 2005, Annual Review of Astronomy and Astrophysics, 43, 861

Wolfe, A. M., Lanzetta, K. M., Foltz, C. B., & Chaffee, F. H. 1995, The Astrophysical Journal, 454, 698

Wolfe, A. M., Prochaska, J. X., & Gawiser, E. 2003b, The Astrophysical Journal, 593, 215

Wolfe, A. M., Prochaska, J. X., Jorgenson, R. A., & Rafelski, M. 2008, The Astrophysical Journal, 681, 881

Wright, E. L., Mather, J. C., Bennett, C. L., Cheng, E. S., Shafer, R. A., Fixsen, D. J., Eplee, R. E., Isaacman, R. B., Read, S. M., Boggess, N. W., Gulkis, S., Hauser, M. G., Janssen, M., Kelsall, T., Lubin, P. M., Meyer, S. S., Moseley, S. H., Murdock, T. L., Silverberg, R. F., Smoot, G. F., Weiss, R., & Wilkinson, D. T. 1991, The Astrophysical Journal, 381, 200

Wu, X.-P., Chiueh, T., Fang, L.-Z., & Xue, Y.-J. 1998, Monthly Notices of the Royal Astronomical Society, 301, 861

York, D. G., Adelman, J., Anderson, J. E., Anderson, S. F., Annis, J., Bahcall, N. A., Bakken, J. A., Barkhouser, R., Bastian, S., Berman, E., Boroski, W. N., Bracker, S., Briegel, C., Briggs, J. W., Brinkmann, J., Brunner, R., Burles, S., Carey, L., Carr, M. A., Castander, F. J., Chen, B., Colestock, P. L., Connolly, A. J., Crocker, J. H., Csabai, I., Czarapata, P. C., Davis, J. E., Doi, M., Dombeck, T., Eisenstein, D., Ellman, N., Elms, B. R., Evans, M. L., Fan, X., Federwitz, G. R., Fiscelli, L., Friedman, S., Frieman, J. A., Fukugita, M., Gillespie, B., Gunn, J. E., Gurbani, V. K., de Haas, E., Haldeman, M., Harris, F. H., Hayes, J., Heckman, T. M., Hennessy, G. S., Hindsley, R. B., Holm, S., Holmgren, D. J., hao Huang, C., Hull, C., Husby, D., ichi Ichikawa, S., Ichikawa, T., Ivezić, Ž., Kent, S., Kim, R. S. J., Kinney, E., Klaene, M., Kleinman, A. N., Kleinman, S., Knapp, G. R., Korienek, J., Kron, R. G., Kunszt, P. Z., Lamb, D. Q., Lee, B., Leger, R. F., Limmongkol, S., Lindenmeyer, C., Long, D. C., Loomis, C., Loveday, J., Lucinio, R., Lupton, R. H., MacKinnon, B., Mannery, E. J., Mantsch, P. M., Margon, B., McGehee, P., McKay, T. A., Meiksin, A., Merelli, A., Monet, D. G., Munn, J. A., Narayanan, V. K., Nash, T., Neilsen, E., Neswold, R., Newberg, H. J., Nichol, R. C., Nicinski, T., Nonino, M., Okada, N., Okamura, S., Ostriker, J. P., Owen, R., Pauls, A. G., Peoples, J., Peterson, R. L., Petravick, D., Pier, J. R., Pope, A., Pordes, R., Prosapio, A., Rechenmacher, R., Quinn, T. R., Richards, G. T., Richmond, M. W., Rivetta, C. H., Rockosi, C. M., Ruthmansdorfer, K., Sandford, D., Schlegel, D. J., Schneider, D. P., Sekiguchi, M., Sergey, G., Shimasaku, K., Siegmund, W. A., Smee, S., Smith, J. A., Snedden, S., Stone, R., Stoughton, C., Strauss, M. A., Stubbs, C., SubbaRao, M., Szalay, A. S., Szapudi, I., Szokoly, G. P., Thakar, A. R., Tremonti, C., Tucker, D. L., Uomoto, A., Berk, D. V., Vogeley, M. S., Waddell, P., i Wang, S., Watanabe, M., Weinberg, D. H., Yanny, B., & Yasuda, N. 2000, The Astronomical Journal, 120, 1579

Chapter 2

Deep Keck u-band imaging of the Hubble Ultra Deep Field: A catalog of $z \sim 3$ Lyman Break Galaxies

2.1 Introduction

The Hubble Ultra Deep Field (UDF; Beckwith et al., 2006) provides the most sensitive high-resolution images ever taken, yielding a unique data set for studying galaxy evolution. These data have contributed to many scientific advances, including constraining the star formation efficiency of gas at $z \sim 3$ (Wolfe & Chen, 2006), aiding in determining the luminosity function in the redshift range $4 \lesssim z \lesssim 6$ (Bouwens et al., 2007), bringing insight into the merger fractions of galaxies (Conselice et al., 2008), and yielding the discovery of clumpy galaxies at high redshift (Elmegreen et al., 2007).

Knowledge of galaxy redshifts is essential to understanding their nature, and various approaches are used to estimate this key attribute. A number of

studies identify objects in the redshift range $4 \lesssim z \lesssim 6$ using the deep multi-filter (BVIZJH) UDF images by identifying so-called "dropout" galaxies which are detectable in certain broadband filters but not in others (Beckwith et al., 2006; Bouwens et al., 2006, 2007). Others use photometric redshifts derived across the entire redshift range $0 < z \lesssim 6$ by analyzing the colors of galaxies in a wider range of filters (Coe et al., 2006). This latter approach has the potential to provide relatively accurate ($\sigma_{\Delta z/(1+z)} \lesssim 0.1$, Fernández-Soto et al., 2001) redshift estimates for a large number of galaxies in a given field, but traditionally has serious problems producing accurate results near $z \sim 3$, a redshift range for which key spectral energy distribution (SED) features fall blueward of the previously available filter set.

The majority of galaxies observed at $z \sim 3$ are Lyman break galaxies (LBGs): star-forming galaxies that are selected based on the break in their SED at the 912 Å Lyman limit primarily by interstellar gas intrinsic to the galaxy, as well as a flux decrement shortward of 1216 Å in the galaxy rest frame due to absorption by the Lyman series of opticallythick hydrogen gas along the line of sight. This Lyman limit discontinuity in the SED significantly dims these galaxies shortward of ~ 3500 Å, allowing them to be found with the U-band dropout technique (Steidel & Hamilton, 1992; Steidel et al., 1995, 1996a,b). Previously, the available observations in the UDF did not include deep u-band imaging. The next prominent broadband signature in the SED is the 4000 Å break, which is redshifted to the near infrared (IR) for $z \sim 3$ LBGs. Without the u-band or very deep IR coverage, it is very difficult to determine from broadband imaging alone whether the observed decrement in the SED near the observed-frame ~ 4800 Å is a low-redshift galaxy with a 4000 Å break, or a high-redshift galaxy with a decrement from the 1216 Å break. This degeneracy causes "catastrophic" errors in the photometric redshifts of galaxies at $z \sim 3$ without u-band data (Ellis, 1997; Fernández-Soto et al., 1999; Benítez, 2000).

The purpose of this paper is to present a reliable sample of LBGs at $z \sim$

3 in the UDF through the introduction of ultra-deep u'-band imaging acquired with the 10m Keck I telescope. The Keck I telescope and the Low Resolution Imaging Spectrometer (LRIS; Oke et al., 1995; McCarthy et al., 1998) form an ideal combination to probe galaxies at the $z \sim 3$ epoch due to the light-gathering power of the 10 m primary mirror and the outstanding efficiency of the LRIS blue channel in the near UV. This allows the u-band filter (with effective wavelength $\lambda_o \sim$ 3400 Å, FWHM$\sim$ 690 Å) used with the blue arm (LRIS-B) to be $\sim$ 300 Å bluer and $\sim$ 360 Å wider than the u-band filter on the Visible Multi-Object Spectrograph (VIMOS; Fevre et al., 2003) instrument ($\lambda_o \sim$ 3700 Å, FWHM$\sim$ 330 Å) at the Very Large Telescope (VLT) and still be effective. Consequently, this enables us to probe the Lyman break efficiently to a lower limit of $z \sim 2.5$, versus the VIMOS limit of $z \sim 2.9$ (as shown by the VIMOS observations of GOODS-South by Nonino et al., 2009). In addition, although the UDF field can only be observed at high air mass from Mauna Kea, the total throughput of LRIS-B and its bluer u-band is approximately twice that of VIMOS with its redder u-band. This gives Keck the unique ability to select lower redshift LBGs via their Lyman break.

We assemble a reliable sample of LBGs in the UDF with a combination of the u-band dropout technique and photometric redshifts, and provide photometric redshifts for all galaxies with good u-band photometry. We find that the u-band imaging improves the photometric redshifts of $z \sim 3$ galaxies by reducing the degeneracy between low and high-redshift galaxies. Furthermore, the combination of deep LRIS u-band and high-resolution multiband Hubble Space Telescope (HST) imaging provides an unprecedented view of $z \sim 3$ LBGs to improve our understanding of their highly irregular rest-frame UV morphologies (Law et al., 2007) down to unprecedented depths.

The deep, high-resolution LBG sample will also extend current constraints on the star formation efficiency of gas at $z \sim 3$. Reservoirs of neutral gas are needed to provide the fuel for star formation. Damped Lyα systems (DLAs), selected for their neutral hydrogen column densities of $N_{\rm HI} \geq 2 \times 10^{20}{\rm cm}^{-2}$, dominate the

neutral-gas content of the universe in the redshift interval $0 < z < 5$. DLAs contain enough gas to account for 50% of the mass content of visible matter in modern galaxies (see Wolfe et al., 2005, for a review) and may act as neutral-gas reservoirs for star formation, since stars form when local values of the H I column density, $N_{\rm HI}$, exceed a critical value. At high redshift, the star formation rate (SFR) is assumed to follow the Kennicutt-Schmidt (KS) law (established for nearby galaxies) which states how the SFR per unit physical area, $\dot{\Sigma}_*$, relates to the neutral gas (i.e., H I and H_2) column density: $\dot{\Sigma}_* \propto N_H^{1.4}$ (Kennicutt, 1998). Strong DLAs with $N_{\rm HI} \geq 1.6 \times 10^{21}{\rm cm}^{-2}$ in the redshift range $2.5 \lesssim z \lesssim 3.5$ are predicted to have emission from star formation in the rest-frame FUV redshifted into the optical such that they are detectable in the UDF F606W image. Wolfe & Chen (2006) searched for low surface-brightness emission from DLAs in the UDF and found the *in situ* SFR efficiency of DLAs to be less than 5% of the KS law. In other words, star formation must occur at much lower rates in DLAs at $z \sim 3$ than in modern galaxies. Whereas the Wolfe & Chen (2006) results set sensitive upper limits on *in situ* star formation in DLAs excluding known galaxy regions, no such limits exist for DLAs containing LBGs. The sample presented here enables a search for spatially extended low-surface-brightness emission around $z \sim 3$ LBGs which will yield constraints on the star formation efficiency at high redshift (Chapter 3). This is one of the main motivations for constructing this sample, and therefore we construct our sample conservatively to minimize the number of potential interlopers.

We present our catalog of $z \sim 3$ LBGs, provide photometric redshifts for the entire sample of objects that have reliable u-band photometry, and make the u-band image available to the public. The observations are described in §2.2.2, and the data reduction and analysis in §2.2.3. We discuss the photometric selection of $z \sim 3$ galaxies in §2.2.4, and summarize our major findings in §2.2.5. Throughout this paper, we adopt the AB magnitude system and an $(\Omega_M, \Omega_\Lambda, h) = (0.3, 0.7, 0.7)$ cosmology with parameters $\Gamma = 0.21, n = 1$, which are largely consistent with

recent values (Hinshaw et al., 2009).

2.2 Observations

The u-band ($\lambda_o \sim 3400$ Å, FWHM$\sim$ 690 Å) images of the UDF ($\alpha(J2000)=03^h32^m39^s$, $\delta(J2000) = -27°47'29.''1$) were obtained with the 10 m Keck I telescope using the LRIS. The u-band data were taken with the new Cassegrain Atmospheric Dispersion Corrector (Cass ADC; Phillips et al., 2006) to minimize image distortions from differential atmospheric refraction. The Cass ADC was critical to the success of these observations because of the low elevation of the UDF from Mauna Kea, and the blue wavelength of our primary band. The data also benefit from the backside illuminated, dual UV-optimized Marconi 2048 × 4096 pixel CCDs on LRIS-B, with 0.″135 pixels and very high UV quantum efficiency ($\sim$50% at $\lambda_o \sim 3450$ Å). Because the quantum efficiency of the two CCD chips varies $\sim$30%–35% in the u-band, we placed the UDF entirely on the more sensitive chip (CCD1). We used a dichroic beam splitter (D460) to simultaneously observe the u-band on the blue side, and the V-band and R-band on the red side. The red channel data were taken for astrometric and photometric consistency checks, and were not used in this study other than for calibration purposes due to the much deeper and higher resolution UDF images available over those wavelength ranges.

The observations were carried out in darktime over two runs, 2007 October 7–9 (three half nights) and 2007 December 3–4 (two half nights). We lost the entire first night of the first run to weather, and had moderate weather and seeing conditions throughout both runs that yielded a median seeing FWHM of $\sim$1.″3 in the u-band. In order to maximize time on sky, we adopted the dither strategy of Sawicki & Thompson (2005, see their Eqn. 1), setting the red channel exposure times such that the last readout of the red channel coincided with the end of the blue channel readout. The u-band images were acquired as a series of 36 × 900s exposures to avoid the nonlinear regime of the CCD, totaling 9 hrs of integration

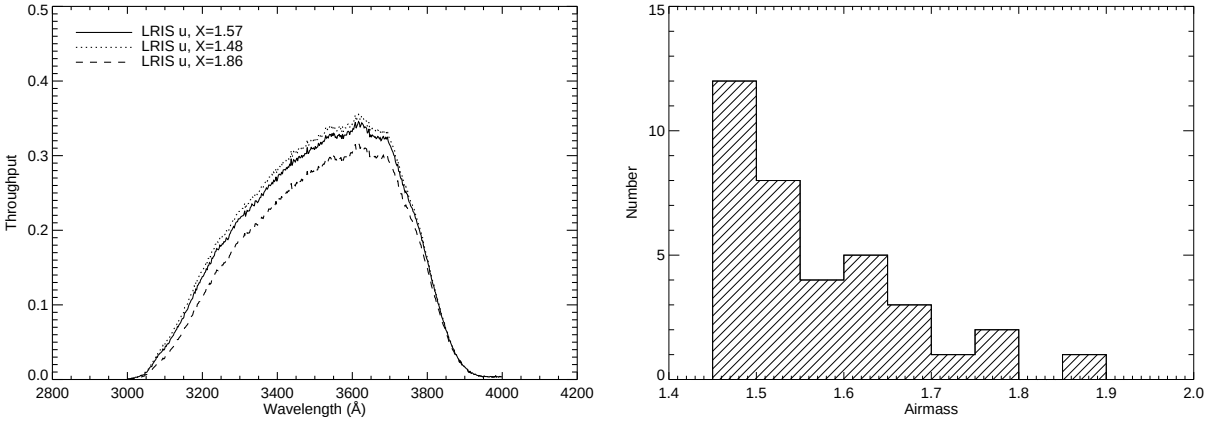

Figure 2.1 Transmission of the u-band filter used in this study for different air masses (X). The filters are corrected for the atmosphere attenuation at different air masses and the CCD quantum efficiency of LRIS-B on the Keck telescope. The histogram shows the range of air masses in the study, with the minimum and maximum air mass being plotted on the transmission curve. The change in the effective wavelength λ_o between air masses is typically $\lesssim 5$ Å.

time on target. We executed a nine-point dither pattern with $10''$ dithers to deal with bad pixels and to create a super-sky flat.

The UDF can only be observed at large air masses at Mauna Kea, which can affect the shape of the u-band throughput. We show a histogram of our observed air masses and the variation of the filter throughput for different air masses in Figure 2.1. We find that the variations in air masses in our sample do not significantly affect the blue side cutoff of our filter. Specifically, we find that the variation between our best and worst air mass yields a change in $\lambda_o \lesssim 10\mathring{A}$, with typical changes in λ_o being $\lesssim 5\mathring{A}$. Given the small variation of λ_o, we derive the final u-band filter transmission curve by convolving the measured filter throughput with the atmospheric attenuation at our average air mass of 1.57 and the CCD quantum efficiency.

Throughout the paper we utilize the B, V, i', and z' band (F435W, F606W, F775W, and F850LP, respectively) observations of the UDF (Beckwith et al., 2006), obtained with the Wide Field Camera (WFC) on the HST Advanced Camera for

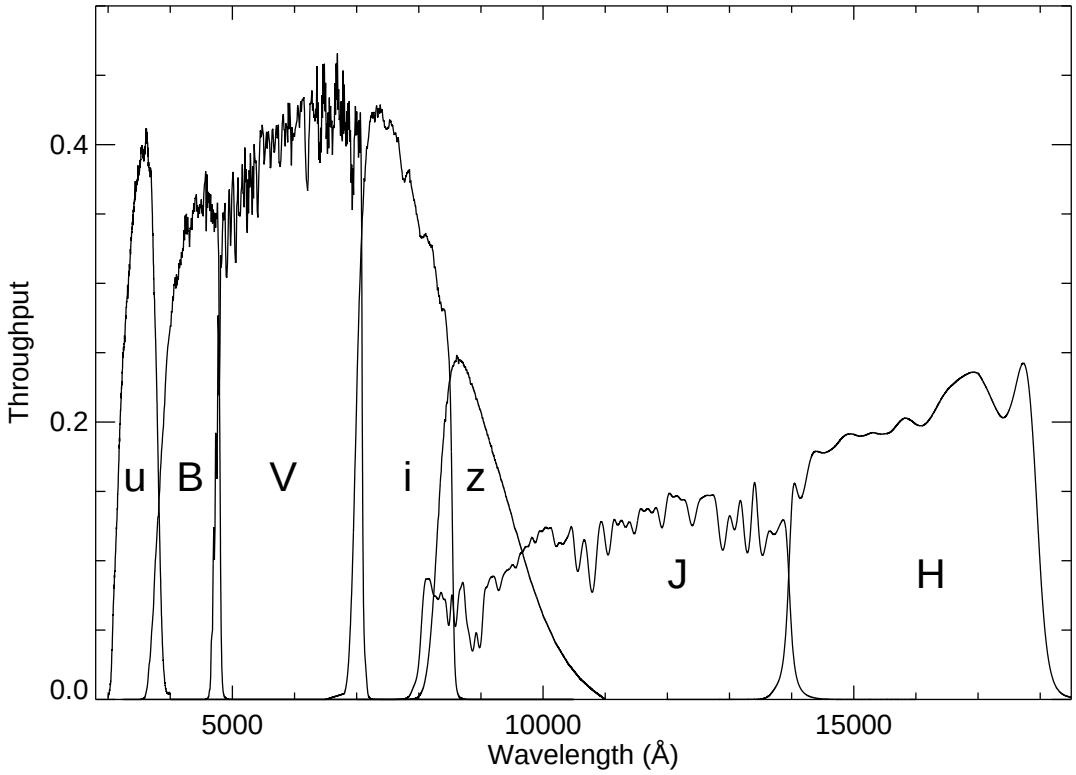

Figure 2.2 Transmissions of the filters used in this paper, corrected for the CCD quantum efficiency, and in the case of the u-band, the atmosphere attenuation at the average air mass of 1.57. The u-band is from LRIS-B on the Keck telescope, the B, V, i', and z' bands from the WFC on the HST ACS, and the J and H bands from the NICMOS camera on HST.

Surveys (ACS; Ford et al., 2002). These images cover 12.80 arcmin^2, although we prune our catalog to the central 11.56 arcmin^2 which contains at least half the average depth of the whole image and overlaps our u-band image with uniform depth. In addition to these ACS images, we also include observations taken with the NICMOS camera NIC3 in the J and H bands (F110W and F160W; Thompson et al., 2006). These red wavelengths cover the central 5.76 arcmin^2 of the UDF, so we only use them whenever the field of view (FOV) overlaps. Figure 2.2 plots the total throughput of the filters used in this paper: the Keck LRIS-B u-band, the HST ACS B, V, i', and z' bands, and the HST NICMOS J and H bands, and include the CCD quantum efficiency and atmospheric attenuation.

2.3 Data Reduction and Analysis

2.3.1 Image processing

The LRIS-B data were processed in a combination of custom code in IDL, and standard data reduction algorithms from IRAF[1]. The images were bias subtracted, first from the overscan region and then from separate bias frames to remove any residuals, before being trimmed to remove any vignetted regions of LRIS. Super-sky flats were created using IRAF from the median of all the unregistered images with sigma clipping to remove objects and cosmic rays, which were then used to flat-field the images. These prove superior to dome and twilight sky flats in determining the CCD response in the u-band because of the short wavelengths, and yield excellent flats. Dithering offsets were determined using custom code and `SExtractor` (Bertin & Arnouts, 1996) to locate bright objects common to all the images. In order to *drizzle* (Fruchter & Hook, 2002) only once and keep correlated noise to a minimum, the images were distortion corrected using the solution provided by J. Cohen & W. Huang (private communication, February 2008) and shifted to correct for the dithering offsets all at once using the `geotran` package in

[1]IRAF is distributed by the National Optical Astronomy Observatory, which is operated by the Association of Universities for Research in Astronomy, Inc., under cooperative agreement with the National Science Foundation.

IRAF. We drizzled with `pixfrac` = `0.5` to improve the point-spread function (PSF) and set the pixel scale such that the pixels are integer multiples of the UDF pixels, 0.″12, for reasons explained in §2.2.3.4. To maximize the signal to noise (S/N), the images were weighted by their inverse variances. The drizzled images were then combined using the IRAF task `imcombine`, with sigma clipping to remove bad pixels and cosmic rays. These images were trimmed to include regions of uniform depth (11.56 arcmin^2), normalized to an effective exposure time of 1s, and then background subtracted using the global background determined with `SExtractor`. An astrometric solution was applied with the IRAF task `ccmap` by matching bright and nearly unresolved objects in the UDF to those in the final stacked image. The final rms astrometric errors are between 0.″02 and 0.″03, negligible in comparison to the 1.″3 FWHM of the u-band PSF.

2.3.2 Photometric Calibration

Moderate weather yielded no completely photometric night for our calibration, and we therefore calibrated to the Multi-wavelength Survey by Yale–Chile (MUSYC; Gawiser et al., 2006), which covers the same part of the sky as our primary observations. We include all our filters (u, V, and R) for this calibration. All our calibrations are in the AB95 system of Fukugita et al. (1996), hereafter referred to as AB magnitudes. We used the IRAF tasks `phot` and `fitparams` to solve for zero-point magnitudes, air-mass correction coefficients, and appropriate color correction coefficients. Specifically, we use the equation:

$$\mathrm{m} = -2.5\log_{10}(\mathrm{F}) + \mathrm{Z} - \mathrm{cX} - \mathrm{Y}, \tag{2.1}$$

where F is the flux in counts/s, Z is the zero-point magnitude, c is the air-mass coefficient, X is the air-mass, and Y is the color term. We allow a color term to account for any differences between the U-band filter used by MUSYC and the u-band filter in our observations, similar to the color term used by Gawiser et al. (2006) to correct for their differences compared to the Johnson-Cousins filter set. The galactic extinction of 0.0384 is subtracted from the zero-point magnitude, using the relation $A(u) = 4.8E(B-V)$ interpreted from Cardelli et al. (1989),

where $E(B-V) = 0.008$ (Beckwith et al., 2006). The final results for the u-band calibration are a zero-point magnitude $Z = 27.80 \pm 0.03$, an air-mass coefficient term $c = 0.41$, an average air-mass $X = 1.57$, and a color term $Y = (0.13 \pm 0.02) \times (U-B)_{AB}$. We double check our calibration using multiple observed photometric standard stars (Landolt, 1992) over a range of air masses, and the zero-point and air-mass correction coefficients are consistent with those found when calibrating to the MUSYC catalog. As a result, we are confident that the u-band image is well calibrated.

2.3.3 Depth of the u-band Image

It is useful to characterize the depth of the u-band image, however, different definitions exist to describe the sensitivity of an image. Two commonly quoted limits are presented here: a measurement of the sky fluctuations of the image, and a limiting magnitude corresponding to a 50% decrease in object counts through Monte Carlo simulations.

The sky noise of the image is measured via the pixel to pixel rms fluctuations in the image, best measured by fitting a Gaussian to the histogram of all pixels without sources. Sources are identified with the program `SExtractor`, with the threshold set such that the negative image has no detections. This yields a depth of 31.0 mag arcsec^{-2}, $1\sigma_u$ sky fluctuations. However, since the image is drizzled, correlated noise between the pixels is introduced. The theoretical increase in noise due to `pixfrac = 0.5` using equation 10 from Fruchter & Hook (2002) is 20%. Alternatively, the correlated noise can be estimated empirically with equation 2 from Fernández-Soto et al. (1999), which uses a covariance matrix to determine a small overestimate of the real error[2]. This results in a slightly more conservative depth of 30.7 mag arcsec^{-2}, $1\sigma_u$ sky fluctuations, which is what we quote here.

Additionally, to get a better sense of the usable depth of the image, a limiting magnitude is often quoted (e.g., Chen et al., 2002; Sawicki & Thompson, 2005). We define $u_{\rm lim}$ as the magnitude limit at which more than 50% of the objects are detected. The best way to determine $u_{\rm lim}$ is through Monte Carlo

[2]The equation has a typographic error. The sum should be over $i_1, i_2 = 1$ to $i_1, i_2 = 3$.

simulations, which take into account both the sky surface brightness and the seeing in our image. Since our image PSF has more flux in the wings than a Gaussian, we plant both Gaussian objects, and objects modeled to fit our PSF using a two-dimensional (2-D) Moffat profile[3]. The custom IDL code was used to extract bright unresolved objects in the u-band image, take the median of all these objects, and create a composite object stack. The composite image was then fit both by a Gaussian, and by a 2-D Moffat profile using `MPFIT` (Markwardt, 2009), with a modification to ensure that the wings of the profile go to 0 for the Moffat profile. We semi-randomly insert these objects with a range of fluxes into the u-band image. The locations of the planted objects are constrained such that they do not: 1) fall off the edges, 2) fall on a real detected object, and 3) fall on any previously planted objects. We find a total $u_{\rm lim}$ of 27.3 mag for the Gaussian and 27.2 mag for the Moffat profile (see Figure 2.3), where the total magnitudes are based on `SExtractor`'s `mag_auto` apertures, which are Kron-like (Kron, 1980) elliptical apertures corrected for possible contamination. While total magnitudes are generally reported, isophotal apertures are more appropriate for LBGs, and yield a $u_{\rm lim}$ of 27.7 mag for the Gaussian and 27.6 mag for the Moffat profile. This is one of the deepest u-band images ever obtained, with our sensitivity being similar to those reported in the Keck Deep Fields (Sawicki & Thompson, 2005).

This detection method does not match the detection method used in §2.2.3.4, and therefore does not constrain our detection efficiency of LBGs. As explained below, we use our prior knowledge of the positions of the sources which yields a different completeness limit. However, this result gives the depth of our u-band image for comparison to other studies.

2.3.4 Photometry through Template Fitting

In order to obtain robust colors across images with varied PSFs, it is necessary to match apertures and correct for PSF differences. If the difference is minor, then methods to apply aperture corrections to account for the variations

[3]The Moffat profile (Moffat, 1969) is a modified Lorentzian with a variable power-law index that takes into account the flux in the wings of the intensity profile which are not included in a Gaussian profile.

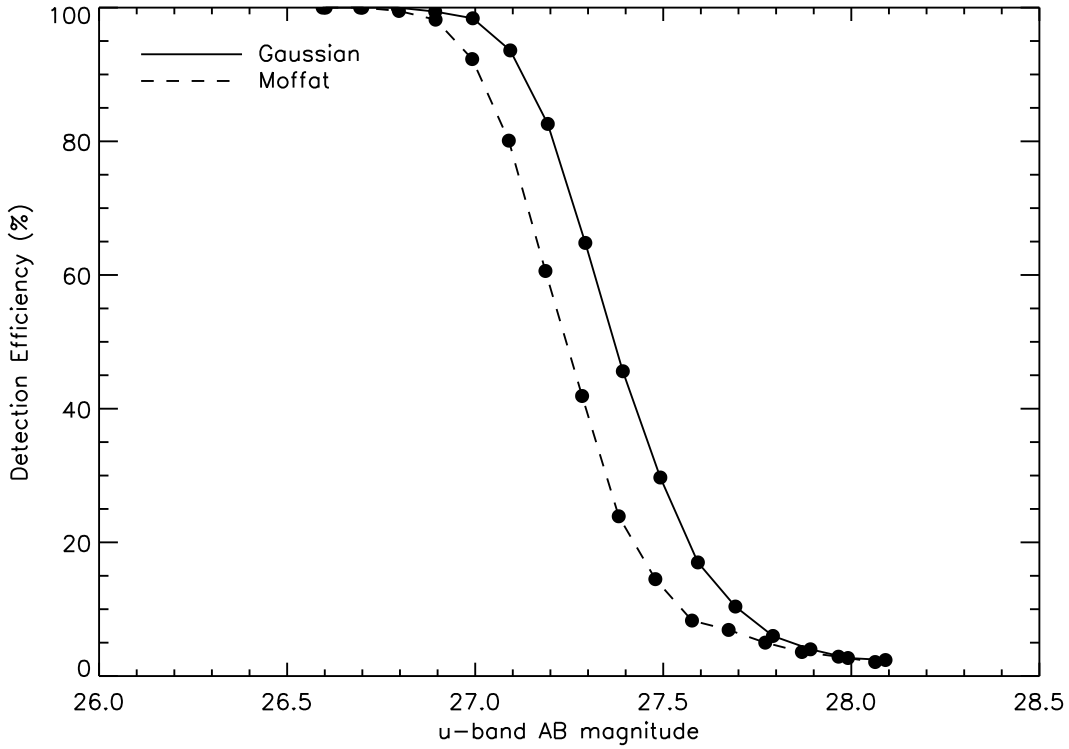

Figure 2.3 Detection efficiency of the u image based on simulations planting objects of different intrinsic profiles into the image. The solid line represents a gaussian profile with a FWHM of 1.″3 and the dashed line represents a Moffat profile with a half-width at half maximum of 1.″2 and a power law index of 3.4. The u values are total magnitudes based on `SExtractor`'s `mag_auto` apertures which are Kron-like (Kron, 1980) elliptical apertures corrected for possible contamination. We find a total $u_{\rm lim}$ of 27.3 mag for the gaussian and 27.2 mag for the Moffat profile, and for isophotal apertures which are more appropriate for LBGs, find a $u_{\rm lim}$ of 27.7 mag for the Gaussian and 27.6 mag for the Moffat profile.

are appropriate, such as the `ColorPro` software by Coe et al. (2006). However, such algorithms don't perform well when the difference in the PSF FWHM is large, such as when combining the high-resolution data from the HST (0.″09 FWHM) with the low-resolution images obtained in this study with Keck (1.″3 FWHM). In this case, the uncertainties in aperture corrections are unreasonably large, and the low-resolution images are crowded such that objects overlap, making object definitions that are valid in both high and low-resolution images difficult to determine.

In order to avoid these uncertainties, we use the `TFIT` (Laidler et al., 2007) template-fitting method that uses prior knowledge of the existence, locations, and morphologies of sources in the deeper high-resolution UDF images to improve the photometric measurements in our low-resolution u-band image. This method creates a template of every object by convolving each object in the high-resolution image with the PSF of the low-resolution image. These templates are then fit to the low-resolution image to determine the flux of all the objects in the u-band, relative to the flux in the UDF V-band image. We chose the V-band as the high-resolution reference image because it is closest in wavelength to the u-band, without being affected by the Ly$-\alpha$ forest over the redshift interval $2.5 \lesssim z \lesssim 3.5$. The result is a very robust color which relates every object in the high-resolution V-band image to the low-resolution u-band, avoiding the problem of aperture matching between the two images while intrinsically correcting for the PSF difference. Using the V-band flux, the color is converted to a u-band flux, which inherits the same isophotal aperture as the high-resolution V-band image. The aperture correction used to obtain total fluxes for the V-band image is then also valid to obtain total fluxes for the u-band. For a more in-depth explanation, see Laidler et al. (2007). This technique is similar to others in the literature (Fernández-Soto et al., 1999; Labbé et al., 2005; Shapley et al., 2005; Grazian et al., 2006), with the original version based on Papovich et al. (2001, 2004).

We chose to use `TFIT` as it is publicly available, well documented, and its performance is carefully tested. Like all the other methods, there are some constraints that had to be met to use this algorithm. The first is that the pixel scale of the u-band image must be an integer multiple of the pixel scale of the UDF

V-band image. This was accomplished by drizzling the images such that the pixel scale of the u-band is 4 times larger than the V-band, as mentioned in §2.2.3.1. The second and third requirements are that the images must not be rotated with respect to each other, and the corner of the V-band image must coincide with the corner of the u-band image. These two requirements were met by rotating and trimming the V-band image using IDL. The resultant image was compared to the original image, and the difference in photometry was negligible compared to the intrinsic uncertainties. We also improved our fit by source weighting the rms map before providing it to the `TFIT` pipeline, as suggested by Laidler et al. (2007).

In order to avoid proliferating different catalogs with minor differences in object definitions, we adopt the object definitions of Coe et al. (2006). These definitions include the catalogs of Beckwith et al. (2006) and Thompson et al. (2006), as well as detections performed on a white light image by Coe et al. (2006). By using identical object definitions as Coe et al. (2006), we can use the careful photometry for the B, V, i', z', J, and H bands already determined, and compare our redshift determinations knowing we have used identical apertures.

`TFIT` requires a `SExtractor` catalog of the V-band image as an input to the pipeline. The program `sexseg` (Coe et al., 2006) was run on the segmentation map of Coe et al. (2006) to provide the necessary information to `TFIT` while using the desired object definitions of Coe et al. (2006). The segmentation map defines which pixels belong to each identified V-band object. The `sexseg` program forces `SExtractor` to run using a predefined segmentation map (for details, see Coe et al., 2006). `TFIT` also requires a representative 2-D model of the u-band PSF, and is sensitive to the quality of its construction. We use the same Moffat profile fit described in §2.2.3.3 to model the PSF of the u-band image, and then use this as the transfer kernel by `TFIT` to convolve the V-band galaxy cutouts. We note that there is no significant spatial variation of the PSF across the field.

In general, the higher the resolution and sensitivity of the high-resolution image, the better `TFIT` can model the sources for the low-resolution image. If an input catalog is not complete enough, then unmodeled objects can act as an unsubtracted background, slightly increasing the flux of all objects (Laidler et al.,

2007). However, this has a limit, and eventually there are so many sources that are too faint to detect in the low-resolution image that galaxies are not well constrained given the substantial number of priors. This yields a large number of galaxies with unconstrained fluxes that increase the uncertainties of the nearby objects without yielding any new information. The UDF V-band image has substantially higher resolution and is deeper than the u-band image, and therefore a limit was put on the faintest galaxy used as a prior in `TFIT`. Only galaxies brighter than $V = 29$ mag are included in the input catalog to `TFIT`. The galaxies fainter than $V = 29$ mag are too faint to be constrained by the u image, and only add noise to the `TFIT` results. We stress that this is a conservative cut, and does not introduce an unsubtracted background.

The quality of the resulting photometric fits can be evaluated through Figure 2.4, which depicts four panels: the V-band image from the UDF, the u image from Keck, the model image, and the residual image. The model and residual images are diagnostics produced by `TFIT`, and are not used in the fitting process. The model image is a collage of the V-band galaxies convolved with the PSF of the u-band image, scaled by the `TFIT` flux measurement for each object. The residual image is the difference of the model and the u-band images. Ideally the residual image would be zero, but this is not the case (especially for bright objects), with multiple effects contributing to the imperfect residual. For instance, if the object in the V-band image is saturated, then it has the wrong profile for the u-band and leaves a residual. Alternatively, imperfections in the modeled PSFs when scaled to large flux measurements of bright objects will also leave a residual. This effect was minimized by using a source-weighted rms map, although photometry of the brightest objects are imperfect. In practice, it is very difficult to perfectly align two images, the distortion correction is not perfect, and images generally have spatially varying PSFs. To minimize these affects, `TFIT` does a "registration dance", where it cross-correlates each region of the model with the region of the data to find any local shifts. This registration dance was performed, which slightly improved the residual image, and leads to more robust photometry.

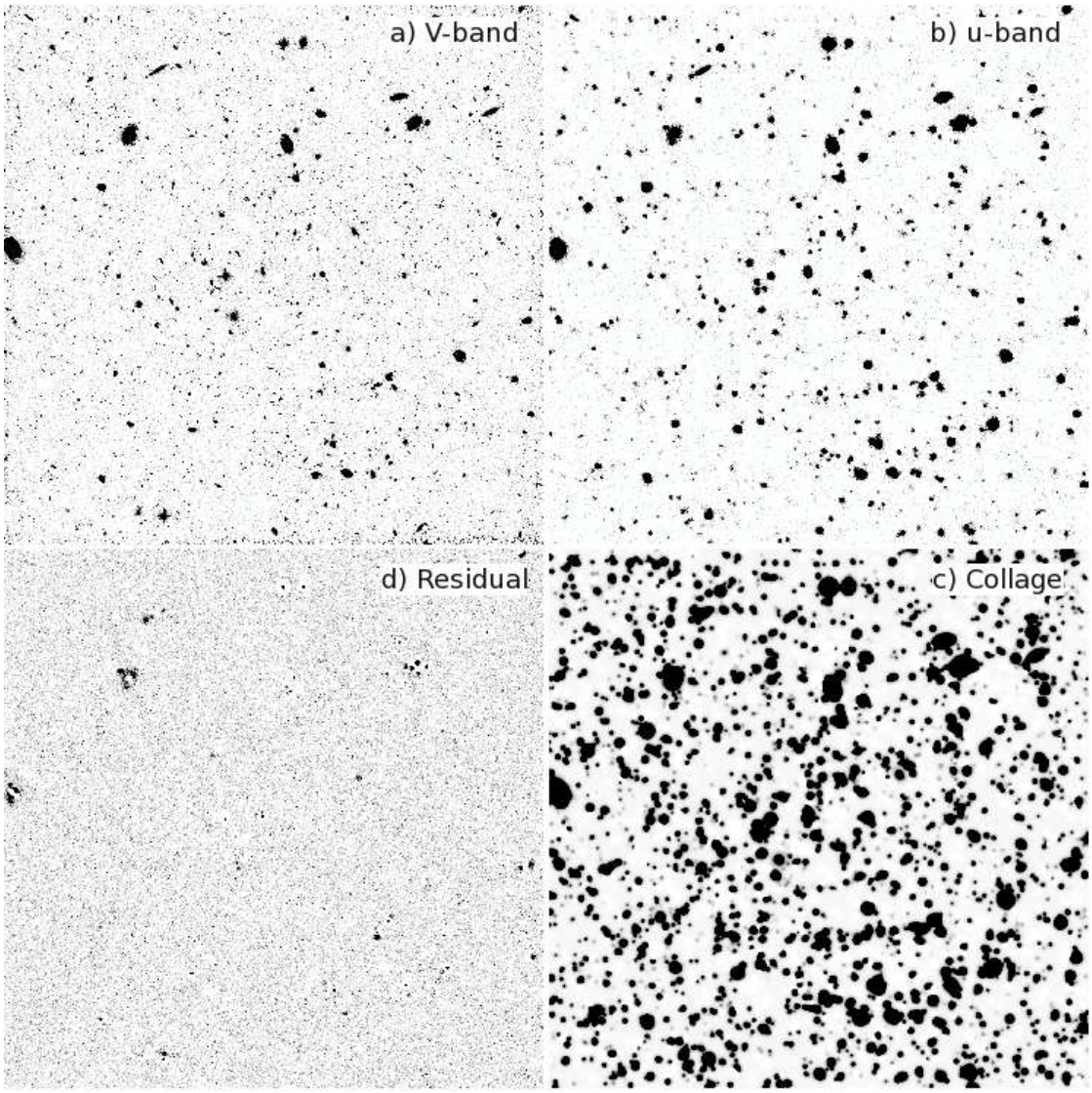

Figure 2.4 Quality of `TFIT` photometric fits of the UDF V-band and LRIS u-band imaging. The images cover the overlap region of the central 11.56 arcmin^2 of the UDF, with North pointing up and East to the left. Clockwise from upper left: (a) the V-band image from the UDF; (b) the u-band image from Keck; (c) the model image; (d) the residual image. The model image is a collage of the V-band galaxies convolved by the PSF of the u-band image, scaled by the `TFIT` flux measurement for each object. The residual image is the difference of the model and the u-band image. Ideally the residual image would be zero, but this is not the case for bright objects (see §2.2.3.4).

2.3.5 Sample Selection

Our aim is to identify a sample of high-redshift galaxies that are suitable for constraining the star formation efficiency of gas at $z \sim 3$. A large fraction of objects for which fluxes are measured with `TFIT` are too faint to yield sufficient information regarding the object's redshift, and we therefore limit our sample to those objects with high S/N. We select objects based on their V-band magnitudes, since cuts in u-band would preferentially remove LBGs. The median u-band S/N of all objects decreases as a function of the V-band magnitude and drops below 3σ at $V \geq 27.6$ mag. We adopt this V-band magnitude cut to include the majority of high S/N u objects, while removing S/N < 3 objects. We note that this is a conservative 3σ cut since most LBGs won't be detected in the u-band reducing the overall median S/N.

In addition to removing low S/N objects, we wish to remove objects with photometry affected by nearby neighbors. `TFIT` can identify such objects with the covariance index diagnostic that uses the covariance matrix (Laidler et al., 2007). During the fitting of an object's photometry as described in §2.2.3.4, `TFIT` uses the singular value decomposition routine to perform a chi-square (χ^2) minimization. This yields a covariance matrix which is used to calculate uncertainties via the square root of the variance (the diagonal element), as well as the covariance (the off diagonal elements) of all objects in the fit. The covariance index is the absolute value of the ratio of the off-diagonal and the diagonal elements (Laidler et al., 2007). The maximum value of the covariance index is saved, along with the corresponding object ID, and yields information about how an object's photometry is affected by its most influential neighbor. Objects for which this ratio is much less than 1 are generally isolated objects, while objects with large covariance index values can have unreliable photometry. Multiple cuts are implemented to remove objects whose photometry have been significantly affected. First, all objects with a covariance index greater than 1 are cut because their measurements are not considered reliable. All remaining objects are kept if one of two conditions apply: either they have a covariance index less than 0.5, or they have a V-band flux greater than twice that of the nearest neighbor. This approach balances the desire for a large sample with

the need to obtain reliable photometry. Lastly, we only consider objects that are detected in all four ACS bands (B, V, i', and z') to facilitate and improve color selection in §2.2.4.2. This requirement removes most galaxies at $z > 4$ as they have little flux in the B or redder bands.

Table 2.1 lists the 1457 galaxies that are left after the V-band magnitude, covariance index, and V-band flux ratio cuts. Each entry includes the object ID (matching those from Coe et al. (2006)), R.A., decl., u magnitudes and uncertainties, and u S/N. It also lists information regarding the most significant neighbor, namely, its object ID, covariance index, V-band flux ratio, and separation distance. The u magnitude uncertainties include the uncertainties due to the V-band aperture correction made in Coe et al. (2006), as the accuracy of our u magnitudes depend on the accuracy of the V-band magnitudes. Objects that are observed with a u-band flux less than 3σ significance are considered undetected in the u-band and are assigned a 3σ upper limit. The magnitude limit is set to:

$$m_{3\sigma} = -2.5 \log_{10}(3\sigma_{\mathrm{TFIT}}) + Z_{\mathrm{LRIS}}, \tag{2.2}$$

where Z_{LRIS} is the zero point magnitude. The error distribution from `TFIT` is normally distributed and the upper limits from `TFIT` are robust, as evaluated in Laidler et al. (2007).

2.4 Photometric Selection of $z \sim 3$ Galaxies

Star-forming galaxies early in their history, such as LBGs, exhibit a clear break in their Spectral Energy Distribution (SED) at the 912 Å Lyman limit (Lyman break), as well as multiple absorption lines shortward of 1216 Å by the Lyman series. Photons bluer than the Lyman limit are not observed because the interstellar gas intrinsic to the galaxy and components of the foreground gas along the line of sight of the galaxy are optically thick at $\lambda \leq 912$ Å. At a redshift of $\gtrsim 2.5$, these spectral features are redshifted to optical wavelengths, with the Lyman break entering the u-band ($\sim$3500 Å). The ability to observe the Lyman break optically allows large samples of high-redshift galaxies to be identified based

Table 2.1. Catalog of u-band Objects

ID[a]	R.A.	Decl.	u (mag)[b]	S/N	Cov. ID[c]	Cov. Index[d]	Flux Ratio[e]	Distance (arcsec)[f]
1	3 32 39.723	–27 49 42.53	24.69±0.01	112.53	12	0.039	0.007	2.546
7	3 32 39.451	-27 49 42.95	25.76±0.02	49.56	10	0.413	0.112	1.138
8	3 32 39.540	-27 49 28.35	26.18±0.04	29.43	80	0.003	0.003	4.335
13	3 32 39.326	-27 49 39.06	26.71±0.05	23.76	16	0.095	0.060	2.099
14	3 32 38.467	-27 49 31.84	25.28±0.02	73.11	56	0.010	0.012	3.319
15	3 32 38.846	-27 49 39.29	28.92±0.34	0.34	22	0.159	0.591	1.800
22	3 32 38.957	-27 49 38.33	28.91±0.35	2.25	19	0.281	12.129	1.440
24	3 32 39.053	-27 49 38.76	27.34±0.08	13.27	22	0.296	0.911	1.484
33	3 32 39.179	-27 49 36.13	27.07±0.06	18.38	48	0.018	0.393	2.902
35	3 32 38.763	-27 49 36.80	27.73±0.11	9.78	19	0.026	10.179	2.880

Note. — Table 2.1 is shown in full in the appendix (Table C.1). A portion is shown here for guidance regarding its form and content.

[a]ID numbers from Coe et al. (2006).

[b]Total u-band magnitudes for the same aperture as the V-band in Coe et al. (2006).

[c]ID of the most significant neighbor affecting the photometry according to the maximum covariance index.

[d]The maximum covariance index is the absolute value of the ratio of the variance and the covariance.

[e]The ratio of object's V-band flux with the V-band flux of its most significant neighbor.

[f]Distance to the most significant neighbor.

on multicolor photometry where LBGs are selected by a strong flux decrement shortward of the Lyman limit, and a continuum longward of rest frame Lyα (1215 Å) (e.g., Steidel & Hamilton, 1992; Steidel et al., 1995, 1996a,b). In addition, photometric redshift determination algorithms can estimate object redshifts using galaxy SED templates[4], which include additional information other than the Lyman break, such as the slope of the SED, the Balmer break at 3646 Å, and the more pronounced 4000 Å break, due to the sudden onset of stellar photospheric opacity by ionized metals and the CaII HK doublet (Hamilton, 1985). Although color selection and photometric redshifts utilize the same SEDs for selecting $z \sim 3$ galaxies, they each have their strengths and weaknesses. We use a combination of color selection and photometric redshifts to create our sample of LBGs (§2.4.2). We provide a description of the photometric redshift process, color selection method, and a catalog of all objects and their photometric redshifts below.

2.4.1 Photometric Redshifts

Photometric redshifts (hereafter, photo-z's) are a well known and robust procedure to determine redshifts of galaxies when spectra are unavailable (e.g. Koo, 1985; Lanzetta et al., 1998; Benítez, 2000; Coe et al., 2006; Hildebrandt et al., 2008). They have the advantage over color selection that they take into account all the colors available simultaneously in χ^2 fits to template SEDs and yield more precise redshift information with clear redshift confidence limits. The photo-z's also sample $z \sim 3$ galaxies in regions of color space that color selected samples avoid because of low-redshift galaxies, and therefore can provide a larger sample. However, photo-z uncertainties do not always include systematic errors caused by variations and evolution of galaxy SEDs compared to SED templates, and possible mismatches of SED templates (see §2.4.1.2). Such systematic problems and the lack of a large spectroscopic sample make it difficult to characterize the contamination fraction of photo-z selected $z \sim 3$ galaxies (see §2.4.1.3). Nonetheless, they provide the largest sample of LBGs for study.

[4]We refer to these templates as SED templates throughout the paper to distinguish them from the galaxy templates discussed in §2.2.3.

For each galaxy, photo-z codes produce a probability distribution function, $P(z)$, representing the probability of a galaxy being at any specific redshift. However, the $P(z)$ can have multiple peaks, especially at $z \sim 3$ where there is a degeneracy with galaxies at $z \sim 0.2$, which then translates into large uncertainties for the photo-z (Benítez, 2000). The introduction of the u-band data helps resolve the photo-z degeneracy and improve the photo-z fits for $z \sim 3$ galaxies as it targets the most dominant signature in their SED, the Lyman break. We present photo-z's for the entire sample of galaxies with u-band data from §2.3.5 in Table 2.2, but caution against using them blindly to select galaxies at $z \sim 3$. We recommend making cuts on the sample to select galaxies with good $\chi^2_{\rm mod}$ and `ODDS` (for a description of these parameters, see §2.4.1.1).

2.4.1.1 Bayesian Photometric Redshifts

There are many different photo-z codes available, and Hildebrandt et al. (2008) explain the benefits of the different algorithms. We chose to use the Bayesian photo-z's (BPZ) (Benítez, 2000; Benítez et al., 2004; Coe et al., 2006) to be consistent with past photo-z's determined for the UDF without u-band data (Coe et al., 2006). Hildebrandt et al. (2008) advise using the SED templates supplied with their respective codes, since user-supplied SED templates can cause problems. However, a re-calibration of the SED template set improves the performance of the photo-z redshifts, and we use the re-calibrated SED templates from Benítez et al. (2004) and Coe et al. (2006) that have been extensively tested with BPZ. These re-calibrated SEDs are based on the star-forming (Im), spiral (Scd, Sbc), and elliptical (El) galaxy templates from Coleman et al. (1980), the star bursting galaxy templates with different reddening (SB2, SB3) from Kinney et al. (1996), and the faint blue galaxy SEDs with ages of 25 and 5 Myr and metallicities of Z=0.08 without dust from Bruzual & Charlot (2003), described in section §2.4.1 of Coe et al. (2006). We interpolate between adjacent galaxy SED templates for an additional two SED templates in the photo-z fit, similar to Benítez et al. (2004) and Coe et al. (2006).

Table 2.2. Catalog of Bayesian Photometric Redshifts

ID[a]	z_b[b]	t_b[c]	ODDS[d]	χ^2_ν[e]	$\chi^2_{\rm mod}$[f]	z_b1[g]	t_b1[c]	ODDS1[h]	z_b2[g]	t_b2[c]	ODDS2[h]
1	$0.17^{+0.11}_{-0.12}$	3.00	1.000	16.40	0.20	$0.17^{+0.07}_{-0.07}$	3.00	1.000	···	···	···
7	$0.01^{+0.10}_{-0.01}$	6.67	0.990	7.59	0.49	$0.01^{+0.10}_{-0.01}$	6.67	0.990	$1.81^{+0.02}_{-0.02}$	6.00	1.000
8	$0.52^{+0.15}_{-0.15}$	1.00	1.000	21.81	0.01	$0.52^{+0.07}_{-0.08}$	1.00	1.000	···	···	···
13	$0.43^{+0.14}_{-0.14}$	3.33	1.000	8.00	0.21	$0.43^{+0.11}_{-0.08}$	3.33	1.000	···	···	···
14	$0.54^{+0.15}_{-0.15}$	2.33	1.000	46.40	0.06	$0.54^{+0.07}_{-0.08}$	2.33	1.000	···	···	···
15	$0.52^{+0.15}_{-0.16}$	1.67	0.970	1.98	0.09	$0.52^{+0.03}_{-0.12}$	1.67	0.520	$0.57^{+0.10}_{-0.02}$	2.00	0.443
22	$3.23^{+0.41}_{-0.41}$	5.00	0.999	7.34	0.44	$3.23^{+0.19}_{-0.29}$	5.00	0.977	$2.90^{+0.04}_{-0.10}$	3.33	0.023
24	$1.39^{+0.78}_{-0.23}$	7.00	0.363	1.56	1.68	$1.39^{+0.12}_{-0.13}$	7.00	0.247	$1.65^{+0.22}_{-0.14}$	6.67	0.429
33	$0.78^{+0.17}_{-0.17}$	3.67	1.000	1.96	0.08	$0.78^{+0.09}_{-0.09}$	3.67	1.000	···	···	···
35	$1.69^{+0.26}_{-0.26}$	6.00	0.996	4.81	0.60	$1.69^{+0.16}_{-0.27}$	6.00	0.996	$0.02^{+0.03}_{-0.01}$	6.67	0.004

Note. — Table 2.2 is shown in full in the appendix (Table C.2). A portion is shown here for guidance regarding its form and content. In addition to the most likely redshift, we report the two most likely redshifts for each galaxy when available, along with the redshift ranges for each peak and the fractions of $P(z)$ contained in those peaks.

[a]ID numbers from Coe et al. (2006).

[b]Bayesian photometric redshift (BPZ) and uncertainty from 95% confidence interval.

[c]Template SEDs used in the BPZ code as described in §2.4.1.1, where 1=El_cww, 2=Scd_cww, 3=Sbc_cww, 4=Im_cww, 5=SB3_kin, 6=SB2_kin , 7=25Myr, and 8=5Myr. Non-interger values are for templates interpolated between adjacent templates.

[d]Integrated $P(z)$ contained within $0.1(1+z_b)$.

[e]Chi square quality of photo-z fit.

[f]Modified reduced chi-square fit, where the templates are given uncertainties.

[g]Redshift ranges for the two most likely peaks.

[h]Integrated $P(z)$ contained within the local minima of $P(z)$ for each peak.

SED templates are not always a good match for each specific galaxy, and when it is not possible to get a good fit to the SED template, then the resulting redshift may not be accurate. As a diagnostic of the goodness of fit, the BPZ code provides a reduced chi square (χ^2_ν) value. However, high χ^2_ν values do not always indicate an unreliable redshift. Bright galaxies with small photometric uncertainties will have larger χ^2_ν values than faint galaxies with larger photometric uncertainties for the same numerator in χ^2 (also known as the variance), yet have more reliable redshifts (see Figure 21 in Coe et al., 2006). This problem occurs because the systematic uncertainties of the SED templates are not taken into account, making χ^2_ν no longer represent the relative quality of the fit. Nonetheless, a mechanism to evaluate the quality of the fits is required to trim the sample to reliable redshifts. To this end, Coe et al. (2006) introduce a modified reduced chi square ($\chi^2_{\rm mod}$) value that assigns an uncertainty to the SED templates in addition to the uncertainty in the photometry of the galaxy. For clarity, we reproduce the equation from Coe et al. (2006) here:

$$\chi^2_{\rm mod} = \sum_\alpha \frac{(f_\alpha - f_{T\alpha})^2}{\sigma^2_{f_\alpha} + \sigma^2_{f_T}}/\nu, \tag{2.3}$$

where f_α are the observed fluxes, σ_{f_α} is the error in observed fluxes, and f_{T_α} are the model fluxes, normalized to the observed fluxes. $\sigma_{f_{T_\alpha}}$ represent the model flux errors, which are set by Coe et al. (2006) to $\sigma_{f_{T_\alpha}} = \max_\alpha(f_{T\alpha})/15$. While the definition of $\sigma_{f_{T_\alpha}}$ is arbitrary, it was picked such that the resultant $\chi^2_{\rm mod}$ is a more realistic measure of the goodness of fit. This is especially important for bright galaxies, as uncertainties in the templates dominate the error budget, and the χ^2_ν values are not useful. The reported χ^2_{mod} values are reduced chi square values, obtained by dividing by the number of degrees of freedom, ν. The number of degrees of freedom is the difference between the number of filters observed and the number of parameters (in this case there are three fit parameters, redshift, template, and amplitude). The minimum number of filters used is 5 and the maximum is 7, so the range of ν in our study is $2 \leq \nu \leq 4$. We note that $\chi^2_{\rm mod}$ is calculated after the photo-z determinations, and does not affect $P(z)$.

If the quality of the fit to the SED template is good, then the `ODDS` parameter is useful in measuring the spread in $P(z)$. A galaxy with high `ODDS` has a

single peak in $P(z)$, while multiple or very wide peaks yield low ODDS. In general, restricting the photometric sample to those objects with ODDS $> 0.9 - -0.99$ yield clearly defined redshifts (Benítez, 2000; Benítez et al., 2004; Coe et al., 2006). In this paper we are conservative and restrict our sample to objects with the best vales of ODDS, those with ODDS > 0.99. Additionally, selecting galaxies based on SED template type (t_b) can useful when selecting a specific type of galaxy, where 1=El_cww, 2=Scd_cww, 3=Sbc_cww, 4=Im_cww, 5=SB3_kin, 6=SB2_kin , 7=25Myr, and 8=5Myr. For instance, in selecting LBGs we constrain ourselves to galaxies with $t_b > 3$, which only include star-forming galaxy templates. The redshifts, redshift uncertainties for a 95% confidence interval, t_b, ODDS, χ^2_ν, and $\chi^2_{\rm mod}$ are all tabulated in Table 2.2.

2.4.1.2 Photometric Redshift Measurement Uncertainties

It is important to understand the origins of photo-z uncertainties in order to have confidence in their values. There are two types of uncertainties in photo-z's: 1) photometric measurement uncertainties and 2) template mismatch variance (Lanzetta et al., 1998; Fernández-Soto et al., 2001, 2002; Chen et al., 2003). Photometric measurement uncertainties are well understood, and they are responsible for the width of $P(z)$, which determines the reported photo-z uncertainties. Faint galaxies with larger photometric measurement uncertainties will yield larger uncertainties in the photo-z's than brighter galaxies. If the photometric measurement uncertainties are very large, then the photo-z will be poorly constrained, because this results in multiple peaks in $P(z)$ corresponding to many possible redshifts. The other possible uncertainty comes from template mismatches, which is a systematic error due to the finite number of templates used in the photo-z determination. Not all galaxies will be well represented by our template SEDs, yielding large χ^2_ν values.

One method to decrease template mismatch errors is to introduce more template SEDs, since that increases the chance that there exist good matching SED templates for each galaxy. While this can improve low-redshift performance, it also increases the number of degenerate solutions and therefore gives poorer high-

redshift performance (Hildebrandt et al., 2008). Degenerate photo-z's occur when different SED templates fit the photometry equally well, resulting in multiple peaks in $P(z)$ and therefore multiple possible redshifts. We consider galaxy redshifts degenerate if they have two or more peaks in $P(z)$ at 95% confidence separated by $\Delta z > 1$. In these cases, the resultant reported uncertainties are very large and the galaxy redshift is poorly constrained. We are mainly interested in good performance at high redshift and therefore do not increase the number of SED templates.

Template mismatches are also the cause for "catastrophic" photo-z errors that occur, where the photo-z is incorrect and the uncertainty does not include the correct redshift (Ellis, 1997; Fernández-Soto et al., 1999; Benítez, 2000). Catastrophic photo-z errors typically occur because multiple peaks in $P(z)$ are incorrectly suppressed, leaving only one peak. The suppression of multiple peaks in bright galaxies likely occur because of their small photometric uncertainties yielding large χ^2_ν values without taking into account the systematic uncertainties in the SED templates, which exaggerate the differences between the different SED template fits that correspond to different peaks in $P(z)$. This suppresses the peaks at other redshifts, resulting in possible "catastrophic" photo-z errors (Dan Coe, private communication).

It is likely that the incorrect suppression of peaks in $P(z)$ can be fixed through the introduction of SED uncertainties in the initial χ^2 fit, although such an addition requires an understanding of those uncertainties using large surveys with both photo-z and spec-z's. This is neither in the scope of the UDF or this paper, and is being investigated elsewhere (Coe et al. in prep). In the mean time, the best we can do is reject photo-z's based on their $\chi^2_{\rm mod}$ values. However, $\chi^2_{\rm mod}$ is not a true statistical test like χ^2_ν, and therefore cuts normally appropriate for χ^2_ν are not valid for $\chi^2_{\rm mod}$. Additionally, galaxies with J and H-bands data have median $\chi^2_{\rm mod}$ larger by ~ 0.7 than those without infrared (IR) data, although the inclusion of the IR data improves the reliability of the photo-z's because of the significantly increased lever arm (Coe et al., 2006). We therefore don't use the same cut as used in Coe et al. (2006) ($\chi^2_{\rm mod} < 1$), but rather use $\chi^2_{\rm mod}$ to conservatively remove

possible bad photo-z fits. While we do present all the photo-z fits, we only include those with $\chi^2_{\rm mod} < 4$ for our $z \sim 3$ galaxy sample. This cut only reduces the total number of galaxies with photo-z's by $\sim$5% (to 1385 galaxies).

2.4.1.3 Comparison of Photometric and Spectroscopic Redshifts

In order to test the accuracy of the photo-z's, we compare the redshifts with spectroscopic redshifts (spec-z's). We compile a list of 100 reliable spec-z's in the UDF that match our sample from §2.3.5 (see Table 2.3)[5]. In this sample, 18 spec-z's are from the VIMOS VLT Deep Survey (VVDS; Fèvre et al., 2004), where we only include redshifts with 95% confidence and multiple lines. Another 22 redshifts come from the GOODS VLT VIMOS survey (VIMOS; Popesso et al., 2009), where we include redshifts with A or B quality spectra. These spectra have good cross-correlation coefficients of the spectra with the templates and multiple lines are well identified. An additional 6 redshifts are from Szokoly et al. (2004) using the VLT FORS1/FORS2 spectrographs, where we use only those flagged as 'reliable' redshifts (quality flags "2" or "2+"). The remaining 57 redshifts are from the GOODS VLT FORS2 survey (FORS2; Vanzella et al., 2005, 2006, 2008, 2009), where we only include redshifts from A or B quality spectra. We do not include redshifts from the slitless spectra obtained as part of the Grism ACS Program for Extragalactic Science (GRAPES) (Pirzkal et al., 2004), since the redshift determinations do not provide an independent check to photo-z's because photo-z's were used to help identify the emission lines (Xu et al., 2007).

The photo-z's agree relatively well with the spec-z's (see left panel of Figure 2.5), and have 100% agreement in the redshift interval of interest ($2.5 \lesssim z \lesssim 3.5$), although only five objects have spec-z's at these redshifts. There are clearly some galaxies that have incorrect photo-z's at lower redshift where the u-band does not sample the Lyman break. Of the 100 galaxies from Table 2.3, 97 have $\chi^2_{\rm mod} < 4$, of which 93 have `ODDS` > 0.99. The galaxy at a spec-z of 1.99 (ID 6834) has a $\chi^2_{\rm mod} \sim 17$ and the resultant photo-z should be ignored.

[5]Most of these redshifts are based on observations made with ESO Telescopes at the La Silla or Paranal Observatories under programme ID(s) 66.A-0270(A), 67.A-0418(A),171.A-3045, 170.A-0788, 074.A-0709, and 275.A-5060.

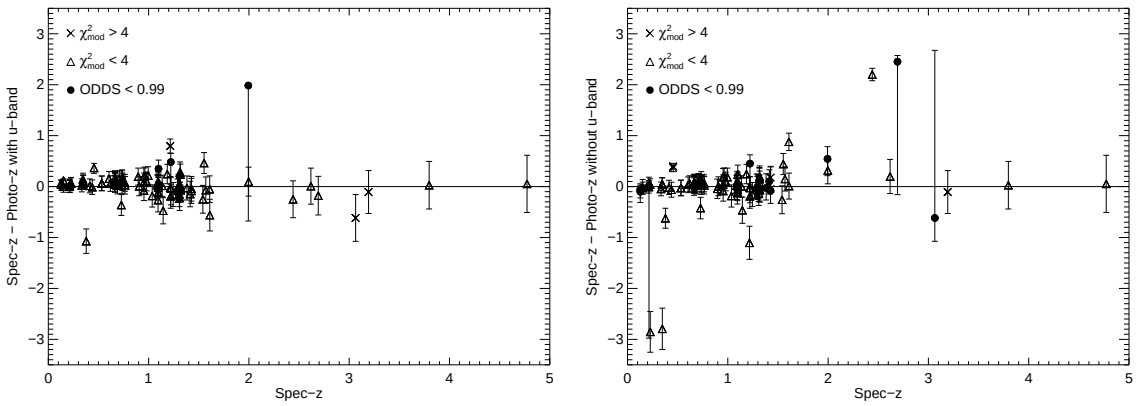

Figure 2.5 Differences in spectroscopic redshifts (spec-z's) and photometric redshifts (photo-z's) compared to the 100 spec-z's described in §2.4.1.3, where the photo-z uncertainties are for a 95% confidence interval. The left panel plots the difference in spec-z and photo-z with u-band, and the right panel plots the same but for the photo-z's without the u-band. The quality of the photometric redshift fit is described by the $\chi^2_{\rm mod}$ (see §2.4.1.1), where objects with good fits, $\chi^2_{\rm mod} < 4$, are marked with triangles, and objects with $\chi^2_{\rm mod} > 4$ are marked with open crosses. There is one point in the left panel at $z \sim$2 that has a large $\chi^2_{\rm mod}$ (~ 17) and should be ignored as it is not a good fit to any SED templates with the u-band.

Table 2.3. Catalog of Galaxies with Reliable Spectroscopic Redshifts in the UDF

ID[a]	Survey	$z_{\rm spec}$	z_b[b]	$\chi^2_{\rm mod}$[c]	ODDS[d]	V (mag)	$u-V$ (mag)	$u-B$ (mag)	$V-z'$ (mag)
3088	FORS2	0.13	$0.06^{+0.10}_{-0.06}$	1.91	1.00	22.85±0.00	1.99±0.01	1.16±0.01	0.48±0.00
5670	VVDS	0.13	$0.09^{+0.11}_{-0.09}$	0.03	1.00	21.23±0.00	2.00±0.00	1.12±0.00	0.54±0.00
1971	VVDS	0.15	$0.03^{+0.10}_{-0.03}$	0.07	1.00	20.46±0.00	1.48±0.00	0.82±0.00	0.37±0.00
2974	VIMOS	0.15	$0.15^{+0.11}_{-0.11}$	1.51	1.00	24.08±0.01	1.97±0.03	0.99±0.03	0.49±0.01
5620	VVDS	0.21	$0.21^{+0.12}_{-0.12}$	0.75	1.00	23.42±0.00	0.88±0.01	0.43±0.01	0.01±0.00
3822	VIMOS	0.21	$0.18^{+0.12}_{-0.12}$	0.59	1.00	19.14±0.00	1.91±0.00	0.87±0.00	0.70±0.00
1000	FORS2	0.21	$0.21^{+0.12}_{-0.13}$	1.08	0.97	23.39±0.00	0.93±0.01	0.46±0.01	-0.01±0.01
5606	VVDS	0.23	$0.16^{+0.11}_{-0.11}$	0.05	1.00	21.14±0.00	1.79±0.00	0.82±0.00	0.55±0.00
5491	VIMOS	0.23	$0.17^{+0.11}_{-0.12}$	1.94	1.00	22.24±0.00	0.64±0.00	0.30±0.00	-0.15±0.00
7847	VVDS	0.33	$0.31^{+0.13}_{-0.13}$	0.02	1.00	22.00±0.00	2.97±0.01	1.36±0.01	1.10±0.00

Note. — Table 2.3 is shown in full in the appendix (Table C.3). A portion is shown here for guidance regarding its form and content. Redshift surveys are VVDS (Fèvre et al., 2004), VIMOS (Popesso et al., 2009), Szokoly et al. (2004), and FORS2 (Vanzella et al., 2005, 2006, 2008, 2009). V magnitudes are total AB magnitudes, and colors are isophotal colors. All photometry other than the u-band are from Coe et al. (2006). Nondetections in u-band are given 3σ limiting magnitudes.

[a]ID numbers from Coe et al. (2006).

[b]Bayesian Photometric Redshift (BPZ) and uncertainty from 95% confidence interval.

[c]Modified reduced chi square fit, where the templates are given uncertainties.

[d]Integrated $P(z)$ contained within $0.1(1+z_b)$.

Only object 8585 meets our criteria, but has a significantly different photo-z than its spec-z and does not include the correct redshift in its $P(z)$. This object, with a spec-z of $z = 0.3775$ (Fèvre et al., 2004) and a photo-z of 1.45 ± 0.24, is a case where the spec-z may be wrong. In general we tried to minimize this possibility by selecting reliable spec-z's, but the spec-z's can still be wrong as seen in some comparisons of Fernández-Soto et al. (2001). In our case, the photometric redshift yields a good fit to the SED templates, and the fit to the SED template at the spec-z is a bad fit. The published spectrum shows that the spec-z is mainly determined by the $H\alpha$ line. This could easily be confused with the OII line for a galaxy with a redshift of $z = 1.43$, which would be consistent with our photo-z. This leaves one galaxy with a possible "catastrophic error", although it is not in the redshift interval of interest ($2.5 \lesssim z \lesssim 3.5$).

2.4.1.4 Improvement of photo-z's with the Addition of the u-band

A comparison of the redshift interval ($2.5 \lesssim z \lesssim 3.5$) in the two panels of Figure 2.5 shows a significant improvement in the photo-z's with u-band data. The left panel depicts photo-z's with u-band data while the right panel depicts photo-z's without u-band data. The u-band helps prevent catastrophic redshift errors that can occur because of a similarity in the colors of low-redshift galaxies and high-redshift galaxies. (Ellis, 1997; Fernández-Soto et al., 1999; Benítez, 2000). Usually, this degeneracy causes $P(z)$ to have multiple peaks representing both possible redshifts in the absence of u-band data (Coe et al., 2006). As discussed in §2.4.1.2, however, sometimes secondary peaks are absent yielding incorrect redshift uncertainties and possibly incorrect redshifts. For example, three galaxies (IDs 830, 4267, 5491) with $\chi^2_{\rm mod} < 4$ and ODDS> 0.99 have catastrophic redshift errors without u-band photometry and gain accurate photo-z's based on their spec-z's after we include the u-band (e.g. see Figure 2.6). As expected, the u data clearly improve the photo-z's of galaxies at $z \sim 3$ when compared to the spec-z's. However, we are constrained to discussing small number statistics, and the true contamination fraction is unknown.

We would ideally like to compare a larger number of $z \sim 3$ photo-z's to

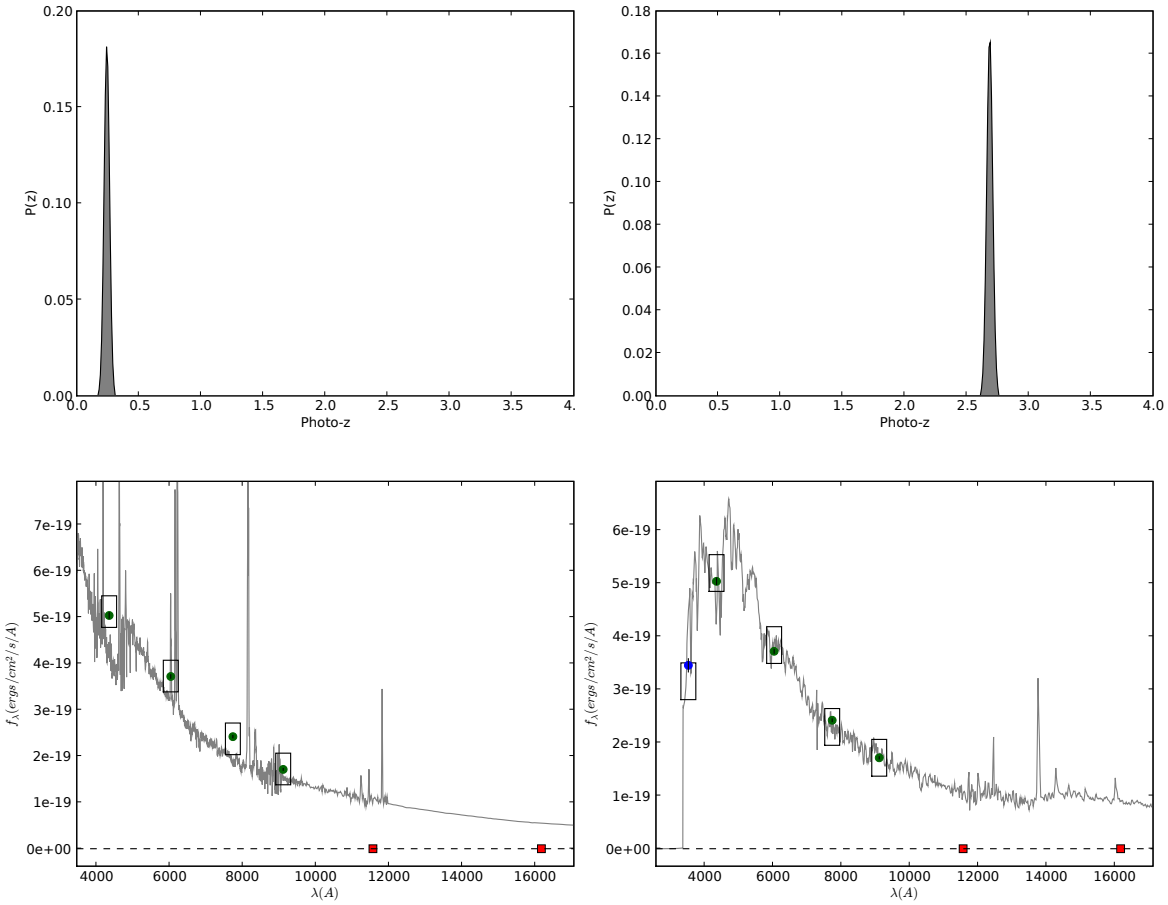

Figure 2.6 Object 830: an example of a galaxy with $z_{\rm spec} = 2.44$ (Popesso et al., 2009) that has a catastrophic redshift error before the addition of the u-band. The left-hand side figures show the photo-z fit without u-band with z=0.24±0.15 and the right-hand side figures show the fit with u-band with z=2.72±0.37. The rectangles represent the assumed uncertainty of the SED template used for $\chi^2_{\rm mod}$, blue points are the u-band data, green are the ACS data, and red are the NICMOS data. Filled circles are for detected and observed data points, and squares are for unobserved data points. The addition of the u-band rules out the possibility of this being a low-redshift galaxy, and corrects the catastrophic redshift.

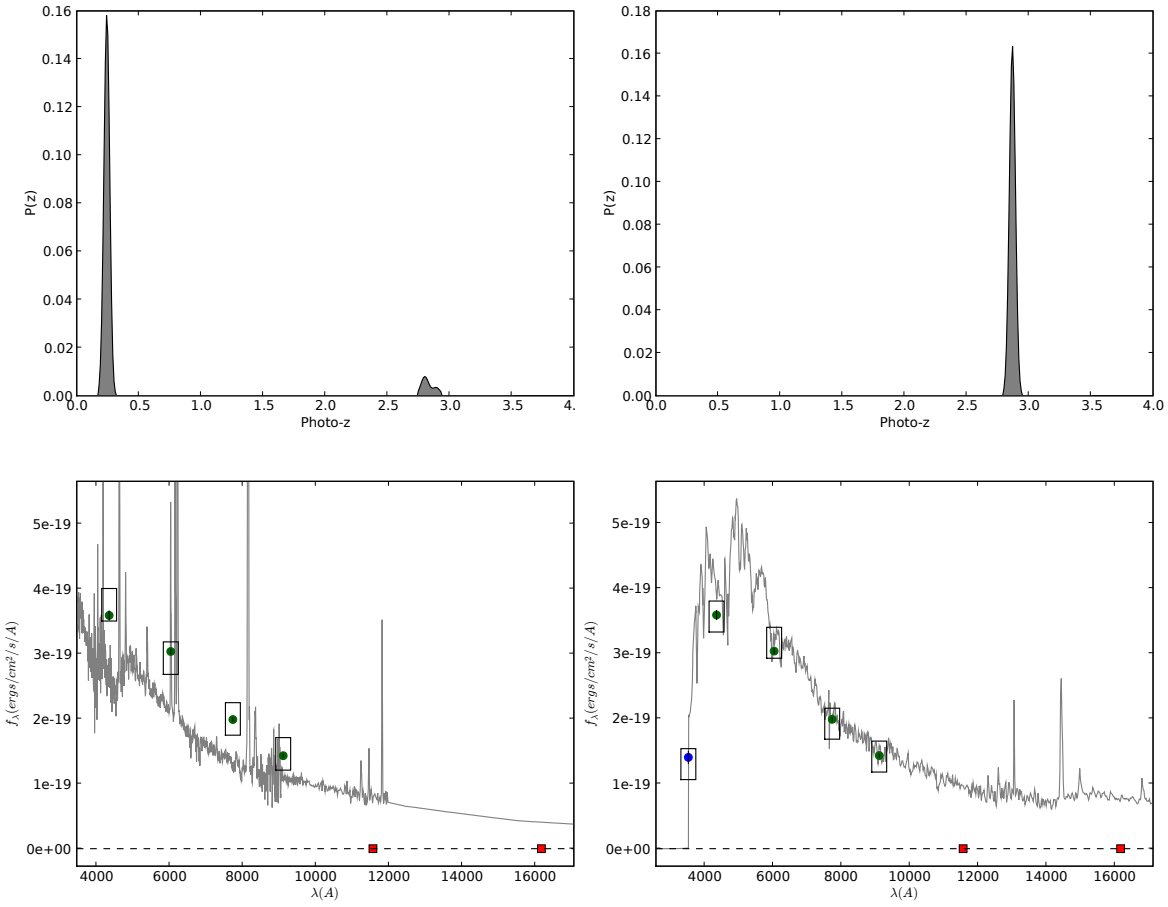

Figure 2.7 Object 97: An example of a galaxy with $z_{\rm spec} = 2.69$ (Popesso et al., 2009) that changes photo-z's with the addition of the u-band. The left-hand side figures shows the photo-z fit without u-band with z=$0.24^{+2.67}_{-0.14}$ and the right-hand side figures show the fit with u-band with z=2.90±0.38. The addition of the u-band rules out the possibility of this being a low-redshift galaxy, and therefore $P(z)$ only has one significant peak.

spec-z's to get a better understanding of the improvement of the photo-z's with the addition of the u-band, although such spectroscopic data are lacking in the UDF. However, since the u-band samples the Lyman break of $z \sim 3$ galaxies, and we know that the photo-z's with u-band are more reliable than those without, we can investigate the changes in the photo-z's. We therefore compare all the photo-z's with $\chi^2_{\rm mod} < 4$ of galaxies with and without the u-band data in Figure 2.8, which highlights two effects. The first is that $P(z)$ changes markedly for 125 galaxies, mostly in the redshift interval $2 \lesssim z \lesssim 3$, where the u-band probes the Lyman break. Of these, 102 change their photo-z's from $z \leq 1$ to $z \sim 2-3$, whereas 23 switch in the other direction. This change is a result of the code selecting different $P(z)$ peaks as the most probable redshift for galaxies having multiple peaks .

The second effect shown in Figure 2.8 is the removal of the degeneracy of $z \sim 3$ and $z \sim 0.2$ photo-z's, due to the removal of one of the peaks in $P(z)$. One hundred seventy five galaxies went from being degenerate to non-degenerate, and are marked by the red crosses in Figure 2.8. Not all of the degenerate photo-z's are removed; however, 51 galaxies are degenerate between these redshifts as marked by the blue crosses in Figure 2.8, of which 17 were not degenerate before the addition of the u-band. The new degeneracies occur when the u-band best fit redshift is different compared to the best-fit to the other bands. The old degeneracies that are not removed occur when the u-band does not conclusively rule out another template, often because they are faint. Figure 2.8 also includes galaxies with $\chi^2_{\rm mod} < 4$ in the photometric redshift fits selected to be at $z \sim 3$ using the color selection method described in §2.4.2 (below), which is useful when comparing the two methods. Figure 2.7 shows an example of both effects, where the u-band changes the photo-z and removes a secondary peak in $P(z)$ for a high-redshift galaxy.

Out of 1384 galaxies with $\chi^2_{\rm mod} < 4$, there are 274 galaxies that have photo-z's in the interval $2.5 \leq z \leq 3.5$ without u-band. The addition of the u-band increases this number by 91, to 365 galaxies that have a photo-z in this redshift interval either with or without the u-band (including the 23 that switched to low redshift). Of these 365 galaxies, 161 galaxies either had their photo-z changed

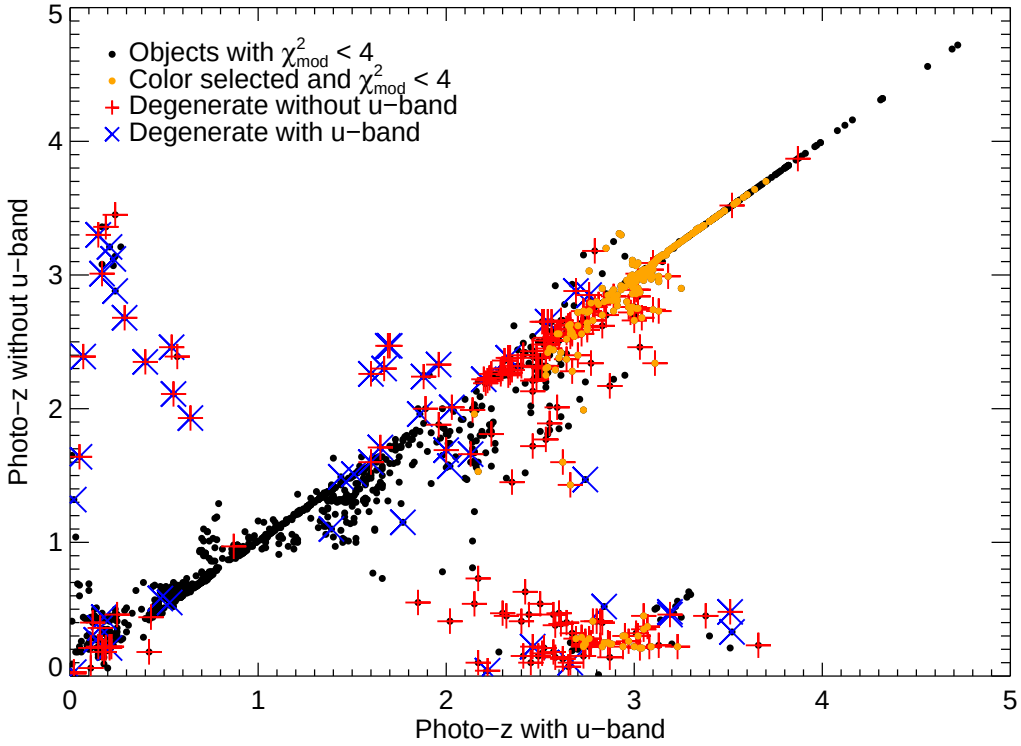

Figure 2.8 Photo-z's without u-band data versus photo-z's with u-band data for objects with $\chi^2_{\rm mod} < 4$ in both cases. The red crosses designate galaxies where the photo-z's are degenerate without u-band, and the blue crosses are for degenerate photo-z's with u-band. The degeneracy in redshift occurs when galaxies have at least two significant peaks in the $P(z)$, usually due to the degeneracy in the colors of a low-redshift galaxies and high-redshift galaxies. The orange dots are those objects that are selected using the color selection technique in §2.4.2. We note although the photo-z's with u-band may be incorrect, the addition of the u-band made a large difference in the photo-z's of $z \sim 3$ galaxies.

or the degeneracy removed with the addition of the u-band. This shows that the addition of the u-band significantly changed the photo-z's of the $z \sim 3$ galaxy sample by $\sim 50\%$.

2.4.2 Color Selection

Color selection is an efficient means to select high-redshift galaxies, and extensive research has been carried out to determine the best color criteria to minimize the interloper fraction from low-redshift galaxies or stars, e.g. Steidel et al. (1996a,b, 1999, 2003); Adelberger et al. (2004); Cooke et al. (2005). The color selection criteria used in these studies are based on predicted colors of model star-forming galaxies at high redshift, which are then confirmed with spec-z's, that result in known contamination fractions between 3%–5% (Steidel et al., 2003; Reddy et al., 2008). Such low contamination fractions are achieved by avoiding colors where low-redshift galaxies reside. While color selection techniques do not provide a complete sample of LBGs, they do an excellent job of selecting galaxies in a specific redshift range, as evidenced by their contamination fractions. While the UDF data provide an extraordinary data set, they also use a different set of filters than used in previous color selection studies, meaning we must define new color criteria for LBG selection. We therefore develop and calibrate new color criteria for selecting $z \sim 3$ LBGs using the same methodology. Since our motivation is to generate a sample of galaxies to put constraints on the star formation efficiency at high redshift, we choose our color selection criteria to best minimize possible low-redshift interlopers (see below).

2.4.2.1 Color Selection Criteria

Using the same approach as Steidel et al. (1996a,b, 1999, 2003), Adelberger et al. (2004), and Cooke et al. (2005), we derive galaxy colors by evolving different galaxy SED templates to high redshift convolved with the total throughput of the different filters shown in Figure 2.2. We include galaxy SED templates consistent with our photometric redshifts described in §2.4.1, with galaxy SED templates from Kinney et al. (1996), Coleman et al. (1980), and Bruzual & Charlot (2003).

In addition we use a 2.0 Gyr Elliptical Galaxy from the Bruzual & Charlot (2003) synthesis code (E2G) since it is quite different than the elliptical galaxy SED template from Coleman et al. (1980) and represents possible low-redshift galaxies we wish to avoid. We apply the K-correction for different redshifts and correct for the opacity from the intergalactic medium by using estimates from Madau (1995). The resultant colors and redshifts of the SED template galaxies are used to determine the appropriate color criteria to maximize the number of LBG candidates at $z \sim 3$ while minimizing the contamination from objects at other redshifts. We test multiple color–color planes and find that for our set of filters, $z \sim 3$ LBGs can best be selected in a $(u - V)$ versus $(V - z')$ color–color plane. Figure 2.9 plots the expected colors of different model galaxies at different redshifts in the $(u - V)$ versus $(V - z')$ diagram.

The region defining candidate $z \sim 3$ LBGs is indicated with the dashed black line in Figure 2.9. In order to avoid selecting low-redshift galaxies, this selection region excludes SED template colors for $z \leq 2.5$. The deviations from SED templates and photometric errors will cause intrinsic scatter in the color–color plane. We therefore leave ~ 0.2 mag between our color selection and the low-redshift elliptical galaxy SEDs that cause the largest contamination for galaxies at $z \sim 3$. In addition to the cut in the $(u - V)$ versus $(V - z')$ diagram, we also apply secondary color cuts using the $(u - B)$ color to improve our color selections by removing potential interlopers. We also include a cut on V-band magnitude, where the bright end does not remove any LBG candidates and the faint end is the V-band magnitude determined in §2.3.5 to keep the S/N of the u-band $> 3\sigma$. The following conservative constraints are used to select LBG candidates:

$$(u - V) \geq 1.0, \tag{2.4}$$

$$(u - B) \geq 0.8, \tag{2.5}$$

$$(V - z') \leq 0.6, \tag{2.6}$$

$$3(V - z') \leq (u - V) - 1.2, \tag{2.7}$$

$$23.5 \leq V \leq 27.6. \tag{2.8}$$

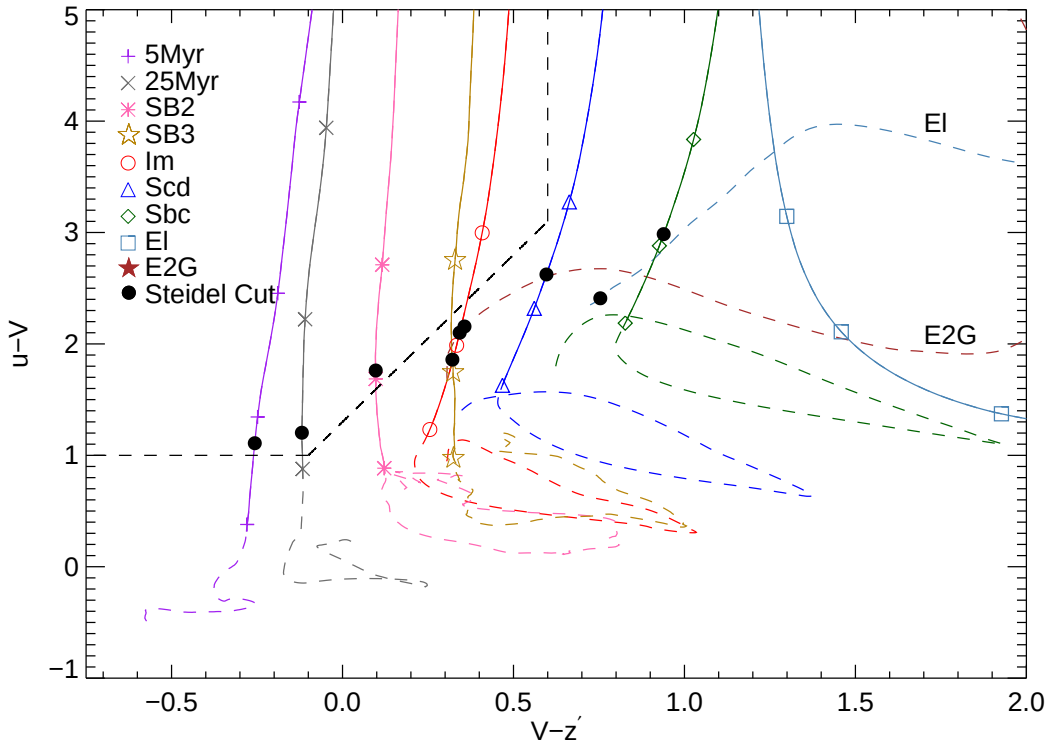

Figure 2.9 $(u-V)$ versus $(V-z')$ color–color diagram depicting different model galaxies at different redshifts, where the solid lines are $z > 2.5$, the dashed lines are $z < 2.5$, and the symbols represent redshifts of 2.5, 2.8, 3.0, and 3.2 which increase with increasing $(u-V)$ color. We include galaxy SED templates from Kinney et al. (1996) for star bursting galaxies with different reddening (SB2, SB3), from Coleman et al. (1980) for star-forming galaxies (Im), spiral galaxies (Scd, Sbc), and elliptical galaxies (El). In addition, we use and two faint blue galaxy SEDs with ages of 25 and 5 Myr and metallicities of Z=0.08 (25Myr, 5Myr), and a 2.0 Gyr Elliptical Galaxy (E2G) from the Bruzual & Charlot (2003) synthesis code. The area above and to the left of the dashed black line is the region selecting candidate LBGs. The filled black circles are the borderline colors for each SED template that correspond to the $z \sim 3$ color cut by Steidel et al. (2003), as described in §2.4.2.2.

2.4.2.2 Reliability of Color Selection

In order to test our selection criteria, we compare our selection of the 100 galaxies with reliable spec-z's as described in §2.4.1.3 and Table 2.3. These spectra allow us to test the efficacy of selecting targets via the $(u - V)$ versus $(V - z')$ color plane (Figure 2.10). No $z < 2.5$ galaxies with reliable spec-z's passed our color cut confirming that our cut effectively excludes low-redshift galaxies. We note that there are three $z > 2.5$ objects that do not meet our color criteria in Figure 2.10. The $z = 3.68$ object (triangle, object 865) is classified as a quasar by Szokoly et al. (2004) due to active galactic nuclei (AGNs) activity. The $z = 4.77$ object with $(V - z')$ is a bright V-band dropout galaxy, whose V-band magnitude (27.26) is just bright enough to remain in the sample before the color cuts. Finally, the $z = 3.80$ is also excluded by our color cut due to a decrease in the V-band magnitude, reddening the color.

There are a number of objects that could contaminate our sample of $z \sim 3$ LBGs because their spectra are unusual and thus do not match our model SEDs. While at brighter magnitudes the color selection criteria include stars and AGNs, for our V > 23.5 sample the color selection criteria are mainly contaminated by low-redshift galaxies at $z \lesssim 0.2$ (Reddy et al., 2008). Additionally, about 1/3 of the Distant Red Galaxies (DRGs) fall within the color selection sample of Steidel (van Dokkum et al., 2006), which is similar to our criteria. DRGs are galaxies at $z \gtrsim 2$ that have faint UV luminosities, have previously undergone their episode(s) of star formation (Franx et al., 2003), and have stellar masses $\gtrsim 10^{11} M_{\odot}$ (van Dokkum et al., 2004, 2006). However, given the DRGs' estimated space density of $(2.2 \pm 0.6) \times 10^{-4}$ Mpc^{-3} (van Dokkum et al., 2006), Reddy & Steidel (2009) conservatively determine that the fractional contribution would be ∼2% for UV-faint sources such as our sample.

As discussed earlier, to get a sense of the number of possible interlopers, we would like to have a large number of spectra to determine the contamination fraction. However, we only have a relatively small number of spectra (100) as shown in Figure 2.10 and Table 2.3. Instead, we compare our color cuts to the $(Un - G)$ versus $(G - R)$ color cuts of Steidel et al. (2003) for redshifts $2.7 \leq z \leq 3.4$, and

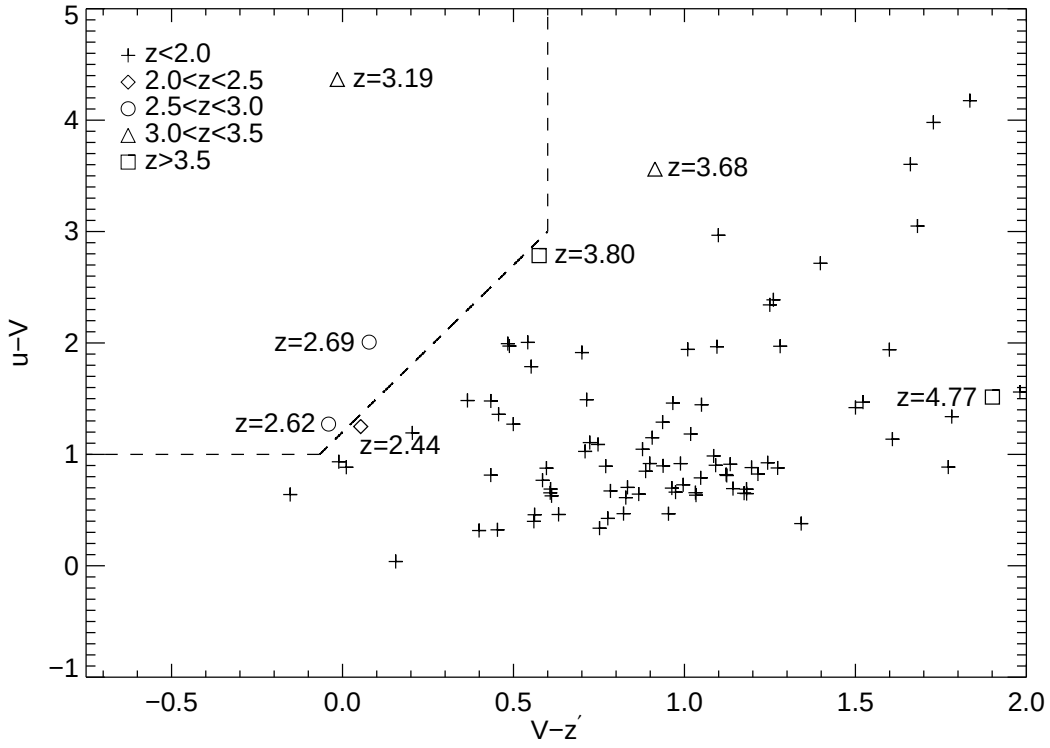

Figure 2.10 Comparison of our selection criteria to 100 reliable spec-z galaxies as described in §2.4.1.3. Object redshifts are binned and represented with different symbols, where crosses are for objects with $z < 2.0$, diamonds for $2.0 < z < 2.5$, open circles for $2.5 < z < 3.0$, triangles for $3.0 < z < 3.5$, and squares for $z > 3.5$. The dashed line depicts our color cut.

assume that our sample has similar contamination. In Figure 2.9, we determine the redshift that corresponds to Steidel's color cut for a given SED template in $(Un - G)$ and $(G - R)$. We then determine the $(u - V)$ and $(V - z')$ colors that this SED template has at this redshift and compare those resulting colors to our color criteria by marking them with filled black circles in Figure 2.9. The filled black circles are outside or near the edge of our color selection criteria, which shows that we are more conservative in our cut for the redder SED templates and about equivalently conservative for the bluer ones as the cut in Steidel et al. (2003). We therefore infer that our contamination fraction is comparable to those of Steidel et al. (2003) and Reddy et al. (2008), where the contamination fraction of $z \sim 3$ LBGs is $\sim 3\%$ for objects $23.5 \leq V \leq 25.5$ mag.

2.5 Sample of z $\sim$ 3 Galaxies

Photometric redshifts and color selection are both good ways to select $z \sim 3$ galaxies. Photometric redshifts have the advantage of creating a larger sample since they can measure redshifts in regions of color space that color selected samples avoid because of low-redshift galaxies. They also use more information than color selection, including all colors simultaneously to constrain the redshift. However, while the error rate of the photo-z's is not well defined, color selection is efficient, has a clearly defined contamination fraction, and allows direct comparisons to other studies. The completeness of our LBG selection is limited primarily on the u-band depth because the ACS bands from HST are deeper. In order to characterize this completeness, we compare our color selected LBGs with other studies in §2.5.3. To justify such comparisons, we compare the redshift distribution of this sample in §2.5.1, and investigate our uncertainties from cosmic variance in §2.5.2.

In choosing our color selection criteria we chose to be conservative and create a less complete catalog with a small contamination fraction similar to that of Steidel et al. (2003) and Reddy et al. (2008) of 3%. Depending on the purpose, a higher contamination fraction is acceptable in exchange for a larger and more complete sample. The photo-z sample yields a more complete sample, and may

even have a similar contamination fraction based on our spectroscopic sample, although due to our small numbers at the redshift of interest, it is not clear at this point. If the lowest contamination fraction possible is needed, a subset of $z \sim 3$ LBGs that are both color selected and photo-z selected are the most robust candidates available.

We present both samples of $z \sim 3$ LBGs in Table 2.4, for a total of 407 candidates, along with their photo-z's and colors. We distinguish the samples by designating them as either color selected, photo-z selected, or both. The photo-z sample consists of galaxies in the redshift interval $2.5 \leq z \leq 3.5$ that have $t_b > 3$, ODDS > 0.99, and $\chi^2_{\rm mod} < 4$, and contains 365 galaxies. Of the 42 galaxies not included in our photo-z sample, two have $z \sim 2.2$, 11 have $z > 3.5$, eight others have ODDS < 0.99, and 21 others have $\chi^2_{\rm mod} > 4$. The color selected sample contains 260 galaxies, all of which have photo-z's with $z > 2$, with 258 that have $z > 2.5$ and 11 that have $z > 3.5$. However, the overlap of the two samples is only 216 galaxies. We show the final LBG selection in Figure 2.11, which plots all objects from Table 2.1 on a color–color diagram, with 287 galaxies falling in the color selection region corresponding to constraints 2.4, 2.6, and 2.7 from §2.4.2.1. There are 27 galaxies that are in the selection area in this diagram, but are rejected by the $(u - B)$ color (constraint 2.5), leaving 260 galaxies that are color selected. The objects marked as blue stars that are selected by photo-z's but not by color selection are generally galaxies at $z \sim 2.8$ that are missed by our color selection criteria in order to avoid elliptical and low-redshift galaxies.

2.5.1 Redshift Distribution

In order to understand the redshift distribution of the color selected LBG sample, we look at the photo-z's that meet the color selection criteria and our photo-z criteria of $\chi^2_{\rm mod} < 4$. This leaves a sample of 235 galaxies that have a mean redshift of 3.0 ± 0.3 in the redshift interval $2.4 \lesssim z \lesssim 3.8$ (see left panel in Figure 2.12), with a median uncertainty in the photo-z's of ± 0.4. Additionally, we investigate the redshift distribution by adding the probability histograms $P(z)$ of the individual galaxies, which yields a similar result (see the right panel in Figure

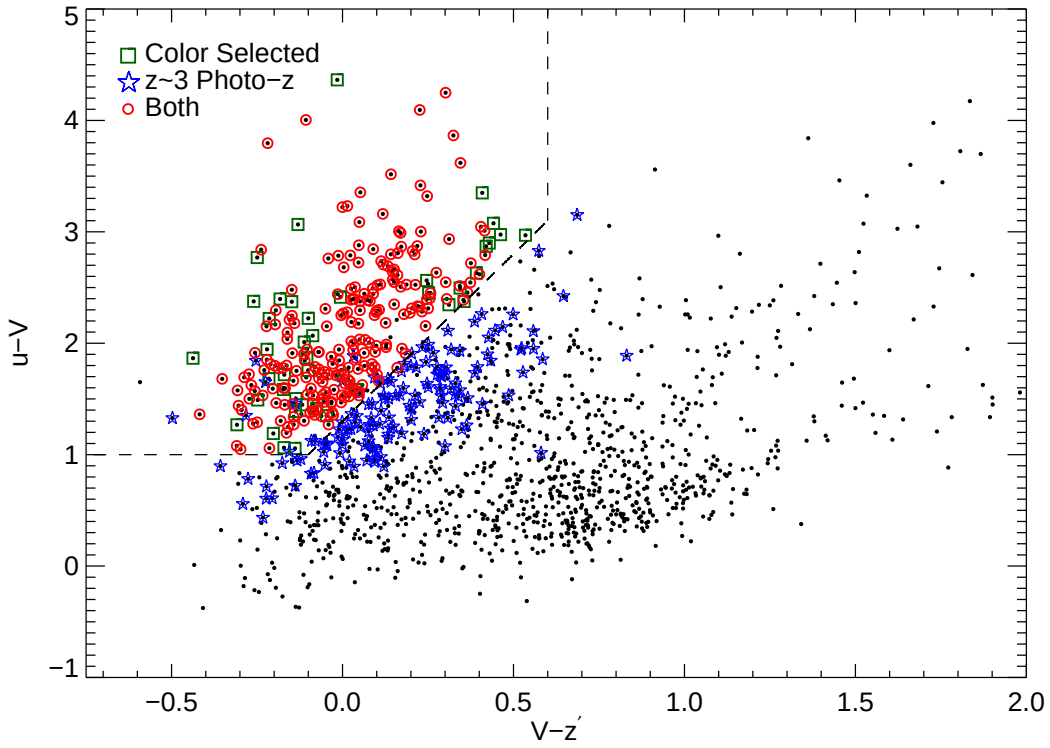

Figure 2.11 All objects from table 2.1 on a color–color diagram, where the dashed line refers to the selection criteria for constraints 2.4, 2.6, and 2.7 from §2.4.2.1. There are 27 objects that are in the color selection area in this diagram but are not color selected because of constraint 2.5 from §2.4.2.1. The 218 galaxies that are both color selected and photo-z selected are marked by red circles, the 42 galaxies that are only color selected are marked by green squares, and the 147 galaxies selected only by photo-z's are marked by blue stars, yielding a total of 407 $z \sim 3$ LBG candidates.

Table 2.4. Catalog of Candidate z∼3 LBGs in the UDF

ID[a]	z_b[b]	$\chi^2_{\rm mod}$[c]	ODDS[d]	Type[e]	V (mag)	$u-V$ (mag)	$u-B$ (mag)	$V-z'$ (mag)
22	$3.23^{+0.41}_{-0.41}$	0.44	1.00	2	27.38±0.03	1.53±0.36	0.96±0.36	0.49±0.04
76	$2.62^{+0.36}_{-0.35}$	0.52	1.00	2	26.47±0.02	1.39±0.16	1.19±0.16	0.11±0.03
84	$3.11^{+0.40}_{-0.40}$	0.01	1.00	1	26.56±0.02	2.40±0.35	1.69±0.35	0.03±0.04
97	$2.87^{+0.38}_{-0.38}$	0.13	1.00	1	25.02±0.01	2.01±0.06	1.48±0.07	0.08±0.01
99	$2.81^{+0.37}_{-0.37}$	0.32	1.00	2	24.74±0.01	1.96±0.07	1.51±0.08	0.52±0.01
101	$2.66^{+0.36}_{-0.36}$	0.17	1.00	2	27.38±0.02	1.45±0.32	1.09±0.32	0.09±0.05
131	$3.06^{+0.40}_{-0.40}$	0.21	1.00	1	26.95±0.02	2.02±0.35	1.43±0.36	0.03±0.05
209	$2.67^{+0.36}_{-0.36}$	9.03	1.00	3	26.92±0.02	1.27±0.34	1.26±0.34	-0.31±0.05
213	$3.14^{+0.41}_{-0.41}$	0.18	1.00	2	26.91±0.02	1.95±0.34	1.19±0.35	0.56±0.04
230	$3.70^{+0.46}_{-0.46}$	0.00	1.00	3	25.68±0.01	3.08±0.35	1.29±0.36	0.44±0.02

Note. — Table 2.4 is shown in full in the appendix (Table C.4). A portion is shown here for guidance regarding its form and content. Photometric redshifts should only be used if they have low $\chi^2_{\rm mod}$ and good ODDS values as described in §2.4.1.1. V magnitudes are total AB magnitudes, and colors are isophotal colors. All photometry other than the u-band are from Coe et al. (2006). Nondetections in u-band are given 3σ limiting magnitudes.

[a]ID numbers from Coe et al. (2006).

[b]Bayesian photometric redshift (BPZ) and uncertainty from 95% confidence interval.

[c]Modified reduced chi-square fit, where the templates are given uncertainties.

[d]Integrated $P(z)$ contained within $0.1(1+z_b)$.

[e]Type of LBG selection, where 1=both color and photo-z selected, 2=only photo-z selected, and 3=only color selected.

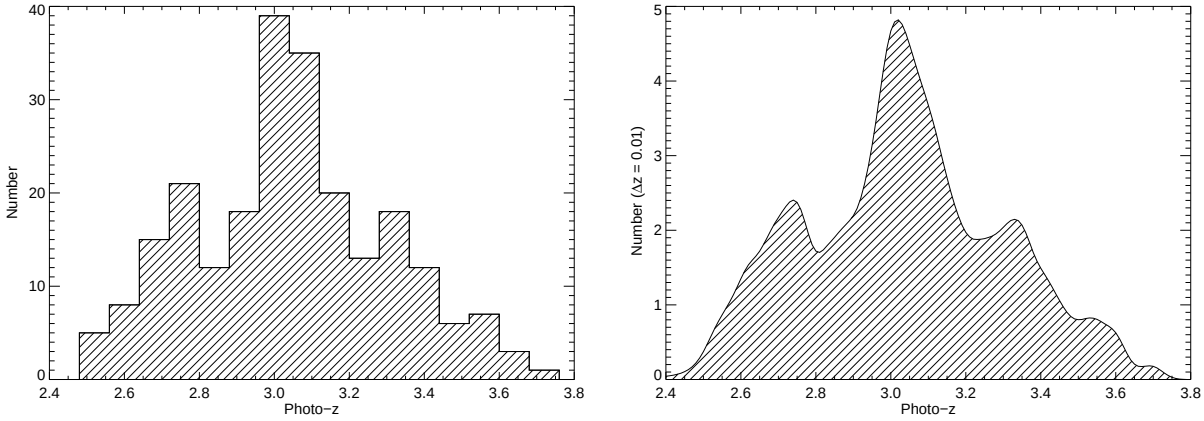

Figure 2.12 Histogram of 235 color selected photometric redshifts with $\chi^2_{\rm mod} < 4$. The mean redshift is 3.0 ± 0.3, and the median uncertainty of the photo-z's is ± 0.4. The left panel is a traditional histogram, and the right panel is the sum of the probability histograms $P(z)$ of the individual galaxies. The redshift distribution selected are similar to those of Steidel et al. (2003).

2.12). The redshifts selected are similar to those of Steidel et al. (2003), with ∼80% of our sample matching their reported redshift interval $2.7 < z < 3.4$. In fact, their distribution is very similar to ours, with a number of their LBGs falling outside of this interval. Given the large uncertainties in our photo-z's, we conclude that our color selected redshift distribution is similar to that of Steidel et al. (2003) within our uncertainties. The similar redshift distribution of our color selected sample justifies our comparison of the number densities of LBGs in §2.5.3.

2.5.2 Cosmic Variance

The UDF has a very small volume, with our overlap area consisting of 11.56 arcmin^2, which in the redshift interval $2.5 \leq z \leq 3.5$ is a comoving volume of $\sim$ 38000 Mpc^3. A single pointing with a small solid angle and such a small volume is likely to be affected by cosmic variance, yielding larger than Poisson uncertainties in the LBG number counts. It is important to estimate the cosmic variance effect in order to understand the systematic uncertainties for comparisons with number densities of LBGs in the literature.

We calculate the cosmic variance using the code from Newman & Davis (2002) and the prescription from Adelberger et al. (2005) to get the fractional error per count σ/N for our given volume in the redshift interval $2.5 \lesssim z \lesssim 3.5$. The variance is determined from the integral of the linear regime of the cold dark matter (CDM) power spectrum ($P(k)$),

$$\sigma^2_{\rm CDM} = \frac{1}{8\pi^3} \int P(k) |\tilde{W}(k)|^2 d^3k \quad , \tag{2.9}$$

where $\tilde{W}(k)$ is the Fourier transform of our survey volume. Since we want the variance of galaxy counts rather than CDM fluctuations, we need to correct for the clustering bias (b) of LBGs to get their variance (σ^2_g), where $\sigma^2_g \simeq b^2 \sigma^2_{\rm CDM}$. The galaxy bias for typical LBGs is then calculated from the ratio of galaxy to CDM fluctuations in spheres of comoving radius 8 h^{-1}Mpc, where $\sigma_8(z)$ represents the CDM fluctuations for our redshift, and $b = \sigma_{8,g}/\sigma_8(z)$ (Adelberger et al., 2005). The resulting variance depends on a fit to the LBG correlation function $\xi_g(r) = (r/r_o)^{-\gamma}$, where r_o is the spatial correlation length and γ the correlation index. The galaxy variance is then

$$\sigma^2_{8,g} = \frac{72(r_o/8\ h^{-1}Mpc)^\gamma}{(3-\gamma)(4-\gamma)(6-\gamma)2^\gamma} \quad , \tag{2.10}$$

(Peebles, 1980, eq. 59.3) from which we can then calculate the fractional error per LBG count.

Empirical fits to the correlation function yield differing values for r_o and γ depending on the sample, redshift distribution, luminosity range, and redshift, which in turn affect the value of $\sigma^2_{8,g}$ and our fractional uncertainty (Adelberger et al., 2005; Hildebrandt et al., 2007, 2009; Kashikawa et al., 2006; Lee et al., 2006; Ouchi et al., 2004, 2005; Yoshida et al., 2008). We avoid looking at samples covering a small area of the sky such as the HDF (Giavalisco & Dickinson, 2001), as such studies are also plagued by cosmic variance as shown in Ouchi et al. (2005). The values in the larger studies generally vary between $r_o \sim 2.8-5.5$ and $\gamma \sim 1.5-2.2$, with an increasing r_o and γ with increasing luminosity, i.e., the brighter LBGs are more strongly clustered. There is also some minor evolution with redshift, where the higher redshift galaxies are more clustered (Hildebrandt et al., 2009).

These values result in $\sigma^2_{8,\mathrm{LBGs}}$ of $\sim 0.56 - -1.1$ which correspond to a fractional error per count of $\sim 0.14 - 0.28$. Our sample includes the fainter less clustered LBGs at $z \sim 3$, so we are on the less clustered side of this range. We therefore adopt a fractional error per count (σ/N) of $\sim$0.2 in the rest of this study, which suggests that we could detect a relatively large over-density or under-density in our small volume. In fact, there is evidence of an over-density of $z \sim 3.7$ galaxies in the Chandra Deep Field South, of which the UDF is a part (Kang & Im, 2009). However, no clear over-density is indicated in the correlation length measured from the GOODs survey covering the same area on the sky (Lee et al., 2006) at slightly higher redshift. We use the above estimate of the cosmic variance for our small field of view to constrain our results of the number densities of LBGs in §2.5.3.

2.5.3 LBG Number Counts

The number counts of $z \sim 3$ LBGs per unit of magnitude indicate the completeness of the LBG selection, and can be compared to number counts from other studies. Such data are only available for color-selected samples, and we therefore only use our color-selected sample in our comparison. The same comparison could be accomplished with the luminosity function, which we do not calculate because we only have one pointing and our comoving volume is small. In other words, we have a small number of LBGs that in conjunction with the uncertainty due to cosmic variance discussed above, would not yield meaningful constraints on the luminosity function. Additionally, to calculate the luminosity function, Monte Carlo simulations need to be run as described in Reddy et al. (2008) that are computationally prohibitive given our complex analysis technique to get reliable photometry with largely varying PSFs (Laidler et al., 2007). We therefore compare our results with the number counts from other studies. We stress that we are comparing number counts that are not corrected for completeness, and therefore the counts will fall at faint magnitudes in each study due to sample incompleteness.

Our ground-based LRIS images have much greater PSF FWHMs ($\sim 1''.3$) than the HST V-band image ($\sim 0.09''$), thus affecting the observed number counts. The dominant effect is caused by the blending of neighboring objects that affects

the color of objects and therefore their selection. In addition, at significantly lower resolution, isolated compact faint objects have part of their flux lost to the noise floor of the background. This causes the faintest objects to go undetected in the low-resolution images, even if they would have been detected in a similarly sensitive high-resolution image. We use the HST V-band image to determine our high-resolution-detection (HRD) number counts and correct for this resolution effect. We convolve the HST V-band image with the PSF modeled from the LRIS V-band image (FWHM of $\sim 1''$) that was taken concurrently with the u-band data. This yields a low-resolution-detection (LRD) image from which a segmentation map is generated using `SExtractor`.

The final photometry is measured with this new segmentation map in all bands using `sexseg` as discussed in §2.3.4, and then the same color selection is used as discussed in §2.4.2.1. Figure 2.13 shows the number counts per half magnitude bin per square arcminute for both the HRD and LRD, along with number counts from Reddy et al. (2008), the Keck Deep Field (KDF) (Sawicki & Thompson, 2006), and Steidel et al. (1999). For the HRD sample, we include only Poisson uncertainties for reference, while for the LRD we include both Poisson uncertainties and the fractional error per count of 0.2 to take into account the cosmic variance (see §2.5.2). The figure shows that we are photometrically complete to $V \sim 27$ mag, after which we start losing LBGs due to the sensitivity of the u-band image. In order to compare to other studies, we convert their R-band magnitudes from Keck to V-band magnitudes from HST with a K-correction at $z \sim 3$ for the Im galaxy template described in §2.4.1, which results in an R-V color of ~ -0.15. The LBG number counts in Figure 2.13 of the LRD's agree at the brighter end to within our uncertainties, however, at the fainter end ($V > 26.0$), our results are larger than the uncorrected KDF results, which is the only survey to probe to equivalent depths.

Based on the turnover in the LBG number counts in Figure 2.13, the KDF and our LRD study appear to be complete to $V \gtrsim 26$ and $V \sim 27$, respectively. The cumulative number counts for $V < 26$ is 3.7 ± 0.6 LBGs arcmin^{-2} in our LRD study and 4.3 ± 0.2 LBGs arcmin^{-2} for the KDF, where the uncertainties

are Poisson. These results are consistent with each other, without invoking cosmic variance, and suggest that the difference in number counts for $V \gtrsim 26$ is due to differing completeness limits.

In order to understand this better, we also include the KDF number counts corrected for LBG completeness in Figure 2.13. This completeness correction is different than the one applied in (Sawicki & Thompson, 2006), as it previously included the volume correction simultaneously. The correction applied here assumes that all $z \sim 3$ LBGs are well-represented by the colors of a fiducial LBG with (1) fixed age of 100 Myr (2) a fixed redshift $z = 3$, and (3) Calzetti et al. (1994) dust extinction for $E(B-V) = 0.2$. The incompleteness is then calculated by planting objects with these colors in the KDF images and determining how many are recovered, with the uncertainties estimated via bootstrap resampling (Marcin Sawicki, private communication). This is not as careful a correction as applied in (Sawicki & Thompson, 2006), but serves to investigate the completeness differences in our studies with respect to LBG detection. Our LRD study number counts are consistent with the KDF LBG completeness corrected number counts down to $V \sim 27$. This helps reinforce that we are likely complete in detecting $z \sim 3$ LBGs to $V \sim 27$ magnitude, making our study the deepest to date.

2.6 Summary

We use newly acquired ground-based u-band imaging with a depth of 30.7 mag arcsec^{-2} ($1\sigma_u$ sky fluctuations) and an isophotal limiting u-band magnitude of 27.6 mag to create a reliable sample of 407 $z \sim 3$ LBGs in the UDF. We use the template-fitting method `TFIT` (Laidler et al., 2007) to measure accurate photometry without the need for aperture corrections, and obtain robust colors across the largely varying PSFs of the UDF ACS images ($0.''09$ FWHM) and the u-band image ($1.''3$ FWHM). The results are as follows:

1) We calculate photometric redshifts for 1457 galaxies using the Bayesian algorithm of Benítez (2000), Benítez et al. (2004), and Coe et al. (2006), of which

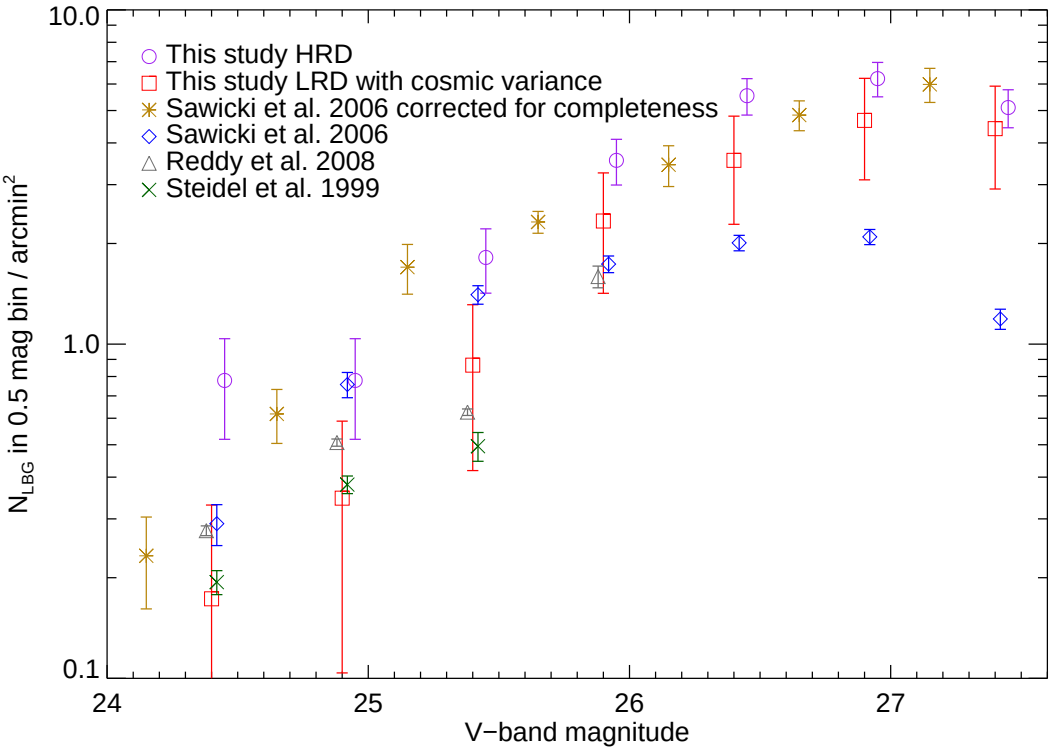

Figure 2.13 Number counts of $z \sim 3$ LBGs in 0.5 mag bins per square arcminute not corrected for completeness. Magnitudes are slightly offset to make the figure more clear. The full number counts based on the high-resolution-detections are marked HRD and are purple circles. The LRDs are marked LRD and are in red squares. The LRD are the number counts that would have been measured if the object detections would have been made using ground-based images with FWHM of $1''.2$. For the HRD sample, we include only Poisson uncertainties, while for the LRD we include both Poisson uncertainties and the cosmic variance estimate (see §2.5.2). Our number counts are plotted along with the studies of Reddy et al. (2008), Sawicki & Thompson (2006), and Steidel et al. (1999). The only points corrected for completeness are the gold crosses for the Sawicki & Thompson (2006) data.

1384 are reliable with $\chi^2_{\rm mod} < 4$. We find that the previous photo-z's by Coe et al. (2006) do a good job of determining redshifts even without the u-band if their uncertainties are taken into account. However, these uncertainties are often quite large at $z \sim 3$ due to the color degeneracy of $z \sim 3$ and $z \sim 0.2$ galaxies.

2) The u-band significantly improves $z \sim 3$ photo-z determinations: out of 1384 galaxies, 175 galaxies no longer have degenerate photo-z's, and 125 of the galaxies changed their primary photo-z with the addition of the u-band. In fact, the addition of the u-band changed the photo-z's of $\sim 50\%$ of the $z \sim 3$ galaxy sample.

3) We find that even when using the u-band photometry and restricting the sample of photo-z's to those with good $\chi^2_{\rm mod}$, catastrophic photo-z errors can still occur, although they are rare (only 1 out of 93 galaxies with spectroscopic redshifts and photometric redshifts with $\chi^2_{\rm mod} < 4$ and ODDS > 0.99). We found *no* catastrophic photo-z's in the redshift interval of interest, ($2.5 \lesssim z \lesssim 3.5$), although only five objects have spec-z's in this interval. In contrast, three galaxies at $2.5 \lesssim z \lesssim 3.5$ had catastrophic photo-z's before the addition of the u-band. The contamination fraction of the $z \sim 3$ photo-z sample is likely small as we sample the Lyman break for these galaxies, and show excellent spectroscopic agreement. However, given the small numbers, the overall error rate of the photo-z's is not well defined.

4) We find excellent agreement of our color selected sample with the spectroscopic $z \sim 3$ sample, with no low-redshift galaxies falling in our color selection area, confirming our chosen criteria. We specifically choose a conservative color criteria that are similar to the cuts of Steidel et al. (2003) such that we can infer that the $\sim 3\%$ contamination fraction for $z \sim 3$ LBGs of Steidel et al. (2003) and Reddy et al. (2008) applies to our data set.

5) The completeness of our LBG selection depends largely on the u-band depth because the ACS bands from HST are deeper. In order to characterize this completeness, we compare our color selected LBGs with other studies and find that we

present the deepest sample of $z \sim 3$ LBGs currently available, likely complete to $V \sim 27$ mag.

This reliable sample of $z \sim 3$ LBGs can be used to further the studies of LBGs and star formation efficiency of gas at $z \sim 3$ through the most sensitive high-resolution images ever taken; the Hubble Ultra Deep Field.

2.7 Acknowledgments

The authors thank, Dan Coe, Victoria Laidler, Eric Gawiser, and Alison Coil for valuable discussions, Marcin Sawicki for providing the KDF number counts, and Narciso Benitez for providing re-calibrated SED templates for BPZ. Support for this work was provided by NSF grant AST 07-09235. J. C. acknowledges generous support by Gary McCue. The W. M. Keck Observatory is operated as a scientific partnership among the California Institute of Technology, the University of California and the National Aeronautics and Space Administration. The Observatory was made possible by the generous financial support of the W. M. Keck Foundation. The authors recognize and acknowledge the very significant cultural role and reverence that the summit of Mauna Kea has always had within the indigenous Hawaiian community. We are most fortunate to have the opportunity to conduct observations from this mountain.

This chapter, in full (with minor exceptions to conform to this thesis), is a reprint of material previously published as "Deep Keck u-band imaging of the Hubble Ultra Deep Field: A catalog of $z \sim 3$ Lyman Break Galaxies", by Marc Rafelski, Arthur M. Wolfe, Jeff Cooke, Hsiao-Wen Chen, Greg Wirth, & Taft E. Armandroff, published in the The Astrophysical Journal, 2009, Vol. 703, p. 2033. I was the primary investigator and author of this paper.

References

Adelberger, K. L., Steidel, C. C., Pettini, M., Shapley, A. E., Reddy, N. A., & Erb, D. K. 2005, The Astrophysical Journal, 619, 697

Adelberger, K. L., Steidel, C. C., Shapley, A. E., Hunt, M. P., Erb, D. K., Reddy, N. A., & Pettini, M. 2004, The Astrophysical Journal, 607, 226

Beckwith, S. V. W., Stiavelli, M., Koekemoer, A. M., Caldwell, J. A. R., Ferguson, H. C., Hook, R., Lucas, R. A., Bergeron, L. E., Corbin, M., Jogee, S., Panagia, N., Robberto, M., Royle, P., Somerville, R. S., & Sosey, M. 2006, The Astronomical Journal, 132, 1729

Benítez, N. 2000, The Astrophysical Journal, 536, 571

Benítez, N., Ford, H., Bouwens, R., Menanteau, F., Blakeslee, J., Gronwall, C., Illingworth, G., Meurer, G., Broadhurst, T. J., Clampin, M., Franx, M., Hartig, G. F., Magee, D., Sirianni, M., Ardila, D. R., Bartko, F., Brown, R. A., Burrows, C. J., Cheng, E. S., Cross, N. J. G., Feldman, P. D., Golimowski, D. A., Infante, L., Kimble, R. A., Krist, J. E., Lesser, M. P., Levay, Z., Martel, A. R., Miley, G. K., Postman, M., Rosati, P., Sparks, W. B., Tran, H. D., Tsvetanov, Z. I., White, R. L., & Zheng, W. 2004, The Astrophysical Journal Supplement Series, 150, 1

Bertin, E. & Arnouts, S. 1996, Astronomy and Astrophysics Supplement, 117, 393

Bouwens, R. J., Illingworth, G. D., Blakeslee, J. P., & Franx, M. 2006, The Astrophysical Journal, 653, 53

Bouwens, R. J., Illingworth, G. D., Franx, M., & Ford, H. 2007, The Astrophysical Journal, 670, 928

Bruzual, G. & Charlot, S. 2003, Monthly Notices of the Royal Astronomical Society, 344, 1000

Calzetti, D., Kinney, A. L., & Storchi-Bergmann, T. 1994, The Astrophysical Journal, 429, 582

Cardelli, J. A., Clayton, G. C., & Mathis, J. S. 1989, The Astrophysical Journal, 345, 245

Chen, H.-W., Marzke, R. O., McCarthy, P. J., Martini, P., Carlberg, R. G., Persson, S. E., Bunker, A., Bridge, C. R., & Abraham, R. G. 2003, The Astrophysical Journal, 586, 745

Chen, H.-W., McCarthy, P. J., Marzke, R. O., Wilson, J., Carlberg, R. G., Firth, A. E., Persson, S. E., Sabbey, C. N., Lewis, J. R., McMahon, R. G., Lahav, O., Ellis, R. S., Martini, P., Abraham, R. G., Oemler, A., Murphy, D. C., Somerville, R. S., Beckett, M. G., & Mackay, C. D. 2002, The Astrophysical Journal, 570, 54

Coe, D., Benítez, N., Sánchez, S. F., Jee, M., Bouwens, R., & Ford, H. 2006, The Astronomical Journal, 132, 926

Coleman, G. D., Wu, C.-C., & Weedman, D. W. 1980, The Astrophysical Journal Supplement Series, 43, 393

Conselice, C. J., Rajgor, S., & Myers, R. 2008, Monthly Notices of the Royal Astronomical Society, 386, 909

Cooke, J., Wolfe, A. M., Prochaska, J. X., & Gawiser, E. 2005, The Astrophysical Journal, 621, 596

Ellis, R. S. 1997, Annual Review of Astronomy and Astrophysics, 35, 389

Elmegreen, D. M., Elmegreen, B. G., Ravindranath, S., & Coe, D. A. 2007, The Astrophysical Journal, 658, 763

Fernández-Soto, A., Lanzetta, K. M., Chen, H.-W., Levine, B., & Yahata, N. 2002, Monthly Notices of the Royal Astronomical Society, 330, 889

Fernández-Soto, A., Lanzetta, K. M., Chen, H.-W., Pascarelle, S. M., & Yahata, N. 2001, The Astrophysical Journal Supplement Series, 135, 41

Fernández-Soto, A., Lanzetta, K. M., & Yahil, A. 1999, The Astrophysical Journal, 513, 34

Fevre, O. L., Vettolani, G., Maccagni, D., Mancini, D., Mazure, A., Mellier, Y., Picat, J. P., Arnaboldi, M., Bardelli, S., Bertin, E., Busarello, G., Cappi, A., Charlot, S., Chincarini, G., Colombi, S., Dantel-Fort, M., Foucaud, S., Garilli, B., Guzzo, L., Iovino, A., Marinoni, C., Mathez, G., McCracken, H., Pello, R., Radovich, M., Ripepi, V., Saracco, P., Scaramella, R., Scoreggio, M., Tresse, L., Zanichelli, A., Zamorani, G., & Zucca, E. 2003, Discoveries and Research Prospects from 6- to 10-Meter-Class Telescopes II. Edited by Guhathakurta, 4834, 173

Fèvre, O. L., Vettolani, G., Paltani, S., Tresse, L., Zamorani, G., Brun, V. L., Moreau, C., Bottini, D., Maccagni, D., Picat, J. P., Scaramella, R., Scodeggio, M., Zanichelli, A., Adami, C., Arnouts, S., Bardelli, S., Bolzonella, M., Cappi, A., Charlot, S., Contini, T., Foucaud, S., Franzetti, P., Garilli, B., Gavignaud, I., Guzzo, L., Ilbert, O., Iovino, A., McCracken, H. J., Mancini, D., Marano, B., Marinoni, C., Mathez, G., Mazure, A., Meneux, B., Merighi, R., Pellò, R., Pollo, A., Pozzetti, L., Radovich, M., Zucca, E., Arnaboldi, M., Bondi, M., Bongiorno, A., Busarello, G., Ciliegi, P., Gregorini, L., Mellier, Y., Merluzzi, P., Ripepi, V., & Rizzo, D. 2004, Astronomy and Astrophysics, 428, 1043

Ford, H. C., Illingworth, G. D., Clampin, M., Hartig, G., Bartko, F., Benitez, N., Blakeslee, J. P., Bouwens, R., Broadhurst, T. J., Brown, R., Burrows, C., Cheng, E., Cross, N., Feldman, P. D., Franx, M., Golimowski, D. A., Gronwall, C., Kimble, R. A., Krist, J., Lesser, M., Magee, D., Martel, A., McCann, W. J., Meurer, G. R., Miley, G., Postman, M., Rosati, P., Sirianni, M., Sparks, W. B., Tran, H. D., Tsvetanov, Z. I., & White, R. L. 2002, American Astronomical Society, 200, 675

Franx, M., Labbé, I., Rudnick, G., van Dokkum, P. G., Daddi, E., Schreiber, N. M. F., Moorwood, A., Rix, H.-W., Röttgering, H., van de Wel, A., van der Werf, P., & van Starkenburg, L. 2003, The Astrophysical Journal, 587, L79

Fruchter, A. S. & Hook, R. N. 2002, The Publications of the Astronomical Society of the Pacific, 114, 144

Fukugita, M., Ichikawa, T., Gunn, J. E., Doi, M., Shimasaku, K., & Schneider, D. P. 1996, The Astronomical Journal, 111, 1748

Gawiser, E., van Dokkum, P. G., Herrera, D., Maza, J., Castander, F. J., Infante, L., Lira, P., Quadri, R., Toner, R., Treister, E., Urry, C. M., Altmann, M., Assef, R., Christlein, D., Coppi, P. S., Durán, M. F., Franx, M., Galaz, G., Huerta, L., Liu, C., López, S., Méndez, R., Moore, D. C., Rubio, M., Ruiz, M. T., Toft, S., & Yi, S. K. 2006, The Astrophysical Journal Supplement Series, 162, 1

Giavalisco, M. & Dickinson, M. 2001, The Astrophysical Journal, 550, 177

Grazian, A., Fontana, A., de Santis, C., Nonino, M., Salimbeni, S., Giallongo, E., Cristiani, S., Gallozzi, S., & Vanzella, E. 2006, Astronomy and Astrophysics, 449, 951

Hamilton, D. 1985, The Astrophysical Journal, 297, 371

Hildebrandt, H., Pielorz, J., Erben, T., Schneider, P., Eifler, T., Simon, P., & Dietrich, J. P. 2007, Astronomy and Astrophysics, 462, 865

Hildebrandt, H., Pielorz, J., Erben, T., van Waerbeke, L., Simon, P., & Capak, P. 2009, eprint arXiv, 0903, 3951

Hildebrandt, H., Wolf, C., & Benítez, N. 2008, Astronomy and Astrophysics, 480, 703

Hinshaw, G., Weiland, J. L., Hill, R. S., Odegard, N., Larson, D., Bennett, C. L., Dunkley, J., Gold, B., Greason, M. R., Jarosik, N., Komatsu, E., Nolta, M. R., Page, L., Spergel, D. N., Wollack, E., Halpern, M., Kogut, A., Limon, M., Meyer, S. S., Tucker, G. S., & Wright, E. L. 2009, The Astrophysical Journal Supplement, 180, 225

Kang, E. & Im, M. 2009, The Astrophysical Journal Letters, 691, L33

Kashikawa, N., Yoshida, M., Shimasaku, K., Nagashima, M., Yahagi, H., Ouchi, M., Matsuda, Y., Malkan, M. A., Doi, M., Iye, M., Ajiki, M., Akiyama, M., Ando, H., Aoki, K., Furusawa, H., Hayashino, T., Iwamuro, F., Karoji, H., Kobayashi, N., Kodaira, K., Kodama, T., Komiyama, Y., Miyazaki, S., Mizumoto, Y., Morokuma, T., Motohara, K., Murayama, T., Nagao, T., Nariai, K., Ohta, K., Okamura, S., Sasaki, T., Sato, Y., Sekiguchi, K., Shioya, Y., Tamura, H., Taniguchi, Y., Umemura, M., Yamada, T., & Yasuda, N. 2006, The Astrophysical Journal, 637, 631

Kennicutt, R. C. 1998, The Astrophysical Journal, 498, 541

Kinney, A. L., Calzetti, D., Bohlin, R. C., McQuade, K., Storchi-Bergmann, T., & Schmitt, H. R. 1996, The Astrophysical Journal, 467, 38

Koo, D. C. 1985, The Astronomical Journal, 90, 418

Kron, R. G. 1980, The Astrophysical Journal Supplement Series, 43, 305

Labbé, I., Huang, J., Franx, M., Rudnick, G., Barmby, P., Daddi, E., van Dokkum, P. G., Fazio, G. G., Schreiber, N. M. F., Moorwood, A. F. M., Rix, H.-W., Röttgering, H., Trujillo, I., & van der Werf, P. 2005, The Astrophysical Journal, 624, L81

Laidler, V. G., Papovich, C., Grogin, N. A., Idzi, R., Dickinson, M., Ferguson, H. C., Hilbert, B., Clubb, K., & Ravindranath, S. 2007, The Publications of the Astronomical Society of the Pacific, 119, 1325

Landolt, A. U. 1992, The Astronomical Journal, 104, 340

Lanzetta, K. M., Fernández-Soto, A., & Yahil, A. 1998, The Hubble Deep Field : Proceedings of the Space Telescope Science Institute Symposium, 143

Law, D. R., Steidel, C. C., Erb, D. K., Pettini, M., Reddy, N. A., Shapley, A. E., Adelberger, K. L., & Simenc, D. J. 2007, The Astrophysical Journal, 656, 1

Lee, K.-S., Giavalisco, M., Gnedin, O. Y., Somerville, R. S., Ferguson, H. C., Dickinson, M., & Ouchi, M. 2006, The Astrophysical Journal, 642, 63

Madau, P. 1995, The Astrophysical Journal, 441, 18

Markwardt, C. B. 2009, eprint arXiv, 0902, 2850

McCarthy, J. K., Cohen, J. G., Butcher, B., Cromer, J., Croner, E., Douglas, W. R., Goeden, R. M., Grewal, T., Lu, B., Petrie, H. L., Weng, T., Weber, B., Koch, D. G., & Rodgers, J. M. 1998, Proc. SPIE Vol. 3355, 3355, 81

Moffat, A. F. J. 1969, Astronomy and Astrophysics, 3, 455

Newman, J. A. & Davis, M. 2002, The Astrophysical Journal, 564, 567

Nonino, M., Dickinson, M., Rosati, P., Grazian, A., Reddy, N., Cristiani, S., Giavalisco, M., Kuntschner, H., Vanzella, E., Daddi, E., Fosbury, R. A. E., & Cesarsky, C. 2009, The Astrophysical Journal Supplement, 183, 244

Oke, J. B., Cohen, J. G., Carr, M., Cromer, J., Dingizian, A., Harris, F. H., Labrecque, S., Lucinio, R., Schaal, W., Epps, H., & Miller, J. 1995, Publications of the Astronomical Society of the Pacific, 107, 375

Ouchi, M., Hamana, T., Shimasaku, K., Yamada, T., Akiyama, M., Kashikawa, N., Yoshida, M., Aoki, K., Iye, M., Saito, T., Sasaki, T., Simpson, C., & Yoshida, M. 2005, The Astrophysical Journal, 635, L117

Ouchi, M., Shimasaku, K., Okamura, S., Furusawa, H., Kashikawa, N., Ota, K., Doi, M., Hamabe, M., Kimura, M., Komiyama, Y., Miyazaki, M., Miyazaki, S., Nakata, F., Sekiguchi, M., Yagi, M., & Yasuda, N. 2004, The Astrophysical Journal, 611, 685

Papovich, C., Dickinson, M., & Ferguson, H. C. 2001, The Astrophysical Journal, 559, 620

Papovich, C., Dickinson, M., Ferguson, H. C., Giavalisco, M., Lotz, J., Madau, P., Idzi, R., Kretchmer, C., Moustakas, L. A., de Mello, D. F., Gardner, J. P., Rieke, M. J., Somerville, R. S., & Stern, D. 2004, The Astrophysical Journal, 600, L111

Peebles, P. 1980, The large-scale structure of the universe (Princeton University Press)

Phillips, A. C., Miller, J., Cowley, D., & Wallace, V. 2006, Ground-based and Airborne Instrumentation for Astronomy. Edited by McLean, 6269, 56

Pirzkal, N., Xu, C., Malhotra, S., Rhoads, J. E., Koekemoer, A. M., Moustakas, L. A., Walsh, J. R., Windhorst, R. A., Daddi, E., Cimatti, A., Ferguson, H. C., Gardner, J. P., Gronwall, C., Haiman, Z., Kümmel, M., Panagia, N., Pasquali, A., Stiavelli, M., di Serego Alighieri, S., Tsvetanov, Z., Vernet, J., & Yan, H. 2004, The Astrophysical Journal Supplement Series, 154, 501

Popesso, P., Dickinson, M., Nonino, M., Vanzella, E., Daddi, E., Fosbury, R. A. E., Kuntschner, H., Mainieri, V., Cristiani, S., Cesarsky, C., Giavalisco, M., Renzini, A., & Team, T. G. 2009, Astronomy and Astrophysics, 494, 443

Reddy, N. A. & Steidel, C. C. 2009, The Astrophysical Journal, 692, 778

Reddy, N. A., Steidel, C. C., Pettini, M., Adelberger, K. L., Shapley, A. E., Erb, D. K., & Dickinson, M. 2008, The Astrophysical Journal Supplement Series, 175, 48

Sawicki, M. & Thompson, D. 2005, The Astrophysical Journal, 635, 100

—. 2006, The Astrophysical Journal, 642, 653

Shapley, A. E., Steidel, C. C., Erb, D. K., Reddy, N. A., Adelberger, K. L., Pettini, M., Barmby, P., & Huang, J. 2005, The Astrophysical Journal, 626, 698

Steidel, C. C., Adelberger, K. L., Giavalisco, M., Dickinson, M., & Pettini, M. 1999, The Astrophysical Journal, 519, 1

Steidel, C. C., Adelberger, K. L., Shapley, A. E., Pettini, M., Dickinson, M., & Giavalisco, M. 2003, The Astrophysical Journal, 592, 728

Steidel, C. C., Giavalisco, M., Dickinson, M., & Adelberger, K. L. 1996a, The Astronomical Journal, 112, 352

Steidel, C. C., Giavalisco, M., Pettini, M., Dickinson, M., & Adelberger, K. L. 1996b, The Astrophysical Journal, 462, L17

Steidel, C. C. & Hamilton, D. 1992, The Astronomical Journal, 104, 941

Steidel, C. C., Pettini, M., & Hamilton, D. 1995, The Astronomical Journal, 110, 2519

Szokoly, G. P., Bergeron, J., Hasinger, G., Lehmann, I., Kewley, L., Mainieri, V., Nonino, M., Rosati, P., Giacconi, R., Gilli, R., Gilmozzi, R., Norman, C., Romaniello, M., Schreier, E., Tozzi, P., Wang, J. X., Zheng, W., & Zirm, A. 2004, The Astrophysical Journal Supplement Series, 155, 271

Thompson, R. I., Bouwens, R. J., & Illingworth, G. 2006, Planets to cosmology : essential science in the final years of the Hubble Space Telescope, 195

van Dokkum, P. G., Franx, M., Schreiber, N. M. F., Illingworth, G. D., Daddi, E., Knudsen, K. K., Labbé, I., Moorwood, A., Rix, H.-W., Röttgering, H., Rudnick, G., Trujillo, I., van der Werf, P., van der Wel, A., van Starkenburg, L., & Wuyts, S. 2004, The Astrophysical Journal, 611, 703

van Dokkum, P. G., Quadri, R., Marchesini, D., Rudnick, G., Franx, M., Gawiser, E., Herrera, D., Wuyts, S., Lira, P., Labbé, I., Maza, J., Illingworth, G. D., Schreiber, N. M. F., Kriek, M., Rix, H.-W., Taylor, E. N., Toft, S., Webb, T., & Yi, S. K. 2006, The Astrophysical Journal, 638, L59

Vanzella, E., Cristiani, S., Dickinson, M., Giavalisco, M., Kuntschner, H., Haase, J., Nonino, M., Rosati, P., Cesarsky, C., Ferguson, H. C., Fosbury, R. A. E., Grazian, A., Moustakas, L. A., Rettura, A., Popesso, P., Renzini, A., Stern, D., & Team, T. G. 2008, Astronomy and Astrophysics, 478, 83

Vanzella, E., Cristiani, S., Dickinson, M., Kuntschner, H., Moustakas, L. A., Nonino, M., Rosati, P., Stern, D., Cesarsky, C., Ettori, S., Ferguson, H. C., Fosbury, R. A. E., Giavalisco, M., Haase, J., Renzini, A., Rettura, A., Serra, P., & the GOODS Team. 2005, Astronomy and Astrophysics, 434, 53

Vanzella, E., Cristiani, S., Dickinson, M., Kuntschner, H., Nonino, M., Rettura, A., Rosati, P., Vernet, J., Cesarsky, C., Ferguson, H. C., Fosbury, R. A. E., Giavalisco, M., Grazian, A., Haase, J., Moustakas, L. A., Popesso, P., Renzini, A., Stern, D., & the GOODS Team. 2006, Astronomy and Astrophysics, 454, 423

Vanzella, E., Giavalisco, M., Dickinson, M., Cristiani, S., Nonino, M., Kuntschner, H., Popesso, P., Rosati, P., Renzini, A., Stern, D., Cesarsky, C., Ferguson, H. C., & Fosbury, R. A. E. 2009, The Astrophysical Journal, 695, 1163

Wolfe, A. M. & Chen, H.-W. 2006, The Astrophysical Journal, 652, 981

Wolfe, A. M., Gawiser, E., & Prochaska, J. X. 2005, Annual Review of Astronomy and Astrophysics, 43, 861

Xu, C., Pirzkal, N., Malhotra, S., Rhoads, J. E., Mobasher, B., Daddi, E., Gronwall, C., Hathi, N. P., Panagia, N., Ferguson, H. C., Koekemoer, A. M., Kümmel, M., Moustakas, L. A., Pasquali, A., di Serego Alighieri, S., Vernet, J., Walsh, J. R., Windhorst, R., & Yan, H. 2007, The Astronomical Journal, 134, 169

Yoshida, M., Shimasaku, K., Ouchi, M., Sekiguchi, K., Furusawa, H., & Okamura, S. 2008, The Astrophysical Journal, 679, 269

Chapter 3

Star Formation from DLA Gas in the Outskirts of Lyman Break Galaxies at z∼3

3.1 Introduction

Understanding how stars form from gas is vital to our comprehension of galaxy formation and evolution. Although the physics involved in this process is not fully understood, we do know something about the principal sites where star formation occurs and where the gas resides. Most of the known star formation at high redshift occurs in Lyman Break galaxies (LBGs), a population of star-forming galaxies selected for their opacity at the Lyman limit and the presence of upper main sequence stars that emit FUV radiation. They also have very high star formation rates (SFRs) of ∼80 $M_\odot$ yr^{-1} after correcting for extinction (Shapley et al., 2003).

While LBGs have a wide range of morphologies, the average half-light radius for $z \sim 3$ LBGs is about $\sim 2-3$ kpc in the optical at ~ 25 mag (e.g. Giavalisco et al., 1996; Law et al., 2007). However, studies of the UDF have shown that fainter

LBGs have smaller half-light radii, around $\sim$ 1 kpc for LBGs with brightnesses similar to those used in this study ($V \sim 26 - 27$ mag) (Bouwens et al., 2004). While we have no empirical knowledge about star formation in the outer regions of LBGs, simulations suggest that stars may be forming further out (e.g. Gnedin & Kravtsov, 2010b). It still remains an unanswered question whether star formation occurs in the outer disks of high redshift galaxies. Local galaxies at $z \sim 0$ are forming stars in their outer disks, as observed in the ultra-violet (Thilker et al., 2005; Bigiel et al., 2010b,a). At low redshift, this star formation occurs in atomic-dominated hydrogen gas (Fumagalli & Gavazzi, 2008; Bigiel et al., 2010b,a), where the majority of the hydrogen gas is atomic but molecules are present. At high redshift such gas resides in Damped Lyα systems (DLAs).

DLAs are a population of H I layers selected for their neutral hydrogen column densities of $N_{\rm HI} \geq 2 \times 10^{20}{\rm cm}^{-2}$, which dominate the neutral-gas content of the Universe in the redshift interval $0 < z < 5$. In fact, DLAs at $z \sim 3$ contain enough gas to account for 25%-50% of the mass content of visible matter in modern galaxies (see Wolfe et al., 2005, for a review) and are neutral-gas reservoirs for star formation.

The locally established Kennicutt-Schmidt (KS) relation (Kennicutt, 1998a; Schmidt, 1959) relates the SFR per unit area and the total gas surface density (atomic and molecular), $\Sigma_{\rm SFR} \propto \Sigma_{\rm gas}^{1.4}$. While it is reasonable to use this relationship at low redshift in normal star forming galaxies, many cosmological simulations use it at all redshifts without distinguishing between atomic and molecular gas (e.g. Nagamine et al., 2004, 2007, 2010; Razoumov et al., 2006; Brooks et al., 2007, 2009; Pontzen et al., 2008; Razoumov et al., 2008; Razoumov, 2009; Tescari et al., 2009; Dekel et al., 2009a,b; Kereš et al., 2009; Barnes & Haehnelt, 2010)[1]. Yet at $z \sim 3$, excluding regions immediately surrounding high surface brightness LBGs, the SFR per unit comoving volume, $\dot{\rho}_*$, of DLAs was found to be less than 5% of

[1]We note that there are also a large number of papers that do not assume the KS relation in their simulations and models (e.g. Kravtsov, 2003; Krumholz et al., 2008, 2009a,b; Tassis et al., 2008; Robertson & Kravtsov, 2008; Gnedin & Kravtsov, 2010a,b; Feldmann et al., 2010).

what is expected from the KS relation (Wolfe & Chen, 2006). This means that a lower level of *in situ* star formation occurs in atomic-dominated hydrogen gas at $z \sim 3$ than in modern galaxies[2].

These results have multiple implications affecting such gas at high redshift. First, the lower SFR efficiencies in DLAs are inconsistent with the 158μm cooling rates of DLAs with purely *in situ* star formation. Specifically, Wolfe et al. (2008) adopt the model of Wolfe et al. (2003b), in which star formation generates FUV radiation that heats the gas by the grain photoelectric mechanism. Assuming thermal balance, they equate the heating rates to the [C II] 158 μm cooling rates of DLAs inferred from the measured C II$^*\lambda$1335.7 absorption of DLAs (Wolfe et al., 2003b). The DLA cooling rates exhibit a bimodal distribution (Wolfe et al., 2008), and the population of DLAs with high cooling rates have inferred heating rates significantly higher than that implied by the upper limits of FUV emission of spatially extended sources (Wolfe & Chen, 2006; Wolfe et al., 2008). Therefore, another source of heat input is required, such as compact star-forming regions embedded in the neutral gas; e.g., LBGs. Second, since $\dot{\rho}_*$ is directly proportional to the metal production rate, the limits on $\dot{\rho}_*$ shift the problem of metal overproduction in DLAs by a factor of 10 (Pettini, 1999, 2004, 2006; Wolfe et al., 2003b, known as the 'Missing Metals' problem for DLAs), to one of underproduction by a factor of 3 (Wolfe & Chen, 2006). Lastly, the multi-component velocity structure of the DLA gas (e.g. Prochaska & Wolfe, 1997) suggests that energy input by supernovae explosions is required to replenish the turbulent kinetic energy lost through cloud collisions; i.e., some *in situ* star formation should be present in DLAs.

One possible way to reconcile the lack of detected *in situ* star formation in DLAs at high redshift and the properties of DLAs that require heating of the gas, is that compact LBG cores embedded in spatially extended DLA gas may cause both the heat input, chemical enrichment, and turbulent kinetic energy observed

[2]We note that the SFR efficiency discussed in this paper relates to the normalization of the KS relation, and is not the same as the star formation efficiency (SFE), which is the inverse of the gas depletion time (e.g. Leroy et al., 2008).

in DLAs. There are several independent lines of evidence linking DLAs and LBGs; e.g. (1) there is a significant cross correlation between LBGs and DLAs (Cooke et al., 2006), (2) the identification of a number of high-z DLAs associated with LBGs (Møller et al., 2002a,b; Chen et al., 2009; Fynbo et al., 2010; Fumagalli et al., 2010; Cooke et al., 2010), (3) the occurrence of Ly-α emission observed in the center of DLA troughs (Møller et al., 2004; Cooke et al., 2010), and 4) the appearance of DLAs in the spectra of rare lensed LBGs at high redshift, where the DLA and LBG have similar redshifts (Pettini et al., 2002b; Cabanac et al., 2008; Dessauges-Zavadsky et al., 2010).

In fact, recent results are consistent with the idea that gas in spatially extended DLAs encompass compact LBGs. Erb (2008) demonstrated that LBGs are rapidly running out of "fuel" for star formation, and cold (T$\sim$100K) gas in DLAs is a natural fuel source. This finding is supported by the measurements of the SFR and gas densities of LBGs by Tacconi et al. (2010). We note that if DLAs are the fuel source for the LBGs, the DLAs in turn would have to be replenished since the comoving density of DLAs at its peak ($z \sim 3.5$) is about 1/3 the current cosmic mass density of stars (Prochaska & Wolfe, 2009). Presumably, they are replenished through accretion of warm (T$\sim 10^4$K) ionized flows[3] (Dekel & Birnboim, 2006, 2008; Dekel et al., 2009a,b; Bauermeister et al., 2010).

While LBGs embedded in spatially extended DLA gas helps resolve some properties of DLAs, it is problematic whether metal-enriched outflows from LBGs can supply the required metals seen in DLAs. Nor is it clear whether such outflows can generate turbulent kinetic energy at rates sufficient to balance dissipative losses arising from cloud collisions implied by the multi-component velocity structure of DLAs[4]. We note that Fumagalli et al. (2011) show that that the filamentary gas

[3]Often referred to as 'cold' flows, but we call them warm flows since cold refers to T$\sim$100K gas in this paper.

[4]The cloud crossing time is $t_{\rm cross} = H/v$ and the cloud collision time is $t_{\rm coll} \simeq \frac{1}{n\sigma v}$, where H is the DLA scale height, v is the cloud velocity, n is the number density of clouds, and σ is the geometric cross section of the clouds. Therefore, the ratio of the cloud crossing time to the cloud collision time is $\frac{t_{\rm cross}}{t_{\rm col}} \simeq n\sigma H \sim \tau$, where τ is the optical depth. Consequently, if $\tau > 1$ as

structures in the cold mode accretion scenario that provide galaxies with fresh fuel (e.g. Dekel et al., 2009a; Kereš et al., 2009) are not sufficiently dense to produce DLA absorption, nor do these filaments have a large enough area covering fraction (Faucher-Giguère & Kereš, 2011). The only location with sufficient covering fraction and high enough densities for the gas to become self shielded is in the vicinity around galaxies (2-10kpc).

To address these issues we adopt the working hypothesis that *in situ* star formation occurs in the presence of atomic-dominated gas in the outskirts of LBGs, similar to the outer disks of local galaxies. Since most of the atomic-dominated gas at high redshift is in DLAs, we assume that this is DLA gas. We emphasize that while the past results (Wolfe & Chen, 2006) set sensitive upper limits on *in situ* star formation in DLAs without compact star-forming regions like LBGs, no such limits exist for DLAs containing such objects.

For these reasons we search for spatially-extended star formation associated with LBGs at $z \sim 3$ by looking for regions of low surface-brightness emission surrounding the LBG cores. We are searching for *in situ* star formation on scales up to ~ 10 kpc, where the detection of faint emission would indicate the presence of spatially extended star formation. It would also uncover a mode of star formation hitherto unknown at high z, and could help solve the dilemmas cited above. We test the hypotheses that (1) the extended star formation is fueled by atomic-dominated gas as probed by the DLAs, and (2) star formation occurs at the KS rate. That is, we consider whether star formation occurs in the outskirts of LBGs, whether that star formation occurs in atomic-dominated gas, and at what SFR efficiency the stars form.

This paper is organized as follows. In §3.2 we describe the observations used, and in §3.3 we we identify a sample of compact LBGs at $z \sim 3$ to search for extended low surface brightness (LSB) emission around the compact cores of

is observed, the clouds would dissipate on a timescale short compared to the crossing time (e.g. McDonald & Miralda-Escudé, 1999).

the LBGs. In §3.4 we describe the image stacking technique, measure a median radial profile of the extended LSB emission, and discuss possible selection biases of the observations. In §3.5, based on the observed radial profile, we calculate the corresponding SFR surface density distribution and the sky covering fraction of the extended LSB emission. We then calculate the in situ SFR density and metal production in these extended LSB regions. In §3.6 we develop a theoretical framework to connect known DLA statistics to the observed surface density distribution of SFR in the outskirts of LBGs, and to obtain an empirical estimate of the star formation efficiency in distant galaxies. In §3.7 we discuss the impacts of our analysis in understanding the star formation relation in the distant universe, and in interpreting the observed low metal content of the DLA population.

Throughout this paper, we adopt the AB magnitude system and an $(\Omega_M, \Omega_\Lambda, h) = (0.3, 0.7, 0.7)$ cosmology.

3.2 Observations

We implement our search for spatially-extended star formation around $z \sim 3$ LBGs in the most sensitive high resolution images available: the V-band image of the Hubble Ultra Deep Field (UDF) taken with the Hubble Space Telescope. This image is ideal because (1) of its high angular resolution (PSF FWHM=0.09″), (2) at $z \sim 3$ the V-band fluxes correspond to rest-frame FUV fluxes, which are sensitive measures of SFRs, since short-lived massive stars produce the observed UV photons, and (3) the 1-σ point source limit of V=30.5 implies high sensitivity. Since most of the LBGs in the UDF are too faint for spectroscopic identification, the u-band is needed to find z$\sim$ 3 LBGs via their flux decrement due to the Lyman limit through color selection and photometric redshifts. To this end, we acquired one of the most sensitive u-band images ever obtained and identified 407 LBGs at z$\sim$ 3 (Rafelski et al., 2009, see also Nonino et al. (2009)).

Throughout the paper we utilize the B, V, i', and z' band (F435W, F606W,

F775W, and F850LP respectively) observations of the UDF (Beckwith et al., 2006), obtained with the Wide Field Camera (WFC) on the HST ACS (Ford et al., 2002). These images cover 12.80 arcmin^2, although we only use the central 11.56 arcmin^2 which overlaps the u-band image from (Rafelski et al., 2009). The u-band image was obtained with the Keck I telescope and the blue channel of the Low Resolution Imaging Spectrometer (LRIS) (Oke et al., 1995; McCarthy et al., 1998), and has a 1σ depth of 30.7 mag arcsec^{-2} and a limiting magnitude of 27.6 mag. The sample described below also makes use of the observations taken with the NICMOS camera NIC3 in the J and H bands (F110W and F160W; Thompson et al., 2006) whenever the field of view (FOV) overlaps.

3.3 Sample Selection

In order to search for spatially-extended star formation associated with $z \sim 3$ LBGs, we require a sample of such galaxies to form a super-stack of LBG images that we describe here. In §3.3.1, we compare the number counts of the $z \sim 3$ LBGs in the UDF to those in the literature. Then in §3.3.2, we select a subsample that are appropriate for stacking in order to improve the signal to noise, S/N, in the LBG outskirts as described in §3.4. Lastly, in §3.3.3 we investigate possible selection biases of the observations.

The samples in this paper are based on the $z \sim 3$ LBG sample of Rafelski et al. (2009), which contains 407 LBGs selected by using a combination of photometric redshifts and the u-band drop out technique (Steidel & Hamilton, 1992; Steidel et al., 1995, 1996a,b). This selection of LBGs is enabled by the extremely deep u-band image described in §3.2, needed to reduce the traditional degeneracy of colors between $z \sim 3$ and $z \sim 0.2$ galaxies that can yield incorrect redshifts at $z \sim 3$ without the u-band (Ellis, 1997; Fernández-Soto et al., 1999; Benítez, 2000; Rafelski et al., 2009). Rafelski et al. (2009) found that the resultant sample is likely to have a contamination fraction of only $\sim 3\%$. Any such contamination

will have a minimal effect on our results, and is included in the uncertainties (see §3.4.3). In addition, Rafelski et al. (2009) found that the LBG sample is complete to $V \sim 27$ magnitude, limited by the depth of the u-band image.

3.3.1 Number Counts

In order to 1) be confident in our sample selection, 2) verify that we are probing the correct comoving volume, and 3) make completeness corrections in §3.5 and §3.6 (as described in Appendix A), we compare the number counts of the $z \sim 3$ LBG selection from Rafelski et al. (2009) to the completeness corrected number counts from Sawicki & Thompson (2006) and Reddy & Steidel (2009) in Figure 3.1. The uncertainties shown from Rafelski et al. (2009) are only poisson, and therefore have smaller error bars than those by Reddy & Steidel (2009). The points from Reddy & Steidel (2009) are offset by 0.05 mags for clarity, and their uncertainties include both poisson and field to field variations. The number counts and the best fit Schechter function (Schechter, 1976) from Reddy & Steidel (2009) are converted to number of LBGs per half magnitude bin using a similar conversion as in Reddy et al. (2008). Specifically, we use the R-band as a tracer of rest-frame 1700$\mathring{A}$ emission. The apparent measured R magnitude, R_{AB}, is converted from the absolute magnitude using the relation:

$$R_{AB} = M_{AB}(1700\text{Å}) + 5\log(d_L/10\text{pc}) + 2.5\log(1+z)\ , \tag{3.1}$$

where $M_{AB}(1700\mathring{A})$ is the absolute magnitude at the rest-frame 1700$\mathring{A}$, and d_L is the luminosity distance. We apply the k-correction from Rafelski et al. (2009) of $R_{AB} - V_{AB} = -0.15$ mag to get the V-band magnitudes. We use a comoving volume of 26436 Mpc^3 for the redshift interval $2.7 < z < 3.4$ and an area of 11.56 arcmin^2 for the number count conversion. We adopt a Schechter function with parameters found by Reddy & Steidel (2009) of $\alpha = -1.73 \pm 0.13$, $M^*_{AB}(1700\mathring{A}) = -20.97 \pm 0.14$, and $\phi^* = (1.71 \pm 0.53) \times 10^{-3}$ Mpc^{-3}.

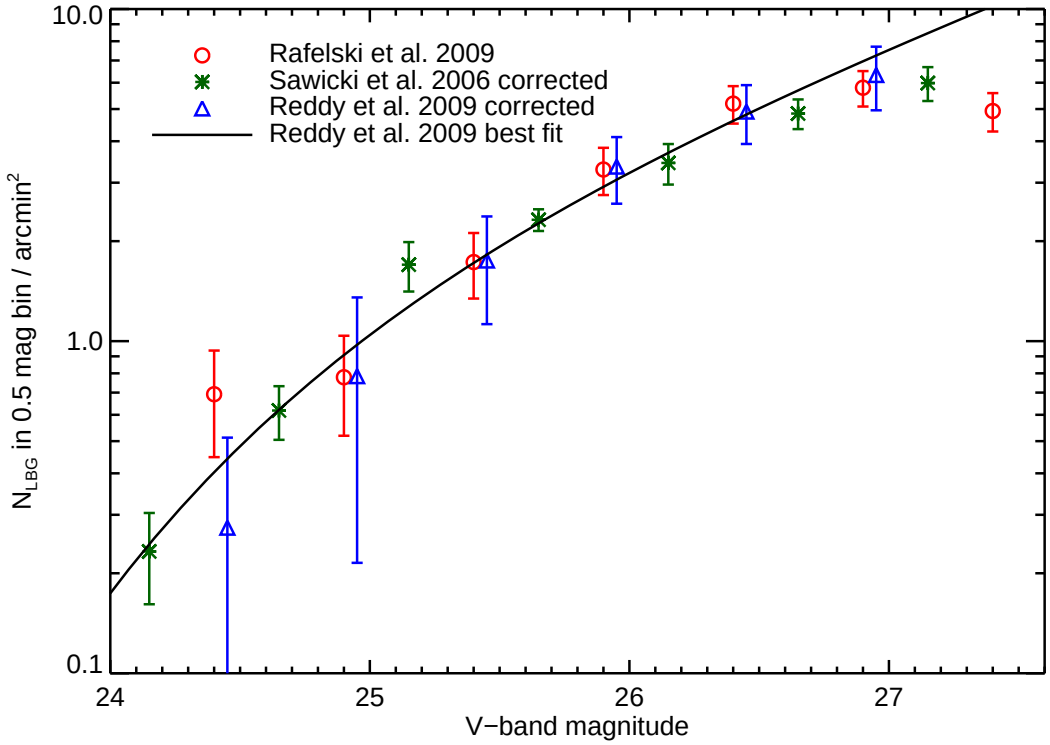

Figure 3.1 Comparison of the number counts of $z \sim 3$ LBGs in 0.5 magnitude bins per square arcminute. The red circles are from Rafelski et al. (2009), the green crosses are from Sawicki & Thompson (2006) corrected for completeness, and the blue triangles are from Reddy & Steidel (2009) also corrected for completeness. The points from Reddy & Steidel (2009) are offset by 0.05 mags in order to avoid overlapping the Rafelski et al. (2009) points. The black line is the best fit Schechter function (Schechter, 1976) from Reddy & Steidel (2009) with $\alpha = -1.73 \pm 0.13$, $M^*_{AB}(1700\mathring{A}) = -20.97 \pm 0.14$, and $\phi^* = (1.71 \pm 0.53) \times 10^{-3}$ Mpc^{-3}.

The resultant number counts agree nicely, and show that the completeness of the Rafelski et al. (2009) $z \sim 3$ LBG sample matches the previous completeness limit found of $V \sim 27$ magnitude. The agreement also suggests that the comoving volume for the redshift interval $2.7< z <3.4$ is appropriate for the sample, which is important for the argument given in §3.5. More importantly, the agreement of the number counts allow us to use the best-fit Schechter function from Reddy & Steidel (2009) to determine the expected number of LBGs at fainter magnitudes, providing the needed information to make completeness corrections in Appendix A. We note that this luminosity function is valid to $R \sim 26.5$, after which the extrapolation to fainter magnitudes could be a potential source of error, and we address this below.

3.3.2 Catalogs of LBGs and Stars

We use two catalogs of $z \sim 3$ LBGs in this paper. The first is the full sample of 407 $z \sim 3$ LBGs as described in Rafelski et al. (2009). The sample redshift distribution is shown in Figure 12. of Rafelski et al. (2009), and has a mean photometric redshift of 3.0 ± 0.3. The second (hereafter referred to as 'subset sample') is a sample of $z \sim 3$ LBGs selected to create a composite image to improve the signal-to-noise of the surface brightness profile described below. These LBGs are selected to be compact, symmetric, and isolated, similar to the selection done at higher redshift by Hathi et al. (2008). The LBGs are selected to be compact and symmetric to aid in stacking LBGs of similar morphology and physical characteristics such that the bright central regions of the LBGs overlap. They were also selected to be isolated from nearby neighbors to avoid coincidental object overlap and dynamically disturbed objects.

To select objects that are compact, symmetric, and isolated, we measure morphological parameters in the V-band image using `SExtractor` (Bertin & Arnouts, 1996). We experimented with different morphological parameters, such as Asymmetry (Schade et al., 1995), Concentration (Abraham et al., 1994, 1996), Gini coefficient (Lotz et al., 2004), and Clumpiness (Conselice, 2003). However, we found that the best sample was selected based on the FWHM for compactness and

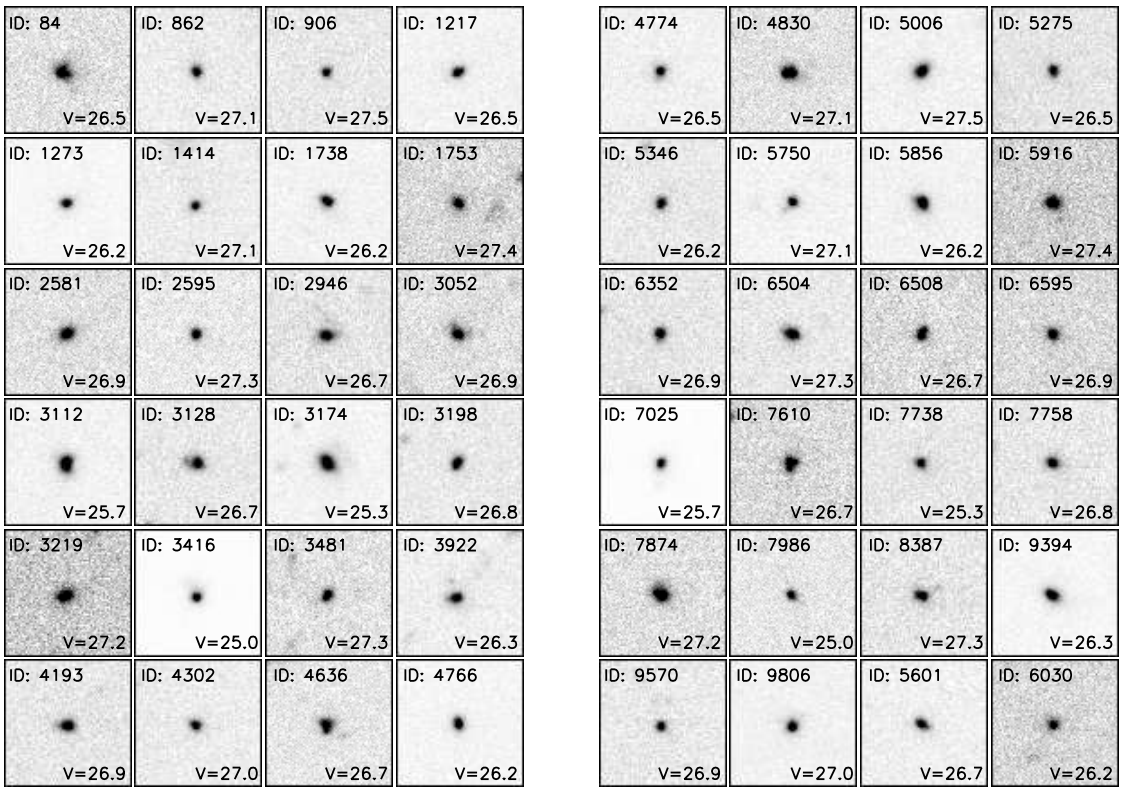

Figure 3.2 Thumbnail images in the V-band of the 48 $z \sim 3$ LBG subsample. The thumbnails are 2.4 arcseconds on a side, the same size as the composite image in Figure 3.3, which corresponds to 18.5 kpc at $z \sim 3$.

ellipticity $\epsilon = (1 - b/a)$ for symmetry, similar to the criteria in Hathi et al. (2008). Specifically, for the subset sample, we require that FWHM$\leq$0.″25 and $\epsilon \leq 0.25$, a slightly more conservative selection than Hathi et al. (2008). Lastly, to select isolated objects, we require that there are no other objects within 1.″4 brighter than 29th mag. These requirements yield a sample of 48 LBGs, representing $\sim 12\%$ of the $z \sim 3$ LBG sample, whose properties are compared in §3.3.3. We show this sample as thumbnails that are 2.4 arcseconds on a side, which corresponds o 18.5 kpc at $z \sim 3$, in Figure 3.2, and a table with relevant information about the 48 LBGs in Table 3.1. Information on the full sample of 407 LBGs is available in Rafelski et al. (2009).

Table 3.1. Properties of LBGs included in image stack

ID[a]	z_{phot} [b]	V mag	$u-V$ mag	$B-V$ mag	$V-z'$ mag	FWHM arcsec	Ellipticity
84	$3.11^{+0.40}_{-0.40}$	26.56±0.02	2.40±0.35	0.70±0.05	0.03±0.04	0.24	0.18
862	$3.18^{+0.41}_{-0.41}$	27.16±0.02	1.87±0.36	0.74±0.05	-0.44±0.05	0.12	0.14
906	$2.68^{+0.36}_{-0.36}$	27.52±0.02	1.50±0.36	-0.10±0.04	-0.14±0.05	0.10	0.04
1217	$2.75^{+0.37}_{-0.37}$	26.53±0.01	2.28±0.30	0.34±0.02	0.01±0.02	0.14	0.23
1273	$3.03^{+0.39}_{-0.39}$	26.24±0.01	2.79±0.37	0.58±0.03	0.02±0.02	0.12	0.12
1414	$2.86^{+0.38}_{-0.38}$	27.19±0.02	1.82±0.37	0.49±0.06	-0.03±0.05	0.10	0.13
1738	$2.67^{+0.36}_{-0.36}$	26.27±0.01	1.05±0.08	0.03±0.02	-0.30±0.03	0.16	0.15
1753	$3.44^{+0.43}_{-0.43}$	27.47±0.03	1.02±0.35	1.39±0.14	0.58±0.04	0.18	0.12
2581	$3.40^{+0.43}_{-0.43}$	26.92±0.02	2.05±0.35	1.04±0.07	0.43±0.03	0.18	0.24
2595	$2.97^{+0.39}_{-0.39}$	27.37±0.02	1.60±0.35	0.22±0.04	-0.17±0.05	0.13	0.05

Note. — Table 3.1 is shown in full in the appendix (Table C.5). A portion is shown here for guidance regarding its form and content. V magnitudes are total AB magnitudes, and colors are isophotal colors. U-band photometry is from Rafelski et al. (2009) and the rest are from Coe et al. (2006). Nondetections in u-band are given 3σ limiting magnitudes.

[a]ID numbers from Rafelski et al. (2009) which match those by Coe et al. (2006).

[b]Bayesian Photometric Redshift (BPZ) and uncertainty from 95% confidence interval from Rafelski et al. (2009).

In addition to the two samples of LBGs, we also need a sample of stars for an accurate measurement of the point spread function (PSF) of the UDF images. We obtain this star sample from Pirzkal et al. (2005), using only those stars with confirmed grism spectra, which mostly consist of M dwarfs. We exclude the stars that are saturated, leaving 15 stars in the V-band image within our FOV with $V = 25.7\pm1.3$, more than adequate to measure the PSF. We note that a comparison of the star PSF with the LBGs show that they are all resolved in the high resolution ACS images.

3.3.3 Comparison of the Subset and Full LBG Samples

We investigate whether the subset sample of 48 LBGs is drawn from the same parent population of the full sample of 407 LBGs by comparing the magnitude, color, and redshifts of two the samples. First, we find little variation in the magnitude distributions of the two samples, with a difference in the mean of ~ 0.3 mag. The subset sample is somewhat fainter, with the full sample having an aver-

age AB magnitude of $V = 26.4 \pm 0.9$ and the subset sample with $V = 26.7 \pm 0.6$. That is, there is a minor systematic selection of fainter LBGs in the subset sample, although this difference is not significant. The similar magnitude distribution of the rest-frame FUV flux suggests that the SFR of the two samples is similar.

Second, we compare the mean colors of the of the two samples, and find the two samples have the same colors. We test this both for the distribution and for stacks of the LBGs. First, the mean of the distribution of the subset sample yields colors of $B-V = 0.5\pm0.4$, $V-i' = 0.0\pm0.2$, and $i'-z' = 0.0\pm0.1$, while the full sample has colors of $B-V = 0.6\pm0.4$, $V-i' = 0.1\pm0.2$, and $i'-z' = 0.0\pm0.1$. Second, the color of the stacked subset sample based on aperture photometry has colors of $B-V = 0.2\pm0.2$, $V-i' = 0.1\pm0.2$, and $i'-z' = 0.1\pm0.2$, while the full sample stack has colors of $B-V = 0.3\pm0.1$, $V-i' = 0.1\pm0.1$, and $i'-z' = 0.2\pm0.1$. These colors are not significantly different based on both the distribution and the stacked photometry uncertainties. The similar distribution of colors suggests that the two samples are made of the same stellar populations and that their star formation histories (SFHs) are similar.

Lastly, the two samples have very similar redshift distributions, with the same mean redshift of 3.0 ± 0.3. We therefore conclude that the subset sample and full sample of LBGs are equivalent in magnitude, color, and redshift, and therefore are probably drawn from the same parent population of LBGs that have similar SFRs, stellar populations, and SFHs. Hence, we are relatively confident that the results determined below for the subset sample of LBGs is applicable to the full sample.

For the sake of completeness, we also consider stacking the full stack of LBGs in Appendix B. We note that stacking the full sample introduces contamination into the stack, such as nearby galaxies. In addition, bright parts of morphologically different galaxies contribute to the faint parts of other galaxies. We therefore do not use this as our primary stack, and take the full stack as an upper limit to the emission from the full sample of LBGs.

3.4 Analysis of UDF Images

The V-band image of the UDF is the most sensitive high resolution image covering the rest-frame FUV at $z \sim 3$ available. However, even this image does not reach the desired sensitivity to search for spatially-extended star formation on scales up to $\sim$10 kpc (as shown below). We wish to increase the signal-to-noise (S/N) ratio high enough to probe down to low values of the SFR surface density ($\Sigma_{\rm SFR}$). Image stacking methods can be used to study the average properties of well defined samples in which individual objects do not have the necessary S/N (e.g. Pascarelle et al., 1996; Zibetti et al., 2004, 2005, 2007; Hathi et al., 2008).

We therefore create super-stacks of the LBG images in §3.4.1, and investigate how the sky subtraction uncertainty affects those stacks in §3.4.2. Using the super-stack of the subset sample of LBGs described in §3.3.2, we determine the radial surface brightness profile of $z \sim 3$ LBGs in §3.4.3, which will be used for much of the analysis throughout the paper. Lastly, in §3.4.4, we investigate the effects of the Ly-α line on the stacked image.

3.4.1 Image Stacks

We create stacked composite images for the LBG subset sample, full LBG sample, and stars sample using custom IDL code. For each object, we fit a 2-D Gaussian using `MPFIT` (Markwardt, 2009) to determine a robust center. We then shift each object to be centered with sub-pixel resolution, interpolating with a damped sinc function. We then create thumbnail images for each object, and combine all the objects by taking the median of all the thumbnails, yielding a robust stacked image which is not sensitive to outliers. While some of the individual thumbnails may have faint emission regions below the level of the isolation criteria, they do not contribute to the median because such emission would need to occur at the same pixels for a significant number objects to affect the median. Therefore, independent of the origin of any such faint regions, they do not affect their median, and therefore do not affect the final stack. While we are most interested in the V-band, we also carry out this procedure for the B, V, i′, and z′ bands and the

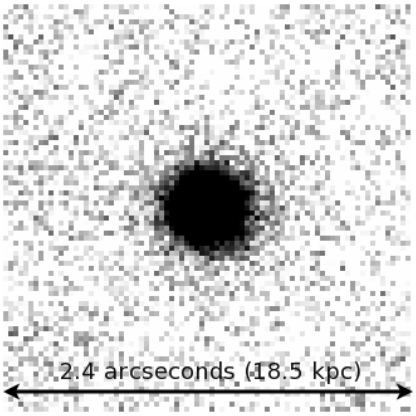

Figure 3.3 Composite image in the V-band of the 48 $z \sim 3$ LBG subsample. Each stamp is 2.4 arcseconds on a side, which corresponds to 18.5 kpc at $z \sim 3$.

stars sample. Figure 3.3 shows the stacked V-band image, as this corresponds to the rest frame FUV luminosity at $z \sim 3$ which is a sensitive measure of the SFR. The image is 2.4 arcseconds on a side, which corresponds to 18.5 kpc at $z \sim 3$.

We showed in §3.3.3 that the subset sample is representative of the full LBG sample, and here investigate any possible variations in the radial surface brightness profile with magnitude and FWHM within the subsample itself. We check if these parameters affect the stack by creating three independent stacks of different brightnesses or FWHM. In the case of magnitude, we create one stack of the brightest 16 LBGs, a second stack of the next 16 LBGs, and a third stack with the faintest 16 LBGs, and repeat for FWHM. We find the profiles to be very similar, and find that the magnitude and FWHM range does not affect our stack. We also investigate the change in the surface brightness profile color. We find that the variations of the LBG composite images for the B, V,i', and z' bands across radius are small compared to their uncertainties, and no clear change in color is obvious at any radius.

We also test the difference between taking the median and the mean of the images in our stack. The profiles of the mean stack are slightly higher at the bright end, but are very similar to the median stack starting at $\sim 0.3''$. We chose to go with the median as it is more robust to possible contamination in the outskirts. In this way, we are not sensitive to contamination if it only occurs in a small subset

of our sample.

In creating a stack of the star data to measure the PSF, we scale each star to the peak of the fitted 2-D gaussian before stacking. For the PSF, we only care about the shape of the PSF, and not the actual value of the flux. Given the wide distribution of magnitudes of the stars, this scaling improves the PSF determination. We do not scale the LBGs before stacking, as we care about the actual measured flux in the outskirts of the LBGs. We find that scaling does not have a significant effect on the LBG stack due to the small range in brightnesses of the selected LBGs, with the radial surface brightness of the two stacks being consistent within the uncertainties, and this would therefore not alter our results.

3.4.2 Sky Subtraction Uncertainty

We hope to accurately characterize the sky background and the uncertainties due to the subtraction of this sky background. The sky-subtraction uncertainty of the UDF was carefully investigated by Hathi et al. (2008), and we follow their prescription for determining the 1σ sky-subtraction error. Hathi et al. (2008) found that it was more reliable to characterize the sky locally rather than globally for the entire image. For this reason, we redetermine the local sky-background for the 407 $z \sim 3$ LBGs in our sample. First, we measure the sky background in each of the thumbnail images of the full LBG sample using IDL and the procedure `MMM.pro`[5], adapted from the DAOPHOT routine by the same name (Stetson, 1987). This procedure iteratively determines the background, removing low probability outliers each time, until the sky background is determined. We then find the 1σ sky value by by fitting a Gaussian to the distribution of sky values. For the V-band, this gives us a value for $\sigma_{sky,ran}$ of 3.52×10^{-5} electrons s^{-1}, very similar to that found by Hathi et al. (2008) of 3.55×10^{-5} electrons s^{-1}. Using this number and the formalism in Hathi et al. (2008), we find a 1σ sky-subtraction error of 30.01 mag arcsec^{-2}.

If the error is random, the uncertainty of the sky subtraction will decrease as we stack more images together. In fact, for a median stack in the Poisson limit,

[5]Part of the IDL Astronomy User's Library

the 1σ uncertainty is $1.25/\sqrt{N}$, where N is the number of images. We test this relation specifically for the UDF data as the error may not be completely random. We stack 48 blank thumbnails and compare the standard deviation of stacked pixels to the median of the standard deviations of each individual thumbnail, and find the above relation holds to 99% accuracy. We are therefore confident that the sky-subtraction noise decreases with stacking as expected, yielding larger S/N values. For the stack of 48 LBGs from our subset sample, we find a 1σ sky-subtraction error of 31.87 mag arcsec^{-2}. We use both of these sky-subtraction errors as our sky limits below in §3.4.3.

3.4.3 Radial Surface Brightness Profile

We extract a radial surface brightness profile from the super-stack of LBG images in Figure 3.4 using custom IDL code which yields identical results to the IRAF[6] procedure `ELLIPSE`. We use circular aperture rings with radial widths of 1.5 pixels in such a way that they do not overlap to avoid correlated data points while still finely probing the profile. We use custom code in order to facilitate using the bootstrap error analysis method to determine the uncertainties. Since we are stacking different objects with different characteristics, the uncertainty for the brighter regions will be dominated by the sample variance, and can be determined with the bootstrap method. Specifically, we bootstrap to get the uncertainty of the median of the LBGs by replacing a random fraction ($1/e \approx 37\%$) of the 48 LBG thumbnails with randomly duplicated thumbnails from the subset sample. We repeat this 1000 times to get a sample of composite images using the method described in §3.4.1, each with its own radial surface brightness profile. The resultant uncertainty is then the standard deviation of all the surface brightness magnitudes at each radius. This method is conservative, but includes all the uncertainties associated with the variance of the sample. Moreover, it helps takes into account possible errors introduced by possible contamination of our LBG sample by other objects, although as mentioned in §3.3, we believe this contamination fraction to

[6]IRAF is distributed by the National Optical Astronomy Observatory, which is operated by the Association of Universities for Research in Astronomy, Inc., under cooperative agreement with the National Science Foundation.

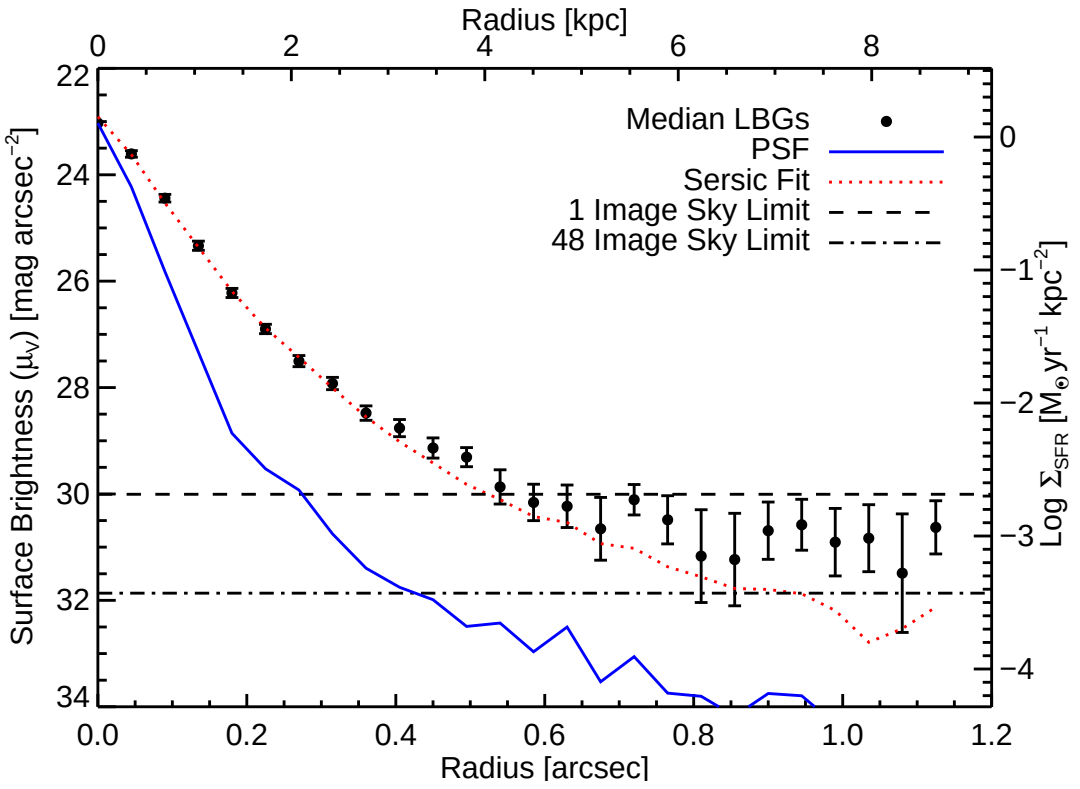

Figure 3.4 The extracted surface brightness profile from the stacked image, where the black points are the 48 LBG composite profile and the blue line is the measured point spread function from stars. The dotted red line is the best fit Sérsic profile convolved with the PSF. The dashed line is the 1σ sky subtraction error for 1 thumbnail image, while the dashed-dotted line is the 1σ sky subtraction error for the composite stack of 48 LBGs, as described in §3.4.2.

be small.

The solid blue line in Figure 3.4 represents the measured ACS V-band PSF determined from a stacked image of the 15 stars described in §3.3.2. The central surface brightness of the stars is scaled to match the LBGs. We note that the S/N of the star stack is higher than that of the LBG stack, even though it has a smaller number of objects in the stack, because the stars are brighter than the LBGs. Therefore the PSF is well determined, and we expect the uncertainties are dominated by the lower S/N LBG stack. The PSF declines more rapidly than the radial surface brightness profile at all radii, which shows that the LBGs are clearly resolved and that the median surface brightness profile of the LBGs is extended.

The dashed line is the 1σ sky subtraction error for 1 thumbnail image, while the dashed-dotted line is the 1σ sky subtraction error for the composite stack of 48 LBGs, as described in §3.4.2.

3.4.3.1 Sersic Profile Fit

The dotted red line in Figure 3.4 shows the best fit Sérsic profile convolved with the ACS V-band PSF. We fit for the best Sérsic model to the composite LBG image by using the Levenberg-Marquardt least-squares minimization, with the χ^2 calculated on a pixel by pixel basis for each possible model. The best fit values are $n = 1.9 \pm 0.04$ and $R_e = 0.074 \pm 0.001$ arcsec, where n is the Sérsic index and R_e is the effective radius, which includes half the light of the LBGs. We use the dimensionless scale factor b(n) from Ciotti & Bertin (1999) such that R_e is the half-light radius. The small R_e value is likely due to our pre-selection of LBGs to be compact (see §3.3.2). While the fit has a good reduced chi-square χ^2/ν of 1.27, it is not a very good fit to the data in the outer regions. The fit is dominated by the inner part of the profile with radii less than $\sim 0.4''$, since the uncertainties are significantly smaller in that region. For radii larger than $\sim 0.4''$, the profile deviates from the inner best fit profile. This deviation is real, being above the PSF and the 1σ sky-subtraction error. This is similar to what Hathi et al. (2008) found when stacking LBGs at $z \sim 4 - 6$. The main constraint we have from this is that it suggests the profile is similar to an exponential disk type profile. If we fit an exponential, it yields a worse fit with a χ^2/ν of 1.4, and $R_e = 0.068 \pm 0.001$ arcsec. A bulge-disk model yields a slightly better fit in the outer regions, but does not improve the overall χ^2/ν. We note that we do not use the fit in the analysis below.

3.4.4 Effects of the Ly-α Line on the Image Stack

We investigate possible contamination from Ly-α emission on the image stack to ensure that the radial surface brightness profile is unaffected by Ly-α emission from the LBGs. First, we note that Ly-α only enters our V-band filter for about half our sample due to the redshift range sampled. Second, we find that due to the large width of the V-band filter, the Ly-α line would have a very small

effect. This is determined by taking the stacked LBG spectrum from Shapley et al. (2003), and comparing the flux in the V-band filter with and without the Ly-α line. We find that the inclusion of the Ly-α line yields an increase of 0.02 magnitudes, a very small effect compared to our uncertainties. While our sample of LBGs is significantly fainter than the LBGs in the stacked spectrum from Shapley et al. (2003), we expect the average strength of the Ly-α line to be similar due to the low escape fraction of ionizing radiation from LBGs (Shapley et al., 2006).

Moreover, we compare the radial surface brightness profile of the V-band stack and an equivalent stack in the i'-band. The Ly-α line does not enter the i'-band filter throughout our redshift range, making the i'-band an excellent test to check if the radial surface brightness profile is affected by the Ly-α line. We find that the V and i'-bands have the same radial surface brightness profile within their uncertainties, with no systematic shifts. This suggests that the Ly-α line has little to no effect, even if the Ly-α line were more extended than the continuum.

3.5 Direct Inferences from the Data

The surface brightness profile of the stacked image indicates the presence of spatially extended star formation around LBGs. In this section, we describe how to connect this emission, which corresponds to the rest-frame FUV radiation intensity, to the SFR surface density. We then compare the covering fraction of this emission to that of the gas responsible for the star formation in §3.5.2. Specifically, in order to determine what types of gas can be responsible for the observed emission, we compare its covering fraction to that of atomic-dominated gas in §3.5.2.1, and to that of molecular-dominated gas in §3.5.2.2. Then in §3.5.3 and §3.5.4, we calculate the *in situ* SFR, $\dot{\rho}_*$, and metal production based on the integrated flux measured in the outskirts of LBGs.

3.5.1 Connecting the Observed Intensity to the SFR Surface Density

In order to investigate how the measured star formation relates to the underlying gas, we require a relation between star formation and gas properties. Star formation occurs in the presence of cold atomic and/or molecular gas, according to the KS relation given by

$$\Sigma_{\rm SFR} = K \times \left(\frac{\Sigma_{gas}}{\Sigma_{\rm c}}\right)^{\beta} . \tag{3.2}$$

This relation holds for nearby disk galaxies in which $\Sigma_{\rm gas}$ is the mass surface density perpendicular to the plane of the disk, $\Sigma_{\rm c} = 1 {\rm M}_{\odot}{\rm pc}^{-2}$, $K = K_{Kenn} = (2.5 \pm 0.5)\times10^{-4}$ ${\rm M}_{\odot}$ ${\rm yr}^{-1}$ ${\rm kpc}^{-2}$, and β=1.4±0.15 (Kennicutt, 1998a,b). There has been much recent work on improving both our understanding of this relation, and measuring the values of K and β (e.g. Leroy et al., 2008; Bigiel et al., 2008; Krumholz et al., 2009b; Gnedin & Kravtsov, 2010b; Genzel et al., 2010; Bigiel et al., 2010b). When only considering molecular gas, the relationship has a flatter slope of β=0.96±0.07 (Bigiel et al., 2008) or $\beta \sim 1.1$ (Wong & Blitz, 2002). We use the original values from (Kennicutt, 1998a) when considering the total gas density to simplify comparisons with other work, and β=1.0 and K=K_{Biegel}=8.7±1.5×10^{-4} ${\rm M}_{\odot}$ ${\rm yr}^{-1}$ ${\rm kpc}^{-2}$ when considering only molecular gas. We note that the K value given here used for molecular gas is modified from Bigiel et al. (2008) to use the same $\Sigma_{\rm c} = 1$ ${\rm M}_{\odot}{\rm pc}^{-2}$ value as above.

Rewriting the KS relation in terms of the column density of the gas, we get

$$\Sigma_{\rm SFR} = K \times \left(\frac{N}{N_c}\right)^{\beta} , \tag{3.3}$$

where the scale factor N_c=1.25×10^{20} ${\rm cm}^{-2}$ (Kennicutt, 1998a,b) and N is the hydrogen column density.[7] We note that this is only valid above the critical column density, which is usually associated with the threshold condition for Toomre insta-

[7]The reader should be aware that when referring to nearby galaxies, N corresponds to $N_{\perp}$, the H I column density perpendicular to the the disk, but when writing about our observations, we are referring to observed column densities N, where we implicitly include the inclination angles in our definitions.

bility. For H I gas in local galaxies, it is observed to range between $5{\times}10^{20}$ cm^{-2} and $2{\times}10^{21}$ cm^{-2} (Kennicutt, 1998b).

In order to connect $\Sigma_{\rm SFR}$ to the observations, we require a relation between observed intensity, corresponding to rest-frame FUV emission, and observed column density, N. Following Wolfe & Chen (2006, eq. 3), we find that for a fixed value of N, the intensity averaged over all disk inclination angles is given by

$$\langle I_{\nu_0}^{obs} \rangle = \frac{C\Sigma_{\rm SFR}}{4\pi(1+z)^3\beta} \ , \tag{3.4}$$

where z is the redshift, and C is the conversion factor from SFR to FUV ($\lambda \sim 1500\mathring{A}$) radiation, with $C = 8.4 \times 10^{-16}$ ergs cm^{-2} s^{-1}Hz^{-1}(M$_\odot$ yr^{-1} kpc^{-2})$^{-1}$ (Madau et al., 1998; Kennicutt, 1998b). We use the same value of C as Wolfe & Chen (2006) corresponding to a Salpeter IMF. The result in equation 3.4 assumes that the star formation occurs in disks inclined on the plane of the sky by randomly selected inclination angles, and averages over all possible angles (see Wolfe & Chen, 2006).

3.5.2 Covering Fraction of LBGs Compared to the Underlying Gas

The covering fraction of observed star formation should be consistent with that of its underlying gas. We therefore investigate whether the covering fraction of the outer parts of LBGs is consistent with the covering fraction of atomic-dominated gas in §3.5.2.1 and molecular-dominated gas in §3.5.2.2. This consistency check yields insights into the nature of the observed star formation, and validates the hypothesis that the outskirts of LBGs consist of atomic-dominated gas, which is used in subsequent sections of the paper.

We calculate the cumulative covering fraction, C_A, for gas columns greater than some column density N, by integrating the H column density distribution function $f(N_H, X)$, where H is either H I or H_2. Specifically,

$$C_A(N) = \int_{X_{min}}^{X_{max}} dX \int_{N}^{N_{max}} dN_H f(N_H, X) \ , \tag{3.5}$$

where $f(N_H, X)$ is the observed column density distribution function of the hydrogen gas, N_{max} is the maximum column density considered, and X is the absorption distance with dX being defined as

$$dX \equiv \frac{H_0}{H(z)}(1+z)^2 dz \ , \tag{3.6}$$

where H_0 is the Hubble constant and $H(z)$ is the Hubble parameter at redshift z. For X_{min} and X_{max} we use the same redshift interval as in §3.3.1, namely $2.7 < z < 3.4$ corresponding to $6.6 < X < 9.2$. The covering fraction depends strongly on the column density distribution function, which is different for atomic and molecular gas. Below we investigate the covering fraction for both cases.

3.5.2.1 Covering Fraction of Atomic-dominated Gas

There is strong evidence to support the association of LBGs and neutral atomic-dominated H I gas, i.e., DLAs (see §3.1), and we therefore investigate whether the covering fraction of the outer parts of LBGs is consistent with the covering fraction of DLAs. If the outer regions of LBGs truly consist of DLA gas, then the covering fractions as functions of the surface brightnesses should be consistent. In this subsection, we work under the hypothesis that the observed FUV emission in the outskirts of LBGs is from *in situ* star formation in atomic-dominated gas, and compare the observed covering fraction to that of the gas distribution.

In order to calculate the covering fraction using equation 3.5, we require $f(N_H, X)$ for atomic-dominated gas. The observed H I column density distribution function, $f(N_{\rm HI}, X)$, is obtained by a double power-law fit to the SDSS data

$$f(N_{\rm HI}, X) = k_3 \left(\frac{N}{N_0}\right)^{\alpha} \ , \tag{3.7}$$

where k_3=(1.12±0.05)×10^{-24} cm^2, α=α_3=−2.00±0.05 for $N \leq N_0$[8] and $\alpha = \alpha_4 = -3.0$ for $N > N_0$, where $N_0 = 3.54^{+0.34}_{-0.24} \times 10^{21}$ cm^{-2} (Prochaska et al., 2005; Prochaska & Wolfe, 2009). The value of α_4 used is different than measured in

[8]We follow Wolfe & Chen (2006) who equated N_0 with N_d, the break in the double power-law expression for $f(N_{\rm HI}, X)$.

(Prochaska & Wolfe, 2009), to remain consistent with our formulation of randomly oriented disks in §3.6, and is predicted to be −3.0, and we use this value for the covering fraction to be consistent. Although this value of α_4 is different than the value in Prochaska & Wolfe (2009), the uncertainties are quite large due to low numbers of very high column density DLAs, and it is quite similar to the value found by Noterdaeme et al. (2009) of α_4=−3.48.

We note that Noterdaeme et al. (2009) find slightly different values for k_3 and α_3 than Prochaska & Wolfe (2009), with k_3=8.1×10^{-24} cm^2 and α=α_3=−1.60 for $N \leq N_0$, corresponding to a flatter slope. We use the values from Prochaska & Wolfe (2009), and describe how the differing values affect our results below. Also, although the normalization of $f(N_{\rm HI}, X)$ varies with redshift, the variations for our redshift interval are not large, and does not strongly affect C_A. Using the Prochaska & Wolfe (2009) values for $f(N_{\rm HI}, X)$, and $N_{max} = 10^{22}$ cm^{-2}, we calculate the covering fraction using equation 3.5 and the corresponding expected μ_V from equations 3.3 and 3.4, where $\mu_V = -2.5\log\langle I_{\nu_0}^{obs}\rangle - Z$, and Z is the AB magnitude zero point of 26.486.

We compare the cumulative covering fraction of DLAs to the observed covering fraction of the outer regions of the LBGs in Figure 3.5. The blue dotted line is the DLA covering fraction for DLAs forming stars according to the KS relation, with $K = K_{Kenn}$. The red lines are for less efficient star formation where the dash-dotted line represents $K = 0.1 \times K_{Kenn}$ and the triple dotted dashed line represents $K = 0.02 \times K_{Kenn}$. The black line is the covering fraction for the observed emission in the outskirts of LBGs in the UDF, which is just the area covered by the outskirts of LBGs up to μ_V divided by the total area probed, 11.56 arcmin^2. The covered area is obtained from the radial surface brightness profile and the 407 observed LBGs in this area. The observed covering fraction depends on the depth of the images, and therefore requires a completeness correction for faint objects that are missed: we discuss this completeness correction in Appendix A. The completeness corrected covering fraction for LBGs is the dashed gold long-dashed line, and is the curve that we compare to the DLA lines below. We ignore the data at a radius > 0.8 arcsec (∼ 6kpc) to only include data with S/N>3, however, we expect

a continuation of the observed trends. We note that we are only sampling the top end of the DLA distribution function, and therefore the covering fraction shown is a small fraction (about a tength) of the total covering fraction of DLAs. When considering all DLAs, we cover about one third of the sky, i.e. $\log(C_A) \sim -0.5$. We note that if we use the Noterdaeme et al. (2009) values for $f(N_{\rm HI}, X)$, then the DLA lines move up and to the left (i.e. cover more of the sky).

Under the hypothesis that the outskirts of LBGs are comprised of atomic-dominated gas (i.e. DLAs) which is responsible for the observed emission, then we expect the covering fraction of the DLA gas to be equal to the covering fraction of the outskirts of LBGs. The blue dotted line for DLAs following the KS relation would therefore only be consistent with the covering fraction of the outskirts of LBGs if much of the DLA gas is not surrounding LBGs. This possibility was constrained by (Wolfe & Chen, 2006), who found that DLAs would need to be forming at significantly lower SFR efficiencies if this was the case. On the other hand, we find that the covering fraction of the outskirts of LBGs is consistent with DLAs having SFR efficiencies of $K \gtrsim 0.1 \times K_{Kenn}$, at which point the covering fraction are roughly equal. This covering-factor analysis provides evidence that if the outskirts of LBGs are comprised of DLA gas, then the SFR efficiency of this atomic-dominated gas at $z \sim 3$ is about 10% of the efficiency for local galaxies.

Moreover, the cumulative covering fraction shows that there is sufficient DLA gas available to be responsible for the emission in the outskirts of LBGs for SFR efficiencies $\gtrsim 10\%$. We investigate this lower SFR efficiency further in §3.6, where we find an efficiency closer to 5%, which is only a factor of $\sim$2 different than the efficiency determined from the covering fraction. We note that systematic uncertainties due to assumptions throughout both quantities could easily be off by a factor of two, and so the general agreement of the covering fraction at low SFR efficiencies is reassuring, and we are not concerned about the minor disagreement.

3.5.2.2 Covering Fraction of Molecular Gas

In the previous subsection, we worked under the hypothesis that the observed FUV emission in the outskirts of LBGs is from *in situ* star formation in

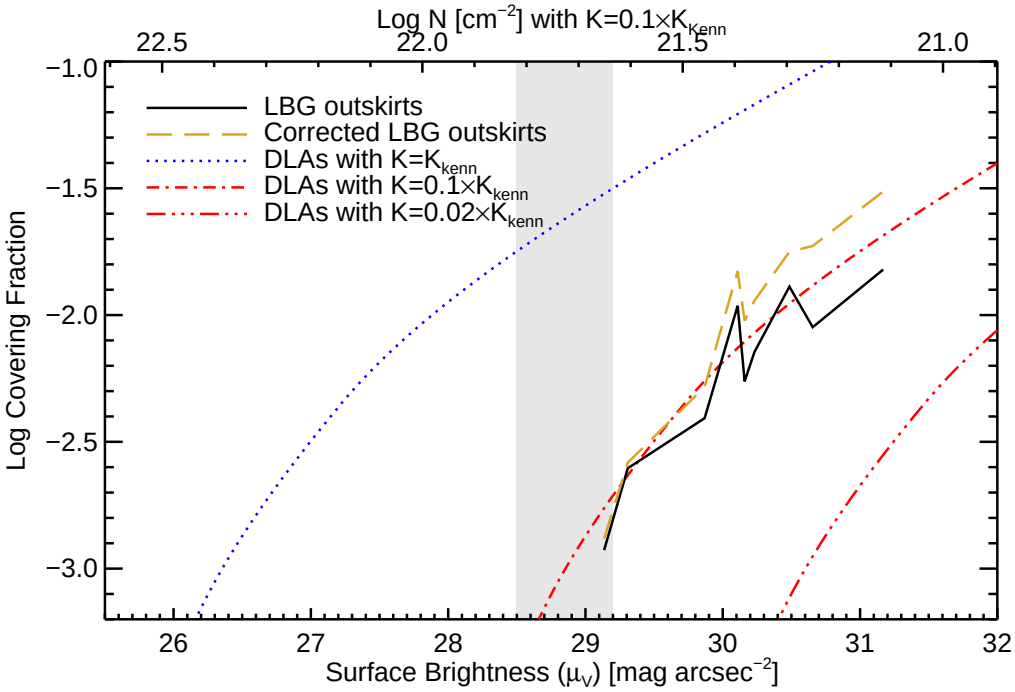

Figure 3.5 Cumulative covering fraction of DLA systems with columns greater than some column density N (and therefore surface brightness), compared to the covering fraction of the observed $z \sim 3$ LBG outskirts greater than some surface brightness. The blue dotted line is the DLA covering fraction for DLAs with $K = K_{Kenn}$, the red dash-dotted line is for $K = 0.1 \times K_{Kenn}$, and the red triple-dotted-dashed line is for $K = 0.02 \times K_{Kenn}$. The solid black line is the covering fraction for the LBG outskirts, while the gold long-dashed line is the same corrected for completeness. The gray filled region represents the transition region mentioned in §3.5.2.2. The top x-axis coordinates are the column densities corresponding to the surface brightnesses using an efficiency of $K = 0.1 \times K_{Kenn}$.

atomic-dominated gas. However, it is possible that this star formation occurs in molecular-dominated gas. We consider this scenario here, and compare the covering fraction of molecular-dominated gas, where the majority of the hydrogen gas is molecular, to our observations.

In order to calculate the covering fraction using equation 3.5, we require $f(N_H, X)$ for molecular-dominated gas. We use the observed molecular column density distribution function, $f(N_{H_2})$, from Zwaan & Prochaska (2006), who obtained a lognormal fit to the BIMA SONG data (Helfer et al., 2003),

$$f(N_{H_2}) = f^* \exp\left[\left(\frac{\log N - \mu}{\sigma}\right)^2 / 2\right] , \tag{3.8}$$

where $\mu = 20.6$, $\sigma = 0.65$, and the normalization f^* is 1.1×10^{-25}cm^2 (Zwaan & Prochaska, 2006)[9]. We use the molecular version of the KS relation discussed in §3.5, where β=1.0 and K=K_{Biegel}=8.7×10^{-4} M$_\odot$ yr^{-1} kpc^{-2}, and we let $N_{max} = 10^{24}$ cm^{-2}, the largest observed value for the $f(N_{H_2})$ function used (Zwaan & Prochaska, 2006). However, $f(N_{H_2})$ is not observationally determined at $z \sim 3$, and likely evolves over time, and we investigate such a possibility below.

The evolution of $f(N_{H_2})$ would either be due to a change in the normalization or a change in the shape. The shape of the atomic gas column density distribution function, $f(N_{H_I})$, has not evolved between $z = 0$ and $z = 3$ (Zwaan et al., 2005; Prochaska et al., 2005; Prochaska & Wolfe, 2009), but the normalization has increased by a factor of 2. In the case of H_2, we consider the instance in which only the normalization (f^*) evolves, then we are looking for a change in Ω_{H_2} at $z = 0$ to Ω_{H_2} at $z = 3$. While theoretical models predict that $\Omega_{H_2}(z = 3)/\Omega_{H_2}(z = 0)$ is ~ 4, their similar prediction for atomic gas does not match observations (Obreschkow & Rawlings, 2009). Alternatively, we can determine an upper limit of the evolution of f^* using the evolution of $\dot{\rho}_*$ for galaxies between $z = 0$ and $z = 3$, assuming that the evolution in $f(N_{H_2})$ is only due to the normalization, and there is no evolution in the KS law for molecular gas between $z = 0$ and $z = 3$ (Bouché et al., 2007; Daddi et al., 2010; Genzel et al., 2010, see §3.6.3). Specifically, studies have found that $\dot{\rho}_*(z = 3)/\dot{\rho}_*(z = 0) \sim 10$ (Schiminovich et al., 2005; Reddy et al., 2008), and

[9]We note that Zwaan & Prochaska (2006) has a typographical error, switching μ and σ.

therefore f^* changes at most by a factor of 10, if we assume that the contribution from atomic gas is small. This is used as an upper limit to the evolution of f^*, and we are not suggesting that this is the correct evolution.

We plot the covering fractions of molecular gas at $z = 3$ in Figure 3.6. We consider 3 cases for $f(N_{H_2})$: 1) no evolution as a purple short-dashed line, 2) evolution with a factor of 4 increase in f^* based on the model by Obreschkow & Rawlings (2009) as a pink triple-dashed line, and 3) evolution with a factor of 10 increase in f^* based on the observed evolution in $\dot{\rho}_*$ as a cyan dotted-dashed line. The gray lines continuing these three lines are extrapolations of the data to lower column densities than observed. We note that the column densities on the top x-axis of the plot now are for $K = K_{Biegel}$.

These covering fractions of molecular gas are compared to the LBG profile including the inner cores in Figure 3.6. *The LBG covering fraction is now modified to include the LBG cores which are composed of molecular-dominated gas*, and the new LBG covering fraction is plotted as a solid brown line. We again ignore the data at a radius > 0.8 arcsec ($\sim$ 6kpc) to only include data with S/N>3. This covering fraction is also corrected for completeness similar to §3.5.2.1, except this time we include the cores of the LBGs, and make no distinction between the outskirts and the inner parts of the LBGs, and is described in Appendix A.1. We plot this corrected covering fraction as a gold long-dashed line. This correction is quite large, as even though the cores cover a smaller area than the outskirts, the cores of fainter missed LBGs contribute at every surface brightness as we go fainter. Since there are significantly more faint LBGs than bright LBGs, there are significantly more LBG cores contributing to each surface brightness than there are LBGs with outskirts at those same surface brightnesses. This correction assumes that all the star formation comes from molecular-dominated gas, and therefore all the cores of fainter LBGs are included.

As in §3.5.2.1, we expect the covering fraction of the gas to be equal to the covering fraction of the LBGs forming out of that gas. In the case of purely molecular gas, the upper limit of the covering fraction ($10 \times f^*$) of the gas is only consistent to $\mu_V \sim 28.5$. At $\mu_V \gtrsim 28.5$, the covering fraction of LBGs is larger

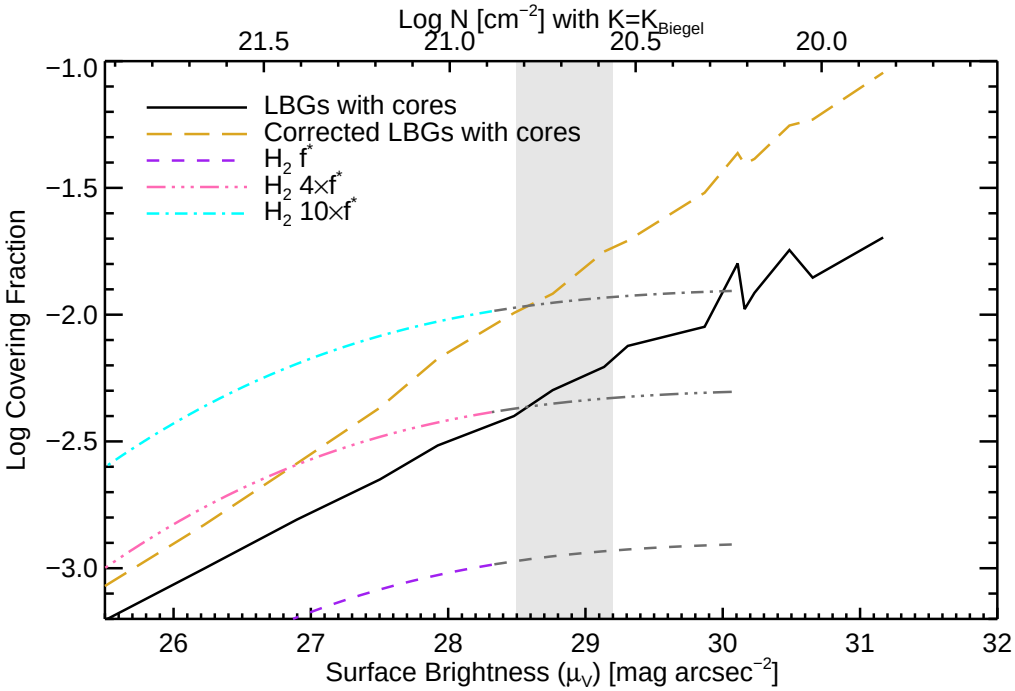

Figure 3.6 Cumulative covering fraction of gas with columns greater than some column density N (and therefore surface brightness). This figure is similar to figure 3.5, but makes comparisons to the covering fractions of molecular gas rather than atomic-dominated gas. The solid black line is the covering fraction for LBGs starting from the center of the LBG core, and the gold long-dashed line is the same corrected for completeness. The purple short-dashed line is the covering fraction of molecular hydrogen with no evolution at $z \sim 3$, the pink triple dotted-dashed line is the same with an evolution of 4 times f^* (the normalization of the column density distribution function of molecular gas) and the cyan dotted-dashed line is the same with an evolution of 10 times f^*. The gray lines continuing the purple, pink, and cyan lines are extrapolations of the data to lower column densities. The gray filled region represents the transition region mentioned in §3.5.2.2. The top x-axis coordinates are the column densities corresponding to the surface brightnesses using an efficiency of $K = K_{Biegel}$ and $\beta = 1$, valid for molecular gas.

than that of the molecular gas. In order to have a covering fraction larger than all the corrected LBG emission, we would require an evolution of f^* by a factor of more than 60, which is not very likely.

We have just shown that the predicted covering factor for molecules is inconsistent with our results for $\mu_V \gtrsim 28.5$. At the same time, our results for atomic-dominated hydrogen do not apply for μ_V brighter than ~ 29, due to the atomic-dominated H I gas cutoff of $N_{\rm HI} \leq 10^{22}{\rm cm}^{-2}$. Therefore, the surface brightness interval from $28.5 \lesssim \mu_V \lesssim 29.2$ is not simultaneously consistent with the neutral atomic-dominated gas nor the molecular gas' covering fractions. This lower bound on μ_V is based on comparing the LBG data compared to 10 times f^*, and for lower evolutions of f^*, this begins at even brighter μ_V. This result is reasonable if the LBG outskirts consist of atomic-dominated gas. In this scenario, there would need to be a transition region between atomic-dominated and molecular-dominated gas, where star formation occurs in both phases. We note that in this hybrid region, the corrected covering fraction of LBGs is not correct, as we would be adding the star formation in the cores of missed LBGs to the outskirts presumably composed of atomic-dominated gas. The true correction would lie somewhere between the black solid line and the gold long-dashed line. We take the molecular gas covering fraction results as evidence that the outskirts of LBGs consist of atomic-dominated gas, which is consistent with our underlying hypothesis for this paper.

3.5.3 Measurements of the SFR and $\dot{\rho_*}$ in the Outskirts of LBGs

In addition to calculating the efficiency of the SFR, we can also calculate the mean SFR, $\langle SFR \rangle$, and $\dot{\rho_*}$ in the outskirts of LBGs by integrating the rest-frame FUV emission in the outer areas. These measurements allow us to calculate the metals produced in the outskirts of LBGs in §3.5.4 and to put a limit on the total $\dot{\rho_*}$ contributed by DLA gas. Similar to Wolfe & Chen (2006), we assume that DLAs are disk like structures, or any other type of gaseous configurations with preferred planes of symmetry. We note that while we work this out for DLA gas, the only assumption in our derivation is that the outskirts have preferred planes of

symmetry such, as disks. Even if the outskirts of LBGs are not DLA gas, such an assumption is still valid given the rotation curves measured for high redshift LBGs (e.g. Schreiber et al., 2009) and the predictions by simulations (Brooks et al., 2009; Ceverino et al., 2010).

For these calculations, we need $\Sigma_\nu^\perp$, the luminosity per unit frequency interval per unit area projected perpendicular to the plane of the disk. Specifically, we solve for $\Sigma_\nu^\perp$ as a function of $\langle I_{\nu_0}^{obs} \rangle$ averaged over all inclination angles. We find that

$$\Sigma_\nu^\perp \equiv \frac{4\pi(1+z)^3 \langle I_{\nu_0}^{obs} \rangle}{\ln(R/H)} \ , \tag{3.9}$$

where R is the radius and H is the scale height of the model disks, which holds in the limit $R \gg H$. We calculate $\Sigma_\nu^\perp$ for a range in aspect ratios, with R/H values from 10 to 100, covering a range from thick disks, as possibly seen at high redshift (e.g. Schreiber et al., 2009), all the way to thin disks resembling the Milky Way. We then calculate the mean SFR by integrating $\Sigma_\nu^\perp$ across the outer region of the LBG stack, and find that

$$\langle SFR \rangle = \frac{8\pi(1+z)^3}{C' \ln(R/H)} \int_{\theta_{\rm low}}^{\theta_{\rm high}} 2\pi {d_A}^2 \langle I_{\nu_0}^{obs}(\theta) \rangle \theta d\theta \ , \tag{3.10}$$

where θ is the radius in arcseconds, $\theta_{\rm low}$ is the minimum radius for the outer region, and $\theta_{\rm high}$ is the maximum radius. $I_{\nu_0}^{obs}(\theta)$ comes from the radial surface brightness profile from §3.4.3 and depends on $\mu_V(\theta)$, namely $I_{\nu_0}^{obs}(\theta) = 10^{-0.4(\mu_V(\theta)+48.6)}$. The SFR depends on the inclination angles of the disks for a given $I_{\nu_0}^{obs}$, and includes a factor of two for averaging over all inclination angles.

In order to find the $\langle SFR \rangle$ in the outer regions of LBGs, we need to designate a radius at which to start integrating the LBG stack, and a comparison of the theoretical model to the data in §3.6.2 yields this radius. The $\langle SFR \rangle$ is independent of the theoretical framework developed later in §3.6, and does not depend on the efficiency of the gas. It is purely a measurement of the star formation occurring in the gas. However, it requires a minimum radius to define the beginning of the outer region of the LBGs. Specifically, we pick the smallest radius that corresponds to the first point in Figure 3.9 where we demonstrate that the small-

est radius of atomic-dominated gas corresponds to $0.4''$.[10] We note that when we refer to spatially extended emission star formation throughout the paper, we are referring to emission at radii larger than $0.4''$. We also require a second point that we integrate out to, for which we use two different values. First, we use the radius of $0.8''$[11], which corresponds to the largest radius above 3σ. Second, we integrate to $1.1''$ [12], corresponding to the furthest point for which we measured μ_V in figure 3.4. Table 3.2 lists the SFRs for different combinations of R/H and $\theta_{\rm high}$. Since we integrate over the radii where the LBG data intersect the theoretical models for the DLA gas, the FUV emission from this region may be from the *in situ* star formation in DLA gas associated with the LBGs (see §3.7).

After we have the SFR we can calculate values for the SFR per unit comoving volume, $\dot{\rho_*}$, via $\dot{\rho_*}$=SFR$\times N_{\rm LBG}/V_{\rm UDF}$, and they are tabulated in Table 3.2. However, since $\dot{\rho_*}$ depends on $N_{\rm LBG}$, we perform a completeness correction as described in Appendix A.2. The resultant completeness corrected $\dot{\rho_*}$ are listed in Table 3.2. While there is a range in the acceptable values for both the SFR and $\dot{\rho_*}$, we find that the extended emission has $\langle SFR \rangle \sim 0.1$ M$_\odot$ yr^{-1} and $\dot{\rho_*} \sim 3 \times 10^{-3}$ M$_\odot$ yr^{-1} Mpc^{-3}.

We take this measured $\dot{\rho_*}$ in conjunction with the upper limit found in Wolfe & Chen (2006) to calculate the total $\dot{\rho_*}$ from neutral atomic-dominated gas at $z \sim 3$. Specifically, Wolfe & Chen (2006) constrain $\dot{\rho_*}$ for regions in the UDF without LBGs, which complements the results from this study for regions containing such objects. Together, we constrain all possibilities for the star formation from such gas. Wolfe & Chen (2006) place a conservative upper limit on $\dot{\rho_*}$ contributed by DLAs with column densities greater than $N_{\rm min} = 2 \times 10^{20}$cm^{-2}, finding $\dot{\rho_*} < 4.0 \times 10^{-3}$ M$_\odot$ yr^{-1} Mpc^{-3}. Combining this with our largest possible value of the completeness corrected $\dot{\rho_*}$ in Table 3.2 of $\dot{\rho_*}$=5.91×10^{-3} M$_\odot$ yr^{-1} Mpc^{-3}, we calculate an upper limit on the total $\dot{\rho_*}$ contributed by DLA gas.

[10]This corresponds to $\mu_V = 28.8 \pm 0.2$ mag arcsec^{-2}, or $\Sigma_{\rm SFR} = (6 \pm 1) \times 10^{-3}$ M$_\odot$ yr^{-1} kpc^{-2} (Figure 3.4).

[11]This corresponds to $\mu_V = 30.5 \pm 0.5$ mag arcsec^{-2}, or $\Sigma_{\rm SFR} = (1.3 \pm 0.6) \times 10^{-3}$ M$_\odot$ yr^{-1} kpc^{-2}(Figure 3.4).

[12]This corresponds to $\mu_V = 30.6 \pm 0.6$ mag arcsec^{-2}, or $\Sigma_{\rm SFR} = (1.2 \pm 0.7) \times 10^{-3}$ M$_\odot$ yr^{-1} kpc^{-2}(Figure 3.4).

Table 3.2. SFR, $\dot{\rho_*}$, and Metallicity

θ_{low}[a] arcsec	θ_{high}[a] arcsec	R/H[b]	SFR $M_\odot$ yr^{-1}	$\dot{\rho_*}$ $M_\odot$ yr^{-1} Mpc^{-3}	$\dot{\rho_*}$ corrected $M_\odot$ yr^{-1} Mpc^{-3}	f[c]	Z $Z_\odot$	$[M/H]$
0.405	0.765	10	0.118 ± 0.002	$(1.82 \pm 0.03) \times 10^{-3}$	$(3.75 \pm 0.03) \times 10^{-3}$	0.084 ± 0.001	0.12 ± 0.05	-0.9 ± 0.4
0.405	0.765	100	0.059 ± 0.001	$(0.91 \pm 0.01) \times 10^{-3}$	$(1.87 \pm 0.01) \times 10^{-3}$	0.084 ± 0.001	0.12 ± 0.05	-0.9 ± 0.4
0.405	1.125	10	0.187 ± 0.005	$(2.87 \pm 0.08) \times 10^{-3}$	$(5.91 \pm 0.08) \times 10^{-3}$	0.126 ± 0.002	0.19 ± 0.07	-0.7 ± 0.4
0.405	1.125	100	0.093 ± 0.002	$(1.44 \pm 0.04) \times 10^{-3}$	$(2.95 \pm 0.04) \times 10^{-3}$	0.126 ± 0.002	0.19 ± 0.07	-0.7 ± 0.4

Note. — The integrated SFR and $\dot{\rho_*}$ in the outskirts of LBGs. We integrate from the point where the theoretical models for DLA gas and the LBG data overlap, in order to probe the hypothesis that the FUV emission in this region is from *in situ* star formation in DLA gas associated with the LBGs.

[a]Radii from the center of the composite LBG stack.

[b]The thickness of the disk, where R is the radius and H is the scale height.

[c]Fraction of $\dot{\rho_*}$ observed in the outer region of the composite LBG stack divided by the total $\dot{\rho_*}$ observed.

We find a conservative upper limit of $\dot{\rho_*} < 9.9 \times 10^{-3}$ M$_\odot$ yr^{-1} Mpc^{-3}, corresponding to $\sim 10\%$ of the $\dot{\rho_*}$ measured in the inner regions of LBGs at $z \sim 3$ (Reddy et al., 2008).

3.5.4 Metal Production in the Outskirts of LBGs

Under the hypothesis that the outskirts of LBGs is composed of atomic-dominated gas, we can calculate the metals produced due to *in situ* star formation from $z = 10$ to $z = 3$, and compare this to the metals observed in DLAs at $z = 3$. The metal production can be measured from the outskirts of the LBG composite since the FUV luminosity is a sensitive measure of star formation, since the massive stars produce the UV photons as well as the majority of the metals. The comoving density of metals produced is obtained by integrating the comoving star formation rate density ($\dot{\rho_*}$) from the most recent galaxy surveys (Bouwens et al., 2010b,a; Reddy & Steidel, 2009). We note that the resultant metallicities are only valid if the outskirts of LBGs are composed of atomic-dominated gas, as we divide by the H I mass density, $\rho_{\rm HI}$, to obtain the metallicity.

First, we integrate $\dot{\rho_*}$ for all LBGs from $z \sim 3$ to $z \sim 10$ using the $\dot{\rho_*}$ values from Bouwens et al. (2010b,a); Reddy & Steidel (2009) to calculate the total mass of metals produced in LBGs by $z \sim 3$ similar to Pettini (1999, 2004, 2006) and Wolfe et al. (2003a). Specifically, we calculate the comoving mass density of stars at $z \sim 3$ by

$$\rho_{*,\rm LBG} = \int_{z=3}^{z=10} \dot{\rho}_{*,\rm LBG} \frac{dt}{dz} dz = 1.1 \times 10^8 \ {\rm M}_\odot \ {\rm Mpc}^{-3} \tag{3.11}$$

where

$$\frac{dt}{dz} = \frac{1}{(1+z)H(z)} \ . \tag{3.12}$$

In order to obtain the comoving mass density of stars in the outskirts of LBGs, we multiply this result by the fraction of $\dot{\rho_*}$ observed in the outer region of the composite LBG stack compared to the total $\dot{\rho_*}$ observed, f, which we list in Table 3.2. We can then calculate the total mass in metals produced by $z \sim 3$ using

the estimated conversion factor $\dot{\rho}_{\rm metals} = (1/64)\ \dot{\rho}_*$ by Conti et al. (2003), which is a factor of 1.5 lower than the metal production rate originally estimated by Madau et al. (1996). The metallicity of the presumed DLA gas is then calculated by dividing by $\rho_{\rm HI}$ at $z \sim 3$, where we use average value of $\rho_{\rm HI}$ over the redshift range $2.4 \lesssim z \lesssim 3.5$ of $(9.0 \pm 0.1) \times 10^7$ M$_\odot$ Mpc^{-3} (Prochaska & Wolfe, 2009). The final metallicities are tabulated in Table 3.2 in terms of the solar metallicity, where $Z_\odot = 0.0134$ (Asplund et al., 2009; Grevesse et al., 2010). The metallicities range from $0.12 Z_\odot$ to $0.19 Z_\odot$, similar to DLA metallicities (see §3.7.6). We note that f is independent of the disk aspect ratio (R/H), and therefore so is the metallicity.

3.6 Star Formation Rate Efficiency in Neutral Atomic-dominated Gas

In our search for spatially extended low surface brightness emission around LBGs, we aim to further our understanding of the connection between the DLA gas studied in absorption and the star formation needed to explain the characteristics of the DLA gas. Specifically, Wolfe & Chen (2006) searched for isolated low surface brightness emission of DLAs, away from known LBGs, in the UDF and found conservative upper limits on the SFR per unit comoving volume, $\dot{\rho}_*$. These limits constrain the *in situ* SFR efficiency of DLAs to be less than 5% of that expected from the KS relation. In other words, star formation must occur at much lower efficiency in neutral atomic-dominated hydrogen gas at $z \sim 3$ than in modern galaxies at $z = 0$.

The surface brightness profile of the super-stack of 48 resolved LBGs (Figure 3.4) reveals the presence of spatially extended star formation around LBGs. The latest evidence suggests that this star formation is most likely occurring in atomic-dominated gas. The most convincing evidence is measurements probing the outer disks of local galaxies that detect star formation in atomic-dominated hydrogen gas (Fumagalli & Gavazzi, 2008; Bigiel et al., 2010b,a). In addition, we find that because the covering fraction of molecular gas is insufficient to explain the observed star formation in the outskirts of LGBs, the observed emission is likely from atomic-

dominated gas (see §3.5.2). Throughout the rest of this investigation, we work under the hypothesis that the observed FUV emission in the outskirts of LBGs is from *in situ* star formation in atomic-dominated gas. In order to quantify the efficiency of star formation at high redshift in atomic-dominated gas, we require a theoretical framework connecting the observed emission around LBGs to the expectations based on known DLA statistics..

We develop such a framework in §3.6.1, where we combine the column density distribution function of DLAs with the KS relation to construct a model that predicts the comoving SFR density per intensity for different SFR efficiencies of the KS relation. We convert the measured radial surface brightness profile from §3.4.3 into this same quantity in §3.6.2, and compare it to the model. Through this comparison, we obtain a SFR efficiency for each surface brightness in the profile which corresponds to both a specific radius in the profile and a gas column density via the KS relation. As a tool to understand the SFR efficiencies and compare our results to those of Wolfe & Chen (2006) and Bigiel et al. (2010b), and simulations such as Gnedin & Kravtsov (2010b), we convert our results to fit onto a standard plot of $\Sigma_{\rm SFR}$ vs. Σ_{gas} in §3.6.3. The $\Sigma_{\rm SFR}$ is determined directly from the measured rest-frame FUV flux, and the Σ_{gas} is determined from the Σ_{gas}, the KS relation, and the SFR efficiency determined through comparisons of the data with the column density distribution function.

3.6.1 Theoretical Framework

We require a theoretical framework for the rest frame FUV emission from DLAs, and we start with the one developed in Wolfe & Chen (2006) for the expected emission from DLAs in the V-band image of the UDF. After summarizing this framework, we expand it to explain the observed emission around LBGs as a function of radius (and therefore surface brightness), taking into account the projection effects of randomly inclined disks. Our resultant model in §6.1.2 yields predictions of the differential $\dot{\rho}_*$ per intensity interval expected from DLAs for different SFR efficiencies. We then compare this model to the data in §3.6.2 to obtain the SFR efficiency of the DLA gas.

3.6.1.1 Original Framework from Wolfe & Chen (2006)

The framework developed in Wolfe & Chen (2006) connects the measured column density distribution function, $f(N_{\rm HI}, X)$, the KS relation, and randomly inclined disks to determine the expected cumulative $\dot{\rho_*}$ for DLAs as a function of column density and therefore surface brightness. Specifically, they develop an expression for $\dot{\rho_*}$ due to DLAs with observed column density greater or equal to N, and we take this expression directly from equation 6, in Wolfe & Chen (2006), namely

$$\dot{\rho_*}(\geq N, X) = \left(\frac{H_0}{c}\right) \int_N^{N_{\rm max}} dN' J(N') \Sigma_{\rm SFR}(N') \ . \tag{3.13}$$

Here H_0 is the Hubble constant, c is the speed of light, $N_{\rm max}$ is the maximum observed column density for DLAs (10^{22} cm^{-2}) and $J(N')$ is

$$J(N') = \int_{N_{\rm min}}^{\min(N_0, N')} dN_\perp g(N_\perp, X) \left(\frac{N_\perp^2}{N'^3}\right) \left(\frac{N_\perp}{N'}\right)^{\beta-1} \quad . \tag{3.14}$$

Here $X(z)$ is the absorption distance and $g(N_\perp, X)$ is the intrinsic column-density distribution of the disk for which the maximum value of $N_\perp$, the H I column density perpendicular to the disk, is N_0. $g(N_\perp, X)$ is related to the observed H I column-density distribution function $f_{HI}(N, X)$ by

$$f_{HI}(N, X) = \int_{N_{min}}^{\min(N_0, N)} dN_\perp g(N_\perp, X)(N_\perp^2/N^3) \tag{3.15}$$

(Fall & Pei, 1993; Wolfe et al., 1995).

A potential problem with using $f(N_{\rm HI}, X)$ in the expression for $\dot{\rho_*}$ is that the measurements of $f(N_{\rm HI}, X)$ originate from absorption-line measurements that sample scales of ~ 1 pc (Lanzetta et al., 2002). On the other hand, the KS relation is established on scales exceeding 0.3 kpc (Kennicutt et al., 2007). This is not an issue, however, because $f(N_{\rm HI}, X)$ typically depends on over 50 measurements per column density bin, and is therefore a statistical average over probed areas that exceed a few kpc^2 (see Wolfe & Chen, 2006).

3.6.1.2 New Differential Approach for LBG Outskirts

The framework developed in Wolfe & Chen (2006) was appropriate for connecting the upper limit measurements of $\dot{\rho_*}$ from DLAs above a limiting column density and therefore surface brightness, to model predictions based on $f(N_{\rm HI}, X)$ and the KS relation. It does not, however, work in the present context of positive detections over a range of surface brightnesses. For this we require a differential expression for $\dot{\rho_*}$, rather than a cumulative version used by Wolfe & Chen (2006). Specifically, assuming that LBGs are at the center of DLAs, we wish to predict the rest-frame FUV emission of DLAs for a range of efficiencies of star formation in such a way that we can distinguish between possible different efficiencies for each surface brightness interval. We find that $d\dot{\rho_*}/dN$ accomplishes this by yielding unique non-overlapping predictions for each efficiency. Each differential interval of $\dot{\rho_*}$ represents a ring around the LBGs corresponding to a surface brightness and a solid angle interval subtended by each ring. This surface brightness corresponds to the column density of gas corresponding to some radius in the radial surface brightness profile and is responsible for the emission covering that area on the sky. If this gas is neutral atomic-dominated H I gas, then we can predict the expected $d\dot{\rho_*}/dN$ using $f(N_{\rm HI}, X)$ and the KS relation.

Specifically, to obtain $d\dot{\rho_*}/dN$, we differentiate equation 3.13 with respect to N. To do so, we need $g(N_\perp, X)$, since Equation 3.13 depends on Equation 3.14, which depends on $g(N_\perp, X)$. We find $g(N_\perp, X)$ from $f(N_{\rm HI}, X)$ to obtain a general form of the equivalent double power-law fit for $g(N_\perp, X)$ when $N_\perp < N_0$ using Equation 3.15. We find that

$$g_{HI}(N_\perp, X) = k_3(\alpha + 3)\left(\frac{N_\perp}{N_0}\right)^\alpha \;\; ; \;\; N_\perp < N_0 \, , \tag{3.16}$$

where k_3 and α are the same as in equation 3.7, and $g(N_\perp, X)$=0 for $N_\perp \geq N_0$. We now differentiate equation 3.13 with respect to N to get

$$\frac{d\dot{\rho_*}}{dN} = h(N)\left(\frac{H_0}{c}\right)\left(\frac{Kk_3}{N_c^\beta}\right)\left(\frac{\alpha+3}{\beta+2+\alpha}\right)\left(\frac{N_0^{-\alpha}}{N^2}\right) \quad , \tag{3.17}$$

where

$$h(N) = \begin{cases} N^{\beta+2+\alpha} - N_{min}^{\beta+2+\alpha} \; ; N < N_0 \; , \\ N_0^{\beta+2+\alpha} - N_{min}^{\beta+2+\alpha} \; ; N > N_0 \; , \end{cases} \tag{3.18}$$

In the case of α=α_3=-2.00 ± 0.05 for $N \leq N_0$ (Prochaska & Wolfe, 2009), this reduces to $g(N_\perp, X)$=$k_3(N_\perp/N_0)^{-2}$ at $N_\perp < N_0$ and $g(N_\perp, X)$=0 for $N_\perp > N_0$. Also, Equations 3.17 and 3.18 reduce to,

$$\frac{d\dot{\rho}_*}{dN} = h(N) \left(\frac{H_0}{c}\right) \left(\frac{K k_3}{\beta N_c^\beta}\right) \left(\frac{N_0}{N}\right)^2 \quad , \; (\alpha = -2) \tag{3.19}$$

where

$$h(N) = \begin{cases} N^\beta - N_{min}^\beta \; ; N < N_0 \; , \\ N_0^\beta - N_{min}^\beta \; ; N > N_0 \; , \end{cases} \; (\alpha = -2) \; . \tag{3.20}$$

We note that the expression for $d\dot{\rho}_*/dN$ is independent of α_4.

We would like to compare $d\dot{\rho}_*/dN$ to the observations, however, we cannot measure $d\dot{\rho}_*/dN$ directly. On the other hand, we can measure $d\dot{\rho}_*/d\langle I_{\nu_0}^{obs}\rangle$, which is easily derived from $d\dot{\rho}_*/dN$. Specifically, we find

$$\frac{d\dot{\rho}_*}{d\langle I_{\nu_0}^{obs}\rangle} = \left(\frac{d\dot{\rho}_*}{dN}\right) \left(\frac{d\Sigma_{\rm SFR}}{dN}\right)^{-1} \left(\frac{d\Sigma_{\rm SFR}}{d\langle I_{\nu_0}^{obs}\rangle}\right) \; . \tag{3.21}$$

Since

$$\frac{d\Sigma_{\rm SFR}}{dN} = \frac{K\beta N^{\beta-1}}{N_c^\beta} \; , \tag{3.22}$$

and

$$\frac{d\Sigma_{\rm SFR}}{d\langle I_{\nu_0}^{obs}\rangle} = \frac{4\pi(1+z)^3\beta}{C} \; , \tag{3.23}$$

we therefore find that

$$\frac{d\dot{\rho}_*}{d\langle I_{\nu_0}^{obs}\rangle} = h(N) \left(\frac{H_0}{c}\right) \left(\frac{4\pi k_3 (1+z)^3}{C}\right) \left(\frac{\alpha+3}{\beta+2+\alpha}\right) \left(\frac{N_0^{-\alpha}}{N^{\beta+1}}\right) \; , \tag{3.24}$$

which for $\alpha = -2$ reduces to

$$\frac{d\dot{\rho}_*}{d\langle I_{\nu_0}^{obs}\rangle} = h(N)\left(\frac{H_0}{c}\right)\left(\frac{4\pi k_3(1+z)^3}{\beta C}\right)\left(\frac{N_0^2}{N^{\beta+1}}\right) , \tag{3.25}$$

where $h(N)$ is the same as in Equations 3.18 and 3.20. Since N is related to $\langle I_{\nu_0}^{obs}\rangle$ through equation 3.4 and the KS relation, we find

$$N = \langle I_{\nu_0}^{obs}\rangle^{-\beta}\left(\frac{4\pi(1+z)^3\beta {N_c}^{\beta}}{CK}\right)^{-\beta} , \tag{3.26}$$

and therefore $d\dot{\rho}_*/d\langle I_{\nu_0}^{obs}\rangle$ is a unique function of $\langle I_{\nu_0}^{obs}\rangle$, and thus surface brightness.

The resulting predictions for the surface brightness, μ_V, versus the differential comoving SFR density per intensity, $d\dot{\rho}_*/d\langle I_{\nu_0}^{obs}\rangle$, is depicted by the blue curve in Figure 3.7. The red curves in this figure depict $d\dot{\rho}_*/d\langle I_{\nu_0}^{obs}\rangle$ for different values of the normalization constant K, where K_{Kenn}=(2.5±0.5)×10^{-4} $M_\odot$ yr^{-1} kpc^{-2} (Kennicutt, 1998a,b). First, we note that $d\dot{\rho}_*/d\langle I_{\nu_0}^{obs}\rangle$ for a given K decreases as μ_V decreases because of the decreasing population of high column-density DLAs (i.e. DLAs with higher surface brightnesses). Second, we note that both $\dot{\rho}_*$ and $\langle I_{\nu_0}^{obs}\rangle$ are linearly proportional to K, and therefore K cancels out in the x-direction, leaving only the observed μ_V to vary with K in the y-direction. We plot μ_V on the y-axis to conceptually facilitate the conversion of these results later in the paper, and note that $d\dot{\rho}_*/d\langle I_{\nu_0}^{obs}\rangle$ is a function of N and therefore μ_V. The curves in this figure predict the amount of star formation that should be observed around LBGs for different efficiencies of star formation, which will be compared to the data in §3.6.2. We plot $d\dot{\rho}_*/d\langle I_{\nu_0}^{obs}\rangle$ for the range in μ_V that corresponds to $N_{\rm min} < N < N_{\rm max}$, where $N_{\rm min} = 5\times10^{20}{\rm cm}^{-2}$, and $N_{\rm max} = 1\times10^{22}{\rm cm}^{-2}$. The value of of $N_{\rm min}$ is lower than the range of threshold column densities of $N_\perp^{\rm crit}$ observed for nearby galaxies (Kennicutt, 1998b), but at a column density high enough such that we may start to see star formation occur. Also, recent results probing in the outer disks of nearby galaxies observe star formation at low column densities in atomic-dominated hydrogen gas (Fumagalli & Gavazzi, 2008; Bigiel et al., 2010b,a). Regardless, our measurements do not probe column densities down to this level, so the exact value for $N_{\rm min}$ doesn't affect the results.

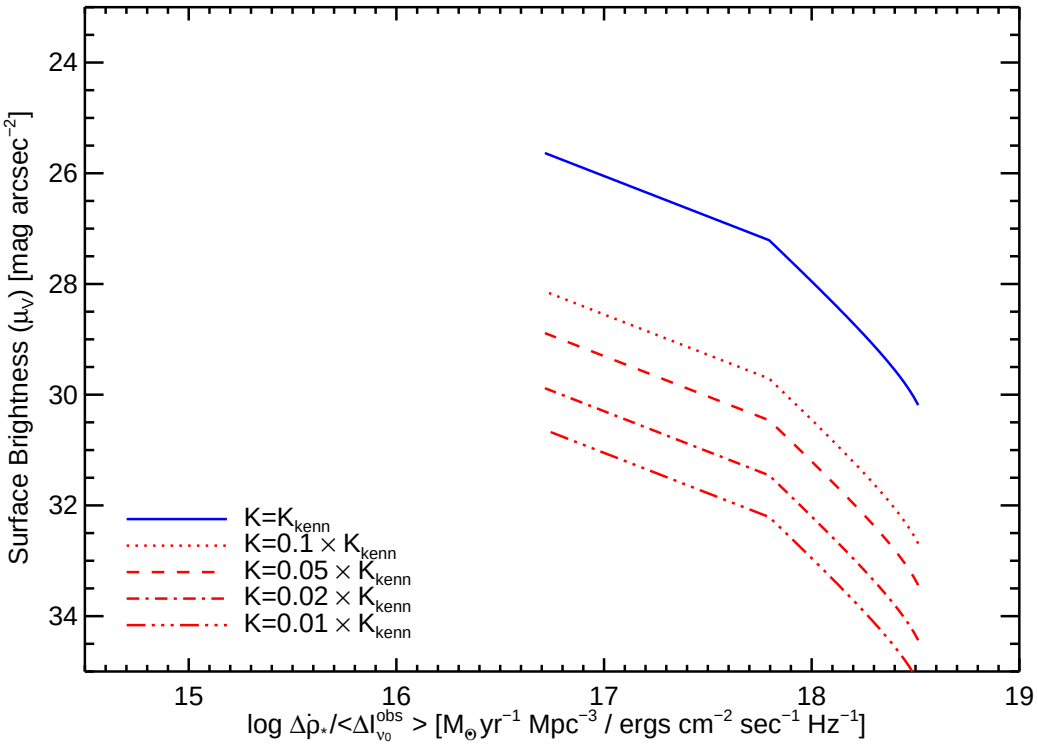

Figure 3.7 The solid blue curve is the surface brightness (μ_V) vs. the differential comoving SFR density per intensity $\Delta\dot{\rho}_*/\Delta\langle I_{\nu_0}^{obs}\rangle$ predicted for Kennicutt-Schmidt relation with $K = K_{Kenn}$. The red curves depict what $\Delta\dot{\rho}_*/\Delta\langle I_{\nu_0}^{obs}\rangle$ looks like for different values of the normalization constant K, where K_{Kenn}=(2.5±0.5)×10^{-4} $M_\odot$ yr^{-1} kpc^{-2} (Kennicutt, 1998a,b). The curves in this figure predict the amount of star formation that should be observed around LBGs for different efficiencies of star formation from equations 3.25 and 3.26. The doted line is for $K = 0.1 \times K_{Kenn}$, the dashed line is for $K = 0.05 \times K_{Kenn}$, the the dotted-dashed line is for $K = 0.02 \times K_{Kenn}$, and the tripple-dotted-dashed line is for $K = 0.01 \times K_{Kenn}$. The range of surface brightnesses correspond to $5 \times 10^{20} < N < 1 \times 10^{22} \mathrm{cm}^{-2}$.

3.6.2 Stacking Randomly Inclined Disks

We wish to compare these theoretical values of $d\dot{\rho}_*/d\langle I_{\nu_0}^{obs}\rangle$, predicted for DLA gas forming stars according to the KS relation, to empirical measurements of $\Sigma_{\rm SFR}$ for our LBG sample. To do this, we require a method to convert the radial surface brightness profile in Figure 3.4 into μ_V versus $d\dot{\rho}_*/d\langle I_{\nu_0}^{obs}\rangle$. For a given ring corresponding to a point in the radial surface brightness profile and covering an area ΔA we can calculate $\Delta\dot{\rho}_*$ from the measured intensity $\langle I_{\nu_0}^{obs}\rangle$. $\Delta\dot{\rho}_*$ is similar to the differential $\dot{\rho}_*$ mentioned above, and is calculated from the flux measured in an annular ring at some radius from the center of the LBGs. Specifically,

$$\Delta\dot{\rho}_* = \frac{\Delta L_\nu N_{\rm LBG}}{C' V_{\rm UDF}} \, , \tag{3.27}$$

where C' is the conversion factor from FUV radiation to SFR[13], $C' = 8 \times 10^{27}$ ergs $\rm s^{-1}$ $\rm hz^{-1}$ $(\rm M_\odot\ yr^{-1})^{-1}$, ΔL_ν is the luminosity per unit frequency interval for a ring with area ΔA, $N_{\rm LBG}$ is the number of $z \sim 3$ LBGs in the UDF, and $V_{\rm UDF}$ is the comoving volume of the UDF. As discussed in §3.3.1, we use a comoving volume of 26436 $\rm Mpc^3$. We recognize that $N_{\rm LBG}$ is dependent on the depth of images available to make selections, and discuss this completeness issue in Appendix A.3. The value of $\Delta\dot{\rho}_*$ depends on ΔL_ν, and therefore on the inclination angle i for a given measured intensity, in the case of planes of preferred symmetry.

In order to determine $\Delta\dot{\rho}_*$, we average over all inclination angles in our determination of ΔL_ν, which depends on $\Sigma_\nu^\perp$ described in §3.5.2. Specifically, we use equation 3.9 in conjunction with $\Delta L_\nu = \Delta A_\perp \Sigma_\nu^\perp$ to find $\Delta\dot{\rho}_*$, where $\Delta A_\perp$ is the area parallel to the plane of the disk. First, we rewrite $\Delta A_\perp$ in terms of ΔA, the projection of $\Delta A_\perp$ perpendicular to the line of sight, and find that averaging over all inclination angles yields $\Delta A_\perp = 2\Delta A$. We can then rewrite $\Delta A_\perp$ in terms of $\Delta\Omega$, the solid angle subtended by one of the rings from the surface brightness profile, and ΔA, yielding $\Delta A_\perp = 2\Delta\Omega d_A^2$. Using this relation, we find

$$\Delta\dot{\rho}_* = \frac{8\pi(1+z)^3 {d_A}^2 N_{\rm LBG} \Delta F_{\nu_0}^{obs}(r)}{\ln(R/H) C' V_{\rm UDF}} \tag{3.28}$$

[13] C' is in different units than the same factor C in equation 3.4.

where d_A is the angular diameter distance, and $\Delta F^{obs}_{\nu_0}(r)$ is the observed integrated flux in a ring as a function of the radius r. We then calculate the change in intensity from one ring to the next, $\Delta\langle I^{obs}_{\nu_0}\rangle$, to get $\Delta\dot{\rho}_*/\Delta\langle I^{obs}_{\nu_0}\rangle$ by measuring the intensity change across each ring by taking the difference between values of the intensity on either side of each point and dividing by two. In the case that $\Delta\langle I^{obs}_{\nu_0}\rangle$ as calculated above is negative, we take the change in intensity over a larger interval.

Figure 3.8 shows a comparison of the theoretical model from §3.5.2.2 and the measured values from the radial surface brightness profile. The measurements are for a range in aspect ratios, with R/H values from 10 to 100, similar to §3.5.2. We display the data in two complementary ways. First, the green diamonds depict results assuming the average value of the possible aspect ratios, with the error bars reflecting the measurement uncertainties (including the uncertainty due to the variance in the image composite) in order to portray the precision of our measurements. Second, we show a filled region, where the gray represent results for the full range in aspect ratios and the gold represents the 1σ uncertainties on top of that range. This shows the region that is acceptable for each of those points. In both portrayals, we only include uncertainties of the aspect ratios, the variance due to stacking different LBGs, and the measurement uncertainties, and do not include uncertainties in the FUV light to SFR conversion factor (C) from equation 3.4, or any other such systematic uncertainties. We truncate the data at a radius of ~ 0.8 arcsec (~ 6 kpc) corresponding to a 3σ cut to include only measurements with high signal to noise. We note that in calculating the S/N values, we include the uncertainties due to the variance of objects in the composite stack. The data beyond a radius of ~ 0.8 arcsec are plotted in gray, and while they yield similar results, they are not included due to their low S/N.

The results shown in Figure 3.8 do not yet include completeness corrections, which we describe in Appendix A.3. We present the completeness corrected comparison between the theoretical models of $d\dot{\rho}_*/d\langle I^{obs}_{\nu_0}\rangle$ for DLAs with measured values of $\Delta\dot{\rho}_*/\Delta\langle I^{obs}_{\nu_0}\rangle$ in Figure 3.9. This shows that, under the hypothesis that the observed extended FUV emission comes from *in situ* star formation of DLA gas, the DLAs have a SFR efficiency at $z \sim 3$ significantly lower than that of local

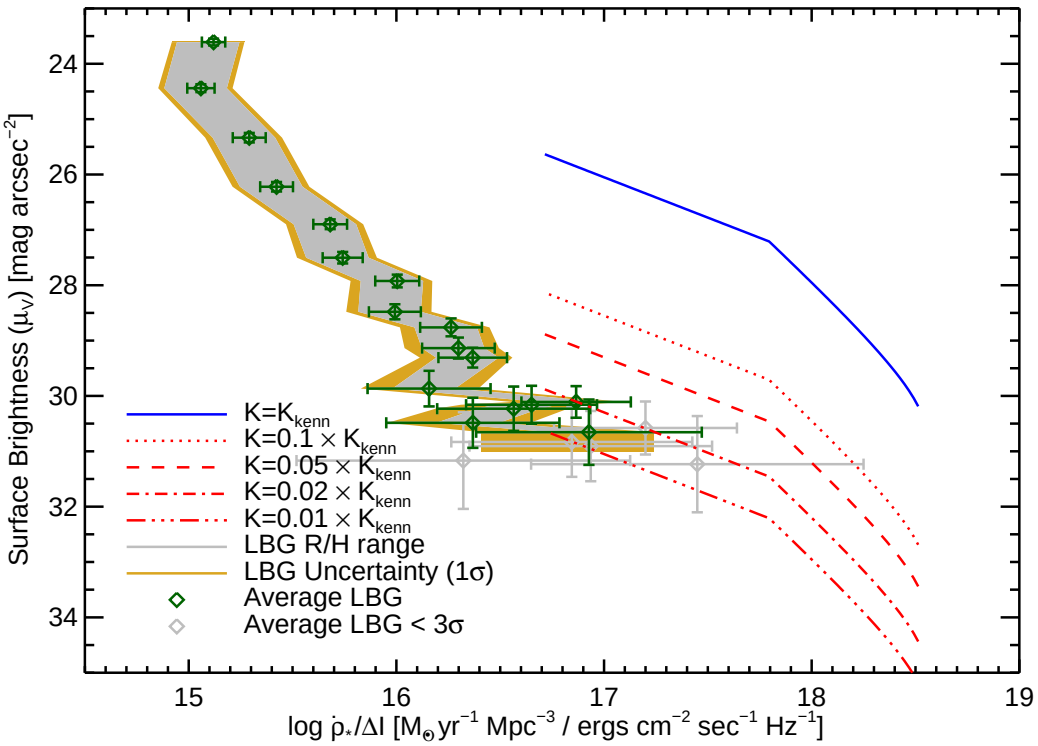

Figure 3.8 The surface brightness (μ_V) vs. the differential comoving SFR density per intensity ($\Delta\dot{\rho}_*/\Delta\langle I_{\nu_0}^{obs}\rangle$), comparing the measured emission in the outskirts of LBGs to the predicted levels for different SFR efficiencies. The blue and red lines are the predictions from Figure 3.7. The filled gray region represents observed emission in the outskirts of LBGs for a range in aspect ratios, with R/H values ranging from 10 to 100, and the filled gold region is its 1σ uncertainty. The green diamonds are the average value of the possible aspect ratios, with the error bars reflecting the measurement uncertainties (including the uncertainty due to the variance in the image composite).

galaxies[14]. In fact, the Kennicutt parameter K needs to be reduced by a factor of 10-50 below the local value, $K = K_{\rm Kenn}$. The values of $\Delta\dot{\rho}_*/\Delta\langle I_{\nu_0}^{obs}\rangle$ that intersect the predictions of the theoretical models for $N = 5\times10^{20} - 1\times10^{22}$ are black crosses and have S/N values ranging from ∼17 to ∼3 suggesting that the measurements are robust. These points correspond to radii of $\sim 0.4 - 0.8$ arcsec ($\sim 3 - 6$ kpc). The point with the largest value of $\Delta\dot{\rho}_*/\Delta\langle I_{\nu_0}^{obs}\rangle$ of ~ 17.4 in Figure 3.9 seems to deviate from what otherwise would be a clear trend. This point corresponds to the point at a radius of 0.72 arcsec in Figure 3.4, which also differs slightly from the general decreasing trend in μ_V. However, it is consistent within their uncertainties for the surface brightness profile, and we are not concerned about it. All the points at radii larger than ~ 0.8 arcsec also intersect the theoretical models with similar efficiencies, but are not included as they have lower S/N. The values of K vary for each data point, and are not constant for a given μ_V. These tantalizing results will be discussed in §3.7, and we consider the affects of stacking different samples of LBGs in Appendix B.

3.6.2.1 Variations in the KS Relation Slope β

The SFR efficiencies can also be decreased by lowering the slope β of the KS relation, while keeping $K = K_{\rm Kenn}$. The value of β in the literature ranges from $\beta \sim 1.0$ (Bigiel et al., 2008) to $\beta \sim 1.7$ (Bouché et al., 2007). Increasing the value of β would increase the SFR efficiency, so we do not consider that here. On the other hand, lower values of β would decrease the SFR efficiency and there are physical motivations to consider β values as low as 1.0 (e.g. Elmegreen, 2002; Kravtsov, 2003). However, even reducing β to values as low as 0.6 does not reduce the SFR efficiency enough to match our observations, and there are no physical motivations nor data to justify values of β lower than 0.6. Lastly, decreasing the value of β not only decreases the SFR efficiency, but it also decreases the value of $d\dot{\rho}_*/d\langle I_{\nu_0}^{obs}\rangle$ (see equation 3.25). While decreasing β would move the blue curve in Figure 3.9 down, it also moves it to the right, and does not help the models match

[14]We remind the reader that if the working hypothesis is not correct, then the results of Wolfe & Chen (2006) already constrain the SFR efficiency.

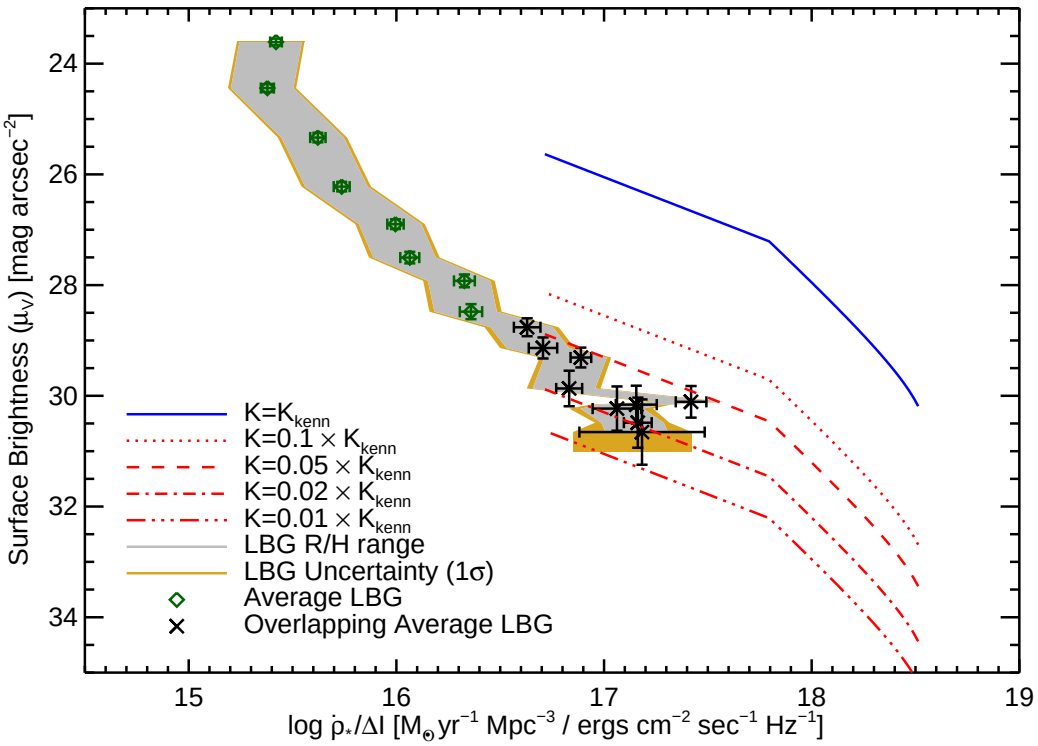

Figure 3.9 Same as Figure 3.8, but corrected for completeness. The points that overlap with the theoretical models are now black crosses, to emphasize the points that will be used for the rest of this work. These points correspond to radii of 0.405″ through 0.765″. We omit the low S/N ($< 3\sigma$) gray data points from figure 3.8. By comparing the measurements in this plot to the predictions, we get the SFR efficiency for each surface brightness.

our observations. Therefore, we focus on other mechanisms for reducing the SFR efficiencies by varying the value of the parameter K.

3.6.3 The Kennicutt Schmidt Relation for Atomic-dominated Gas at High Redshift

As a tool to understand the low SFR efficiencies, and in order to compare our results to those of Wolfe & Chen (2006) and Bigiel et al. (2010b), and simulations such as those by Gnedin & Kravtsov (2010b), we translate the result from §3.6.2 and Figure 3.9 to a common set of parameters to obtain a plot of $\Sigma_{\rm SFR}$ vs. Σ_{gas}. We derive this conversion for the emission in the outskirts of LBGs in §3.6.3.1, and for the DLA upper limits from Wolfe & Chen (2006) in §3.6.3.2.

3.6.3.1 Converting the LBG Results to $\Sigma_{\rm SFR}$ versus $\Sigma_{\rm gas}$

We calculate $\Sigma_{\rm SFR}$ directly using equation 3.4, where the average intensity is obtained from the radial surface brightness profile of the composite LBG stack in rings as explained in §3.4.3 (Figure 3.4). As μ_V algebraically increases with increasing radius, $\Sigma_{\rm SFR}$ will generally decrease with increasing radius. We compute $\Sigma_{\rm gas}$ by first inferring the value of K for each data point that intersects the theoretical curves in the μ_V versus $\Delta\dot{\rho}_*/\Delta\langle I_{\nu_0}^{obs}\rangle$ plane, since each theoretical curve is parameterized by a fixed value of K. We precisely find the corresponding efficiency by calculating a grid of models with K varying by 0.001. We then use this value of K and the KS relation (equation 3.2) to calculate Σ_{gas} for each value of $\Sigma_{\rm SFR}$ inferred from the measured μ_V.

In short, we directly measure $\Sigma_{\rm SFR}$ through the emitted FUV radiation, and then calculate Σ_{gas} for the corresponding K that matches the DLA model. We note that $\Sigma_{\rm SFR}$ is a direct measurement, while Σ_{gas} comes from the DLA model which is based on the column density distribution function of DLA gas. The result is shown in Figure 3.10, which plots $\Sigma_{\rm SFR}$ vs. Σ_{gas}. We truncate the plot to include only data that overlaps with observed DLA gas densities, namely $N \leq 1 \times 10^{22}$ cm^{-2}, where N is calculated from equation 3.3 using the K value determined for that μ_V. The

dashed line black represents the KS relation with $K = K_{Kenn}$=(2.5±0.5)×10^{-4} $M_\odot$ yr^{-1} kpc^{-2}, while the pink triple dot-dashed line represents $K = 0.1 \times K_{Kenn}$. The gray filled area with the 1σ uncertainty and the black points represent the same data as in Figure 3.9. The green upper limits will be described in §3.6.3.2.

The LBG outskirts in Figure 3.10 clearly have lower SFR efficiencies than predicted by the KS relation. In addition, they appear to follow a power law that is steeper than the KS relation at low redshift. However, there is a large scatter caused by the uncertainty introduced by the sky subtraction uncertainty (see §3.4.2), and the sample variance due to stacking different objects (see §3.4.3). We are therefore cautious about fitting a power law to this data by itself, and investigate this trend further in §3.7.3.1.

3.6.3.2 Converting DLA Data to $\Sigma_{\rm SFR}$ vs. Σ_{gas}

To convert the DLA points from Wolfe & Chen (2006), we use the same idea as that of the LBG data, except that in this case we do not have detected star formation, and therefore we use upper limits. Also, rather than using the new framework developed above, we use the formalism developed for DLAs without central bulges of star formation (Wolfe & Chen, 2006). We start with Figure 7 of Wolfe & Chen (2006), which basically plots the SFR density due to star formation in neutral atomic-dominated hydrogen gas (i.e., DLAs) with column densities greater than N ($\dot{\rho_*}(> N)$) vs. μ_V[15]. Similar to our Figure 3.9, Figure 7 of Wolfe & Chen (2006) has DLA models with different Kennicutt parameters K. We follow the same technique of using the intersection of these models with the data to find K values for each μ_V. However, in this case the values of μ_V do not correspond to detected surface brightnesses of LBGs, but rather correspond to threshold surface brightnesses, i.e., the lowest values of $\langle I_{\nu_0}^{obs} \rangle$ that would be measured for a DLA of a given angular diameter. Therefore, we cannot calculate $\Sigma_{\rm SFR}$ the same way as in §3.6.3.1.

To determine $\Sigma_{\rm SFR}$, we first calculate an effective minimum column density,

[15]The x-axis of the plot is actually $\Sigma_{\rm SFR}$, but $\Sigma_{\rm SFR}$ corresponds to a value of μ_V, which is easier to understand and makes more sense in this context.

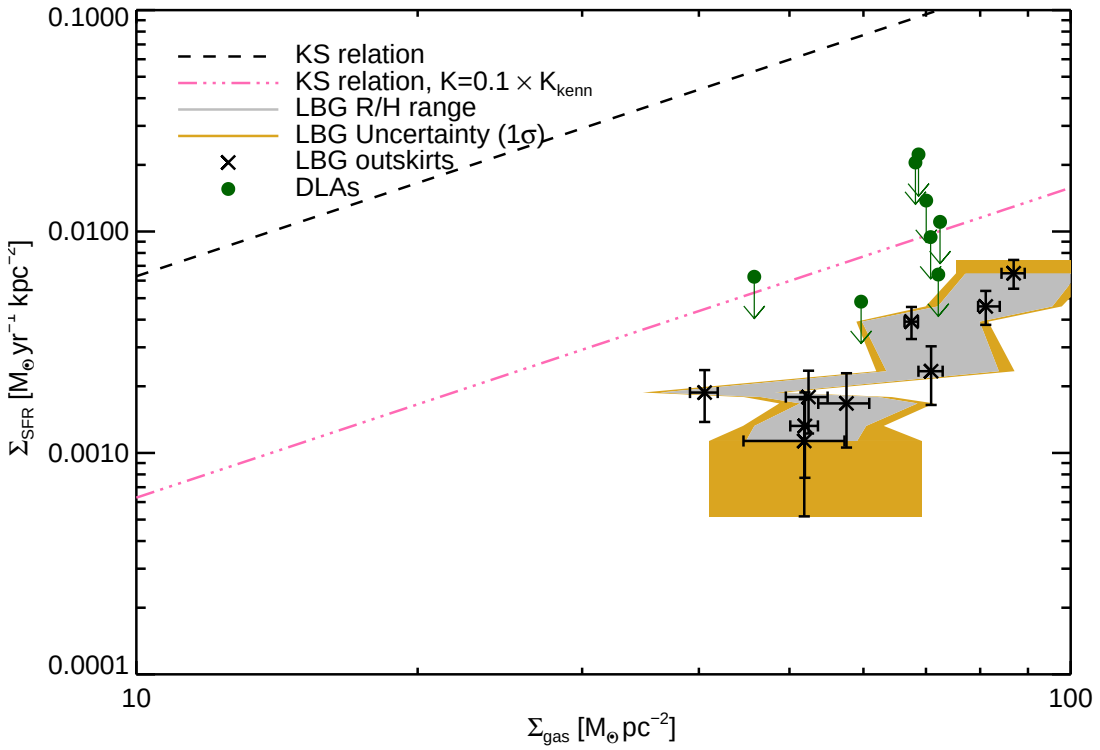

Figure 3.10 Star formation rate per unit area ($\Sigma_{\rm SFR}$) versus gas density ($\Sigma_{\rm gas}$). The dashed line represents the KS relation with $K = K_{Kenn}$=(2.5±0.5)×10^{-4} $M_\odot$ yr^{-1} kpc^{-2}, while the triple dot-dashed line is for $K = 0.1 \times K_{Kenn}$. The gray filled region, the gold filled region, and the black crosses represent the same data as in Figure 3.9. The green data points corresponding to upper limits derived for DLAs without central bulges of star formation from Wolfe & Chen (2006) converted to work with this plot. Since DLA sizes are not known, the upper limits are derived for angular diameters $\theta_{\rm kern}$=4″, 2″, 1″, 0.6″, 0.5″, 0.4″, 0.3″, and 0.25 ″, from left to right. The data all fall at or below 10% of the KS relation, showing a lower SFR efficiency than predicted. (A color version of this figure is available in the online journal.)

$N_{\rm eff}$, corresponding to the threshold surface brightness of Wolfe & Chen (2006). We do this using the K values from the intersection points, the thresholds μ_V, and Equation 3.3. We then calculate $\Sigma_{\rm SFR}$, the average over all possible column densities above $N_{\rm eff}$, as

$$\Sigma_{\rm SFR} = \langle \Sigma_{\rm SFR}(> N_{\rm eff}) \rangle = \frac{c}{H_0} \frac{\dot{\rho_*}(> N_{\rm eff})}{\int_{N_{\rm eff}}^{N_{\rm max}} J(N') dN'} \tag{3.29}$$

where $J(N)$ is the integral in Equation 3.14. We then calculate $\Sigma_{\rm gas}$ using these $\Sigma_{\rm SFR}$, the above K values, and Equation 3.2. The resulting values are overlaid on the LBG results in Figure 3.10. We emphasize that the two results are independent tests. The DLA upper limits put constraints on the KS relation in the case of no central bulge of star formation, while the LBG outskirts data put constraints on *in situ* star formation in DLAs associated with LBGs. Together, these results show that the SFR efficiency in diffuse atomic-dominated gas at $z \sim 3$ is less efficient than predicted by the KS relation for local galaxies.

3.7 Discussion of Results

We present, for the first time, evidence for low surface brightness emission around LBGs on spatial scales large compared to the LBG cores due to *in situ* star formation in gas associated with LBGs (see Figure 3.4). Using the theoretical framework developed in §3.6.1.2, we model this emission as the average *in situ* star formation in atomic-dominated gas surrounding LBGs at $z \sim 3$. Since most of the atomic-dominated gas at high redshift is in DLAs, we assume that this is DLA gas. We find that under this hypothesis, the efficiency of star formation in the atomic-dominated gas is significantly lower than what is expected for predictions by the Kennicutt-Schmidt relation. This is clearly evident in Figure 3.10, which compares the local KS relation directly to the observations. The efficiency of *in situ* star formation in atomic-dominated gas appear to be a factor of $10 - 50$ lower than that of local galaxies that follow KS relation. In addition, the SFR efficiency of atomic-dominated gas around galaxies without bright cores is constrained by the the thresholds measured by Wolfe & Chen (2006), who impose similar efficiencies

on the *in situ* star formation in DLAs, as shown by the green upper limits in Figure 3.10. Therefore, together with the results from Wolfe & Chen (2006), we constrain the SFR efficiency of *all* neutral atomic-dominated hydrogen gas (DLAs) at $z \sim 3$.

There are multiple possible effects contributing to the observed lower SFR efficiencies, including a higher background radiation field at high redshift, low metallicity of DLAs, and the role of molecular vs. atomic hydrogen in star formation. We start the discussion by comparing our results to the models of low metallicity high-redshift galaxies by Gnedin & Kravtsov (2010b) in §3.7.1. We then consider the roles of molecular and atomic-dominated gas in the KS relation in the context of the saturation of atomic dominated in §3.7.2. We investigate whether there is a variation of the KS relation with redshift in §3.7.3, and compare our results at high redshift with those in the outer disks of local galaxies in §3.7.3.1. We then consider the effect that a bimodality of the DLA population would have on the results in §3.7.4, and a caveat on the results based on DLA sizes in §3.7.5. Lastly, we address the 'Missing Metals' problem of DLAs in §3.7.6.

3.7.1 Models of the Kennicutt Schmidt Relation in High Redshift Galaxies

Here we discuss two effects contributing to the observed lower efficiencies: First, at higher redshifts the background radiation field (Haardt & Madau, 1996) is stronger, yielding a higher UV-flux environment. This photo-dissociates the molecular hydrogen (H_2) content of the gas, raising the threshold for the gas to become molecular, therefore requiring higher gas densities to form stars. Second, the metallicity of DLAs at high redshift are considerably lower than solar (Pettini et al., 1994, 1995, 1997, 2002a; Prochaska et al., 2003), and therefore have a lower dust content, which is needed to form molecular hydrogen and to shield the gas from photo-dissociating radiation.

Recent theoretical work (Krumholz et al., 2008; Gnedin et al., 2009; Gnedin & Kravtsov, 2010a,b; Krumholz et al., 2009b,a) suggests that the most important part in determining the amplitude and slope of the KS relation is the dust abundance, and therefore the metallicity. Gnedin & Kravtsov (2010b) investigate the

KS relation at high redshift using their metallicity dependent model of molecular hydrogen (Gnedin et al., 2009). They find that while the higher UV flux does lower the SFR, it also lowers the surface density of the neutral gas, leaving the KS relation mostly unaffected. However, they find that the lower metallicity, and therefore lower dust-to-gas ratio, causes a steepening and lower amplitude in the KS relation. This yields lower molecular gas fractions, which in turn reduces SFR for a given gas surface density, $\Sigma_{\rm gas}$. This would yield lower observed SFR efficiencies similar to what is measured in this study.

We compare our results with the $z = 3$ model KS relation (Gnedin & Kravtsov, 2010b) in Figure 3.11, with a plot showing our data overlaid with the model results, and find that their predictions are consistent with our findings. This plot is similar to Figure 3 in Gnedin & Kravtsov (2010b), as we provided them with our preliminary results for comparison. However, there was previously an error in our implementation of the theoretical framework, yielding slightly different results than presented here. Also, here we split the figure into two panels, with the top panel including gas of all metallicities for galaxies at $z = 3$, and the bottom panel including only the gas with metallicities below $0.1Z_{\odot}$. Each plot includes the same points as shown in Figure 3.10. In addition, the plots show the KS relation for the simulated galaxies at $z = 3$ for the total neutral gas (atomic and molecular), with the solid lines showing the mean value and the hatched area showing the rms scatter around the mean. The dotted purple line shows the mean KS relation only considering the atomic gas, while the dot-dashed cyan line shows it for the molecular gas. The dashed black line is the best-fit relation of Kennicutt (1998a) for $z \sim 0$ galaxies, while the triple dot-dashed line is for $K = 0.1 \times K_{Kenn}$. The blue line in the bottom panel is closer to the range of observed metallicities observed in DLAs of $\sim 0.04Z_{\odot}$ (Prochaska et al., 2003, Rafelski et al. 2011 in prep). The use of a metallicity cut of $0.1Z_{\odot}$ is reasonable, since the mass-weighted and volume-weighted metallicity of the atomic gas is $\sim 0.02Z_{\odot}$ and $\sim 0.03Z_{\odot}$ respectively (private communication, N. Gnedin 2010), matching the observed DLA metallicities nicely. In addition, although the dispersion of DLA metallicities is large, the majority of DLAs have metallicities below 0.1 $Z_{\odot}$, making

this a good choice for a cut to compare to DLA gas.

The spatially extended emission around LBGs is consistent with both the total and low metallicity gas models in Figure 3.11. While the uncertainties in both the model and the data are large, taking the results at face value, we can gain insights into the nature of the gas reservoirs around LBGs. The data is a better match to the model with the metallicity cut of $0.1Z_{\odot}$, coinciding with the mean relation for this model. On the other hand, the emission from gas around LBGs is also consistent within the 1σ uncertainties of the model including gas with all metallicities for the part of the rms scatter *below* the mean. This lower part of the hatched area in the top panel of Figure 3.11 represents the gas at the lower end of the metallicity distribution shown in Gnedin et al. (2009), having a mass-weighted and volume-weighted metallicity of the atomic gas of $\sim 0.26\ Z_{\odot}$ (private communication, N. Gnedin 2010), which is consistent with that of $z = 3$ galaxies having an average metallicity of $\sim 0.25\ \mathrm{Z}_{\odot}$ (Shapley et al., 2003; Mannucci et al., 2009). Since the observations fall below the mean model for the higher metallicity model, and coincide with the model for the lower metallicity model, we conclude that the metallicity of the gas is most likely around the mean metallicity of the low metallicity model, $\sim 0.04Z_{\odot}$, and is definitely below $\sim 0.26\ Z_{\odot}$, the metallicity of the model including gas of all metallicities The results therefore imply that the gas in the outskirts of LBGs has lower metallicities than the LBG cores. In fact, the observed SFRs and the implied metallicities from the models are fully consistent with the outer regions of LBGs consisting of DLA gas.

3.7.2 The Roles of Molecular and Atomic-dominated Gas in the Kennicutt Schmidt Relation

The reduction in SFR efficiency will also be affected by the competing roles played by atomic and molecular gas in the KS relation. There has been some debate as to whether the KS relation should include both atomic and molecular gas. All stars are believed to form from molecular gas, and some workers argue that Σ_{SFR} correlates better with molecular gas than atomic gas (Wong & Blitz, 2002; Kennicutt et al., 2007; Bigiel et al., 2008). On the other hand, other observations

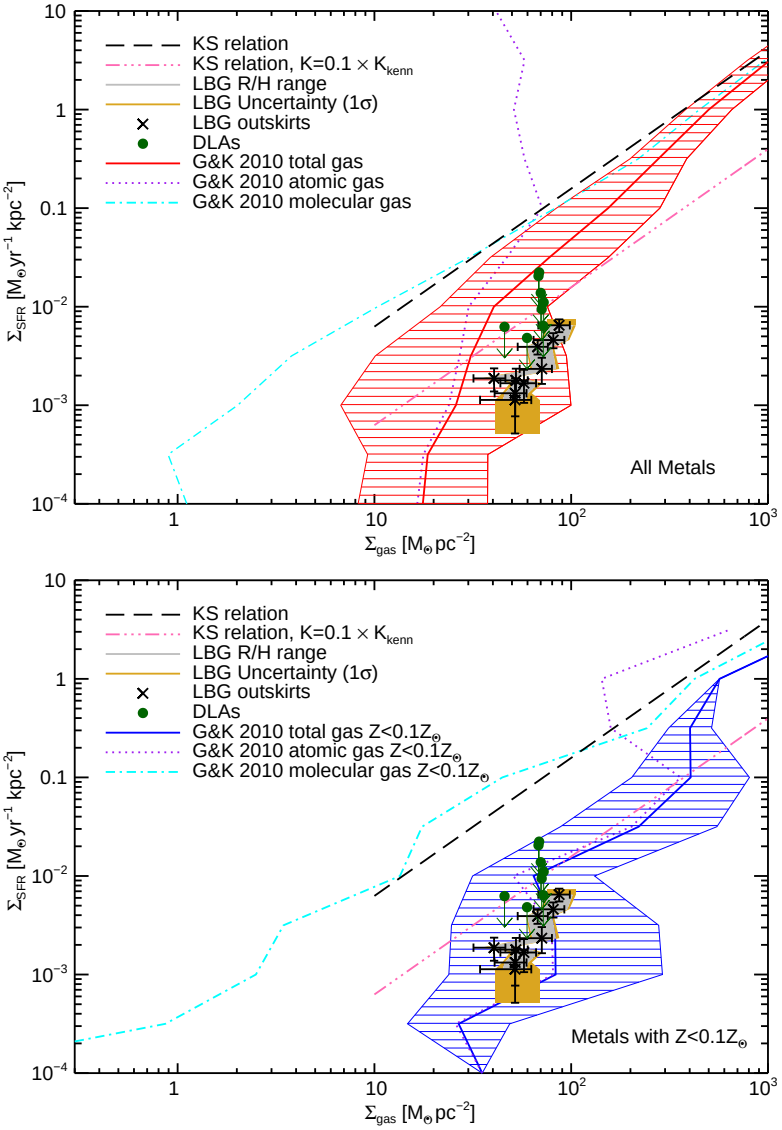

Figure 3.11 Star formation rate per unit area ($\Sigma_{\rm SFR}$) versus gas density ($\Sigma_{\rm gas}$) for both the data as shown in Figure 3.10, and the KS relation for simulated galaxies at $z = 3$ from (Gnedin et al., 2009). The top panel includes gas of all metallicities while the bottom panel considers only the gas with metallicities below $0.1Z_{\odot}$. The solid red and blue lines are the mean relation for the total neutral gas surface density (atomic and molecular) and the hatched area shows the rms scatter around the mean. The dotted purple line shows the mean KS relation only considering the atomic gas, while the dot-dashed cyan line shows it for the molecular gas. The long dashed line is the Kennicutt relation for local ($z \sim 0$) galaxies (Kennicutt, 1998a), while the triple dot-dashed line is for $K = 0.1 \times K_{Kenn}$. The gray and gold lines and the black and green points are the data and are the same as in Figure 3.10.

show a clear correlation of the total gas surface density, $\Sigma_{\rm gas}$, with $\Sigma_{\rm SFR}$ (Kennicutt, 1989, 1998a; Schuster et al., 2007; Crosthwaite & Turner, 2007), and the atomic gas surface density, $\Sigma_{\rm HI}$, with $\Sigma_{\rm SFR}$ (Bigiel et al., 2010b).

These differences can be understood in the context of the saturation of atomic-dominated gas at high column densities. Above a specified threshold of $\Sigma_{\rm HI}$, the atomic gas is converted into molecular gas and no longer correlates with $\Sigma_{\rm SFR}$. This saturation of atomic hydrogen gas above a threshold surface density is clearly observed (see Figure 8, Bigiel et al., 2008) for local galaxies at $z = 0$, and occurs at surface densities of $\sim 10 {\rm M}_{\odot}$ pc^{-2} (Wong & Blitz, 2002; Bigiel et al., 2008). However, below this threshold surface density, there is a correlation of $\Sigma_{\rm HI}$ and $\Sigma_{\rm SFR}$. This is most clearly seen in the results analyzing the *outer disks of nearby galaxies* (Bigiel et al., 2010b), where a clear correlation of $\Sigma_{\rm HI}$ with $\Sigma_{\rm SFR}$ is observed. In fact, they find that the key regulating quantity for star formation in outer disks is the column density of atomic gas. Further evidence is seen in the outskirts of M83, where the distribution of FUV flux again follows the $\Sigma_{\rm HI}$ (Bigiel et al., 2010a). In fact, Bigiel et al. (2010a) find that in the outskirts of M83, massive star formation proceeds almost everywhere H I is observed. While these outer disks must contain some molecular gas in order for star formation to occur, they are nonetheless dominated by atomic gas with surface densities lower than the saturation threshold seen in Bigiel et al. (2008).

The saturation of atomic gas above a threshold surface density is investigated in theoretical models (Krumholz et al., 2009a; Gnedin & Kravtsov, 2010b,a), which reproduce the saturation threshold for atomic gas in local galaxies. Moreover, the authors find that the threshold surface density for saturation varies with metallicity, where lower metallicity systems have higher thresholds (see Figure 4, Krumholz et al., 2009a). In addition, the simulations of $z = 3$ galaxies by Gnedin & Kravtsov (2010b) show an increased saturation surface density of atomic gas of $\sim 50 {\rm M}_{\odot}$ pc^{-2}, as seen in the purple dotted line in Figure 3.11. The line clearly saturates, with no clear relation between $\Sigma_{\rm HI}$ and $\Sigma_{\rm SFR}$ above $\sim 50 {\rm M}_{\odot}$ pc^{-2}, but with a clear relation below this density. Since $z = 3$ galaxies are typically LBGs with metallicities of $\sim 0.25 {\rm Z}_{\odot}$ (Shapley et al., 2003; Mannucci et al., 2009), this

is consistent with predictions from Krumholz et al. (2009a). The model with only lower metallicity gas (bottom panel of Figure 3.11) saturates at even higher atomic gas surface densities (Gnedin & Kravtsov, 2010b), continuing the relation of the threshold saturation of $\Sigma_{\rm HI}$ with metallicity. It appears that $\Sigma_{\rm HI}$ tracks $\Sigma_{\rm gas}$ to large values of $\Sigma_{\rm SFR}$, and no saturation occurs in $\Sigma_{\rm HI}$ until $\sim$ 200-300 $\rm M_\odot$ $\rm pc^{-2}$.

Comparison of the saturation thresholds found by Gnedin & Kravtsov (2010b) with our data in the bottom panel of Figure 3.11 reveals that the data are below this threshold for saturation of atomic gas for all values of $\Sigma_{\rm HI}$ for the model with the $0.1Z_\odot$ cut, which most closely matches our results. We therefore conclude that the measured decrease in SFR efficiency is not due to the saturation of atomic-dominated gas. In fact, our data confirms that the atomic-dominated gas doesn't saturate for $\Sigma_{\rm HI}$ of at least $\gtrsim 100 \rm M_\odot$ $\rm pc^{-2}$. This number is larger than predicted for LBG metallicities, yet smaller than predicted for DLA metallicities. This suggests that the average metallicity of the gas in the outskirts of LBGs is between $0.1Z_\odot$ and $0.25Z_\odot$. This is consistent with the metallicity estimate made in §3.5.4 of $0.12Z_\odot$ to $0.19Z_\odot$ based on the metal production rate of star formation.

While molecular gas is very likely needed to form stars, it is also clear from results for local outer disks (Bigiel et al., 2010b) and our results at high redshift that star formation can be observed even when molecular gas does not dominate azimuthal averages in rings of galactic dimensions. We do not suggest that stars are forming from purely atomic gas, but rather that in the presence of high density atomic gas, there are sufficient molecules to cool the gas such that star formation can be initiated by gravitational collapse. We predict that more sensitive measurements of molecular gas in local outer disks would result in the detection of molecular gas. On the other hand, recent models by Low & Glover (2010) suggest that molecular hydrogen may not be the cause of star formation, but rather a consequence of the star formation. In this scenario, CO traces dense gas that is already gravitationally unstable and would probably form stars regardless. More investigations are needed to better understand what is fundamentally required for star formation, and our work provides some observational constraints for such work.

We note that even though large amounts of molecular gas are not observed in DLAs (Curran et al., 2003, 2004), the molecular gas has a very small covering fraction, and therefore is unlikely to be seen along random sight lines (Zwaan & Prochaska, 2006). We also note that Bigiel et al. (2010b) finds that the FUV emission reflects the recently formed stars without large biases from external extinction. We similarly do not expect much extinction in the outer parts of the LBGs, as DLAs have low dust-to-gas ratios (Pettini, 2004; Frank & Péroux, 2010). Therefore, unless the gas in the outskirts of LBGs is due to star formation in molecular-dominated gas, we do not expect large extinction corrections to be necessary.

3.7.3 Is There a Variation of the Kennicutt Schmidt Relation with Redshift?

Recent studies of star forming galaxies at high redshift have suggested that the KS relation does not vary with redshift (Bouché et al., 2007; Tacconi et al., 2010; Daddi et al., 2010; Genzel et al., 2010). These studies do a careful job of comparing $\Sigma_{\rm SFR}$ and the molecular gas surface density, $\Sigma_{\rm H_2}$, of high and low redshift systems, and find that the galaxies fit a single KS relation. This is starkly different than our finding a lower SFR efficiency at high redshift. Furthermore, these studies differ from, simulations of high redshift galaxies that do find a reduced SFR efficiency (Gnedin & Kravtsov, 2010b).

These differences may be due to comparisons of different types of gas. In our results, we consider atomic-dominated gas as found in DLAs, while the other observational studies are focused on molecular-dominated gas with galaxies having high molecular fractions and higher metal abundances. Similarly, Bigiel et al. (2010b) also found a lower SFR efficiency in the outskirts of otherwise normal local galaxies when probing atomic-dominated gas. There are two different possible scenarios that explain the results. First, the KS relation for atomic-dominated gas follows a different KS relation than the KS relation for molecular-dominated gas. This possibility would explain the observed lower efficiencies of star formation in 1) the outskirts of $z \sim 3$ LBGs as measured here, 2) the DLAs without star forming

bulges as measured by Wolfe & Chen (2006), and 3) the outskirts of local galaxies as measured by Bigiel et al. (2010b).

On the other hand, the simulations by Gnedin & Kravtsov (2010b) focus on galaxies with low metallicities similar to those observed of LBGs ($\sim 0.26\ Z_{\odot}$) and find reduced SFR efficiencies in both their molecular-dominated and their atomic-dominated gas. They also find that the efficiency is directly related to the metallicity of the gas, suggesting that the decreased star formation efficiency is most likely due to decreased metallicities. These models accurately predict the SFR efficiencies we measure in the outskirts of the LBGs if they are associated with DLAs. The outskirts of the local galaxies measured by Bigiel et al. (2010b) are also generally of lower metallicities (e.g. de Paz et al., 2007; Cioni, 2009; Bresolin et al., 2009), so the decreased efficiencies could also be due to the lower metallicity. The SFR efficiencies in Bigiel et al. (2010b) are similar to this study, and we discuss this below in §3.7.3.1.

In addition, Bigiel et al. (2010a) find a clear correlation of the FUV light (representing star formation) with the location of the H I gas in M83. In the inner region they find a much steeper radial decline in $\Sigma_{\rm SFR}$ than in $\Sigma_{\rm H_I}$, while in the outer region of the disk, $\Sigma_{\rm SFR}$ declines less steeply, if at all (see Figure 4, Bigiel et al., 2010a). Similarly, the metallicity in the inner part of M83 drops pretty steeply, and then flattens out at larger radii (Bresolin et al., 2009). These results are consistent with the scenario that the metallicity is driving the efficiency of the SFR.

While it is not yet clear what the causes the decrease in SFR efficiency in DLAs, the results suggest it is either due to a different KS relation for atomic-dominated gas or due to the metallicity of the gas rather than the redshift. Given the excellent agreement of our results with the predictions by Gnedin & Kravtsov (2010b), and the suggestive results of the outer regions of M83, we give extra credence to the metallicities driving the SFR efficiencies. In fact, these two effects may be the same, as the outskirts of galaxies generally probably have lower metallicities, and therefore lower SFR efficiencies. While all the gas at high redshift may not have a reduced efficiency, care must be taken when using the KS relation in

cosmological models, as the properties of gas vary with redshift, thereby affecting the SFR efficiencies.

3.7.3.1 Comparison of the $z \sim 3$ SFR Efficiency with Local $z = 0$ Outer Disks

The environment for star formation at large galactic radii is significantly different than in the inner regions of star-forming galaxies, having lower metallicities and dust abundances, consisting of more H I than H_2 gas, and being spread out over large volumes. These environmental factors undoubtably have effects on the conversion of gas into stars, and perhaps the SFR efficiency. Similar to our results at high redshift, the SFR efficiency in the local ($z = 0$) outer disks is also less efficient than the KS relation (Bigiel et al., 2010b). Figure 3.12 plots our results of H I dominated gas in the outskirts of LBGs at $z \sim 3$ from Figure 3.10, in conjunction with the measurements of Bigiel et al. (2010b) of the outskirts of local spiral galaxies. These measurements combine data from the H I Nearby Galaxy Survey and the GALEX Nearby Galaxy Survey to measure both the atomic hydrogen gas surface density and the FUV emission tracing the SFR in 17 spiral galaxies. The blue diamonds in Figure 3.12 represent the best estimate for the true relation of $\Sigma_{\rm SFR}$ and $\Sigma_{\rm HI}$ from Bigiel et al. (2010b) accounting for their sensitivity, and the error bars represent the scatter in the measurements. The SFRs determined in Bigiel et al. (2010b) from the FUV luminosity use a Kroupa-type IMF and the Salim et al. (2007) FUV-SFR calibration, while we use a Salpeter IMF and the FUV-SFR calibration from Madau et al. (1998) and Kennicutt (1998b). For comparison with our LBG results, we convert the SFRs from Bigiel et al. (2010b) to Salpeter by multiplying by a factor of 1.59, and to the Kennicutt (1998b) FUV-SFR calibration by multiplying by a factor of 1.30.

While these populations probe very different redshifts and gas densities, they both probe diffuse atomic dominated gas in the outskirts of galaxies and have low metallicities. In fact, the differing redshifts enable a comparison of drastically different gas surface densities not possible at low redshift alone, due to the saturation of H I gas above a threshold surface density as described in §3.7.2. Specifically,

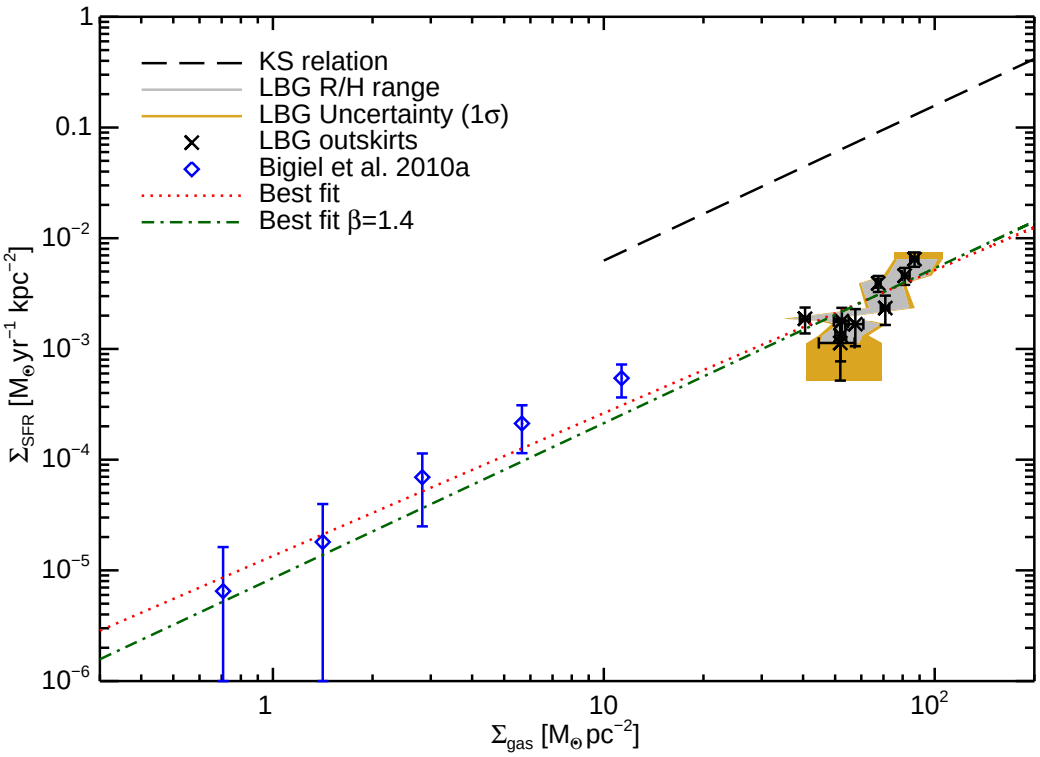

Figure 3.12 Star formation rate per unit area ($\Sigma_{\rm SFR}$) versus gas density ($\Sigma_{\rm gas}$) for the data as shown in Figure 3.10 and the results from the outer regions of spiral galaxies from (Bigiel et al., 2010b). The blue diamonds represent the best estimate for the true relation of $\Sigma_{\rm SFR}$ and $\Sigma_{\rm HI}$ from Bigiel et al. (2010b) accounting for their sensitivity, and the error bars represent the scatter. These points have been converted to use the same IMF and FUV-SFR conversion as used in this work. The long dashed line is the Kennicutt relation for local ($z \sim 0$) galaxies (Kennicutt, 1998a). The gray and gold lines and the black points are the data as shown in Figure 3.10. The dotted red line represents a power law fit to the data with both the normalization and the slope as free parameters, and the green dotted-dashed line is a power law fit with the slope set to $\beta = 1.4$, as described in §3.7.2.1.

Bigiel et al. (2010b) cannot probe significantly higher gas densities, as at $z = 0$ the H I gas saturates at threshold surface densities of $\sim 10 M_\odot$ pc^{-2} (see Figure 8 in Bigiel et al., 2008). On the other hand, as described in §3.7.2, at $z \sim 3$ the H I gas does not saturate until much higher gas surface densities. However, our measurements at $z \sim 3$ are also limited in the other direction, as we cannot probe lower gas surface densities due to insufficient surface-brightness sensitivity, and therefore we are left with non-overlapping results for $10 \lesssim \Sigma_{\rm gas} \lesssim 30 M_\odot {\rm pc}^2$.

It is not likely a coincidence that the SFR is less efficient in the outer regions of galaxies at both low and high redshift. It may be that the SFR is less efficient in the outer regions of galaxies at all redshifts, and this possibility needs to be investigated. There is evidence that the metallicities in the inner regions of galaxies observed in emission are higher than that in the outer parts sampled by quasar absorption line systems at $z \sim 0.6$ (Chen et al., 2005, 2007). If the SFR efficiency depends on the metallicity, then we would expect lower efficiencies in the outer parts of these $z \sim 0.6$ galaxies as observed.

Comparing the data at low redshift with those at high redshift, we find that they appear to fall on a straight line in log space. We therefore fit a power law to the outer disk measurements in Figure 3.12, using the KS relation in equation 3.2 and setting $\Sigma_{\rm c} = 1$ M$_\odot$pc^{-2}. Leaving both the normalization and the slope as free parameters, our least squares solution results in a normalization of $K = (1.4 \pm 0.7) \times 10^{-5}$ M$_\odot$ yr^{-1} kpc^{-2} and a slope of β=1.3$\pm$0.1, and is plotted as a dotted red line in Figure 3.12. In addition, we also fit a power law where we set the slope to the same value as in the KS relation (Kennicutt, 1998a,b), namely β=1.4. This fit has a normalization of $K = (8.5 \pm 0.7) \times 10^{-6}$ M$_\odot$ yr^{-1} kpc^{-2}, and is plotted as a dot-dashed green line in Figure 3.12. The fit is consistent for both the low and high redshift galaxy outskirts, and the normalization is significantly lower than that of the KS relation, with a K value that is 0.03 times the local value. We note that the slope of the LBG outskirts is larger than the slope for the outskirts of local galaxies. The metallicities of the outskirts of local galaxies are probably somewhat higher than those in the outskirts of LBGs, assuming they consist of DLA gas, and therefore this difference may be a result of differing metallicities.

We acknowledge that we may be comparing different environments when considering the high and low redshift outer disks, but they may be similar enough to tell us about star formation in the outskirts of galaxies. Indeed, both populations exhibit similar SFR efficiencies. Measurements of the SFR efficiency across a range of redshifts are needed to further explore if variations of the slope are real and evolve over time.

3.7.4 Bimodality of DLAs

There is evidence to suggest that there are two populations of DLAs (high cool and low cool), since the distribution of cooling rates of DLAs is bimodal (Wolfe et al., 2008). These two populations have significant differences in their cooling rates (and therefore SFRs), velocity widths, metallicity, dust-to-gas ratio, and Si II equivalent widths. The gas in the high cool population cannot be heated by background and/or *in situ* star formation alone, and so Wolfe et al. (2008) suggest that the high cool population is associated with compact star forming bulges, or LBGs. These high cool DLAs typically have metallicities ($Z = 0.09 \pm 0.03\ Z_{\odot}$), higher than the average for DLAs (Wolfe et al., 2008). The low cool population may also be associated with LBGs, although it is possible that this population is heated solely by *in situ* star formation. These low cool DLAs generally have lower than average metallicities ($Z = 0.02 \pm 0.01\ Z_{\odot}$) (Wolfe et al., 2008).

Given that our measurements in the outskirts of LBGs are consistent with both metallicities, it is possible that all DLAs are in the outskirts of LBGs. Alternatively, it would also be logical to associate the high cool population of DLAs with the gas responsible for the star formation in the outskirts of the LBGs, and the low cool population would then naturally be represented by the DLA upper limits from Wolfe & Chen (2006). While those DLAs are also likely associated with galaxies, their lower surface brightness may result in this being included in the Wolfe & Chen (2006) sample.

If we are mainly probing the high cool DLAs with the extended low surface brightness emission around LBGs, and are mainly probing the low cool DLAs in the upper limits from Wolfe et al. (2008), then the number count statistics would

need to be modified to account for the different percentages of high cool and low cool DLAs. However, these percentages are not yet very well constrained. A reasonable first try to modify the DLA models is to use the current observational result that about half the DLAs are high cool and half are low cool. If only high cool DLAs are included, it would lower the expected $\dot{\rho}_*$, which would increase the efficiencies of the SFR, moving the data to the left in Figure 3.11. Assuming that each of the two DLA populations represents half the DLAs, we find the data move to the left by about ~ 0.1 dex. This does slightly worsen the agreement of the outskirts of LBGs with the blue low metallicity model, but not by much. Also, in this scenario, the gas would have higher metallicities ($Z \sim 0.09$), and therefore we would expect the outskirts of the LBGs to fall to the left of the blue line. Regardless, the uncertainties in the models and the data are large enough that they could be compatible with a wide range of interpretations. In short, our SFR efficiency results do not drastically change whether or not there is a bimodality in the DLA population.

3.7.5 Effects of Different DLA Sizes

One caveat remains, which is the possibility that *if* DLAs are not associated with LBGs, *and* the FWHM linear diameters of DLAs at $z \sim 3$ are less than 1.9 kpc, then we have not put a limit on the *in situ* star formation in DLAs. However, as discussed in §3.1 of Wolfe & Chen (2006), all models suggested so far predict that the bulk of DLAs will have diameters larger than 1.9 kpc (e.g. Prochaska & Wolfe, 1997; Mo et al., 1998; Haehnelt et al., 2000; Boissier et al., 2003; Nagamine et al., 2006, 2007; Tescari et al., 2009; Hong et al., 2010), which is in agreement with the observations (Wolfe et al., 2005; Cooke et al., 2010). Rauch et al. (2008) find spatially extended Ly-α emission from objects with radii up to $4''$ ($\sim$30kpc) and mean radii of $\sim 1''$ ($\sim$8kpc) which they argue corresponds to the H I diameters of DLAs. While continuum emission has not been detected on these scales, it may have been observed from associated compact objects. In fact, almost all of the Ly-α selected objects have at least one plausible continuum counterpart (Michael Rauch, 2010, private communication).

If we assume that the sources of Ly-α photons are distributed throughout the gas, then we can compare the $\Sigma_{\rm SFR}$ values from Rauch et al. (2008) to ours. In this scenario, the *in situ* star formation in the DLA gas is the source of the Ly-α photons, which is possibly associated with LBGs detected in the continuum. We note that currently there is no evidence for this assumption, and it is counter to the interpretation by Rauch et al. (2008), who assume that Ly-α radiation originates in a compact object embedded in the more extended DLA gas. On the other hand, we cannot rule out this possibility and it is intriguing, so we consider it here. Using the median size of their measured extended Lyα emission of $\sim 1''$, we convert their SFRs to $\Sigma_{\rm SFR}$ of $4{\times}10^{-4}$ - $8{\times}10^{-3}$ $M_\odot$ yr^{-1} kpc^{-2}. This range in $\Sigma_{\rm SFR}$ overlaps our measured $\Sigma_{\rm SFR}$ shown in Figures 3.4 & 3.10, suggesting that we may be measuring the same star formation in DLAs in two very different methods. If this is the case, then the sizes of DLAs may be even larger than otherwise expected. Whether or not this interpretation is correct, we are definitely above the minimum size probed by Wolfe & Chen (2006) of 1.9 kpc, implying that the above mentioned caveat is unimportant. We are therefore confident that we have shown in §3.5 and §3.6 that the SFR efficiency in diffuse atomic-dominated gas at $z \sim 3$ is less efficient than for local galaxies.

3.7.6 The 'Missing Metals' Problem

The metal production by LBGs can be compared to the metals observed in DLAs. Previously, the metal content produced in LBGs was found to be significantly larger than that observed in DLAs by a factor of 10, and was called the 'Missing Metals' problem for DLAs (Pettini, 1999, 2004, 2006; Pagel, 2002; Wolfe et al., 2003a; Bouché et al., 2005). However, Wolfe & Chen (2006) found that when taking into account a reduced efficiency of star formation as found in DLAs at $z \sim 3$, then the metal over production by a factor of 10 changed to one of underproduction by a factor of 3.

In this study, we calculated the metal production in the outskirts of LBGs, and found that the metals produced there yield metallicities in the range of $0.12 \pm 0.05 Z_\odot$ to $0.19 \pm 0.07 Z_\odot$, depending on the outer radius for the integration of the

SFR (see §3.5.3 and Table 3.2). The average metallicities of DLAs at $z \sim 3$ is $Z \sim 0.04 Z_{\odot}$ (Prochaska et al., 2003, Rafelski et al. 2011 in prep), and the metallicity of the high cool DLAs likely associated with LBGs (see §3.7.1.1) typically have metallicities of $Z = 0.09 \pm 0.03\ Z_{\odot}$. We therefore find that if all the metallicity enrichment of DLAs were mainly due to *in situ* star formation in the outskirts of LBGs, then there would be no 'Missing Metals' problem.

In order for the metallicity enrichment of DLAs to arise primarily from *in situ* star formation in the outskirts of LBGs, we would require some mechanism for the LBG cores, where the metallicity is high, to not enrich the IGM significantly from $z \sim 10$ to $z \sim 3$ (~ 2 billion years). However, large scale outflows of several hundred km s^{-1} are observed in LBGs (e.g. Franx et al., 1997; Steidel et al., 2001; Pettini et al., 2002b; Adelberger et al., 2003; Shapley et al., 2003; Steidel et al., 2010). Therefore, the lack of enrichment would require that either these outflows do not mix significantly with the circumgalactic medium (CGM, as defined by Steidel et al. (2010) to be within 300 kpc of the galaxies) in the given time frame, or that the outflows do not move sufficient amounts of metal enriched gas to the outer regions of the LBGs to significantly affect the metallicity. We note that we also expect some atomic gas to be in the inner regions of LBGs, and therefore a subsample of DLA gas may be enriched locally, although with a smaller covering fraction.

While there are many theoretical models and numerical simulations to understand the nature of DLAs (e.g. Haehnelt et al., 1998; Gardner et al., 2001; Maller et al., 2001; Razoumov et al., 2006; Nagamine et al., 2007; Pontzen et al., 2008; Hong et al., 2010), none of them are able to match the column densities, metallicity range, kinematic properties, and DLA cross sections in a cosmological simulation. In addition, other than Pontzen et al. (2008), they do not reproduce the distribution of metallicities in DLAs. Pontzen et al. (2008) do not yet address the mixing of metals nor the effects of large outflows on these metals, and can therefore not address this question either. These are essential for understanding the production and mixing of the metals, and it is therefore unclear at this time if outflows from LBGs mix significantly with the CGM, or if they move enough

metal content from the inner core to the outskirts to significantly increase the metallicity. If the outskirts are not significantly enriched by the cores, then the observed metallicity of DLAs would be consistent with expectations from the *in situ* star formation in the outskirts of LBGs.

3.8 Summary and Concluding Remarks

In this work we aim to unify two pictures of the high redshift universe: absorption line systems such as DLAs that provide the fuel for star formation, and compact star forming regions such as LBGs which form the majority of stars. Each population provides valuable but independent information about the early Universe (for reviews, see Giavalisco, 2002; Wolfe et al., 2005). Connecting these two populations helps us to better understand how stars form from gas, an important part in understanding galaxy formation and evolution. In doing so, we begin to bridge two separate but complementary fields in astrophysics.

Wolfe & Chen (2006) start to bridge these fields by setting sensitive upper limits on star formation in DLAs without compact star forming regions, finding that the *in situ* star formation in DLAs is less than 5% of what is expected from the KS relation. However, they do not constrain DLAs associated with bright star-forming cores such as LBGs. In the present paper we address this caveat by searching for spatially-extended star formation in the outskirts of LBGs at $z \sim 3$ on scales up to $\sim$10 kpc. We find the following:

1) Using the sample of 407 $z \sim 3$ LBGs in the UDF from Rafelski et al. (2009), we create a composite image stack in the V-band, corresponding to the rest frame FUV emission which is a sensitive measure of the SFR, for 48 resolved, compact, symmetric, and isolated LBGs at $z \sim 3$ (Figure 3.3). We detect spatially extended low surface brightness emission in the outskirts of LBGs, as shown in the radial surface brightness profile in Figure 3.4. This is evidence for the presence of *in situ* star formation in gas in the outskirts of LBGs.

2) We find that the area covered by DLAs is larger than the area of the outskirts of LBGs for SFR efficiencies of $K = K_{Kenn}$, and is consistent with DLAs having SFR efficiencies of $K \sim 0.1 \times K_{Kenn}$ (Figure 3.5). On the other hand, the covering fraction of molecular gas is inadequate to explain the star formation in the outskirts of LBGs (Figure 3.6). This suggests that the outskirts of LBGs consist of atomic-dominated gas, supporting the underlying hypothesis of this paper. In fact, the covering fraction provides evidence that the SFR efficiency of atomic-dominated gas at $z \sim 3$ is on the order of 10 times lower than for local galaxies.

3) We integrate the rest frame FUV emission in the outskirts of LBGs and find that the average SFR is $\sim$ 0.1 $M_\odot$ yr^{-1} and $\dot{\rho_*}$ is $\sim 3 \times 10^{-3}$ $M_\odot$ yr^{-1} Mpc^{-3} (see table 3.2). Combining our largest possible value of $\dot{\rho_*}$ in the outskirts of LBGs with the upper limit found in Wolfe & Chen (2006), we obtain a conservative upper limit on the total $\dot{\rho_*}$ contributed by atomic-dominated gas of $\dot{\rho_*} < 9.9 \times 10^{-3}$ $M_\odot$ yr^{-1} Mpc^{-3}. This corresponds to $\sim$ 10% of the $\dot{\rho_*}$ measured in the inner regions of LBGs at $z \sim 3$ (Reddy et al., 2008).

4) We integrate $\dot{\rho_*}$ in the redshift range $3 \lesssim z \lesssim 10$, and calculate the total metal production in DLAs and get a metallicity of $\sim 0.15 Z_\odot$. This is comparable to the metallicity of the high cool DLAs believed to be associated with LBGs with metallicities of $\sim 0.09 Z_\odot$. If the large observed outflows of several hundred km s^{-1} of LBGs do not significantly contaminate the CGM, then the metallicity of DLAs would be consistent with expectations from the *in situ* star formation in the outskirts of LBGs. This is a potential solution to the 'Missing Metals' problem.

5) Under the hypothesis that the observed FUV emission in the outskirts of LBGs in from *in situ* star formation in atomic-dominated gas, we develop a theoretical framework connecting the emission observed around LBGs to the expected emission from DLAs. Such a framework is necessary to interpret the spatially extended star formation around LBGs. This framework develops a differential expression for the comoving star formation rate density, $\dot{\rho_*}$, corresponding to a given interval of

surface brightness using the KS relation and the column-density distribution function (equation 3.25). We also develop a method to convert the measured radial surface brightness profile of the LBG composite into the same differential expression for $\dot{\rho_*}$ (equation 3.28).

6) We compare the predictions for the surface brightnesses and $d\dot{\rho_*}/d\langle I_{\nu_0}^{obs}\rangle$ to the measured values in Figure 3.9, and find that the two overlap if the efficiency of star formation in neutral atomic-dominated gas is lower than the local KS relation by factors of 10-50. Using these reduced efficiencies, we convert our results and those from Wolfe & Chen (2006) into the standard $\Sigma_{\rm SFR}$ versus $\Sigma_{\rm gas}$ plot generally used to study SFRs (Figure 3.10). We find that $\Sigma_{\rm SFR}$ is lower than the upper limits found by Wolfe & Chen (2006) for a similar range in $\Sigma_{\rm gas}$, and both results have significantly lower SFR efficiencies than predicted by the local KS relation.

7) The reduced SFR efficiencies in the outskirts of LBGs are consistent with the predictions by Gnedin & Kravtsov (2010b) for star formation at $z \sim 3$ in neutral atomic-dominated gas with low ($< 0.1\ Z_{\odot}$) metallicities (right panel, Figure 3.11). These models find that the primary cause for the lower SFRs is due to the decreased metallicities, suggesting that this is likely the primary driver for the reduced SFR efficiencies.

8) Our results correspond to gas surface densities below the predicted threshold for saturation of atomic gas at $z = 3$ for DLA metallicities, and therefore the low measured SFR efficiencies are not due to the saturation of the atomic-dominated gas. In fact, our data supports the theoretical predictions (Krumholz et al., 2009a; Gnedin & Kravtsov, 2010b) that the atomic-dominated gas doesn't saturate for $\Sigma_{\rm HI}$ of at least $\gtrsim 100 {\rm M}_{\odot}\ {\rm pc}^{-2}$.

9) Our finding of star formation in atomic-dominated gas in the outskirts of LBGs is similar to the recent results by Bigiel et al. (2010b) who find that star formation in the outskirts of local ($z = 0$) galaxies also arise in atomic-dominated gas

(Figure 3.12). In fact, the two results are consistent with the same power law, and both results find that the SFR efficiency in this gas is lower than expected from the KS relation. It is possible that the SFR efficiencies in the outskirts of galaxies may be lower at all redshifts, and this tantalizing possibility should be investigated.

10) We find that the reduced efficiencies of star formation are likely due to either a different KS relation for atomic-dominated gas or due to the metallicity of the gas. It is possible that the lower efficiencies are due to atomic-dominated gas following a different KS relation than molecular-dominated gas, however, we favor the idea that the metallicity of the gas drives the SFR (e.g. Krumholz et al., 2009a; Gnedin & Kravtsov, 2010b,a). In fact, these two effects may be the same, as the outskirts of galaxies generally probably have lower metallicities, and therefore lower SFR efficiencies. While the reduced efficiency may not be observed for all gas at high redshift, care must be taken when applying the KS relation, as the properties of gas vary with redshift, thereby affecting the SFR efficiencies.

Moreover, simulations of galaxy formation incorporating star formation need to take these latest results into account, as the local KS relation may not be valid when dealing with either atomic-dominated gas or gas with lower metallicities. Further observations of star formation in atomic-dominated gas are needed to differentiate between these two possibilities responsible for reducing the SFR efficiencies. Future studies similar to this one at a range of redshifts will help give a clearer picture, as will further studies of star formation in the outskirts of local galaxies. In addition, progress will also hopefully be made by measurements of the CII 158μm line emission in DLAs using the Atacama Large Millimeter Array (e.g. Nagamine et al., 2006).

3.9 Acknowledgments

The authors thank Frank Bigiel, Jeff Cooke, Nickolay Gnedin, Andrey Kravtsov, and J. Xavier Prochaska for valuable discussions. Support for this work

was provided by NSF grant AST 07-09235. This work was made possible by data taken at the W.M. Keck Observatory, which is operated as a scientific partnership among the California Institute of Technology, the University of California and the National Aeronautics and Space Administration. The Observatory was made possible by the generous financial support of the W. M. Keck Foundation. The authors recognize and acknowledge the very significant cultural role and reverence that the summit of Mauna Kea has always had within the indigenous Hawaiian community. We are most fortunate to have the opportunity to conduct observations from this mountain.

This chapter, in full (with minor exceptions to conform to this thesis), is a reprint of material previously submitted as "Star Formation from DLA Gas in the Outskirts of Lyman Break Galaxies at z$\sim$3", by Marc Rafelski, Arthur M. Wolfe, &, Hsiao-Wen Chen, to the The Astrophysical Journal, 2010. I was the primary investigator and author of this paper.

References

Abraham, R. G., Tanvir, N. R., Santiago, B. X., Ellis, R. S., Glazebrook, K., & van den Bergh, S. 1996, Monthly Notices of the Royal Astronomical Society, 279, L47

Abraham, R. G., Valdes, F., Yee, H. K. C., & van den Bergh, S. 1994, The Astrophysical Journal, 432, 75

Adelberger, K. L., Steidel, C. C., Shapley, A. E., & Pettini, M. 2003, The Astrophysical Journal, 584, 45

Asplund, M., Grevesse, N., Sauval, A. J., & Scott, P. 2009, Annual Review of Astronomy and Astrophysics, 47, 481

Barnes, L. A. & Haehnelt, M. G. 2010, Monthly Notices of the Royal Astronomical Society, 403, 870

Bauermeister, A., Blitz, L., & Ma, C.-P. 2010, The Astrophysical Journal, 717, 323

Beckwith, S. V. W., Stiavelli, M., Koekemoer, A. M., Caldwell, J. A. R., Ferguson, H. C., Hook, R., Lucas, R. A., Bergeron, L. E., Corbin, M., Jogee, S., Panagia, N., Robberto, M., Royle, P., Somerville, R. S., & Sosey, M. 2006, The Astronomical Journal, 132, 1729

Benítez, N. 2000, The Astrophysical Journal, 536, 571

Bertin, E. & Arnouts, S. 1996, Astronomy and Astrophysics Supplement, 117, 393

Bigiel, F., Leroy, A., Seibert, M., Walter, F., Blitz, L., Thilker, D., & Madore, B. 2010a, The Astrophysical Journal Letters, 720, L31

Bigiel, F., Leroy, A., Walter, F., Blitz, L., Brinks, E., de Blok, W. J. G., & Madore, B. 2010b, The Astronomical Journal, 140, 1194

Bigiel, F., Leroy, A., Walter, F., Brinks, E., de Blok, W. J. G., Madore, B., & Thornley, M. D. 2008, The Astronomical Journal, 136, 2846

Boissier, S., Péroux, C., & Pettini, M. 2003, Monthly Notice of the Royal Astronomical Society, 338, 131

Bouché, N., Cresci, G., Davies, R., Eisenhauer, F., Schreiber, N. M. F., Genzel, R., Gillessen, S., Lehnert, M., Lutz, D., Nesvadba, N., Shapiro, K. L., Sternberg, A., Tacconi, L. J., Verma, A., Cimatti, A., Daddi, E., Renzini, A., Erb, D. K., Shapley, A., & Steidel, C. C. 2007, The Astrophysical Journal, 671, 303

Bouché, N., Lehnert, M. D., & Péroux, C. 2005, Monthly Notices of the Royal Astronomical Society, 364, 319

Bouwens, R. J., Illingworth, G. D., Blakeslee, J. P., Broadhurst, T. J., & Franx, M. 2004, The Astrophysical Journal, 611, L1

Bouwens, R. J., Illingworth, G. D., González, V., Labbé, I., Franx, M., Conselice, C. J., Blakeslee, J., van Dokkum, P., Holden, B., Magee, D., Marchesini, D., & Zheng, W. 2010a, The Astrophysical Journal, 725, 1587

Bouwens, R. J., Illingworth, G. D., Oesch, P. A., Labbe, I., Trenti, M., van Dokkum, P., Franx, M., Stiavelli, M., Carollo, C. M., Magee, D., & Gonzalez, V. 2010b, arXiv, astro-ph.CO

Bresolin, F., Ryan-Weber, E., Kennicutt, R. C., & Goddard, Q. 2009, The Astrophysical Journal, 695, 580

Brooks, A. M., Governato, F., Booth, C. M., Willman, B., Gardner, J. P., Wadsley, J., Stinson, G., & Quinn, T. 2007, The Astrophysical Journal, 655, L17

Brooks, A. M., Governato, F., Quinn, T., Brook, C. B., & Wadsley, J. 2009, The Astrophysical Journal, 694, 396

Cabanac, R. A., Valls-Gabaud, D., & Lidman, C. 2008, Monthly Notices of the Royal Astronomical Society, 386, 2065

Ceverino, D., Dekel, A., & Bournaud, F. 2010, Monthly Notices of the Royal Astronomical Society, 404, 2151

Chen, H.-W., Kennicutt, R. C., & Rauch, M. 2005, The Astrophysical Journal, 620, 703

—. 2007, The Astrophysical Journal, 659, 863

Chen, H.-W., Perley, D. A., Pollack, L. K., Prochaska, J. X., Bloom, J. S., Dessauges-Zavadsky, M., Pettini, M., Lopez, S., Dall'aglio, A., & Becker, G. D. 2009, The Astrophysical Journal, 691, 152

Cioni, M.-R. L. 2009, Astronomy and Astrophysics, 506, 1137

Ciotti, L. & Bertin, G. 1999, Astronomy and Astrophysics, 352, 447

Coe, D., Benítez, N., Sánchez, S. F., Jee, M., Bouwens, R., & Ford, H. 2006, The Astronomical Journal, 132, 926

Conselice, C. J. 2003, The Astrophysical Journal Supplement Series, 147, 1

Conti, A., Connolly, A. J., Hopkins, A. M., Budavári, T., Szalay, A. S., Csabai, I., Schmidt, S. J., Adams, C., & Petrovic, N. 2003, The Astronomical Journal, 126, 2330

Cooke, J., Wolfe, A. M., Gawiser, E., & Prochaska, J. X. 2006, The Astrophysical Journal, 652, 994

Cooke, R., Pettini, M., Steidel, C. C., King, L. J., Rudie, G. C., & Rakic, O. 2010, Monthly Notices of the Royal Astronomical Society, 409, 679

Crosthwaite, L. P. & Turner, J. L. 2007, The Astronomical Journal, 134, 1827

Curran, S. J., Murphy, M. T., Pihlström, Y. M., Webb, J. K., Bolatto, A. D., & Bower, G. C. 2004, Monthly Notices of the Royal Astronomical Society, 352, 563

Curran, S. J., Murphy, M. T., Webb, J. K., & Pihlström, Y. M. 2003, Monthly Notice of the Royal Astronomical Society, 340, 139

Daddi, E., Bournaud, F., Walter, F., Dannerbauer, H., Carilli, C. L., Dickinson, M., Elbaz, D., Morrison, G. E., Riechers, D., Onodera, M., Salmi, F., Krips, M., & Stern, D. 2010, The Astrophysical Journal, 713, 686

de Paz, A. G., Madore, B. F., Boissier, S., Thilker, D., Bianchi, L., Contreras, C. S., Barlow, T. A., Conrow, T., Forster, K., Friedman, P. G., Martin, D. C., Morrissey, P., Neff, S. G., Rich, R. M., Schiminovich, D., Seibert, M., Small, T., Donas, J., Heckman, T. M., Lee, Y.-W., Milliard, B., Szalay, A. S., Wyder, T. K., & Yi, S. 2007, The Astrophysical Journal, 661, 115

Dekel, A. & Birnboim, Y. 2006, Monthly Notices of the Royal Astronomical Society, 368, 2

—. 2008, Monthly Notices of the Royal Astronomical Society, 383, 119

Dekel, A., Birnboim, Y., Engel, G., Freundlich, J., Goerdt, T., Mumcuoglu, M., Neistein, E., Pichon, C., Teyssier, R., & Zinger, E. 2009a, Nature, 457, 451

Dekel, A., Sari, R., & Ceverino, D. 2009b, The Astrophysical Journal, 703, 785

Dessauges-Zavadsky, M., D'Odorico, S., Schaerer, D., Modigliani, A., Tapken, C., & Vernet, J. 2010, Astronomy and Astrophysics, 510, 26

Ellis, R. S. 1997, Annual Review of Astronomy and Astrophysics, 35, 389

Elmegreen, B. G. 2002, The Astrophysical Journal, 577, 206

Erb, D. K. 2008, The Astrophysical Journal, 674, 151

Fall, S. M. & Pei, Y. C. 1993, The Astrophysical Journal, 402, 479

Faucher-Giguère, C.-A. & Kereš, D. 2011, Monthly Notices of the Royal Astronomical Society: Letters, L208

Feldmann, R., Gnedin, N. Y., & Kravtsov, A. V. 2010, eprint arXiv, 1010, 1539

Fernández-Soto, A., Lanzetta, K. M., & Yahil, A. 1999, The Astrophysical Journal, 513, 34

Ford, H. C., Illingworth, G. D., Clampin, M., Hartig, G., Bartko, F., Benitez, N., Blakeslee, J. P., Bouwens, R., Broadhurst, T. J., Brown, R., Burrows, C., Cheng, E., Cross, N., Feldman, P. D., Franx, M., Golimowski, D. A., Gronwall, C., Kimble, R. A., Krist, J., Lesser, M., Magee, D., Martel, A., McCann, W. J., Meurer, G. R., Miley, G., Postman, M., Rosati, P., Sirianni, M., Sparks, W. B., Tran, H. D., Tsvetanov, Z. I., & White, R. L. 2002, American Astronomical Society, 200, 675

Frank, S. & Péroux, C. 2010, Monthly Notices of the Royal Astronomical Society, 837

Franx, M., Illingworth, G. D., Kelson, D. D., van Dokkum, P. G., & Tran, K.-V. 1997, The Astrophysical Journal Letters, 486, L75

Fumagalli, M. & Gavazzi, G. 2008, Astronomy and Astrophysics, 490, 571

Fumagalli, M., O'Meara, J. M., Prochaska, J. X., & Kanekar, N. 2010, Monthly Notices of the Royal Astronomical Society, 408, 362

Fumagalli, M., Prochaska, J. X., Kasen, D., Dekel, A., Ceverino, D., & Primack, J. R. 2011, arXiv, astro-ph.CO

Fynbo, J. P. U., Laursen, P., Ledoux, C., Durgapal, A. K., Møller, P., Goldoni, P., Gullberg, B., Kaper, L., Maund, J., Noterdaeme, P., Ostlin, G., Strandet, M. L., Toft, S., Vreeswijk, P. M., & Zafar, T. 2010, eprint arXiv, 1002, 4626

Gardner, J. P., Katz, N., Hernquist, L., & Weinberg, D. H. 2001, The Astrophysical Journal, 559, 131

Genzel, R., Tacconi, L. J., Gracia-Carpio, J., Sternberg, A., Cooper, M. C., Shapiro, K., Bolatto, A., Bouché, N., Bournaud, F., Burkert, A., Combes, F., Comerford, J., Cox, P., Davis, M., Schreiber, N. M. F., Garcia-Burillo, S., Lutz, D., Naab, T., Neri, R., Omont, A., Shapley, A., & Weiner, B. 2010, Monthly Notices of the Royal Astronomical Society, 407, 2091

Giavalisco, M. 2002, Annual Review of Astronomy and Astrophysics, 40, 579

Giavalisco, M., Steidel, C. C., & Macchetto, F. D. 1996, The Astrophysical Journal, 470, 189

Gnedin, N. Y. & Kravtsov, A. V. 2010a, eprint arXiv, 1004, 3

—. 2010b, The Astrophysical Journal, 714, 287

Gnedin, N. Y., Tassis, K., & Kravtsov, A. V. 2009, The Astrophysical Journal, 697, 55

Grevesse, N., Asplund, M., Sauval, A. J., & Scott, P. 2010, Astrophysics and Space Science, 328, 179

Haardt, F. & Madau, P. 1996, The Astrophysical Journal, 461, 20

Haehnelt, M. G., Steinmetz, M., & Rauch, M. 1998, The Astrophysical Journal, 495, 647

—. 2000, The Astrophysical Journal, 534, 594

Hathi, N. P., Jansen, R. A., Windhorst, R. A., Cohen, S. H., Keel, W. C., Corbin, M. R., & Ryan, R. E. 2008, The Astronomical Journal, 135, 156

Helfer, T. T., Thornley, M. D., Regan, M. W., Wong, T., Sheth, K., Vogel, S. N., Blitz, L., & Bock, D. C.-J. 2003, The Astrophysical Journal Supplement Series, 145, 259

Hong, S., Katz, N., Davé, R., Fardal, M., Kereš, D., & Oppenheimer, B. D. 2010, arXiv, astro-ph.CO

Kennicutt, R. C. 1989, The Astrophysical Journal, 344, 685

—. 1998a, The Astrophysical Journal, 498, 541

—. 1998b, Annual Review of Astronomy and Astrophysics, 36, 189

Kennicutt, R. C., Calzetti, D., Walter, F., Helou, G., Hollenbach, D. J., Armus, L., Bendo, G., Dale, D. A., Draine, B. T., Engelbracht, C. W., Gordon, K. D., Prescott, M. K. M., Regan, M. W., Thornley, M. D., Bot, C., Brinks, E., de Blok, E., de Mello, D., Meyer, M., Moustakas, J., Murphy, E. J., Sheth, K., & Smith, J. D. T. 2007, The Astrophysical Journal, 671, 333

Kereš, D., Katz, N., Fardal, M., Davé, R., & Weinberg, D. H. 2009, Monthly Notices of the Royal Astronomical Society, 395, 160

Kravtsov, A. V. 2003, The Astrophysical Journal, 590, L1

Krumholz, M. R., McKee, C. F., & Tumlinson, J. 2008, The Astrophysical Journal, 689, 865

—. 2009a, The Astrophysical Journal, 693, 216

—. 2009b, The Astrophysical Journal, 699, 850

Lanzetta, K. M., Yahata, N., Pascarelle, S., Chen, H.-W., & Fernández-Soto, A. 2002, The Astrophysical Journal, 570, 492

Law, D. R., Steidel, C. C., Erb, D. K., Pettini, M., Reddy, N. A., Shapley, A. E., Adelberger, K. L., & Simenc, D. J. 2007, The Astrophysical Journal, 656, 1

Leroy, A. K., Walter, F., Brinks, E., Bigiel, F., de Blok, W. J. G., Madore, B., & Thornley, M. D. 2008, The Astronomical Journal, 136, 2782

Lotz, J. M., Primack, J., & Madau, P. 2004, The Astronomical Journal, 128, 163

Low, M.-M. M. & Glover, S. C. O. 2010, arXiv, astro-ph.GA

Madau, P., Ferguson, H. C., Dickinson, M. E., Giavalisco, M., Steidel, C. C., & Fruchter, A. 1996, Monthly Notices of the Royal Astronomical Society, 283, 1388

Madau, P., Pozzetti, L., & Dickinson, M. 1998, The Astrophysical Journal, 498, 106

Maller, A. H., Prochaska, J. X., Somerville, R. S., & Primack, J. R. 2001, Monthly Notices of the Royal Astronomical Society, 326, 1475

Mannucci, F., Cresci, G., Maiolino, R., Marconi, A., Pastorini, G., Pozzetti, L., Gnerucci, A., Risaliti, G., Schneider, R., Lehnert, M., & Salvati, M. 2009, Monthly Notices of the Royal Astronomical Society, 398, 1915

Markwardt, C. B. 2009, eprint arXiv, 0902, 2850

McCarthy, J. K., Cohen, J. G., Butcher, B., Cromer, J., Croner, E., Douglas, W. R., Goeden, R. M., Grewal, T., Lu, B., Petrie, H. L., Weng, T., Weber, B., Koch, D. G., & Rodgers, J. M. 1998, Proc. SPIE Vol. 3355, 3355, 81

McDonald, P. & Miralda-Escudé, J. 1999, The Astrophysical Journal, 519, 486

Mo, H. J., Mao, S., & White, S. D. M. 1998, Monthly Notices of the Royal Astronomical Society, 295, 319

Møller, P., Fynbo, J. P. U., & Fall, S. M. 2004, Astronomy and Astrophysics, 422, L33

Møller, P., Fynbo, J. P. U., Hjorth, J., Thomsen, B., Egholm, M. P., Andersen, M. I., Gorosabel, J., Holland, S. T., Jakobsson, P., Jensen, B. L., Pedersen, H., Pedersen, K., & Weidinger, M. 2002a, Astronomy and Astrophysics, 396, L21

Møller, P., Warren, S. J., Fall, S. M., Fynbo, J. U., & Jakobsen, P. 2002b, The Astrophysical Journal, 574, 51

Nagamine, K., Choi, J.-H., & Yajima, H. 2010, The Astrophysical Journal Letters, 725, L219

Nagamine, K., Springel, V., & Hernquist, L. 2004, Monthly Notices of the Royal Astronomical Society, 348, 435

Nagamine, K., Wolfe, A. M., & Hernquist, L. 2006, The Astrophysical Journal, 647, 60

Nagamine, K., Wolfe, A. M., Hernquist, L., & Springel, V. 2007, The Astrophysical Journal, 660, 945

Nonino, M., Dickinson, M., Rosati, P., Grazian, A., Reddy, N., Cristiani, S., Giavalisco, M., Kuntschner, H., Vanzella, E., Daddi, E., Fosbury, R. A. E., & Cesarsky, C. 2009, The Astrophysical Journal Supplement, 183, 244

Noterdaeme, P., Petitjean, P., Ledoux, C., & Srianand, R. 2009, Astronomy and Astrophysics, 505, 1087

Obreschkow, D. & Rawlings, S. 2009, The Astrophysical Journal Letters, 696, L129

Oke, J. B., Cohen, J. G., Carr, M., Cromer, J., Dingizian, A., Harris, F. H., Labrecque, S., Lucinio, R., Schaal, W., Epps, H., & Miller, J. 1995, Publications of the Astronomical Society of the Pacific, 107, 375

Pagel, B. E. J. 2002, Cosmic chemical evolution. Proceedings of the 187th Symposium of the International Astronomical Union, 187, 209

Pascarelle, S. M., Windhorst, R. A., Keel, W. C., & Odewahn, S. C. 1996, Nature, 383, 45

Pettini, M. 1999, Chemical Evolution from Zero to High Redshift, 233

—. 2004, Cosmochemistry. The melting pot of the elements (Cambridge University Press)

—. 2006, arXiv, astro-ph

Pettini, M., Ellison, S. L., Bergeron, J., & Petitjean, P. 2002a, Astronomy and Astrophysics, 391, 21

Pettini, M., King, D. L., Smith, L. J., & Hunstead, R. W. 1997, The Astrophysical Journal, 478, 536

Pettini, M., Lipman, K., & Hunstead, R. W. 1995, The Astrophysical Journal, 451, 100

Pettini, M., Rix, S. A., Steidel, C. C., Adelberger, K. L., Hunt, M. P., & Shapley, A. E. 2002b, The Astrophysical Journal, 569, 742

Pettini, M., Smith, L. J., Hunstead, R. W., & King, D. L. 1994, The Astrophysical Journal, 426, 79

Pirzkal, N., Sahu, K. C., Burgasser, A., Moustakas, L. A., Xu, C., Malhotra, S., Rhoads, J. E., Koekemoer, A. M., Nelan, E. P., Windhorst, R. A., Panagia, N., Gronwall, C., Pasquali, A., & Walsh, J. R. 2005, The Astrophysical Journal, 622, 319

Pontzen, A., Governato, F., Pettini, M., Booth, C. M., Stinson, G., Wadsley, J., Brooks, A., Quinn, T., & Haehnelt, M. 2008, Monthly Notices of the Royal Astronomical Society, 390, 1349

Prochaska, J. X., Gawiser, E., Wolfe, A. M., Castro, S., & Djorgovski, S. G. 2003, The Astrophysical Journal, 595, L9

Prochaska, J. X., Herbert-Fort, S., & Wolfe, A. M. 2005, The Astrophysical Journal, 635, 123

Prochaska, J. X. & Wolfe, A. M. 1997, The Astrophysical Journal, 487, 73

—. 2009, The Astrophysical Journal, 696, 1543

Rafelski, M., Wolfe, A. M., Cooke, J., Chen, H.-W., Armandroff, T. E., & Wirth, G. D. 2009, The Astrophysical Journal, 703, 2033

Rauch, M., Haehnelt, M., Bunker, A., Becker, G., Marleau, F., Graham, J., Cristiani, S., Jarvis, M., Lacey, C., Morris, S., Peroux, C., Röttgering, H., & Theuns, T. 2008, The Astrophysical Journal, 681, 856

Razoumov, A. O. 2009, The Astrophysical Journal, 707, 738

Razoumov, A. O., Norman, M. L., Prochaska, J. X., Sommer-Larsen, J., Wolfe, A. M., & Yang, Y.-J. 2008, The Astrophysical Journal, 683, 149

Razoumov, A. O., Norman, M. L., Prochaska, J. X., & Wolfe, A. M. 2006, The Astrophysical Journal, 645, 55

Reddy, N. A. & Steidel, C. C. 2009, The Astrophysical Journal, 692, 778

Reddy, N. A., Steidel, C. C., Pettini, M., Adelberger, K. L., Shapley, A. E., Erb, D. K., & Dickinson, M. 2008, The Astrophysical Journal Supplement Series, 175, 48

Robertson, B. E. & Kravtsov, A. V. 2008, The Astrophysical Journal, 680, 1083

Salim, S., Rich, R. M., Charlot, S., Brinchmann, J., Johnson, B. D., Schiminovich, D., Seibert, M., Mallery, R., Heckman, T. M., Forster, K., Friedman, P. G., Martin, D. C., Morrissey, P., Neff, S. G., Small, T., Wyder, T. K., Bianchi, L., Donas, J., Lee, Y.-W., Madore, B. F., Milliard, B., Szalay, A. S., Welsh, B. Y., & Yi, S. K. 2007, The Astrophysical Journal Supplement Series, 173, 267

Sawicki, M. & Thompson, D. 2006, The Astrophysical Journal, 642, 653

Schade, D., Lilly, S. J., Crampton, D., Hammer, F., Fevre, O. L., & Tresse, L. 1995, The Astrophysical Journal Letters, 451, L1

Schechter, P. 1976, The Astrophysical Journal, 203, 297

Schiminovich, D., Ilbert, O., Arnouts, S., Milliard, B., Tresse, L., Fèvre, O. L., Treyer, M., Wyder, T. K., Budavári, T., Zucca, E., Zamorani, G., Martin, D. C., Adami, C., Arnaboldi, M., Bardelli, S., Barlow, T., Bianchi, L., Bolzonella, M., Bottini, D., Byun, Y.-I., Cappi, A., Contini, T., Charlot, S., Donas, J., Forster, K., Foucaud, S., Franzetti, P., Friedman, P. G., Garilli, B., Gavignaud, I., Guzzo, L., Heckman, T. M., Hoopes, C., Iovino, A., Jelinsky, P., Brun, V. L., Lee, Y.-W., Maccagni, D., Madore, B. F., Malina, R., Marano, B., Marinoni, C., McCracken, H. J., Mazure, A., Meneux, B., Morrissey, P., Neff, S., Paltani, S., Pellò, R., Picat, J. P., Pollo, A., Pozzetti, L., Radovich, M., Rich, R. M., Scaramella, R., Scodeggio, M., Seibert, M., Siegmund, O., Small, T., Szalay, A. S., Vettolani, G., Welsh, B., Xu, C. K., & Zanichelli, A. 2005, The Astrophysical Journal, 619, L47

Schmidt, M. 1959, The Astrophysical Journal, 129, 243

Schreiber, N. M. F., Genzel, R., Bouché, N., Cresci, G., Davies, R., Buschkamp, P., Shapiro, K., Tacconi, L. J., Hicks, E. K. S., Genel, S., Shapley, A. E., Erb, D. K., Steidel, C. C., Lutz, D., Eisenhauer, F., Gillessen, S., Sternberg, A., Renzini, A., Cimatti, A., Daddi, E., Kurk, J., Lilly, S., Kong, X., Lehnert, M. D., Nesvadba, N., Verma, A., Mccracken, H., Arimoto, N., Mignoli, M., & Onodera, M. 2009, The Astrophysical Journal, 706, 1364

Schuster, K. F., Kramer, C., Hitschfeld, M., Garcia-Burillo, S., & Mookerjea, B. 2007, Astronomy and Astrophysics, 461, 143

Shapley, A. E., Steidel, C. C., Pettini, M., & Adelberger, K. L. 2003, The Astrophysical Journal, 588, 65

Shapley, A. E., Steidel, C. C., Pettini, M., Adelberger, K. L., & Erb, D. K. 2006, The Astrophysical Journal, 651, 688

Steidel, C. C., Erb, D. K., Shapley, A. E., Pettini, M., Reddy, N., Bogosavljević, M., Rudie, G. C., & Rakic, O. 2010, The Astrophysical Journal, 717, 289

Steidel, C. C., Giavalisco, M., Dickinson, M., & Adelberger, K. L. 1996a, The Astronomical Journal, 112, 352

Steidel, C. C., Giavalisco, M., Pettini, M., Dickinson, M., & Adelberger, K. L. 1996b, The Astrophysical Journal, 462, L17

Steidel, C. C. & Hamilton, D. 1992, The Astronomical Journal, 104, 941

Steidel, C. C., Pettini, M., & Adelberger, K. L. 2001, The Astrophysical Journal, 546, 665

Steidel, C. C., Pettini, M., & Hamilton, D. 1995, The Astronomical Journal, 110, 2519

Stetson, P. B. 1987, Astronomical Society of the Pacific, 99, 191

Tacconi, L. J., Genzel, R., Neri, R., Cox, P., Cooper, M. C., Shapiro, K., Bolatto, A., Bouché, N., Bournaud, F., Burkert, A., Combes, F., Comerford, J., Davis, M., Schreiber, N. M. F., Garcia-Burillo, S., Gracia-Carpio, J., Lutz, D., Naab, T., Omont, A., Shapley, A., Sternberg, A., & Weiner, B. 2010, Nature, 463, 781

Tassis, K., Kravtsov, A. V., & Gnedin, N. Y. 2008, The Astrophysical Journal, 672, 888

Tescari, E., Viel, M., Tornatore, L., & Borgani, S. 2009, Monthly Notices of the Royal Astronomical Society, 1

Thilker, D. A., Bianchi, L., Boissier, S., de Paz, A. G., Madore, B. F., Martin, D. C., Meurer, G. R., Neff, S. G., Rich, R. M., Schiminovich, D., Seibert, M., Wyder, T. K., Barlow, T. A., Byun, Y.-I., Donas, J., Forster, K., Friedman, P. G., Heckman, T. M., Jelinsky, P. N., Lee, Y.-W., Malina, R. F., Milliard, B., Morrissey, P., Siegmund, O. H. W., Small, T., Szalay, A. S., & Welsh, B. Y. 2005, The Astrophysical Journal, 619, L79

Thompson, R. I., Bouwens, R. J., & Illingworth, G. 2006, Planets to cosmology : essential science in the final years of the Hubble Space Telescope, 195

Wolfe, A. M. & Chen, H.-W. 2006, The Astrophysical Journal, 652, 981

Wolfe, A. M., Gawiser, E., & Prochaska, J. X. 2003a, The Astrophysical Journal, 593, 235

—. 2005, Annual Review of Astronomy and Astrophysics, 43, 861

Wolfe, A. M., Lanzetta, K. M., Foltz, C. B., & Chaffee, F. H. 1995, The Astrophysical Journal, 454, 698

Wolfe, A. M., Prochaska, J. X., & Gawiser, E. 2003b, The Astrophysical Journal, 593, 215

Wolfe, A. M., Prochaska, J. X., Jorgenson, R. A., & Rafelski, M. 2008, The Astrophysical Journal, 681, 881

Wong, T. & Blitz, L. 2002, The Astrophysical Journal, 569, 157

Zibetti, S., Ménard, B., Nestor, D., & Turnshek, D. 2005, The Astrophysical Journal, 631, L105

Zibetti, S., Ménard, B., Nestor, D. B., Quider, A. M., Rao, S. M., & Turnshek, D. A. 2007, The Astrophysical Journal, 658, 161

Zibetti, S., White, S. D. M., & Brinkmann, J. 2004, Monthly Notices of the Royal Astronomical Society, 347, 556

Zwaan, M. A. & Prochaska, J. X. 2006, The Astrophysical Journal, 643, 675

Zwaan, M. A., van der Hulst, J. M., Briggs, F. H., Verheijen, M. A. W., & Ryan-Weber, E. V. 2005, Monthly Notices of the Royal Astronomical Society, 364, 1467

Chapter 4

Metallicity Evolution of Damped Lyman Alpha Systems out to $z \sim 5$

4.1 Introduction

The recent detection of star-forming galaxies out to $z \sim 8$ (Bouwens et al., 2010; Bunker et al., 2010) provides new information about the crucial formative stages of galaxy evolution. One of the important goals of these studies is to identify the high-redshift progenitors of current galaxies and their stellar populations. A valuable diagnostic tool that links the properties of high-redshift galaxies to their descendants is their chemical properties (Pettini, 2006). While chemical properties are exceedingly difficult to extract from the faint starlight emitted by star-forming galaxies at high redshift, they are more easily determined from protogalactic gas detected in absorption against bright background quasars (Pettini, 2006; Prochaska et al., 2003b). If the metallicity of such gas were to resemble the metallicity of, say, globular clusters, then a reasonable first guess is that stars in globular clusters form out of this gas. The evolution of the metallicity and other properties of this

gas could then provide information about the sequence of events leading to the formation of current galaxies. The challenge then is to find gas in objects that are representative of the high-z protogalaxies.

The high-redshift Universe is occupied by populations of objects spanning a wide range of metallicities. While the mean metal abundances of dense, compact objects such as quasars is given by [M/H][1] ≈ 0 (Hamann & Ferland, 1999), diffuse large-scale configurations such as the Ly-α forest clouds have [M/H]=-3 (Aguirre et al., 2004). With a mean metal abundance of [M/H]=$-$ 1.4 (Pettini, 2006), the damped Ly-α absorption systems (DLAs; see Wolfe et al., 2005, for a review) are galactic-scale objects that lie between these two extremes. The purpose of this paper is to present the results of a new survey for the metal abundances of DLAs out to $z \approx 5$. We focus on the DLAs for several reasons. First, since they are detected in absorption, DLAs are unbiassed with respect to luminosity and presumably mass; i.e., they are representative objects. Second, in contrast to all other classes of quasar absorption systems, the gas in DLAs is mainly neutral. In fact, DLAs dominate the neutral-gas content of the Universe out to $z \approx 5$, (Wolfe et al., 2005), and exhibit properties indicating that they are neutral-gas reservoirs for star formation at high redshift (Nagamine et al., 2004b,a; Wolfe & Chen, 2006). Third, because DLA gas likely originates in the outer regions of high-z galaxies, chemical and dynamical information would be preserved due to the long time-scales for dissipation and dynamical mixing (Freeman & Bland-Hawthorn, 2002). Fourth, the large optical depth at the Lyman limit of the neutral gas in DLAs (typically $\tau_{\rm LL} \approx 10^4$), eliminates the need for uncertain ionization corrections to deduce the metal abundances. Accordingly the most accurately determined abundances at high redshift are for DLAs (Wolfe et al., 2005).

Our primary goal is to measure the cosmic metallicity:
$\langle {\rm Z} \rangle \equiv \log_{10}(\Omega_{\rm metals}/\Omega_{\rm gas}) - \log_{10}({\rm M/H})_\odot$ (Lanzetta et al., 1995)

[1]We adopt the standard notation in which the metal abundance [M/H] signifies the logarithmic abundance of element M relative to solar; i.e., [M/H]$\equiv \log_{10}({\rm M/H}) - \log_{10}({\rm M/H})_\odot$.

at redshifts $z > 4$. Previously we determined $\langle \mathrm{Z} \rangle$ by measuring the column-density weighted mean metal abundances (see Prochaska et al., 2003a) in redshift bins containing equal numbers of DLAs. The data revealed a statistically significant decline in $\langle \mathrm{Z} \rangle$ with increasing redshift, given by $\langle \mathrm{Z} \rangle = (-0.26 \pm 0.07)z - (0.59 \pm 0.18)$, which was confirmed at $z < 4$ by independent measurements (Kulkarni et al., 2005, 2010). While the evolution of $\langle \mathrm{Z} \rangle$ is linear in redshift, it is non-linear in time, with the slope, $\mathrm{d}\langle \mathrm{Z} \rangle / \mathrm{dt}$, becoming significantly steeper at earlier cosmic times, t. Since the Prochaska et al. (2003a) sample contained only 10 DLAs with $z > 4$, $\langle \mathrm{Z} \rangle$ and its derivatives were poorly determined at such high redshifts. Therefore, another primary goal is to find whether this trend continues back to $z \approx 5$. Prochaska et al. (2003a) also discovered (1) a "metallicity floor" at [M/H]$=-3.0$, because no metal abundances were found below this value despite our sensitivity to [M/H] values well below -4.0, and (2) a large dispersion of [M/H] at all redshifts. We wish to investigate whether these phenomena persist at higher redshifts. Although increasing the redshift range of our survey to $z \approx 5$ corresponds to an increase in survey time interval of only ≈ 0.5 Gyr, we shall show that this is a critical time interval in which, as stated above, $\mathrm{d}\langle \mathrm{Z} \rangle / \mathrm{dt}$ becomes increasingly steep with decreasing t.

Another goal is to compare the metallicity distribution of DLAs with those of known stellar populations. Previous studies (Pettini, 2004, 2006) have shown that the distribution of metallicities at $z > 2$ disagree with known stellar populations in the Galaxy. However, if high redshift galaxies are surrounded by a thick disk of neutral gas (Wolfe et al., 2003, 2008; Rafelski et al., 2010), then stars that formed *in situ* in such gas at high redshift should be observable in $z = 0$ galaxies, such as the Milk Way. These stars would presumably have a similar metallicity distribution as the DLA gas. We wish to investigate whether or not this disagreement persists in our sample that is larger in size and extends to higher redshifts.

The outline of this paper is as follows: The observations and data reduction are presented in §4.2 and the analysis of the resultant spectra is detailed in §4.3.

In §4.3.1, Voigt profiles are fitted to the damped Ly-α profiles to determine the H I column densities, $N_{\rm HI}$. Column densities of the metal lines are determined from the apparent optical depth method (Savage & Sembach, 1991; Prochaska et al., 2001), and combined with the $N_{\rm HI}$ values to determine element abundances for the DLAs in §4.3.2. The determination of $\langle$Z$\rangle$ as function of redshift and time is presented in §4.3.3, and a comparison of the DLA metallicity distribution with that of halo stars is shown in §4.3.4. In §4.4 we discuss the metallicity distribution and its implications for halo star formation. In §4.5 we summarize the results.

Throughout this paper we adopt a cosmology of $(\Omega_{\rm M}, \Omega_\Lambda, h)$=(0.3,0.7.0.7).

4.2 Observations and Data Reduction

The observations presented in this paper were acquired with the Echellette Spectrograph and Imager (ESI; Sheinis et al., 2002) and followup observations were obtained with the High Resolution Echelle Spectrometer (HIRES; Vogt et al., 1994) on the Keck I and II 10m telescopes. As reported in Prochaska et al. (2003b), ESI is a highly efficient instrument for determining metal abundances from the narrow metal absorption lines produced in the spectra of high-redshift quasars by foreground DLAs. The primary new quasar sample, obtained in 2009 and 2010, comprises objects with emission redshifts $z_{em} > 4.1$ that were selected from the Sloan Digital Sky Surveys SDSS5, and SDSS7 (Adelman-McCarthy et al., 2007; Abazajian et al., 2009). These high-z_{em} quasars are systematically fainter than the lower z_{em} quasars in the Prochaska et al. (2003b) sample, and therefore longer integration times were typically required to achieve a given signal-to-noise (S/N) ratio. The effective upper limit to the redshifts of our DLA sample is about 5.2, since DLAs with higher redshifts are essentially undetectable because line blanketing by the Ly-α forest severely attenuates the quasar continuum at wavelengths shortward of Ly-α emission; i.e. at wavelengths where such DLAs would be located. In addition to the primary high redshift quasar sample, we also

include observations of lower redshift quasars ($2.5 \lesssim z \lesssim 3.5$) obtained in 2008 to augment the number of unbiased metallicity measurements (see below).

The new observations comprise a total of 6 nights (effectively 5 nights due to bad weather) on ESI and 3 nights on HIRES. In Table 4.1 we present a journal of observations describing the 50 quasars in our sample. Column (1) gives the quasar coordinate name obtained from the SDSS survey. Columns (2) and (3) give the RA and Dec. of the quasar in J2000 coordinates. Columns (4) and (5) give the AB r and i magnitudes of the quasar: in most cases the i magnitude gives a realistic measure of the unattenuated quasar brightness since at the redshifts of most of the DLAs, the i filter is placed redward of Ly-α emission. Column (6) gives the emission redshift of the quasars, and column (7) lists candidate DLA absorption redshifts obtained from SDSS. Column (8) provides the UT date of the observations, column (9) states the instrument used, and column (10) lists the slit size. Column (11) gives the exposure time, and column (12) the S/N pixel^{-1} of the data.

In general we aimed at obtaining S/N values larger than 15 pixel^{-1} for each quasar, and for the ESI observations, we obtained 2-3 exposures per object. After the first exposure was obtained, the data was quickly reduced to determine if the DLA candidate were a false positive. If the candidate was definitely a false positive, then we abandoned obtaining more exposures, resulting in reduced S/N values for those targets. These quasars are nonetheless listed in Table 4.1, and they are marked with the footnote *a*.

Table 4.1. Journal of Observations

QSO	R.A. (J2000)	Dec. (J2000)	r (AB)	i (AB)	z_{em}	z_{abs}	Date (UT)	Instr.	Slit (arcsec)	t_{exp} (s)	S/N pixel^{-1}
(1)	(2)	(3)	(4)	(5)	(6)	(7)	(8)	(9)	(10)	(11)	(12)
J0040−0915	00 40 54.7	−09 15 27	20.48	19.18	4.98	4.74	2010 Jan 20	ESI	0.50	2280	17
J0210−0018	02 10 43.2	−00 18 18	20.48	19.20	4.72	4.57[a]	2010 Jan 20	ESI	0.50	2880	11
J0331−0741	03 31 19.7	−07 41 43	20.56	19.12	4.71	4.19[a]	2010 Jan 20	ESI	0.75	4320	21
J0747+4434	07 47 49.7	+44 34 17	19.62	17.35	4.43	4.02	2009 Mar 22	ESI	0.75	3600	15
J0759+1800	07 59 07.6	+18 00 55	21.06	19.16	4.86	4.66	2010 Jan 20	ESI	0.75	4320	20
J0813+3508	08 13 33.3	+35 08 11	20.81	19.13	4.92	4.30[a]	2010 Apr 21	ESI	0.75	1400	16
J0817+1351	08 17 40.5	+13 51 35	19.86	19.22	4.39	4.26,3.49	2010 Jan 20	ESI	0.75	3600	18
J0825+3544	08 25 40.1	+35 44 14	18.45	18.38	3.85	3.66	2008 Mar 05	ESI	0.75	2700	40
							2008 Mar 25	HIRESr	0.86	10800	20
J0825+5127	08 25 35.2	+51 27 06	18.18	17.93	3.51	3.21,3.32	2008 Mar 05	ESI	0.75	2700	28

Note. — Table 4.1 is shown in full in the appendix (Table C.6). A portion is shown here for guidance regarding its form and content. Units of right ascension are in hours, minutes, and seconds, and units of declination are in degrees, arcminutes, and arcseconds

[a]Marked as a DLA in SDSS, but is not a DLA based on higher resolution ESI data

All ESI observations prior to 2010, and all HIRES observations were observed at the same slit position to facilitate the removal of cosmic rays between exposures. In order to decrease the effects of fringing in ESI observations ($\sim 15\%$ at 9000Å; Sheinis et al., 2002) at the longest wavelengths ($\lambda > 8,000$), we used a three point dither pattern along the slit for all ESI observations starting in 2010. Throughout the ESI observations, we primarily used the 0.″75 slit, except in two cases when we used the 0.″5 slit, which correspond to a resolution of FWHM of ~ 33 and ~ 44 km s^{-1} respectively ($R \approx 10,000$). For the HIRES observations, we used the CI decker, with a 0.″86 slit corresponding to a resolution of FWHM of 6.3 km s^{-1} ($R \approx 50,000$). ESI has a fixed format echellette that covers the spectral region λ = 4,000 to 11,000Å, while the HIRES echellette coverage varies with each setup. The HIRES observations are all followup observations of the ESI observations, and we therefore targeted the appropriate metal lines for metallicity determination with the HIRES setups.

The primary high redshift ESI survey was designed to systematically measure metallicities of DLAs with $z > 4$ in order to determine the metallicity evolution of DLAs out to $z \sim 5$. Figure 4.1 shows the 25 quasar spectra containing 30 confirmed DLAs with $z > 4$ (see §4.3.1 regarding confirmation of DLAs), in order of increasing value of the largest redshift DLA for each spectrum. We note that while these spectra also contain other lower redshift DLAs, we only show those with $z > 4$. In addition to the quasars containing $z > 4$ DLAs, we also include ESI observations and HIRES followup from 2008 which were obtained in a similar unbiased fashion.

Specifically, the ESI quasar observations with candidate $z > 4$ DLAs obtained in 2009 and 2010 were selected based on their brightness, redshift, and meeting the threshold criteria for being a DLA, i.e. N(HI)$\geq 2 \times 10^{20}$cm^{-2}. The ESI quasar observations obtained in 2008 were similarly selected for their brightness and DLA threshold, and were also selected such that the CII* ($\lambda = 1335.7$Å) line is redward of the Ly-α forest. Therefore, all the DLA candidates observed in this study are unbiased with regard to their $N_{\rm HI}$ column density and metallicity.

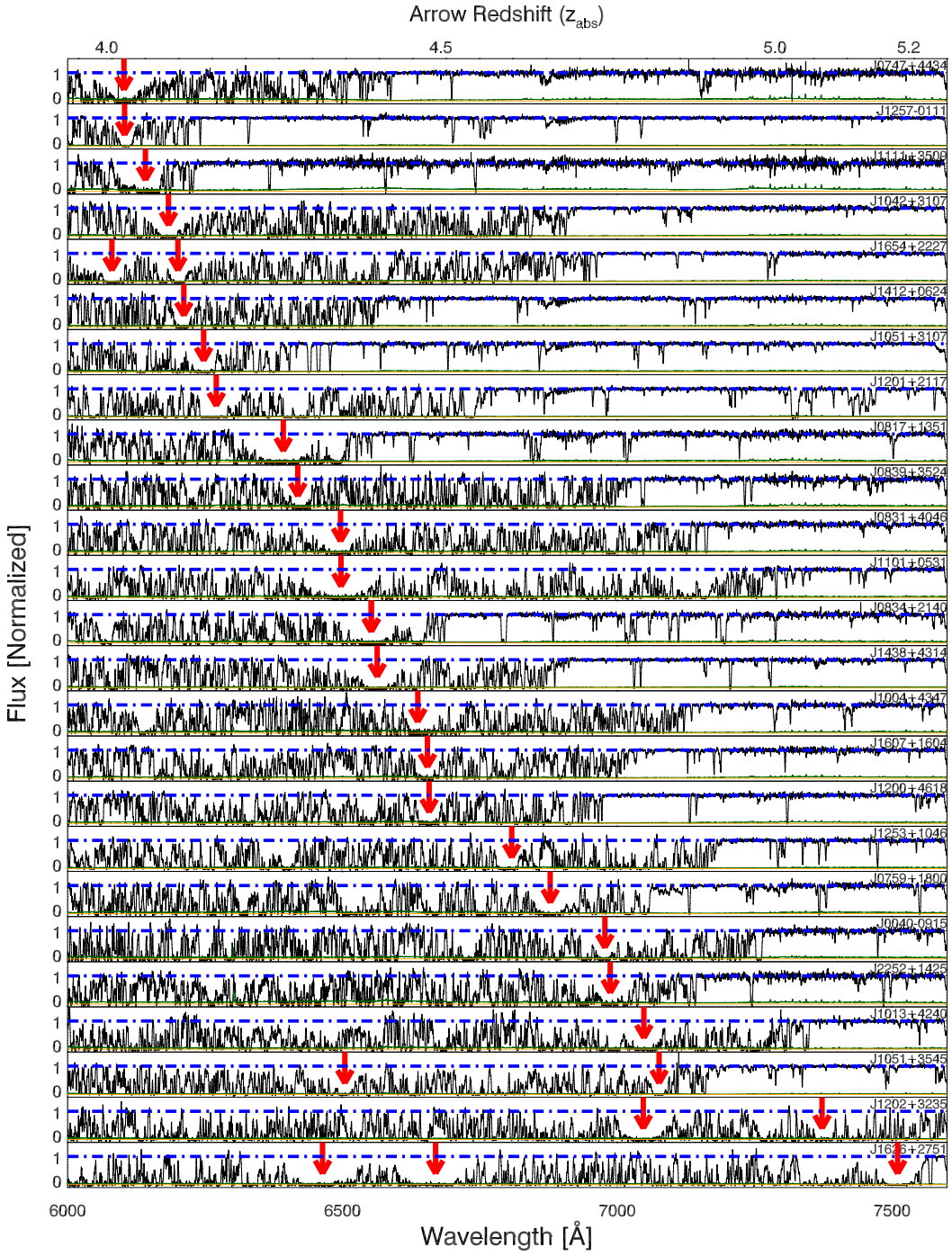

Figure 4.1 ESI spectra of 25 quasars with 30 DLAs at $z > 4$. Fluxes (black curves) and 1-σ error arrays (green curves) are normalized to unit continuum (blue curve). $z > 4$ Damped Lyα lines, denoted by red arrows, are listed in order of increasing value of the largest redshift DLA for each spectrum

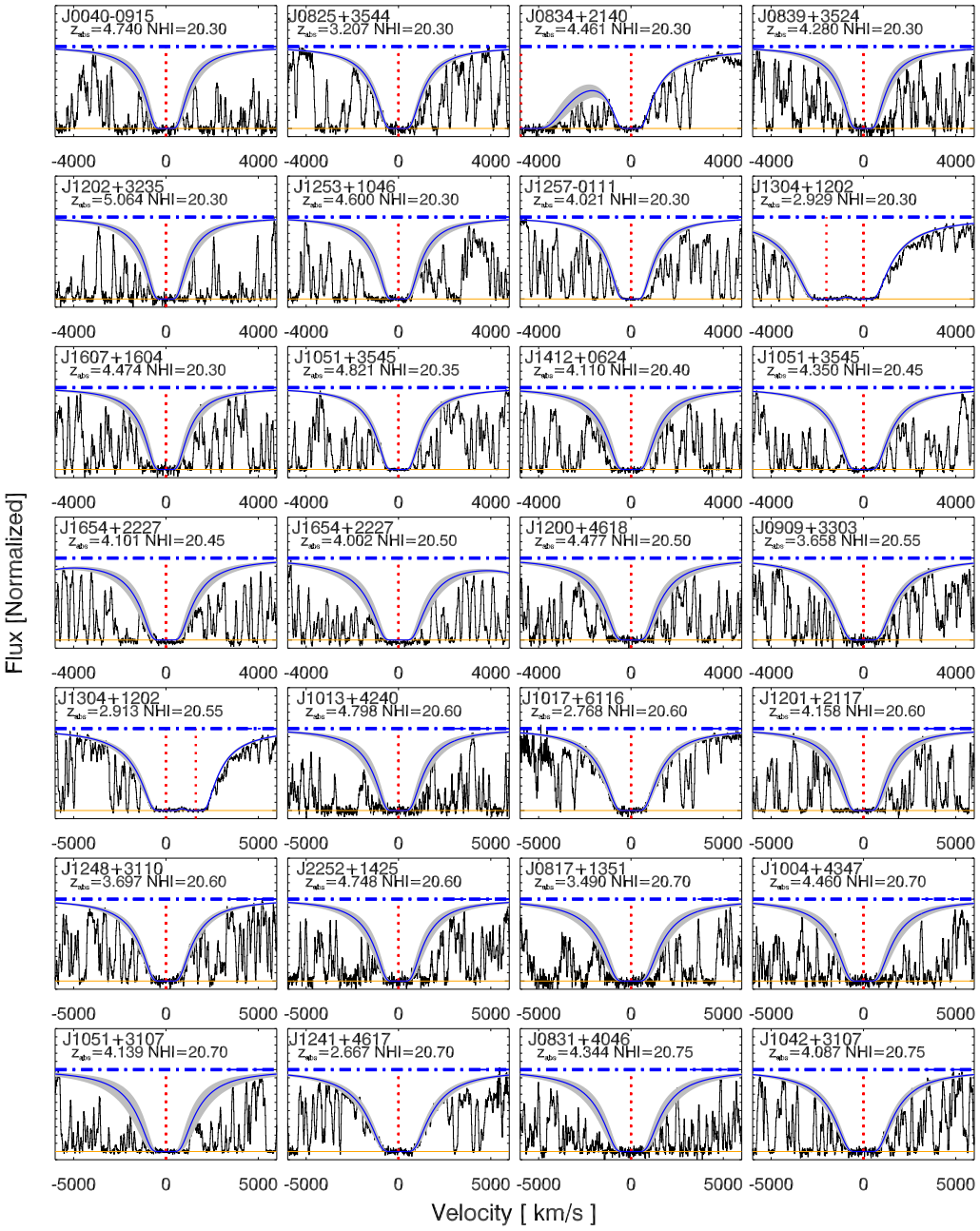

Figure 4.2 Voigt profile fits to 51 confirmed DLAs. Blue curves are best-fit profiles and gray shade includes 95% confidence limits surrounding best fits. Individual panels include quasar name, DLA redshift and H I column density. The red dotted line marks the velocity centroid of the DLA determined from the metal limes. The blue dot-dashed line represents the normalized continuum, and the orange line shows the zero line. The DLAs are ordered by $N_{\rm HI}$, with the x-range based on the $N_{\rm HI}$.

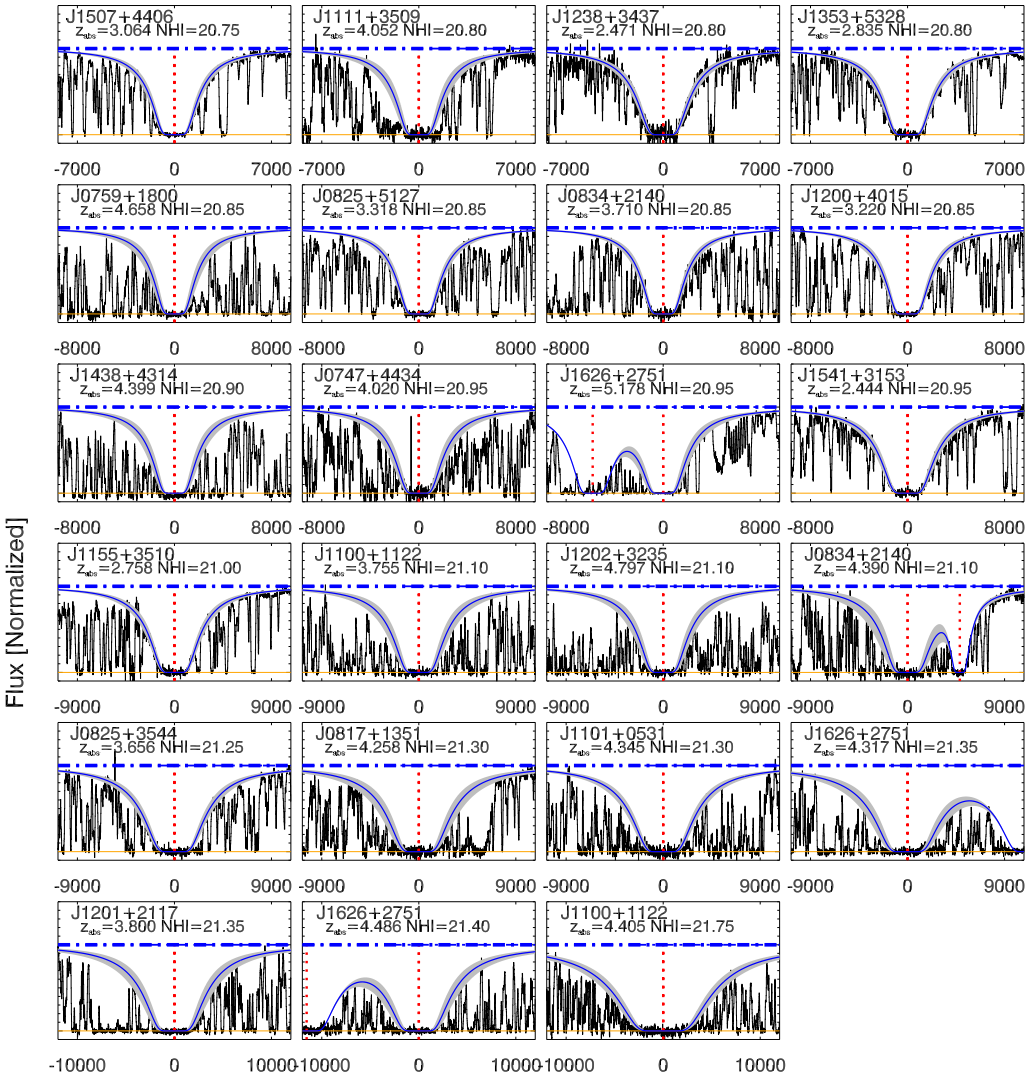

Figure 4.3 Continuation of Figure 4.2.

All the data were reduced with the XIDL[2] package developed in IDL by J. X. Prochaska. Specifically, the ESI observations were reduced with ESIRedux[3] (Prochaska et al., 2003b) and the HIRES observations were reduced with HIRedux[4], both of which are publicly available. All the data were extracted with optimal extraction, and the data were continuum fit using the x_continuum routine within XIDL.

4.3 Analysis and Results

In this section we present the analysis of the quasar spectra obtained in this survey. We first confirm the DLA candidates using Voigt profile fitting and determine their $N_{\rm HI}$ values. We then describe the derivation of elemental abundances, and determine $\langle {\rm Z} \rangle$ as function of redshift. Lastly, we compare the metallicity distribution of DLAs to that of known stellar populations in the Milk Way, focusing on the halo stars.

4.3.1 Voigt Profile Fitting

We determine the $N_{\rm HI}$ values of the damped Ly-α systems in our sample using the same methodology as Prochaska et al. (2003b). Specifically, we fit the Ly-α line with a Voigt profile in the fluxed, but not continuum fit, spectra using the routine x_fitdla, part of the IDL package. We tie the centroid of the Voigt profile to the redshift of the metal-line transitions, which yields a velocity centroid to within $\sim$ 30 km s^{-1} of the true line center. We simultaneously fit the Voigt profile and the continuum to obtain a fit that matches both the core and wings of the profile. While this fitting procedure is not completely quantitative, it is the standard methodology used by our group. In our experience, a standard χ^2 analysis yields unrealistically small error estimates (Prochaska et al., 2003b). We place very conservative error estimates on the $N_{\rm HI}$ values, and the reader should consider them to be roughly at the 95% confidence level.

[2]See http://www.ucolick.org/~xavier/IDL/
[3]See http://www2.keck.hawaii.edu/inst/esi/ESIRedux/
[4]See http://www.ucolick.org/~xavier/HIRedux/

The sample of candidate DLAs all have $N_{\rm HI}\geq 2\times10^{20}{\rm cm}^{-2}$ based on the SDSS spectra with spectral resolution FWHM ~ 2Å. At low redshift, this is sufficiently high resolution to obtain relatively accurate $N_{\rm HI}$, and therefore yields only a small number of false candidates. However, as we move to higher redshift, the Ly-α forest becomes significantly more dense, and the damped Ly-α profiles in the SDSS spectra are significantly affected by line-blending with random Ly-α forest clouds. Since the ESI spectra resolve out the Ly-α forest, we can therefore obtain more robust values of $\rm N_{HI}$. In order to confirm a candidate DLA from SDSS to be a true DLA, we require $N_{\rm HI}\geq 2\times10^{20}{\rm cm}^{-2}$ in the ESI spectrum. We fitted $N_{\rm HI}$ Voigt profiles to 70 candidate DLAs from SDSS, and confirm 51 as bona-fide DLAs. Figures 4.2 and 4.3 show the Voigt profile fits of 51 newly confirmed DLAs ordered by increasing $\rm N_{HI}$. Some panels have more than one DLA candidate marked, and in those cases the central DLA is the confirmed DLA. The velocity interval of the individual panels varies with column density such that they show the wings of the damped profile.

The false candidates consisted of multiple lower column density lines that are blended together in the lower resolution SDSS data. Of the 70 candidate DLAs in Table 4.1, 47 of them have $z > 4$. Of those 47 candidate $z > 4$ DLAs, 15 are false positives, leaving a total of 32 confirmed DLAs with $z > 4$. As a result, we find that $\sim$30% of $z > 4$ DLAs are misidentified in SDSS due to line-blending. In contrast, for our sample of 23 $z < 4$ DLAs, we found 4 false candidates, and none of them are from our 14 $z \sim 3$ candidate DLAs from our 2008 run. In our survey for DLAs, we reject proximate DLA systems that are found to be within 3000 km $\rm s^{-1}$ of the quasar emission redshift, as these DLAs may be physically associated or otherwise affected by the quasar (see Prochaska et al., 2008; Ellison et al., 2010, 2011). This removes our highest redshift confirmed DLA ($z = 5.18$, J1626+275), and it is not included in our metallicity measurements determined below.

4.3.2 Element Abundances

In this subsection we describe the derivation of ionic column densities for all of the new confirmed DLAs using the apparent optical depth method (AODM;

Savage & Sembach, 1991). This method can uncover hidden saturated lines by comparing the apparent column density, N_a, for multiple transitions of a single ion. We then calculate N_a for each pixel from the optical depth equation, and sum over the velocity profile of each transition to obtain the total column density, N. If multiple lines for a single ion are available, then we take the weighted mean of the column densities. The AODM technique yields accurate column densities that agree well with line fitting, and it is easier to apply to a large data sets such as this one (Prochaska et al., 2001). For consistency with past results (e.g. Prochaska et al., 2003a), we use the wavelengths and oscillator strengths shown in Table 2 of Prochaska et al. (2003b) and the elemental abundances shown in Table 3 of Prochaska et al. (2003b).

Whenever possible, we use α-elements to determine the metallicity, [M/H], in decreasing priority: Si, S, O, Zn. In this survey, the O transitions are often in the Ly-α forest and saturated, the Zn transitions are unavailable due to the high redshift, and therefore we are left with the Si and S transitions for metallicity measurements. Si is the most common α-element used, as multiple transitions fall outside of the forest with varying oscillator strengths. Si is a mildly refractory element which is only very mildly depleted, and therefore the observed Si column density reflects the actual total Si column density (Prochaska & Wolfe, 2002). S is a non-refractory element, and provides robust undepleted metallicities, although is often in the Ly-α forest or too weak to be measured. In a small number of cases (11), these elements are not available, in which case we determine a [M/H] value by taking the [Fe/H] value and assuming an offset of 0.4 dex, which match the median and mean of [α/Fe] for DLAs (Prochaska & Wolfe, 2002). In addition, we also calculate the metallicity of a depleted element to get a handle on the dust-to-gas ratio, and therefore determine a [Fe/H] value for each DLA. In cases where Fe is not available, we use Ni with a 0.1 dex correction, or Al. Figure 4.4 shows example ESI velocity profiles for some of the metal-line transitions used in this study.

In Table 4.2 we present new metallicity measurements for 49 DLAs, with 30 of them at $z > 4$ (two DLAs don't have measurable metallicities and are not

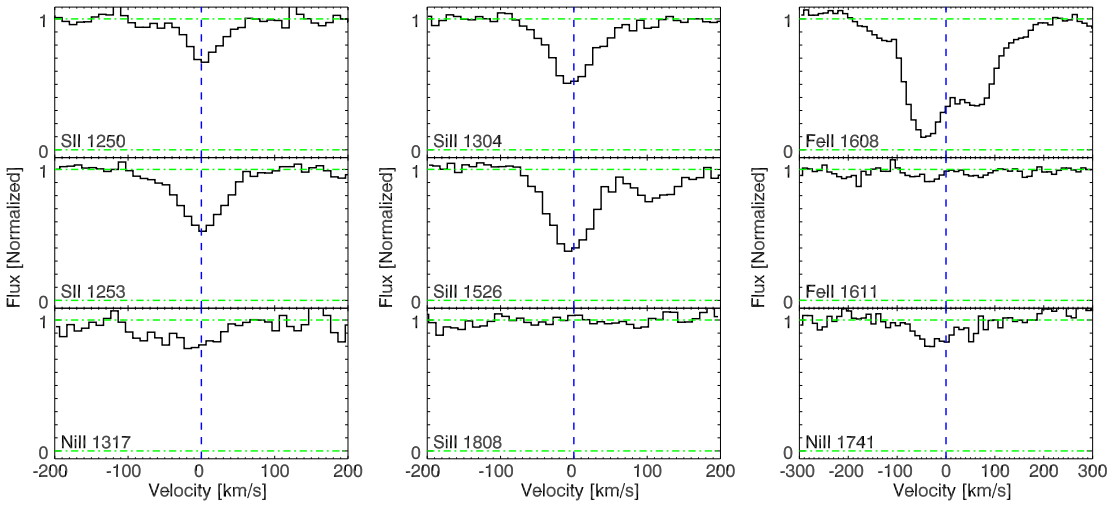

(a) J0817+1351 (b) J1051+3107 (c) J1626+2751

Figure 4.4 Example velocity profiles of metal-line transitions showcasing some of the transitions used to obtain metallicities in this study. We primarily use SiII and SII transitions as described in the text. These velocity profiles are from ESI spectra of a) J0817+1351 at $z_{\rm abs} = 4.2583$, b) J1051+3107 at $z_{\rm abs} = 4.1391$, and c) J1626+2751 at $z_{\rm abs} = 4.3111$. Some of the transitions are saturated (i.e. FeII 1608), while others are upper limits (i.e. SiII 1808). These are just example lines from these DLAs, and each DLA has more usable metal lines than shown. The blue dashed line marks the center of the velocity profile, and the green dot-dashed lines indicate the range of flux between 0 and 1.

Table 4.2. New DLA metallicities

QSO (1)	z_{abs} (2)	log$N_{\rm HI}$ (3)	f_α[a] (4)	[α/H] (5)	$f_{\rm Fe}$[b] (6)	[Fe/H] (7)	$f_{\rm mtl}$[c] (8)	[M/H] (9)
J0040−0915	4.7395	20.30±0.15	1	-1.74±0.03	6	-2.04±0.09	1	-1.74±0.15
J0747+4434	4.0197	20.95±0.15	3	-1.38±0.00	1	-2.72±0.14	2	-2.32±0.25
J0759+1800	4.6577	20.85±0.15	4	-1.60±0.04	1	-2.03±0.03	1	-1.60±0.16
J0817+1351	3.4901	20.70±0.15	1	-1.14±0.10	3	-0.98±0.00	1	-1.14±0.18
J0817+1351	4.2583	21.30±0.15	4	-1.36±0.05	4	-1.52±0.04	1	-1.36±0.16
J0825+3544	3.2073	20.30±0.10	2	-1.83±0.02	1	-1.98±0.03	2	-1.58±0.13
J0825+3544	3.6567	21.25±0.10	1	-1.82±0.10	4	-1.95±0.04	1	-1.82±0.14
J0825+5127	3.3180	20.85±0.10	1	-1.67±0.10	1	-2.07±0.01	1	-1.67±0.14
J0831+4046	4.3440	20.75±0.15	1	-2.36±0.03	1	-2.41±0.07	1	-2.36±0.15
J0834+2140	3.7102	20.85±0.10	1	-1.65±0.14	1	-1.86±0.02	1	-1.65±0.17

Note. — Table 4.2 is shown in full in the appendix (Table C.7). A portion is shown here for guidance regarding its form and content. Note that none of the reported limits take into account the uncertainty in $N_{\rm HI}$.

[a]0 = No measurement; 1= Si measurement; 2 = Si lower limit; 3 = Si upper limit; 4 = [S/H].

[b]0 = No measurement; 1= Fe measurement; 2 = Fe lower limit; 3 = Fe upper limit; 4 = [Ni/H]−0.1 dex; 5 = [Cr/H]−0.2 dex; 6 = [Al/H].

[c]1 = [α/H]; 2=[Fe/H]. In the later case, we use [M/H] = [Fe/H]+0.4 dex.

[d]This is a proximate DLA, and is therefore not included in the analysis of the metallicity evolution.

in the table, and one is a proximate DLA and is included in the table). Column (1) gives the quasar coordinate name obtained from the SDSS survey, column (2) gives the DLA absorption redshifts determined from the metal transition lines, and column (3) gives the logarithm of the measured $N_{\rm HI}$ values. Columns (4) and (5) give the alpha element flag and metallicity, and column (6) and (7) give the Fe flag and metallicity. Column (8) and (9) give the flag and final metallicity used in this paper. The flags in columns (4) and (6) state which transitions are used and if they are detections or limits, as described in the Table notes. Also, the uncertainty in columns (5) and (7) do not include the uncertainty in $N_{\rm HI}$, while the final metallicity in column (9) adds it in quadrature.

The uncertainty in [M/H] is dominated by the uncertainty in $N_{\rm HI}$, and the given values generally over-estimate the statistical error while underestimating the systematic errors from line blending or continuum fitting. The uncertainties for [α/H] and [Fe/H] in Table 4.2 include only the measurement uncertainty of the metal column density, while the [M/H] values add the uncertainty of $N_{\rm HI}$ in

quadrature. We note that we ignore the error in the continuum fit in our error calculations, although it may be important in very weak transitions. We set a minimum error of 0.1 dex for all metallicity measurements, and our main results are not sensitive to the uncertainties in individual measurements (see bootstrap method below).

In Figure 4.5, we plot the 48 metallicities obtained in this paper as a function of redshift (not including the proximate DLA). The figure outlines which elements are used to obtain [M/H] and the uncertainties of those measurements. The symbols and colors indicate the origin of the [M/H] measurements, with green squares representing Si II, blue triangles representing S II, and red plus signs representing Fe II. The metallicity measurements are directly from Table 4.2, and therefore the the Fe II values use [M/H] = [Fe/H]+0.4 dex.

4.3.3 Evolution of Cosmic Metallicity

The evolution of the chemical elemental abundances of DLAs provide constraints for theories of galaxy formation, and we therefore investigate the metallicity evolution out to $z \approx 5$. In Figure 4.6, we plot the metallicity as a function of redshift for both our measurements and those from the literature with a total of 179 abundances. Specifically, we plot the metallicities from Prochaska et al. (2003a) as red plus signs, which include numerous DLAs from studies with high resolution ($R > 5000$) and high S/N (15 pixel^{-1}) obtained at large telescopes. We overplot our new [M/H] measurements as stars, with ESI measurements as green stars and HIRES measurements as gold stars. Of these new [M/H] measurements, 29 are at $z > 4$.

There are three interesting features in this plot: 1) there exists a large dispersion in [M/H] at all redshifts, 2) there exists a metallicity "floor" at [M/H]≈ -3, and 3) the average [M/H] decreases with increasing redshift. The large dispersion in Figure 4.6 is not an observational error, but is due to intrinsic scatter amongst the DLAs. The dispersion in [M/H] is ~ 0.5 dex, and does not evolve with redshift. The metallicity "floor" occurs at [M/H]≈ -3, with no DLAs existing at [M/H] < -2.8 despite the sensitivity of our spectra for finding DLAs with [M/H] ≥ -4.5.

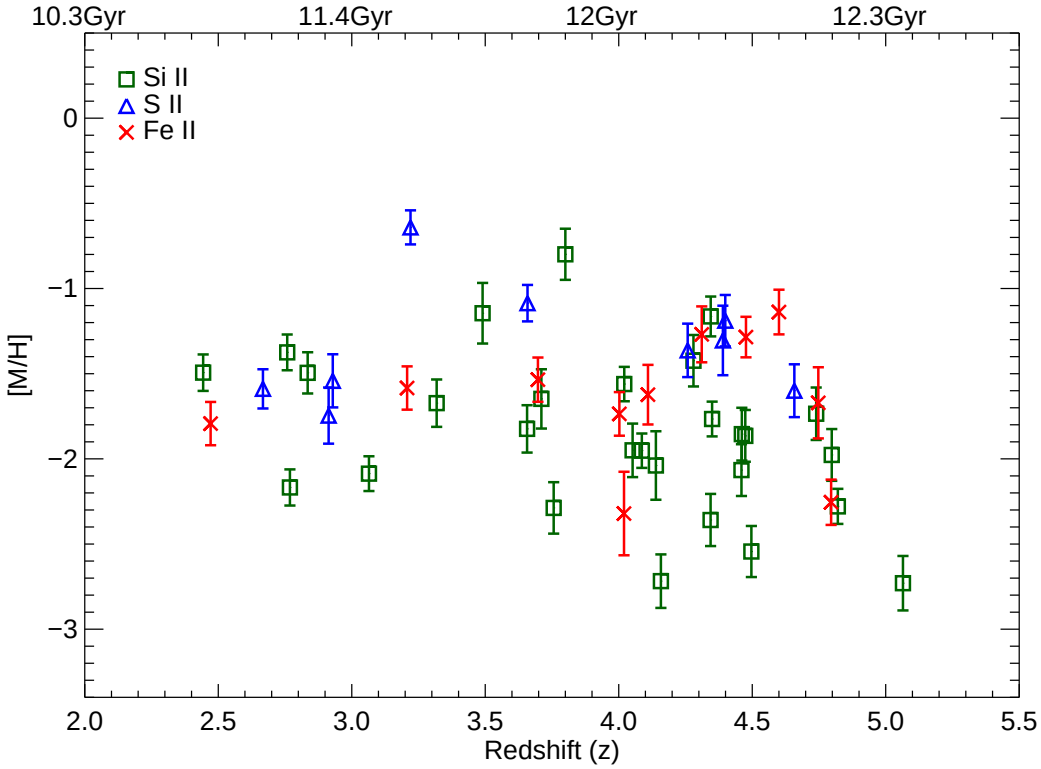

Figure 4.5 DLA metal abundance, [M/H], versus redshift for the DLAs in Table 4.2 (not including the proximate DLA). The symbols and colors indicate the origin of the [M/H] values: Si II measurements (green squares) S II measurements (blue triangles), and Fe II measurements (red crosses). We note that the Fe II [M/H] values are [Fe/H]+0.4 dex.

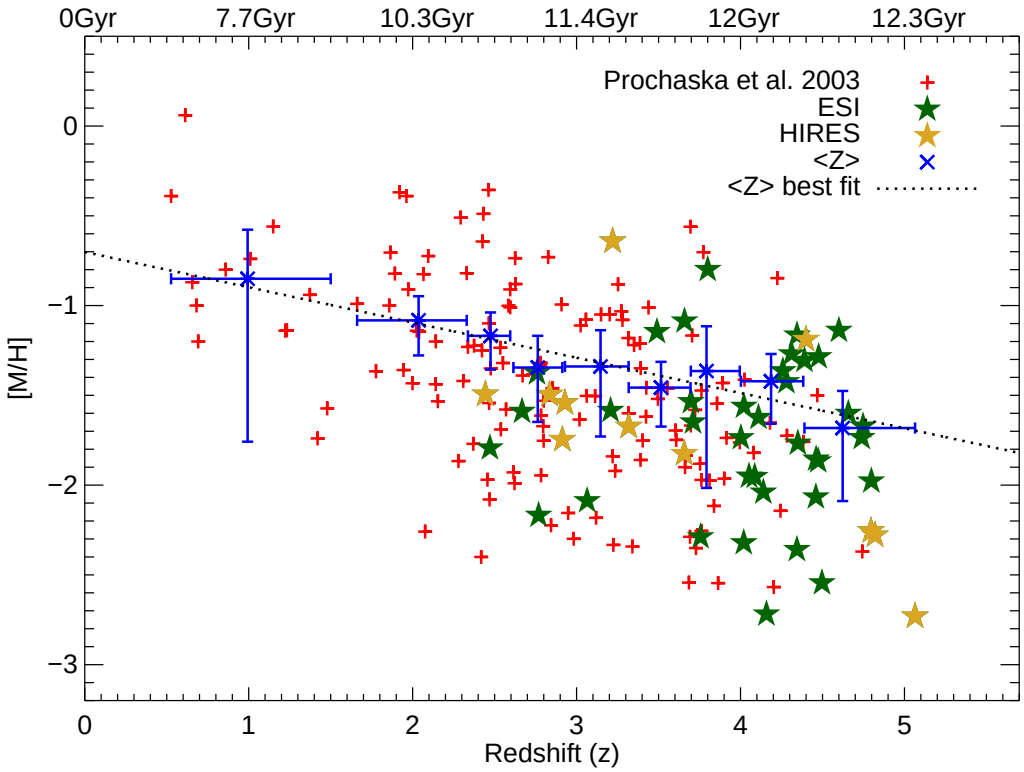

Figure 4.6 DLA metal abundance, [M/H], versus redshift. Red plus signs from (Prochaska et al., 2003a). The metallicities from ESI are green stars and those from HIRES are gold stars. The 9 blue crosses with error bars show cosmic metallicity, $\langle Z \rangle$, where horizontal error bars are determined such that there are equal numbers of data points per redshift bin. The vertical error bars represent 95% confidence levels given from our bootstrap analysis. Black straight line is linear fit to the $\langle Z \rangle$ data points.

The implications of these will be discussed in §4.4.

The evolution of [M/H] is investigated by computing the cosmological mean metallicity, $\langle \mathrm{Z} \rangle$, where

$$\langle \mathrm{Z} \rangle = \log \left(\sum_i 10^{[M/H]_i} N(\mathrm{HI})_i / \sum_i N(\mathrm{HI})_i \right), \tag{4.1}$$

and i represents each bin of DLAs as a function of redshift (Prochaska et al., 2003a). We bin the data such that each bin has an equal number of DLAs per bin (22 DLAs/bin), except for the lowest and highest redshift bins which contain 13 and 17 DLAs respectively. $\langle \mathrm{Z} \rangle$ is plotted as blue crosses in Figure 4.6, and the error bars represent 95% confidence limits based on a bootstrap error analysis described below.

The $\langle \mathrm{Z} \rangle$ statistic is dominated by the systems with the largest N_{HI} and [M/H] values, and therefore the measurement uncertainty is dominated by sample variance rather than statistical error. Therefore, we calculate the uncertainties on $\langle \mathrm{Z} \rangle$ by using a bootstrap method, where we replace a random fraction ($1/e \approx 37\%$) of the DLAs in each bin with other DLAs from that bin. We repeat this 1000 times, and then take the standard deviation of all the column density weighted metallicity measurements. This method is conservative, and includes all the uncertainties associated with the variance of the sample, if the distribution of the bootstrap values are Gaussian. The only bin which is not Gaussian is the lowest redshift bin, where the distribution is bimodal due to a single high N_{HI} value in that bin. We note that we have sufficient high N_{HI} DLAs in our sample such that the results are insensitive to the addition of any single DLA for all but the lowest redshift bin (see Prochaska et al., 2003a).

The black dotted line in Figure 4.6 is a linear least-squares fit to the $\langle \mathrm{Z} \rangle$ values and their bootstrap uncertainties, and we find that $\langle \mathrm{Z} \rangle = (-0.21 \pm 0.04)z - (0.69 \pm 0.13)$. This yields a 5σ detection in the evolution of $\langle \mathrm{Z} \rangle$, which is a significant improvement over the previous 3σ detection by Prochaska et al. (2003a). We note that the fit values are completely consistent with the previous measurements by Prochaska et al. (2003a), confirming that the mean metallicity of the universe in neutral gas is doubling about every billion years at $z \sim 3$.

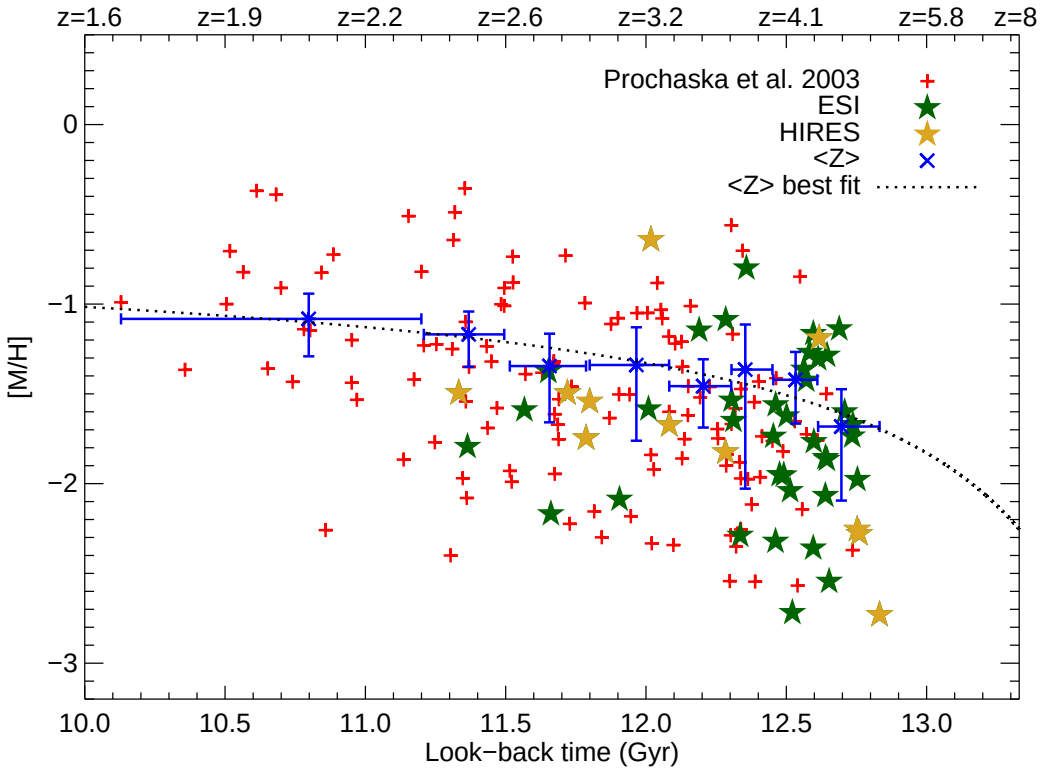

Figure 4.7 DLA metal abundance [M/H] versus time. Red plus signs from (Prochaska et al., 2003a). The metallicities from ESI are green stars and those from HIRES are gold stars. The 9 blue data points with error bars show cosmic metallicity, $\langle Z \rangle$, where horizontal error bars are determined such that there are equal numbers of data points per redshift bin. Black straight line is linear fit to $\langle Z \rangle$ data points as a function of redshift. We note that we show only the values at $z > 1.6$ to focus on the area of interest at higher redshift.

While the evolution of $\langle Z \rangle$ is linear in redshift, it is non-linear in time, with the slope, $d\langle Z \rangle/dt$, becoming significantly steeper at earlier cosmic times, t. In Figure 4.7, we plot the metallicity as a function of time rather than redshift. We truncate the plot at $z = 1.6$ in order to focus on the higher redshift part of the plot which contains the most rapidly changing metal abundances. The black dotted line is the linear fit to $\langle Z \rangle$ as a function of redshift, and clearly shows the steepening of $\langle Z \rangle$ going back in time. This shows the importance of obtaining metallicities of the highest redshift DLA systems, as undertaken in this study. Future observations should focus on obtaining metallicities at $z > 4.7$ to further constrain the metallicity evolution of DLAs.

4.3.4 Comparison of DLA Metallicities with those of Halo Stars

DLAs are widely believed to be the progenitors of today's disk galaxies and act as neutral gas reservoirs for star formation at high redshifts (Nagamine et al., 2004b,a; Wolfe & Chen, 2006; Wolfe et al., 2008; Rafelski et al., 2010). Stars forming *in situ* out of the low metallicity DLA gas would result in low metallicity stars, which should be observable in the Milky Way today. However, previous studies found that the metallicity distribution of DLAs disagree with known stellar populations in the Galaxy (Pettini, 2004, 2006). Here we investigate weather the increase in sample size and redshift yields a metallicity a better agreement with these populations. We compare the thin disk stars, thick disk stars, and halo stars, although we mainly focus on the halo stars as the metallicities of the other two are systematically too high (as we will show below).

Halo stars generally have low metallicities and are often selected based on their metallicities (e.g. Beers & Sommer-Larsen, 1995), however, there is an overlap in the metallicity of different stellar components in the galaxy (Unavane et al., 1996; Chiba & Beers, 2000). Therefore, Venn et al. (2004) select stars based purely on their kinematics, compile a large dataset from a number of publications, and provide probabilities of each star consisting of a thin disk, thick disk, or halo star, based on their kinematics. Here, we select stars from the Venn et al. (2004) sample with an 80% or better probability of being identified as each type of star and having both α and Fe element abundances measured. This results in a sample of 201 thin disk stars, 109 thick disk stars, and 207 halo stars (Venn et al., 2004; Edvardsson et al., 1993; Hanson et al., 1998; Fulbright, 2000, 2002; Reddy et al., 2003).

In Figure 4.8, we plot histograms comparing the abundances of 161 DLAs at redshifts $z > 2$ (red), with a) thin disk stars, b) thick disk stars, and c) halo stars (blue). For the DLAs, we use the same metal abundances as used in Table 4.2 and Figure 4.6. For the stars, we use the α-element abundances tabulated in Venn et al. (2004). The histograms are normalized to have equal area and a maximum value of 1.0. We compare the stars to DLAs with $z > 2$, as the majority of the

halo stars are believed to have formed by then (Freeman & Bland-Hawthorn, 2002; Bullock & Johnston, 2005; Robertson et al., 2005; Johnston et al., 2008). This cut includes the vast majority of our sample, and therefore has a negligible effect on the comparisons. A visual comparison of histograms immediately rules out the possibility of any agreement of the metallicity distributions of the thin disk or thick disk stars with DLAs. However, the halo star metallicity distributions look similar, and the median [M/H] of the two distributions are -1.58 and -1.53 for the DLAs and halo stars respectively.

We apply the Kolmogorov-Smirnov (K-S) test to find the probability of each of the distributions being drawn from the same parent population as the DLA metallicities. Similar to the visual comparison, the thin disk and thick disk stars are ruled out with a probability of $\sim 10^{-39}\%$, i.e., the null hypothesis can be rejected at a high confidence level. However, the halo stars have a probability of 3%, i.e., the null hypothesis cannot be rejected with more than 2σ confidence. The K-S test is only powerful at rejecting hypotheses, not proving them, and it cannot confidently rule out halo stars, i.e. they are not inconsistent. This comparison hints at an overlap between the metallicity distributions of high redshift DLAs and halo stars in the Milky Way.

Another possible comparison of DLAs and halo stars can be made by studying the chemistry of the two populations. Specifically we can compare the ratio of α-elements to Fe abundances to determine whether gas is α-enhanced. α-elements are produced in high mass stars and then are ejected by type II supernovae, while Fe is produced in both type II and type Ia supernovae. Therefore, if stars are formed shortly after the type II supernovae go off, but before the type Ia supernovae do, they will have enhanced [α/Fe] ratios. We note that Type II supernovae need $\sim 10^7$ years to go off, while Type Ia supernovae need more than 10^9 years (Fulbright, 2000). In Figure 4.9, we plot histograms of the [α/Fe] ratios for the 207 halo stars (blue) and a) 115 $z > 2$ DLAs that have abundances for both an Fe and an α-element, and b) a subset 100 of those 115 DLAs that also have [M/H] < -1. We note that it is possible that the Fe abundances are depleted onto dust grains, especially for the higher metallicity systems. However, at lower metallicities, the

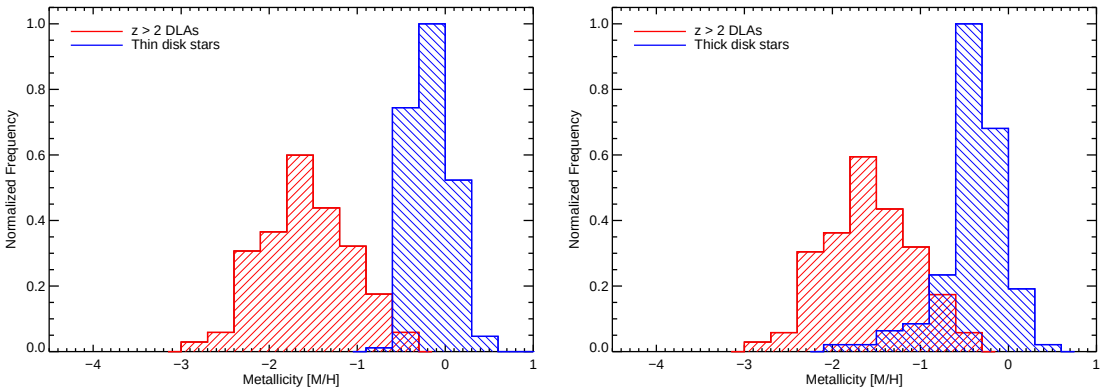

(a) Thin disk stars

(b) Thick disk stars

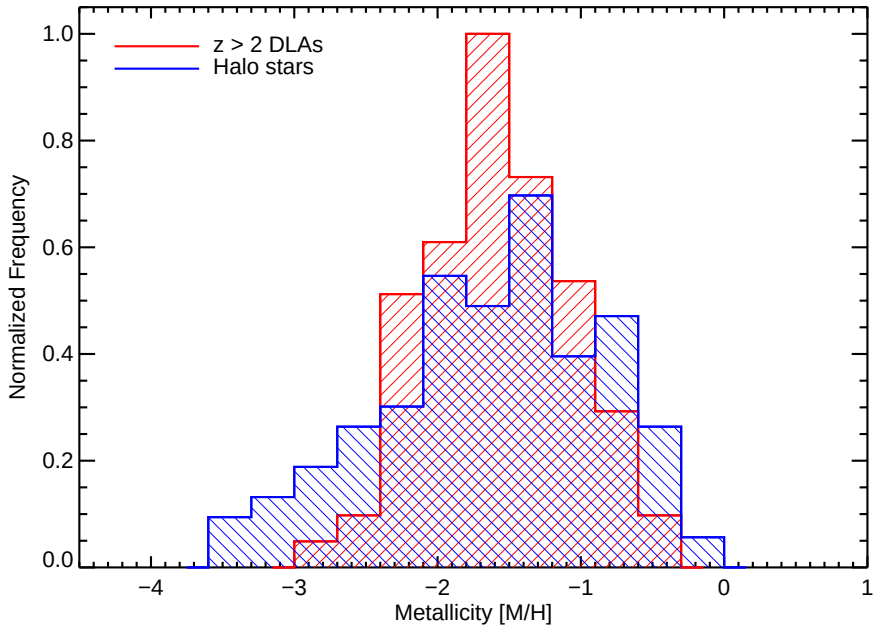

(c) Halo stars

Figure 4.8 Histograms comparing abundances of 161 DLAs at $z > 2$ with a) 201 thin disk stars, b) 109 thick disk stars, and c) 207 halo stars (Venn et al., 2004). The histograms are normalized to have equal area and a maximum value of 1.0 The red left shaded region represent the DLAs and the blue right shaded region represent the thin disk, thick disk, and halo stars. The only population of stars in the Milk Way that is not inconsistent with the DLA metallicity distribution are the halo stars.

[α/Fe] ratio of DLAs is relatively constant (Prochaska & Wolfe, 2002; Wolfe et al., 2005). If there was dust depletion in the sample, it would move the red histogram to the left in Figure 4.9a. The sample in Figure 4.9b reduces such depletion issues, as the lower metallicity DLAs will have Fe less or not at all depleted.

We apply the K-S test to the [α/Fe] ratios for DLAs and halo stars, and find the probability that the two distributions are drawn from the same parent population to be 7% for the 115 DLAs in Figure 4.9a, and 50% for the 100 DLAs in Figure 4.9b. We therefore cannot reject the null hypothesis with more than 1σ, and find that the [α/Fe] ratio distribution for the DLA sample and the halo stars is compatible. This indicates that both the halo stars and the DLA gas is α-enhanced by ≈ 0.3 dex, suggesting that the Type Ia supernovae have not yet contaminated the gas.

4.4 Discussion

The principle result of this study is that we find a continued decrease in the metallicity of DLAs with increasing redshift out to $z \approx 5$. We improve the significance of this trend to 5σ and extend it to higher redshifts. These observations of the metallicity evolution tightly constrain the star formation history of $z \sim 5$ galaxies and the processes that transport metals from star-forming regions to the ambient ISM. They do so by multiple observed characteristics in the metallicity evolution plots (Figures 4.6 and 4.7).

In addition to the continued decrease in metallicity, Figures 4.6 and 4.7 reveal two interesting features. The first is the large dispersion of [M/H] at $z > 4$ that matches the results at lower redshift (Prochaska et al., 2003a). This result is not an observational error but is due to intrinsic scatter amongst the DLAs. The scatter does not appear to evolve with redshift, suggesting that it is intrinsic to the DLAs, possibly due to the wide range of masses of the galaxies hosting DLAs, as suggested by the mass-metallicity correlation found both at low redshift (Tremonti et al., 2004) and at high redshift (Erb et al., 2006). The second feature is a metallicity "floor" at [M/H]≈ -3, which is also consistent with the results at

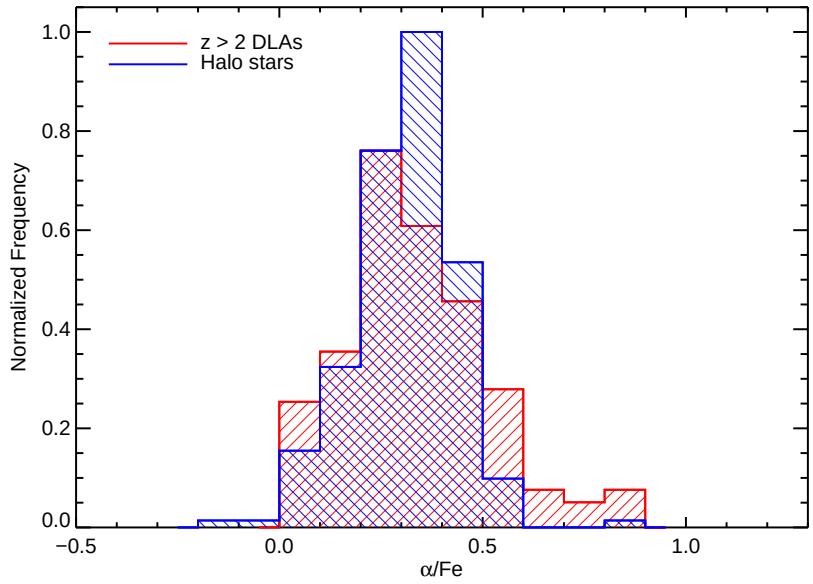

(a) $z > 2$ DLAs

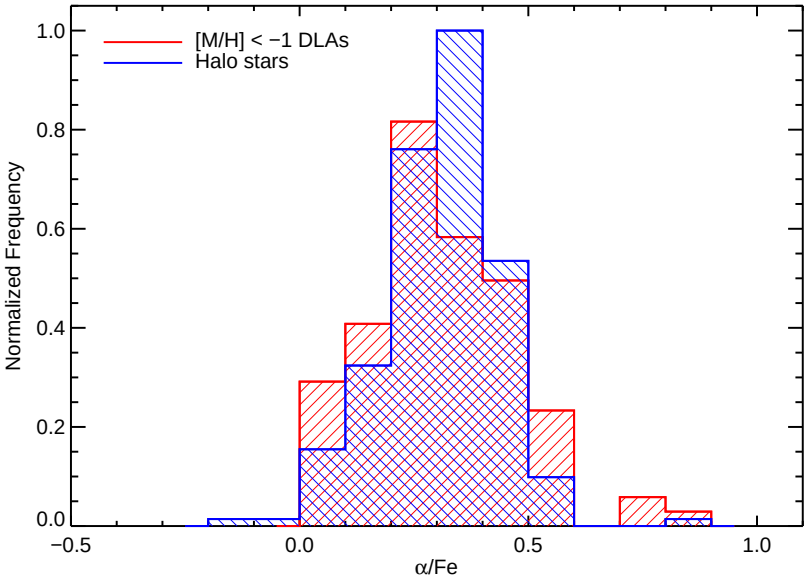

(b) $z > 2$ and [M/H] < -1 DLAs

Figure 4.9 Histogram comparing α/Fe ratios of 207 halo stars with a) 115 DLAs at $z > 2$ and b) 100 DLAs at $z > 2$ with [M/H] < -1. The DLAs are selected such that they have both α and Fe elemental abundances measured. The histograms are normalized to have equal area and a maximum value of 1.0 The red left shaded region represent the DLAs and the blue right shaded region represent the halo stars. The α/Fe ratios of DLAs is consistent with that of halo stars.

lower redshift (Prochaska et al., 2003a). This is likely a physical lower limit of the metallicity of DLAs out to at least $z \approx 5$, which may continue out to even larger redshifts. These metallicities are systematically higher than those of the Ly-α forest clouds which have [M/H]=-3 (Aguirre et al., 2004), and therefore even the lowest metallicity DLA gas is part of a distinctly different population. Moreover, the extension of this lower limit of [M/H] at higher redshift has implications for the primordial gas (gas without metals) in these galaxies. Either the primordial gas does not exist in the neutral phase in high redshift galaxies, or it is surrounded by gas enriched by metals (Prochaska et al., 2003a). Either way, this suggests that all DLA gas has had multiple generations of stars formed by the time it is observable as a DLA.

An intriguing property of the [M/H] values in Figure 4.6 is that the highest redshift DLAs in our sample appear to have metallicities below the linear trend in $\langle$Z$\rangle$. Specifically, the 7 DLAs at $z > 4.7$ all have [M/H] values below the linear fit ($\langle$Z$\rangle = -1.6$ at $z = 4.8$), with a mean $\langle$Z$\rangle = -2.1^{+0.2}_{-0.3}$ (2σ confidence limits from the bootstrap method). Although the sample size is currently small, and this result may just be due to small number statistics, future work should test whether this departure of $\langle$Z$\rangle$ below the linear fit persists at these redshifts.

The metallicity measurements at high redshift also enable us to investigate wether any known populations in our Galaxy have the same metallicity distribution as the high redshift DLAs. Previously, no known population was known to have the same metallicity distribution as DLAs (Pettini, 2004, 2006). This was because the metallicity of thin and thick disks were too metal rich for DLAs, while the halo stars were too metal poor. However, we showed in §4.3.4 that it is possible that the metallicity distribution of DLAs at $z > 2$ is compatible with that of halo stars. Specifically, we cannot rule out, with a high degree of confidence, that DLAs are the progenitors of halo stars. We stress that this is the first time that any known population of stars have been shown to not have inconsistent metallicity distributions with DLAs.

There are two primary differences between our study and previous studies, which compared the DLA metallicity distributions to known stellar populations

(Pettini, 2004, 2006). First, we use α-enhanced elements for abundance measurements (primarily Si), while the other studies use Zn. Second we probe a higher redshift range out to $z \sim 5$, as opposed to $z \sim 3.5$. Both Zn and Si yield reliable abundance measurements, which are consistent with each other. Figure 4.10 plots [Si/Zn] measurements for the 30 DLAs in this sample with both elements detected and not saturated, and it shows that the Zn and Si metallicities are consistent with each other, with a median value of $[\mathrm{Si/Zn}] = -0.02 \pm 0.1$, similar to the results by Prochaska & Wolfe (2002). However, the oscillator strengths of Zn are smaller than Si, making it much more difficult to detect low metallicity DLAs. In addition, the wavelengths of Zn transitions are larger than Si, making Zn measurements at high redshift more difficult to obtain as they are redshifted into the near-infrared. The past comparisons of the metallicity distributions included upper limits of Zn together with detections, skewing the distribution towards metallicities higher than that of the intrinsic population. In addition, by sampling higher redshifts, we include lower metallicity DLAs, since the metallicity of DLAs evolve with time. Together, our sensitivity to lower metallicity systems and our inclusion of higher redshift systems account for the different metallicity distribution presented here.

In addition to the metallicity distribution, the chemistry of the DLAs and halo stars is consistent, based on the comparison of the $[\alpha/\mathrm{Fe}]$ ratios. Both populations have enhanced α-elements ($[\alpha/\mathrm{Fe}] \approx 0.3$), suggesting that stars formed shortly after the ISM was enriched by type II supernovae, but before the type Ia supernovae had a chance to go off (Matteucci, 2003; Venn et al., 2004). Together, these results suggest that the halo stars formed out of gas that has undergone the same number of generations of star formation as DLAs, which occurred before type Ia supernovae contributed significantly. It is therefore possible that the halo stars in the Milky Way formed out of $z > 2$ DLA gas. We note that if the halo stars formed out of DLA gas, then the differences in the kinematics of halo stars and DLAs would necessarily be caused mergers, which randomize and increase the kinetic energy of the orbits of the stars formed in the quiescent DLAs.

The metallicity evolution also has implications for the star formation rate (SFR) efficiency at high redshift. In general, the SFR per unit area is related to

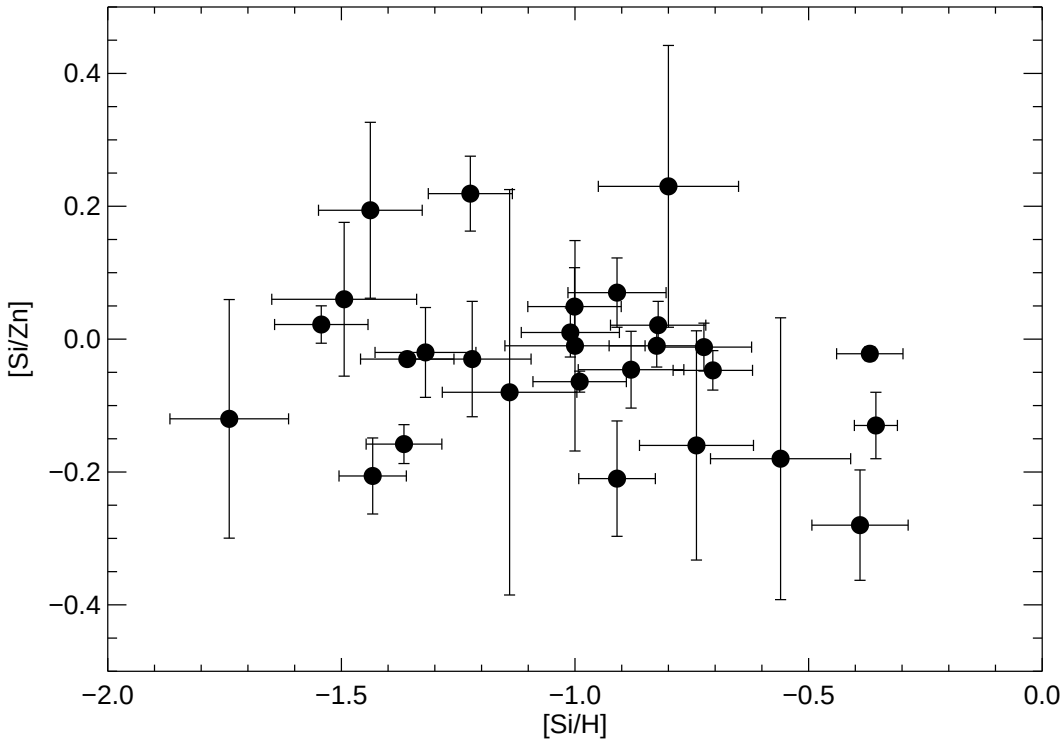

Figure 4.10 Plot of [Si/Zn] as a function of the [Si/H] metallicity. This compares the abundances Si and Zn abundances for the 30 DLAs in our sample that have detected and unsaturated lines for both transitions. The [Si/Zn] values are consistent with 0, with a median [Si/Zn] = −0.03. This suggests that both Si and Zn yield comparable metallicities.

the gas density via the locally established Kennicutt-Schmidt (KS) relation ($\Sigma_{SFR} \propto \Sigma_{gas}^{\beta}$). At $z \sim 3$, the *in situ* SFR of DLA gas was found to be less than 5% of what is expected from the KS relation in isolated regions (Wolfe & Chen, 2006), and $\sim$ 10% of the expected rate in the outskirts of LBGs (Rafelski et al., 2009, 2010). This means that the SFR of DLA gas is less efficient than what would be predicted by the KS relation. Gnedin & Kravtsov (2010) conclude that the main reason for the decreased efficiency of star formation is that the diffuse ISM in high redshift galaxies has a lower metallicity and dust-to-gas ratio, both of which are needed to cool the gas and form stars. In this case, since the metallicities of DLAs decrease with redshift, we expect that the efficiency of star formation should be correlated with redshift. In order to further our understanding of the effect of metallicity on the SFR efficiency, and measure the evolution of the KS relation with redshift, measurements over a range in redshift are required. This study provides the metallicities of the DLA gas over a large redshift range, setting the stage for such studies.

4.5 Summary

The purpose of this study is to measure the metallicities of DLAs with $z > 4$ in order to determine the metallicity evolution of DLAs out to $z \sim 5$. We obtained high resolution spectroscopy of 51 quasars (see Table 4.1, with 39 at $z > 4.1$) using the ESI and HIRES instruments on the Keck Telescopes and find the following:

(1) We fit $N_{\rm HI}$ Voigt profiles to 70 candidate DLAs from SDSS, and confirm 51 of them to have $N_{\rm HI} \geq 2 \times 10^{20} {\rm cm}^{-2}$ (see Figures 4.2 and 4.3). For the 47 $z > 4$ DLA candidates, 15 are false positives leaving 32 confirmed DLAs with $z > 4$ (see Figure 4.1), tripling the sample of $z > 4$ DLAs that have high resolution metallicity measurements to a total of 39. While at lower redshifts the majority of candidate DLAs from SDSS are confirmed, at $z > 4$ the number of false positives is large, with $\sim$30% misidentified due to line-blending with random Ly-α forest clouds.

(2) We measure metal abundances, [M/H], for a total of 48 DLAs (see Table 4.2 and Figure 4.5), with 30 at $z > 4$ (one of which is a proximate DLA). We find that the cosmic metallicity, $\langle Z \rangle$, continues to decrease in metallicity with increasing redshift to $z \approx 5$ (see Figure 4.6). Specifically, we find that $\langle Z \rangle = (-0.21 \pm 0.04)z - (0.69 \pm 0.13)$, which is a 5σ detection in the evolution of $\langle Z \rangle$ and is a significant improvement over the previous 3σ detection by Prochaska et al. (2003a). The fit values are completely consistent with the previous measurements by Prochaska et al. (2003a), confirming that the mean metallicity of the universe in neutral gas is doubling about every billion years at $z \sim 3$.

(3) We find that the large dispersion of [M/H] measured at $z \lesssim 4$(Prochaska et al., 2003a) continues out to $z \sim 5$ (see Figure 4.5). This result is not an observational error, but is due to intrinsic scatter amongst the DLAs. The scatter does not appear to evolve with redshift, suggesting that it is intrinsic to the DLAs, possibly due to the wide range of masses of the galaxies hosting DLAs.

(4) We find that the metallicity "floor" at [M/H]≈ -3 measured at $z \lesssim 4$ (Prochaska et al., 2003a) continues out to $z \sim 5$ (see Figure 4.5). Stated differently, we find no DLAs with [M/H] < -2.8 despite the sensitivity of our spectra for finding DLAs with [M/H] ≥ -4.5. This is likely a physical lower limit of the metallicity of DLAs out to at least $z \approx 5$, which may continue out to even larger redshifts.

(5) We find that the metallicity distribution and the α/Fe ratios of $z > 2$ DLAs are not inconsistent with those for halo stars (see Figures 4.8 and 4.9). This is the first time that any known population of stars have been shown to not have inconsistent metallicity distributions with that of DLAs. It is therefore possible that the halo stars in the Milky Way formed out of DLA gas.

Altogether, we have measured the evolution of the metal abundances of DLAs out to $z \sim 5$, which tightly constrain the star formation history of $z \sim 5$ galaxies and the processes that transport metals from star-forming regions to the

ambient ISM. We note that while the evolution of $\langle Z \rangle$ is linear in redshift, it is non-linear in time, with the slope, $d\langle Z \rangle/dt$, becoming significantly steeper at earlier cosmic times, t (see Figure 4.7). In addition, the 7 highest redshift DLAs at $z > 4.7$ in our sample all have both [M/H] and $\langle Z \rangle$ values below the linear fit. Future observations should therefore focus on obtaining metallicities at $z > 4.7$ to further constrain the metallicity evolution of DLAs, as they will have the largest impact.

4.6 Acknowledgements

The authors thank Max Pettini for alerting us to the work by Venn et al. (2004) on halo-star metal abundances. Support for this work was provided by NSF grant AST 07-09235 and the Chancellor's associates fund at UCSD. The W. M. Keck Observatory is operated as a scientific partnership among the California Institute of Technology, the University of California and the National Aeronautics and Space Administration. The Observatory was made possible by the generous financial support of the W. M. Keck Foundation. The authors wish to recognize and acknowledge the very significant cultural role and reverence that the summit of Mauna Kea has always had within the indigenous Hawaiian community. We are most fortunate to have the opportunity to conduct observations from this mountain.

This chapter is a draft of material that will be submitted as "Metallicity Evolution of Damped Lyman Alpha Systems out to $z \sim 5$" by Marc Rafelski, Arthur M. Wolfe, J. Xavier Prochaska, & Alexander Mendez, to the
The Astrophysical Journal. I am the primary investigator and author of this paper.

References

Abazajian, K. N., Adelman-McCarthy, J. K., Agüeros, M. A., Allam, S. S., Prieto, C. A., An, D., Anderson, K. S. J., Anderson, S. F., Annis, J., Bahcall, N. A., Bailer-Jones, C. A. L., Barentine, J. C., Bassett, B. A., Becker, A. C., Beers, T. C., Bell, E. F., Belokurov, V., Berlind, A. A., Berman, E. F., Bernardi, M., Bickerton, S. J., Bizyaev, D., Blakeslee, J. P., Blanton, M. R., Bochanski, J. J., Boroski, W. N., Brewington, H. J., Brinchmann, J., Brinkmann, J., Brunner, R. J., Budavári, T., Carey, L. N., Carliles, S., Carr, M. A., Castander, F. J., Cinabro, D., Connolly, A. J., Csabai, I., Cunha, C. E., Czarapata, P. C., Davenport, J. R. A., de Haas, E., Dilday, B., Doi, M., Eisenstein, D. J., Evans, M. L., Evans, N. W., Fan, X., Friedman, S. D., Frieman, J. A., Fukugita, M., Gänsicke, B. T., Gates, E., Gillespie, B., Gilmore, G., Gonzalez, B., Gonzalez, C. F., Grebel, E. K., Gunn, J. E., Györy, Z., Hall, P. B., Harding, P., Harris, F. H., Harvanek, M., Hawley, S. L., Hayes, J. J. E., Heckman, T. M., Hendry, J. S., Hennessy, G. S., Hindsley, R. B., Hoblitt, J., Hogan, C. J., Hogg, D. W., Holtzman, J. A., Hyde, J. B., ichi Ichikawa, S., Ichikawa, T., Im, M., Ivezić, Ž., Jester, S., Jiang, L., Johnson, J. A., Jorgensen, A. M., Jurić, M., Kent, S. M., Kessler, R., Kleinman, S. J., Knapp, G. R., Konishi, K., Kron, R. G., Krzesinski, J., Kuropatkin, N., Lampeitl, H., Lebedeva, S., Lee, M. G., Lee, Y. S., Leger, R. F., Lépine, S., Li, N., Lima, M., Lin, H., Long, D. C., Loomis, C. P., Loveday, J., Lupton, R. H., Magnier, E., Malanushenko, O., Malanushenko, V., Mandelbaum, R., Margon, B., Marriner, J. P., Martínez-Delgado, D., Matsubara, T., McGehee, P. M., McKay, T. A., Meiksin, A., Morrison, H. L., Mullally, F., Munn, J. A., Murphy, T., Nash, T., Nebot, A., Neilsen, E. H., Newberg, H. J., Newman, P. R., Nichol, R. C., Nicinski, T., Nieto-Santisteban, M., Nitta, A., Okamura, S., Oravetz, D. J., Ostriker, J. P., Owen, R., Padmanabhan, N., Pan, K., Park, C., Pauls, G., Peoples, J., Percival, W. J., Pier, J. R., Pope, A. C., Pourbaix, D., Price, P. A., Purger, N., Quinn, T., Raddick, M. J., Fiorentin, P. R., Richards, G. T., Richmond, M. W., Riess, A. G., Rix, H.-W., Rockosi, C. M., Sako, M., Schlegel, D. J., Schneider, D. P., Scholz, R.-D., Schreiber, M. R., Schwope, A. D., Seljak, U., Sesar, B., Sheldon, E., Shimasaku, K., Sibley, V. C., Simmons, A. E., Sivarani, T., Smith, J. A., Smith, M. C., Smolčić, V., Snedden, S. A., Stebbins, A., Steinmetz, M., Stoughton, C., Strauss, M. A., Rao, M. S., Suto, Y., Szalay, A. S., Szapudi, I., Szkody, P., Tanaka, M., Tegmark, M., Teodoro, L. F. A.,

Thakar, A. R., Tremonti, C. A., Tucker, D. L., Uomoto, A., Berk, D. E. V., Vandenberg, J., Vidrih, S., Vogeley, M. S., Voges, W., Vogt, N. P., Wadadekar, Y., Watters, S., Weinberg, D. H., West, A. A., White, S. D. M., Wilhite, B. C., Wonders, A. C., Yanny, B., Yocum, D. R., York, D. G., Zehavi, I., Zibetti, S., & Zucker, D. B. 2009, The Astrophysical Journal Supplement Series, 182, 543

Adelman-McCarthy, J. K., Agüeros, M. A., Allam, S. S., Anderson, K. S. J., Anderson, S. F., Annis, J., Bahcall, N. A., Bailer-Jones, C. A. L., Baldry, I. K., Barentine, J. C., Beers, T. C., Belokurov, V., Berlind, A., Bernardi, M., Blanton, M. R., Bochanski, J. J., Boroski, W. N., Bramich, D. M., Brewington, H. J., Brinchmann, J., Brinkmann, J., Brunner, R. J., Budavári, T., Carey, L. N., Carliles, S., Carr, M. A., Castander, F. J., Connolly, A. J., Cool, R. J., Cunha, C. E., Csabai, I., Dalcanton, J. J., Doi, M., Eisenstein, D. J., Evans, M. L., Evans, N. W., Fan, X., Finkbeiner, D. P., Friedman, S. D., Frieman, J. A., Fukugita, M., Gillespie, B., Gilmore, G., Glazebrook, K., Gray, J., Grebel, E. K., Gunn, J. E., de Haas, E., Hall, P. B., Harvanek, M., Hawley, S. L., Hayes, J., Heckman, T. M., Hendry, J. S., Hennessy, G. S., Hindsley, R. B., Hirata, C. M., Hogan, C. J., Hogg, D. W., Holtzman, J. A., ichi Ichikawa, S., Ichikawa, T., Ivezić, Ž., Jester, S., Johnston, D. E., Jorgensen, A. M., Jurić, M., Kauffmann, G., Kent, S. M., Kleinman, S. J., Knapp, G. R., Kniazev, A. Y., Kron, R. G., Krzesinski, J., Kuropatkin, N., Lamb, D. Q., Lampeitl, H., Lee, B. C., Leger, R. F., Lima, M., Lin, H., Long, D. C., Loveday, J., Lupton, R. H., Mandelbaum, R., Margon, B., Martínez-Delgado, D., Matsubara, T., McGehee, P. M., McKay, T. A., Meiksin, A., Munn, J. A., Nakajima, R., Nash, T., Neilsen, E. H., Newberg, H. J., Nichol, R. C., Nieto-Santisteban, M., Nitta, A., Oyaizu, H., Okamura, S., Ostriker, J. P., Padmanabhan, N., Park, C., Peoples, J., Pier, J. R., Pope, A. C., Pourbaix, D., Quinn, T. R., Raddick, M. J., Fiorentin, P. R., Richards, G. T., Richmond, M. W., Rix, H.-W., Rockosi, C. M., Schlegel, D. J., Schneider, D. P., Scranton, R., Seljak, U., Sheldon, E., Shimasaku, K., Silvestri, N. M., Smith, J. A., Smolčić, V., Snedden, S. A., Stebbins, A., Stoughton, C., Strauss, M. A., SubbaRao, M., Suto, Y., Szalay, A. S., Szapudi, I., Szkody, P., Tegmark, M., Thakar, A. R., Tremonti, C. A., Tucker, D. L., Uomoto, A., Berk, D. E. V., Vandenberg, J., Vidrih, S., Vogeley, M. S., Voges, W., Vogt, N. P., Weinberg, D. H., West, A. A., White, S. D. M., Wilhite, B., Yanny, B., Yocum, D. R., York, D. G., Zehavi, I., Zibetti, S., & Zucker, D. B. 2007, The Astrophysical Journal Supplement Series, 172, 634

Aguirre, A., Schaye, J., Kim, T.-S., Theuns, T., Rauch, M., & Sargent, W. L. W. 2004, The Astrophysical Journal, 602, 38

Beers, T. C. & Sommer-Larsen, J. 1995, The Astrophysical Journal Supplement Series, 96, 175

Bouwens, R. J., Illingworth, G. D., Oesch, P. A., Stiavelli, M., van Dokkum, P.,

Trenti, M., Magee, D., Labbé, I., Franx, M., Carollo, C. M., & Gonzalez, V. 2010, The Astrophysical Journal Letters, 709, L133

Bullock, J. S. & Johnston, K. V. 2005, The Astrophysical Journal, 635, 931

Bunker, A. J., Wilkins, S., Ellis, R. S., Stark, D. P., Lorenzoni, S., Chiu, K., Lacy, M., Jarvis, M. J., & Hickey, S. 2010, Monthly Notices of the Royal Astronomical Society, 409, 855

Chiba, M. & Beers, T. C. 2000, The Astronomical Journal, 119, 2843

Edvardsson, B., Andersen, J., Gustafsson, B., Lambert, D. L., Nissen, P. E., & Tomkin, J. 1993, Astronomy and Astrophysics, 275, 101

Ellison, S. L., Prochaska, J. X., Hennawi, J., Lopez, S., Usher, C., Wolfe, A. M., Russell, D. M., & Benn, C. R. 2010, Monthly Notices of the Royal Astronomical Society, 406, 1435

Ellison, S. L., Prochaska, J. X., & Mendel, J. T. 2011, Monthly Notices of the Royal Astronomical Society, 412, 448

Erb, D. K., Shapley, A. E., Pettini, M., Steidel, C. C., Reddy, N. A., & Adelberger, K. L. 2006, The Astrophysical Journal, 644, 813, (c) 2006: The American Astronomical Society

Freeman, K. & Bland-Hawthorn, J. 2002, Annual Review of Astronomy and Astrophysics, 40, 487

Fulbright, J. P. 2000, The Astronomical Journal, 120, 1841

—. 2002, The Astronomical Journal, 123, 404

Gnedin, N. Y. & Kravtsov, A. V. 2010, The Astrophysical Journal, 714, 287

Hamann, F. & Ferland, G. 1999, Annual Review of Astronomy and Astrophysics, 37, 487

Hanson, R. B., Sneden, C., Kraft, R. P., & Fulbright, J. 1998, The Astronomical Journal, 116, 1286

Johnston, K. V., Bullock, J. S., Sharma, S., Font, A., Robertson, B. E., & Leitner, S. N. 2008, The Astrophysical Journal, 689, 936

Kulkarni, V. P., Fall, S. M., Lauroesch, J. T., York, D. G., Welty, D. E., Khare, P., & Truran, J. W. 2005, The Astrophysical Journal, 618, 68

Kulkarni, V. P., Khare, P., Som, D., Meiring, J., York, D. G., Péroux, C., & Lauroesch, J. T. 2010, New Astronomy, 15, 735

Lanzetta, K. M., Wolfe, A. M., & Turnshek, D. A. 1995, The Astrophysical Journal, 440, 435

Matteucci, F. 2003, Astrophysics and Space Science, 284, 539

Nagamine, K., Springel, V., & Hernquist, L. 2004a, Monthly Notices of the Royal Astronomical Society, 348, 421

—. 2004b, Monthly Notices of the Royal Astronomical Society, 348, 435

Pettini, M. 2004, Cosmochemistry. The melting pot of the elements (Cambridge University Press)

—. 2006, arXiv, astro-ph

Prochaska, J. X., Gawiser, E., Wolfe, A. M., Castro, S., & Djorgovski, S. G. 2003a, The Astrophysical Journal, 595, L9

Prochaska, J. X., Gawiser, E., Wolfe, A. M., Cooke, J., & Gelino, D. 2003b, The Astrophysical Journal Supplement Series, 147, 227

Prochaska, J. X., Hennawi, J. F., & Herbert-Fort, S. 2008, The Astrophysical Journal, 675, 1002

Prochaska, J. X. & Wolfe, A. M. 2002, The Astrophysical Journal, 566, 68

Prochaska, J. X., Wolfe, A. M., Tytler, D., Burles, S., Cooke, J., Gawiser, E., Kirkman, D., O'Meara, J. M., & Storrie-Lombardi, L. 2001, The Astrophysical Journal Supplement Series, 137, 21

Rafelski, M., Wolfe, A. M., & Chen, H.-W. 2010, eprint arXiv, 1011, 6390

Rafelski, M., Wolfe, A. M., Cooke, J., Chen, H.-W., Armandroff, T. E., & Wirth, G. D. 2009, The Astrophysical Journal, 703, 2033

Reddy, B. E., Tomkin, J., Lambert, D. L., & Prieto, C. A. 2003, Monthly Notice of the Royal Astronomical Society, 340, 304

Robertson, B., Bullock, J. S., Font, A. S., Johnston, K. V., & Hernquist, L. 2005, The Astrophysical Journal, 632, 872

Savage, B. D. & Sembach, K. R. 1991, Astrophysical Journal, 379, 245

Sheinis, A. I., Bolte, M., Epps, H. W., Kibrick, R. I., Miller, J. S., Radovan, M. V., Bigelow, B. C., & Sutin, B. M. 2002, The Publications of the Astronomical Society of the Pacific, 114, 851

Tremonti, C. A., Heckman, T. M., Kauffmann, G., Brinchmann, J., Charlot, S., White, S. D. M., Seibert, M., Peng, E. W., Schlegel, D. J., Uomoto, A., Fukugita, M., & Brinkmann, J. 2004, The Astrophysical Journal, 613, 898

Unavane, M., Wyse, R. F. G., & Gilmore, G. 1996, Monthly Notices of the Royal Astronomical Society, 278, 727

Venn, K. A., Irwin, M., Shetrone, M. D., Tout, C. A., Hill, V., & Tolstoy, E. 2004, The Astronomical Journal, 128, 1177

Vogt, S. S., Allen, S. L., Bigelow, B. C., Bresee, L., Brown, B., Cantrall, T., Conrad, A., Couture, M., Delaney, C., Epps, H. W., Hilyard, D., Hilyard, D. F., Horn, E., Jern, N., Kanto, D., Keane, M. J., Kibrick, R. I., Lewis, J. W., Osborne, J., Pardeilhan, G. H., Pfister, T., Ricketts, T., Robinson, L. B., Stover, R. J., Tucker, D., Ward, J., & Wei, M. Z. 1994, Proc. SPIE Instrumentation in Astronomy VIII, 2198, 362

Wolfe, A. M. & Chen, H.-W. 2006, The Astrophysical Journal, 652, 981

Wolfe, A. M., Gawiser, E., & Prochaska, J. X. 2003, The Astrophysical Journal, 593, 235

—. 2005, Annual Review of Astronomy and Astrophysics, 43, 861

Wolfe, A. M., Prochaska, J. X., Jorgenson, R. A., & Rafelski, M. 2008, The Astrophysical Journal, 681, 881

Chapter 5

Photometric Stellar Variability in the Galactic Center

5.1 Introduction

The stellar cluster at the Galactic center (GC) presents a unique opportunity to study the evolution and properties of stars within the sphere of influence of a $3 - 4 \times 10^6 M_\odot$ supermassive black hole (SMBH) (Ghez et al., 2003, 2005b; Schödel et al., 2003). Photometric variability offers a useful approach to a number of outstanding questions regarding this stellar population which is composed of a mixture of old giants and young, massive stars. (Krabbe et al., 1991, 1995; Blum et al., 1996a,b, 2003; Figer et al., 2003; Paumard et al., 2001, 2004, 2006). For example, light curves can easily reveal close binary stars, which are relevant in several ways to our understanding of stars at the Galactic center.

First, binaries on radial orbits that are disrupted by the central black hole may provide a mechanism for capturing young stars from large galacto-centric radii, where the conditions are conducive to star formation, and retaining them at the smaller less hospitable radii where many young stars are found today (Gould & Quillen, 2003). Second, binary companions may facilitate the production of

dust around the WC sub-class of Wolf-Rayet stars, which are massive post-main sequence stars undergoing rapid mass loss. While conditions in the hostile environment (high temperatures in particular) of the stellar winds do not favor the formation of dust (Williams et al., 1987), compression within wind-colliding binary systems could overcome this challenge (White & Becker, 1995; Veen et al., 1998; Williams & van der Hucht, 2000; Lefèvre et al., 2005). Third, binaries provide a direct measurement of stellar masses. This is especially helpful for the most massive stars in the Galactic center as it would assist our understanding of the recent star formation history.

Another way in which a photometric variability study constrains the recent star formation history, as well as our understanding of massive star evolution, is the possibility of identifying luminous blue variables (LBVs). There are currently only 12 confirmed Galactic LBVs and 23 additional candidates, with 6 candidates in the Galactic center IRS 16 cluster of stars alone (Clark et al., 2005). The LBV phase plays an important, although poorly constrained, role in stellar evolution, because, during this phase, stars experience significant mass loss, with rates of $\sim 10^{-2} M_{\odot}$/yr during eruptions and as high as high as $10^{-4.5} M_{\odot}$/yr during quiescent phases (Abbott & Conti, 1987; Humphreys & Davidson, 1994; Massey, 2003). From a star formation history stand point, the LBV phase is notable because it is the first of several post main sequence phases that only the most massive stars ($M \gtrsim 60 - 85 M_{\odot}$) may go through before becoming supernovae. Stars stay in this phase for only $\sim 10^4$ years (Stothers & Chin, 1996) before entering the Wolf-Rayet phase, which typically lasts a few $\times 10^6$ years (Meynet & Maeder, 2005). Less massive stars ($M \gtrsim 40 M_{\odot}$) will skip the LBV phase and become Wolf-Rayet stars, but on time-scales longer than that of the more massive stars that experienced an LBV phase. Therefore, in principle, the numbers of LBVs and WR stars can constrain recent star formation histories (e.g. Paumard et al. 2006; Figer 2004). In this context the candidate LBVs at the Galactic center are perplexing in the context of the $\gtrsim 25$ Wolf-Rayet stars located in their immediate vicinity, since in a single

starburst event one would not expect to see any WR stars if the most massive stars are just now evolving through the LBV phase. This is similar to the problem posed by the presence of two LBVs in the Quintuplet cluster Figer (2004). If confirmed, the LBV candidates would suggest that this region has undergone multiple recent star forming events or that our understanding of LBV evolution is incomplete.

The photometry of stars in close proximity to the SMBH can also be used to constrain the properties of a possible cold, geometrically-thin inactive accretion disk around Sgr A* which could explain the present-day low luminosity of Sgr A* (Nayakshin & Sunyaev, 2003; Cuadra et al., 2003). In the presence of such a disk, we would expect to see nearby stars eclipsed or reddened when they pass behind the disk.

Very few photometric variable studies of the Galactic center exist. Tamura et al. (1996) introduced the idea that stars close to the Galactic center are expected to have a higher fraction of ellipsoidal[1] and eclipsing variable binaries than the stars in the solar neighborhood, but found very few variable stars and no binary stars. Seeing-limited studies (Tamura et al., 1996; Blum et al., 1996a) are limited to the brightest stars, due to stellar confusion caused by the high stellar densities and proper motions close to the central black hole. With high angular resolution data, Ott et al. (1999) have identified the only known eclipsing binary system in this region (see also Depoy et al. 2004; Martins et al. 2006). Furthermore, they suggest that as much as half of their sample (K $\lesssim$13) may be variable. However, the variability fraction decreases at smaller galactocentric radii starting from $\sim 5''$, suggesting that even at a high resolution of $0''.13$ their sensitivity to variability is limited by stellar confusion.

In this paper, we present the results of a stellar variability study of the central $5''\times5''$ of our Galaxy, based on ten years of K[2.2 μm] diffraction-limited images from the W. M. Keck I Telescope ($\theta = 0''.05$). The observations are de-

[1]Ellipsoidal variables are non-eclipsing binaries that are elongated by mutual tidal forces (Sterken & Jaschek, 1996).

scribed in §5.2, and the data and methodology to determine variability in §5.3. We discuss the variable star population in §5.4, which includes identification of asymmetries in the light curve of the eclipsing binary star IRS 16SW and the discovery of a likely wind colliding binary star in IRS 29N, and summarize our major findings in §5.5.

5.2 Observations

K-band (λ_o = 2.2μm, $\Delta\lambda$=0.4μm) speckle imaging observations of the Galaxy's central stellar cluster were obtained with the W. M. Keck I 10 m telescope using the facility near-infrared camera, NIRC (Matthews & Soifer, 1994). Observations taken from 1995 to 2004 have been described in detail elsewhere (Ghez et al., 1998, 2000, 2005b; Lu et al., 2005) and new observations on 2005 April 24-25 were conducted in a similar manner, resulting in diffraction-limited images. Each night several thousand short-exposure frames were taken in sets of $\sim$ 200, with NIRC in its fine plate scale mode, which has a scale of 20.40 $\pm$ 0.04 mas pixel^{-1} and a corresponding field of view (FOV) of 5.″22 $\times$ 5.″22 (Matthews et al., 1996). Table 5.1 lists the date and number of frames obtained for each of the 50 nights of observations used in this study.

5.3 Data Analysis and Results

5.3.1 Image Processing

The individual frames are processed in two steps to create a final average image for each night of observation. First, the standard image reduction steps of sky subtraction, flat-fielding, bad pixel correction, optical distortion correction[2], and pixel magnification by a factor of two are carried out on each frame. Sec-

[2]http://www.keck.hawaii.edu/inst/nirc/Distortion.html

Table 5.1. List of Observations

Date	Frames[a] (Obs.)	Frames[b] (Used)	Num. Stars[c] (Initial)	Num. Stars[d] (Final)	SNR[e]	Strehl
1995 Jun 10	1200	425	54	66	10.3	0.08
1995 Jun 11	2700	1604	95	110	15.0	0.06
1995 Jun 12	2100	1082	107	108	12.0	0.04
1996 Jun 26	4200	585	116	119	19.8	0.04
1996 Jun 27	2300	1260	117	121	20.5	0.04
1997 May 14	3600	1851	63	82	16.7	0.06
1998 Apr 02	2660	1649	119	121	16.3	0.05
1998 May 14	4560	1748	96	114	16.7	0.04
1998 May 15	7030	1953	41	55	9.9	0.06
1998 Jul 04	2280	943	108	114	17.8	0.08

Note. — Table 5.1 is shown in full in the appendix (Table C.8). A portion is shown here for guidance regarding its form and content. All observations are speckle K-band (λ_o = 2.2μm, $\Delta\lambda$=0.4μm) images.

[a]The number of frames observed in the night in stacks of 190 frames.

[b]The number of frames used in weighted shift-and-add routine described in Hornstein (2006).

[c]Number of stars in initial source list.

[d]Number of stars in final source list.

[e]The signal to noise ratio determined from median uncertainties of the six faintest non-variable stars detected in all the nights (S0-14, S1-25, S0-13, S1-68, S2-5, S1-34) with $m_k \sim 13.4$ mag.

ond, the frames from each night of observation are combined using the method of "Shift-and-Add" (Christou, 1991) with the frame selection and weighting scheme prescribed by Hornstein (2006). In short, each frame is analyzed for Strehl quality using the peak pixel value of IRS 16C, and low quality frames, which do not improve the cumulative signal to noise ratio (SNR) for the observations from each night, are rejected. This typically leaves ∼1600 frames for each night or 37% of the original data set (see column 3 of Table 5.1). The remaining frames for a given night are combined with Shift-and-Add in an average that is weighted by each frame's peak pixel value for IRS 16C. The final images have typical Strehl ratios of ∼0.07 (see column 8 of Table 5.1). The dataset from each night is also divided into three equivalent quality (and randomized in time) subsets to make three independent weighted Shift-and-Add image subsets, which are used to determine measurement uncertainties and to reject spurious sources.

Sources are identified in individual images and cross-identified between images using the strategy developed in Ghez et al. (1998, 2000, 2005b) and Lu et al. (2009), which for this study entails four separate steps. In the first step of the source identification process, we generate a conservative initial list of sources for each night of data to help minimize spurious source detection. This is done using the point-spread-function (PSF) fitting routine *StarFinder* (Diolaiti et al., 2000) to identify sources in both the average images and the subset images. StarFinder identifies sources through cross-correlation of each image with its PSF model, which, for our implementation, is generated from the two bright stars IRS 16C and IRS 16NW. The initial source list for each night of data is composed of only sources detected in the average images with correlation values above 0.8 and in all three subset images with correlation values above 0.6. In the second step of the source identification process, the source lists from all nights are cross-identified to produce a master list of sources, using a process that is described in Ghez et al. (1998) and that also solves for the sources' proper motions. To further ensure that no spurious sources have been detected we require that sources be detected in a minimum of 13 nights[3].

Figure 5.1 displays the 131 sources contained in our final master list. In the third step of the source identification process, we return to the original images to search more aggressively for the sources on the master list that were missed in some of the images. We explicitly feed the master list of sources into StarFinder and search for only these sources at their predicted positions with more lenient criteria, which require correlation values above 0.4 for both average and subset images. In the fourth and final step, we impose a restriction on our source detections to ensure photometric reliability: we exclude source detections that occur in regions of the average images covered by less than 50% frames that went into making a particular image. These regions, which are on the edges of the image, have relatively low signal to noise and the PSFs in these regions may not be well represented by the

[3]The threshold for the minimum number of nights was chosen by looking for a drop in the distribution of the number of nights that the sources were detected in the first pass at source identification. A minor drop is seen at 13 nights. The final results are not very sensitive to this choice and we therefore have made a fairly conservative choice.

PSF model. We also exclude individual measurements in which known stars are blended with each other (i.e., sources as listed in Ghez et al. (2005b) as well as Sgr A* IR.) This procedure, in its entirety, produces 4795 detections among 131 sources, which range in m_K magnitude from 9.0 to 16.1 mag (see Figure 5.2).

Photometric zeropoints are established on the basis of the work done by Blum et al. (1996a). While we share 7 stars in common with Blum et al. (1996a) (IRS 16NW, 16SW, 16C, 16NE, 29N, 29S, and 16CC), only IRS 16C ($m_K = 9.83 \pm 0.05$ mag) is a suitable photometric reference source. IRS 16SW is a known variable star in the K-band (Ott et al., 1999; Depoy et al., 2004) and IRS 29N is noted as possibly variable in Hornstein et al. (2002). IRS 16CC appears to be variable in the L-band; Blum et al. (1996a) list a re-calibrated value from Depoy & Sharp (1991) of 8.7 ± 0.2 mag, while Simons & Becklin (1996) measure 10.2 ± 0.2 mag. Among the remaining sources, only IRS 16C is in the final source lists of all the images. Several non-variable sources (see §5.3.2.1) are used *a posteriori* to confirm that IRS 16C is non-varying. Specifically, we check for any systematic shifts in the zero points by examining the normalized flux densities ($Q_j = \sum_i^N \frac{Flux_{i,j}}{NFlux_{avg_i}}$ where index i represents each star in an image of epoch j, $Flux_{avg_i}$ is the weighted average of the flux for that star over all images, and N is the number of stars used) of the 7 least variable bright stars that are identified in all 50 images (S1-3, S1-5, S2-22, S2-5, S1-68, S0-13, and S1-25) (see §5.3.2.1). The photometric stability of IRS 16C is shown in Figure 5.3, which plots Q_j versus the observing dates. The reference source IRS 16C appears to be stable over time, since the standard deviation of Q_j is 0.05, which is consistent with our measurement uncertainty for bright stars. Increasing the number of reference stars to 11 non-variable sources present in all frames in all 50 nights yields the same result. We therefore conclude that IRS 16C is non-varying to within our measurement uncertainties, and include it in our list of non-varying sources. Uncertainty in each of our reported relative photometry values is initially estimated as the root mean square (RMS) deviation from the average of the measurements from the three different subset images. The RMS value is added in quadrature with the uncertainty in the brightness of IRS 16C (0.05 mag) determined from the standard deviation of the normalized flux

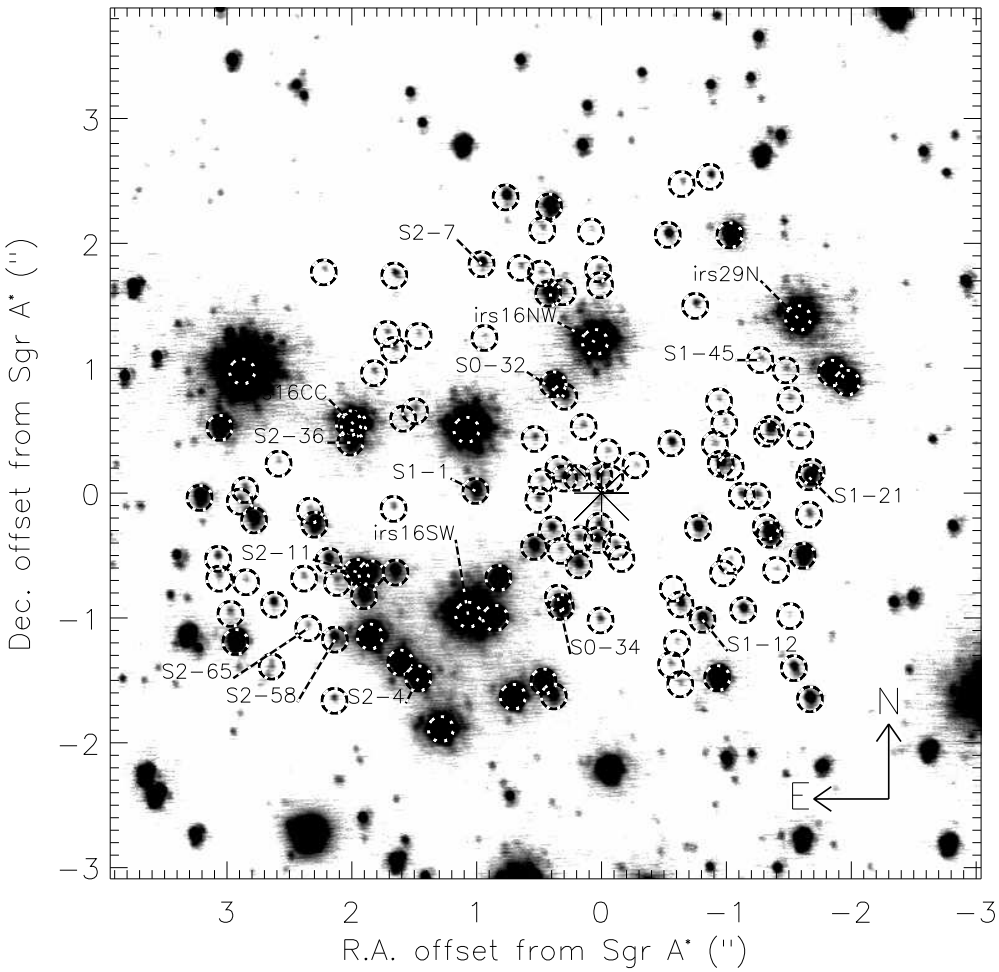

Figure 5.1 Identification of sources from this study overlaid on a 6″ x 6″ region of an LGS K′-band ($\lambda_o = 2.1\mu$m) image from Ghez et al. (2008) taken on June 30, 2005. All 131 sources are circled, but only variable sources are labeled. The location of Sgr A* is marked with an asterisk.

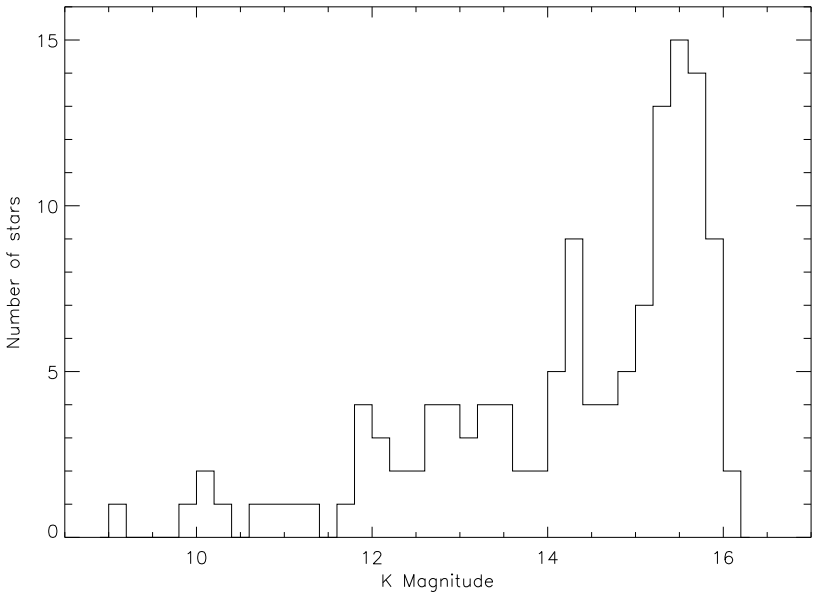

Figure 5.2 A m_K histogram of the 131 stars in our sample which range in magnitude from 9.0 to 16.1 mag.

densities Q_j. As Figure 5.4 shows, the median uncertainties grow from a floor of about 0.06 mag to 0.21 mag for the K= 16 mag sources.

5.3.2 Variability

5.3.2.1 Identifying Variables

There is a wide range of methods for testing photometric variability and the challenge for these various approaches is to avoid declaring a non-variable source variable on the basis of a few outlying data points (Welch & Stetson, 1993). We therefore have chosen to use the Kolmogorov-Smirnov (KS) test to calculate the probability that a *distribution* of data points is consistent with a model of a distribution of measurements for a non-variable source. This approach is less sensitive to outlying data points than the commonly used χ^2 test, which is an analysis of a single number description of how well a data set matches a model. In the KS test, we adopt as our model a non-variable light curve with gaussian-distributed uncertainties and we test the consistency of the measurements with

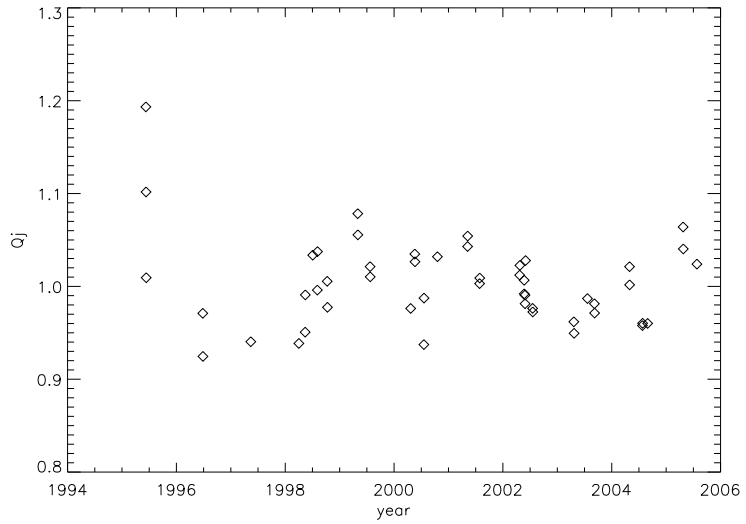

Figure 5.3 The average normalized flux densities (Q_j, as defined in §5.3.1) as a function of time. The variations seen are consistent with the measurement uncertainties for bright stars and are therefore demonstrative of the stability of our calibrator IRS 16C. This quantity is used as a scale factor to improve the quality of our relative photometry.

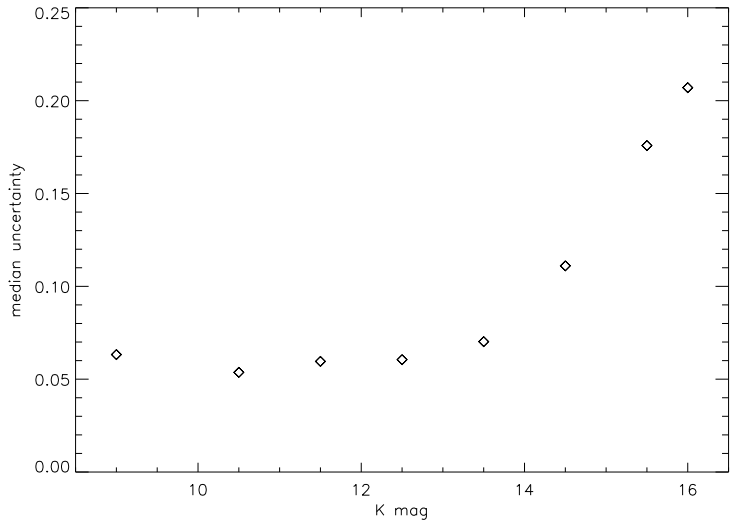

Figure 5.4 The median measurement uncertainty of stars binned by magnitude. The median uncertainties grow from a floor of about 0.06 mag to 0.21 mag for the K= 16 mag sources.

the model. Specifically, we examine the distribution of $X_j = \frac{Flux_j - Flux_{avg}}{\sigma_{Flux_j}}$ where $Flux_j$ is the flux of a star in a image of epoch j, σ_{Flux_j} is the corresponding uncertainty, and $Flux_{avg}$ is the weighted average of the flux for that star over all images. The resulting KS probabilities, which have allowed values between 0 and 1, describe how likely it is that a source's measurements are consistent with a non-variable source. Therefore variable stars, whose intensity variations are larger or comparable to our measurement uncertainties, should have very low KS probabilities. We classify a star as variable if it has a KS probability of less than 2.7×10^{-3}, which is the equivalent to a 3σ cut for gaussian distributed uncertainties (see Figure 5.5). To ensure all our low KS probability stars are truly variable, we also require these stars to have positive estimates of their intrinsic flux density variance, $\sigma^2_{intrinsic} = \sigma^2_{measured} - \langle\delta\rangle^2$, where the first term is the dispersion of the measured flux densities and the second term removes the bias introduced by the measurement uncertainties, δ. At this point, the 7 least variable bright stars detected in all images, used in §5.3.1 to define Q_j, are identified. We then scale all our photometry by Q_j in order to reduce the fluctuations induced by measurement errors on IRS 16C. The KS and intrinsic variance tests are then repeated. Table 5.2 and 5.3 list the properties of the variable and non-variable stars in our sample, respectively, and the light curves of all variable stars and a few key non-variable stars are shown below in Figures 5.9, 5.10, 5.11, 5.12, 5.13, and 5.15. While there are almost certainly other variable stars that we have excluded, our uncertainties limit our ability to classify more of these stars as variable, especially at the fainter end.

Among the 131 stars in our sample, 15 are identified as photometric variables in K-band (see Figure 5.1). To this we also add IRS 16CC, known to be variable in the L-band (see §5.3.1). Since the relative photometric uncertainties are roughly uniform down to a m_K magnitude of ~ 14 and then grow at fainter magnitudes (see Figure 5.4), we report a frequency of variable stars based on the stars brighter than 14 mag. Within this brighter sample of 44 stars, there are 10 variable stars, suggesting a minimum frequency of variable stars of 23%. There is no evidence for radial dependence, suggesting that we are not limited by stellar

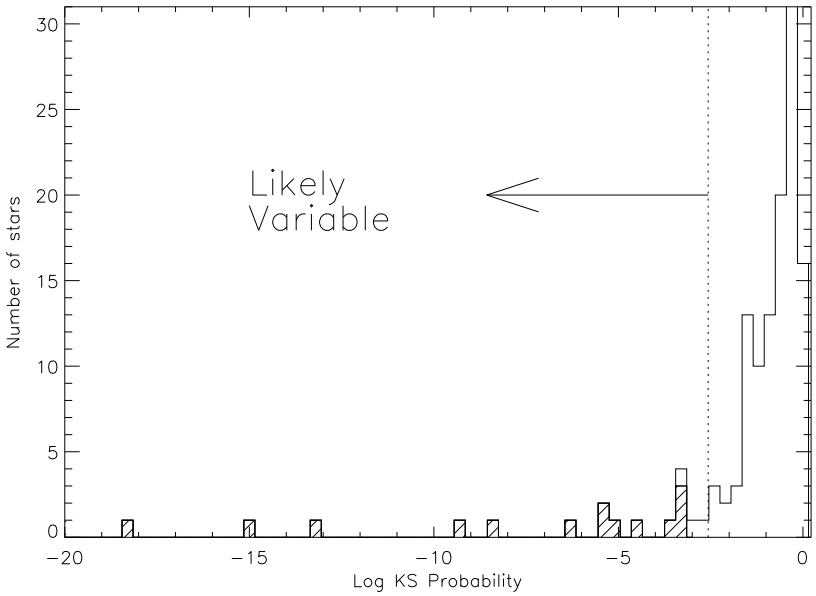

Figure 5.5 KS test probabilities of all the stars, with low values implying a low probability for a star to be non-variable. We classify a star as variable if it has a KS probability of less than 2.7×10^{-3}, which is equivalent to a 3σ cutoff value for gaussian distributed uncertainties and is marked by the dashed line. To ensure all our low KS probability stars are truly variable, we require all variable stars to have positive intrinsic variance. We mark all variable stars identified in this survey with hatches.

Table 5.2. List of Variable Stars

Star ID	Other ID	K[a] (mag)	Int. Var. (mag)	p (arcsec)	ΔR.A. (arcsec)	ΔDec. (arcsec)	Probability	Nights (days)	Type
IRS16SW	E23	10.06±0.19	0.17	1.41	1.04	-0.95	2.3E-23	50	Ofpe/WN9[h]
IRS16NW	E19	10.09±0.09	0.07	1.21	-0.01	1.21	3.3E-05	49	Ofpe/WN9[g]
IRS29N	E31	10.33±0.20	0.18	2.15	-1.63	1.40	1.1E-15	35	WC9[g]
IRS16CC	E27	10.60±0.05	0.01	2.07	1.99	0.57	3.0E-01	50	O9.5-B0.5 I[ci]
S2-11	GEN+2.03-0.63	11.99±0.13	0.11	2.07	1.99	-0.58	4.9E-19	49	Late[g]
S2-4	E28:GEN+1.46-1.49	12.26±0.17	0.15	2.05	1.45	-1.45	6.1E-14	47	B0-0.5 I[g]
S1-1	GEN+1.01+0.02	13.00±0.11	0.08	0.98	0.98	0.05	3.6E-04	49	Early[f]
S2-36	···	13.28±0.13	0.12	2.08	2.04	0.43	3.7E-09	48	Early[f]
S1-21	E24:W7	13.33±0.17	0.15	1.69	-1.69	0.13	4.2E-06	42	O9-9.5 III?[g]
S1-12	E21:W13	13.82±0.18	0.17	1.31	-0.85	-1.00	4.2E-07	45	OB I?[c]

Note. — Table 5.2 is shown in full in the appendix (Table C.9). A portion is shown here for guidance regarding its form and content. Photometry is relative to IRS 16C (m_k=9.83 mag). Positions are in arcseconds offset from Sgr A* in 1999.56 and p is the projected distance. The K-S probability is equal to 1 for an ideal non variable source, and approaches 0 for a very variable source. Other ID's are from Paumard et al. (2006) and Genzel et al. (2003) respectively. We classify IRS 29N as an early type star according to Paumard et al. (2006) although Figer et al. (2003) classifies it as a late type star.

[a]The magnitudes are Q_j corrected using 7 bright non-variable stars, and the uncertainties do not include the 5 % absolute calibration uncertainties. Comparison to other sources requires adding them in quadrature. Uncertainties are calculated as the standard deviation of the mean.

[b]Spectroscopic identification by Eisenhauer et al. (2005).

[c]Spectroscopic identification by Paumard et al. (2006).

[d]Spectroscopic identification by Figer et al. (2003).

[e]Spectroscopic identification by Ott (2003). We denote sources with clear CO or He lines as Early and Late respectively.

[f]Identification based on the interpretation by Genzel et al. (2003) of $m(CO)$ index of Ott (2003) where Genzel et al. (2003) identify stars with $m(CO) \geq 0.04$ as late type stars and stars with $m(CO) < 0.04$ as early type stars.

[g]Identified as nonvariable by Ott et al. (1999).

[h]Identified as possibly variable by Ott et al. (1999).

[i]IRS 16CC appears to be variable in the L-band as discussed in §5.3.1.

confusion down to 14 mag.

We compare our results to those of Ott et al. (1999), the only other high spatial resolution study of the variability of sources in the Galactic center. Those authors give an upper limit of possible variable stars of approximately 50% of their 218 sources with $m_K < 13$ mag over $18'' \times 18''$. While this variable star frequency is higher than our reported value (and consistent), a comparison limited to the stars in common leads to a number of discrepancies. In the overlap sample of 33 stars, Ott et al. find 2 of the stars to be variable (IRS 16SW, S1-3), while our sample has 6 (IRS 16SW, IRS 16NW, IRS 29N, S2-11, S2-4, S1-21) and only IRS 16SW is in common. There are a number of differences between these two studies, including the data analysis approach used (PSF fitting vs. aperture photometry), the time baseline (10 years vs. 5 years), and the angular resolution ($0\farcs05$ vs. $0\farcs13$). Since our study covers twice the time baseline, we can pick out variations on longer time scales, which helps explain our additional variables. Also, the high stellar crowding makes the area we observe the most uncertain region for the lower resolution Ott et al. study. Only one star, S1-3, in our non-variable sample is identified as variable by Ott et al., and it is very close to their threshold for variability.

5.3.2.2 Variability Characterization and Periodicity Search

We attempt to characterize the minimum time-scale for variation by searching for daily and monthly variability using KS tests similar to the test for variability in §5.3.2.1 where we adopt as our model a non-variable light curve with gaussian-distributed uncertainties. For the daily variations, we group the consecutive nights in pairs and examine the distribution of the pairs in sets i for each star of $X_i = \frac{Flux_j - Flux_k}{\sqrt{\sigma^2_{Flux_j} + \sigma^2_{Flux_k}}}$ where $Flux_j$ and $Flux_k$ are the fluxes of stars in images of consecutive epochs j and k respectively, σ_{Flux_j} and σ_{Flux_k} are the corresponding uncertainties. For the monthly variation, all measurements made within days of each other are averaged together and the pairs separated by one month are examined with the same KS test. The only stars showing daily variability in excess of 3σ is IRS 16SW, and the stars showing monthly variations are IRS 16SW and S2-36.

Table 5.3. List of Non-variable Stars

Star ID	Other ID	K (mag)	p (arcsec)	ΔR.A. (arcsec)	ΔDec. (arcsec)	Nights (days)	Type
IRS16NE	E39	9.00±0.05	3.06	2.85	1.10	35	Ofpe/WN9[g]
IRS16C	E20	9.83±0.05	1.23	1.13	0.50	50	Ofpe/WN9[ġ]
S2-17	E34:GEN+1.27-1.87	10.90±0.07	2.23	1.27	-1.84	35	B0.5-1 I[g]
IRS16SW-E	E32:16SE1	11.00±0.08	2.15	1.85	-1.11	50	WC8/9[g]
IRS29S	···	11.31±0.06	2.08	-1.86	0.93	30	K3 III[d]
S1-24	E26:GEN+0.76-1.55	11.64±0.07	1.72	0.73	-1.55	45	O8-9.5 I[g]
S2-16	E35:29NE1	11.85±0.08	2.29	-1.01	2.05	33	WC8/9[g]
S1-23	GEN-0.90-1.46	11.86±0.09	1.73	-0.92	-1.46	33	Late[g]
S3-2	GEN+3.07+0.56	12.00±0.11	3.09	3.03	0.60	31	Early[f]
S2-6	E30:GEN+1.60-1.36	12.06±0.08	2.07	1.59	-1.31	50	O8.5-9.5 I[c]

Note. — Table 5.3 is shown in full in the appendix (Table C.10). A portion is shown here for guidance regarding its form and content. See notes from table 5.1.

[a]The magnitudes are Q_j corrected using 7 bright non-variable stars, and the uncertainties do not include the 5 % calibration uncertainties. Comparison to other sources requires adding them in quadrature.

[b−h]Type from Paumard et al. (2006), Figer et al. (2003), Eisenhauer et al. (2005), and Ott (2003) as described in table 5.1.

[g]Identified as nonvariable by Ott et al. (1999).

[h]Identified as possibly variable by Ott et al. (1999).

[i]This is our main calibration star and is included in this table only for completeness.

[j]The 7 least variable bright stars detected in all images used for scaling of the photometry in order to reduce the fluctuations induced by measurement errors on IRS 16C (see §5.3.1).

The light curves of the variable stars are searched for periodicities using three different methods. First, the Lomb and Scargle periodogram technique (Lomb, 1976; Scargle, 1982; Press et al., 1992), which fits fourier components to the data points, is applied and is expected to yield a larger power spectral density at intrinsic harmonics of a data set in which there is a periodic signal. Second, Dworetsky's (1983) string length method, a variant of the Lafler-Kinman method (1965), phases the data for every possible period and then sums over the total separation between points in phase space, with the best period and its aliases corresponding to the smallest lengths. Third, Stetson's (1996) string length technique is similar to Dworetsky's, but also weights these lengths by their uncertainties and how close in phase the points are. Our criterion for considering a star periodic is that it show similar periods from all three techniques. The periodicity search shows only one periodic star: IRS 16SW. We find a photometric period of 9.724 ± 0.001 days, which is consistent with Ott et al. (1999), Depoy et al. (2004) and the reanalysis of the Ott et al. data in Martins et al. (2006). Figure 5.6 shows the determination of IRS 16SW's period using Dworetsky's (1983) string length algorithm, showing the 9.724 day period and its other harmonics at multiples of its period. The top panel in Figure 5.7 shows the phased light curve of IRS 16SW at 9.724 days and depicts a clearly periodic signal with an amplitude of ~ 0.55 mag. The phased light curve of IRS 16SW is asymmetric (see Figure 5.7) with a rise-time that is ~ 1.6 times longer than the fall-time.

5.4 Discussion

The 16 variable stars identified in this study cover a wide variety of different types of stars, as we only limited our search by location and brightness. As Figure 5.8 shows, based on the K magnitudes alone, this sample is expected to contain early-type (O & B) main sequence stars, late-type (K & M) giant stars, and most types of supergiants. Fortunately, all but two of the variable stars have spectral classifications (see column 10 in Table 5.2). While 9 of the variable stars are securely identified from spectroscopic work (Paumard et al., 2006; Eisenhauer et al.,

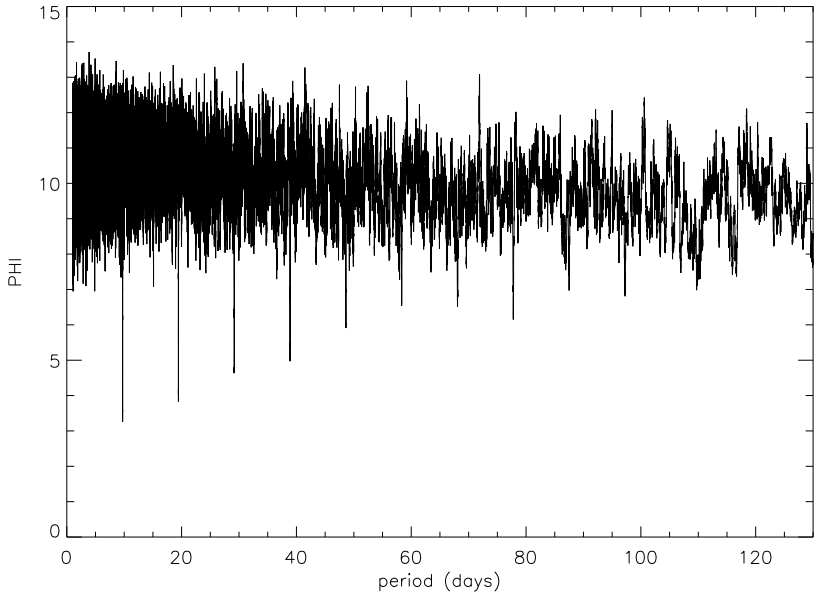

Figure 5.6 Determination of IRS 16SW's period using Dworetsky's string length method Dworetsky (1983). Phi is the string length where shorter lengths and therefore smaller values of Phi indicate a periodic signal. Note that the other harmonics are also found at multiples of the original period.

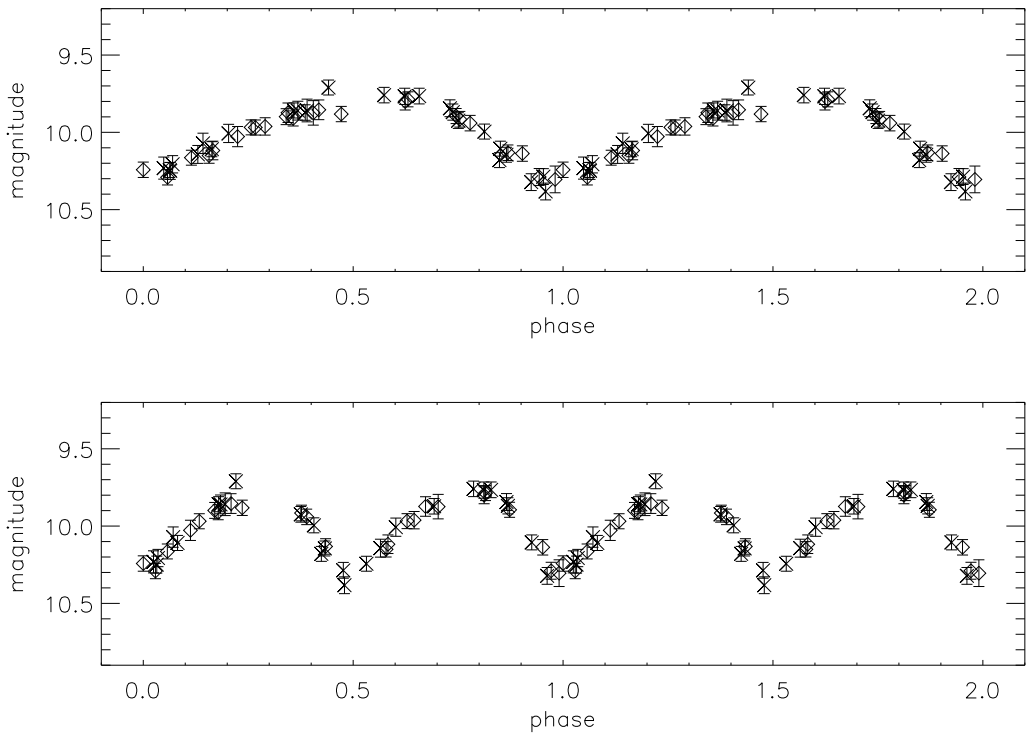

Figure 5.7 The phased light curve of IRS 16SW at its period of 9.724 (top panel) and 19.448 days (bottom panel). The points are plotted twice for clarity. Both phased diagrams show a rise-time that is ~ 1.6 times longer than the fall-time. The similarity of the first half of the data set (1995-2000; diamonds) to the second half (2001-2005; crosses) shows that the asymmetry has been constant over the past ten years. This effect could be produced by tidal deformation of two equal mass stars in an eclipsing binary star system.

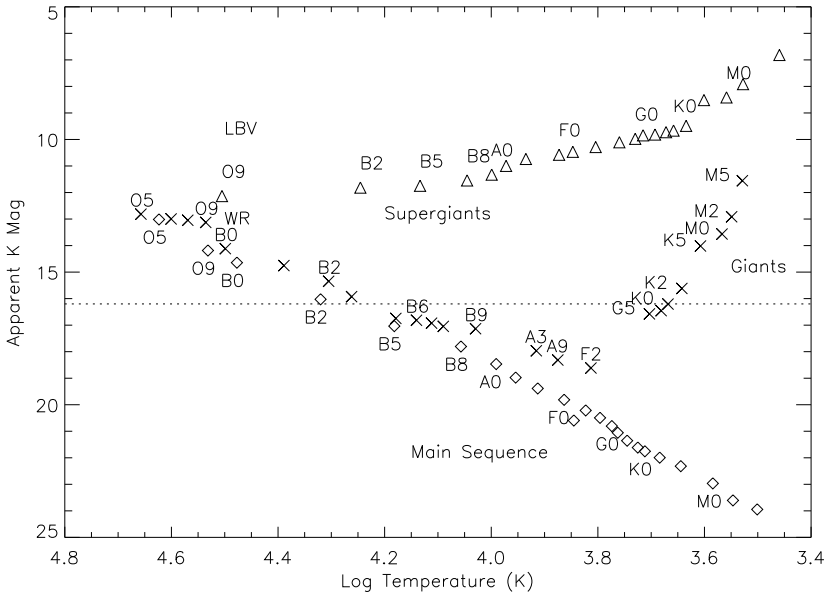

Figure 5.8 Apparent K magnitudes versus spectral type assuming a distance of r = 8.0 kpc (Reid, 1993) and an extinction A_K=3.3 mag (Blum et al., 1996a) based on compilations of data from Cox (2000) where available, and by (Jager & Nieuwenhuijzen, 1987; Wegner, 1994, 2006; Vacca et al., 1996; Grenier et al., 1985; Blackwell & Lynas-Gray, 1994; Theodossiou & Danezis, 1991) for Giants of type O-F . The lower dotted line is the magnitude limit of this sample, and the locations of WR and LBV stars are highly variable and average locations are marked for reference only. The triangles represent supergiant stars, the crosses represent giant stars, and the diamonds represent main sequence stars.

2005; Figer et al., 2003; Ott, 2003), an additional 5 stars are classified on the basis of narrowband photometry of CO absorption (Ott, 2003; Genzel et al., 2003). In summary, four stars are LBV candidates (IRS 16SW, 16NW, 16NE, & 16C; see §5.4.1) one is a WC9 (IRS 29N; see §5.4.2), four are OB supergiants (S2-4, S1-12, S2-7, & IRS 16CC; see §5.4.3), one is an O giant (S1-21), five more are classified as some sort of early-type star from narrowband filter photometric measurements (S1-1, S2-36, S0-32, S2-58, S1-45), and one is classified as a late-type star from narrowband filter photometric measurements (S2-11; see §5.4.3). The variability of stars in each spectral classification is discussed in turn below, along with a discussion of the possibility of external agents causing variability.

5.4.1 Ofpe/WN9 Stars

5.4.1.1 Luminous Blue Variable Candidates

Four stars in our sample are Ofpe/WN9 stars and have been previously classified as candidate LBVs (IRS 16NE, 16C, 16SW, and 16NW) based on their bright luminosity, their narrow emission lines, and their proximity and similarity to IRS 34W (Clark et al., 2005; Paumard et al., 2004; Trippe et al., 2006)[4]. In our observations, both IRS 16NE and 16C are non-variable over a ten-year time frame to within our uncertainties. The other two LBV candidates (IRS 16NW and 16SW) show variability, but not the characteristic LBV eruptions, which in the context of this study are the $\Delta M_v \simeq 1-2$ mag events occurring every 10-40 years and lasting as long as several years (Humphreys & Davidson, 1994). IRS 16SW has periodic variability that is explained by an eclipsing binary system (see §5.4.1.2 below) and IRS 16NW has an overall flat light curve with a decrease in brightness ($\Delta m_K \simeq 0.2$) mag between 1997 and 1999 (see Figure 5.9). The apparent dimming of IRS 16NW can be explained by ejected circumstellar material obscuring the star, with an amplitude that is smaller than is characteristic of a typical LBV. These variations do not require it to be an LBV, just that it has strong stochastic winds. While none of these stars shows the classic characteristics of LBVs, our time baseline is too short to rule them out as LBVs as they may be in a quiescent phase. Nonetheless, our observations do not demand the complication of multiple recent star formation events that would be suggested with the presence of both LBVs and WR stars.

5.4.1.2 Asymmetric Periodic Light Variations in IRS 16SW: Tidal Deformation?

The periodic variation in IRS 16SW has recently been attributed to either an equal mass contact eclipsing-binary or a massive pulsating star (Ott et al.,

[4]The classification of IRS 34W as an LBV is based on its bright luminosity, narrow emission lines, along with a multi-year obscuration event (Paumard et al., 2004; Trippe et al., 2006). However, more recent studies have cast doubt on IRS 34W's categorization as an LBV since it lacks spectroscopic variability and since the eruption event responsible for the obscuration event was not observed(Trippe et al., 2006).

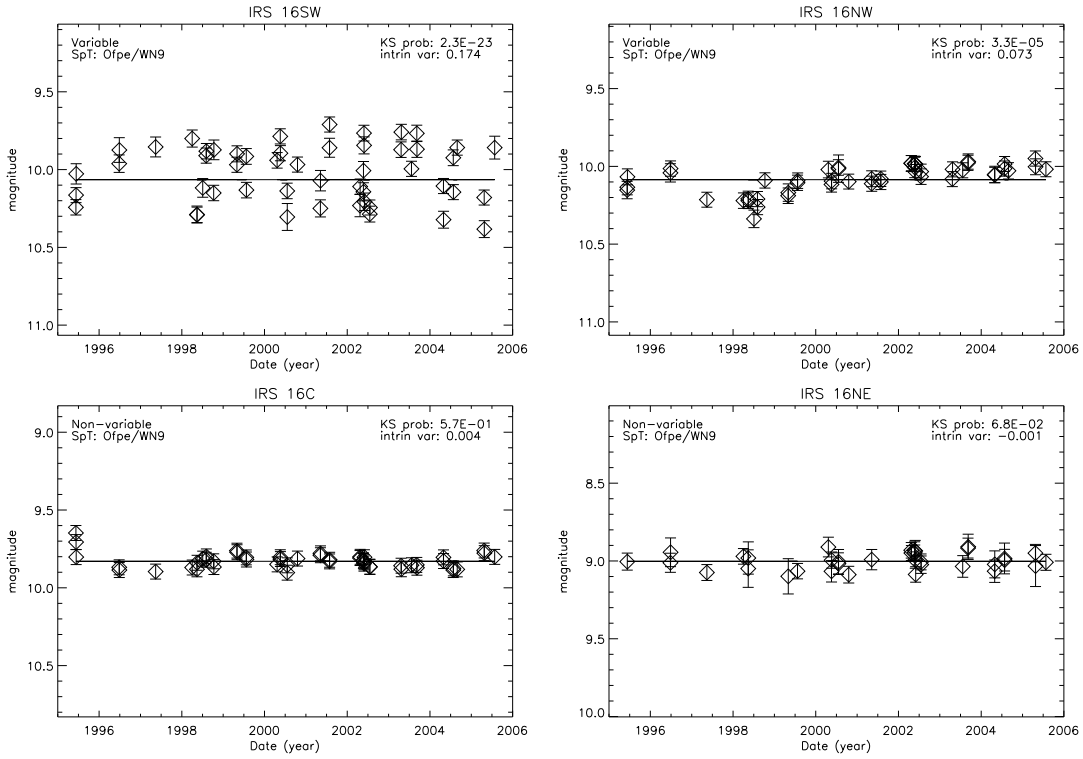

Figure 5.9 Light curves of the four stars in our sample that are classified as candidate LBVs (IRS 16SW, 16NW, 16NE, 16C). The top two panels denote the two variable stars, while the bottom two panels are non-variable stars. The given intrinsic variance is in magnitudes.

1999; Depoy et al., 2004; Martins et al., 2006), although the measurement of a spectroscopic radial velocity period by Martins et al. (2006) strongly suggests it is an eclipsing binary star system. Also, a re-analysis of the data suggesting a pulsating star now agrees with IRS 16SW probably being an eclipsing binary (Peeples et al., 2007). The asymmetries that we observe in the phased light curve of IRS 16SW are difficult to explain in the context of an eclipsing binary star system. Figure 5.7 shows the properly phased light curve (19.448 ± 0.002 days), in which asymmetries in its rise and fall-times are still readily detected. The asymmetry is remarkably similar for both halves of the phased light curve. While this was not detected in earlier photometric studies[5], our study is likely more sensitive to small photometric variations due to our higher angular resolution (see §5.3.2.1). The observed asymmetry has been sustained over 10 years; if the asymmetry has been changing over time, it would show up as a dispersion in the vertical placements of the points in the phase diagram that is much larger than what we observe. In figure 5.7 we explicitly show that the asymmetries are the same during the first half and second half of the data-set and we see no period drifts, with the period of the first half and second half not differing at the 3σ confidence level. Magnetic hot spots can explain light curve asymmetries (Djurašević et al., 2000; Cohen et al., 2004), however, they can not maintain this asymmetry over long periods of time. Furthermore, the similarity in the asymmetry between the first and second half would require the spots to be the same on both stars. Likewise, heating in the contact region of the binary or any third light in this region produces a light curve that is a mirror reflection between the 1st and 2nd half (see Moffat et al., 2004) and is therefore inconsistent with our observations. Other heating mechanisms such as irradiation effects are unlikely to be the cause of the asymmetry as they barely change the light curve (Bauer, 2005). Given that this is suspected to be a contact binary, we suggest that the asymmetric light curve may be due to tidal deformations caused by the proximity of the stars in asynchronous orbits. Since these two stars are equal in mass ($\sim 50 M_{\odot}$), equal in radius ($66 R_{\odot}$) and appear to

[5]Our light curve is similar to the light curve presented by Ott et al. (1999), although the asymmetry was not explicitly reported and the reanalysis of the data by (Martins et al., 2006) does not show the asymmetry.

be in contact (Martins et al., 2006), they fall within the tidal radius of $\sim 163 R_{\odot}$, and are likely tidally deformed. In order to produce the asymmetric light curve, the rotation of the stars needs to be asynchronous with their orbital periods so that the rotational inertia of the stars prevents their tidal bulges from being aligned with the line joining the stars' centers of mass. Two stars in such close contact will eventually synchronize their orbital period with their rotation period. The synchronization time scale of stars with convective cores and radiative envelopes is longer than for stars with convective envelopes, albeit more difficult to calculate (Zahn, 1977). We therefore calculate the convective envelope synchronization time as a minimum time for synchronization based on formalism developed by Zahn (1977) and find a minimum age of $\sim 6 \times 10^8$ yrs. This time scale is far larger than the lifetime of stars as massive as IRS 16SW and asynchronous orbits are therefore acceptable. The equality of the two halves of the light curve implies that the rotation rate of the two stars is very similar. Since these two stars are identical in every other respect, this equality is not surprising. It is therefore possible that the asymmetric light curve is due to tidal deformations.

5.4.1.3 Eclipsing Binary Fraction

Stars close to the Galactic center are expected to have a higher fraction of ellipsoidal and eclipsing variable binaries than the stars in the solar neighborhood. However, IRS 16SW is the only eclipsing binary star detected in our sample. The stars' orbits may be smaller due to hardening by encounters with other stars producing tightly bound binaries, such that eclipses would be more likely. In addition, collisions and tidal capture produce binaries, making ellipsoidal variations or eclipses more probable (Tamura et al., 1996). Of the 164 Galactic O stars in clusters or associations in the sample by Mason et al. (1998), 50 are confirmed as spectroscopic binaries, 40 are unconfirmed spectroscopic binaries, 4 are confirmed eclipsing variables, and 14 are either ellipsoidal or eclipsing binaries. This yields local rates of eclipsing O star binaries between 2% and 11%. Our sample contains 11 spectroscopically confirmed O stars, 4 Ofpe/WN9 stars, and possibly more unconfirmed. If the Galactic center fraction of eclipsing binaries is similar to the

cluster results, we would expect on the order of one eclipsing binary. Our detection of one eclipsing variable star suggests that the frequency of eclipsing binaries is not significantly increased at the Galactic center over the local neighborhood.

5.4.2 Late-type WC Wolf-Rayet Stars: Variations Associated with a Wind Colliding Binary

Three stars in our sample are spectroscopically identified as WC stars (IRS 29N, IRS 16SW-E and S2-16) (Paumard et al., 2006), and all three are dust producers as evidenced by their red colors (K-L $\sim$ 3; Blum et al. 1996a). In this study, only IRS 29N is variable (see Fig 5.10). IRS 29N's intensity shows a gradual drop and then rise in brightness of $\Delta m_K \simeq 0.7$ mag over a time scale of ≈ 5 years. Its light curve is similar to the variations seen in WC stars elsewhere in the Galaxy (e.g. compilation by van der Hucht et al. 2001); these sources are thought to be variable due to periodic or episodic dust production in the wind collision zone of long period eccentric binary star systems (1000d $<$ P $<$ 10000d) during periastron passage. When the dust forms, the star exhibits a rising infrared flux followed by fading emission when dust formation stops and dust grains are dispersed by stellar winds (Moffat et al., 1987; White & Becker, 1995; Veen et al., 1998; Williams & van der Hucht, 2000). Currently, only seven WC stars have been observed to produce dust episodically, all of which are confirmed or suspected massive binaries with elliptical orbits (van der Hucht, 2001; Williams et al., 2005; Lefèvre et al., 2005). Two of these are known to exhibit pinwheel nebulae, a tell-tale sign of wind-colliding binaries (Tuthill et al., 1999; Monnier et al., 1999). The time-scales and magnitude of the photometric variability of IRS 29N is consistent with it being a wind-colliding binary; we therefore conclude that IRS 29N is likely to be a wind-colliding binary.

5.4.3 Comments on Other Stars

Our sample includes at least 10 other variable young massive stars in addition to those discussed in §5.4.1 & §5.4.2. Five are spectroscopically identified OB

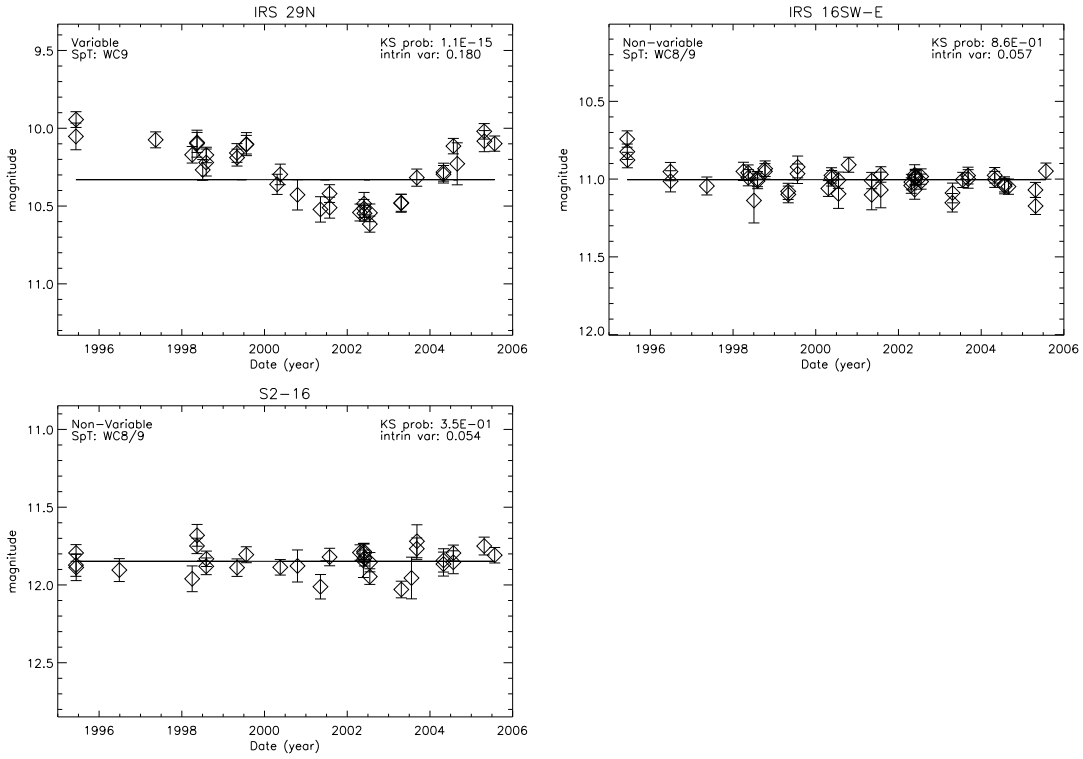

Figure 5.10 Light curves of Wolf-Rayet stars of type WC in our sample. The first panel is the variable star IRS 29N, which is probably a wind-colliding binary, while the other two are non-variable stars. The given intrinsic variance is expressed in magnitudes.

stars (IRS 16CC[6], S2-4, S1-21, S1-12, S2-7; see Figure 5.11) (Paumard et al., 2006), and five are early-type stars classified as on the basis of narrowband filter photometric measurements (S1-1, S2-36, S0-32, S2-58, S1-45; see Figure 5.12) (Genzel et al., 2003; Ott, 2003). The majority of these variables are likely associated with mass loss, although interstellar extinction could also play a role, as discussed below. In particular, the two K-band variable OB supergiants each show a dip (0.3 - 0.9 mag) in their brightness that lasts for 1-6 years. OB supergiants have stochastic winds with high mass loss rates ($0.2 - 20 \times 10^{-6} M_{\odot}$/yr) (Massey, 2003); it is therefore likely the large variations seen are due to ejection of circumstellar material. Another example of an OB star with variations potentially due to mass loss is S2-7, which is either luminosity class III or V based on its assumed distance. S2-7 shows a decrease in luminosity between 2000 and 2005 with $\Delta m_K \simeq 0.5 - 1.0$ mag. This is reminiscent of Be stars, which sometimes show fading events due to the formation of an equatorial disk on time scales of several years (Mennickent et al., 1994; Pavlovski et al., 1997; Percy & Bakos, 2001). The remaining young variable stars in our sample have variations that are more difficult to characterize, although S2-36 seems to have significant variations on monthly time-scales (see §5.3.2.2). Nonetheless, it is likely that mass loss also plays a central role in generating the observed variations.

5.4.4 Interstellar Material

5.4.4.1 Apparent Variations Caused by Stellar Motion Through the Line of Sight Extinction

Periods of reduced luminosity in stars can also be due to external effects such as obscuration by foreground interstellar matter. The central parsec has several gas patches that are a few arcseconds wide and that can cause local extinction enhancements of ~ 1 magnitude in K-band (Paumard et al., 2004). As our FOV is only $5'' \times 5''$, these patches would cover a sizable region and many neighboring stars

[6]IRS 16CC is not identified as variable in this survey, although reported differences in L-band magnitudes from previous studies suggest it is variable (Depoy & Sharp, 1991; Simons & Becklin, 1996; Blum et al., 1996a) (see §5.3.1).

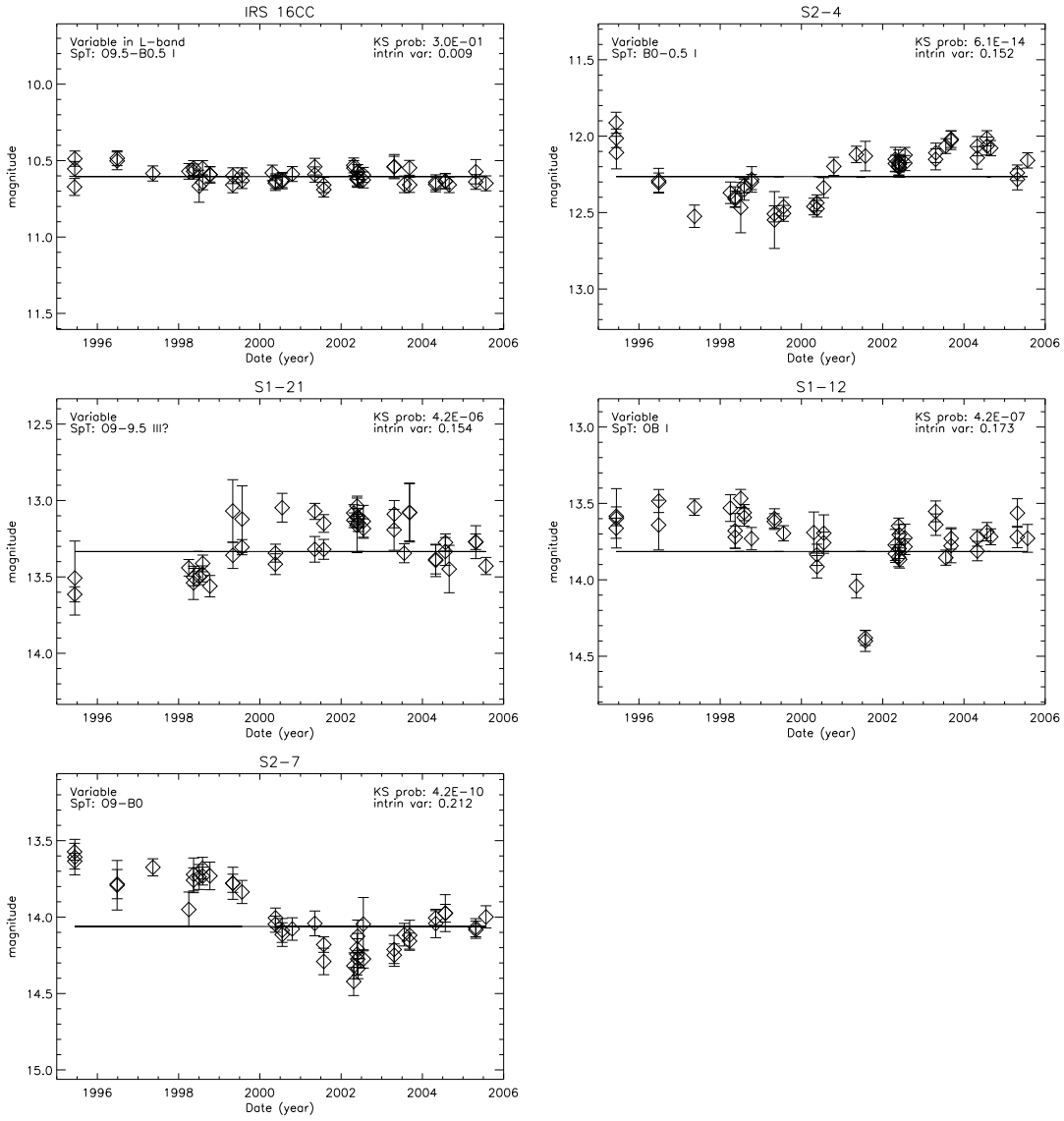

Figure 5.11 Light curves of variable OB stars in our sample. IRS 16CC is not variable in K band, but shows variability at L (see §5.3.1). We propose that S2-4 and S1-12 are variable due to ejection of circumstellar material obscuring the stars, while S2-7 is probably a Be star with the formation of an equatorial disk obscuring the star. The given intrinsic variance is expressed in magnitudes.

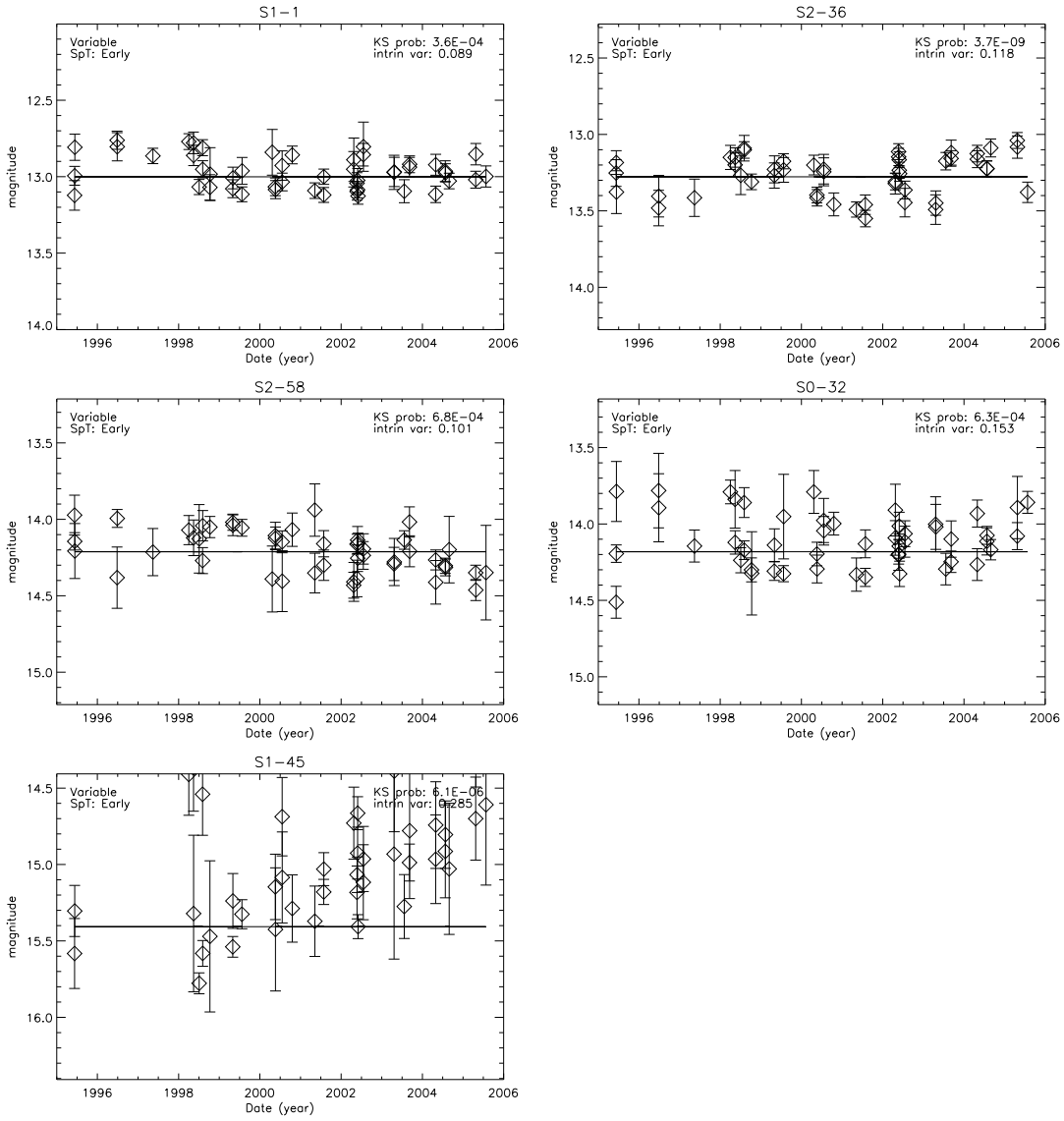

Figure 5.12 Light curves of early-type variable stars in our sample. S2-36 is variable on a monthly basis and its variation is therefore probably intrinsic. The variations in S1-45 and S2-58 may be due to obscuration by high density streamers. The given intrinsic variance is expressed in magnitudes.

would show similar variations. Interstellar material closer to Earth in the line of sight is unlikely, as its proximity would make the clouds even larger in projection (Trippe et al., 2006). Since neighboring stars do not experience similar effects of obscuration, the large scale structure in the interstellar medium (ISM) is unlikely to be the cause.

In some cases it is possible that the variable obscuration is caused by the relative motion of the foreground high density streamers and the background stars, such as are observed in the L-band associated with the Northern Arm (Clénet et al., 2004; Ghez et al., 2005a). In this area we see unresolved streamers that are small in projected width (< 80 mas). These streamers may be due to shocks heating the neighboring dust with the streamers tracing thin shells of compressed gas from one or several shocks (Clénet et al., 2004). These streamers may cause dips in our light curves due to small-scale structure obscuration in the line of sight. This causes photometric variability due to the relative lateral motion between the absorbing feature and the star. The projected implied width of the small-scale structure is approximately $\sim 10 - 40$ mas assuming a projected stellar velocity of ~ 5 mas/yr which is typical of stars at projected distances of $\sim 2''$ from Sgr A*. The three stars whose variability is most likely ascribable to these thin high density streamers are S2-11, S1-45, S2-58. The most clear case is the late-type star S2-11 (Ott, 2003), which shows an interval of reduced luminosity between 2001 and 2005 with $\Delta m_K \simeq 0.3$ mag and is otherwise constant over our time frame (see Figure 5.13). Using a Galactic center distance of $r = 8.0$ kpc (Reid, 1993) and an extinction A_K=3.3 mag (Blum et al., 1996a) , we determine its spectral type based on luminosity and late-type classification as M3-5 III. Stars with spectral type M5 and luminosity class III are generally classified as asymptotic giant branch stars (AGB), but the variations observed are not typical of AGB stars which have periods between 0.5 - 1.5 yrs (Habing, 1996). This star is likely obscured by dust given its red color (K-L ~ 2). It is located in the middle of the Northern Arm (see Figure 5.14) and its reduced luminosity is likely due to a high density streamer in the line of sight. The two other stars whose variability can probably be attributed to high density streamers have long term variations over ten years; S1-45 appears

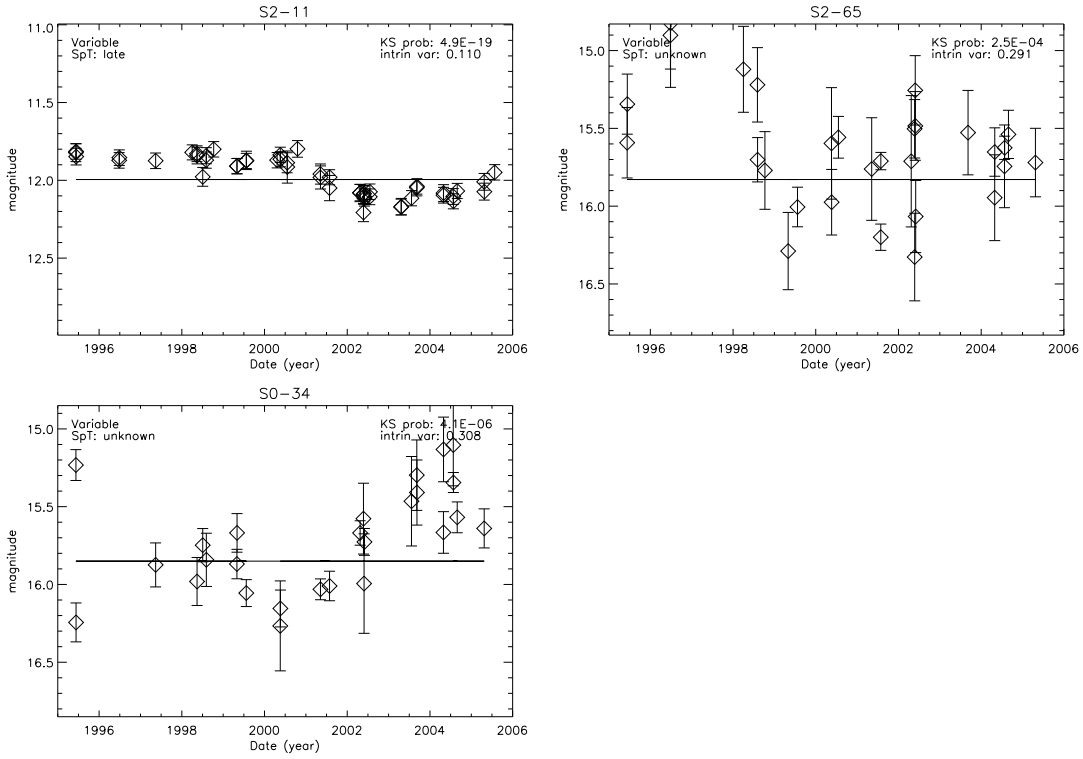

Figure 5.13 Light curves of a late-type star, and two unknown type stars in our sample. The late-type star, S2-11, is probably an AGB star of spectral type M3-5 III, while we are unable to classify the two stars of unknown spectral type. The given intrinsic variance is expressed in magnitudes.

to brighten by $\Delta m_K \simeq 0.5 - 1.0$ mag and S2-58 appears to dim by $\Delta m_K \simeq 0.2$ mag (see Figure 5.12). It is also possible that the dips in the light curves of stars speculated to be variable due to high stellar winds such as S2-4, S1-12, S2-7, and S2-36 are actually variable due to obscuration in the line of sight. Measurements at multiple wavelengths throughout future variations would help to establish the role of variable extinction in the observed K-band variations. Furthermore, foreground material would be polarized due to the magnetic fields at the Galactic center, and therefore polarization variations of stars would provide a test of the hypothesis that the relative motion of streamers and stars are responsible for stellar intensity variations.

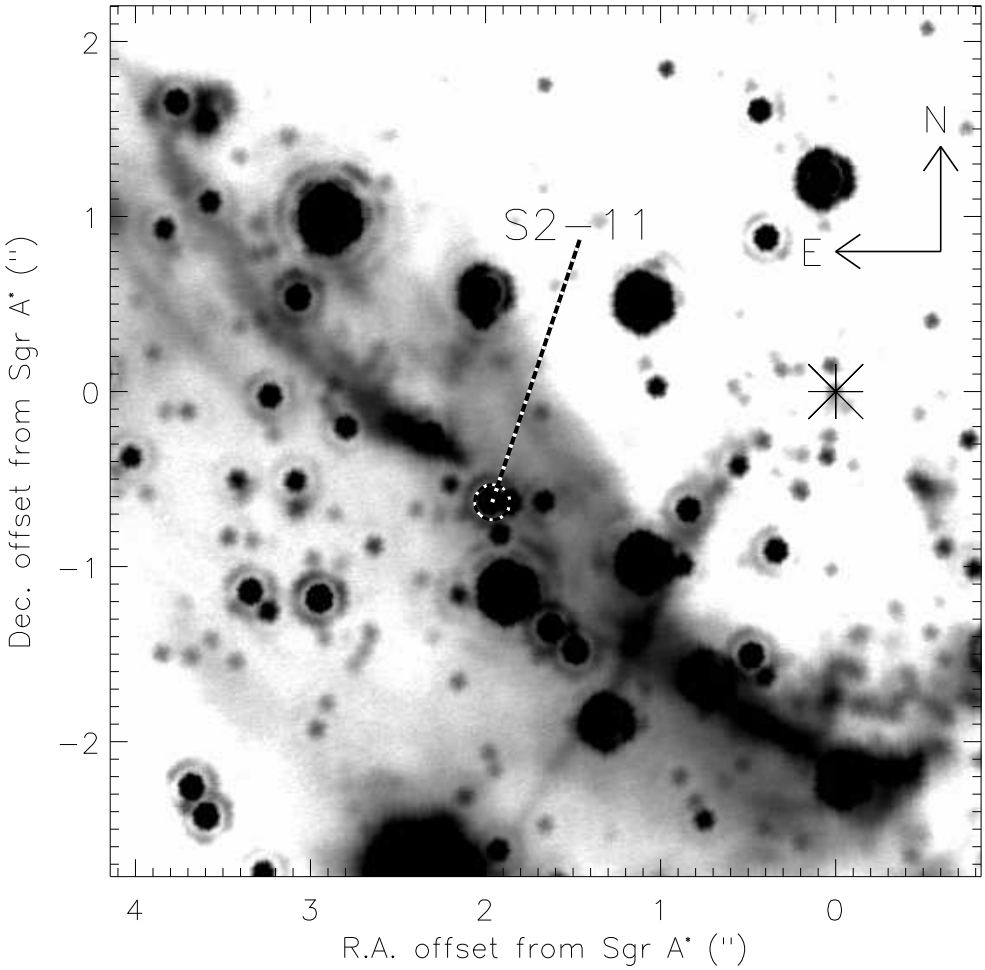

Figure 5.14 Identification of the source S2-11 from this study overlaid on a 5″ x 5″ region of an LGS L′-band ($\lambda_o = 3.8\mu$m) image from Ghez et al. (2008) taken on June 30, 2005. The star S2-11 is situated in the middle of the Northern Arm and it is therefore likely that the interval of reduced luminosity is due to the stellar motion through a high density streamer in the line of sight. The location of Sgr A* is marked with an asterisk.

5.4.4.2 Variability of Stars Near Closest Approach

We detect no variability in the 7 central arcsecond sources that have known 3-dimensional orbits (S0-1, S0-2, S0-4, S0-5, S0-16, S0-19, S0-20) (see Figure 5.15). The three fainter stars (S0-16, S0-19, S0-20) have missing measurements that are due to insufficient image sensitivity, although they are detected in higher signal-to-noise images made from multiple nights of data (Ghez et al., 2005b). The photometry of these stars constrains the properties of a cold, geometrically-thin inactive accretion disk around Sgr A*, since in the presence of such a disk we would expect to see nearby stars significantly flaring in the NIR as they passed through and interacted with the disk, and eclipsed at other times. When a nearby star approaches such a disk we would see enhanced NIR flux from reprocessed UV and optical starlight incident on the disk (which we call a flare). Also, we would expect the disk to eclipse the star, reducing the flux from the star in varying amounts depending on the properties of the disk. The time-scales vary based on the geometry of the disk but are on the order of a year and months for the eclipses and flares, respectively (Nayakshin & Sunyaev, 2003; Cuadra et al., 2003). An optically thin disk may not fully eclipse stars, and gaps in our observations would allow different geometries of the disk to account for any one star not showing eclipses or flares as was calculated for S0-2 (Cuadra et al., 2003). However, with the ensemble of stars that we have monitored, the effects of a disk with any orientation should be evident. We constrain the NIR optical depth to be $\lesssim 0.1$. If we assume the NIR standard interstellar dust opacity at 2.2μmwhere the dust extinction is approximately $\sim 5 \times 10^{-22} cm^2$ per hydrogen atom (see Fig. 2 in Voshchinnikov 2002), we find the column density of the disc to be $\sim 2 \times 10^{20} cm^{-2}$. However, dust grains may be larger in size or non-existant in the disc (Cuadra et al., 2003; Nayakshin et al., 2004), and such constraints should therefore be approached cautiously. Regardless, the lack of observed flares or eclipses in the 7 central arcsecond sources that have known 3-dimensional orbits puts such severe constrains on the density and size of any possible disc disk around Sgr A* that such a disk is unlikely to exist.

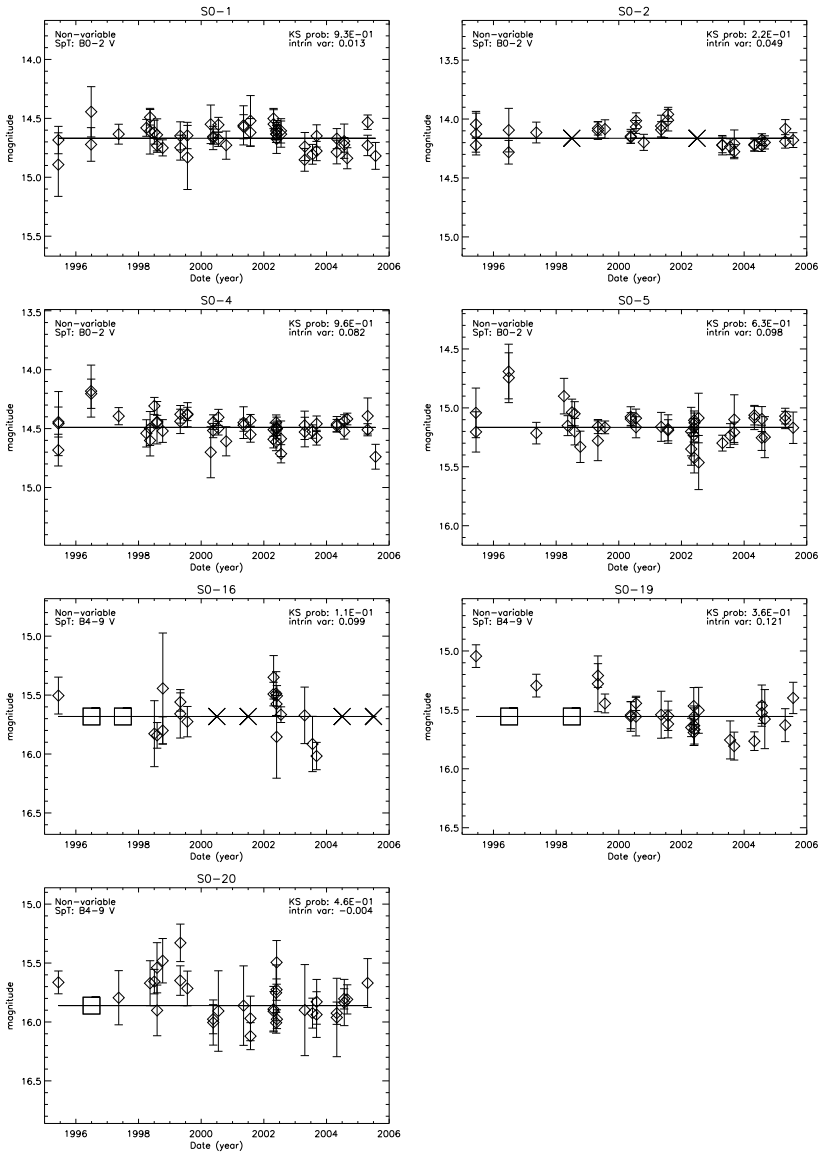

Figure 5.15 Light curves of 7 central arcsecond sources that have known 3-dimensional orbits. The X's mark observations that are rejected due to confusion with other sources, and the boxes are areas where the nightly images have missing measurements due to insufficient image sensitivity and correspond to detections in monthly averaged images. None of these stars are variable, which is evidence against the presence of a dusty disk around Sgr A*. The given intrinsic variance is expressed in magnitudes.

5.5 Summary

We use ten years of diffraction-limited K-band speckle data to determine the photometric stellar variability in the central $5'' \times 5''$ of our Galaxy. Within this study's limiting magnitude of $m_K < 16$ mag, we find 15 K-band variable stars out of 131 well-sampled stars. Among 46 stars brighter than $m_K < 14$ mag with uniform photometric uncertainties, there are 10 variable stars, suggesting a minimum variable star frequency of 23%. We find one periodic star, IRS 16SW, with a period of P=19.448$\pm$0.002 days, in agreement with Ott et al. (1999), Depoy et al. (2004), and Martins et al. (2006). Our data are consistent with an eclipsing binary and show a rise-time that is $\sim$ 1.6 times longer than the fall time and we suggest that the asymmetric light curve results from tidal deformations of the two stars in the presence of asynchronous rotation. We expect to see on the order of one eclipsing binary in our sample for conditions similar to the rest of the Galaxy, suggesting that the frequency of eclipsing binaries is not significantly increased at the Galactic center over the local neighborhood. We identify IRS 29N as a wind colliding binary based on its light curve and spectral classification. This rare object warrants further investigation to confirm its binary nature. None of the IRS 16 stars shows the classic eruptive events of LBVs, although our time baseline is too short to rule them out as LBVs. Among the remaining variable early-type stars in our sample, 3 exhibit large variations on time-scales of a year, which are either due to obscuration from mass loss events or from line of sight extinction variations. Three more stars in our sample exhibit long term variations of $\sim$5-10 yrs probably due to line of sight extinction variations due to high density streamers. Seven stars in the central arcsecond do not show photometric variations indicative of a cold geometrically thin inactive accretion disk which puts such severe constraints on the density and size of any possible disk around Sgr A* that such a disk is unlikely to exist.

5.6 Acknowledgements

The authors thank Eric Becklin, Jill Naiman and Andrea Stolte for helpful conversations and useful comments on the manuscript and an anonymous referee for a helpful review. Support for this work was provided by NSF grant AST-0406816. The W. M. Keck Observatory is operated as a scientific partnership among the California Institute of Technology, the University of California and the National Aeronautics and Space Administration. The Observatory was made possible by the generous financial support of the W. M. Keck Foundation. The authors wish to recognize and acknowledge the very significant cultural role and reverence that the summit of Mauna Kea has always had within the indigenous Hawaiian community. We are most fortunate to have the opportunity to conduct observations from this mountain.

This chapter, in full (with minor exceptions to conform to this thesis), is a reprint of "Photometric Stellar Variability in the Galactic Center", by Marc Rafelski, Andrea. M. Ghez, Seth D. Hornstein, Jessica R. Lu, & Mark Morris, published in the The Astrophysical Journal, 2007, Vol. 659, p. 1241. I was the primary investigator and author of this paper.

References

Abbott, D. C. & Conti, P. S. 1987, Annual Review of Astronomy and Astrophysics, 25, 113

Bauer, M. 2005, Astrophysics and Space Science, 296, 255

Blackwell, D. E. & Lynas-Gray, A. E. 1994, Astronomy and Astrophysics, 282, 899

Blum, R. D., Ramírez, S. V., Sellgren, K., & Olsen, K. 2003, The Astrophysical Journal, 597, 323

Blum, R. D., Sellgren, K., & Depoy, D. L. 1996a, The Astrophysical Journal, 470, 864

—. 1996b, The Astronomical Journal, 112, 1988

Christou, J. C. 1991, Astronomical Society of the Pacific, 103, 1040

Clark, J. S., Larionov, V. M., & Arkharov, A. 2005, Astronomy and Astrophysics, 435, 239

Clénet, Y., Rouan, D., Gendron, E., Lacombe, F., Lagrange, A.-M., Mouillet, D., Magnard, Y., Rousset, G., Fusco, T., Montri, J., Genzel, R., Schödel, R., Ott, T., Eckart, A., Marco, O., & Tacconi-Garman, L. 2004, Astronomy and Astrophysics, 417, L15

Cohen, R. E., Herbst, W., & Williams, E. C. 2004, The Astronomical Journal, 127, 1602

Cox, A. N. 2000, Allen's astrophysical quantities (New York: AIP Press; Springer)

Cuadra, J., Nayakshin, S., & Sunyaev, R. 2003, Astronomy and Astrophysics, 411, 405

Depoy, D. L., Pepper, J., Pogge, R. W., Stutz, A., Pinsonneault, M., & Sellgren, K. 2004, The Astrophysical Journal, 617, 1127

Depoy, D. L. & Sharp, N. A. 1991, The Astronomical Journal, 101, 1324

Diolaiti, E., Bendinelli, O., Bonaccini, D., Close, L., Currie, D., & Parmeggiani, G. 2000, Astronomy and Astrophysics Supplement, 147, 335

Djurašević, G., Rovithis-Livaniou, H., & Rovithis, P. 2000, Astronomy and Astrophysics, 364, 543

Dworetsky, M. M. 1983, Royal Astronomical Society, 203, 917

Eisenhauer, F., Genzel, R., Alexander, T., Abuter, R., Paumard, T., Ott, T., Gilbert, A., Gillessen, S., Horrobin, M., Trippe, S., Bonnet, H., Dumas, C., Hubin, N., Kaufer, A., Kissler-Patig, M., Monnet, G., Ströbele, S., Szeifert, T., Eckart, A., Schödel, R., & Zucker, S. 2005, The Astrophysical Journal, 628, 246

Figer, D. F. 2004, The Formation and Evolution of Massive Young Star Clusters, 322, 49

Figer, D. F., Gilmore, D., Kim, S. S., Morris, M., Becklin, E. E., McLean, I. S., Gilbert, A. M., Graham, J. R., Larkin, J. E., Levenson, N. A., & Teplitz, H. I. 2003, The Astrophysical Journal, 599, 1139

Genzel, R., Schödel, R., Ott, T., Eisenhauer, F., Hofmann, R., Lehnert, M., Eckart, A., Alexander, T., Sternberg, A., Lenzen, R., Clénet, Y., Lacombe, F., Rouan, D., Renzini, A., & Tacconi-Garman, L. E. 2003, The Astrophysical Journal, 594, 812

Ghez, A. M., Duchêne, G., Matthews, K., Hornstein, S. D., Tanner, A., Larkin, J., Morris, M., Becklin, E. E., Salim, S., Kremenek, T., Thompson, D., Soifer, B. T., Neugebauer, G., & McLean, I. 2003, The Astrophysical Journal, 586, L127

Ghez, A. M., Hornstein, S. D., Lu, J. R., Bouchez, A., Mignant, D. L., van Dam, M. A., Wizinowich, P., Matthews, K., Morris, M., Becklin, E. E., Campbell, R. D., Chin, J. C. Y., Hartman, S. K., Johansson, E. M., Lafon, R. E., Stomski, P. J., & Summers, D. M. 2005a, The Astrophysical Journal, 635, 1087

Ghez, A. M., Klein, B. L., Morris, M., & Becklin, E. E. 1998, The Astrophysical Journal, 509, 678

Ghez, A. M., Morris, M., Becklin, E. E., Tanner, A., & Kremenek, T. 2000, Nature, 407, 349

Ghez, A. M., Salim, S., Hornstein, S. D., Tanner, A., Lu, J. R., Morris, M., Becklin, E. E., & Duchêne, G. 2005b, The Astrophysical Journal, 620, 744

Ghez, A. M., Salim, S., Weinberg, N. N., Lu, J. R., Do, T., Dunn, J. K., Matthews, K., Morris, M. R., Yelda, S., Becklin, E. E., Kremenek, T., Milosavljevic, M., & Naiman, J. 2008, The Astrophysical Journal, 689, 1044

Gould, A. & Quillen, A. C. 2003, The Astrophysical Journal, 592, 935

Grenier, S., Gomez, A. E., Jaschek, C., Jaschek, M., & Heck, A. 1985, Astronomy and Astrophysics, 145, 331

Habing, H. J. 1996, The Astronomy and Astrophysics Review, 7, 97

Hornstein, S. 2006, PhD thesis, University of California, Los Angeles

Hornstein, S. D., Ghez, A. M., Tanner, A., Morris, M., Becklin, E. E., & Wizinowich, P. 2002, The Astrophysical Journal, 577, L9

Humphreys, R. M. & Davidson, K. 1994, Astronomical Society of the Pacific, 106, 1025

Jager, C. D. & Nieuwenhuijzen, H. 1987, Astronomy and Astrophysics, 177, 217

Krabbe, A., Genzel, R., Drapatz, S., & Rotaciuc, V. 1991, The Astrophysical Journal, 382, L19

Krabbe, A., Genzel, R., Eckart, A., Najarro, F., Lutz, D., Cameron, M., Kroker, H., Tacconi-Garman, L. E., Thatte, N., Weitzel, L., Drapatz, S., Geballe, T., Sternberg, A., & Kudritzki, R. 1995, The Astrophysical Journal Letters, 447, L95

Lafler, J. & Kinman, T. D. 1965, The Astrophysical Journal Supplement, 11, 216

Lefèvre, L., Marchenko, S. V., Lépine, S., Moffat, A. F. J., Acker, A., Harries, T. J., Annuk, K., Bohlender, D. A., Demers, H., Grosdidier, Y., Hill, G. M., Morrison, N. D., Knauth, D. C., Skalkowski, G., & Viti, S. 2005, Monthly Notices of the Royal Astronomical Society, 360, 141

Lomb, N. R. 1976, Astrophysics and Space Science, 39, 447

Lu, J. R., Ghez, A. M., Hornstein, S. D., Morris, M., & Becklin, E. E. 2005, The Astrophysical Journal, 625, L51

Lu, J. R., Ghez, A. M., Hornstein, S. D., Morris, M. R., Becklin, E. E., & Matthews, K. 2009, The Astrophysical Journal, 690, 1463

Martins, F., Trippe, S., Paumard, T., Ott, T., Genzel, R., Rauw, G., Eisenhauer, F., Gillessen, S., Maness, H., & Abuter, R. 2006, The Astrophysical Journal, 649, L103

Mason, B. D., Gies, D. R., Hartkopf, W. I., Bagnuolo, W. G., ten Brummelaar, T., & McAlister, H. A. 1998, The Astronomical Journal, 115, 821

Massey, P. 2003, Annual Review of Astronomy and Astrophysics, 41, 15

Matthews, K., Ghez, A. M., Weinberger, A. J., & Neugebauer, G. 1996, Publications of the Astronomical Society of the Pacific, 108, 615

Matthews, K. & Soifer, B. T. 1994, Infrared Astronomy with Arrays, 190, 239

Mennickent, R. E., Vogt, N., & Sterken, C. 1994, Astronomy and Astrophysics Supplment, 108, 237

Meynet, G. & Maeder, A. 2005, Astronomy and Astrophysics, 429, 581

Moffat, A. F. J., Lamontagne, R., Williams, P. M., Horn, J., & Seggewiss, W. 1987, The Astrophysical Journal, 312, 807

Moffat, A. F. J., Poitras, V., Marchenko, S. V., Shara, M. M., Zurek, D. R., Bergeron, E., & Antokhina, E. A. 2004, The Astronomical Journal, 128, 2854

Monnier, J. D., Tuthill, P. G., & Danchi, W. C. 1999, The Astrophysical Journal, 525, L97

Nayakshin, S., Cuadra, J., & Sunyaev, R. 2004, Astronomy and Astrophysics, 413, 173

Nayakshin, S. & Sunyaev, R. 2003, Monthly Notice of the Royal Astronomical Society, 343, L15

Ott, T. 2003, PhD thesis, Max-Planck-Institut für Extraterrestrische Physik

Ott, T., Eckart, A., & Genzel, R. 1999, The Astrophysical Journal, 523, 248

Paumard, T., Genzel, R., Martins, F., Nayakshin, S., Beloborodov, A. M., Levin, Y., Trippe, S., Eisenhauer, F., Ott, T., Gillessen, S., Abuter, R., Cuadra, J., Alexander, T., & Sternberg, A. 2006, The Astrophysical Journal, 643, 1011

Paumard, T., Maillard, J.-P., & Morris, M. 2004, Astronomy and Astrophysics, 426, 81

Paumard, T., Maillard, J. P., Morris, M., & Rigaut, F. 2001, Astronomy and Astrophysics, 366, 466

Pavlovski, K., Harmanec, P., Bozic, H., Koubsky, P., Hadrava, P., Kriiz, S., Ruzic, Z., & Stefl, S. 1997, Astronomy and Astrophysics Supplement, 125, 75

Peeples, M. S., Bonanos, A. Z., Depoy, D. L., Stanek, K. Z., Pepper, J., Pogge, R. W., Pinsonneault, M. H., & Sellgren, K. 2007, The Astrophysical Journal, 654, L61

Percy, J. R. & Bakos, A. G. 2001, The Publications of the Astronomical Society of the Pacific, 113, 748

Press, W., Teukolsky, S., Vetterling, W., & Flannery, B. 1992, Numerical Recipes in C Second Edition (Cambridge Univ. Press)

Reid, M. J. 1993, Annual Review of Astronomy and Astrophysics, 31, 345

Scargle, J. D. 1982, The Astrophysical Journal, 263, 835

Schödel, R., Ott, T., Genzel, R., Eckart, A., Mouawad, N., & Alexander, T. 2003, The Astrophysical Journal, 596, 1015

Simons, D. A. & Becklin, E. E. 1996, The Astronomical Journal, 111, 1908

Sterken, C. & Jaschek, C. 1996, Light Curves of Variable Stars, A Pictorial Atlas (Cambridge University Press)

Stetson, P. B. 1996, Publications of the Astronomical Society of the Pacific, 108, 851

Stothers, R. B. & Chin, C.-W. 1996, The Astrophysical Journal, 468, 842

Tamura, M., Werner, M. W., Becklin, E. E., & Phinney, E. S. 1996, The Astrophysical Journal, 467, 645

Theodossiou, E. & Danezis, E. 1991, Astrophysics and Space Science, 183, 91

Trippe, S., Martins, F., Ott, T., Paumard, T., Abuter, R., Eisenhauer, F., Gillessen, S., Genzel, R., Eckart, A., & Schödel, R. 2006, Astronomy and Astrophysics, 448, 305

Tuthill, P. G., Monnier, J. D., & Danchi, W. C. 1999, Nature, 398, 487

Vacca, W. D., Garmany, C. D., & Shull, J. M. 1996, The Astrophysical Journal, 460, 914

van der Hucht, K. A. 2001, New Astronomy Reviews, 45, 135

van der Hucht, K. A., Williams, P. M., & Morris, P. W. 2001, The Promise of the Herschel Space Observatory. Eds. G.L. Pilbratt, 460, 273

Veen, P. M., van der Hucht, K. A., Williams, P. M., Catchpole, R. M., Duijsens, M. F. J., Glass, I. S., & Gunawan, D. Y. A. S. 1998, Astronomy and Astrophysics, 339, L45

Voshchinnikov, N. V. 2002, Optics of Cosmic Dust, 1

Wegner, W. 1994, Monthly Notices of the Royal Astronomical Society, 270, 229

—. 2006, Monthly Notices of the Royal Astronomical Society, 371, 185

Welch, D. L. & Stetson, P. B. 1993, The Astronomical Journal, 105, 1813

White, R. L. & Becker, R. H. 1995, The Astrophysical Journal, 451, 352

Williams, P. M. & van der Hucht, K. A. 2000, Monthly Notices of the Royal Astronomical Society, 314, 23

Williams, P. M., van der Hucht, K. A., & Rauw, G. 2005, Proceedings of "Massive Stars and High-Energy Emission in OB Associations", 65

Williams, P. M., van der Hucht, K. A., & The, P. S. 1987, Astronomy and Astrophysics, 182, 91

Zahn, J.-P. 1977, Astronomy and Astrophysics, 57, 383

Appendix A

Completeness Corrections

Throughout the paper, we use the number of $z \sim 3$ LBGs in the UDF, $N_{\rm LBG}$. However, the number of LBGs detected depends on the depth of our images, and there are large numbers of LBGs fainter than our detection limit that are not identified. These LBGs are part of the underlying sample and contribute to C_A, $\dot{\rho}_*$, and $\Delta\dot{\rho}_*/\Delta\langle I_{\nu_0}^{obs}\rangle$. We describe our completeness corrections for each of these in the following sections.

A.1 Covering Fraction Completeness Correction

The covering fraction of LBGs depends on $N_{\rm LBG}$, and we recover the underlying covering fraction for all $z \sim 3$ LBGs by applying a completeness correction which assumes that the undetected LBGs have a similar radial surface brightness profile as the brighter detected LBGs. We acknowledge that the size of LBGs vary with brightness, but do not have measurements of its variation at these faint magnitudes, and therefore make this assumption. If the fainter LBGs were smaller, then their μ_V would be larger at smaller radii, and it would decrease the slope of the covering fraction completeness correction. This would not make much of a difference for the correction in Figure 3.5, but it could potentially have a small effect on the completeness correction in Figure 3.6.

The first step in calculating the completeness correction is determining the total number of LBGs expected in each half magnitude bin from the number counts derived from the best fit Schecter function from Reddy & Steidel (2009) in §3.3.1. Since the number counts in Figure 3.1 agree well with the number counts of the sample from Rafelski et al. (2009), we are confident that this is the appropriate number of expected LBGs. We then subtract the number of detected LBGs in each bin yielding the number of missed LBGs per half magnitude bin, $N_{j(\mathrm{mis})}$, where j is the index in the sum in equation A.1 representing the half magnitude bins. We repeat this for 20 bins from V $\sim$27 to V $\sim$37 magnitude. The results are insensitive to the faint limit, as described below.

We then determine the ratio of the flux that needs a correction for each half magnitude bin, $\mathrm{F(mag)}_j$, to the total flux of the composite LBG, $\mathrm{F_{comp}}$, such that the flux ratio is $R_j = \mathrm{F(mag)}_j/\mathrm{F_{comp}}$. For each half magnitude bin, we scale the profile by R_j, and then determine the area, A_j, that the scaled profile covers for each μ_V. The missed covering fraction, $(C_A)_{\mathrm{mis}}$, as a function of μ_V is just the sum over all half magnitude bins, namely

$$(C_A)_{\mathrm{mis}} = \sum_{j=1}^{20} A_j N_{j(\mathrm{mis})} \ . \tag{A.1}$$

We treat the completeness correction differently for atomic-dominated and molecular dominated gas. For the atomic-dominated gas, we only consider the light from the outskirts of these missed galaxies, and not the inner cores. On the other hand, for the molecular-dominated gas, we consider light from the entire LBG, making no distinction between the outskirts and the inner parts of the LBGs. In this scenario, both the cores and the outskirts are composed of molecular gas, so the cores also contribute to the surface brightness in the outskirts for each μ_V. The gold long-dashed lines in Figures 3.5 and 3.6 correspond to the covering fraction for the LBGs corrected for completeness.

We note that while $N_{j(\mathrm{mis})}$ increases steeply with increasing magnitude,

$R_{j(\mathrm{ratio})}$ decreases more steeply, and therefore the completeness correction is dominated by the bright end. To give an idea of the magnitude range of the LBGs contributing the most to the correction, we discuss the correction for the entire LBG profile here. The missed LBGs fainter than $V \sim 33$ have basically no effect, since the surface brightnesses barely overlap the area of interest. We could have truncated the completeness correction at this magnitude with no changes to our results. The amount of correction depends on the μ_V being considered, and half the completeness correction for the faintest μ_V values is due to LBGs brighter than $V \sim 31$. Additionally, those $V \lesssim 31$ LBGs only contribute to $\mu_V \gtrsim 28$. In other words, for $\mu_V \lesssim 28$, we could have truncated the completeness correction at $V \sim 31$ without any change.

Hence, the luminosity function used at the fainter magnitudes is not crucial, as those points add negligible amounts to the correction. However, if there was a significant deviation in the faint end of the luminosity function between $27 \lesssim V \lesssim 31$, it would affect our completeness corrections when considering both the cores and the outskirts. (see Figure 3.6). We note, however, that even if we only correct for completeness for missed LBGs with $V \lesssim 29$, where a drastic change in the luminosity function is unlikely, an evolution of f^* in $f(N_{H_2})$ of $\sim$40 would be needed to account for the low surface brightness emission in the outskirts of LBGs. Therefore, variations in the faint end luminosity function are not responsible for the disagreement observed in Figure 3.6. In the case of the atomic-dominated gas where we only consider the outskirts, the completeness correction is even more dominated by the brightest missed LBGs, since the fainter outskirts quickly do not overlap the μ_V of interest, making the total correction very small (see Figure 3.5).

A.2 $\dot{\rho}_*$ Completeness Correction

Our determination of $\dot{\rho}_*$ also depends on $N_{\rm LBG}$, and we use a similar completeness correction to Appendix A.1 here. We use the same formalism, using the flux ratio R_j and the number of missed LBGs, $N_{j(\rm mis)}$ as calculated there. We also once again assume that the undetected LBGs have a similar radial surface brightness profile as the brighter detected LBGs. However, this time in addition to summing over all half magnitude bins j, we also sum over all μ_V to get the total $\dot{\rho}_*$ missed due to completeness, $\dot{\rho}_{*\rm mis}$. Specifically, we find

$$\dot{\rho}_{*\rm mis} = \sum_{\mu_V} \sum_{j=1}^{20} \dot{\rho}_* \; R_j N_{j(\rm mis)} / N_{\rm LBG} \; . \tag{A.2}$$

We note that similar to Appendix A.1, this result is again not sensitive to the correction at the faint end, making the uncertainty of the luminosity function out there unimportant.

A.3 $\Delta\dot{\rho}_*$ Completeness Corrections

The determination of $\Delta\dot{\rho}_*$ depends on $N_{\rm LBG}$, which again depends on the depth of our images. These missed LBGs are part of the underlying sample and contribute to the true value of $\Delta\dot{\rho}_*$, but are not included in Figure 3.8. We recover the underlying true $\Delta\dot{\rho}_*$ for all $z \sim 3$ LBGs by applying a completeness correction similar to Appendices A.1 and A.2. We use the same formalism developed in A.1, and once again assume that the undetected LBGs have a similar radial surface brightness profile as the brighter detected LBGs. Just like in Appendix A.1, we determine the flux ratio, R_j, and the number of missed LBGs, $N_{j(\rm mis)}$, where the index j represents half magnitude bins for different missed LBGs. For each bin, we calculate the missed $\Delta\dot{\rho}_*/\Delta\langle I_{\nu_0}^{obs}\rangle$ as a function of μ_V, and then sum over the half magnitude bins to to get the final correction to be applied to $\Delta\dot{\rho}_*/\Delta\langle I_{\nu_0}^{obs}\rangle$. Specifically, we find

$$\left(\frac{\Delta\dot{\rho}_*}{\Delta\langle I_{\nu_0}^{obs}\rangle}\right)_{\rm mis} = \sum_{j=1}^{20} \frac{\Delta\dot{\rho}_*}{\Delta\langle I_{\nu_0}^{obs}\rangle} R_j N_{j({\rm mis})}/N_{\rm LBG} \ . \tag{A.3}$$

We note that similar to Appendix B.1, this result is not sensitive to the correction at the faint end, making the uncertainty of the luminosity function out there unimportant. The completeness corrected μ_V versus $\Delta\dot{\rho}_*/\Delta\langle I_{\nu_0}^{obs}\rangle$ is shown in Figure 3.9.

Appendix B

Comparison of the Subset and Full LBG Stacks

In §3.3.3 we compared the subset and full LBG samples, and found them to have similar magnitude, color, and redshift distributions. This implies that the two samples of LBGs have similar SFRs, stellar populations, and SFHs, and justifies using only the subset sample in the analysis to avoid contamination. In addition, the KS relation works the same on galaxies of different morphologies and environments, so we do not expect an effect based on sample selection. Nonetheless, for completeness we investigate how the results would differ if we had stacked the full sample of LBGs rather than the subsample. A stack of the full sample of LBGS would include contamination and different morphological areas as described in §3.3.3, and therefore these stacks yield an upper limit to the star formation occurring in the outskirts of LBGs.

We repeat the analysis for the full sample stack, and find that it yields SFR efficiencies slightly higher than discussed in §3.6.2 for the subsample stack. Specifically, the Kennicutt parameter K needs to be reduced by a factor of ~ 9 below the local value for the entire outskirt region. The slope of the surface brightness versus $\Delta\dot{\rho}_*/\Delta\langle I_{\nu_0}^{obs}\rangle$ is similar to the model $d\dot{\rho}_*/d\langle I_{\nu_0}^{obs}\rangle$, and therefore yields an

efficiency that does vary with radius. This effect is largely due to contamination from nearby galaxies, and if we repeat the analysis for half the sample including only isolated galaxies, we find a varying SFR efficiency with radius. We conclude that the correct sample to stack is the subsample stack, but a stack of the full sample does not drastically increase our SFR efficiencies. Therefore, the result of lower SFR efficiencies is robust and not due to any sample selections.

We also repeat the covering fraction analysis of §3.5.2 for the full sample stack and half sample stacks mentioned above. In both cases the SFR efficiencies of atomic-dominated gas would need to be increased by a factor of about two over the results from the subset sample stack to be compatible with the covering fraction of DLAs. Since these stacks include contamination and morphologically different galaxies, molecular-dominated gas from parts of some of these galaxies will be contributing throughout. Therefore, these results are also upper limits to the covering fraction of the atomic-dominated gas. Regardless, even with significant contamination, this analysis also indicates that our results are robust and not due to sample selections. In addition, the molecular-dominated covering fraction based on the full LBG stack is still insufficient to account for the emission in the outskirts of the LBGs.

References

Rafelski, M., Wolfe, A. M., Cooke, J., Chen, H.-W., Armandroff, T. E., & Wirth, G. D. 2009, The Astrophysical Journal, 703, 2033

Reddy, N. A. & Steidel, C. C. 2009, The Astrophysical Journal, 692, 778

Appendix C

Full Tables

Throughout the text, I included shorter versions of the tables. I include the full versions of the tables here in the appendix.

Table C.1. Catalog of u-band Objects

ID[a]	R.A.	Decl.	u (mag)[b]	S/N	Cov. ID[c]	Cov. Index[d]	Flux Ratio[e]	Distance (arcsec)[f]
1	3 32 39.723	-27 49 42.53	24.69±0.01	112.53	12	0.039	0.007	2.546
7	3 32 39.451	-27 49 42.95	25.76±0.02	49.56	10	0.413	0.112	1.138
8	3 32 39.540	-27 49 28.35	26.18±0.04	29.43	80	0.003	0.003	4.335
13	3 32 39.326	-27 49 39.06	26.71±0.05	23.76	16	0.095	0.060	2.099
14	3 32 38.467	-27 49 31.84	25.28±0.02	73.11	56	0.010	0.012	3.319
15	3 32 38.846	-27 49 39.29	28.92±0.34	0.34	22	0.159	0.591	1.800
22	3 32 38.957	-27 49 38.33	28.91±0.35	2.25	19	0.281	12.129	1.440
24	3 32 39.053	-27 49 38.76	27.34±0.08	13.27	22	0.296	0.911	1.484
33	3 32 39.179	-27 49 36.13	27.07±0.06	18.38	48	0.018	0.393	2.902
35	3 32 38.763	-27 49 36.80	27.73±0.11	9.78	19	0.026	10.179	2.880
36	3 32 39.820	-27 49 33.94	28.94±0.36	3.04	65	0.139	0.088	1.800
48	3 32 39.000	-27 49 34.59	28.11±0.16	6.08	55	0.174	5.700	1.939
55	3 32 39.042	-27 49 32.98	26.47±0.04	29.23	48	0.166	0.175	1.939
64	3 32 40.521	-27 49 32.52	27.00±0.06	17.04	50381	0.038	0.183	2.596
68	3 32 38.819	-27 49 28.43	28.59±0.27	4.17	87	0.188	0.019	1.610
76	3 32 40.482	-27 49 30.59	27.87±0.15	6.56	77	0.535	0.480	1.138
84	3 32 37.834	-27 49 29.92	28.96±0.35	0.63	50457	0.201	0.138	1.836
86	3 32 40.113	-27 49 28.09	26.55±0.05	22.31	107	0.373	0.038	1.298
89	3 32 38.182	-27 49 29.97	28.93±0.32	3.21	14	0.002	35.114	4.680
95	3 32 40.072	-27 49 26.67	26.64±0.05	21.82	101	0.216	0.312	1.610
97	3 32 40.948	-27 49 25.60	27.02±0.06	16.61	50478	0.005	0.039	3.706
99	3 32 40.730	-27 49 25.77	26.70±0.07	13.47	103	0.754	0.492	0.720
100	3 32 40.345	-27 49 23.50	26.44±0.04	29.15	140	0.017	0.032	3.097
101	3 32 39.983	-27 49 27.46	28.83±0.32	3.20	95	0.268	3.202	1.610
104	3 32 37.572	-27 49 27.61	28.56±0.36	-1.47	50477	0.571	0.261	1.018
126	3 32 37.603	-27 49 22.99	27.02±0.06	16.71	122	0.016	0.070	2.812
131	3 32 39.642	-27 49 24.25	28.97±0.35	-1.97	148	0.102	0.545	2.621
152	3 32 40.967	-27 49 23.46	27.23±0.08	11.78	163	0.443	1.289	1.298
153	3 32 39.596	-27 49 9.60	27.66±0.18	7.01	295	0.015	0.083	3.260
163	3 32 41.016	-27 49 22.46	28.64±0.32	0.06	152	0.361	0.776	1.298
166	3 32 38.530	-27 49 21.69	26.68±0.04	24.93	177	0.160	0.295	2.190
168	3 32 37.415	-27 49 20.01	25.23±0.01	96.72	267	0.012	0.116	3.319
176	3 32 38.011	-27 49 22.18	27.23±0.08	12.83	180	0.575	0.103	0.805
177	3 32 38.654	-27 49 22.15	27.39±0.08	11.78	166	0.162	3.391	2.190
178	3 32 38.659	-27 49 18.89	25.11±0.01	100.05	266	0.013	0.022	3.319
188	3 32 41.208	-27 49 21.16	27.28±0.08	11.75	179	0.209	0.376	1.484

Table C.1—Continued

ID[a]	R.A.	Decl.	u (mag)[b]	S/N	Cov. ID[c]	Cov. Index[d]	Flux Ratio[e]	Distance (arcsec)[f]
206	3 32 41.216	-27 49 18.43	24.88±0.01	128.08	232	0.029	0.017	2.596
209	3 32 38.207	-27 49 20.60	28.19±0.34	0.99	210	0.888	0.177	0.360
213	3 32 41.511	-27 49 19.90	28.86±0.34	0.60	202	0.546	0.350	1.440
221	3 32 41.431	-27 49 17.11	25.18±0.01	92.47	213	0.017	0.083	3.220
224	3 32 37.050	-27 49 17.33	24.57±0.01	170.53	230	0.211	0.271	1.800
230	3 32 36.958	-27 49 16.26	28.75±0.35	-1.97	317	0.385	0.126	1.138
235	3 32 40.914	-27 49 17.74	27.35±0.08	12.74	232	0.018	0.098	3.055
237	3 32 39.369	-27 49 17.88	28.54±0.25	4.26	216	0.010	0.099	3.415
251	3 32 36.907	-27 49 17.40	26.66±0.05	21.47	259	0.442	0.782	1.138
252	3 32 38.106	-27 49 18.49	28.81±0.33	-1.45	253	0.460	0.640	1.440
259	3 32 36.835	-27 49 16.97	28.81±0.34	-0.83	251	0.496	1.279	1.138
267	3 32 37.284	-27 49 17.27	27.42±0.10	11.37	286	0.268	0.316	2.099
268	3 32 40.218	-27 49 15.20	28.57±0.29	-0.13	283	0.463	0.537	1.080
285	3 32 38.122	-27 49 13.28	26.21±0.03	35.06	294	0.018	0.085	2.742
287	3 32 39.859	-27 49 13.97	27.12±0.07	15.09	359	0.028	0.628	2.546
295	3 32 39.581	-27 49 12.79	26.22±0.03	36.24	340	0.120	0.085	1.939
296	3 32 38.373	-27 49 15.27	28.30±0.23	4.56	312	0.552	0.266	0.720
310	3 32 41.625	-27 49 13.02	26.55±0.04	26.83	369	0.447	0.078	1.298
313	3 32 36.681	-27 49 14.68	28.94±0.34	-4.08	50784	0.279	0.535	1.836
324	3 32 38.353	-27 49 13.23	27.54±0.10	9.86	312	0.522	0.259	1.484
341	3 32 40.051	-27 49 12.66	28.91±0.34	1.14	359	0.049	1.462	2.902
344	3 32 37.573	-27 49 11.51	26.71±0.06	14.06	394	0.599	0.243	1.138
345	3 32 40.961	-27 49 12.87	27.26±0.09	12.13	371	0.485	0.110	0.805
347	3 32 41.295	-27 49 12.30	26.88±0.06	19.19	386	0.353	0.174	1.527
349	3 32 38.589	-27 49 12.89	26.97±0.06	18.11	392	0.370	0.247	1.138
355	3 32 38.806	-27 49 9.31	25.14±0.02	64.51	401	0.427	0.089	1.018
357	3 32 41.499	-27 49 11.26	26.77±0.07	16.65	380	0.622	0.139	1.080
359	3 32 39.902	-27 49 11.40	28.96±0.35	-0.58	341	0.050	0.684	2.902
366	3 32 42.078	-27 49 11.58	28.75±0.35	-3.60	396	0.734	0.480	1.080
367	3 32 36.296	-27 49 11.11	26.78±0.05	21.45	381	0.252	0.364	1.610
379	3 32 36.513	-27 49 11.60	28.96±0.34	1.56	381	0.040	0.990	2.621
381	3 32 36.339	-27 49 12.40	28.97±0.36	1.98	367	0.266	2.749	1.610
388	3 32 41.416	-27 49 10.78	27.26±0.11	8.89	386	0.515	0.208	0.805
403	3 32 36.352	-27 49 9.73	26.45±0.03	31.16	367	0.221	0.908	1.527
405	3 32 37.324	-27 49 10.05	28.99±0.35	-1.03	387	0.085	0.319	2.036
407	3 32 38.566	-27 49 9.06	28.93±0.36	-2.05	408	0.297	0.281	1.298

Table C.1—Continued

ID[a]	R.A.	Decl.	u (mag)[b]	S/N	Cov. ID[c]	Cov. Index[d]	Flux Ratio[e]	Distance (arcsec)[f]
408	3 32 38.650	-27 49 9.78	28.14±0.17	6.11	355	0.304	33.016	2.546
409	3 32 41.361	-27 49 9.58	28.89±0.34	-1.93	388	0.391	1.322	1.800
412	3 32 38.790	-27 49 7.62	28.69±0.34	-1.59	489	0.298	1.154	1.484
423	3 32 39.163	-27 48 44.66	22.98±0.00	334.69	949	0.006	0.001	5.315
424	3 32 36.623	-27 49 6.35	26.12±0.03	36.06	477	0.183	0.055	1.800
428	3 32 40.031	-27 49 6.53	25.55±0.02	67.94	522	0.038	0.121	2.621
435	3 32 40.230	-27 49 8.99	27.88±0.13	8.41	480	0.061	0.857	2.742
446	3 32 39.408	-27 49 6.49	25.69±0.02	53.95	533	0.075	0.840	2.190
461	3 32 41.230	-27 49 7.11	27.59±0.10	10.68	517	0.048	0.465	3.076
475	3 32 38.857	-27 49 6.26	25.99±0.04	28.03	489	0.792	0.383	0.720
480	3 32 40.292	-27 49 6.71	27.94±0.20	4.71	508	0.701	0.325	0.805
500	3 32 37.293	-27 49 6.26	28.98±0.35	-2.93	548	0.004	0.364	4.025
501	3 32 40.262	-27 49 0.09	25.06±0.01	81.36	582	0.217	0.217	1.800
503	3 32 42.150	-27 49 3.13	26.78±0.05	20.91	591	0.059	0.062	2.546
513	3 32 36.019	-27 49 4.60	28.81±0.32	-0.90	524	0.328	0.223	1.298
518	3 32 40.622	-27 49 3.54	26.59±0.05	22.90	597	0.487	0.138	0.720
520	3 32 41.717	-27 49 5.37	28.10±0.16	6.79	478	0.231	0.428	1.484
521	3 32 40.786	-27 49 4.35	26.71±0.05	21.30	512	0.242	0.199	1.138
522	3 32 40.083	-27 49 4.05	28.80±0.32	-3.30	612	0.147	0.615	1.800
529	3 32 36.816	-27 49 5.19	28.35±0.34	-2.00	531	0.829	0.436	0.509
533	3 32 39.379	-27 49 4.40	26.16±0.03	37.31	584	0.288	0.062	2.036
542	3 32 41.071	-27 48 53.01	23.47±0.00	262.73	807	0.027	0.002	3.097
551	3 32 41.597	-27 49 1.83	25.63±0.02	62.72	543	0.004	0.043	3.600
552	3 32 35.682	-27 49 3.78	27.83±0.21	4.87	558	0.685	0.327	0.805
559	3 32 39.271	-27 49 2.66	27.65±0.17	5.88	584	0.798	0.166	0.509
566	3 32 42.764	-27 49 0.99	26.52±0.04	22.47	607	0.307	0.372	1.484
582	3 32 40.363	-27 49 1.08	27.28±0.08	14.07	501	0.350	4.612	1.800
599	3 32 40.900	-27 49 1.75	28.96±0.35	-1.96	601	0.022	0.204	3.220
600	3 32 39.015	-27 49 1.80	27.54±0.10	10.79	637	0.063	3.454	2.546
602	3 32 38.463	-27 49 2.49	27.05±0.19	5.20	613	0.954	0.362	0.360
604	3 32 39.951	-27 49 2.12	28.81±0.34	0.40	628	0.412	0.224	1.440
607	3 32 42.735	-27 49 2.29	28.46±0.23	4.67	566	0.390	2.689	1.484
631	3 32 40.085	-27 49 1.19	28.85±0.36	-2.47	612	0.500	0.487	1.080
636	3 32 37.764	-27 48 59.51	27.52±0.12	8.24	714	0.568	0.139	0.720
637	3 32 39.004	-27 48 59.56	28.26±0.19	5.80	756	0.084	0.028	1.836
643	3 32 42.314	-27 49 0.57	27.74±0.11	9.49	691	0.175	0.357	1.527

Table C.1—Continued

ID[a]	R.A.	Decl.	u (mag)[b]	S/N	Cov. ID[c]	Cov. Index[d]	Flux Ratio[e]	Distance (arcsec)[f]
647	3 32 36.212	-27 49 0.68	27.78±0.15	6.50	649	0.655	0.281	0.720
648	3 32 38.575	-27 48 58.68	26.43±0.04	29.64	613	0.004	0.067	4.105
656	3 32 39.473	-27 48 55.29	25.88±0.03	39.65	719	0.423	0.373	1.138
657	3 32 42.187	-27 48 59.64	26.02±0.03	34.89	691	0.645	0.193	0.805
662	3 32 41.882	-27 48 53.83	23.59±0.00	364.31	887	0.048	0.006	2.812
666	3 32 39.903	-27 48 58.94	26.33±0.03	33.02	700	0.153	0.110	2.190
669	3 32 36.365	-27 49 0.02	28.07±0.15	7.20	647	0.086	0.913	2.277
674	3 32 41.903	-27 48 58.95	28.74±0.29	3.41	657	0.004	1.425	4.380
679	3 32 37.031	-27 48 57.35	25.50±0.02	67.79	725	0.033	0.026	2.742
697	3 32 35.276	-27 48 57.23	26.89±0.06	17.93	51275	0.031	0.125	2.902
702	3 32 42.787	-27 48 56.87	28.38±0.21	5.04	704	0.092	1.150	2.277
703	3 32 41.624	-27 48 56.58	25.76±0.02	58.09	736	0.163	0.046	1.836
704	3 32 42.932	-27 48 57.44	26.30±0.03	35.57	683	0.018	0.092	2.742
711	3 32 35.570	-27 48 58.20	27.32±0.08	13.77	782	0.080	0.160	2.277
719	3 32 39.448	-27 48 56.45	26.41±0.04	23.21	656	0.466	2.681	1.138
726	3 32 38.259	-27 48 57.03	27.78±0.12	8.73	779	0.167	0.172	1.610
731	3 32 41.559	-27 48 48.03	25.61±0.02	53.16	881	0.034	0.094	3.220
732	3 32 36.256	-27 48 58.16	28.98±0.35	1.25	669	0.043	0.820	2.305
733	3 32 40.953	-27 48 56.79	26.04±0.03	35.50	760	0.599	0.061	0.805
734	3 32 41.354	-27 48 57.54	26.94±0.06	19.44	687	0.261	0.165	1.527
735	3 32 35.533	-27 48 55.58	26.37±0.04	25.88	793	0.405	0.101	1.138
741	3 32 38.937	-27 48 56.76	28.86±0.35	-3.18	756	0.245	0.072	1.610
754	3 32 41.078	-27 48 57.08	27.60±0.10	10.51	733	0.125	5.916	2.190
766	3 32 39.777	-27 48 56.57	28.18±0.17	6.40	744	0.218	0.626	1.527
769	3 32 37.881	-27 48 53.12	25.33±0.02	65.97	857	0.303	0.259	1.484
772	3 32 40.486	-27 48 54.32	28.85±0.34	-0.48	803	0.194	0.283	1.836
776	3 32 37.753	-27 48 56.15	27.39±0.08	12.52	829	0.012	0.200	3.396
778	3 32 36.027	-27 48 54.82	25.63±0.02	65.81	761	0.005	0.054	3.894
784	3 32 36.887	-27 48 53.91	27.37±0.10	9.69	808	0.357	0.134	1.080
791	3 32 35.352	-27 48 54.56	27.29±0.10	11.09	831	0.339	0.063	1.298
794	3 32 38.019	-27 48 55.11	26.96±0.06	18.33	829	0.269	0.170	1.298
797	3 32 35.975	-27 48 50.40	22.81±0.00	740.46	975	0.021	0.013	3.097
817	3 32 36.958	-27 48 52.81	26.52±0.04	25.14	784	0.355	0.912	1.527
830	3 32 42.323	-27 48 53.11	26.04±0.02	45.77	879	0.058	0.110	2.277
833	3 32 38.002	-27 48 53.49	27.32±0.09	11.68	866	0.325	0.400	1.484
838	3 32 36.465	-27 48 52.75	27.57±0.10	10.64	915	0.107	0.087	2.415

Table C.1—Continued

ID[a]	R.A.	Decl.	u (mag)[b]	S/N	Cov. ID[c]	Cov. Index[d]	Flux Ratio[e]	Distance (arcsec)[f]
841	3 32 35.319	-27 48 53.51	27.34±0.09	12.21	791	0.368	2.506	1.138
853	3 32 38.199	-27 48 49.46	26.20±0.03	33.28	918	0.274	0.496	1.800
857	3 32 37.886	-27 48 51.83	25.69±0.02	53.83	769	0.412	3.856	1.484
862	3 32 41.399	-27 48 53.40	29.03±0.36	-0.07	807	0.038	0.629	2.902
865	3 32 39.673	-27 48 50.61	28.86±0.36	-0.44	952	0.132	0.044	2.415
870	3 32 40.168	-27 48 52.65	27.98±0.14	7.46	798	0.072	0.385	2.277
872	3 32 38.394	-27 48 51.91	27.69±0.16	6.55	890	0.740	0.169	0.720
879	3 32 42.162	-27 48 52.42	28.14±0.16	6.60	887	0.116	0.395	2.190
881	3 32 41.378	-27 48 49.48	28.79±0.34	1.60	731	0.042	10.589	3.220
883	3 32 40.818	-27 48 52.30	27.10±0.06	16.30	542	0.088	321.899	3.671
895	3 32 39.335	-27 48 51.99	27.75±0.25	4.27	891	0.945	0.325	0.805
898	3 32 38.961	-27 48 49.50	26.70±0.05	23.58	423	0.009	408.808	5.692
900	3 32 44.435	-27 48 18.99	23.01±0.00	520.58	2222	0.000	0.001	6.440
901	3 32 40.363	-27 48 46.59	24.71±0.01	143.09	1071	0.210	0.037	1.800
906	3 32 43.435	-27 48 51.33	29.03±0.36	1.33	750	0.000	0.501	7.200
911	3 32 35.057	-27 48 44.36	27.58±0.11	11.07	1220	0.001	0.006	4.320
916	3 32 40.690	-27 48 49.56	27.58±0.12	8.46	944	0.462	0.903	1.138
918	3 32 38.304	-27 48 48.41	26.71±0.06	18.33	958	0.540	0.133	1.298
926	3 32 35.689	-27 48 49.96	27.45±0.09	10.49	976	0.372	0.328	1.138
941	3 32 42.935	-27 48 48.67	27.35±0.08	12.97	998	0.112	0.215	1.939
944	3 32 40.763	-27 48 49.15	27.84±0.14	7.29	916	0.498	1.107	1.138
951	3 32 42.482	-27 48 49.50	28.90±0.34	-0.50	914	0.306	0.836	1.484
955	3 32 42.358	-27 48 48.45	28.30±0.23	4.74	987	0.549	0.234	1.138
966	3 32 39.938	-27 48 46.42	27.21±0.07	14.21	1089	0.080	0.127	2.305
968	3 32 37.535	-27 48 38.94	22.67±0.00	600.96	1142	0.012	0.003	3.618
969	3 32 43.280	-27 48 48.62	27.84±0.15	7.10	963	0.500	0.696	1.138
973	3 32 36.808	-27 48 48.36	27.72±0.11	9.53	817	0.000	1.116	5.154
975	3 32 35.856	-27 48 47.99	28.81±0.33	-0.55	976	0.118	0.389	2.415
985	3 32 38.007	-27 48 48.34	28.87±0.33	-0.44	1004	0.111	0.194	2.190
997	3 32 40.940	-27 48 46.94	27.75±0.11	9.59	972	0.020	0.170	3.097
1000	3 32 36.747	-27 48 43.51	24.32±0.01	197.55	1188	0.035	0.016	2.546
1003	3 32 35.607	-27 48 46.41	27.84±0.13	7.36	1037	0.218	0.409	2.277
1006	3 32 41.859	-27 48 45.80	26.53±0.04	28.32	1049	0.051	1.996	2.160
1016	3 32 43.524	-27 48 45.54	26.92±0.05	19.95	963	0.002	0.322	4.394
1018	3 32 36.489	-27 48 45.94	28.74±0.30	3.38	1014	0.083	0.281	1.800
1025	3 32 43.039	-27 48 45.08	26.23±0.04	30.46	1052	0.422	0.997	1.018

Table C.1—Continued

ID[a]	R.A.	Decl.	u (mag)[b]	S/N	Cov. ID[c]	Cov. Index[d]	Flux Ratio[e]	Distance (arcsec)[f]
1041	3 32 39.437	-27 48 38.84	25.79±0.02	47.18	1274	0.006	0.027	3.877
1044	3 32 35.447	-27 48 45.84	28.31±0.35	-1.99	1037	0.876	0.494	0.360
1049	3 32 41.854	-27 48 43.39	26.53±0.04	27.98	1006	0.048	0.501	2.160
1052	3 32 43.077	-27 48 44.24	26.45±0.04	22.94	1025	0.438	1.003	1.018
1057	3 32 43.180	-27 48 42.28	26.10±0.03	34.65	1052	0.097	0.393	2.596
1058	3 32 43.109	-27 48 45.37	28.83±0.36	1.14	1025	0.438	2.602	1.138
1063	3 32 37.680	-27 48 43.79	27.24±0.07	14.63	1151	0.095	0.158	2.036
1072	3 32 37.444	-27 48 45.21	28.25±0.19	5.68	1091	0.214	1.578	1.610
1088	3 32 42.599	-27 48 40.07	27.02±0.07	15.79	1087	0.000	0.037	5.014
1091	3 32 37.499	-27 48 43.90	28.25±0.19	5.27	1072	0.203	0.634	1.610
1095	3 32 39.598	-27 48 42.14	28.96±0.36	-1.00	1181	0.162	0.159	1.610
1105	3 32 38.600	-27 48 42.58	27.10±0.06	17.46	1180	0.038	0.120	2.596
1106	3 32 43.731	-27 48 42.17	26.92±0.05	19.50	1016	0.001	0.747	4.582
1107	3 32 41.102	-27 48 43.72	29.02±0.36	-8.18	1182	0.020	0.369	2.812
1112	3 32 40.669	-27 48 37.10	27.50±0.13	7.15	1231	0.022	0.060	3.097
1120	3 32 37.976	-27 48 41.29	28.90±0.34	-3.46	1113	0.045	0.244	2.160
1160	3 32 42.139	-27 48 40.41	26.59±0.04	26.70	1205	0.210	0.513	1.610
1174	3 32 36.281	-27 48 41.52	28.97±0.35	1.11	1206	0.146	0.353	2.099
1189	3 32 36.398	-27 48 39.14	26.34±0.03	33.72	1291	0.044	0.224	2.596
1205	3 32 42.098	-27 48 38.90	27.13±0.07	14.69	1160	0.200	1.950	1.610
1217	3 32 43.312	-27 48 39.93	28.81±0.30	3.60	1057	0.036	4.775	3.055
1236	3 32 38.772	-27 48 38.91	28.39±0.23	4.42	1219	0.479	0.401	1.298
1242	3 32 41.375	-27 48 35.20	27.27±0.09	11.25	1270	0.017	0.107	3.055
1253	3 32 35.103	-27 48 38.09	28.83±0.33	-2.03	1228	0.265	0.275	1.527
1265	3 32 40.189	-27 48 38.31	28.94±0.34	1.41	1190	0.001	0.560	4.830
1266	3 32 34.821	-27 48 35.48	25.12±0.01	100.26	1383	0.054	0.120	2.546
1267	3 32 38.522	-27 48 38.32	27.37±0.09	12.37	1269	0.318	1.345	1.484
1269	3 32 38.606	-27 48 37.63	26.39±0.04	29.48	1267	0.329	0.743	1.484
1273	3 32 38.146	-27 48 37.98	29.03±0.37	0.27	1320	0.121	0.676	1.610
1285	3 32 39.861	-27 48 37.25	27.81±0.12	8.61	1274	0.039	0.261	2.902
1287	3 32 38.726	-27 48 37.02	28.85±0.33	2.41	1269	0.169	2.407	1.939
1291	3 32 36.311	-27 48 37.06	26.65±0.04	26.03	1338	0.193	0.202	1.527
1299	3 32 44.599	-27 48 35.88	27.26±0.07	15.26	1352	0.039	0.033	2.880
1316	3 32 37.189	-27 48 33.81	25.58±0.02	59.73	1365	0.172	0.022	1.800
1320	3 32 38.183	-27 48 36.20	28.92±0.34	3.13	1273	0.117	1.480	1.610
1332	3 32 33.961	-27 48 35.86	27.14±0.07	14.11	1355	0.442	0.221	1.080

Table C.1—Continued

ID[a]	R.A.	Decl.	u (mag)[b]	S/N	Cov. ID[c]	Cov. Index[d]	Flux Ratio[e]	Distance (arcsec)[f]
1344	3 32 36.879	-27 48 32.20	25.45±0.02	73.32	1458	0.224	0.035	1.484
1354	3 32 38.911	-27 48 34.91	28.92±0.35	2.59	1429	0.273	0.104	1.484
1358	3 32 33.185	-27 48 33.62	26.75±0.05	20.06	51644	0.405	2.072	1.800
1362	3 32 44.279	-27 48 33.56	26.81±0.05	18.82	1415	0.077	0.228	2.160
1375	3 32 33.014	-27 48 29.39	24.73±0.01	115.61	1426	0.276	0.438	1.484
1383	3 32 34.698	-27 48 33.84	28.94±0.35	-1.99	1266	0.060	8.340	2.546
1386	3 32 35.231	-27 48 33.90	28.93±0.35	0.20	1275	0.002	0.255	4.025
1396	3 32 42.520	-27 48 32.21	28.47±0.32	1.77	1419	0.498	0.363	1.138
1403	3 32 42.578	-27 48 33.57	28.74±0.35	1.22	1374	0.395	0.722	1.138
1414	3 32 36.849	-27 48 33.75	29.01±0.37	-3.32	1344	0.209	16.477	1.939
1416	3 32 37.715	-27 48 31.71	25.64±0.02	62.17	1531	0.255	0.154	1.484
1421	3 32 41.678	-27 48 29.69	25.45±0.02	71.77	1682	0.009	0.052	3.319
1426	3 32 33.052	-27 48 30.81	25.13±0.01	87.79	1375	0.347	2.285	1.484
1428	3 32 37.258	-27 48 31.54	25.30±0.01	82.69	1509	0.082	0.281	2.190
1430	3 32 43.289	-27 48 33.06	27.92±0.13	8.01	1492	0.016	0.318	3.220
1440	3 32 35.742	-27 48 31.58	28.75±0.34	2.86	1529	0.474	0.234	1.018
1446	3 32 39.182	-27 48 32.30	28.73±0.31	-3.14	1412	0.103	0.350	1.800
1448	3 32 36.457	-27 48 32.15	28.35±0.33	0.97	1487	0.798	0.306	0.509
1449	3 32 43.577	-27 48 32.37	27.43±0.09	11.57	1492	0.262	0.375	1.610
1453	3 32 38.687	-27 48 29.27	27.18±0.07	13.21	1662	0.055	0.392	2.415
1454	3 32 40.391	-27 48 29.48	26.60±0.04	24.60	1603	0.052	0.047	2.520
1469	3 32 35.028	-27 48 30.72	25.35±0.01	76.70	1576	0.203	0.089	1.298
1476	3 32 37.428	-27 48 31.40	27.76±0.12	9.11	1428	0.078	5.229	2.546
1477	3 32 39.698	-27 48 31.19	27.04±0.06	14.98	1526	0.044	0.222	2.880
1478	3 32 38.400	-27 48 29.00	26.44±0.04	26.36	1593	0.308	0.063	1.298
1481	3 32 39.986	-27 48 30.61	26.41±0.03	31.27	1477	0.003	0.443	4.380
1494	3 32 36.249	-27 48 31.39	28.31±0.20	5.12	1559	0.158	2.231	1.800
1499	3 32 44.085	-27 48 30.38	27.55±0.18	5.60	1568	0.819	0.336	0.509
1509	3 32 37.224	-27 48 29.43	27.45±0.09	10.27	1665	0.135	0.142	2.099
1531	3 32 37.736	-27 48 30.27	26.84±0.05	19.33	1416	0.263	6.480	1.484
1551	3 32 40.330	-27 48 26.69	25.38±0.02	72.33	1668	0.100	0.270	2.520
1559	3 32 36.238	-27 48 29.63	28.78±0.34	1.15	1597	0.515	0.463	1.080
1564	3 32 39.539	-27 48 28.46	28.95±0.36	3.00	1702	0.249	0.031	1.527
1571	3 32 44.665	-27 48 28.38	26.54±0.04	26.31	1518	0.001	0.125	4.610
1589	3 32 42.531	-27 48 28.04	26.62±0.05	21.15	1607	0.394	1.083	1.440
1592	3 32 41.968	-27 48 28.68	26.51±0.04	25.62	1640	0.617	0.495	1.610

Table C.1—Continued

ID[a]	R.A.	Decl.	u (mag)[b]	S/N	Cov. ID[c]	Cov. Index[d]	Flux Ratio[e]	Distance (arcsec)[f]
1597	3 32 36.316	-27 48 29.43	28.30±0.24	4.36	1540	0.471	0.966	1.018
1607	3 32 42.614	-27 48 28.12	26.22±0.03	34.80	1589	0.451	0.923	1.440
1612	3 32 37.397	-27 48 27.42	26.89±0.05	18.76	1718	0.023	0.826	2.742
1616	3 32 35.940	-27 48 28.82	28.93±0.34	2.62	1529	0.027	0.437	3.055
1619	3 32 42.778	-27 48 27.44	25.68±0.02	59.01	1607	0.068	0.492	2.277
1626	3 32 38.354	-27 48 25.70	25.85±0.02	41.99	1727	0.366	0.810	1.018
1640	3 32 42.062	-27 48 28.22	26.64±0.08	13.03	1673	0.803	0.156	0.509
1650	3 32 39.891	-27 48 26.69	28.88±0.35	-4.40	1753	0.177	0.568	1.800
1662	3 32 38.763	-27 48 27.13	28.95±0.37	-0.55	1738	0.077	1.951	2.036
1666	3 32 41.322	-27 48 21.17	24.21±0.01	181.27	1888	0.206	0.054	1.800
1668	3 32 40.482	-27 48 26.54	25.47±0.01	75.34	1551	0.122	3.709	2.520
1678	3 32 36.447	-27 48 26.99	26.88±0.05	18.47	1637	0.131	0.197	1.836
1681	3 32 37.201	-27 48 25.91	26.05±0.04	29.60	1763	0.801	0.353	0.720
1683	3 32 43.051	-27 48 27.30	27.37±0.08	12.98	1674	0.019	0.243	2.902
1693	3 32 37.874	-27 48 26.73	26.70±0.04	24.67	1751	0.123	0.262	1.939
1718	3 32 37.332	-27 48 24.70	28.74±0.31	-0.80	1763	0.141	0.651	1.836
1720	3 32 32.743	-27 48 25.42	27.69±0.11	9.30	1830	0.141	2.164	1.836
1722	3 32 35.252	-27 48 25.78	28.98±0.36	1.53	1792	0.076	0.260	2.305
1725	3 32 33.105	-27 48 24.93	27.40±0.09	12.42	1814	0.133	0.358	1.800
1727	3 32 38.408	-27 48 24.68	27.23±0.08	13.90	1626	0.434	1.235	1.018
1732	3 32 33.113	-27 48 23.05	26.61±0.05	21.65	1814	0.355	0.237	1.484
1738	3 32 38.854	-27 48 25.42	27.31±0.08	14.44	1662	0.088	0.513	2.036
1739	3 32 42.132	-27 48 24.83	26.82±0.05	20.86	1673	0.023	0.072	2.902
1753	3 32 39.819	-27 48 25.28	28.49±0.35	0.84	1771	0.888	0.354	0.805
1774	3 32 41.540	-27 48 24.43	26.29±0.03	31.19	1780	0.361	0.099	1.138
1775	3 32 42.826	-27 48 23.45	25.97±0.03	38.69	1907	0.451	0.207	1.018
1787	3 32 34.594	-27 48 23.87	27.83±0.13	7.61	1938	0.211	0.229	1.800
1789	3 32 38.927	-27 48 19.57	24.86±0.01	106.78	1904	0.013	0.175	4.025
1809	3 32 35.050	-27 48 23.21	28.90±0.36	0.56	1792	0.179	0.054	2.036
1810	3 32 45.038	-27 48 24.31	27.40±0.10	11.29	1851	0.541	0.249	1.298
1814	3 32 33.028	-27 48 23.55	27.81±0.13	8.04	1732	0.456	4.218	1.484
1830	3 32 32.750	-27 48 23.62	26.68±0.04	23.69	1720	0.138	0.462	1.836
1849	3 32 33.379	-27 48 22.50	27.32±0.10	10.60	1912	0.629	0.084	1.018
1858	3 32 40.569	-27 48 23.05	28.86±0.32	1.52	1788	0.113	0.683	2.415
1859	3 32 45.329	-27 48 22.30	28.82±0.33	-1.47	1985	0.075	0.121	2.277
1874	3 32 43.719	-27 48 20.77	25.65±0.02	52.01	1942	0.110	0.096	2.036

Table C.1—Continued

ID[a]	R.A.	Decl.	u (mag)[b]	S/N	Cov. ID[c]	Cov. Index[d]	Flux Ratio[e]	Distance (arcsec)[f]
1880	3 32 38.673	-27 48 21.90	28.36±0.28	3.85	1981	0.703	0.121	0.805
1881	3 32 34.126	-27 48 22.62	28.41±0.34	-0.09	1885	0.804	0.330	0.509
1888	3 32 41.199	-27 48 21.23	28.57±0.34	-0.74	1947	0.615	0.186	0.805
1889	3 32 41.572	-27 48 22.14	26.90±0.06	17.39	1995	0.459	0.094	1.080
1898	3 32 33.155	-27 48 21.65	26.70±0.05	22.87	1732	0.282	0.721	1.484
1904	3 32 38.698	-27 48 17.58	25.97±0.03	41.56	2280	0.049	0.050	2.621
1905	3 32 36.285	-27 48 19.99	25.63±0.02	57.06	1977	0.062	0.056	2.415
1922	3 32 36.702	-27 48 20.73	26.54±0.05	22.81	1936	0.528	0.441	0.805
1940	3 32 33.993	-27 48 20.84	28.79±0.36	0.97	1982	0.534	0.106	0.805
1955	3 32 37.789	-27 48 20.64	27.13±0.07	13.64	2004	0.354	0.199	1.836
1960	3 32 35.964	-27 48 11.88	24.85±0.01	117.53	2477	0.094	0.003	2.190
1971	3 32 41.944	-27 47 57.53	21.94±0.00	834.03	2873	0.008	0.005	4.394
1992	3 32 37.972	-27 48 20.60	27.24±0.08	13.99	2060	0.332	0.352	1.527
2007	3 32 42.931	-27 48 19.26	27.37±0.09	11.56	2087	0.393	1.425	1.138
2012	3 32 35.912	-27 48 17.26	26.92±0.07	15.13	2211	0.304	0.024	1.484
2017	3 32 33.006	-27 48 18.74	28.66±0.28	3.76	2139	0.209	0.142	1.610
2032	3 32 37.612	-27 48 19.47	27.54±0.10	10.03	1976	0.365	0.623	1.484
2034	3 32 36.588	-27 48 18.75	26.58±0.04	26.46	2070	0.111	0.160	2.190
2042	3 32 39.608	-27 48 19.08	27.09±0.08	12.39	2080	0.572	0.195	0.805
2044	3 32 36.789	-27 48 19.53	28.04±0.15	6.60	1922	0.222	3.047	2.036
2045	3 32 33.305	-27 48 17.69	27.22±0.08	12.37	2199	0.482	0.188	1.018
2087	3 32 43.006	-27 48 18.60	28.87±0.36	-0.76	2007	0.367	0.702	1.138
2088	3 32 36.971	-27 48 18.66	28.43±0.21	5.13	2044	0.031	1.226	2.621
2093	3 32 40.797	-27 48 18.29	28.32±0.32	0.90	2101	0.794	0.449	0.720
2102	3 32 45.501	-27 48 17.64	28.89±0.33	-1.25	2205	0.017	0.237	3.319
2104	3 32 32.710	-27 48 14.88	26.50±0.05	21.96	2316	0.498	0.109	1.018
2107	3 32 45.780	-27 48 12.89	25.47±0.02	72.89	52796	0.004	0.011	3.564
2162	3 32 35.701	-27 48 15.48	24.71±0.01	136.32	2202	0.422	0.047	1.138
2170	3 32 41.203	-27 48 16.41	26.79±0.05	20.23	2061	0.063	1.985	3.260
2174	3 32 42.327	-27 48 16.60	26.41±0.04	28.52	2230	0.348	0.136	1.610
2189	3 32 40.575	-27 48 13.37	27.34±0.08	12.90	2392	0.079	0.041	2.160
2201	3 32 33.989	-27 48 14.69	25.43±0.01	76.63	2265	0.300	0.089	1.484
2215	3 32 33.084	-27 48 13.02	25.76±0.02	51.77	2241	0.066	0.358	2.190
2228	3 32 35.860	-27 48 15.80	28.80±0.34	-0.40	2211	0.375	0.281	1.298
2240	3 32 33.781	-27 48 14.36	25.79±0.02	53.86	2265	0.295	0.070	1.440
2241	3 32 33.054	-27 48 15.18	27.34±0.08	14.05	2215	0.085	2.792	2.190

Table C.1—Continued

ID[a]	R.A.	Decl.	u (mag)[b]	S/N	Cov. ID[c]	Cov. Index[d]	Flux Ratio[e]	Distance (arcsec)[f]
2245	3 32 37.068	-27 48 14.53	27.26±0.08	14.68	2333	0.010	0.668	3.546
2248	3 32 39.315	-27 48 14.78	26.49±0.04	24.66	2331	0.816	0.110	0.805
2265	3 32 33.885	-27 48 14.52	28.77±0.32	-0.32	2201	0.280	11.281	1.484
2267	3 32 35.446	-27 48 14.39	26.49±0.04	29.18	2162	0.006	3.955	4.105
2281	3 32 43.380	-27 48 14.37	27.38±0.11	9.65	2274	0.698	0.306	1.080
2290	3 32 44.793	-27 48 13.23	26.77±0.05	22.72	2242	0.063	0.196	1.939
2291	3 32 39.443	-27 48 13.41	28.34±0.32	2.54	2347	0.974	0.407	0.509
2293	3 32 42.494	-27 48 14.46	28.96±0.35	-3.69	2340	0.099	2.790	1.939
2306	3 32 39.908	-27 48 13.46	28.66±0.30	3.37	2416	0.382	0.275	1.018
2322	3 32 39.220	-27 47 58.37	26.10±0.04	34.32	3216	0.022	0.003	3.618
2329	3 32 36.888	-27 48 12.07	27.26±0.09	12.10	2333	0.381	0.670	1.298
2332	3 32 43.549	-27 48 11.27	27.54±0.10	10.26	2391	0.007	0.098	3.894
2333	3 32 36.853	-27 48 13.09	27.22±0.08	13.39	2329	0.386	1.493	1.298
2340	3 32 42.458	-27 48 12.47	26.60±0.04	23.66	2476	0.257	0.117	1.800
2350	3 32 36.385	-27 48 12.03	28.74±0.34	0.27	2358	0.374	1.434	1.440
2358	3 32 36.373	-27 48 13.21	26.53±0.04	26.13	2350	0.421	0.697	1.440
2387	3 32 35.750	-27 47 58.85	26.31±0.05	25.70	3320	0.020	0.002	3.600
2414	3 32 33.065	-27 48 7.54	28.80±0.36	0.77	2667	0.181	0.055	1.836
2415	3 32 44.743	-27 48 11.79	26.69±0.04	24.65	2290	0.202	1.915	1.610
2445	3 32 38.693	-27 48 10.40	27.25±0.10	9.74	2480	0.359	0.119	1.138
2461	3 32 41.598	-27 48 8.11	26.10±0.03	36.99	2669	0.167	0.068	1.800
2462	3 32 37.103	-27 48 3.92	25.82±0.03	43.28	2925	0.083	0.027	2.742
2463	3 32 39.403	-27 48 9.84	26.88±0.05	20.23	2634	0.060	0.029	2.099
2468	3 32 35.402	-27 48 10.56	28.65±0.33	0.98	2530	0.577	0.345	1.018
2499	3 32 41.560	-27 48 9.92	27.89±0.14	7.46	2461	0.153	4.699	1.836
2516	3 32 44.768	-27 48 8.96	28.31±0.20	5.18	2602	0.329	0.411	1.484
2518	3 32 35.756	-27 48 9.05	28.88±0.35	-3.59	2656	0.245	0.190	1.527
2525	3 32 43.591	-27 48 4.71	24.70±0.01	135.24	2765	0.119	0.021	1.939
2526	3 32 32.695	-27 48 9.88	26.46±0.03	30.77	2675	0.104	0.097	1.939
2538	3 32 41.742	-27 48 9.69	27.46±0.09	10.54	2426	0.126	0.473	1.939
2540	3 32 42.302	-27 48 9.69	28.87±0.33	-0.51	2476	0.095	0.341	2.036
2542	3 32 32.520	-27 48 9.26	26.94±0.05	19.63	2526	0.044	1.121	2.546
2546	3 32 36.423	-27 48 9.33	28.40±0.37	-4.41	2554	0.658	0.208	0.805
2547	3 32 33.032	-27 48 9.53	28.96±0.35	0.06	2414	0.115	3.580	1.939
2558	3 32 44.648	-27 48 7.80	27.23±0.10	11.19	2602	0.649	0.081	0.805
2565	3 32 34.138	-27 48 8.46	27.84±0.14	7.39	2611	0.378	1.086	1.018

Table C.1—Continued

ID[a]	R.A.	Decl.	u (mag)[b]	S/N	Cov. ID[c]	Cov. Index[d]	Flux Ratio[e]	Distance (arcsec)[f]
2566	3 32 46.293	-27 48 8.85	28.94±0.34	1.29	53125	0.135	0.463	1.836
2573	3 32 45.304	-27 48 7.96	26.53±0.04	28.36	2681	0.188	0.383	1.800
2581	3 32 40.378	-27 48 8.71	28.97±0.35	0.82	2452	0.015	0.374	2.902
2595	3 32 33.844	-27 48 8.89	28.96±0.35	1.93	2633	0.220	0.609	1.610
2607	3 32 43.257	-27 47 56.12	23.91±0.01	193.62	3311	0.011	0.004	4.025
2611	3 32 34.079	-27 48 7.54	28.81±0.33	-1.86	2565	0.385	0.921	1.018
2639	3 32 36.591	-27 48 7.87	27.30±0.10	10.47	2613	0.706	0.326	1.080
2652	3 32 39.930	-27 48 6.58	26.41±0.04	28.20	2801	0.014	0.084	3.319
2681	3 32 45.213	-27 48 6.88	28.99±0.36	2.47	2573	0.194	2.612	1.800
2688	3 32 45.961	-27 48 6.53	28.93±0.35	-2.66	2706	0.247	0.401	1.610
2693	3 32 32.604	-27 48 6.05	26.54±0.04	27.09	2675	0.027	0.112	2.812
2697	3 32 42.411	-27 48 6.53	28.85±0.32	-4.73	2795	0.088	0.573	2.099
2705	3 32 35.164	-27 48 6.35	27.91±0.13	7.53	2723	0.008	0.658	3.618
2728	3 32 41.913	-27 48 5.63	28.96±0.35	-4.32	2936	0.017	0.155	2.969
2734	3 32 42.892	-27 48 6.00	28.58±0.35	-3.99	2730	0.747	0.334	0.509
2750	3 32 38.609	-27 48 4.03	28.89±0.34	-3.55	2838	0.096	0.119	1.939
2753	3 32 37.749	-27 47 54.47	25.76±0.02	46.66	3432	0.339	0.026	1.298
2763	3 32 36.613	-27 48 1.43	25.73±0.02	44.38	20148	0.389	0.058	1.138
2764	3 32 34.185	-27 48 3.21	25.94±0.02	46.20	2881	0.016	0.127	3.076
2770	3 32 43.164	-27 48 1.91	26.54±0.05	17.55	2898	0.389	0.143	1.440
2778	3 32 35.668	-27 48 5.56	27.92±0.23	4.47	2830	0.657	0.212	0.360
2781	3 32 40.791	-27 48 4.56	27.14±0.12	7.89	2804	0.829	0.476	0.360
2785	3 32 35.934	-27 48 4.28	27.04±0.06	16.73	2736	0.080	0.107	1.939
2798	3 32 33.432	-27 48 4.83	28.97±0.35	0.01	2857	0.004	0.197	4.335
2799	3 32 38.931	-27 48 4.39	26.67±0.04	24.72	2838	0.039	0.115	2.902
2813	3 32 45.374	-27 48 3.56	27.00±0.06	17.80	2935	0.061	0.075	2.415
2825	3 32 30.995	-27 48 3.88	28.97±0.35	-1.00	2960	0.066	0.621	2.546
2826	3 32 31.785	-27 48 4.47	28.77±0.28	3.72	2882	0.035	2.510	2.742
2837	3 32 36.764	-27 48 3.79	28.83±0.34	1.84	2877	0.252	0.349	1.610
2848	3 32 35.341	-27 48 3.00	27.06±0.07	16.05	2841	0.402	0.229	1.138
2861	3 32 40.339	-27 48 3.48	28.06±0.15	6.66	2978	0.110	0.665	2.305
2872	3 32 42.960	-27 48 2.78	28.35±0.20	5.40	2866	0.064	0.081	2.099
2873	3 32 41.796	-27 48 1.26	28.84±0.33	-4.28	2912	0.054	0.323	2.305
2878	3 32 36.889	-27 48 3.73	27.91±0.15	7.11	2925	0.456	0.555	1.018
2879	3 32 33.833	-27 48 3.61	27.90±0.13	7.79	2881	0.040	0.831	2.596
2881	3 32 33.981	-27 48 2.05	28.98±0.37	-3.87	2879	0.038	1.203	2.596

Table C.1—Continued

ID[a]	R.A.	Decl.	u (mag)[b]	S/N	Cov. ID[c]	Cov. Index[d]	Flux Ratio[e]	Distance (arcsec)[f]
2882	3 32 31.950	-27 48 3.22	28.35±0.20	5.42	2826	0.034	0.398	2.742
2912	3 32 41.682	-27 48 2.98	28.93±0.35	0.86	2856	0.253	0.559	1.484
2927	3 32 35.493	-27 47 58.91	25.80±0.02	53.63	2387	0.031	8.515	3.960
2933	3 32 40.766	-27 48 0.46	27.44±0.09	12.23	2963	0.017	0.063	3.319
2934	3 32 37.696	-27 48 2.41	26.69±0.05	24.01	3004	0.301	0.170	1.610
2941	3 32 40.032	-27 48 2.22	28.33±0.20	5.31	3001	0.087	0.541	2.277
2943	3 32 46.702	-27 48 0.82	25.99±0.02	42.49	53369	0.015	0.063	2.969
2946	3 32 36.102	-27 48 1.95	28.67±0.27	3.91	2785	0.010	2.229	3.564
2954	3 32 31.184	-27 48 1.22	28.77±0.34	0.50	3059	0.431	0.291	1.138
2960	3 32 30.875	-27 48 2.26	28.10±0.18	5.91	2980	0.502	0.402	0.720
2974	3 32 41.593	-27 47 57.26	26.05±0.03	39.11	3125	0.082	0.102	2.596
2987	3 32 36.964	-27 48 1.23	27.54±0.10	10.60	2925	0.144	0.412	1.836
2993	3 32 40.053	-27 47 55.27	25.29±0.02	52.01	3186	0.553	0.121	0.720
2998	3 32 36.290	-27 47 55.35	25.24±0.01	86.86	3458	0.097	0.027	1.939
3006	3 32 30.635	-27 47 59.89	28.00±0.15	7.11	3251	0.018	0.307	3.220
3013	3 32 40.359	-27 47 59.42	28.93±0.37	3.05	2978	0.008	0.114	3.600
3021	3 32 31.107	-27 47 58.62	27.58±0.11	9.77	3154	0.133	0.348	1.939
3031	3 32 36.383	-27 47 58.50	25.46±0.02	44.29	3094	0.510	0.181	1.018
3033	3 32 32.513	-27 48 0.83	27.03±0.07	14.55	3076	0.454	1.635	1.138
3048	3 32 39.818	-27 47 58.98	26.98±0.06	17.91	3101	0.142	0.384	2.099
3052	3 32 38.412	-27 48 0.16	27.90±0.14	7.35	3161	0.651	0.220	1.080
3058	3 32 31.523	-27 47 58.25	27.05±0.07	16.42	3185	0.348	0.260	1.138
3060	3 32 34.788	-27 47 59.59	28.85±0.35	-0.21	3102	0.410	0.243	1.080
3068	3 32 42.744	-27 47 59.80	26.47±0.04	30.42	3192	0.072	0.596	2.742
3088	3 32 36.430	-27 47 50.59	24.84±0.01	112.84	3531	0.097	0.005	2.160
3091	3 32 34.330	-27 47 59.55	28.63±0.34	-0.31	3176	0.570	0.094	0.720
3101	3 32 39.698	-27 47 57.92	27.72±0.12	8.54	3187	0.132	0.241	1.836
3112	3 32 33.893	-27 47 58.45	28.98±0.36	0.51	3128	0.160	0.412	1.836
3123	3 32 42.951	-27 47 55.22	25.51±0.02	60.33	3291	0.437	0.175	1.138
3128	3 32 34.011	-27 47 59.08	28.97±0.36	-4.52	3112	0.162	2.426	1.836
3136	3 32 45.199	-27 47 56.89	27.26±0.08	14.34	3301	0.015	0.100	3.319
3143	3 32 33.249	-27 47 58.03	25.71±0.02	52.74	3037	0.032	0.192	2.969
3154	3 32 31.147	-27 47 56.85	28.85±0.32	1.32	3021	0.154	2.877	1.939
3159	3 32 31.335	-27 47 58.14	27.54±0.10	10.74	3185	0.344	1.830	1.484
3174	3 32 37.524	-27 47 56.30	28.16±0.17	6.34	2753	0.006	2.407	4.025
3178	3 32 37.027	-27 47 58.18	27.56±0.13	7.69	3228	0.380	0.111	1.610

Table C.1—Continued

ID[a]	R.A.	Decl.	u (mag)[b]	S/N	Cov. ID[c]	Cov. Index[d]	Flux Ratio[e]	Distance (arcsec)[f]
3180	3 32 37.880	-27 47 51.00	23.99±0.01	192.75	3432	0.025	0.008	2.969
3185	3 32 31.430	-27 47 57.88	28.88±0.35	-1.14	3058	0.345	3.846	1.138
3190	3 32 36.953	-27 47 56.54	28.38±0.30	3.38	3228	0.621	0.151	1.138
3192	3 32 42.922	-27 47 58.40	27.97±0.29	-3.52	3075	0.828	0.286	0.805
3198	3 32 34.418	-27 47 57.99	28.63±0.27	3.98	3294	0.189	0.170	1.484
3203	3 32 33.833	-27 47 47.93	24.29±0.01	184.33	3720	0.005	0.006	4.350
3205	3 32 34.690	-27 47 57.66	28.74±0.28	3.55	3102	0.051	0.437	2.190
3214	3 32 33.705	-27 47 56.64	27.31±0.08	13.14	3310	0.138	0.067	1.939
3219	3 32 47.021	-27 47 57.19	28.91±0.34	1.75	3184	0.154	0.695	1.484
3221	3 32 46.171	-27 47 56.71	27.44±0.09	12.22	3501	0.004	0.299	3.759
3223	3 32 34.939	-27 47 56.01	28.84±0.33	-3.93	3379	0.147	0.139	1.800
3247	3 32 45.055	-27 47 52.97	27.45±0.10	10.80	3467	0.311	0.174	1.484
3248	3 32 35.206	-27 47 56.66	27.32±0.08	12.79	3314	0.470	0.276	1.298
3257	3 32 38.957	-27 47 55.05	26.24±0.03	29.82	3470	0.271	0.088	1.527
3259	3 32 38.313	-27 47 56.37	27.11±0.07	14.65	3300	0.479	0.541	1.018
3268	3 32 41.404	-27 47 46.90	23.47±0.00	317.94	3445	0.125	0.256	2.621
3274	3 32 32.491	-27 47 56.12	27.45±0.09	12.16	3157	0.206	0.699	2.190
3280	3 32 37.992	-27 47 55.69	28.06±0.16	6.59	3376	0.291	0.992	1.484
3288	3 32 40.422	-27 47 52.37	26.81±0.06	19.60	3416	0.179	0.813	1.836
3299	3 32 46.160	-27 47 52.33	25.98±0.03	39.48	3501	0.305	0.055	1.610
3306	3 32 36.984	-27 47 54.44	27.54±0.11	9.28	3327	0.476	0.389	1.080
3309	3 32 30.130	-27 47 54.63	27.26±0.07	14.76	53335	0.044	2.049	2.621
3315	3 32 44.682	-27 47 54.55	28.20±0.19	5.68	3333	0.270	1.526	1.610
3319	3 32 30.976	-27 47 54.27	25.99±0.02	43.86	3519	0.035	0.147	2.902
3332	3 32 38.357	-27 47 54.10	27.39±0.09	11.74	3436	0.241	0.179	1.610
3333	3 32 44.739	-27 47 53.25	28.10±0.19	5.65	3472	0.418	1.440	1.018
3345	3 32 39.133	-27 47 54.52	28.92±0.35	0.94	3257	0.064	2.408	2.546
3347	3 32 44.276	-27 47 54.31	29.00±0.36	-2.76	3672	0.002	0.682	4.105
3349	3 32 41.673	-27 47 50.51	25.35±0.02	68.88	3445	0.039	1.760	3.220
3351	3 32 32.639	-27 47 55.14	28.16±0.16	6.30	3274	0.065	1.624	2.415
3354	3 32 35.517	-27 47 53.88	26.25±0.03	32.78	3528	0.381	0.085	1.138
3357	3 32 41.342	-27 47 54.10	28.91±0.35	-1.57	3573	0.006	0.395	3.671
3372	3 32 42.282	-27 47 46.08	23.22±0.00	416.39	3957	0.153	0.004	2.621
3373	3 32 40.048	-27 47 51.71	24.62±0.01	146.03	3637	0.022	0.024	2.969
3376	3 32 37.982	-27 47 54.33	27.65±0.11	9.03	3280	0.286	1.008	1.484
3390	3 32 35.265	-27 47 53.32	28.00±0.15	7.05	3344	0.049	0.237	2.812

Table C.1—Continued

ID[a]	R.A.	Decl.	u (mag)[b]	S/N	Cov. ID[c]	Cov. Index[d]	Flux Ratio[e]	Distance (arcsec)[f]
3416	3 32 40.296	-27 47 52.63	27.92±0.14	7.81	3288	0.217	1.230	1.836
3418	3 32 36.277	-27 47 53.45	28.49±0.33	-0.80	3458	0.670	0.307	1.080
3424	3 32 38.889	-27 47 52.92	27.02±0.08	14.21	3470	0.606	0.135	1.080
3425	3 32 42.984	-27 47 53.69	28.14±0.17	5.92	3123	0.268	7.939	1.836
3436	3 32 38.261	-27 47 53.36	27.55±0.10	10.18	3332	0.264	5.574	1.610
3440	3 32 45.243	-27 47 52.73	28.21±0.19	5.22	3462	0.329	0.423	1.298
3442	3 32 41.119	-27 47 52.14	26.14±0.03	38.38	3643	0.286	0.089	1.527
3445	3 32 41.560	-27 47 47.95	24.98±0.01	87.10	3885	0.215	0.015	1.527
3454	3 32 40.722	-27 47 49.22	27.48±0.11	9.54	3518	0.371	0.441	1.298
3459	3 32 39.574	-27 47 52.66	27.48±0.09	9.49	3364	0.009	0.273	3.097
3460	3 32 32.573	-27 47 51.76	25.25±0.01	85.47	3560	0.195	0.071	1.800
3461	3 32 31.204	-27 47 52.73	28.96±0.34	2.67	3620	0.042	0.380	2.546
3467	3 32 44.961	-27 47 53.29	27.47±0.09	11.36	3247	0.378	5.749	1.484
3468	3 32 33.820	-27 47 52.50	28.80±0.36	2.47	3544	0.414	0.215	1.484
3472	3 32 44.784	-27 47 52.28	27.74±0.13	8.10	3333	0.468	0.694	1.018
3475	3 32 41.306	-27 47 49.08	25.21±0.01	90.94	3573	0.179	0.033	1.484
3481	3 32 45.982	-27 47 53.21	28.94±0.34	1.80	3378	0.219	0.512	1.610
3483	3 32 36.389	-27 47 47.03	24.26±0.01	182.27	3886	0.167	0.009	1.800
3484	3 32 47.520	-27 47 48.30	24.75±0.01	119.15	3845	0.190	0.021	1.800
3492	3 32 45.107	-27 47 38.45	22.30±0.00	666.49	3914	0.242	0.256	2.277
3504	3 32 45.564	-27 47 51.42	27.87±0.13	8.10	3592	0.027	0.114	2.880
3507	3 32 35.446	-27 47 52.61	28.87±0.34	-0.86	3528	0.327	0.384	1.484
3512	3 32 32.274	-27 47 51.20	26.69±0.06	18.92	20153	0.612	0.108	0.720
3514	3 32 31.886	-27 47 52.61	27.16±0.12	8.41	3488	0.856	0.281	0.720
3518	3 32 40.785	-27 47 50.25	28.19±0.21	4.63	3454	0.350	2.270	1.298
3519	3 32 30.820	-27 47 52.83	29.02±0.35	-3.02	3319	0.043	6.823	2.902
3521	3 32 40.576	-27 47 52.38	29.01±0.36	-1.12	3288	0.125	8.634	2.520
3523	3 32 33.677	-27 47 51.08	28.86±0.36	2.17	3720	0.114	0.258	2.036
3527	3 32 33.029	-27 47 51.37	27.01±0.07	15.58	3513	0.440	1.249	1.610
3547	3 32 36.596	-27 47 51.76	28.98±0.36	-2.46	3088	0.060	48.306	2.742
3567	3 32 34.623	-27 47 51.78	28.95±0.35	-4.45	3389	0.008	0.481	3.319
3569	3 32 32.326	-27 47 50.11	27.86±0.14	7.55	3512	0.241	3.046	1.298
3573	3 32 41.290	-27 47 50.70	29.01±0.38	-0.52	3475	0.198	30.005	1.484
3574	3 32 39.121	-27 47 51.54	28.96±0.36	-0.60	3345	0.014	1.015	3.240
3581	3 32 40.515	-27 47 49.03	25.82±0.02	50.22	3454	0.027	1.112	3.260
3583	3 32 33.149	-27 47 50.76	27.15±0.07	14.14	3513	0.393	1.491	1.484

Table C.1—Continued

ID[a]	R.A.	Decl.	u (mag)[b]	S/N	Cov. ID[c]	Cov. Index[d]	Flux Ratio[e]	Distance (arcsec)[f]
3584	3 32 41.045	-27 47 50.32	27.43±0.15	6.59	3643	0.731	0.224	0.720
3591	3 32 34.082	-27 47 50.65	28.96±0.36	1.16	3502	0.110	0.244	2.160
3595	3 32 34.322	-27 47 50.31	28.37±0.33	2.82	3607	0.745	0.359	0.805
3602	3 32 47.300	-27 47 49.58	27.38±0.09	11.36	3608	0.141	1.018	1.800
3605	3 32 36.771	-27 47 49.52	27.77±0.12	8.32	3801	0.185	0.203	1.610
3608	3 32 47.239	-27 47 51.11	27.71±0.11	9.46	3602	0.152	0.982	1.800
3610	3 32 38.710	-27 47 43.68	25.50±0.02	53.18	3823	0.384	0.457	1.080
3613	3 32 37.620	-27 47 44.14	24.12±0.01	210.76	4192	0.033	0.090	2.902
3650	3 32 38.111	-27 47 49.80	28.81±0.35	1.78	3651	0.316	0.177	1.298
3655	3 32 37.566	-27 47 50.16	27.37±0.08	12.85	3180	0.005	22.619	4.735
3677	3 32 37.308	-27 47 29.29	25.32±0.03	48.47	55220	0.009	0.002	4.350
3680	3 32 38.582	-27 47 46.50	26.80±0.05	18.91	3906	0.093	0.117	1.939
3682	3 32 47.609	-27 47 50.12	26.33±0.03	32.66	53972	0.305	0.947	1.440
3688	3 32 31.394	-27 47 46.33	26.18±0.03	36.39	3827	0.285	0.077	1.440
3689	3 32 31.643	-27 47 48.15	26.79±0.05	19.97	3758	0.150	0.226	2.277
3690	3 32 42.675	-27 47 48.83	28.28±0.19	5.08	3582	0.014	0.373	3.076
3693	3 32 31.250	-27 47 49.18	28.72±0.34	2.17	3781	0.515	0.178	1.018
3701	3 32 29.798	-27 47 49.12	27.23±0.07	15.04	3856	0.002	0.317	4.394
3745	3 32 47.242	-27 47 46.85	25.90±0.02	46.00	3953	0.161	0.082	1.800
3752	3 32 43.368	-27 47 43.49	25.61±0.02	52.61	3933	0.231	0.277	1.939
3772	3 32 37.171	-27 47 47.91	28.93±0.35	-2.01	3898	0.171	0.659	1.484
3777	3 32 35.023	-27 47 47.49	27.42±0.09	12.67	4034	0.006	0.257	3.600
3778	3 32 41.714	-27 47 46.84	28.71±0.34	-0.93	3885	0.447	0.156	1.080
3785	3 32 37.371	-27 47 43.57	26.95±0.06	16.92	3977	0.136	4.539	1.939
3799	3 32 38.344	-27 47 44.47	26.20±0.03	28.09	4023	0.032	0.052	2.880
3802	3 32 44.105	-27 47 47.23	27.68±0.11	10.37	3672	0.006	0.295	3.546
3804	3 32 39.746	-27 47 46.39	27.72±0.12	8.22	4004	0.033	1.067	3.055
3819	3 32 44.775	-27 47 47.17	26.95±0.06	18.78	3739	0.058	0.212	2.415
3822	3 32 44.865	-27 47 27.61	21.05±0.00	2161.39	4929	0.002	0.110	5.091
3823	3 32 38.716	-27 47 44.90	25.18±0.01	77.63	3610	0.451	2.189	1.080
3838	3 32 29.401	-27 47 46.77	27.98±0.14	7.13	3922	0.154	2.625	1.836
3840	3 32 46.481	-27 47 44.41	28.70±0.30	3.64	3878	0.078	0.664	2.190
3844	3 32 34.141	-27 47 43.44	25.92±0.03	41.25	4136	0.050	0.251	2.596
3869	3 32 45.140	-27 47 44.67	26.24±0.03	37.47	3492	0.000	34.429	6.162
3871	3 32 32.740	-27 47 43.91	27.06±0.08	12.38	4149	0.516	0.149	1.018
3878	3 32 46.512	-27 47 46.58	28.52±0.23	4.50	3840	0.092	1.506	2.190

Table C.1—Continued

ID[a]	R.A.	Decl.	u (mag)[b]	S/N	Cov. ID[c]	Cov. Index[d]	Flux Ratio[e]	Distance (arcsec)[f]
3881	3 32 33.742	-27 47 44.18	25.84±0.02	52.03	4183	0.014	0.101	3.097
3893	3 32 32.949	-27 47 44.97	26.82±0.06	17.84	3969	0.473	0.139	1.298
3895	3 32 36.111	-27 47 44.66	25.92±0.02	43.83	3940	0.040	0.173	2.812
3915	3 32 47.844	-27 47 44.20	26.24±0.03	34.50	4041	0.413	0.105	1.138
3922	3 32 29.420	-27 47 45.00	28.92±0.36	-2.11	4062	0.242	0.554	1.527
3933	3 32 43.254	-27 47 44.05	26.65±0.05	21.67	3752	0.299	3.609	1.939
3936	3 32 41.979	-27 47 45.98	27.94±0.18	5.72	3847	0.570	0.337	1.298
3938	3 32 32.785	-27 47 45.18	26.69±0.07	15.63	3958	0.667	0.181	0.805
3939	3 32 35.596	-27 47 45.50	27.38±0.09	12.37	3909	0.122	0.138	2.277
3940	3 32 35.969	-27 47 46.22	27.72±0.11	9.57	3895	0.047	5.793	2.812
3967	3 32 47.467	-27 47 44.69	28.51±0.23	4.63	3953	0.049	0.364	2.621
3977	3 32 37.409	-27 47 41.65	24.39±0.01	167.65	4355	0.179	0.019	2.099
3985	3 32 36.648	-27 47 44.31	26.19±0.03	32.87	4119	0.535	0.103	0.805
4000	3 32 42.306	-27 47 42.91	27.99±0.15	6.84	4123	0.042	0.288	2.902
4010	3 32 33.064	-27 47 43.96	28.86±0.35	-4.23	3893	0.201	0.821	2.099
4015	3 32 40.551	-27 47 43.88	27.38±0.10	10.09	4089	0.474	0.587	1.138
4027	3 32 30.019	-27 47 43.46	26.81±0.06	17.30	4191	0.544	0.149	0.720
4036	3 32 38.862	-27 47 42.96	28.20±0.19	5.35	3610	0.100	12.430	2.277
4037	3 32 35.262	-27 47 44.07	28.93±0.34	0.93	4060	0.163	1.908	1.939
4040	3 32 41.912	-27 47 43.36	28.54±0.25	4.17	3996	0.083	0.059	2.160
4052	3 32 40.630	-27 47 39.93	25.92±0.03	39.46	4177	0.375	0.469	1.138
4058	3 32 30.496	-27 47 42.10	26.57±0.05	21.39	4100	0.545	0.286	1.298
4061	3 32 31.435	-27 47 43.18	28.95±0.36	1.10	3688	0.012	1.967	3.319
4062	3 32 29.346	-27 47 43.86	28.97±0.36	-0.88	3922	0.268	1.804	1.527
4065	3 32 32.447	-27 47 43.86	28.42±0.21	4.92	4093	0.123	0.692	2.160
4069	3 32 39.691	-27 47 42.92	26.32±0.03	35.04	4215	0.051	0.167	2.742
4070	3 32 34.820	-27 47 43.46	26.97±0.06	17.68	4148	0.100	0.315	2.099
4084	3 32 30.677	-27 47 41.27	25.14±0.01	77.00	4072	0.487	0.980	1.080
4087	3 32 34.593	-27 47 43.58	27.76±0.12	8.54	4085	0.123	4.168	2.277
4092	3 32 40.199	-27 47 42.69	25.58±0.02	66.10	4202	0.037	0.170	2.812
4094	3 32 37.630	-27 47 40.39	25.78±0.03	28.12	4187	0.425	0.860	1.018
4096	3 32 29.354	-27 47 41.63	26.56±0.04	28.03	4062	0.058	0.146	2.160
4100	3 32 30.439	-27 47 42.74	26.95±0.08	11.51	4189	0.467	0.452	1.018
4126	3 32 36.986	-27 47 42.32	27.88±0.13	8.28	4483	0.002	0.387	4.214
4136	3 32 34.065	-27 47 41.18	28.45±0.23	4.63	3844	0.063	3.984	2.596
4137	3 32 29.511	-27 47 42.84	27.67±0.11	9.40	4013	0.385	0.451	1.440

Table C.1—Continued

ID[a]	R.A.	Decl.	u (mag)[b]	S/N	Cov. ID[c]	Cov. Index[d]	Flux Ratio[e]	Distance (arcsec)[f]
4142	3 32 44.198	-27 47 33.47	23.37±0.00	459.42	4611	0.010	0.011	3.396
4148	3 32 34.948	-27 47 42.37	27.49±0.11	8.91	4124	0.680	0.217	1.018
4159	3 32 30.217	-27 47 42.36	27.26±0.08	12.73	4172	0.360	2.038	1.298
4172	3 32 30.138	-27 47 41.75	26.41±0.04	29.58	4159	0.372	0.491	1.298
4177	3 32 40.551	-27 47 39.43	28.33±0.28	2.74	4430	0.410	0.270	1.018
4178	3 32 46.942	-27 47 42.27	28.94±0.35	2.94	4150	0.266	0.321	1.610
4183	3 32 33.918	-27 47 42.30	27.93±0.14	7.41	4136	0.059	2.521	2.415
4184	3 32 31.857	-27 47 42.14	28.44±0.35	-1.12	4241	0.796	0.286	0.509
4188	3 32 41.744	-27 47 41.80	28.73±0.30	3.51	4111	0.309	0.893	1.484
4193	3 32 47.649	-27 47 42.12	27.83±0.12	8.85	4028	0.033	0.419	2.621
4202	3 32 40.317	-27 47 40.74	28.94±0.35	1.16	4447	0.099	0.131	1.939
4216	3 32 44.709	-27 47 41.85	27.77±0.12	8.79	4302	0.242	1.497	1.610
4225	3 32 42.052	-27 47 40.56	28.79±0.34	-3.98	4381	0.375	0.079	1.298
4228	3 32 30.350	-27 47 39.48	26.91±0.06	16.65	4418	0.298	0.077	1.484
4243	3 32 39.508	-27 47 39.60	25.57±0.02	63.82	4215	0.063	0.088	2.546
4245	3 32 28.994	-27 47 37.98	25.77±0.03	30.06	4466	0.999	0.249	1.138
4253	3 32 39.888	-27 47 38.05	24.83±0.01	112.90	4307	0.018	0.020	3.076
4254	3 32 43.390	-27 47 39.17	28.87±0.35	-0.29	4246	0.008	0.145	3.600
4258	3 32 36.008	-27 47 38.08	26.56±0.06	16.16	4458	0.693	0.152	0.805
4262	3 32 38.868	-27 47 33.25	24.37±0.01	153.34	4445	0.267	4.459	2.036
4267	3 32 48.336	-27 47 38.84	25.82±0.03	39.13	54455	0.543	0.167	1.080
4268	3 32 35.667	-27 47 40.95	27.21±0.07	14.76	4379	0.122	0.815	1.800
4276	3 32 44.645	-27 47 40.70	27.55±0.14	7.79	4304	0.662	0.135	0.805
4280	3 32 37.347	-27 47 39.31	28.03±0.28	3.06	4355	0.807	0.382	0.360
4287	3 32 31.883	-27 47 39.01	26.60±0.04	26.26	4241	0.038	0.131	2.621
4289	3 32 37.730	-27 47 40.22	27.60±0.13	6.88	4264	0.519	0.340	0.805
4301	3 32 33.629	-27 47 40.32	27.72±0.12	8.83	4197	0.270	2.079	1.836
4302	3 32 44.763	-27 47 40.67	28.91±0.35	-2.61	4216	0.245	0.668	1.610
4315	3 32 37.109	-27 47 35.66	23.96±0.00	250.19	4702	0.125	0.008	1.939
4316	3 32 36.616	-27 47 37.85	28.83±0.36	-1.31	4349	0.419	0.159	1.018
4320	3 32 38.703	-27 47 34.19	28.59±0.32	-8.43	4445	0.089	19.967	2.415
4321	3 32 30.976	-27 47 38.11	26.57±0.04	25.34	4543	0.166	0.199	1.836
4322	3 32 32.378	-27 47 40.01	28.15±0.17	6.34	4213	0.236	0.358	1.800
4338	3 32 41.887	-27 47 39.45	28.64±0.28	3.46	4348	0.245	2.450	1.610
4348	3 32 41.791	-27 47 38.60	28.74±0.33	-1.70	4338	0.211	0.408	1.610
4349	3 32 36.683	-27 47 38.50	28.55±0.29	1.89	4316	0.387	6.278	1.018

Table C.1—Continued

ID[a]	R.A.	Decl.	u (mag)[b]	S/N	Cov. ID[c]	Cov. Index[d]	Flux Ratio[e]	Distance (arcsec)[f]
4350	3 32 32.750	-27 47 38.75	27.16±0.08	14.32	4370	0.441	0.155	1.138
4360	3 32 29.939	-27 47 34.67	26.09±0.03	37.79	4761	0.255	0.027	1.484
4361	3 32 33.856	-27 47 39.29	27.90±0.13	7.82	4492	0.033	0.693	2.546
4368	3 32 40.744	-27 47 36.43	28.71±0.30	3.36	4404	0.141	2.273	2.099
4369	3 32 35.247	-27 47 37.92	28.82±0.32	-1.53	4407	0.154	0.946	1.836
4371	3 32 43.727	-27 47 38.37	25.99±0.03	40.08	4446	0.511	0.121	1.138
4373	3 32 41.381	-27 47 38.07	28.54±0.36	-1.14	4459	0.734	0.167	0.805
4376	3 32 41.486	-27 47 38.79	28.91±0.34	2.12	4373	0.294	2.123	1.939
4379	3 32 35.599	-27 47 39.36	28.96±0.35	-9.79	4268	0.123	1.228	1.800
4389	3 32 46.527	-27 47 35.87	25.22±0.01	91.74	4604	0.132	0.012	2.190
4390	3 32 30.515	-27 47 37.94	26.17±0.03	38.20	4318	0.030	0.121	2.277
4394	3 32 31.361	-27 47 24.99	23.05±0.00	457.48	5459	0.001	0.002	4.897
4396	3 32 35.800	-27 47 34.69	26.22±0.03	31.92	4732	0.127	0.065	2.277
4404	3 32 40.633	-27 47 37.69	26.99±0.07	15.15	4430	0.562	0.159	1.138
4407	3 32 35.380	-27 47 37.55	27.83±0.14	7.52	4572	0.267	0.149	1.484
4410	3 32 48.057	-27 47 37.50	25.27±0.01	90.01	4540	0.167	0.015	1.836
4411	3 32 47.005	-27 47 38.05	28.96±0.37	0.13	4412	0.230	0.318	1.800
4438	3 32 33.043	-27 47 30.96	23.89±0.01	223.09	5080	0.005	0.006	3.877
4445	3 32 38.775	-27 47 32.09	22.26±0.00	1074.34	4262	0.248	0.224	2.036
4461	3 32 39.618	-27 47 37.18	26.49±0.04	29.59	4243	0.021	1.006	2.812
4479	3 32 42.569	-27 47 37.28	27.45±0.09	11.37	4568	0.132	0.458	1.939
4481	3 32 39.261	-27 47 36.72	25.49±0.02	70.65	4655	0.013	0.050	3.546
4491	3 32 40.216	-27 47 33.07	24.19±0.01	186.79	4674	0.301	0.215	1.298
4492	3 32 33.748	-27 47 37.20	28.97±0.36	-1.07	4361	0.032	1.443	2.546
4496	3 32 36.721	-27 47 37.28	27.05±0.08	12.92	4588	0.433	0.746	1.018
4502	3 32 41.229	-27 47 37.19	27.34±0.08	12.97	4459	0.182	0.357	1.800
4527	3 32 41.405	-27 47 17.13	25.74±0.03	39.56	33867	0.007	0.005	4.610
4532	3 32 37.449	-27 47 37.48	28.17±0.17	6.22	4280	0.113	0.879	2.596
4545	3 32 44.066	-27 47 37.40	28.02±0.15	7.30	4313	0.032	0.433	2.520
4547	3 32 45.476	-27 47 36.40	28.93±0.35	0.94	3492	0.011	149.941	6.152
4563	3 32 47.664	-27 47 36.05	26.67±0.04	25.39	4441	0.005	0.076	4.073
4578	3 32 30.164	-27 47 36.23	27.82±0.13	8.06	4544	0.115	0.379	1.939
4587	3 32 40.674	-27 47 30.99	25.65±0.02	52.62	4767	0.482	0.279	1.298
4591	3 32 41.118	-27 47 34.59	25.36±0.01	72.08	4746	0.076	0.039	2.520
4592	3 32 33.069	-27 47 36.49	28.96±0.36	2.61	4682	0.105	0.883	2.099
4601	3 32 43.158	-27 47 36.01	27.89±0.14	7.26	4724	0.359	0.339	1.138

Table C.1—Continued

ID[a]	R.A.	Decl.	u (mag)[b]	S/N	Cov. ID[c]	Cov. Index[d]	Flux Ratio[e]	Distance (arcsec)[f]
4603	3 32 43.041	-27 47 35.75	28.61±0.28	3.98	4724	0.152	0.186	1.800
4607	3 32 41.448	-27 47 35.74	28.98±0.36	-5.22	4373	0.056	2.154	2.415
4611	3 32 44.320	-27 47 36.28	27.49±0.15	7.10	4614	0.799	0.231	0.509
4616	3 32 42.733	-27 47 33.93	27.27±0.09	11.99	4954	0.010	0.073	3.415
4620	3 32 35.377	-27 47 36.02	28.83±0.33	-5.35	4407	0.220	1.758	1.800
4626	3 32 34.644	-27 47 35.01	28.96±0.36	0.19	4658	0.036	0.185	2.902
4636	3 32 40.989	-27 47 35.87	28.89±0.33	3.14	4746	0.233	0.233	1.610
4638	3 32 32.219	-27 47 32.82	26.62±0.04	20.02	4875	0.082	0.150	2.969
4641	3 32 46.208	-27 47 34.82	27.52±0.09	11.30	4627	0.100	0.294	2.099
4642	3 32 47.124	-27 47 35.54	28.88±0.32	3.44	4411	0.016	1.009	2.902
4648	3 32 29.176	-27 47 34.12	28.38±0.32	-3.97	4800	0.615	0.158	0.805
4651	3 32 31.216	-27 47 34.81	26.50±0.04	26.69	4777	0.357	0.117	1.527
4657	3 32 36.546	-27 47 32.96	26.38±0.04	29.44	4972	0.095	0.057	1.939
4660	3 32 32.069	-27 47 34.32	28.88±0.34	1.45	4638	0.047	2.057	2.812
4661	3 32 35.525	-27 47 34.37	28.94±0.36	-2.27	4732	0.113	0.227	2.190
4662	3 32 39.484	-27 47 34.63	26.48±0.04	27.68	4771	0.181	0.211	1.800
4668	3 32 31.400	-27 47 34.55	28.87±0.33	-1.63	4685	0.187	2.120	1.800
4673	3 32 34.822	-27 47 33.81	28.96±0.37	2.48	4658	0.124	0.239	1.800
4674	3 32 40.305	-27 47 33.80	28.84±0.34	-7.74	4491	0.417	4.661	1.298
4678	3 32 44.748	-27 47 34.07	28.97±0.36	1.57	4625	0.018	0.848	3.260
4686	3 32 31.688	-27 47 35.22	28.34±0.20	5.31	4787	0.140	0.432	1.610
4699	3 32 33.253	-27 47 33.83	27.05±0.06	16.36	4438	0.006	23.773	4.073
4701	3 32 37.950	-27 47 33.16	27.51±0.10	10.11	4734	0.153	0.250	1.800
4714	3 32 36.304	-27 47 32.67	26.56±0.04	26.94	4749	0.220	0.084	1.610
4717	3 32 48.654	-27 47 32.47	26.84±0.05	20.85	54757	0.010	0.102	2.969
4764	3 32 43.234	-27 47 31.42	26.88±0.05	19.85	4724	0.004	0.123	3.546
4766	3 32 30.744	-27 47 33.44	29.02±0.37	0.73	4785	0.025	0.175	2.880
4767	3 32 40.611	-27 47 30.20	25.83±0.03	36.90	4587	0.407	3.590	1.298
4774	3 32 41.275	-27 47 33.42	28.27±0.18	5.87	4591	0.076	5.635	2.742
4779	3 32 29.361	-27 47 33.22	28.00±0.15	6.91	4800	0.096	0.232	2.160
4801	3 32 36.906	-27 47 26.35	24.88±0.01	72.61	5271	0.438	0.214	0.805
4805	3 32 40.056	-27 47 31.92	28.13±0.17	5.89	4825	0.193	3.676	1.800
4807	3 32 31.578	-27 47 32.45	26.97±0.06	16.67	4787	0.301	0.163	1.610
4813	3 32 46.997	-27 47 31.22	28.09±0.22	4.78	4969	0.559	0.227	0.805
4814	3 32 32.433	-27 47 32.23	28.48±0.35	1.37	4875	0.767	0.283	0.509
4816	3 32 44.182	-27 47 29.52	25.50±0.02	62.88	4979	0.054	0.019	2.596

Table C.1—Continued

ID[a]	R.A.	Decl.	u (mag)[b]	S/N	Cov. ID[c]	Cov. Index[d]	Flux Ratio[e]	Distance (arcsec)[f]
4825	3 32 40.157	-27 47 30.71	25.99±0.03	32.35	4870	0.865	0.110	1.080
4830	3 32 36.740	-27 47 32.61	28.98±0.36	-3.62	4657	0.039	3.165	2.902
4835	3 32 34.867	-27 47 30.72	26.41±0.04	30.25	5037	0.098	0.193	2.099
4838	3 32 38.549	-27 47 30.38	27.75±0.14	7.46	4944	0.516	0.300	1.018
4841	3 32 35.021	-27 47 32.10	27.97±0.15	7.55	4835	0.047	5.148	2.415
4849	3 32 39.323	-27 47 32.17	27.03±0.06	17.24	4771	0.183	0.403	1.800
4860	3 32 35.810	-27 47 29.29	28.59±0.33	0.83	5032	0.411	0.067	1.298
4874	3 32 34.045	-27 47 31.76	28.89±0.34	1.80	4855	0.018	0.677	3.260
4878	3 32 48.543	-27 47 25.37	25.21±0.02	72.67	5420	0.210	0.044	2.190
4880	3 32 30.953	-27 47 31.63	27.11±0.06	16.59	4766	0.007	1.833	3.706
4907	3 32 46.772	-27 47 29.54	27.65±0.12	8.66	4990	0.447	0.160	1.138
4908	3 32 45.912	-27 47 30.33	28.09±0.27	3.75	5031	0.833	0.344	0.805
4913	3 32 41.458	-27 47 29.40	28.92±0.36	-0.20	5060	0.213	0.781	1.610
4927	3 32 48.000	-27 47 30.51	28.96±0.36	-2.46	4829	0.075	0.097	2.812
4929	3 32 45.107	-27 47 24.01	23.49±0.00	400.70	5621	0.010	0.001	3.396
4930	3 32 39.944	-27 47 31.37	27.96±0.14	7.23	4805	0.204	5.008	1.939
4947	3 32 40.454	-27 47 29.59	26.47±0.04	29.57	4767	0.166	2.599	2.277
4950	3 32 30.023	-27 47 26.80	25.86±0.02	45.14	5126	0.143	0.030	2.036
4983	3 32 35.425	-27 47 30.44	27.45±0.09	11.85	4928	0.200	0.223	1.484
4999	3 32 36.341	-27 47 27.91	26.33±0.06	15.38	5095	0.599	0.275	0.720
5005	3 32 45.325	-27 47 29.06	26.40±0.03	31.19	5044	0.048	0.067	2.546
5006	3 32 35.050	-27 47 29.72	28.98±0.36	0.10	5015	0.049	0.274	2.902
5010	3 32 32.124	-27 47 27.92	26.62±0.05	20.88	5181	0.473	0.205	1.138
5022	3 32 46.484	-27 47 27.22	26.36±0.03	32.58	5106	0.044	0.091	2.621
5037	3 32 34.799	-27 47 28.91	28.34±0.22	4.59	5124	0.348	0.720	1.610
5052	3 32 38.926	-27 47 28.89	28.38±0.21	5.05	5205	0.028	1.362	2.969
5053	3 32 48.340	-27 47 28.45	28.10±0.17	6.69	4878	0.003	16.737	4.335
5056	3 32 36.198	-27 47 26.15	28.36±0.28	-3.08	4999	0.124	1.312	2.812
5060	3 32 41.405	-27 47 27.89	27.11±0.07	13.71	5206	0.233	0.307	1.484
5063	3 32 47.386	-27 47 26.02	28.88±0.37	-0.46	5480	0.008	0.116	3.220
5089	3 32 32.856	-27 47 26.40	26.14±0.03	38.78	5115	0.026	0.292	2.969
5093	3 32 38.313	-27 47 28.05	27.72±0.19	5.38	5105	0.801	0.168	0.720
5098	3 32 41.761	-27 47 27.68	28.95±0.36	-0.44	5251	0.069	0.753	2.190
5102	3 32 40.377	-27 47 27.69	28.93±0.35	2.66	5198	0.194	0.413	1.836
5106	3 32 46.319	-27 47 28.14	28.93±0.36	1.04	5055	0.262	0.337	1.440
5107	3 32 35.893	-27 47 27.42	28.87±0.34	0.40	4860	0.127	2.436	2.099

Table C.1—Continued

ID[a]	R.A.	Decl.	u (mag)[b]	S/N	Cov. ID[c]	Cov. Index[d]	Flux Ratio[e]	Distance (arcsec)[f]
5109	3 32 31.956	-27 47 27.65	28.95±0.35	0.22	5181	0.118	0.369	2.277
5111	3 32 33.478	-27 47 28.06	28.47±0.22	4.85	5178	0.078	1.628	2.036
5115	3 32 32.664	-27 47 27.38	27.33±0.08	12.98	5089	0.026	3.427	2.969
5120	3 32 35.220	-27 47 28.05	26.86±0.06	19.32	5134	0.359	0.444	1.484
5134	3 32 35.314	-27 47 27.71	28.76±0.34	0.91	5200	0.391	2.277	1.018
5136	3 32 35.978	-27 47 25.57	27.62±0.13	7.87	5107	0.089	0.255	2.596
5159	3 32 38.501	-27 47 25.31	24.45±0.01	183.63	5263	0.055	0.144	2.546
5177	3 32 48.457	-27 47 19.67	25.71±0.02	54.41	5820	0.078	0.013	2.277
5178	3 32 33.587	-27 47 26.68	28.18±0.17	6.22	5111	0.077	0.614	2.036
5182	3 32 39.784	-27 47 26.78	27.96±0.15	5.90	5099	0.089	0.277	2.036
5187	3 32 44.356	-27 47 23.76	25.43±0.02	53.60	5299	0.642	0.137	0.805
5190	3 32 34.822	-27 47 21.92	24.67±0.01	135.79	5358	0.094	0.153	2.190
5196	3 32 42.766	-27 47 26.77	27.32±0.10	10.68	5143	0.598	0.252	0.805
5200	3 32 35.356	-27 47 26.74	26.82±0.05	20.09	5134	0.442	0.439	1.018
5201	3 32 34.438	-27 47 26.41	27.02±0.10	10.10	5214	0.842	0.243	0.360
5205	3 32 38.970	-27 47 26.35	28.94±0.35	0.97	5052	0.028	0.734	2.969
5212	3 32 43.682	-27 47 25.51	28.51±0.26	4.08	5315	0.536	0.201	1.298
5216	3 32 34.259	-27 47 24.01	25.66±0.02	53.51	5408	0.049	0.211	2.546
5231	3 32 44.295	-27 47 25.48	27.22±0.10	10.67	5239	0.563	0.109	0.805
5249	3 32 32.207	-27 47 25.68	28.97±0.35	-3.19	5181	0.078	0.586	2.099
5251	3 32 41.775	-27 47 25.51	27.00±0.06	17.35	5331	0.222	0.267	1.484
5253	3 32 49.102	-27 47 25.64	26.83±0.05	16.08	55239	0.122	0.311	1.484
5254	3 32 29.629	-27 47 26.19	27.60±0.10	10.96	5125	0.018	0.433	3.319
5261	3 32 41.048	-27 47 25.71	28.58±0.33	1.45	5247	0.656	0.358	0.805
5263	3 32 38.678	-27 47 25.21	27.59±0.11	9.53	5159	0.057	6.959	2.546
5267	3 32 43.101	-27 47 22.50	26.57±0.04	24.60	5749	0.005	0.063	3.600
5268	3 32 40.324	-27 47 22.81	24.49±0.01	168.46	5618	0.112	0.015	2.099
5275	3 32 36.745	-27 47 25.81	28.93±0.34	-0.51	4801	0.167	15.705	2.546
5276	3 32 41.402	-27 47 23.93	26.94±0.07	14.59	5330	0.333	0.704	1.138
5286	3 32 45.648	-27 47 23.52	27.96±0.17	6.20	5458	0.503	0.365	1.138
5292	3 32 37.639	-27 47 23.63	27.02±0.07	16.35	5386	0.360	0.553	1.298
5304	3 32 34.674	-27 47 25.27	27.22±0.08	13.93	5321	0.130	0.109	2.190
5330	3 32 41.474	-27 47 24.55	26.89±0.07	13.01	5398	0.558	0.341	0.509
5331	3 32 41.805	-27 47 23.87	28.63±0.33	1.70	5452	0.547	0.351	0.805
5341	3 32 40.733	-27 47 24.21	28.90±0.34	-2.47	5210	0.030	0.301	2.742
5346	3 32 42.759	-27 47 24.69	28.99±0.36	-4.69	5449	0.133	0.294	2.036

Table C.1—Continued

ID[a]	R.A.	Decl.	u (mag)[b]	S/N	Cov. ID[c]	Cov. Index[d]	Flux Ratio[e]	Distance (arcsec)[f]
5348	3 32 40.171	-27 47 24.40	28.41±0.35	0.02	5371	0.680	0.313	0.805
5358	3 32 34.794	-27 47 24.08	26.88±0.06	16.73	5306	0.175	0.108	1.939
5365	3 32 29.807	-27 47 19.44	25.33±0.02	60.07	5577	0.580	0.134	1.018
5367	3 32 32.555	-27 47 24.61	28.67±0.26	4.08	5456	0.025	2.178	2.902
5377	3 32 35.110	-27 47 24.54	27.27±0.08	13.77	5322	0.230	0.418	1.939
5380	3 32 36.299	-27 47 22.12	27.13±0.08	12.16	5385	0.501	0.340	1.138
5388	3 32 41.858	-27 47 21.92	25.89±0.02	44.13	5527	0.221	0.047	1.800
5399	3 32 42.360	-27 47 22.94	26.49±0.04	30.69	5328	0.012	0.078	3.396
5405	3 32 38.545	-27 47 23.04	26.37±0.03	30.78	5159	0.053	4.845	2.621
5408	3 32 34.076	-27 47 23.70	28.77±0.30	3.57	5216	0.061	4.749	2.546
5411	3 32 48.821	-27 47 22.03	27.85±0.14	7.91	5563	0.287	0.085	1.484
5415	3 32 36.786	-27 47 22.79	28.69±0.33	1.57	5461	0.356	0.097	1.018
5417	3 32 39.883	-27 47 15.08	23.48±0.00	326.09	6008	0.099	0.039	2.190
5431	3 32 41.350	-27 47 21.78	28.28±0.20	4.90	5608	0.245	0.146	1.836
5435	3 32 36.199	-27 47 22.71	26.98±0.06	17.23	5385	0.198	0.328	1.939
5443	3 32 37.467	-27 47 23.23	28.94±0.35	-2.35	5386	0.222	0.565	1.800
5456	3 32 32.637	-27 47 22.23	28.39±0.21	4.95	5543	0.103	0.145	2.160
5473	3 32 45.966	-27 47 21.19	28.37±0.29	3.75	5558	0.737	0.371	0.805
5491	3 32 46.959	-27 47 15.94	22.88±0.00	658.38	6040	0.042	0.017	2.812
5496	3 32 45.712	-27 47 21.35	27.58±0.11	8.05	5498	0.348	0.458	1.018
5497	3 32 37.769	-27 47 21.19	26.70±0.05	22.80	5677	0.056	0.171	2.742
5501	3 32 35.833	-27 47 18.70	25.58±0.02	61.13	5709	0.063	0.091	2.621
5526	3 32 34.457	-27 47 20.88	28.92±0.36	1.27	5529	0.068	0.520	2.520
5529	3 32 34.635	-27 47 20.87	28.76±0.33	2.30	5526	0.061	1.922	2.520
5533	3 32 42.588	-27 47 21.98	28.85±0.33	-2.72	5449	0.158	0.316	2.036
5536	3 32 29.932	-27 47 21.83	27.47±0.15	7.28	5617	0.848	0.234	0.509
5540	3 32 46.496	-27 47 16.32	25.93±0.03	41.61	5882	0.128	0.034	1.610
5545	3 32 38.253	-27 47 20.80	27.36±0.09	12.52	5538	0.172	0.369	1.610
5548	3 32 47.590	-27 47 20.96	28.92±0.36	-2.05	5731	0.273	0.121	1.484
5569	3 32 35.323	-27 47 18.54	24.99±0.01	110.54	5841	0.149	0.012	1.836
5579	3 32 33.185	-27 47 20.10	28.91±0.36	0.67	5574	0.358	0.199	1.484
5605	3 32 47.178	-27 47 20.93	26.84±0.05	20.37	5669	0.398	0.463	1.080
5606	3 32 34.110	-27 47 12.11	22.92±0.00	598.14	6376	0.014	0.002	3.220
5614	3 32 45.965	-27 47 19.28	26.63±0.05	21.04	5558	0.547	0.404	1.138
5615	3 32 38.651	-27 47 18.08	27.28±0.11	9.20	5863	0.585	0.174	0.805
5620	3 32 43.570	-27 47 16.77	24.30±0.01	199.74	5831	0.009	0.188	3.564

Table C.1—Continued

ID[a]	R.A.	Decl.	u (mag)[b]	S/N	Cov. ID[c]	Cov. Index[d]	Flux Ratio[e]	Distance (arcsec)[f]
5626	3 32 30.881	-27 47 20.80	28.30±0.23	4.56	5609	0.516	0.255	1.298
5627	3 32 30.408	-27 47 20.03	27.72±0.11	9.45	5750	0.026	1.783	2.969
5628	3 32 37.007	-27 47 20.99	28.80±0.33	2.48	5562	0.287	0.436	1.610
5634	3 32 46.780	-27 47 19.49	27.53±0.12	9.17	5802	0.568	0.193	0.720
5649	3 32 47.926	-27 47 20.10	26.87±0.10	11.24	5657	0.645	0.108	0.509
5658	3 32 41.769	-27 47 16.82	25.24±0.02	68.15	5894	0.269	0.194	1.527
5661	3 32 31.775	-27 47 20.19	26.71±0.04	23.58	5459	0.004	0.150	3.877
5662	3 32 36.314	-27 47 19.78	28.70±0.29	3.33	5380	0.074	4.380	2.546
5670	3 32 46.542	-27 47 8.88	23.23±0.00	332.49	6520	0.015	0.003	3.827
5679	3 32 47.344	-27 47 18.72	27.94±0.15	7.00	5707	0.335	0.339	1.440
5683	3 32 39.727	-27 47 17.27	27.53±0.11	9.72	5867	0.089	0.152	2.099
5685	3 32 38.683	-27 47 16.22	25.90±0.02	42.17	5863	0.186	0.069	1.800
5686	3 32 41.728	-27 47 18.54	27.23±0.08	13.14	5658	0.202	4.976	1.836
5687	3 32 42.423	-27 47 19.09	28.11±0.16	6.89	5766	0.006	0.763	3.759
5688	3 32 41.128	-27 47 19.84	27.91±0.15	7.19	5783	0.363	0.415	1.018
5694	3 32 43.469	-27 47 12.97	24.68±0.01	94.53	6118	0.433	0.271	0.805
5697	3 32 30.175	-27 47 16.86	26.21±0.04	22.38	5864	0.541	0.261	1.080
5701	3 32 48.277	-27 47 17.32	27.23±0.08	13.81	5849	0.136	0.209	1.836
5707	3 32 47.249	-27 47 18.55	27.12±0.07	14.64	5679	0.328	2.950	1.440
5709	3 32 35.667	-27 47 19.14	26.76±0.05	22.51	5501	0.076	11.019	2.621
5716	3 32 44.764	-27 47 18.85	28.90±0.36	1.91	5639	0.378	0.263	1.298
5726	3 32 33.624	-27 47 17.75	27.45±0.09	10.93	5732	0.072	0.146	2.036
5735	3 32 34.523	-27 47 18.51	27.75±0.12	8.55	5856	0.058	2.091	2.305
5748	3 32 43.956	-27 47 15.64	25.70±0.02	45.58	5983	0.237	0.545	1.800
5750	3 32 30.220	-27 47 19.20	27.97±0.14	7.55	5812	0.197	1.804	1.939
5753	3 32 32.325	-27 47 18.33	26.57±0.04	25.29	5714	0.284	0.510	1.610
5766	3 32 42.665	-27 47 17.86	28.36±0.21	4.47	5727	0.046	0.344	2.305
5771	3 32 44.543	-27 47 17.33	27.52±0.10	11.19	5716	0.008	0.944	3.706
5778	3 32 44.261	-27 47 18.32	28.95±0.36	-5.03	5603	0.015	0.707	3.260
5787	3 32 43.948	-27 47 13.68	25.53±0.02	50.24	5983	0.407	0.460	1.298
5805	3 32 46.095	-27 47 13.86	24.23±0.01	193.33	6135	0.023	0.019	3.076
5808	3 32 40.722	-27 47 17.06	28.89±0.35	1.37	5870	0.210	0.202	1.800
5812	3 32 30.253	-27 47 17.48	26.39±0.05	23.79	5864	0.693	0.257	0.805
5815	3 32 47.598	-27 47 16.13	27.91±0.14	8.38	5887	0.049	0.702	2.277
5827	3 32 38.800	-27 47 14.86	25.84±0.02	45.41	6090	0.220	0.134	1.800
5831	3 32 43.396	-27 47 14.40	25.76±0.02	46.33	5694	0.361	2.267	1.800

Table C.1—Continued

ID[a]	R.A.	Decl.	u (mag)[b]	S/N	Cov. ID[c]	Cov. Index[d]	Flux Ratio[e]	Distance (arcsec)[f]
5837	3 32 38.844	-27 47 17.64	28.17±0.17	5.82	5615	0.045	2.482	2.969
5839	3 32 45.094	-27 47 17.52	28.91±0.36	-8.41	5886	0.409	0.428	1.138
5843	3 32 35.093	-27 47 17.06	27.51±0.10	11.16	5937	0.172	0.271	1.800
5849	3 32 48.140	-27 47 17.36	28.48±0.23	4.43	5701	0.155	4.788	1.836
5856	3 32 34.415	-27 47 16.81	28.97±0.36	-3.27	5735	0.060	0.478	2.305
5860	3 32 36.552	-27 47 16.72	26.20±0.03	34.77	5954	0.356	0.089	1.298
5867	3 32 39.596	-27 47 16.01	28.83±0.32	-1.86	5683	0.105	6.561	2.099
5877	3 32 44.319	-27 47 15.09	28.32±0.35	-1.78	6012	0.707	0.375	0.509
5878	3 32 35.525	-27 47 15.59	25.82±0.02	49.42	6171	0.030	0.032	3.600
5887	3 32 47.436	-27 47 16.97	28.60±0.25	4.18	5679	0.077	4.115	2.305
5888	3 32 42.209	-27 47 16.66	28.93±0.36	2.47	5869	0.321	0.459	1.484
5894	3 32 41.834	-27 47 15.65	26.73±0.05	21.57	5658	0.408	5.159	1.527
5896	3 32 36.966	-27 47 15.72	25.81±0.02	51.44	5924	0.201	0.082	1.800
5898	3 32 31.398	-27 47 13.45	25.72±0.02	51.54	6047	0.159	0.426	2.305
5916	3 32 47.263	-27 47 16.21	27.73±0.11	9.43	5707	0.048	1.603	2.520
5920	3 32 37.176	-27 47 15.28	28.76±0.30	3.42	5853	0.059	0.634	2.305
5922	3 32 31.568	-27 47 11.13	25.53±0.02	50.03	6047	0.351	0.326	1.298
5932	3 32 42.532	-27 47 14.34	28.89±0.34	-3.17	5995	0.081	3.803	2.099
5933	3 32 42.778	-27 47 14.25	27.19±0.08	12.82	6074	0.556	0.053	1.138
5946	3 32 31.370	-27 47 6.54	24.77±0.01	82.87	6399	0.025	0.045	3.877
5952	3 32 34.044	-27 47 15.37	28.86±0.33	-1.44	6014	0.018	0.248	2.880
5959	3 32 39.382	-27 47 14.27	25.31±0.01	89.55	6162	0.011	0.392	3.319
5962	3 32 47.419	-27 47 11.01	26.93±0.07	17.55	6289	0.009	0.263	3.618
5975	3 32 41.691	-27 47 13.56	25.92±0.02	46.93	5894	0.021	0.435	3.055
5989	3 32 38.629	-27 47 11.42	25.18±0.01	87.41	6196	0.170	0.442	1.610
5995	3 32 42.661	-27 47 13.06	25.48±0.02	72.14	5933	0.131	0.599	2.099
5999	3 32 30.778	-27 47 12.27	26.27±0.03	33.53	5996	0.001	0.082	4.610
6009	3 32 42.971	-27 47 9.95	25.58±0.03	40.14	6311	0.625	0.236	1.298
6017	3 32 34.925	-27 47 14.65	27.63±0.12	8.96	6117	0.395	0.247	1.298
6018	3 32 32.690	-27 47 12.03	27.52±0.11	10.22	6282	0.553	0.094	1.527
6027	3 32 39.637	-27 47 9.12	27.07±0.08	13.51	6508	0.054	0.084	2.742
6038	3 32 37.734	-27 47 6.96	27.75±0.16	6.85	6348	0.049	0.032	3.097
6047	3 32 31.512	-27 47 12.26	28.19±0.20	4.53	5922	0.427	3.071	1.298
6051	3 32 32.408	-27 47 12.52	26.30±0.03	31.97	6076	0.095	0.260	2.036
6056	3 32 34.380	-27 47 12.60	26.02±0.03	38.47	5606	0.009	61.625	3.976
6060	3 32 47.025	-27 47 11.07	26.23±0.03	34.50	6289	0.090	0.171	2.546

Table C.1—Continued

ID[a]	R.A.	Decl.	u (mag)[b]	S/N	Cov. ID[c]	Cov. Index[d]	Flux Ratio[e]	Distance (arcsec)[f]
6066	3 32 44.296	-27 47 13.11	28.85±0.34	-6.34	6012	0.529	0.268	1.440
6076	3 32 32.294	-27 47 13.76	27.28±0.07	14.19	6051	0.112	3.847	2.036
6079	3 32 33.458	-27 47 12.40	26.26±0.03	35.30	6322	0.048	0.223	2.277
6082	3 32 34.732	-27 47 7.57	23.70±0.00	337.67	6535	0.081	0.009	2.099
6090	3 32 38.730	-27 47 13.69	27.53±0.10	10.77	5827	0.282	7.464	1.800
6103	3 32 31.978	-27 47 12.20	28.19±0.35	1.25	6178	0.628	0.201	0.509
6108	3 32 47.852	-27 47 12.93	28.77±0.30	3.61	6236	0.037	0.563	2.596
6110	3 32 40.637	-27 47 13.33	28.85±0.32	-4.71	6273	0.158	0.343	1.800
6112	3 32 48.432	-27 47 13.56	27.77±0.13	8.31	6062	0.391	0.593	1.138
6119	3 32 37.012	-27 47 13.31	26.64±0.05	23.15	6214	0.267	0.204	1.138
6123	3 32 41.093	-27 47 12.81	28.78±0.32	-1.46	6115	0.338	0.527	1.298
6128	3 32 37.383	-27 47 13.09	28.98±0.36	0.46	6187	0.016	1.451	3.220
6133	3 32 30.258	-27 47 10.27	25.21±0.01	85.82	6265	0.091	0.013	2.415
6139	3 32 37.950	-27 47 11.00	28.96±0.37	-7.14	6025	0.003	0.198	3.618
6143	3 32 40.299	-27 47 11.32	28.20±0.18	5.84	6306	0.023	0.222	2.969
6151	3 32 32.210	-27 47 12.03	26.95±0.06	18.85	6076	0.070	1.002	2.305
6162	3 32 39.233	-27 47 11.89	27.07±0.06	17.65	6201	0.174	0.446	2.160
6187	3 32 37.480	-27 47 10.44	26.73±0.05	23.06	6348	0.064	0.189	1.939
6188	3 32 42.379	-27 47 7.63	28.68±0.37	3.32	6704	0.006	0.048	3.600
6190	3 32 41.013	-27 47 10.85	27.63±0.11	7.97	6352	0.273	1.233	1.298
6196	3 32 38.515	-27 47 10.67	25.95±0.02	47.58	5989	0.202	2.262	1.610
6197	3 32 42.818	-27 47 10.22	27.74±0.17	5.89	6334	0.684	0.311	0.720
6201	3 32 39.108	-27 47 11.91	27.04±0.06	17.78	6244	0.178	0.280	1.484
6203	3 32 43.388	-27 47 10.55	26.23±0.03	38.16	6118	0.103	0.315	2.036
6206	3 32 38.487	-27 47 2.40	25.54±0.02	52.28	6919	0.062	0.026	2.305
6227	3 32 32.836	-27 47 10.04	27.95±0.18	5.67	6341	0.611	0.175	0.805
6250	3 32 46.136	-27 47 9.63	26.38±0.03	31.01	6391	0.381	0.142	1.484
6260	3 32 44.813	-27 47 10.58	28.87±0.36	-1.30	6290	0.478	1.507	1.138
6274	3 32 45.811	-27 47 5.18	28.17±0.26	2.91	6584	0.515	0.201	0.805
6278	3 32 44.772	-27 47 8.89	27.62±0.12	9.45	6290	0.317	0.705	1.484
6288	3 32 40.878	-27 47 6.95	25.32±0.01	82.86	6425	0.021	0.016	3.220
6289	3 32 47.173	-27 47 10.70	28.97±0.36	2.45	6060	0.108	5.838	2.546
6290	3 32 44.739	-27 47 10.19	27.63±0.12	8.45	6260	0.408	0.663	1.138
6317	3 32 36.273	-27 47 9.54	28.25±0.19	4.56	6416	0.034	0.326	2.742
6322	3 32 33.399	-27 47 10.19	27.76±0.12	9.17	6388	0.140	0.202	2.277
6335	3 32 32.863	-27 47 8.62	27.23±0.08	13.79	6341	0.455	0.230	1.018

Table C.1—Continued

ID[a]	R.A.	Decl.	u (mag)[b]	S/N	Cov. ID[c]	Cov. Index[d]	Flux Ratio[e]	Distance (arcsec)[f]
6352	3 32 40.979	-27 47 9.58	28.69±0.31	3.25	6404	0.490	0.202	1.484
6377	3 32 38.370	-27 47 8.81	27.52±0.09	11.51	6196	0.027	3.841	2.812
6386	3 32 32.444	-27 47 8.45	28.99±0.36	1.00	6519	0.010	1.272	3.396
6391	3 32 46.102	-27 47 8.05	27.26±0.13	7.64	6477	0.783	0.235	0.805
6394	3 32 40.074	-27 47 5.01	25.73±0.02	48.55	6488	0.057	0.163	2.305
6396	3 32 39.139	-27 47 8.20	28.14±0.17	6.17	6244	0.004	0.248	3.894
6399	3 32 31.611	-27 47 8.02	28.38±0.21	4.80	5946	0.067	22.352	3.877
6411	3 32 30.948	-27 47 8.50	27.87±0.13	8.17	6421	0.116	0.181	2.160
6438	3 32 35.773	-27 47 6.21	26.48±0.04	26.09	6614	0.353	0.136	1.527
6451	3 32 36.372	-27 47 7.26	28.86±0.35	-3.75	6568	0.358	0.111	1.527
6462	3 32 43.589	-27 46 59.26	24.63±0.01	103.60	6886	0.278	0.187	1.440
6478	3 32 46.015	-27 47 6.38	28.48±0.33	2.31	6609	0.458	0.189	1.138
6487	3 32 45.428	-27 47 6.60	28.78±0.35	-1.43	6570	0.536	0.316	0.805
6488	3 32 40.170	-27 47 6.86	28.89±0.33	-2.24	6394	0.074	6.153	2.305
6490	3 32 41.344	-27 47 6.69	27.09±0.06	17.54	6630	0.011	0.332	3.546
6498	3 32 47.318	-27 47 7.02	28.05±0.24	4.52	6530	0.761	0.307	0.509
6499	3 32 35.013	-27 47 4.85	26.40±0.04	27.54	6494	0.200	0.118	1.800
6502	3 32 33.258	-27 47 6.54	28.86±0.35	1.83	6541	0.317	0.793	1.440
6504	3 32 32.985	-27 47 6.84	28.98±0.36	-1.14	6590	0.067	0.148	2.546
6506	3 32 35.950	-27 47 5.97	26.79±0.05	21.27	6614	0.223	0.150	1.939
6508	3 32 39.580	-27 47 6.89	28.96±0.35	-2.34	6027	0.085	11.881	2.742
6518	3 32 42.993	-27 47 6.16	27.27±0.08	12.86	6542	0.246	3.219	1.440
6519	3 32 32.574	-27 47 5.76	28.94±0.36	0.04	6684	0.035	0.405	2.742
6520	3 32 46.701	-27 47 5.85	28.88±0.33	-2.19	5670	0.049	312.608	3.827
6523	3 32 34.435	-27 46 59.57	28.55±0.35	0.25	6839	0.011	0.716	3.319
6527	3 32 43.480	-27 47 6.33	28.97±0.36	-2.54	6595	0.139	0.604	2.277
6533	3 32 47.218	-27 47 5.16	28.97±0.37	-0.79	6498	0.076	0.472	2.546
6539	3 32 42.084	-27 47 4.91	28.95±0.35	2.39	6777	0.083	0.172	2.099
6542	3 32 42.881	-27 47 5.83	27.54±0.10	10.69	6518	0.240	0.311	1.440
6543	3 32 31.930	-27 47 4.08	28.78±0.33	1.01	6674	0.395	1.605	1.484
6554	3 32 30.599	-27 47 5.94	28.64±0.35	-2.98	6515	0.625	0.233	0.805
6558	3 32 46.115	-27 47 4.32	26.22±0.03	30.83	6609	0.208	0.163	1.527
6576	3 32 40.643	-27 47 5.94	27.10±0.06	16.96	6288	0.009	15.820	3.759
6595	3 32 43.355	-27 47 5.76	28.98±0.35	-1.42	6527	0.143	1.657	2.277
6607	3 32 42.517	-27 47 2.76	26.03±0.03	42.35	6704	0.140	0.045	1.836
6614	3 32 35.843	-27 47 5.35	27.90±0.15	6.55	6438	0.371	7.357	1.527

Table C.1—Continued

ID[a]	R.A.	Decl.	u (mag)[b]	S/N	Cov. ID[c]	Cov. Index[d]	Flux Ratio[e]	Distance (arcsec)[f]
6627	3 32 35.385	-27 47 4.27	26.14±0.03	36.36	6624	0.441	0.200	1.080
6642	3 32 38.963	-27 47 3.99	26.70±0.04	25.06	6936	0.015	0.081	2.902
6645	3 32 33.176	-27 47 3.67	26.10±0.03	33.59	6648	0.332	0.259	1.298
6648	3 32 33.251	-27 47 4.45	27.26±0.08	12.15	6645	0.396	3.862	1.298
6649	3 32 36.967	-27 47 2.99	28.03±0.21	4.65	6799	0.487	0.200	1.080
6658	3 32 38.108	-27 47 4.59	26.78±0.19	5.58	6708	0.623	0.422	0.509
6670	3 32 43.148	-27 47 3.38	27.83±0.12	8.99	6518	0.006	0.720	3.564
6671	3 32 42.711	-27 47 4.48	28.57±0.32	3.13	6657	0.720	0.216	0.805
6673	3 32 34.767	-27 47 4.39	27.57±0.10	11.04	6585	0.046	0.247	2.546
6675	3 32 44.645	-27 47 2.34	27.62±0.11	9.60	6926	0.199	0.102	1.800
6680	3 32 31.156	-27 47 2.74	25.49±0.02	67.82	6754	0.118	0.533	2.190
6695	3 32 46.339	-27 47 3.77	28.98±0.36	0.46	6710	0.040	4.153	2.812
6700	3 32 36.124	-27 47 1.93	26.46±0.04	28.55	41136	0.340	0.052	1.610
6701	3 32 34.155	-27 47 3.75	28.93±0.36	-5.06	6774	0.243	0.203	1.610
6710	3 32 46.221	-27 47 1.69	25.98±0.03	38.91	6893	0.412	0.839	1.298
6715	3 32 32.959	-27 47 2.06	27.63±0.15	6.48	6828	0.626	0.403	0.805
6722	3 32 44.263	-27 47 3.71	28.96±0.35	-3.12	6820	0.032	0.994	3.097
6732	3 32 42.837	-27 47 2.54	28.94±0.37	-2.85	6808	0.367	0.084	1.298
6747	3 32 38.792	-27 46 48.92	26.93±0.08	15.32	20061	0.042	0.045	3.319
6749	3 32 32.327	-27 47 3.45	27.65±0.11	9.92	6684	0.227	0.481	1.527
6754	3 32 31.298	-27 47 2.33	25.94±0.02	48.31	6680	0.130	1.875	2.190
6776	3 32 36.346	-27 47 2.10	28.55±0.25	3.94	41136	0.121	0.487	1.939
6778	3 32 36.963	-27 47 1.68	28.82±0.33	1.99	6649	0.355	1.753	1.440
6781	3 32 43.658	-27 47 1.21	27.19±0.08	12.22	6941	0.205	4.193	1.800
6782	3 32 32.507	-27 47 2.03	26.62±0.04	26.17	6992	0.057	0.311	2.277
6785	3 32 45.975	-27 46 57.59	24.56±0.01	137.00	6939	0.178	0.185	1.527
6808	3 32 42.910	-27 47 1.76	28.84±0.34	-3.54	6732	0.362	11.919	1.298
6820	3 32 44.418	-27 47 2.21	29.00±0.36	-3.46	6926	0.048	0.400	2.415
6821	3 32 42.773	-27 46 59.08	24.45±0.01	177.55	7045	0.017	0.059	3.671
6827	3 32 42.399	-27 47 1.69	28.91±0.35	1.16	6912	0.193	0.652	1.484
6834	3 32 41.839	-27 46 57.20	25.73±0.02	49.83	7169	0.223	0.034	1.939
6837	3 32 45.970	-27 47 1.82	27.70±0.11	8.96	6558	0.019	1.742	3.319
6839	3 32 34.588	-27 47 1.98	28.98±0.36	0.62	6523	0.022	1.396	3.319
6846	3 32 44.297	-27 46 60.00	26.23±0.04	28.75	6949	0.825	0.265	1.138
6853	3 32 36.441	-27 46 58.31	24.72±0.01	145.17	7144	0.128	0.025	1.836
6854	3 32 41.302	-27 47 1.76	27.42±0.08	11.86	6899	0.126	0.199	2.160

Table C.1—Continued

ID[a]	R.A.	Decl.	u (mag)[b]	S/N	Cov. ID[c]	Cov. Index[d]	Flux Ratio[e]	Distance (arcsec)[f]
6862	3 32 41.430	-27 46 51.47	24.85±0.01	102.74	7270	0.040	0.012	2.546
6870	3 32 46.926	-27 47 1.50	27.77±0.12	8.96	6994	0.021	0.199	3.220
6874	3 32 44.205	-27 47 0.71	27.68±0.16	6.85	6949	0.841	0.486	0.509
6893	3 32 46.262	-27 47 0.71	27.13±0.07	14.84	6710	0.462	1.191	1.298
6894	3 32 31.132	-27 47 0.31	26.88±0.06	19.82	7017	0.351	0.102	1.298
6912	3 32 42.382	-27 47 0.09	28.85±0.33	2.82	6827	0.195	1.534	1.484
6919	3 32 38.392	-27 47 0.60	28.88±0.32	-0.56	6206	0.126	38.321	2.305
6922	3 32 36.189	-27 46 57.13	26.09±0.03	30.32	7202	0.350	0.136	1.440
6933	3 32 33.428	-27 46 50.41	24.56±0.01	103.06	7424	0.484	0.159	0.720
6937	3 32 37.837	-27 46 59.93	28.97±0.36	-0.26	7137	0.020	0.313	2.969
6939	3 32 46.064	-27 46 58.69	25.98±0.02	43.25	6785	0.251	5.412	1.527
6941	3 32 43.738	-27 46 59.93	26.00±0.03	35.26	6911	0.456	0.614	1.484
6953	3 32 36.668	-27 46 57.70	25.64±0.02	64.63	7161	0.033	0.035	2.621
6957	3 32 35.063	-27 46 58.69	26.10±0.03	42.43	6942	0.009	0.076	3.396
6959	3 32 42.364	-27 46 57.20	26.64±0.05	23.72	7166	0.194	0.059	1.939
6967	3 32 40.296	-27 46 59.44	26.96±0.06	17.59	7013	0.150	0.234	1.800
6974	3 32 37.965	-27 46 51.93	23.16±0.00	448.60	7308	0.020	0.004	3.220
6993	3 32 44.803	-27 46 58.21	26.80±0.06	18.41	7011	0.545	0.452	1.080
6997	3 32 33.193	-27 46 56.32	26.60±0.04	23.50	7153	0.023	0.051	2.969
6999	3 32 40.993	-27 46 59.32	28.88±0.33	2.27	7113	0.108	0.160	1.836
7012	3 32 41.942	-27 46 58.22	27.15±0.08	12.28	7086	0.321	0.531	1.836
7022	3 32 44.770	-27 46 55.03	25.87±0.02	46.37	7194	0.129	0.162	1.939
7025	3 32 46.977	-27 46 57.79	29.02±0.37	-1.60	6994	0.023	0.034	3.055
7028	3 32 39.491	-27 46 59.21	28.05±0.15	6.73	7077	0.022	0.209	2.969
7036	3 32 45.682	-27 46 55.20	24.77±0.01	127.86	7060	0.058	0.037	2.160
7037	3 32 35.764	-27 46 54.93	26.51±0.04	25.23	7247	0.182	0.063	1.800
7046	3 32 38.631	-27 46 58.27	27.77±0.13	8.38	7030	0.272	0.385	1.939
7067	3 32 32.446	-27 46 56.44	26.09±0.04	28.95	7154	0.662	0.121	0.805
7071	3 32 36.447	-27 46 55.05	24.97±0.01	97.81	7144	0.235	0.028	1.440
7072	3 32 40.145	-27 46 57.93	27.66±0.11	9.23	7125	0.298	0.741	1.610
7076	3 32 46.279	-27 46 56.98	27.74±0.12	8.73	7065	0.186	0.567	1.939
7086	3 32 42.074	-27 46 57.79	28.00±0.25	4.12	56971	0.840	0.273	0.720
7104	3 32 31.419	-27 46 57.33	26.52±0.05	21.60	7126	0.669	0.143	0.805
7112	3 32 39.810	-27 46 53.54	25.14±0.01	94.35	7230	0.081	0.282	2.546
7121	3 32 40.966	-27 46 55.10	26.88±0.05	20.99	7219	0.076	0.136	2.190
7129	3 32 47.430	-27 46 57.36	28.49±0.23	4.73	57075	0.105	0.339	2.099

Table C.1—Continued

ID[a]	R.A.	Decl.	u (mag)[b]	S/N	Cov. ID[c]	Cov. Index[d]	Flux Ratio[e]	Distance (arcsec)[f]
7131	3 32 32.462	-27 46 54.03	26.20±0.03	37.34	7211	0.105	0.042	2.099
7146	3 32 31.172	-27 46 56.12	26.30±0.03	34.74	7151	0.105	0.174	1.939
7148	3 32 47.136	-27 46 55.53	27.59±0.10	10.36	7275	0.021	0.182	3.076
7151	3 32 31.053	-27 46 57.05	28.80±0.35	-1.34	7092	0.478	0.321	1.018
7172	3 32 41.680	-27 46 55.38	28.81±0.35	0.94	7169	0.352	0.527	1.484
7185	3 32 44.234	-27 46 55.13	27.97±0.15	7.23	7158	0.192	0.298	1.440
7188	3 32 35.409	-27 46 56.08	28.31±0.19	5.64	7097	0.111	0.269	1.939
7189	3 32 40.309	-27 46 55.24	28.76±0.34	1.18	7190	0.412	0.226	1.138
7193	3 32 33.432	-27 46 55.41	27.68±0.12	8.53	7291	0.270	0.225	1.484
7194	3 32 44.648	-27 46 56.00	26.83±0.05	21.92	7022	0.166	6.156	1.939
7199	3 32 38.486	-27 46 55.30	27.89±0.13	7.40	7030	0.038	0.629	2.546
7203	3 32 34.795	-27 46 50.94	26.36±0.04	27.22	7478	0.189	0.182	1.939
7209	3 32 35.588	-27 46 55.75	28.86±0.35	2.46	7247	0.423	0.433	1.298
7219	3 32 40.815	-27 46 55.46	27.73±0.11	8.64	7121	0.081	7.341	2.190
7227	3 32 35.255	-27 46 54.40	25.56±0.02	52.74	7319	0.528	0.046	1.018
7230	3 32 39.643	-27 46 53.80	26.27±0.03	32.43	7112	0.088	3.543	2.546
7234	3 32 31.940	-27 46 53.78	26.16±0.03	37.68	7326	0.004	0.231	3.894
7244	3 32 38.743	-27 46 54.15	28.92±0.35	2.01	7120	0.055	0.172	2.621
7246	3 32 41.991	-27 46 54.26	28.68±0.27	4.06	7268	0.142	0.710	2.190
7268	3 32 41.861	-27 46 53.65	27.47±0.09	11.94	7246	0.142	1.407	2.190
7269	3 32 41.862	-27 46 51.09	25.38±0.02	65.84	7459	0.078	0.166	2.812
7274	3 32 46.876	-27 46 53.91	28.54±0.36	2.63	7332	0.679	0.166	0.805
7290	3 32 36.930	-27 46 53.97	27.17±0.07	16.46	7382	0.037	1.845	3.097
7312	3 32 46.530	-27 46 52.72	28.86±0.33	3.26	7347	0.010	1.939	3.618
7313	3 32 36.355	-27 46 52.89	27.34±0.08	13.89	7071	0.054	5.630	2.596
7316	3 32 33.153	-27 46 52.95	27.97±0.15	7.41	7352	0.243	0.126	1.484
7318	3 32 32.273	-27 46 52.74	27.30±0.08	11.35	7326	0.132	0.864	2.099
7326	3 32 32.173	-27 46 51.51	28.60±0.32	-0.56	7427	0.839	0.394	1.298
7328	3 32 42.974	-27 46 49.90	28.79±0.36	-0.04	7406	0.377	1.081	1.527
7330	3 32 35.045	-27 46 51.74	27.01±0.08	12.60	7465	0.577	0.237	0.509
7338	3 32 35.126	-27 46 52.68	28.76±0.34	-2.85	7400	0.332	1.456	1.080
7347	3 32 46.290	-27 46 52.34	27.11±0.06	16.59	9078	0.038	0.201	2.415
7370	3 32 32.711	-27 46 51.55	26.39±0.04	24.76	7447	0.608	0.087	1.018
7375	3 32 40.387	-27 46 51.81	28.47±0.36	1.29	7374	0.795	0.153	0.509
7392	3 32 33.712	-27 46 51.33	27.07±0.07	14.42	7409	0.540	0.120	1.018
7394	3 32 38.990	-27 46 51.05	26.61±0.04	24.29	7489	0.418	0.271	1.018

Table C.1—Continued

ID[a]	R.A.	Decl.	u (mag)[b]	S/N	Cov. ID[c]	Cov. Index[d]	Flux Ratio[e]	Distance (arcsec)[f]
7398	3 32 42.319	-27 46 51.09	25.67±0.02	65.52	7492	0.015	0.176	3.319
7400	3 32 35.145	-27 46 51.55	28.73±0.33	1.41	7338	0.341	0.687	1.080
7406	3 32 43.023	-27 46 48.88	27.52±0.11	10.18	7328	0.423	0.925	1.527
7423	3 32 37.019	-27 46 51.28	28.13±0.21	4.90	7443	0.676	0.204	0.720
7428	3 32 34.508	-27 46 51.08	28.29±0.25	4.18	7487	0.670	0.275	0.805
7432	3 32 37.360	-27 46 45.41	25.40±0.02	55.52	8897	0.408	0.252	1.018
7452	3 32 44.198	-27 46 47.12	25.69±0.02	54.53	7695	0.306	0.063	1.610
7459	3 32 41.708	-27 46 49.53	27.21±0.08	12.88	9211	0.428	0.321	1.138
7469	3 32 45.619	-27 46 49.99	28.50±0.36	-0.82	9146	0.710	0.306	0.805
7471	3 32 39.891	-27 46 49.97	28.14±0.17	6.05	9016	0.061	0.216	2.596
7478	3 32 34.913	-27 46 50.29	28.82±0.33	-4.66	7465	0.320	0.323	1.800
7490	3 32 32.106	-27 46 48.59	26.85±0.06	17.16	8972	0.180	0.526	1.836
7492	3 32 42.093	-27 46 50.39	27.64±0.12	8.58	7720	0.473	0.833	1.298
7495	3 32 44.422	-27 46 41.86	24.53±0.01	135.06	8089	0.051	0.010	2.812
7506	3 32 38.286	-27 46 11.65	28.35±0.24	4.24	7563	0.466	0.816	1.080
7526	3 32 37.081	-27 46 47.01	25.32±0.01	77.44	9010	0.035	0.036	2.812
7529	3 32 36.250	-27 46 13.05	27.99±0.15	6.79	7602	0.287	0.278	1.298
7534	3 32 40.461	-27 46 11.97	28.80±0.32	2.39	9110	0.079	0.643	2.415
7555	3 32 41.805	-27 46 12.13	27.64±0.11	9.48	9120	0.316	0.168	1.298
7556	3 32 40.781	-27 46 15.68	22.60±0.00	512.67	7749	0.004	0.001	4.694
7559	3 32 38.097	-27 46 13.93	24.21±0.01	207.27	7535	0.041	0.024	2.305
7587	3 32 45.696	-27 46 47.87	27.19±0.07	15.39	9146	0.266	0.097	1.610
7593	3 32 38.670	-27 46 13.21	27.08±0.07	16.28	7501	0.267	0.230	1.484
7600	3 32 34.718	-27 46 16.00	29.01±0.37	-8.15	7816	0.003	0.165	3.546
7608	3 32 38.403	-27 46 15.65	25.89±0.02	47.94	7660	0.324	0.092	1.138
7610	3 32 37.152	-27 46 49.40	28.93±0.35	1.91	9010	0.321	0.439	1.298
7613	3 32 42.638	-27 46 18.02	27.40±0.08	12.69	7987	0.089	0.263	2.160
7617	3 32 43.109	-27 46 14.10	28.88±0.34	0.00	7712	0.193	1.096	1.484
7633	3 32 39.779	-27 46 47.36	28.72±0.33	-1.41	9016	0.452	0.230	1.138
7647	3 32 41.426	-27 46 15.35	26.18±0.03	29.43	7639	0.365	0.125	1.018
7658	3 32 37.100	-27 46 14.34	28.86±0.33	-0.79	7751	0.086	0.302	2.099
7664	3 32 36.955	-27 46 15.57	25.50±0.02	60.27	7786	0.101	1.967	2.036
7669	3 32 37.291	-27 46 14.44	28.81±0.34	1.10	7670	0.377	0.465	1.138
7671	3 32 35.584	-27 46 48.92	28.94±0.36	-2.28	8964	0.253	2.113	1.527
7675	3 32 38.830	-27 46 14.33	28.88±0.34	-6.27	7678	0.064	5.320	2.621
7678	3 32 38.991	-27 46 15.30	25.80±0.02	50.16	7790	0.116	0.084	2.036

Table C.1—Continued

ID[a]	R.A.	Decl.	u (mag)[b]	S/N	Cov. ID[c]	Cov. Index[d]	Flux Ratio[e]	Distance (arcsec)[f]
7681	3 32 37.448	-27 46 15.43	26.42±0.04	27.37	7609	0.282	0.110	1.484
7687	3 32 36.141	-27 46 16.30	23.91±0.00	202.72	7688	0.433	3.243	1.800
7688	3 32 36.148	-27 46 18.07	23.26±0.00	315.79	7687	0.236	0.308	1.800
7705	3 32 37.565	-27 46 46.78	25.95±0.02	41.12	8930	0.223	0.431	1.800
7710	3 32 36.117	-27 46 47.07	28.96±0.35	-2.72	7630	0.085	0.765	1.836
7711	3 32 34.547	-27 46 47.01	26.77±0.05	22.82	7701	0.069	0.082	2.190
7712	3 32 43.070	-27 46 15.65	27.90±0.14	7.38	7963	0.252	0.073	1.610
7720	3 32 42.053	-27 46 49.52	28.81±0.34	0.44	7492	0.487	1.201	1.298
7725	3 32 35.082	-27 46 15.74	24.83±0.01	112.92	7878	0.007	0.020	4.335
7737	3 32 35.284	-27 46 12.22	25.64±0.02	58.67	7516	0.222	0.019	1.527
7738	3 32 38.974	-27 46 17.77	28.91±0.35	-4.43	8105	0.249	3.990	1.440
7743	3 32 41.342	-27 46 46.27	26.37±0.04	29.89	8346	0.284	0.094	1.800
7750	3 32 37.425	-27 46 12.29	28.66±0.30	-5.20	7670	0.092	0.324	1.939
7756	3 32 33.912	-27 46 17.06	26.48±0.04	24.07	58328	0.250	0.284	1.298
7758	3 32 38.383	-27 46 45.82	28.97±0.36	-0.52	8987	0.205	0.312	1.610
7760	3 32 43.087	-27 46 46.12	26.78±0.05	21.24	8872	0.095	0.376	2.277
7762	3 32 35.475	-27 46 16.93	26.17±0.03	34.44	7776	0.274	0.063	1.298
7775	3 32 41.303	-27 46 13.39	27.66±0.12	9.21	7639	0.311	0.088	1.527
7780	3 32 34.382	-27 46 16.52	27.48±0.09	11.25	7838	0.027	0.051	2.546
7786	3 32 37.072	-27 46 17.19	25.49±0.02	62.43	8126	0.300	0.062	1.800
7815	3 32 32.739	-27 46 40.70	28.93±0.35	-8.57	8905	0.065	0.220	2.305
7827	3 32 36.673	-27 46 17.84	28.37±0.22	4.58	7806	0.147	0.298	2.160
7845	3 32 34.892	-27 46 47.04	26.66±0.05	21.20	8954	0.174	0.495	1.939
7847	3 32 41.759	-27 46 19.40	24.96±0.01	103.93	8039	0.027	0.007	2.742
7862	3 32 45.242	-27 46 43.00	27.99±0.33	1.36	7925	0.699	0.296	0.509
7868	3 32 39.296	-27 46 44.67	28.96±0.35	-0.94	8926	0.131	0.153	1.800
7874	3 32 37.700	-27 46 48.97	28.98±0.36	0.05	7705	0.027	2.272	3.055
7879	3 32 40.437	-27 46 18.98	28.64±0.26	4.10	7805	0.026	0.338	3.076
7900	3 32 40.975	-27 46 19.99	27.55±0.10	9.90	8006	0.283	0.639	1.484
7905	3 32 39.576	-27 46 43.42	25.42±0.02	64.20	7868	0.003	0.230	4.554
7907	3 32 43.245	-27 46 44.39	28.65±0.32	1.35	7812	0.358	0.131	1.298
7909	3 32 39.643	-27 46 20.48	27.80±0.14	7.59	7928	0.466	0.166	1.080
7938	3 32 39.066	-27 46 42.28	26.78±0.05	21.39	8926	0.018	0.125	2.902
7953	3 32 36.691	-27 46 20.99	25.34±0.01	84.65	7827	0.011	0.139	3.260
7957	3 32 35.692	-27 46 22.59	28.72±0.34	-0.82	8021	0.417	0.072	1.080
7962	3 32 42.816	-27 46 20.07	28.90±0.35	2.18	7994	0.441	1.610	1.298

Table C.1—Continued

ID[a]	R.A.	Decl.	u (mag)[b]	S/N	Cov. ID[c]	Cov. Index[d]	Flux Ratio[e]	Distance (arcsec)[f]
7966	3 32 34.974	-27 46 20.76	27.79±0.12	8.23	7878	0.079	0.220	2.099
7974	3 32 37.734	-27 46 42.77	24.90±0.01	110.36	8941	0.245	0.128	1.610
7983	3 32 35.142	-27 46 41.92	26.27±0.03	36.06	8020	0.189	0.121	1.800
7986	3 32 38.904	-27 46 21.23	28.96±0.36	1.76	7942	0.122	0.410	1.836
7994	3 32 42.763	-27 46 18.67	28.06±0.29	3.42	7987	0.807	0.221	0.720
7995	3 32 42.251	-27 46 25.40	24.37±0.01	158.64	8120	0.112	0.018	1.800
7998	3 32 39.121	-27 46 21.01	28.86±0.35	-0.21	7942	0.418	0.328	1.440
8003	3 32 35.705	-27 46 18.13	28.93±0.35	-3.58	7754	0.247	0.288	1.527
8006	3 32 40.989	-27 46 21.43	26.59±0.06	16.42	7952	0.693	0.231	0.805
8015	3 32 33.536	-27 46 23.39	23.72±0.00	308.43	8058	0.007	0.002	3.759
8017	3 32 39.406	-27 46 22.40	28.66±0.34	-2.11	8070	0.558	0.106	1.080
8022	3 32 41.781	-27 46 22.67	28.71±0.34	-0.28	8039	0.564	0.454	1.018
8024	3 32 34.084	-27 46 41.74	28.83±0.35	-2.81	8046	0.459	0.393	0.805
8026	3 32 36.291	-27 46 22.23	25.58±0.02	65.21	7515	0.007	0.060	3.759
8037	3 32 40.458	-27 46 22.55	27.79±0.12	9.18	8259	0.120	0.652	2.546
8038	3 32 34.004	-27 46 23.15	25.21±0.01	79.87	7984	0.046	0.023	2.546
8040	3 32 38.872	-27 46 26.03	23.88±0.00	234.46	8297	0.092	0.005	2.277
8042	3 32 39.014	-27 46 22.29	28.82±0.34	0.80	7942	0.251	0.158	1.484
8049	3 32 38.971	-27 46 30.25	22.98±0.00	518.07	8297	0.025	0.002	3.055
8051	3 32 37.424	-27 46 22.54	25.84±0.02	46.43	7997	0.289	0.097	1.138
8053	3 32 38.755	-27 46 20.91	28.78±0.30	3.51	7986	0.090	0.927	2.190
8062	3 32 37.547	-27 46 20.01	28.69±0.31	-5.33	7960	0.140	0.393	2.099
8069	3 32 36.251	-27 46 38.31	26.20±0.03	37.45	8812	0.232	0.267	1.610
8071	3 32 39.335	-27 46 23.54	28.65±0.34	2.25	8070	0.619	0.096	1.080
8082	3 32 37.137	-27 46 25.93	28.71±0.32	-6.08	8315	0.087	0.310	1.800
8084	3 32 40.238	-27 46 23.37	27.93±0.15	6.48	8259	0.459	0.846	1.298
8092	3 32 44.560	-27 46 23.52	28.89±0.34	-2.72	58496	0.005	7.664	3.600
8105	3 32 39.084	-27 46 17.87	28.79±0.35	-2.89	7790	0.412	0.167	1.138
8125	3 32 41.521	-27 46 40.22	24.22±0.01	185.15	8801	0.144	0.166	2.190
8126	3 32 37.177	-27 46 17.01	28.59±0.29	-2.61	7786	0.312	16.108	1.800
8138	3 32 35.522	-27 46 28.86	26.26±0.03	30.75	8398	0.357	0.170	1.080
8150	3 32 37.989	-27 46 38.79	25.01±0.01	109.15	8757	0.213	0.336	1.939
8156	3 32 34.597	-27 46 24.79	24.87±0.01	119.67	8085	0.053	0.018	2.812
8161	3 32 35.421	-27 46 38.71	27.22±0.09	9.25	8272	0.507	0.364	0.805
8171	3 32 41.647	-27 46 25.25	26.93±0.06	17.46	8198	0.403	0.434	1.484
8177	3 32 45.109	-27 46 37.57	28.75±0.29	3.77	8750	0.051	1.714	2.546

Table C.1—Continued

ID[a]	R.A.	Decl.	u (mag)[b]	S/N	Cov. ID[c]	Cov. Index[d]	Flux Ratio[e]	Distance (arcsec)[f]
8181	3 32 35.677	-27 46 28.33	28.79±0.33	-1.58	8261	0.347	2.737	1.939
8182	3 32 41.491	-27 46 23.17	28.85±0.32	-1.73	8196	0.033	0.907	2.621
8196	3 32 41.461	-27 46 25.68	28.95±0.35	1.23	8305	0.232	0.312	1.610
8198	3 32 41.732	-27 46 25.05	28.27±0.20	4.70	8171	0.417	2.302	1.484
8207	3 32 35.640	-27 46 38.20	28.82±0.34	-4.47	8686	0.280	0.461	1.610
8217	3 32 44.002	-27 46 25.60	28.40±0.24	4.50	8342	0.021	0.080	3.097
8230	3 32 42.778	-27 46 26.37	28.71±0.35	1.96	8313	0.522	0.165	1.080
8238	3 32 36.923	-27 46 28.33	28.68±0.36	-0.81	8260	0.244	0.297	1.484
8242	3 32 34.954	-27 46 24.33	26.80±0.05	22.92	8114	0.029	0.205	3.240
8255	3 32 34.627	-27 46 37.78	26.39±0.05	22.76	8263	0.695	0.151	0.805
8257	3 32 38.589	-27 46 31.62	23.79±0.01	211.97	8316	0.129	0.384	2.546
8259	3 32 40.304	-27 46 22.79	28.55±0.35	3.05	8106	0.566	0.356	0.805
8261	3 32 35.780	-27 46 27.49	26.21±0.04	26.97	8277	0.279	0.025	1.440
8262	3 32 35.348	-27 46 39.20	25.94±0.03	30.87	8272	0.656	0.107	0.720
8270	3 32 43.973	-27 46 32.57	24.70±0.01	105.50	8273	0.807	0.308	1.298
8275	3 32 36.494	-27 46 28.98	23.03±0.00	436.32	8551	0.062	0.323	2.902
8283	3 32 36.178	-27 46 27.57	27.81±0.14	6.96	8337	0.155	0.195	1.939
8293	3 32 43.615	-27 46 28.52	26.68±0.05	21.83	8400	0.340	0.118	1.138
8294	3 32 43.859	-27 46 28.82	27.01±0.06	18.06	8420	0.019	0.139	3.076
8304	3 32 34.385	-27 46 27.40	28.97±0.35	-2.97	8098	0.004	0.345	3.600
8311	3 32 45.111	-27 46 30.44	27.39±0.08	12.77	58692	0.010	0.164	3.319
8314	3 32 36.681	-27 46 31.12	25.56±0.02	51.21	8275	0.052	5.291	3.600
8316	3 32 38.437	-27 46 31.91	26.34±0.04	27.82	8257	0.245	2.606	2.546
8327	3 32 41.763	-27 46 28.83	28.98±0.36	1.84	8376	0.016	0.268	3.894
8337	3 32 36.124	-27 46 29.27	28.30±0.20	4.28	8283	0.179	5.118	1.939
8351	3 32 38.304	-27 46 28.44	26.30±0.03	28.91	20037	0.173	3.474	1.610
8354	3 32 39.229	-27 46 30.05	28.25±0.19	5.39	8401	0.122	0.159	1.610
8355	3 32 37.407	-27 46 28.73	27.74±0.12	9.23	8410	0.107	0.220	2.036
8363	3 32 38.020	-27 46 26.15	28.70±0.35	0.94	8214	0.607	0.344	1.440
8372	3 32 35.620	-27 46 32.82	24.70±0.01	126.55	8398	0.013	0.020	3.220
8374	3 32 35.391	-27 46 30.50	26.90±0.05	18.37	8398	0.154	0.401	1.836
8387	3 32 40.224	-27 46 29.00	28.97±0.35	-1.76	8352	0.076	0.325	2.415
8392	3 32 34.185	-27 46 34.67	26.85±0.05	20.27	8640	0.190	0.132	1.800
8398	3 32 35.517	-27 46 30.06	28.09±0.17	6.08	8138	0.392	5.866	1.080
8409	3 32 41.471	-27 46 34.85	28.21±0.21	5.05	8643	0.464	0.151	1.080
8419	3 32 33.997	-27 46 29.77	28.99±0.36	-1.72	8247	0.016	0.426	2.969

Table C.1—Continued

ID[a]	R.A.	Decl.	u (mag)[b]	S/N	Cov. ID[c]	Cov. Index[d]	Flux Ratio[e]	Distance (arcsec)[f]
8428	3 32 44.073	-27 46 31.95	27.02±0.06	17.02	8270	0.331	16.121	1.610
8446	3 32 39.972	-27 46 30.93	28.56±0.25	4.26	8352	0.136	0.243	2.099
8449	3 32 40.336	-27 46 30.95	28.94±0.34	-3.06	8563	0.064	0.269	2.596
8454	3 32 42.812	-27 46 31.74	26.76±0.05	21.24	8523	0.199	1.030	1.610
8461	3 32 44.621	-27 46 32.21	24.95±0.01	102.25	8659	0.003	0.012	4.105
8467	3 32 44.250	-27 46 32.66	28.07±0.15	7.17	8428	0.042	0.696	2.969
8486	3 32 33.416	-27 46 29.46	27.48±0.09	12.14	8334	0.031	0.157	2.812
8491	3 32 34.116	-27 46 32.81	27.59±0.10	10.28	8392	0.102	2.606	2.099
8501	3 32 44.746	-27 46 37.30	27.53±0.09	11.74	8652	0.001	0.197	4.680
8504	3 32 40.239	-27 46 33.75	27.40±0.13	7.38	8563	0.712	0.243	0.360
8520	3 32 34.640	-27 46 35.25	28.41±0.24	4.41	8665	0.511	0.200	1.138
8523	3 32 42.762	-27 46 33.25	26.13±0.03	39.82	8454	0.209	0.971	1.610
8530	3 32 37.910	-27 46 32.89	28.70±0.29	-2.33	8470	0.140	0.406	1.610
8551	3 32 36.424	-27 46 31.58	24.22±0.01	167.73	8275	0.086	3.092	2.902
8553	3 32 45.654	-27 46 36.08	27.73±0.11	9.61	8587	0.024	0.293	2.621
8555	3 32 40.671	-27 46 41.50	28.91±0.34	-2.01	8602	0.003	0.122	4.335
8561	3 32 39.879	-27 46 33.47	27.32±0.08	13.90	8446	0.021	0.458	2.742
8576	3 32 43.449	-27 46 34.25	26.52±0.05	25.34	8519	0.002	0.011	4.803
8577	3 32 40.927	-27 46 33.73	27.43±0.09	11.32	8444	0.040	0.624	2.596
8580	3 32 38.298	-27 46 36.22	28.36±0.35	-0.31	8514	0.988	0.134	0.805
8585	3 32 35.504	-27 46 26.22	22.77±0.00	486.73	8138	0.074	0.041	2.546
8597	3 32 41.860	-27 46 34.51	27.60±0.10	10.52	8629	0.021	3.392	2.742
8603	3 32 36.918	-27 46 34.80	25.56±0.02	55.75	8701	0.034	0.086	2.742
8614	3 32 38.422	-27 46 34.88	25.50±0.02	66.47	8580	0.168	0.123	2.099
8624	3 32 37.791	-27 46 35.22	26.68±0.05	19.15	8710	0.073	0.301	2.277
8626	3 32 40.412	-27 46 34.48	27.52±0.09	10.83	8504	0.039	1.312	2.621
8629	3 32 41.776	-27 46 37.15	26.70±0.05	23.10	8597	0.019	0.295	2.742
8637	3 32 32.667	-27 46 34.85	26.98±0.06	17.63	8541	0.273	0.304	1.610
8650	3 32 36.359	-27 46 40.93	28.89±0.35	-1.46	8803	0.251	0.235	1.440
8653	3 32 39.219	-27 46 36.08	25.80±0.02	55.35	8608	0.049	0.100	2.546
8671	3 32 41.901	-27 46 40.33	28.88±0.36	-1.87	8785	0.490	0.285	1.018
8680	3 32 35.468	-27 46 37.02	25.44±0.01	74.13	8161	0.215	0.169	1.610
8686	3 32 35.734	-27 46 39.02	28.92±0.36	-0.10	8207	0.309	2.168	1.610
8687	3 32 37.245	-27 46 36.56	28.30±0.33	1.64	8681	0.772	0.418	0.720
8693	3 32 44.349	-27 46 38.83	24.78±0.01	90.44	8169	0.354	0.010	1.610
8698	3 32 43.024	-27 46 36.92	28.28±0.24	4.45	8654	0.608	0.244	0.805

Table C.1—Continued

ID[a]	R.A.	Decl.	u (mag)[b]	S/N	Cov. ID[c]	Cov. Index[d]	Flux Ratio[e]	Distance (arcsec)[f]
8702	3 32 34.990	-27 46 45.53	27.25±0.11	8.88	8907	0.709	0.499	0.720
8705	3 32 43.165	-27 46 37.08	28.75±0.29	3.65	8698	0.173	1.492	1.836
8710	3 32 37.747	-27 46 37.50	28.01±0.17	5.88	8741	0.393	1.712	1.080
8721	3 32 32.636	-27 46 37.52	28.90±0.33	-0.07	8637	0.025	2.718	2.546
8731	3 32 33.614	-27 46 39.06	27.50±0.15	6.60	8754	0.731	0.352	0.805
8740	3 32 34.027	-27 46 40.05	27.99±0.14	6.81	8024	0.137	2.017	1.939
8741	3 32 37.753	-27 46 38.68	28.83±0.35	1.99	8710	0.406	0.584	1.080
8744	3 32 35.187	-27 46 38.97	25.85±0.02	50.72	8262	0.125	1.473	2.546
8749	3 32 34.855	-27 46 40.44	25.63±0.02	58.22	8000	0.105	0.034	2.277
8750	3 32 45.235	-27 46 39.19	28.79±0.34	3.10	8336	0.431	0.259	0.805
8757	3 32 37.879	-27 46 39.23	28.86±0.34	3.06	8150	0.226	2.973	1.939
8759	3 32 45.783	-27 46 40.95	28.97±0.36	-1.89	8841	0.158	0.248	1.800
8765	3 32 36.560	-27 46 40.62	25.41±0.02	62.91	8776	0.522	0.375	1.138
8768	3 32 36.885	-27 46 39.65	28.68±0.30	1.98	8735	0.225	0.440	1.440
8782	3 32 40.304	-27 46 41.05	25.70±0.02	56.51	9026	0.108	0.042	1.836
8801	3 32 41.510	-27 46 42.19	26.16±0.03	34.04	8125	0.188	6.016	2.190
8805	3 32 33.540	-27 46 40.56	27.35±0.08	12.27	8731	0.292	1.373	1.800
8810	3 32 37.257	-27 46 10.35	24.01±0.00	235.42	9264	0.111	0.747	2.277
8812	3 32 36.299	-27 46 39.75	28.30±0.22	4.58	8803	0.372	0.128	1.138
8816	3 32 35.673	-27 46 41.33	27.72±0.13	7.36	8822	0.435	1.078	1.484
8822	3 32 35.753	-27 46 41.37	28.66±0.30	3.36	8816	0.466	0.928	1.484
8841	3 32 45.783	-27 46 42.76	28.31±0.20	5.18	8759	0.155	4.032	1.800
8844	3 32 34.875	-27 46 43.83	28.01±0.31	-0.65	8860	0.777	0.460	0.360
8852	3 32 43.174	-27 46 41.24	27.55±0.10	11.12	7934	0.111	0.440	2.305
8872	3 32 43.040	-27 46 44.12	27.39±0.09	11.08	7760	0.095	2.657	2.277
8880	3 32 34.676	-27 46 44.51	26.92±0.06	17.54	7959	0.196	0.606	1.800
8893	3 32 35.712	-27 46 44.06	28.08±0.17	5.20	9159	0.380	9.639	1.484
8918	3 32 36.688	-27 46 48.44	26.26±0.04	29.75	7606	0.500	0.100	1.018
8924	3 32 37.889	-27 46 45.11	27.88±0.14	7.27	8863	0.103	0.234	2.546
8930	3 32 37.500	-27 46 45.36	26.93±0.06	16.58	7705	0.233	2.323	1.800
8941	3 32 37.644	-27 46 41.82	26.79±0.05	20.94	7974	0.302	7.807	1.610
8942	3 32 40.103	-27 46 45.68	27.59±0.11	10.03	9021	0.425	0.593	1.138
8948	3 32 39.351	-27 46 46.88	28.95±0.34	-1.02	7868	0.051	1.812	2.277
8950	3 32 43.688	-27 46 46.36	26.29±0.03	33.93	8970	0.029	0.029	2.546
8954	3 32 34.781	-27 46 46.13	28.82±0.32	-1.08	7845	0.190	2.020	1.939
8964	3 32 35.661	-27 46 47.84	28.89±0.35	-4.09	7671	0.238	0.473	1.527

Table C.1—Continued

ID[a]	R.A.	Decl.	u (mag)[b]	S/N	Cov. ID[c]	Cov. Index[d]	Flux Ratio[e]	Distance (arcsec)[f]
8972	3 32 32.087	-27 46 47.08	27.75±0.13	8.01	7694	0.308	1.825	1.484
8994	3 32 35.080	-27 46 47.54	28.82±0.33	2.04	8907	0.256	0.343	2.036
8997	3 32 35.803	-27 46 47.67	27.93±0.14	7.43	8964	0.131	3.094	2.190
9000	3 32 35.466	-27 45 56.28	25.92±0.03	39.26	9604	0.562	0.049	1.138
9006	3 32 44.476	-27 46 48.00	27.94±0.13	8.26	7452	0.004	12.201	4.025
9018	3 32 35.300	-27 46 42.32	24.63±0.01	137.57	7983	0.082	0.276	2.546
9019	3 32 39.698	-27 46 48.25	28.41±0.27	3.78	9016	0.635	0.344	0.720
9024	3 32 38.024	-27 46 48.46	27.65±0.11	8.80	6974	0.015	88.871	3.671
9034	3 32 40.652	-27 46 48.57	27.00±0.06	18.35	7677	0.032	0.364	3.076
9074	3 32 38.270	-27 46 4.02	28.96±0.38	-0.99	9274	0.050	0.180	2.742
9088	3 32 35.127	-27 46 12.30	26.49±0.04	29.88	7516	0.161	0.067	1.527
9090	3 32 39.348	-27 46 8.75	25.66±0.02	50.14	9155	0.203	0.037	1.800
9092	3 32 42.091	-27 46 9.06	28.92±0.35	-1.00	9215	0.276	1.242	1.610
9097	3 32 37.579	-27 46 3.14	28.37±0.22	4.58	9305	0.360	2.214	1.298
9102	3 32 39.729	-27 46 11.17	25.82±0.03	38.41	7638	0.002	0.055	4.073
9110	3 32 40.322	-27 46 10.91	27.55±0.10	10.74	7534	0.085	1.556	2.415
9112	3 32 39.166	-27 45 54.27	27.63±0.11	9.49	9396	0.096	4.789	2.277
9113	3 32 34.343	-27 46 49.75	27.54±0.10	10.42	7487	0.183	0.250	2.099
9123	3 32 36.554	-27 46 12.33	25.07±0.01	96.04	9204	0.176	3.507	2.415
9125	3 32 39.919	-27 46 6.93	24.59±0.01	130.12	9185	0.031	0.081	2.902
9135	3 32 39.154	-27 46 6.71	27.31±0.09	12.92	9180	0.412	0.286	1.484
9139	3 32 36.193	-27 46 8.88	26.47±0.04	28.26	9178	0.066	0.071	2.277
9159	3 32 35.812	-27 46 43.70	25.95±0.03	36.39	7757	0.374	0.025	1.298
9171	3 32 39.514	-27 46 4.95	27.02±0.06	16.98	9155	0.025	0.187	2.902
9179	3 32 41.816	-27 46 8.72	27.77±0.12	8.11	9120	0.052	0.115	2.277
9182	3 32 40.010	-27 46 3.95	28.97±0.35	-1.86	9495	0.102	1.044	2.305
9183	3 32 38.441	-27 46 9.49	25.02±0.01	95.23	9064	0.513	0.054	1.800
9185	3 32 39.824	-27 46 4.51	28.97±0.35	-2.42	9125	0.050	12.305	2.902
9194	3 32 34.784	-27 46 9.50	26.82±0.05	18.80	9394	0.052	1.301	2.621
9204	3 32 36.618	-27 46 10.25	24.50±0.01	112.33	9123	0.088	0.285	2.415
9211	3 32 41.635	-27 46 49.69	28.81±0.35	1.90	7459	0.454	3.120	1.138
9215	3 32 42.139	-27 46 7.51	28.51±0.35	3.03	9213	0.790	0.306	0.805
9225	3 32 35.983	-27 46 5.12	27.70±0.11	8.87	9266	0.039	0.445	2.520
9227	3 32 37.534	-27 46 14.38	28.37±0.33	-2.14	7609	0.793	0.444	0.360
9230	3 32 37.923	-27 46 9.06	22.39±0.00	1041.23	7535	0.013	0.001	3.076
9235	3 32 35.497	-27 46 5.80	26.96±0.06	17.89	9175	0.035	0.181	2.902

Table C.1—Continued

ID[a]	R.A.	Decl.	u (mag)[b]	S/N	Cov. ID[c]	Cov. Index[d]	Flux Ratio[e]	Distance (arcsec)[f]
9244	3 32 38.765	-27 46 3.40	25.00±0.01	104.57	9184	0.057	0.034	2.596
9253	3 32 42.810	-27 46 5.69	23.00±0.00	440.72	9351	0.026	0.080	3.076
9264	3 32 37.192	-27 46 8.08	28.53±0.39	2.35	8810	0.076	1.340	2.277
9269	3 32 36.849	-27 46 10.02	27.21±0.08	12.83	9204	0.065	10.685	3.240
9273	3 32 40.168	-27 46 5.70	25.99±0.04	22.92	9495	0.696	0.333	0.805
9289	3 32 40.338	-27 46 4.65	28.93±0.35	2.90	9219	0.246	0.978	1.527
9299	3 32 40.784	-27 46 6.00	28.94±0.36	-5.98	9285	0.008	0.056	3.415
9304	3 32 42.381	-27 46 7.00	28.94±0.34	-2.65	9111	0.021	0.323	2.742
9305	3 32 37.534	-27 46 4.20	26.85±0.06	18.23	9236	0.307	0.151	1.484
9308	3 32 37.845	-27 46 4.37	26.87±0.06	18.65	9344	0.199	0.102	1.527
9312	3 32 41.223	-27 45 57.07	28.94±0.35	-0.66	9414	0.142	0.368	2.036
9328	3 32 37.000	-27 46 1.34	28.79±0.32	3.06	9347	0.269	18.274	1.800
9330	3 32 41.217	-27 46 0.02	28.75±0.34	-0.44	9282	0.420	0.658	1.080
9332	3 32 43.118	-27 46 7.67	25.43±0.02	47.06	9169	0.625	0.250	1.138
9341	3 32 38.367	-27 46 0.62	25.23±0.01	81.75	9585	0.205	0.095	1.836
9347	3 32 36.917	-27 46 2.33	24.76±0.01	129.49	9328	0.234	0.055	1.800
9348	3 32 36.871	-27 46 4.11	25.53±0.02	56.19	9200	0.306	0.053	1.440
9349	3 32 39.321	-27 46 0.07	28.12±0.17	6.05	9331	0.199	2.711	1.440
9356	3 32 36.423	-27 45 59.94	26.78±0.05	18.97	9532	0.358	5.430	1.440
9360	3 32 41.031	-27 46 1.69	27.38±0.08	13.22	9406	0.055	0.385	2.415
9361	3 32 39.273	-27 46 2.86	26.75±0.05	21.73	9331	0.281	1.416	1.610
9368	3 32 36.538	-27 46 2.16	28.83±0.32	-3.73	9321	0.156	0.288	1.939
9371	3 32 42.141	-27 46 3.22	26.99±0.06	18.75	9270	0.019	0.635	2.742
9372	3 32 38.006	-27 46 5.75	27.46±0.09	10.08	9308	0.033	1.563	2.596
9385	3 32 35.151	-27 46 5.92	28.52±0.25	3.74	9265	0.214	0.249	1.800
9393	3 32 38.520	-27 45 57.88	28.51±0.35	1.51	9207	0.730	0.220	0.805
9394	3 32 34.620	-27 46 8.62	27.43±0.09	12.76	9194	0.063	0.769	2.621
9396	3 32 39.325	-27 45 55.16	25.88±0.02	44.59	9112	0.079	0.209	2.277
9397	3 32 39.085	-27 46 1.80	21.20±0.00	2483.76	9365	0.073	0.004	2.190
9402	3 32 35.063	-27 45 59.66	24.75±0.01	115.07	57616	0.115	0.272	2.546
9409	3 32 36.828	-27 45 58.04	27.98±0.22	4.94	9275	0.667	0.132	0.720
9414	3 32 41.127	-27 45 58.71	26.97±0.07	13.00	9406	0.592	0.458	0.720
9419	3 32 40.424	-27 45 58.79	28.96±0.35	-1.86	9379	0.058	0.256	2.621
9425	3 32 39.521	-27 45 59.78	26.94±0.06	18.17	9349	0.027	0.609	3.260
9432	3 32 35.544	-27 45 56.72	27.09±0.07	14.97	9000	0.460	2.187	1.298
9437	3 32 35.813	-27 45 49.25	24.20±0.01	136.73	56720	0.603	0.441	1.018

Table C.1—Continued

ID[a]	R.A.	Decl.	u (mag)[b]	S/N	Cov. ID[c]	Cov. Index[d]	Flux Ratio[e]	Distance (arcsec)[f]
9444	3 32 37.299	-27 45 57.86	26.22±0.03	33.69	9429	0.118	0.029	2.305
9452	3 32 36.211	-27 45 56.98	26.68±0.05	22.22	9510	0.037	0.165	2.596
9455	3 32 41.336	-27 45 54.35	23.75±0.00	232.30	9294	0.046	0.009	2.812
9474	3 32 39.467	-27 45 57.10	25.68±0.02	55.91	9396	0.039	1.030	3.055
9487	3 32 40.175	-27 46 0.55	28.89±0.35	-0.36	9787	0.358	1.207	1.440
9505	3 32 37.477	-27 45 53.37	28.96±0.35	2.21	9580	0.005	0.229	4.025
9532	3 32 36.326	-27 46 0.10	25.86±0.02	47.40	9356	0.341	0.184	1.440
9543	3 32 39.584	-27 45 54.45	28.88±0.36	2.36	9547	0.095	0.040	2.099
9570	3 32 37.845	-27 45 57.76	28.65±0.27	3.89	9442	0.149	0.715	1.610
9585	3 32 38.247	-27 46 0.21	27.65±0.11	8.52	9341	0.239	10.555	1.836
9588	3 32 41.874	-27 45 51.88	27.73±0.11	9.71	57164	0.037	0.335	2.546
9593	3 32 39.610	-27 45 50.86	27.43±0.09	12.21	9547	0.007	0.367	3.319
9598	3 32 38.627	-27 45 15.26	28.36±0.27	3.59	9566	0.693	0.497	1.080
9599	3 32 37.700	-27 45 50.40	26.68±0.05	22.81	9580	0.072	0.046	2.190
9609	3 32 37.768	-27 45 44.19	27.01±0.06	15.65	10004	0.043	0.438	2.621
9617	3 32 41.320	-27 45 49.15	27.38±0.09	11.55	9720	0.467	0.161	1.080
9624	3 32 41.691	-27 45 55.10	26.91±0.05	19.15	9517	0.273	0.214	1.484
9640	3 32 36.414	-27 45 48.46	26.98±0.06	18.68	9711	0.134	0.348	1.836
9649	3 32 40.197	-27 46 2.86	26.64±0.04	23.78	9487	0.045	0.298	2.546
9672	3 32 37.861	-27 45 22.52	25.88±0.02	41.13	9813	0.029	0.111	2.880
9674	3 32 38.922	-27 45 44.30	26.63±0.04	24.74	9858	0.015	0.201	3.220
9675	3 32 39.252	-27 45 46.97	27.54±0.09	11.26	9739	0.160	0.283	2.190
9676	3 32 37.357	-27 45 49.68	28.82±0.35	0.14	9673	0.367	0.110	1.138
9678	3 32 39.335	-27 45 22.44	28.13±0.16	6.42	60146	0.075	12.377	2.969
9689	3 32 36.869	-27 45 45.31	27.72±0.12	9.03	9810	0.263	0.191	1.484
9706	3 32 36.519	-27 45 40.24	27.15±0.07	13.17	56612	0.244	3.904	1.836
9711	3 32 36.284	-27 45 48.93	28.90±0.34	-0.77	9640	0.133	2.870	1.836
9712	3 32 37.887	-27 45 18.76	25.26±0.01	88.68	60080	0.007	0.034	3.396
9713	3 32 40.164	-27 45 45.96	27.32±0.08	14.03	9789	0.026	0.286	2.621
9724	3 32 39.733	-27 45 47.10	26.51±0.05	19.12	9779	0.688	0.499	0.805
9731	3 32 38.281	-27 45 19.19	28.22±0.18	5.89	9784	0.019	1.081	2.902
9759	3 32 38.327	-27 45 44.22	25.02±0.01	86.58	9742	0.010	0.041	3.706
9765	3 32 36.330	-27 45 41.08	26.35±0.04	22.50	56612	0.485	2.939	1.138
9778	3 32 36.565	-27 45 42.58	26.36±0.04	26.84	9834	0.169	4.350	2.969
9783	3 32 37.351	-27 45 37.77	27.22±0.07	14.85	10001	0.026	0.171	2.742
9787	3 32 40.082	-27 46 0.29	27.73±0.12	8.52	9487	0.347	0.828	1.440

Table C.1—Continued

ID[a]	R.A.	Decl.	u (mag)[b]	S/N	Cov. ID[c]	Cov. Index[d]	Flux Ratio[e]	Distance (arcsec)[f]
9806	3 32 36.991	-27 45 34.83	27.16±0.07	16.46	9872	0.049	0.117	2.277
9807	3 32 36.904	-27 45 49.54	27.21±0.08	13.52	9763	0.045	0.065	2.902
9834	3 32 36.371	-27 45 43.29	24.47±0.01	123.71	9778	0.100	0.230	2.969
9837	3 32 36.674	-27 45 39.02	26.37±0.03	30.60	9955	0.064	0.144	2.305
9839	3 32 37.618	-27 45 32.15	25.91±0.03	32.61	9923	0.573	0.181	1.018
9847	3 32 38.971	-27 45 23.83	27.36±0.09	12.40	10013	0.029	0.092	2.902
9848	3 32 38.217	-27 45 26.11	26.86±0.07	15.27	9808	0.466	1.096	1.138
9859	3 32 38.874	-27 45 26.95	27.30±0.09	11.27	10039	0.382	0.517	1.484
9889	3 32 38.648	-27 45 36.35	27.75±0.11	9.03	9989	0.072	0.445	2.621
9895	3 32 40.410	-27 45 38.17	24.58±0.01	131.44	10042	0.054	0.043	2.546
9903	3 32 37.023	-27 45 40.83	26.73±0.04	24.07	10001	0.021	0.096	2.812
9925	3 32 39.424	-27 45 27.59	27.00±0.06	17.40	9964	0.156	0.494	1.800
9927	3 32 37.487	-27 45 30.18	27.34±0.10	10.05	9998	0.529	0.358	0.805
9944	3 32 38.555	-27 45 29.83	26.85±0.05	20.81	10039	0.002	0.529	4.394
9947	3 32 37.850	-27 45 33.66	28.15±0.17	6.34	9970	0.040	0.222	2.596
9959	3 32 38.680	-27 45 19.82	28.94±0.35	2.23	9457	0.127	0.232	1.836
9962	3 32 37.493	-27 45 26.59	25.86±0.02	52.26	9998	0.024	0.043	2.902
9964	3 32 39.498	-27 45 29.02	27.56±0.10	10.82	9925	0.166	2.025	1.800
9972	3 32 40.245	-27 45 35.79	27.52±0.10	11.08	9983	0.167	0.336	2.190
9974	3 32 38.097	-27 45 26.83	25.58±0.02	57.40	9848	0.241	0.287	1.939
9980	3 32 37.268	-27 45 28.19	26.69±0.05	23.83	59855	0.316	0.728	1.484
9983	3 32 40.120	-27 45 35.47	28.78±0.32	-4.33	9972	0.156	2.974	2.190
9990	3 32 39.545	-27 45 41.54	28.94±0.34	-4.12	9525	0.008	0.231	3.546
9999	3 32 38.540	-27 45 33.87	27.48±0.09	11.91	9889	0.016	0.741	2.902
10004	3 32 37.946	-27 45 43.50	28.93±0.34	2.65	9609	0.051	2.281	2.621
10016	3 32 41.548	-27 45 46.88	28.85±0.32	3.33	9556	0.185	0.123	1.800
10018	3 32 36.680	-27 45 49.16	28.65±0.32	0.61	9659	0.309	0.435	1.080
10020	3 32 38.837	-27 45 40.33	27.03±0.06	17.60	9993	0.119	0.164	1.800
10021	3 32 37.458	-27 45 41.92	26.50±0.04	29.51	9727	0.013	0.212	3.546
10025	3 32 40.907	-27 45 40.95	23.41±0.00	409.02	9697	0.039	0.007	2.742
10035	3 32 38.576	-27 45 20.00	27.63±0.11	8.92	9959	0.277	1.413	1.836
10042	3 32 40.243	-27 45 37.66	28.14±0.16	6.45	9972	0.115	3.611	2.160
10043	3 32 37.819	-27 45 53.87	26.71±0.07	14.13	9582	0.435	0.425	1.080
20037	3 32 38.246	-27 46 30.10	25.74±0.02	48.37	8351	0.157	0.288	1.610
20061	3 32 38.992	-27 46 49.27	26.70±0.05	20.31	7489	0.352	0.298	1.018
40448	3 32 40.903	-27 47 50.28	27.79±0.18	5.96	3522	0.640	0.234	0.805

Table C.1—Continued

ID[a]	R.A.	Decl.	u (mag)[b]	S/N	Cov. ID[c]	Cov. Index[d]	Flux Ratio[e]	Distance (arcsec)[f]
50139	3 32 39.093	-27 49 46.10	27.27±0.08	14.24	5	0.002	0.247	4.511
50721	3 32 36.798	-27 49 19.09	27.34±0.08	13.55	259	0.048	1.796	2.277
50947	3 32 36.016	-27 49 10.66	28.17±0.31	-2.60	50960	0.530	0.143	0.509
51093	3 32 35.622	-27 49 5.45	28.73±0.30	3.32	552	0.193	1.748	2.099
51179	3 32 35.264	-27 49 0.83	28.40±0.32	3.30	51213	0.877	0.112	0.720
51644	3 32 33.131	-27 48 34.85	25.70±0.02	46.37	1358	0.324	0.483	1.800
51711	3 32 33.735	-27 48 42.10	28.86±0.33	2.36	1232	0.005	0.236	3.894
52596	3 32 31.843	-27 48 20.18	26.34±0.03	33.31	52756	0.040	0.110	2.520
52761	3 32 31.671	-27 48 15.67	28.38±0.21	4.63	52786	0.282	1.885	1.836
52786	3 32 31.565	-27 48 15.71	28.81±0.33	0.32	52791	0.573	0.195	1.440
52950	3 32 46.386	-27 48 11.18	26.36±0.04	20.32	52978	0.191	0.069	2.099
52966	3 32 46.446	-27 48 9.51	26.75±0.06	16.65	53125	0.515	0.143	0.805
53090	3 32 31.131	-27 48 9.57	28.97±0.34	-0.83	2579	0.120	0.293	2.190
53163	3 32 30.460	-27 48 3.04	25.88±0.02	48.61	3006	0.003	0.087	3.827
53335	3 32 30.084	-27 47 57.04	26.75±0.05	22.70	53380	0.148	4.896	1.800
53380	3 32 29.944	-27 47 57.15	26.92±0.07	17.76	53335	0.123	0.204	1.800
53540	3 32 47.135	-27 47 59.17	27.19±0.08	14.01	3184	0.441	0.289	1.610
53790	3 32 29.695	-27 47 53.57	26.75±0.04	23.92	3577	0.022	0.162	2.812
53972	3 32 47.709	-27 47 50.14	28.94±0.36	1.87	3682	0.317	1.055	1.440
54717	3 32 28.344	-27 47 35.56	27.77±0.12	9.49	54801	0.109	1.270	2.305
54735	3 32 49.307	-27 47 26.27	23.32±0.00	385.42	55239	0.041	0.003	2.742
54801	3 32 28.232	-27 47 34.21	26.68±0.05	22.32	54717	0.090	0.787	2.305
55351	3 32 49.355	-27 47 23.47	28.04±0.16	6.34	55406	0.161	0.912	2.277
55406	3 32 49.480	-27 47 23.10	28.90±0.34	2.24	55351	0.168	1.097	2.277
55515	3 32 49.218	-27 47 21.65	28.32±0.34	3.10	55593	0.777	0.248	0.720
55812	3 32 49.131	-27 47 15.59	28.49±0.28	3.82	55978	0.449	0.129	1.138
55969	3 32 49.112	-27 47 14.38	28.28±0.20	5.35	55812	0.302	0.981	1.484
56017	3 32 29.696	-27 47 13.72	27.11±0.07	16.42	55970	0.245	0.292	1.800
56215	3 32 48.350	-27 47 8.58	28.32±0.23	4.58	56261	0.352	0.072	1.298
56333	3 32 48.415	-27 47 7.34	28.87±0.37	-0.84	56467	0.447	0.335	1.138
56463	3 32 48.554	-27 47 7.57	28.97±0.36	-3.04	56333	0.146	0.910	2.160
56611	3 32 30.488	-27 47 4.07	26.64±0.04	25.46	6554	0.057	0.549	2.546
56612	3 32 36.404	-27 45 40.63	24.45±0.01	158.21	9765	0.475	0.340	1.138
56987	3 32 41.742	-27 45 45.96	28.49±0.24	4.29	10016	0.023	0.625	2.969
57116	3 32 41.960	-27 45 48.86	28.19±0.30	1.59	57186	0.732	0.245	0.805
57353	3 32 47.018	-27 46 48.70	28.25±0.23	4.58	59600	0.467	0.086	1.138

Table C.1—Continued

ID[a]	R.A.	Decl.	u (mag)[b]	S/N	Cov. ID[c]	Cov. Index[d]	Flux Ratio[e]	Distance (arcsec)[f]
57577	3 32 42.829	-27 45 59.54	25.88±0.02	44.52	57513	0.009	0.029	3.415
57616	3 32 34.908	-27 46 0.28	26.11±0.03	34.54	9402	0.151	3.679	2.546
57909	3 32 46.696	-27 46 44.56	28.81±0.36	1.24	57563	0.421	0.477	1.298
58328	3 32 33.832	-27 46 16.37	27.66±0.12	9.35	7756	0.295	3.521	1.298
58728	3 32 32.736	-27 46 29.97	25.31±0.01	77.23	58344	0.326	0.078	1.484
58772	3 32 32.559	-27 46 31.89	25.57±0.02	57.75	8541	0.030	0.037	2.812
58779	3 32 32.794	-27 46 31.08	28.77±0.35	0.76	58344	0.448	0.443	1.018
58909	3 32 32.498	-27 46 35.29	28.90±0.35	-0.86	58933	0.326	0.489	1.610
59220	3 32 31.606	-27 46 45.75	26.91±0.06	19.51	7702	0.001	1.201	5.507
59307	3 32 31.242	-27 46 51.04	25.85±0.03	40.98	59352	0.222	0.238	1.939
59352	3 32 31.134	-27 46 51.67	27.03±0.07	14.12	59307	0.271	4.201	1.939
59855	3 32 37.175	-27 45 27.84	28.80±0.32	-3.62	9980	0.310	1.374	1.484
59970	3 32 37.248	-27 45 24.89	28.24±0.18	5.68	59855	0.010	0.858	3.076
60088	3 32 38.493	-27 45 9.16	28.46±0.31	3.23	60069	0.718	0.434	0.805
60146	3 32 39.525	-27 45 21.55	25.37±0.02	44.01	60198	0.547	0.291	0.805
60162	3 32 39.603	-27 45 20.16	24.53±0.01	111.24	60198	0.538	0.213	1.138
60302	3 32 39.241	-27 45 18.73	28.85±0.33	0.46	60300	0.262	0.329	1.610
60303	3 32 39.779	-27 45 23.99	25.90±0.02	46.29	60301	0.213	0.068	1.800

Note. — See notes from Table 2.1.

Table C.2. Catalog of Bayesian Photometric Redshifts

ID[a]	z_b[b]	t_b[c]	ODDS[d]	χ^2_ν[e]	$\chi^2_{\rm mod}$[f]	z_b1[g]	t_b1[c]	ODDS1[h]	z_b2[g]	t_b2[c]	ODDS2[h]
1	$0.17^{+0.11}_{-0.12}$	3.00	1.000	16.40	0.20	$0.17^{+0.07}_{-0.07}$	3.00	1.000	... + −	...	...
7	$0.01^{+0.10}_{-0.01}$	6.67	0.990	7.59	0.49	$0.01^{+0.10}_{-0.01}$	6.67	0.990	$1.81^{+0.02}_{-0.02}$	6.00	1.000
8	$0.52^{+0.15}_{-0.15}$	1.00	1.000	21.81	0.01	$0.52^{+0.07}_{-0.08}$	1.00	1.000	... + −	...	...
13	$0.43^{+0.14}_{-0.14}$	3.33	1.000	8.00	0.21	$0.43^{+0.11}_{-0.08}$	3.33	1.000	... + −	...	...
14	$0.54^{+0.15}_{-0.15}$	2.33	1.000	46.40	0.06	$0.54^{+0.07}_{-0.08}$	2.33	1.000	... + −	...	...
15	$0.52^{+0.15}_{-0.16}$	1.67	0.970	1.98	0.09	$0.52^{+0.03}_{-0.12}$	1.67	0.520	$0.57^{+0.10}_{-0.02}$	2.00	0.443
22	$3.23^{+0.41}_{-0.41}$	5.00	0.999	7.34	0.44	$3.23^{+0.19}_{-0.29}$	5.00	0.977	$2.90^{+0.04}_{-0.10}$	3.33	0.023
24	$1.39^{+0.78}_{-0.23}$	7.00	0.363	1.56	1.68	$1.39^{+0.12}_{-0.13}$	7.00	0.247	$1.65^{+0.22}_{-0.14}$	6.67	0.429
33	$0.78^{+0.17}_{-0.17}$	3.67	1.000	1.96	0.08	$0.78^{+0.09}_{-0.09}$	3.67	1.000	... + −	...	...
35	$1.69^{+0.26}_{-0.26}$	6.00	0.996	4.81	0.60	$1.69^{+0.16}_{-0.27}$	6.00	0.996	$0.02^{+0.03}_{-0.01}$	6.67	0.004
36	$0.56^{+0.15}_{-0.15}$	1.33	1.000	1.42	0.01	$0.56^{+0.08}_{-0.07}$	1.33	1.000	... + −	...	...
48	$1.59^{+0.25}_{-0.25}$	6.00	0.999	5.91	2.28	$1.59^{+0.15}_{-0.19}$	6.00	0.999	$1.32^{+0.01}_{-0.01}$	6.33	0.001
55	$2.48^{+0.34}_{-0.34}$	5.67	1.000	6.57	0.12	$2.48^{+0.09}_{-0.11}$	5.67	1.000	... + −	...	...
64	$1.85^{+0.45}_{-0.28}$	7.00	0.947	0.51	0.26	$1.85^{+0.29}_{-0.29}$	7.00	0.948	$2.30^{+0.15}_{-0.16}$	7.33	0.052
68	$0.75^{+0.17}_{-0.17}$	1.00	1.000	7.89	0.01	$0.75^{+0.07}_{-0.07}$	1.00	1.000	... + −	...	...
76	$2.62^{+0.36}_{-0.35}$	6.33	1.000	4.97	0.52	$2.62^{+0.12}_{-0.15}$	6.33	1.000	... + −	...	...
84	$3.11^{+0.40}_{-0.40}$	6.67	1.000	0.03	0.01	$3.11^{+0.12}_{-0.18}$	6.67	0.902	$3.29^{+0.13}_{-0.06}$	7.33	0.098
86	$0.01^{+0.10}_{-0.01}$	2.00	1.000	4.04	0.05	$0.01^{+0.10}_{-0.01}$	2.00	1.000	... + −	...	...
89	$0.10^{+0.11}_{-0.10}$	5.33	0.987	3.93	1.26	$0.10^{+0.09}_{-0.08}$	5.33	0.987	$0.44^{+0.04}_{-0.03}$	5.67	0.013
95	$2.30^{+0.32}_{-0.32}$	6.33	1.000	0.17	0.01	$2.30^{+0.14}_{-0.14}$	6.33	1.000	... + −	...	...
97	$2.87^{+0.38}_{-0.38}$	6.33	1.000	4.12	0.13	$2.87^{+0.08}_{-0.08}$	6.33	1.000	... + −	...	...
99	$2.81^{+0.37}_{-0.37}$	5.00	1.000	30.59	0.32	$2.81^{+0.08}_{-0.07}$	5.00	1.000	... + −	...	...
100	$0.56^{+0.15}_{-0.15}$	3.00	1.000	3.22	0.03	$0.56^{+0.08}_{-0.08}$	3.00	1.000	... + −	...	...
101	$2.66^{+0.36}_{-0.36}$	6.33	1.000	0.46	0.17	$2.66^{+0.20}_{-0.33}$	6.33	1.000	... + −	...	...
104	$3.56^{+0.45}_{-0.45}$	4.00	1.000	0.10	0.01	$3.56^{+0.16}_{-0.15}$	4.00	1.000	... + −	...	...
126	$1.52^{+0.25}_{-0.25}$	2.67	1.000	18.45	0.06	$1.52^{+0.10}_{-0.09}$	2.67	0.999	$1.65^{+0.01}_{-0.01}$	2.33	0.001
131	$3.06^{+0.40}_{-0.40}$	6.67	1.000	0.83	0.21	$3.06^{+0.14}_{-0.17}$	6.67	0.905	$3.26^{+0.14}_{-0.06}$	7.33	0.095
152	$1.69^{+0.27}_{-1.52}$	7.33	0.553	0.39	0.43	$1.69^{+0.46}_{-0.39}$	7.33	0.580	$0.44^{+0.30}_{-0.18}$	7.33	0.343
153	$0.88^{+0.18}_{-0.18}$	1.00	1.000	40.04	0.01	$0.88^{+0.07}_{-0.08}$	1.00	1.000	... + −	...	...
163	$3.28^{+0.42}_{-0.44}$	3.33	0.973	2.47	0.14	$3.28^{+0.20}_{-0.19}$	3.33	0.968	$2.86^{+0.05}_{-0.08}$	2.33	0.014
166	$1.51^{+0.25}_{-0.25}$	3.33	1.000	4.26	0.03	$1.51^{+0.09}_{-0.08}$	3.33	1.000	... + −	...	...
168	$0.60^{+0.16}_{-0.16}$	5.33	1.000	12.22	0.13	$0.60^{+0.09}_{-0.07}$	5.33	1.000	... + −	...	...
176	$0.63^{+0.16}_{-0.16}$	3.67	1.000	3.66	0.11	$0.63^{+0.08}_{-0.08}$	3.67	1.000	... + −	...	...
177	$1.35^{+0.23}_{-0.23}$	7.00	0.985	1.00	1.31	$1.35^{+0.17}_{-0.19}$	7.00	0.985	$1.98^{+0.07}_{-0.08}$	7.00	0.015
178	$0.58^{+0.16}_{-0.15}$	5.33	1.000	6.85	0.09	$0.58^{+0.09}_{-0.09}$	5.33	1.000	... + −	...	...
188	$2.51^{+0.34}_{-0.34}$	8.00	0.985	1.39	0.96	$2.51^{+0.15}_{-0.30}$	8.00	0.985	$2.03^{+0.09}_{-0.09}$	7.00	0.015

Table C.2—Continued

ID[a]	z_b[b]	t_b[c]	ODDS[d]	χ^2_ν[e]	$\chi^2_{\rm mod}$[f]	z_b1[g]	t_b1[c]	ODDS1[h]	z_b2[g]	t_b2[c]	ODDS2[h]
206	$0.74^{+0.17}_{-0.17}$	5.00	1.000	4.92	0.05	$0.74^{+0.08}_{-0.08}$	5.00	1.000	$\cdots$ $^{+}_{-}$	$\cdots$	$\cdots$
209	$2.67^{+0.36}_{-0.36}$	8.00	1.000	6.34	9.03	$2.67^{+0.12}_{-0.14}$	8.00	1.000	$\cdots$ $^{+}_{-}$	$\cdots$	$\cdots$
213	$3.14^{+0.41}_{-0.41}$	4.33	1.000	1.77	0.18	$3.14^{+0.23}_{-0.33}$	4.33	1.000	$\cdots$ $^{+}_{-}$	$\cdots$	$\cdots$
221	$0.66^{+0.16}_{-0.16}$	3.67	1.000	18.37	0.16	$0.66^{+0.07}_{-0.07}$	3.67	1.000	$\cdots$ $^{+}_{-}$	$\cdots$	$\cdots$
224	$1.62^{+0.26}_{-0.26}$	5.67	1.000	2.46	0.06	$1.62^{+0.09}_{-0.08}$	5.67	1.000	$\cdots$ $^{+}_{-}$	$\cdots$	$\cdots$
230	$3.70^{+0.46}_{-0.46}$	6.00	1.000	0.05	0.00	$3.70^{+0.09}_{-0.09}$	6.00	1.000	$\cdots$ $^{+}_{-}$	$\cdots$	$\cdots$
235	$0.56^{+0.15}_{-0.15}$	4.67	1.000	14.62	0.52	$0.56^{+0.12}_{-0.11}$	4.67	1.000	$\cdots$ $^{+}_{-}$	$\cdots$	$\cdots$
237	$0.50^{+0.15}_{-0.15}$	3.33	1.000	11.99	0.79	$0.50^{+0.10}_{-0.09}$	3.33	1.000	$\cdots$ $^{+}_{-}$	$\cdots$	$\cdots$
251	$1.54^{+0.25}_{-0.25}$	3.67	1.000	2.83	0.03	$1.54^{+0.14}_{-0.08}$	3.67	0.634	$1.38^{+0.08}_{-0.08}$	5.00	0.366
252	$3.31^{+0.42}_{-0.42}$	8.00	1.000	1.23	1.35	$3.31^{+0.17}_{-0.43}$	8.00	1.000	$\cdots$ $^{+}_{-}$	$\cdots$	$\cdots$
259	$3.59^{+0.45}_{-0.45}$	4.33	1.000	1.80	0.10	$3.59^{+0.13}_{-0.16}$	4.33	0.612	$3.81^{+0.10}_{-0.09}$	5.67	0.388
267	$1.39^{+0.23}_{-0.23}$	4.00	1.000	4.46	0.38	$1.39^{+0.13}_{-0.12}$	4.00	1.000	$\cdots$ $^{+}_{-}$	$\cdots$	$\cdots$
268	$3.11^{+0.40}_{-0.40}$	7.67	1.000	3.67	2.15	$3.11^{+0.17}_{-0.18}$	7.67	0.870	$2.82^{+0.11}_{-0.12}$	6.67	0.130
285	$0.15^{+0.11}_{-0.11}$	5.33	1.000	2.01	0.10	$0.15^{+0.08}_{-0.09}$	5.33	1.000	$\cdots$ $^{+}_{-}$	$\cdots$	$\cdots$
287	$0.61^{+0.16}_{-0.16}$	3.33	1.000	1.76	0.05	$0.61^{+0.09}_{-0.09}$	3.33	1.000	$\cdots$ $^{+}_{-}$	$\cdots$	$\cdots$
295	$2.16^{+0.31}_{-0.45}$	5.33	0.969	6.77	0.17	$2.16^{+0.10}_{-0.11}$	5.33	0.969	$1.69^{+0.06}_{-0.06}$	4.00	0.031
296	$2.75^{+0.37}_{-0.37}$	8.00	1.000	1.38	1.12	$2.75^{+0.13}_{-0.15}$	8.00	1.000	$\cdots$ $^{+}_{-}$	$\cdots$	$\cdots$
310	$2.71^{+0.36}_{-0.36}$	5.67	1.000	5.52	0.10	$2.71^{+0.08}_{-0.09}$	5.67	1.000	$\cdots$ $^{+}_{-}$	$\cdots$	$\cdots$
313	$3.13^{+0.40}_{-0.41}$	6.67	1.000	0.03	0.02	$3.13^{+0.12}_{-0.24}$	6.67	0.758	$3.32^{+0.17}_{-0.07}$	7.33	0.242
324	$0.63^{+0.16}_{-0.16}$	5.33	1.000	0.32	0.04	$0.63^{+0.09}_{-0.11}$	5.33	1.000	$\cdots$ $^{+}_{-}$	$\cdots$	$\cdots$
341	$2.74^{+0.37}_{-2.73}$	5.00	0.878	9.78	0.89	$2.74^{+0.19}_{-0.14}$	5.00	0.878	$0.03^{+0.08}_{-0.02}$	4.67	0.122
344	$1.89^{+0.28}_{-0.28}$	6.33	0.994	0.74	0.13	$1.89^{+0.36}_{-0.25}$	6.33	1.000	$\cdots$ $^{+}_{-}$	$\cdots$	$\cdots$
345	$2.18^{+0.31}_{-0.31}$	5.67	1.000	2.42	0.16	$2.18^{+0.13}_{-0.22}$	5.67	1.000	$\cdots$ $^{+}_{-}$	$\cdots$	$\cdots$
347	$0.02^{+2.24}_{-0.02}$	6.67	0.891	0.44	0.21	$0.02^{+0.08}_{-0.01}$	6.67	0.891	$2.24^{+0.08}_{-0.09}$	6.33	0.092
349	$0.40^{+1.36}_{-0.17}$	7.33	0.873	1.06	0.50	$0.40^{+0.18}_{-0.23}$	7.33	0.922	$1.74^{+0.16}_{-0.18}$	6.67	0.070
355	$0.52^{+0.15}_{-0.15}$	3.00	1.000	27.53	0.10	$0.52^{+0.08}_{-0.08}$	3.00	1.000	$\cdots$ $^{+}_{-}$	$\cdots$	$\cdots$
357	$2.66^{+0.36}_{-0.36}$	6.00	1.000	5.33	0.14	$2.66^{+0.12}_{-0.10}$	6.00	1.000	$\cdots$ $^{+}_{-}$	$\cdots$	$\cdots$
359	$3.45^{+0.44}_{-0.44}$	6.00	1.000	0.43	0.03	$3.45^{+0.14}_{-0.15}$	6.00	1.000	$\cdots$ $^{+}_{-}$	$\cdots$	$\cdots$
366	$5.67^{+0.65}_{-0.65}$	8.00	1.000	2.11	0.01	$5.67^{+0.07}_{-0.04}$	8.00	0.646	$5.60^{+0.03}_{-0.08}$	6.00	0.354
367	$2.14^{+0.31}_{-0.31}$	6.00	1.000	3.57	0.16	$2.14^{+0.12}_{-0.16}$	6.00	1.000	$\cdots$ $^{+}_{-}$	$\cdots$	$\cdots$
379	$3.10^{+0.40}_{-0.40}$	7.67	1.000	0.55	0.36	$3.10^{+0.16}_{-0.20}$	7.67	0.923	$2.82^{+0.08}_{-0.10}$	7.00	0.077
381	$3.05^{+0.40}_{-0.40}$	8.00	0.991	3.12	2.06	$3.05^{+0.16}_{-0.18}$	8.00	0.660	$2.73^{+0.14}_{-0.12}$	7.00	0.340
388	$2.63^{+0.36}_{-0.36}$	7.33	1.000	2.62	2.61	$2.63^{+0.19}_{-0.32}$	7.33	1.000	$\cdots$ $^{+}_{-}$	$\cdots$	$\cdots$
403	$1.39^{+0.23}_{-0.23}$	4.00	1.000	1.42	0.02	$1.39^{+0.09}_{-0.09}$	4.00	1.000	$\cdots$ $^{+}_{-}$	$\cdots$	$\cdots$
405	$3.05^{+0.40}_{-0.40}$	8.00	1.000	0.63	0.51	$3.05^{+0.13}_{-0.15}$	8.00	1.000	$\cdots$ $^{+}_{-}$	$\cdots$	$\cdots$
407	$3.81^{+0.47}_{-0.47}$	6.33	1.000	1.13	0.09	$3.81^{+0.09}_{-0.08}$	6.33	1.000	$\cdots$ $^{+}_{-}$	$\cdots$	$\cdots$

Table C.2—Continued

ID[a]	z_b[b]	t_b[c]	ODDS[d]	χ^2_ν[e]	$\chi^2_{\rm mod}$[f]	z_b1[g]	t_b1[c]	ODDS1[h]	z_b2[g]	t_b2[c]	ODDS2[h]
408	$0.24^{+2.50}_{-0.12}$	6.67	0.798	1.13	0.89	$0.24^{+0.10}_{-0.10}$	6.67	0.793	$2.65^{+0.18}_{-0.18}$	6.00	0.168
409	$3.42^{+0.43}_{-0.43}$	7.00	1.000	0.48	0.22	$3.42^{+0.08}_{-0.13}$	7.00	0.666	$3.54^{+0.17}_{-0.04}$	7.33	0.334
412	$4.32^{+0.52}_{-0.52}$	7.33	1.000	3.11	0.81	$4.32^{+0.11}_{-0.20}$	7.33	0.688	$4.02^{+0.10}_{-0.13}$	6.00	0.312
423	$0.29^{+0.13}_{-0.13}$	1.33	1.000	33.53	1.43	$0.29^{+0.07}_{-0.08}$	1.33	1.000	··· $^{+}_{-}$	···	···
424	$0.72^{+0.17}_{-0.17}$	5.67	0.991	14.78	0.40	$0.72^{+0.13}_{-0.08}$	5.67	0.960	$0.88^{+0.05}_{-0.03}$	5.33	0.040
428	$2.25^{+0.32}_{-0.32}$	6.00	1.000	1.73	0.05	$2.25^{+0.12}_{-0.11}$	6.00	1.000	··· $^{+}_{-}$	···	···
435	$2.38^{+0.33}_{-0.33}$	7.00	0.996	0.35	0.20	$2.38^{+0.10}_{-0.39}$	7.00	0.741	$2.53^{+0.17}_{-0.05}$	7.33	0.259
446	$1.10^{+0.21}_{-0.21}$	5.33	1.000	4.89	0.42	$1.10^{+0.08}_{-0.08}$	5.33	1.000	··· $^{+}_{-}$	···	···
461	$1.47^{+0.24}_{-0.24}$	4.00	1.000	2.58	0.18	$1.47^{+0.11}_{-0.11}$	4.00	1.000	··· $^{+}_{-}$	···	···
475	$1.49^{+0.24}_{-0.24}$	4.00	1.000	10.78	0.14	$1.49^{+0.08}_{-0.08}$	4.00	0.645	$1.34^{+0.07}_{-0.07}$	5.67	0.355
480	$1.52^{+0.25}_{-0.25}$	4.00	0.997	0.31	0.03	$1.52^{+0.19}_{-0.08}$	4.00	0.658	$1.39^{+0.05}_{-0.15}$	5.67	0.342
500	$2.99^{+0.39}_{-0.39}$	8.00	1.000	2.13	1.65	$2.99^{+0.14}_{-0.34}$	8.00	1.000	··· $^{+}_{-}$	···	···
501	$1.37^{+0.23}_{-0.23}$	3.00	0.998	3.24	0.01	$1.37^{+0.08}_{-0.07}$	3.00	0.786	$1.19^{+0.07}_{-0.07}$	3.33	0.214
503	$0.56^{+0.15}_{-0.15}$	3.33	1.000	9.89	0.20	$0.56^{+0.09}_{-0.09}$	3.33	1.000	··· $^{+}_{-}$	···	···
513	$3.29^{+0.42}_{-0.42}$	3.33	1.000	7.80	0.30	$3.29^{+0.16}_{-0.16}$	3.33	1.000	··· $^{+}_{-}$	···	···
518	$0.67^{+0.16}_{-0.16}$	5.33	1.000	0.36	0.01	$0.67^{+0.07}_{-0.08}$	5.33	1.000	··· $^{+}_{-}$	···	···
520	$2.49^{+0.34}_{-0.34}$	6.67	1.000	1.46	0.52	$2.49^{+0.15}_{-0.21}$	6.67	1.000	··· $^{+}_{-}$	···	···
521	$0.88^{+0.18}_{-0.18}$	3.67	1.000	9.26	0.21	$0.88^{+0.15}_{-0.10}$	3.67	1.000	··· $^{+}_{-}$	···	···
522	$3.09^{+0.40}_{-0.40}$	8.00	1.000	0.17	0.22	$3.09^{+0.18}_{-0.21}$	8.00	0.959	$2.83^{+0.05}_{-0.10}$	7.00	0.041
529	$3.29^{+0.42}_{-0.42}$	6.67	1.000	0.02	0.01	$3.29^{+0.27}_{-0.28}$	6.67	1.000	··· $^{+}_{-}$	···	···
533	$2.42^{+0.34}_{-0.34}$	6.67	1.000	0.95	0.89	$2.42^{+0.09}_{-0.10}$	6.67	1.000	··· $^{+}_{-}$	···	···
542	$0.18^{+0.12}_{-0.12}$	1.67	1.000	1.09	0.13	$0.18^{+0.08}_{-0.10}$	1.67	1.000	··· $^{+}_{-}$	···	···
551	$1.48^{+0.24}_{-0.24}$	5.00	1.000	4.62	0.03	$1.48^{+0.08}_{-0.08}$	5.00	1.000	··· $^{+}_{-}$	···	···
552	$0.48^{+0.15}_{-0.14}$	3.67	1.000	0.88	0.08	$0.48^{+0.13}_{-0.09}$	3.67	1.000	··· $^{+}_{-}$	···	···
559	$2.46^{+0.34}_{-0.34}$	6.33	1.000	2.35	1.52	$2.46^{+0.15}_{-0.16}$	6.33	0.943	$2.25^{+0.05}_{-0.11}$	6.00	0.057
566	$2.16^{+0.31}_{-0.31}$	6.00	1.000	0.89	0.05	$2.16^{+0.13}_{-0.17}$	6.00	1.000	··· $^{+}_{-}$	···	···
582	$0.92^{+0.19}_{-0.19}$	2.33	1.000	6.14	0.03	$0.92^{+0.09}_{-0.09}$	2.33	1.000	··· $^{+}_{-}$	···	···
599	$2.87^{+0.38}_{-0.38}$	5.33	1.000	3.67	0.58	$2.87^{+0.24}_{-0.17}$	5.33	1.000	··· $^{+}_{-}$	···	···
600	$0.47^{+0.14}_{-0.14}$	3.33	1.000	3.11	1.01	$0.47^{+0.09}_{-0.08}$	3.33	1.000	··· $^{+}_{-}$	···	···
602	$0.29^{+2.28}_{-0.13}$	7.33	0.945	0.21	0.08	$0.29^{+0.21}_{-0.13}$	7.33	0.969	$2.64^{+0.09}_{-0.13}$	7.67	0.031
604	$3.13^{+0.40}_{-0.41}$	6.33	1.000	0.42	0.46	$3.13^{+0.14}_{-0.19}$	6.33	1.000	··· $^{+}_{-}$	···	···
607	$2.74^{+0.37}_{-0.37}$	8.00	1.000	2.48	1.65	$2.74^{+0.13}_{-0.13}$	8.00	1.000	··· $^{+}_{-}$	···	···
631	$3.82^{+0.47}_{-0.47}$	6.33	1.000	1.57	1.38	$3.82^{+0.18}_{-0.11}$	6.33	0.985	$4.02^{+0.07}_{-0.02}$	7.33	0.015
636	$2.21^{+0.32}_{-0.32}$	5.67	0.993	0.50	0.08	$2.21^{+0.26}_{-0.32}$	5.67	0.993	$0.09^{+0.05}_{-0.05}$	6.67	0.007
637	$3.31^{+0.42}_{-0.42}$	6.00	1.000	7.22	0.09	$3.31^{+0.08}_{-0.10}$	6.00	1.000	··· $^{+}_{-}$	···	···
643	$2.61^{+0.35}_{-0.35}$	7.00	1.000	1.86	0.62	$2.61^{+0.11}_{-0.13}$	7.00	1.000	··· $^{+}_{-}$	···	···

Table C.2—Continued

ID[a]	z_b[b]	t_b[c]	ODDS[d]	χ^2_ν[e]	$\chi^2_{\rm mod}$[f]	z_b1[g]	t_b1[c]	ODDS1[h]	z_b2[g]	t_b2[c]	ODDS2[h]
647	$2.54^{+0.35}_{-2.28}$	7.33	0.778	0.64	1.44	$2.54^{+0.22}_{-0.40}$	7.33	0.799	$2.00^{+0.14}_{-0.33}$	6.67	0.146
648	$0.46^{+0.14}_{-0.14}$	3.67	1.000	8.66	0.25	$0.46^{+0.08}_{-0.07}$	3.67	1.000	$\cdots$ $^{+}_{-}$	$\cdots$	$\cdots$
656	$1.24^{+0.22}_{-0.22}$	2.00	1.000	11.14	1.53	$1.24^{+0.08}_{-0.08}$	2.00	1.000	$\cdots$ $^{+}_{-}$	$\cdots$	$\cdots$
657	$1.73^{+0.27}_{-0.27}$	6.33	0.992	2.14	0.54	$1.73^{+0.12}_{-0.11}$	6.33	0.981	$1.47^{+0.05}_{-0.05}$	6.67	0.019
662	$0.53^{+0.15}_{-0.15}$	4.67	1.000	19.19	0.18	$0.53^{+0.08}_{-0.08}$	4.67	1.000	$\cdots$ $^{+}_{-}$	$\cdots$	$\cdots$
666	$1.26^{+0.22}_{-0.22}$	5.67	1.000	5.42	1.45	$1.26^{+0.08}_{-0.09}$	5.67	1.000	$\cdots$ $^{+}_{-}$	$\cdots$	$\cdots$
669	$1.47^{+0.24}_{-0.33}$	3.33	0.918	0.56	0.01	$1.47^{+0.12}_{-0.14}$	3.33	0.856	$1.23^{+0.10}_{-0.16}$	4.33	0.144
674	$2.81^{+0.37}_{-0.37}$	6.67	1.000	0.81	0.18	$2.81^{+0.11}_{-0.11}$	6.67	0.828	$3.01^{+0.19}_{-0.09}$	7.33	0.172
679	$0.71^{+0.17}_{-0.17}$	5.00	1.000	10.83	0.13	$0.71^{+0.07}_{-0.07}$	5.00	1.000	$\cdots$ $^{+}_{-}$	$\cdots$	$\cdots$
697	$1.53^{+0.25}_{-0.25}$	3.33	1.000	8.32	0.09	$1.53^{+0.09}_{-0.09}$	3.33	1.000	$\cdots$ $^{+}_{-}$	$\cdots$	$\cdots$
702	$2.95^{+0.39}_{-0.39}$	4.67	1.000	4.01	0.05	$2.95^{+0.10}_{-0.11}$	4.67	1.000	$\cdots$ $^{+}_{-}$	$\cdots$	$\cdots$
703	$0.69^{+0.17}_{-0.17}$	6.00	1.000	3.97	0.15	$0.69^{+0.07}_{-0.07}$	6.00	1.000	$\cdots$ $^{+}_{-}$	$\cdots$	$\cdots$
704	$0.70^{+0.17}_{-0.17}$	6.00	1.000	4.03	0.16	$0.70^{+0.07}_{-0.07}$	6.00	1.000	$\cdots$ $^{+}_{-}$	$\cdots$	$\cdots$
711	$2.57^{+0.35}_{-0.35}$	6.67	1.000	2.30	0.23	$2.57^{+0.10}_{-0.09}$	6.67	1.000	$\cdots$ $^{+}_{-}$	$\cdots$	$\cdots$
719	$0.77^{+0.17}_{-0.17}$	5.33	1.000	4.71	0.18	$0.77^{+0.09}_{-0.09}$	5.33	1.000	$\cdots$ $^{+}_{-}$	$\cdots$	$\cdots$
726	$0.21^{+0.12}_{-0.12}$	5.00	0.999	1.87	0.21	$0.21^{+0.09}_{-0.12}$	5.00	0.999	$0.44^{+0.01}_{-0.01}$	4.00	0.001
731	$0.05^{+0.10}_{-0.05}$	1.33	1.000	5.78	0.13	$0.05^{+0.12}_{-0.04}$	1.33	1.000	$\cdots$ $^{+}_{-}$	$\cdots$	$\cdots$
732	$2.98^{+0.39}_{-0.39}$	8.00	1.000	2.95	2.12	$2.98^{+0.13}_{-0.36}$	8.00	1.000	$\cdots$ $^{+}_{-}$	$\cdots$	$\cdots$
733	$2.13^{+0.31}_{-0.31}$	6.33	1.000	3.29	0.10	$2.13^{+0.13}_{-0.06}$	6.33	0.690	$2.04^{+0.03}_{-0.12}$	6.33	0.310
734	$0.97^{+0.19}_{-0.19}$	4.00	1.000	3.79	0.19	$0.97^{+0.09}_{-0.16}$	4.00	1.000	$\cdots$ $^{+}_{-}$	$\cdots$	$\cdots$
735	$1.61^{+0.26}_{-0.26}$	3.33	1.000	6.14	0.03	$1.61^{+0.09}_{-0.09}$	3.33	1.000	$\cdots$ $^{+}_{-}$	$\cdots$	$\cdots$
741	$3.55^{+0.45}_{-0.45}$	4.67	1.000	4.22	3.27	$3.55^{+0.12}_{-0.15}$	4.67	1.000	$\cdots$ $^{+}_{-}$	$\cdots$	$\cdots$
754	$1.32^{+0.24}_{-0.27}$	6.67	0.882	0.51	0.31	$1.32^{+0.15}_{-0.13}$	6.67	0.729	$1.10^{+0.09}_{-0.10}$	7.00	0.222
766	$0.95^{+0.19}_{-0.24}$	5.67	0.928	5.61	1.83	$0.95^{+0.21}_{-0.16}$	5.67	0.908	$0.73^{+0.06}_{-0.07}$	5.67	0.092
769	$2.73^{+0.37}_{-0.37}$	4.67	1.000	1.18	0.01	$2.73^{+0.07}_{-0.08}$	4.67	1.000	$\cdots$ $^{+}_{-}$	$\cdots$	$\cdots$
772	$3.99^{+0.49}_{-0.49}$	4.00	1.000	8.65	1.51	$3.99^{+0.13}_{-0.14}$	4.00	0.639	$4.21^{+0.10}_{-0.09}$	5.67	0.361
776	$2.32^{+0.33}_{-0.32}$	7.00	1.000	2.10	1.23	$2.32^{+0.11}_{-0.26}$	7.00	0.780	$2.50^{+0.12}_{-0.07}$	7.33	0.220
778	$1.46^{+0.24}_{-0.24}$	5.33	1.000	12.97	0.20	$1.46^{+0.08}_{-0.09}$	5.33	1.000	$\cdots$ $^{+}_{-}$	$\cdots$	$\cdots$
784	$2.53^{+0.35}_{-0.35}$	6.67	1.000	2.29	0.76	$2.53^{+0.12}_{-0.14}$	6.67	1.000	$\cdots$ $^{+}_{-}$	$\cdots$	$\cdots$
791	$2.82^{+0.37}_{-0.37}$	5.33	1.000	3.31	0.06	$2.82^{+0.09}_{-0.09}$	5.33	1.000	$\cdots$ $^{+}_{-}$	$\cdots$	$\cdots$
794	$1.32^{+0.23}_{-0.23}$	5.67	1.000	4.82	0.31	$1.32^{+0.10}_{-0.09}$	5.67	1.000	$\cdots$ $^{+}_{-}$	$\cdots$	$\cdots$
797	$1.53^{+0.25}_{-0.25}$	3.67	1.000	2.73	0.01	$1.53^{+0.08}_{-0.07}$	3.67	1.000	$\cdots$ $^{+}_{-}$	$\cdots$	$\cdots$
817	$0.69^{+0.17}_{-0.17}$	6.33	1.000	5.28	0.59	$0.69^{+0.07}_{-0.07}$	6.33	1.000	$\cdots$ $^{+}_{-}$	$\cdots$	$\cdots$
830	$2.69^{+0.36}_{-0.36}$	6.33	1.000	8.33	0.20	$2.69^{+0.07}_{-0.08}$	6.33	1.000	$\cdots$ $^{+}_{-}$	$\cdots$	$\cdots$
833	$0.92^{+0.19}_{-0.19}$	5.67	1.000	4.72	0.50	$0.92^{+0.09}_{-0.08}$	5.67	1.000	$\cdots$ $^{+}_{-}$	$\cdots$	$\cdots$
838	$0.58^{+0.16}_{-0.15}$	2.67	1.000	1.25	0.02	$0.58^{+0.08}_{-0.09}$	2.67	1.000	$\cdots$ $^{+}_{-}$	$\cdots$	$\cdots$

Table C.2—Continued

ID[a]	z_b[b]	t_b[c]	ODDS[d]	χ^2_ν[e]	$\chi^2_{\rm mod}$[f]	z_b1[g]	t_b1[c]	ODDS1[h]	z_b2[g]	t_b2[c]	ODDS2[h]
841	$2.53^{+0.35}_{-0.35}$	7.00	1.000	1.18	0.15	$2.53^{+0.07}_{-0.10}$	7.00	0.563	$2.66^{+0.11}_{-0.06}$	7.33	0.437
853	$1.74^{+0.27}_{-0.27}$	3.00	1.000	24.65	2.77	$1.74^{+0.10}_{-0.10}$	3.00	1.000	$\cdots\ ^{+}_{-}$	···	···
857	$1.58^{+0.25}_{-0.25}$	5.67	1.000	6.66	0.22	$1.58^{+0.10}_{-0.09}$	5.67	1.000	$\cdots\ ^{+}_{-}$	···	···
862	$3.18^{+0.41}_{-0.41}$	8.00	1.000	11.70	4.12	$3.18^{+0.14}_{-0.16}$	8.00	0.655	$2.94^{+0.08}_{-0.14}$	7.33	0.345
865	$3.68^{+0.46}_{-0.46}$	3.33	1.000	6.96	21.40	$3.68^{+0.10}_{-0.11}$	3.33	1.000	$\cdots\ ^{+}_{-}$	···	···
870	$0.73^{+0.17}_{-0.17}$	6.00	1.000	10.68	1.87	$0.73^{+0.15}_{-0.08}$	6.00	1.000	$\cdots\ ^{+}_{-}$	···	···
872	$0.10^{+0.11}_{-0.10}$	3.33	0.986	2.59	1.38	$0.10^{+0.04}_{-0.09}$	3.33	0.583	$0.17^{+0.08}_{-0.03}$	3.67	0.417
879	$0.02^{+2.20}_{-0.02}$	7.00	0.309	9.08	9.04	$0.02^{+0.08}_{-0.01}$	7.00	0.309	$2.14^{+0.16}_{-0.18}$	6.33	0.691
881	$3.22^{+0.41}_{-0.41}$	3.33	1.000	4.80	0.05	$3.22^{+0.11}_{-0.11}$	3.33	1.000	$\cdots\ ^{+}_{-}$	···	···
883	$1.18^{+0.21}_{-0.24}$	6.33	0.954	2.61	1.85	$1.18^{+0.12}_{-0.10}$	6.33	0.684	$1.00^{+0.08}_{-0.10}$	6.67	0.316
895	$0.55^{+0.15}_{-0.15}$	6.67	0.994	0.27	0.09	$0.55^{+0.18}_{-0.14}$	6.67	0.995	$0.10^{+0.03}_{-0.03}$	6.33	0.005
898	$1.40^{+0.27}_{-0.24}$	6.33	0.952	1.75	1.43	$1.40^{+0.12}_{-0.14}$	6.33	0.754	$1.60^{+0.14}_{-0.08}$	6.00	0.246
900	$0.40^{+0.14}_{-0.14}$	2.33	1.000	21.78	0.08	$0.40^{+0.08}_{-0.08}$	2.33	1.000	$\cdots\ ^{+}_{-}$	···	···
901	$0.75^{+0.17}_{-0.17}$	4.67	1.000	8.60	0.67	$0.75^{+0.08}_{-0.08}$	4.67	1.000	$\cdots\ ^{+}_{-}$	···	···
906	$2.68^{+0.36}_{-0.36}$	8.00	1.000	10.36	12.26	$2.68^{+0.12}_{-0.18}$	8.00	1.000	$\cdots\ ^{+}_{-}$	···	···
911	$0.79^{+0.17}_{-0.18}$	1.00	1.000	147.10	0.09	$0.79^{+0.08}_{-0.07}$	1.00	1.000	$\cdots\ ^{+}_{-}$	···	···
916	$2.15^{+0.36}_{-0.31}$	7.00	0.953	6.41	3.69	$2.15^{+0.23}_{-0.17}$	7.00	0.920	$2.47^{+0.14}_{-0.09}$	7.33	0.078
918	$1.11^{+0.21}_{-0.21}$	3.67	1.000	25.15	2.97	$1.11^{+0.08}_{-0.08}$	3.67	1.000	$\cdots\ ^{+}_{-}$	···	···
926	$2.61^{+0.35}_{-0.35}$	8.00	1.000	0.30	0.29	$2.61^{+0.12}_{-0.17}$	8.00	1.000	$\cdots\ ^{+}_{-}$	···	···
941	$0.48^{+0.15}_{-0.14}$	5.33	0.991	2.33	0.18	$0.48^{+0.13}_{-0.09}$	5.33	0.991	$0.67^{+0.03}_{-0.03}$	6.00	0.009
944	$0.94^{+0.19}_{-0.19}$	4.00	1.000	3.93	1.18	$0.94^{+0.12}_{-0.15}$	4.00	1.000	$\cdots\ ^{+}_{-}$	···	···
951	$3.03^{+0.39}_{-0.39}$	5.67	0.997	0.76	0.19	$3.03^{+0.22}_{-0.45}$	5.67	1.000	$\cdots\ ^{+}_{-}$	···	···
955	$2.88^{+0.38}_{-0.38}$	6.33	1.000	5.80	0.26	$2.88^{+0.13}_{-0.12}$	6.33	1.000	$\cdots\ ^{+}_{-}$	···	···
966	$1.03^{+0.20}_{-0.20}$	3.67	0.998	6.12	0.54	$1.03^{+0.09}_{-0.06}$	3.67	0.532	$0.91^{+0.06}_{-0.09}$	5.00	0.468
968	$0.50^{+0.15}_{-0.15}$	4.67	1.000	32.93	0.27	$0.50^{+0.09}_{-0.08}$	4.67	1.000	$\cdots\ ^{+}_{-}$	···	···
969	$0.63^{+0.16}_{-0.19}$	6.33	0.928	1.63	1.08	$0.63^{+0.09}_{-0.05}$	6.33	0.502	$0.54^{+0.04}_{-0.14}$	6.33	0.498
973	$0.60^{+0.16}_{-0.16}$	4.67	1.000	10.89	0.57	$0.60^{+0.09}_{-0.09}$	4.67	1.000	$\cdots\ ^{+}_{-}$	···	···
975	$3.75^{+0.47}_{-0.46}$	6.00	1.000	0.12	0.02	$3.75^{+0.23}_{-0.15}$	6.00	1.000	$\cdots\ ^{+}_{-}$	···	···
985	$3.68^{+0.46}_{-0.46}$	6.67	1.000	0.51	0.71	$3.68^{+0.26}_{-0.14}$	6.67	1.000	$\cdots\ ^{+}_{-}$	···	···
997	$0.67^{+0.16}_{-0.18}$	5.67	0.965	5.03	0.84	$0.67^{+0.08}_{-0.07}$	5.67	0.846	$0.53^{+0.07}_{-0.08}$	5.33	0.154
1000	$0.21^{+0.12}_{-0.13}$	6.33	0.973	20.54	1.08	$0.21^{+0.07}_{-0.07}$	6.33	0.971	$0.07^{+0.04}_{-0.04}$	6.00	0.029
1003	$0.66^{+0.16}_{-0.16}$	3.67	1.000	0.41	0.05	$0.66^{+0.09}_{-0.16}$	3.67	1.000	$\cdots\ ^{+}_{-}$	···	···
1006	$1.41^{+0.24}_{-0.24}$	2.67	1.000	0.34	0.00	$1.41^{+0.08}_{-0.09}$	2.67	1.000	$\cdots\ ^{+}_{-}$	···	···
1016	$0.77^{+0.17}_{-0.17}$	5.33	1.000	1.27	0.06	$0.77^{+0.11}_{-0.09}$	5.33	1.000	$\cdots\ ^{+}_{-}$	···	···
1018	$0.60^{+0.16}_{-0.16}$	3.33	1.000	2.82	0.54	$0.60^{+0.10}_{-0.13}$	3.33	1.000	$\cdots\ ^{+}_{-}$	···	···
1025	$1.09^{+0.20}_{-0.21}$	3.00	1.000	12.09	0.10	$1.09^{+0.13}_{-0.08}$	3.00	1.000	$\cdots\ ^{+}_{-}$	···	···

Table C.2—Continued

ID[a]	z_b[b]	t_b[c]	ODDS[d]	χ^2_ν[e]	$\chi^2_{\rm mod}$[f]	z_b1[g]	t_b1[c]	ODDS1[h]	z_b2[g]	t_b2[c]	ODDS2[h]
1041	$0.56^{+0.15}_{-0.15}$	3.00	1.000	33.89	3.54	$0.56^{+0.08}_{-0.07}$	3.00	1.000	$\cdots$ $^{+}_{-}$	$\cdots$	$\cdots$
1044	$2.56^{+0.35}_{-0.35}$	8.00	0.988	7.80	12.49	$2.56^{+0.16}_{-0.28}$	8.00	0.988	$2.13^{+0.08}_{-0.06}$	7.00	0.012
1049	$2.67^{+0.36}_{-0.36}$	3.33	1.000	6.67	0.02	$2.67^{+0.08}_{-0.09}$	3.33	1.000	$\cdots$ $^{+}_{-}$	$\cdots$	$\cdots$
1052	$2.29^{+0.32}_{-0.32}$	6.33	1.000	0.84	0.06	$2.29^{+0.20}_{-0.14}$	6.33	1.000	$\cdots$ $^{+}_{-}$	$\cdots$	$\cdots$
1057	$0.59^{+0.16}_{-0.16}$	3.00	1.000	9.91	0.05	$0.59^{+0.08}_{-0.08}$	3.00	1.000	$\cdots$ $^{+}_{-}$	$\cdots$	$\cdots$
1058	$2.86^{+0.38}_{-0.38}$	8.00	1.000	5.49	4.61	$2.86^{+0.20}_{-0.26}$	8.00	1.000	$\cdots$ $^{+}_{-}$	$\cdots$	$\cdots$
1063	$0.61^{+0.16}_{-0.16}$	3.67	1.000	4.90	0.48	$0.61^{+0.08}_{-0.09}$	3.67	1.000	$\cdots$ $^{+}_{-}$	$\cdots$	$\cdots$
1072	$1.73^{+0.47}_{-0.27}$	6.00	0.891	2.70	0.99	$1.73^{+0.22}_{-0.16}$	6.00	0.875	$2.17^{+0.12}_{-0.10}$	5.67	0.089
1088	$0.19^{+0.12}_{-0.12}$	2.33	1.000	2.81	0.05	$0.19^{+0.08}_{-0.08}$	2.33	1.000	$\cdots$ $^{+}_{-}$	$\cdots$	$\cdots$
1091	$2.55^{+0.35}_{-0.35}$	7.00	1.000	2.24	1.65	$2.55^{+0.07}_{-0.12}$	7.00	0.502	$2.67^{+0.16}_{-0.05}$	7.33	0.498
1095	$3.15^{+0.41}_{-0.41}$	4.00	1.000	0.39	0.43	$3.15^{+0.32}_{-0.24}$	4.00	1.000	$\cdots$ $^{+}_{-}$	$\cdots$	$\cdots$
1105	$0.70^{+0.17}_{-0.17}$	5.00	1.000	7.12	1.52	$0.70^{+0.08}_{-0.08}$	5.00	1.000	$\cdots$ $^{+}_{-}$	$\cdots$	$\cdots$
1106	$2.48^{+0.34}_{-0.34}$	5.67	1.000	1.26	0.05	$2.48^{+0.12}_{-0.17}$	5.67	1.000	$\cdots$ $^{+}_{-}$	$\cdots$	$\cdots$
1107	$3.36^{+0.43}_{-0.43}$	5.67	1.000	0.18	0.10	$3.36^{+0.17}_{-0.26}$	5.67	0.990	$3.00^{+0.09}_{-0.06}$	4.33	0.010
1112	$3.04^{+0.40}_{-0.40}$	5.33	1.000	6.37	1.43	$3.04^{+0.08}_{-0.09}$	5.33	1.000	$\cdots$ $^{+}_{-}$	$\cdots$	$\cdots$
1120	$3.29^{+0.42}_{-0.42}$	6.33	1.000	0.81	0.65	$3.29^{+0.13}_{-0.19}$	6.33	1.000	$\cdots$ $^{+}_{-}$	$\cdots$	$\cdots$
1160	$0.92^{+0.19}_{-0.19}$	5.67	1.000	4.50	0.26	$0.92^{+0.08}_{-0.09}$	5.67	0.936	$1.05^{+0.06}_{-0.05}$	4.00	0.064
1174	$2.97^{+0.39}_{-0.39}$	8.00	1.000	1.10	1.10	$2.97^{+0.20}_{-0.20}$	8.00	1.000	$\cdots$ $^{+}_{-}$	$\cdots$	$\cdots$
1189	$2.77^{+0.37}_{-0.37}$	5.33	1.000	3.95	0.05	$2.77^{+0.08}_{-0.08}$	5.33	1.000	$\cdots$ $^{+}_{-}$	$\cdots$	$\cdots$
1205	$1.07^{+0.20}_{-0.28}$	5.67	0.902	0.40	0.07	$1.07^{+0.14}_{-0.14}$	5.67	0.879	$0.84^{+0.08}_{-0.11}$	6.00	0.121
1217	$2.75^{+0.37}_{-0.37}$	6.67	1.000	1.85	0.52	$2.75^{+0.10}_{-0.10}$	6.67	1.000	$\cdots$ $^{+}_{-}$	$\cdots$	$\cdots$
1236	$0.39^{+0.14}_{-0.20}$	3.67	0.887	0.29	0.16	$0.39^{+0.12}_{-0.05}$	3.67	0.521	$0.29^{+0.05}_{-0.19}$	5.00	0.479
1242	$2.83^{+0.38}_{-0.38}$	5.33	1.000	2.23	0.46	$2.83^{+0.10}_{-0.09}$	5.33	1.000	$\cdots$ $^{+}_{-}$	$\cdots$	$\cdots$
1253	$3.42^{+0.43}_{-0.43}$	6.33	1.000	0.11	0.02	$3.42^{+0.15}_{-0.18}$	6.33	1.000	$\cdots$ $^{+}_{-}$	$\cdots$	$\cdots$
1265	$3.00^{+0.39}_{-0.39}$	6.67	1.000	0.34	0.24	$3.00^{+0.18}_{-0.18}$	6.67	0.948	$3.21^{+0.15}_{-0.03}$	7.33	0.052
1266	$1.40^{+0.24}_{-0.24}$	2.33	1.000	3.54	0.01	$1.40^{+0.08}_{-0.07}$	2.33	1.000	$\cdots$ $^{+}_{-}$	$\cdots$	$\cdots$
1267	$1.39^{+0.23}_{-0.23}$	4.00	1.000	4.03	2.33	$1.39^{+0.11}_{-0.12}$	4.00	1.000	$\cdots$ $^{+}_{-}$	$\cdots$	$\cdots$
1269	$1.20^{+0.22}_{-0.22}$	7.00	1.000	1.33	0.37	$1.20^{+0.14}_{-0.13}$	7.00	1.000	$\cdots$ $^{+}_{-}$	$\cdots$	$\cdots$
1273	$3.03^{+0.39}_{-0.39}$	6.67	1.000	1.06	0.16	$3.03^{+0.10}_{-0.11}$	6.67	1.000	$\cdots$ $^{+}_{-}$	$\cdots$	$\cdots$
1285	$0.68^{+0.17}_{-0.17}$	5.33	1.000	3.24	0.61	$0.68^{+0.07}_{-0.14}$	5.33	1.000	$\cdots$ $^{+}_{-}$	$\cdots$	$\cdots$
1287	$3.54^{+0.44}_{-0.44}$	7.33	1.000	2.60	2.03	$3.54^{+0.20}_{-0.29}$	7.33	1.000	$\cdots$ $^{+}_{-}$	$\cdots$	$\cdots$
1291	$0.67^{+0.16}_{-0.16}$	7.00	0.990	5.40	3.00	$0.67^{+0.12}_{-0.12}$	7.00	0.990	$1.93^{+0.04}_{-0.04}$	6.33	0.010
1299	$0.01^{+0.10}_{-0.01}$	2.33	1.000	28.09	0.30	$0.01^{+0.10}_{-0.01}$	2.33	1.000	$\cdots$ $^{+}_{-}$	$\cdots$	$\cdots$
1316	$1.79^{+0.27}_{-0.27}$	2.67	1.000	51.59	6.67	$1.79^{+0.11}_{-0.11}$	2.67	1.000	$\cdots$ $^{+}_{-}$	$\cdots$	$\cdots$
1320	$0.59^{+0.16}_{-0.16}$	3.00	1.000	6.88	0.25	$0.59^{+0.09}_{-0.10}$	3.00	1.000	$\cdots$ $^{+}_{-}$	$\cdots$	$\cdots$
1332	$1.33^{+0.23}_{-0.23}$	5.67	1.000	2.49	0.15	$1.33^{+0.10}_{-0.09}$	5.67	0.987	$1.45^{+0.04}_{-0.02}$	4.00	0.013

Table C.2—Continued

ID[a]	z_b[b]	t_b[c]	ODDS[d]	χ^2_ν[e]	$\chi^2_{\rm mod}$[f]	z_b1[g]	t_b1[c]	ODDS1[h]	z_b2[g]	t_b2[c]	ODDS2[h]
1344	$0.28^{+0.12}_{-0.12}$	3.67	1.000	2.75	1.44	$0.28^{+0.07}_{-0.08}$	3.67	1.000	$\cdots$ $^{+}_{-}$	$\cdots$	$\cdots$
1354	$3.05^{+0.40}_{-0.40}$	6.67	1.000	1.30	1.54	$3.05^{+0.12}_{-0.14}$	6.67	1.000	$\cdots$ $^{+}_{-}$	$\cdots$	$\cdots$
1358	$0.02^{+0.10}_{-0.02}$	5.00	1.000	8.18	0.36	$0.02^{+0.07}_{-0.01}$	5.00	1.000	$\cdots$ $^{+}_{-}$	$\cdots$	$\cdots$
1362	$1.98^{+0.29}_{-0.29}$	6.33	0.975	0.19	0.02	$1.98^{+0.35}_{-0.26}$	6.33	0.980	$0.09^{+0.06}_{-0.07}$	7.00	0.020
1375	$0.55^{+0.15}_{-0.15}$	3.67	1.000	21.62	0.14	$0.55^{+0.08}_{-0.08}$	3.67	1.000	$\cdots$ $^{+}_{-}$	$\cdots$	$\cdots$
1383	$3.21^{+0.41}_{-0.41}$	5.67	1.000	0.15	0.02	$3.21^{+0.16}_{-0.18}$	5.67	1.000	$\cdots$ $^{+}_{-}$	$\cdots$	$\cdots$
1386	$3.08^{+0.40}_{-0.40}$	5.67	1.000	0.90	0.08	$3.08^{+0.17}_{-0.14}$	5.67	1.000	$\cdots$ $^{+}_{-}$	$\cdots$	$\cdots$
1396	$3.07^{+0.40}_{-0.40}$	6.33	1.000	0.72	0.11	$3.07^{+0.13}_{-0.13}$	6.33	1.000	$\cdots$ $^{+}_{-}$	$\cdots$	$\cdots$
1403	$3.51^{+0.44}_{-3.31}$	3.33	0.732	0.13	0.05	$3.51^{+0.29}_{-0.20}$	3.33	0.732	$0.29^{+0.08}_{-0.19}$	2.00	0.146
1414	$2.86^{+0.38}_{-0.38}$	7.00	1.000	1.24	0.97	$2.86^{+0.16}_{-0.14}$	7.00	0.844	$3.06^{+0.18}_{-0.04}$	7.33	0.156
1416	$2.53^{+0.35}_{-0.35}$	6.33	1.000	7.22	1.30	$2.53^{+0.08}_{-0.08}$	6.33	1.000	$\cdots$ $^{+}_{-}$	$\cdots$	$\cdots$
1421	$2.55^{+0.35}_{-0.35}$	5.33	1.000	13.51	1.17	$2.55^{+0.09}_{-0.10}$	5.33	1.000	$\cdots$ $^{+}_{-}$	$\cdots$	$\cdots$
1426	$1.52^{+0.25}_{-0.25}$	4.00	1.000	3.73	0.04	$1.52^{+0.09}_{-0.08}$	4.00	1.000	$\cdots$ $^{+}_{-}$	$\cdots$	$\cdots$
1428	$1.19^{+0.21}_{-0.22}$	6.33	1.000	5.10	0.78	$1.19^{+0.07}_{-0.09}$	6.33	1.000	$\cdots$ $^{+}_{-}$	$\cdots$	$\cdots$
1430	$1.64^{+0.26}_{-0.26}$	6.00	1.000	5.30	1.75	$1.64^{+0.15}_{-0.12}$	6.00	1.000	$\cdots$ $^{+}_{-}$	$\cdots$	$\cdots$
1440	$3.31^{+0.42}_{-0.42}$	6.00	1.000	0.06	0.01	$3.31^{+0.16}_{-0.20}$	6.00	1.000	$\cdots$ $^{+}_{-}$	$\cdots$	$\cdots$
1446	$2.78^{+0.37}_{-0.37}$	1.67	1.000	0.27	0.52	$2.78^{+0.07}_{-0.12}$	1.67	1.000	$\cdots$ $^{+}_{-}$	$\cdots$	$\cdots$
1448	$0.47^{+0.14}_{-0.31}$	5.67	0.974	4.67	3.04	$0.47^{+0.15}_{-0.09}$	5.67	0.974	$0.12^{+0.06}_{-0.08}$	5.00	0.026
1449	$1.44^{+0.55}_{-1.41}$	6.67	0.635	0.99	1.31	$1.44^{+0.13}_{-0.15}$	6.67	0.414	$1.68^{+0.55}_{-0.11}$	6.33	0.508
1453	$0.42^{+0.14}_{-0.27}$	3.67	0.612	2.75	0.52	$0.42^{+0.09}_{-0.08}$	3.67	0.575	$0.25^{+0.08}_{-0.16}$	3.33	0.425
1454	$2.70^{+0.36}_{-0.36}$	6.67	1.000	1.84	0.76	$2.70^{+0.08}_{-0.08}$	6.67	1.000	$\cdots$ $^{+}_{-}$	$\cdots$	$\cdots$
1469	$1.40^{+0.24}_{-0.24}$	4.00	1.000	2.72	0.02	$1.40^{+0.08}_{-0.08}$	4.00	1.000	$\cdots$ $^{+}_{-}$	$\cdots$	$\cdots$
1476	$1.52^{+0.25}_{-0.25}$	3.67	1.000	1.32	0.35	$1.52^{+0.13}_{-0.25}$	3.67	1.000	$\cdots$ $^{+}_{-}$	$\cdots$	$\cdots$
1477	$1.79^{+0.27}_{-0.27}$	6.33	0.995	1.62	0.67	$1.79^{+0.35}_{-0.24}$	6.33	1.000	$\cdots$ $^{+}_{-}$	$\cdots$	$\cdots$
1478	$1.46^{+0.24}_{-0.24}$	3.33	1.000	6.51	1.11	$1.46^{+0.09}_{-0.09}$	3.33	1.000	$\cdots$ $^{+}_{-}$	$\cdots$	$\cdots$
1481	$0.91^{+0.19}_{-0.19}$	5.67	1.000	5.09	0.43	$0.91^{+0.08}_{-0.08}$	5.67	1.000	$\cdots$ $^{+}_{-}$	$\cdots$	$\cdots$
1494	$0.21^{+2.60}_{-0.12}$	5.33	0.447	1.38	0.44	$0.21^{+0.09}_{-0.11}$	5.33	0.447	$2.68^{+0.22}_{-0.23}$	4.00	0.553
1499	$2.49^{+0.34}_{-0.55}$	5.33	0.594	2.06	0.25	$2.49^{+0.15}_{-0.24}$	5.33	0.577	$2.04^{+0.18}_{-0.18}$	4.00	0.423
1509	$0.73^{+0.17}_{-0.17}$	3.33	1.000	1.42	0.32	$0.73^{+0.09}_{-0.10}$	3.33	1.000	$\cdots$ $^{+}_{-}$	$\cdots$	$\cdots$
1531	$1.55^{+0.25}_{-0.32}$	6.33	0.905	0.82	0.19	$1.55^{+0.14}_{-0.17}$	6.33	0.882	$1.27^{+0.11}_{-0.11}$	6.67	0.118
1551	$0.21^{+0.12}_{-0.12}$	3.67	1.000	10.39	1.42	$0.21^{+0.07}_{-0.07}$	3.67	1.000	$\cdots$ $^{+}_{-}$	$\cdots$	$\cdots$
1559	$3.01^{+0.39}_{-0.39}$	6.67	1.000	1.15	0.13	$3.01^{+0.12}_{-0.13}$	6.67	0.974	$3.18^{+0.06}_{-0.05}$	7.33	0.026
1564	$3.34^{+0.43}_{-0.42}$	6.00	1.000	5.46	0.14	$3.34^{+0.09}_{-0.09}$	6.00	1.000	$\cdots$ $^{+}_{-}$	$\cdots$	$\cdots$
1571	$1.50^{+0.25}_{-0.25}$	2.67	1.000	4.29	0.01	$1.50^{+0.09}_{-0.07}$	2.67	0.896	$1.41^{+0.02}_{-0.07}$	3.00	0.104
1589	$1.70^{+0.26}_{-0.27}$	3.33	1.000	2.01	0.03	$1.70^{+0.12}_{-0.05}$	3.33	0.569	$1.61^{+0.04}_{-0.10}$	3.67	0.431
1592	$1.57^{+0.25}_{-0.25}$	4.00	1.000	1.26	0.25	$1.57^{+0.11}_{-0.12}$	4.00	1.000	$\cdots$ $^{+}_{-}$	$\cdots$	$\cdots$

Table C.2—Continued

ID[a]	z_b[b]	t_b[c]	ODDS[d]	χ^2_ν[e]	$\chi^2_{\rm mod}$[f]	z_b1[g]	t_b1[c]	ODDS1[h]	z_b2[g]	t_b2[c]	ODDS2[h]
1597	$0.56^{+0.15}_{-0.15}$	3.67	1.000	2.16	1.97	$0.56^{+0.12}_{-0.10}$	3.67	1.000	$\cdots$ $^{+}_{-}$	$\cdots$	$\cdots$
1607	$1.57^{+0.25}_{-0.25}$	6.33	1.000	7.81	0.96	$1.57^{+0.10}_{-0.11}$	6.33	1.000	$\cdots$ $^{+}_{-}$	$\cdots$	$\cdots$
1612	$2.13^{+0.31}_{-0.31}$	6.67	1.000	2.18	2.41	$2.13^{+0.19}_{-0.21}$	6.67	1.000	$\cdots$ $^{+}_{-}$	$\cdots$	$\cdots$
1616	$0.67^{+0.16}_{-0.16}$	3.33	1.000	11.02	1.50	$0.67^{+0.13}_{-0.11}$	3.33	1.000	$\cdots$ $^{+}_{-}$	$\cdots$	$\cdots$
1619	$1.30^{+0.23}_{-0.22}$	3.67	1.000	0.62	0.00	$1.30^{+0.08}_{-0.07}$	3.67	1.000	$\cdots$ $^{+}_{-}$	$\cdots$	$\cdots$
1626	$1.37^{+0.23}_{-0.23}$	6.00	1.000	5.41	0.23	$1.37^{+0.16}_{-0.08}$	6.00	1.000	$\cdots$ $^{+}_{-}$	$\cdots$	$\cdots$
1640	$1.12^{+0.21}_{-0.21}$	6.67	1.000	0.24	0.22	$1.12^{+0.11}_{-0.10}$	6.67	1.000	$\cdots$ $^{+}_{-}$	$\cdots$	$\cdots$
1650	$3.82^{+0.47}_{-0.47}$	6.00	1.000	2.46	0.53	$3.82^{+0.23}_{-0.13}$	6.00	1.000	$\cdots$ $^{+}_{-}$	$\cdots$	$\cdots$
1662	$2.55^{+0.35}_{-0.35}$	2.67	1.000	4.66	0.17	$2.55^{+0.27}_{-0.33}$	2.67	1.000	$\cdots$ $^{+}_{-}$	$\cdots$	$\cdots$
1666	$1.35^{+0.23}_{-0.23}$	6.00	1.000	20.45	0.88	$1.35^{+0.08}_{-0.07}$	6.00	1.000	$\cdots$ $^{+}_{-}$	$\cdots$	$\cdots$
1668	$0.99^{+0.19}_{-0.19}$	7.00	1.000	7.26	1.45	$0.99^{+0.08}_{-0.08}$	7.00	1.000	$\cdots$ $^{+}_{-}$	$\cdots$	$\cdots$
1678	$1.57^{+0.25}_{-0.25}$	6.00	1.000	2.01	0.19	$1.57^{+0.11}_{-0.10}$	6.00	1.000	$\cdots$ $^{+}_{-}$	$\cdots$	$\cdots$
1681	$0.12^{+1.82}_{-0.11}$	7.33	0.788	3.67	4.39	$0.12^{+0.09}_{-0.09}$	7.33	0.788	$1.62^{+0.22}_{-0.14}$	7.00	0.160
1683	$2.52^{+0.35}_{-0.35}$	7.33	1.000	0.20	0.09	$2.52^{+0.17}_{-0.13}$	7.33	0.983	$2.35^{+0.04}_{-0.07}$	7.00	0.017
1693	$1.11^{+0.21}_{-0.21}$	6.33	1.000	4.13	0.87	$1.11^{+0.10}_{-0.11}$	6.33	1.000	$\cdots$ $^{+}_{-}$	$\cdots$	$\cdots$
1718	$3.66^{+0.46}_{-0.46}$	5.33	1.000	2.47	1.11	$3.66^{+0.17}_{-0.35}$	5.33	1.000	$\cdots$ $^{+}_{-}$	$\cdots$	$\cdots$
1720	$0.45^{+0.14}_{-0.14}$	5.67	0.989	2.23	0.37	$0.45^{+0.12}_{-0.08}$	5.67	0.989	$0.67^{+0.03}_{-0.03}$	6.00	0.011
1722	$0.48^{+3.00}_{-0.14}$	3.00	0.503	2.72	1.01	$0.48^{+0.14}_{-0.13}$	3.00	0.503	$3.40^{+0.16}_{-0.16}$	3.33	0.486
1725	$2.69^{+0.36}_{-2.51}$	4.33	0.912	1.51	0.03	$2.69^{+0.16}_{-0.11}$	4.33	0.601	$2.37^{+0.10}_{-0.14}$	3.33	0.251
1727	$0.25^{+0.12}_{-0.12}$	3.33	1.000	0.75	0.31	$0.25^{+0.09}_{-0.09}$	3.33	1.000	$\cdots$ $^{+}_{-}$	$\cdots$	$\cdots$
1732	$0.61^{+0.16}_{-0.16}$	3.67	1.000	6.06	0.16	$0.61^{+0.09}_{-0.09}$	3.67	1.000	$\cdots$ $^{+}_{-}$	$\cdots$	$\cdots$
1738	$2.67^{+0.36}_{-0.36}$	7.67	1.000	5.54	2.36	$2.67^{+0.10}_{-0.13}$	7.67	1.000	$\cdots$ $^{+}_{-}$	$\cdots$	$\cdots$
1739	$2.51^{+0.34}_{-0.34}$	6.33	1.000	2.81	0.79	$2.51^{+0.10}_{-0.09}$	6.33	1.000	$\cdots$ $^{+}_{-}$	$\cdots$	$\cdots$
1753	$3.44^{+0.43}_{-0.43}$	4.00	1.000	0.37	0.26	$3.44^{+0.30}_{-0.36}$	4.00	1.000	$\cdots$ $^{+}_{-}$	$\cdots$	$\cdots$
1774	$1.91^{+0.28}_{-0.28}$	6.67	0.996	1.27	0.67	$1.91^{+0.19}_{-0.19}$	6.67	0.996	$0.11^{+0.02}_{-0.03}$	7.00	0.004
1775	$2.15^{+0.31}_{-0.31}$	6.33	1.000	0.63	0.04	$2.15^{+0.11}_{-0.17}$	6.33	0.821	$2.32^{+0.09}_{-0.06}$	6.67	0.179
1787	$0.67^{+0.16}_{-0.16}$	3.67	1.000	0.38	0.05	$0.67^{+0.11}_{-0.17}$	3.67	1.000	$\cdots$ $^{+}_{-}$	$\cdots$	$\cdots$
1789	$0.17^{+0.11}_{-0.12}$	3.00	1.000	3.65	0.39	$0.17^{+0.08}_{-0.07}$	3.00	1.000	$\cdots$ $^{+}_{-}$	$\cdots$	$\cdots$
1809	$3.60^{+0.45}_{-0.45}$	5.33	1.000	1.14	0.03	$3.60^{+0.09}_{-0.09}$	5.33	1.000	$\cdots$ $^{+}_{-}$	$\cdots$	$\cdots$
1810	$1.37^{+0.23}_{-0.23}$	4.00	1.000	3.46	0.22	$1.37^{+0.09}_{-0.11}$	4.00	1.000	$\cdots$ $^{+}_{-}$	$\cdots$	$\cdots$
1814	$1.48^{+0.73}_{-0.24}$	5.00	0.715	0.84	0.15	$1.48^{+0.33}_{-0.13}$	5.00	0.727	$2.14^{+0.18}_{-0.33}$	5.00	0.273
1830	$2.22^{+0.32}_{-2.17}$	6.00	0.964	1.59	0.04	$2.22^{+0.08}_{-0.15}$	6.00	0.505	$2.40^{+0.11}_{-0.10}$	6.33	0.460
1849	$2.58^{+0.35}_{-0.35}$	6.33	1.000	0.60	0.05	$2.58^{+0.13}_{-0.12}$	6.33	1.000	$\cdots$ $^{+}_{-}$	$\cdots$	$\cdots$
1858	$3.52^{+0.44}_{-0.44}$	5.33	1.000	0.31	0.11	$3.52^{+0.20}_{-0.37}$	5.33	1.000	$\cdots$ $^{+}_{-}$	$\cdots$	$\cdots$
1859	$4.08^{+0.50}_{-0.50}$	7.00	1.000	0.02	0.01	$4.08^{+0.06}_{-0.17}$	7.00	0.582	$4.18^{+0.12}_{-0.04}$	7.33	0.418
1874	$1.44^{+0.24}_{-0.24}$	4.00	1.000	5.11	0.06	$1.44^{+0.08}_{-0.08}$	4.00	0.919	$1.32^{+0.04}_{-0.06}$	5.33	0.081

Table C.2—Continued

ID[a]	z_b[b]	t_b[c]	ODDS[d]	χ^2_ν[e]	$\chi^2_{\rm mod}$[f]	z_b1[g]	t_b1[c]	ODDS1[h]	z_b2[g]	t_b2[c]	ODDS2[h]
1880	$3.31^{+0.42}_{-0.42}$	6.00	1.000	2.21	0.23	$3.31^{+0.10}_{-0.12}$	6.00	1.000	$\cdots$ $^{+}_{-}$	$\cdots$	$\cdots$
1881	$3.19^{+0.41}_{-3.06}$	4.00	0.897	0.82	0.07	$3.19^{+0.27}_{-0.44}$	4.00	0.899	$0.15^{+0.16}_{-0.12}$	2.67	0.074
1888	$3.07^{+0.40}_{-0.40}$	6.33	1.000	0.61	0.18	$3.07^{+0.19}_{-0.20}$	6.33	1.000	$\cdots$ $^{+}_{-}$	$\cdots$	$\cdots$
1889	$2.24^{+0.32}_{-0.54}$	5.00	0.799	4.64	1.44	$2.24^{+0.26}_{-0.25}$	5.00	0.799	$1.75^{+0.14}_{-0.11}$	3.67	0.201
1898	$0.17^{+2.32}_{-0.12}$	3.33	0.796	1.87	0.08	$0.17^{+0.08}_{-0.11}$	3.33	0.796	$2.46^{+0.08}_{-0.09}$	3.00	0.204
1904	$0.61^{+0.16}_{-0.16}$	4.33	1.000	4.82	1.67	$0.61^{+0.09}_{-0.09}$	4.33	1.000	$\cdots$ $^{+}_{-}$	$\cdots$	$\cdots$
1905	$0.58^{+0.16}_{-0.15}$	3.67	1.000	9.76	0.54	$0.58^{+0.09}_{-0.08}$	3.67	1.000	$\cdots$ $^{+}_{-}$	$\cdots$	$\cdots$
1922	$2.29^{+0.32}_{-0.32}$	6.33	1.000	4.45	2.01	$2.29^{+0.21}_{-0.13}$	6.33	1.000	$\cdots$ $^{+}_{-}$	$\cdots$	$\cdots$
1940	$3.62^{+0.45}_{-0.45}$	5.67	1.000	0.18	0.01	$3.62^{+0.11}_{-0.12}$	5.67	1.000	$\cdots$ $^{+}_{-}$	$\cdots$	$\cdots$
1955	$2.02^{+0.30}_{-0.30}$	6.67	1.000	0.56	0.25	$2.02^{+0.31}_{-0.26}$	6.67	1.000	$\cdots$ $^{+}_{-}$	$\cdots$	$\cdots$
1960	$0.45^{+0.14}_{-0.14}$	1.67	1.000	54.80	0.09	$0.45^{+0.07}_{-0.08}$	1.67	1.000	$\cdots$ $^{+}_{-}$	$\cdots$	$\cdots$
1971	$0.03^{+0.10}_{-0.03}$	3.00	1.000	0.87	0.07	$0.03^{+0.08}_{-0.02}$	3.00	1.000	$\cdots$ $^{+}_{-}$	$\cdots$	$\cdots$
1992	$1.98^{+0.31}_{-0.29}$	7.00	0.972	4.05	2.84	$1.98^{+0.19}_{-0.29}$	7.00	0.910	$2.25^{+0.13}_{-0.08}$	7.00	0.082
2007	$1.31^{+0.23}_{-0.23}$	5.33	1.000	0.93	0.11	$1.31^{+0.18}_{-0.10}$	5.33	1.000	$\cdots$ $^{+}_{-}$	$\cdots$	$\cdots$
2012	$2.98^{+0.39}_{-0.39}$	5.33	1.000	7.35	1.02	$2.98^{+0.08}_{-0.08}$	5.33	1.000	$\cdots$ $^{+}_{-}$	$\cdots$	$\cdots$
2017	$0.05^{+0.49}_{-0.05}$	2.00	0.874	9.22	0.33	$0.05^{+0.12}_{-0.04}$	2.00	0.874	$0.51^{+0.08}_{-0.07}$	3.67	0.126
2032	$2.23^{+0.32}_{-0.32}$	6.67	0.979	0.26	0.08	$2.23^{+0.22}_{-0.41}$	6.67	0.991	$0.10^{+0.05}_{-0.06}$	7.00	0.009
2034	$2.36^{+0.33}_{-0.33}$	6.00	1.000	2.78	0.53	$2.36^{+0.15}_{-0.15}$	6.00	1.000	$\cdots$ $^{+}_{-}$	$\cdots$	$\cdots$
2042	$1.27^{+0.25}_{-0.22}$	7.00	0.973	2.80	2.28	$1.27^{+0.23}_{-0.18}$	7.00	0.971	$1.55^{+0.11}_{-0.05}$	6.67	0.029
2044	$2.51^{+0.34}_{-0.34}$	6.33	0.998	1.05	0.61	$2.51^{+0.15}_{-0.12}$	6.33	0.643	$2.33^{+0.06}_{-0.20}$	6.00	0.357
2045	$2.58^{+0.35}_{-0.35}$	6.33	1.000	4.05	0.20	$2.58^{+0.10}_{-0.11}$	6.33	1.000	$\cdots$ $^{+}_{-}$	$\cdots$	$\cdots$
2087	$3.81^{+0.47}_{-0.47}$	7.67	1.000	0.02	0.02	$3.81^{+0.11}_{-0.12}$	7.67	0.781	$3.63^{+0.06}_{-0.09}$	7.00	0.219
2088	$0.57^{+0.15}_{-0.15}$	4.00	1.000	2.62	1.75	$0.57^{+0.12}_{-0.13}$	4.00	1.000	$\cdots$ $^{+}_{-}$	$\cdots$	$\cdots$
2093	$3.06^{+0.40}_{-0.40}$	6.67	1.000	1.49	1.20	$3.06^{+0.19}_{-0.22}$	6.67	0.965	$3.30^{+0.13}_{-0.05}$	7.33	0.035
2102	$3.04^{+0.40}_{-0.40}$	8.00	1.000	1.17	0.87	$3.04^{+0.15}_{-0.21}$	8.00	0.987	$2.76^{+0.07}_{-0.05}$	7.00	0.013
2104	$0.87^{+0.18}_{-0.18}$	3.67	1.000	6.78	0.17	$0.87^{+0.09}_{-0.11}$	3.67	1.000	$\cdots$ $^{+}_{-}$	$\cdots$	$\cdots$
2107	$0.47^{+0.14}_{-0.14}$	1.33	1.000	16.54	0.01	$0.47^{+0.07}_{-0.07}$	1.33	1.000	$\cdots$ $^{+}_{-}$	$\cdots$	$\cdots$
2162	$0.95^{+0.19}_{-0.19}$	6.33	1.000	17.33	2.46	$0.95^{+0.08}_{-0.07}$	6.33	1.000	$\cdots$ $^{+}_{-}$	$\cdots$	$\cdots$
2170	$2.61^{+0.35}_{-0.55}$	5.33	0.756	8.47	3.20	$2.61^{+0.10}_{-0.14}$	5.33	0.756	$2.11^{+0.15}_{-0.10}$	3.67	0.244
2174	$1.98^{+0.29}_{-0.29}$	6.67	1.000	1.37	1.37	$1.98^{+0.22}_{-0.18}$	6.67	1.000	$\cdots$ $^{+}_{-}$	$\cdots$	$\cdots$
2189	$2.83^{+0.38}_{-0.38}$	6.33	1.000	6.25	0.20	$2.83^{+0.08}_{-0.08}$	6.33	1.000	$\cdots$ $^{+}_{-}$	$\cdots$	$\cdots$
2201	$1.41^{+0.24}_{-0.24}$	3.33	1.000	0.63	0.00	$1.41^{+0.08}_{-0.07}$	3.33	1.000	$\cdots$ $^{+}_{-}$	$\cdots$	$\cdots$
2215	$0.70^{+0.17}_{-0.17}$	6.00	1.000	11.17	0.34	$0.70^{+0.07}_{-0.07}$	6.00	1.000	$\cdots$ $^{+}_{-}$	$\cdots$	$\cdots$
2228	$2.89^{+0.38}_{-0.38}$	6.67	1.000	1.18	0.66	$2.89^{+0.40}_{-0.16}$	6.67	1.000	$\cdots$ $^{+}_{-}$	$\cdots$	$\cdots$
2240	$2.61^{+0.35}_{-0.35}$	7.00	1.000	7.17	0.40	$2.61^{+0.08}_{-0.07}$	7.00	1.000	$\cdots$ $^{+}_{-}$	$\cdots$	$\cdots$
2241	$0.59^{+0.16}_{-0.16}$	6.00	1.000	10.17	1.28	$0.59^{+0.08}_{-0.08}$	6.00	1.000	$\cdots$ $^{+}_{-}$	$\cdots$	$\cdots$

Table C.2—Continued

ID[a]	z_b[b]	t_b[c]	ODDS[d]	χ^2_ν[e]	$\chi^2_{\rm mod}$[f]	z_b1[g]	t_b1[c]	ODDS1[h]	z_b2[g]	t_b2[c]	ODDS2[h]
2245	$1.66^{+0.26}_{-0.26}$	3.00	1.000	13.70	0.24	$1.66^{+0.16}_{-0.10}$	3.00	1.000	$\cdots$ $^{+}_{-}$	$\cdots$	$\cdots$
2248	$2.52^{+0.35}_{-0.35}$	7.33	1.000	1.08	1.07	$2.52^{+0.13}_{-0.09}$	7.33	1.000	$\cdots$ $^{+}_{-}$	$\cdots$	$\cdots$
2265	$0.05^{+2.72}_{-0.05}$	3.67	0.343	4.66	3.74	$0.05^{+0.13}_{-0.04}$	3.67	0.343	$2.63^{+0.28}_{-0.49}$	4.67	0.657
2267	$1.49^{+0.24}_{-0.24}$	4.00	1.000	7.88	3.82	$1.49^{+0.09}_{-0.09}$	4.00	1.000	$\cdots$ $^{+}_{-}$	$\cdots$	$\cdots$
2281	$1.03^{+0.20}_{-0.20}$	3.67	1.000	1.00	0.10	$1.03^{+0.09}_{-0.11}$	3.67	1.000	$\cdots$ $^{+}_{-}$	$\cdots$	$\cdots$
2290	$2.41^{+0.33}_{-0.53}$	5.67	0.939	0.60	0.01	$2.41^{+0.14}_{-0.17}$	5.67	0.939	$0.07^{+0.04}_{-0.05}$	6.33	0.025
2291	$3.65^{+0.46}_{-0.46}$	6.33	1.000	2.31	1.13	$3.65^{+0.18}_{-0.19}$	6.33	1.000	$\cdots$ $^{+}_{-}$	$\cdots$	$\cdots$
2293	$0.35^{+0.27}_{-0.13}$	1.00	0.716	2.05	0.30	$0.35^{+0.12}_{-0.10}$	1.00	0.624	$0.48^{+0.22}_{-0.01}$	1.67	0.376
2306	$0.64^{+0.16}_{-0.16}$	5.67	0.992	3.78	1.98	$0.64^{+0.09}_{-0.20}$	5.67	1.000	$\cdots$ $^{+}_{-}$	$\cdots$	$\cdots$
2322	$0.59^{+0.16}_{-0.16}$	1.00	1.000	4.59	0.37	$0.59^{+0.07}_{-0.07}$	1.00	1.000	$\cdots$ $^{+}_{-}$	$\cdots$	$\cdots$
2329	$0.24^{+0.12}_{-0.12}$	3.33	1.000	1.21	0.48	$0.24^{+0.10}_{-0.11}$	3.33	1.000	$\cdots$ $^{+}_{-}$	$\cdots$	$\cdots$
2332	$0.08^{+0.11}_{-0.08}$	3.33	0.992	2.40	0.20	$0.08^{+0.15}_{-0.07}$	3.33	1.000	$\cdots$ $^{+}_{-}$	$\cdots$	$\cdots$
2333	$1.24^{+0.22}_{-0.22}$	3.33	1.000	5.43	0.54	$1.24^{+0.10}_{-0.09}$	3.33	1.000	$\cdots$ $^{+}_{-}$	$\cdots$	$\cdots$
2340	$1.32^{+0.23}_{-0.23}$	5.67	1.000	9.76	1.36	$1.32^{+0.10}_{-0.09}$	5.67	0.974	$1.46^{+0.04}_{-0.04}$	4.00	0.026
2350	$3.09^{+0.40}_{-0.40}$	5.67	1.000	3.44	0.34	$3.09^{+0.13}_{-0.13}$	5.67	1.000	$\cdots$ $^{+}_{-}$	$\cdots$	$\cdots$
2358	$2.41^{+0.33}_{-0.33}$	6.67	1.000	0.86	0.97	$2.41^{+0.10}_{-0.11}$	6.67	0.991	$2.28^{+0.02}_{-0.04}$	6.33	0.009
2387	$0.62^{+0.16}_{-0.16}$	1.00	1.000	16.32	0.17	$0.62^{+0.07}_{-0.07}$	1.00	1.000	$\cdots$ $^{+}_{-}$	$\cdots$	$\cdots$
2414	$0.94^{+0.19}_{-0.19}$	1.00	1.000	6.89	0.00	$0.94^{+0.08}_{-0.07}$	1.00	1.000	$\cdots$ $^{+}_{-}$	$\cdots$	$\cdots$
2415	$1.50^{+0.25}_{-0.25}$	6.67	0.992	0.59	0.12	$1.50^{+0.31}_{-0.13}$	6.67	1.000	$\cdots$ $^{+}_{-}$	$\cdots$	$\cdots$
2445	$2.57^{+0.35}_{-0.35}$	3.67	1.000	0.83	0.27	$2.57^{+0.15}_{-0.19}$	3.67	1.000	$\cdots$ $^{+}_{-}$	$\cdots$	$\cdots$
2461	$1.22^{+0.22}_{-0.22}$	5.67	1.000	8.34	1.62	$1.22^{+0.09}_{-0.11}$	5.67	1.000	$\cdots$ $^{+}_{-}$	$\cdots$	$\cdots$
2462	$0.18^{+0.12}_{-0.12}$	3.00	1.000	8.37	0.62	$0.18^{+0.08}_{-0.07}$	3.00	1.000	$\cdots$ $^{+}_{-}$	$\cdots$	$\cdots$
2463	$2.89^{+0.38}_{-0.38}$	5.67	1.000	3.01	0.39	$2.89^{+0.08}_{-0.08}$	5.67	1.000	$\cdots$ $^{+}_{-}$	$\cdots$	$\cdots$
2468	$2.88^{+0.38}_{-0.38}$	6.67	1.000	1.44	1.43	$2.88^{+0.26}_{-0.15}$	6.67	1.000	$\cdots$ $^{+}_{-}$	$\cdots$	$\cdots$
2499	$0.69^{+0.26}_{-0.17}$	6.00	0.860	3.54	0.63	$0.69^{+0.08}_{-0.07}$	6.00	0.860	$0.92^{+0.07}_{-0.06}$	6.00	0.140
2516	$2.93^{+0.41}_{-0.38}$	6.67	0.933	4.74	1.00	$2.93^{+0.14}_{-0.12}$	6.67	0.505	$3.29^{+0.11}_{-0.17}$	8.00	0.495
2518	$3.89^{+0.48}_{-0.48}$	4.00	1.000	0.59	0.34	$3.89^{+0.16}_{-0.17}$	4.00	0.911	$4.06^{+0.12}_{-0.01}$	5.33	0.089
2525	$0.63^{+0.16}_{-0.16}$	3.33	1.000	33.30	0.13	$0.63^{+0.08}_{-0.09}$	3.33	1.000	$\cdots$ $^{+}_{-}$	$\cdots$	$\cdots$
2526	$1.26^{+0.28}_{-0.22}$	6.67	0.934	4.92	1.39	$1.26^{+0.09}_{-0.10}$	6.67	0.836	$1.45^{+0.04}_{-0.10}$	6.33	0.091
2538	$2.56^{+0.35}_{-0.35}$	6.67	1.000	1.83	0.62	$2.56^{+0.12}_{-0.14}$	6.67	1.000	$\cdots$ $^{+}_{-}$	$\cdots$	$\cdots$
2540	$3.10^{+0.40}_{-0.40}$	6.00	1.000	1.71	0.58	$3.10^{+0.21}_{-0.19}$	6.00	1.000	$\cdots$ $^{+}_{-}$	$\cdots$	$\cdots$
2542	$1.46^{+0.24}_{-0.24}$	3.67	1.000	0.74	0.01	$1.46^{+0.15}_{-0.09}$	3.67	0.907	$1.31^{+0.06}_{-0.07}$	5.00	0.093
2546	$3.68^{+0.46}_{-0.46}$	6.33	1.000	0.47	0.46	$3.68^{+0.15}_{-0.12}$	6.33	1.000	$\cdots$ $^{+}_{-}$	$\cdots$	$\cdots$
2547	$3.18^{+0.41}_{-0.41}$	8.00	1.000	0.92	0.32	$3.18^{+0.14}_{-0.25}$	8.00	0.989	$2.88^{+0.05}_{-0.06}$	7.00	0.011
2558	$3.02^{+0.39}_{-0.39}$	5.67	1.000	1.86	0.02	$3.02^{+0.08}_{-0.08}$	5.67	1.000	$\cdots$ $^{+}_{-}$	$\cdots$	$\cdots$
2565	$0.95^{+0.19}_{-0.28}$	6.00	0.866	2.03	0.87	$0.95^{+0.22}_{-0.16}$	6.00	0.865	$0.70^{+0.08}_{-0.06}$	6.33	0.135

Table C.2—Continued

ID[a]	z_b[b]	t_b[c]	ODDS[d]	χ^2_ν[e]	$\chi^2_{\rm mod}$[f]	z_b1[g]	t_b1[c]	ODDS1[h]	z_b2[g]	t_b2[c]	ODDS2[h]
2566	$3.48^{+0.44}_{-0.44}$	4.67	1.000	0.32	0.03	$3.48^{+0.19}_{-0.07}$	4.67	0.560	$3.38^{+0.03}_{-0.32}$	4.33	0.440
2573	$0.89^{+0.19}_{-0.19}$	5.33	1.000	8.29	0.23	$0.89^{+0.09}_{-0.17}$	5.33	1.000	··· $^{+}_{-}$	···	···
2581	$3.40^{+0.43}_{-0.43}$	5.33	1.000	5.97	2.24	$3.40^{+0.16}_{-0.22}$	5.33	1.000	··· $^{+}_{-}$	···	···
2595	$2.97^{+0.39}_{-0.39}$	8.00	1.000	1.81	1.41	$2.97^{+0.14}_{-0.05}$	8.00	0.461	$2.91^{+0.01}_{-0.18}$	8.00	0.461
2607	$0.60^{+0.16}_{-0.16}$	2.00	1.000	90.94	0.08	$0.60^{+0.08}_{-0.07}$	2.00	1.000	··· $^{+}_{-}$	···	···
2611	$3.23^{+0.41}_{-0.41}$	7.67	1.000	1.64	0.70	$3.23^{+0.17}_{-0.15}$	7.67	0.747	$3.01^{+0.07}_{-0.20}$	6.67	0.253
2639	$0.91^{+0.26}_{-0.19}$	6.33	0.730	3.53	1.38	$0.91^{+0.09}_{-0.12}$	6.33	0.544	$1.12^{+0.11}_{-0.12}$	6.00	0.456
2652	$0.56^{+0.15}_{-0.15}$	3.33	1.000	12.74	0.07	$0.56^{+0.09}_{-0.08}$	3.33	1.000	··· $^{+}_{-}$	···	···
2681	$3.55^{+0.45}_{-0.45}$	6.00	1.000	0.00	0.01	$3.55^{+0.15}_{-0.16}$	6.00	1.000	··· $^{+}_{-}$	···	···
2688	$3.28^{+0.42}_{-0.42}$	6.33	1.000	0.08	0.03	$3.28^{+0.21}_{-0.26}$	6.33	1.000	··· $^{+}_{-}$	···	···
2693	$1.50^{+0.25}_{-0.28}$	6.00	0.929	1.57	0.06	$1.50^{+0.11}_{-0.11}$	6.00	0.808	$1.27^{+0.07}_{-0.09}$	6.33	0.192
2697	$3.75^{+0.47}_{-0.46}$	5.33	1.000	0.54	0.59	$3.75^{+0.19}_{-0.38}$	5.33	1.000	··· $^{+}_{-}$	···	···
2705	$0.68^{+0.17}_{-0.17}$	6.33	1.000	4.06	2.18	$0.68^{+0.07}_{-0.07}$	6.33	1.000	··· $^{+}_{-}$	···	···
2728	$3.17^{+0.41}_{-0.41}$	6.33	1.000	0.44	0.09	$3.17^{+0.12}_{-0.16}$	6.33	1.000	··· $^{+}_{-}$	···	···
2734	$3.03^{+0.39}_{-0.39}$	8.00	1.000	0.87	1.02	$3.03^{+0.14}_{-0.22}$	8.00	0.977	$2.78^{+0.03}_{-0.07}$	7.00	0.023
2750	$3.64^{+0.45}_{-0.46}$	6.33	1.000	1.80	0.82	$3.64^{+0.13}_{-0.13}$	6.33	1.000	··· $^{+}_{-}$	···	···
2753	$0.53^{+0.15}_{-0.15}$	3.00	1.000	13.70	0.10	$0.53^{+0.07}_{-0.08}$	3.00	1.000	··· $^{+}_{-}$	···	···
2763	$1.54^{+0.25}_{-0.25}$	3.33	1.000	5.72	2.71	$1.54^{+0.09}_{-0.08}$	3.33	1.000	··· $^{+}_{-}$	···	···
2764	$1.51^{+0.25}_{-0.25}$	4.00	1.000	11.79	3.31	$1.51^{+0.08}_{-0.09}$	4.00	1.000	··· $^{+}_{-}$	···	···
2770	$1.71^{+0.27}_{-0.27}$	6.33	0.996	0.68	0.65	$1.71^{+0.06}_{-0.16}$	6.33	0.519	$1.81^{+0.22}_{-0.04}$	6.33	0.481
2778	$2.48^{+0.34}_{-0.34}$	6.67	0.994	3.29	2.99	$2.48^{+0.19}_{-0.45}$	6.67	1.000	··· $^{+}_{-}$	···	···
2781	$2.13^{+0.31}_{-0.34}$	7.00	0.965	1.14	1.33	$2.13^{+0.22}_{-0.49}$	7.00	1.000	··· $^{+}_{-}$	···	···
2785	$1.55^{+0.25}_{-0.25}$	3.00	1.000	16.04	0.49	$1.55^{+0.11}_{-0.09}$	3.00	1.000	··· $^{+}_{-}$	···	···
2798	$0.60^{+0.16}_{-0.16}$	2.33	1.000	3.83	0.24	$0.60^{+0.10}_{-0.13}$	2.33	1.000	··· $^{+}_{-}$	···	···
2799	$0.91^{+0.19}_{-0.19}$	5.67	1.000	4.10	1.54	$0.91^{+0.08}_{-0.07}$	5.67	1.000	··· $^{+}_{-}$	···	···
2813	$2.67^{+0.36}_{-0.36}$	3.33	1.000	2.68	0.01	$2.67^{+0.08}_{-0.09}$	3.33	0.934	$2.76^{+0.07}_{-0.01}$	3.67	0.066
2825	$3.86^{+0.48}_{-0.48}$	6.33	1.000	0.07	0.02	$3.86^{+0.18}_{-0.19}$	6.33	1.000	··· $^{+}_{-}$	···	···
2826	$2.53^{+0.35}_{-0.35}$	7.00	1.000	1.20	1.30	$2.53^{+0.21}_{-0.22}$	7.00	1.000	··· $^{+}_{-}$	···	···
2837	$3.38^{+0.43}_{-0.43}$	4.67	1.000	1.57	1.10	$3.38^{+0.16}_{-0.20}$	4.67	1.000	··· $^{+}_{-}$	···	···
2848	$0.06^{+0.23}_{-0.06}$	6.00	0.764	5.68	2.37	$0.06^{+0.08}_{-0.05}$	6.00	0.764	$0.26^{+0.07}_{-0.06}$	6.33	0.236
2861	$1.39^{+0.23}_{-0.23}$	4.00	1.000	1.96	0.21	$1.39^{+0.15}_{-0.15}$	4.00	1.000	··· $^{+}_{-}$	···	···
2872	$3.01^{+0.39}_{-0.39}$	6.67	1.000	2.59	0.46	$3.01^{+0.12}_{-0.13}$	6.67	1.000	··· $^{+}_{-}$	···	···
2873	$3.46^{+0.44}_{-0.44}$	5.33	1.000	0.36	0.17	$3.46^{+0.14}_{-0.27}$	5.33	1.000	··· $^{+}_{-}$	···	···
2878	$2.29^{+0.32}_{-0.32}$	6.67	0.982	0.69	0.30	$2.29^{+0.24}_{-0.42}$	6.67	0.992	$0.11^{+0.05}_{-0.04}$	7.00	0.008
2879	$1.70^{+0.26}_{-0.27}$	6.00	1.000	2.09	0.59	$1.70^{+0.20}_{-0.15}$	6.00	1.000	··· $^{+}_{-}$	···	···
2881	$4.69^{+0.56}_{-0.56}$	4.67	1.000	0.25	0.18	$4.69^{+0.12}_{-0.11}$	4.67	1.000	··· $^{+}_{-}$	···	···

Table C.2—Continued

ID[a]	z_b[b]	t_b[c]	ODDS[d]	χ^2_ν[e]	$\chi^2_{\rm mod}$[f]	z_b1[g]	t_b1[c]	ODDS1[h]	z_b2[g]	t_b2[c]	ODDS2[h]
2882	$2.94^{+0.39}_{-0.39}$	6.33	1.000	4.38	0.48	$2.94^{+0.16}_{-0.14}$	6.33	1.000	$\cdots$ $^{+}_{-}$	$\cdots$	$\cdots$
2912	$0.57^{+0.15}_{-0.15}$	3.33	1.000	7.88	1.85	$0.57^{+0.12}_{-0.11}$	3.33	1.000	$\cdots$ $^{+}_{-}$	$\cdots$	$\cdots$
2927	$0.20^{+0.12}_{-0.12}$	3.00	0.989	7.84	0.06	$0.20^{+0.06}_{-0.08}$	3.00	0.857	$0.28^{+0.08}_{-0.02}$	3.33	0.143
2933	$0.55^{+0.15}_{-0.15}$	2.67	1.000	9.26	0.12	$0.55^{+0.08}_{-0.08}$	2.67	1.000	$\cdots$ $^{+}_{-}$	$\cdots$	$\cdots$
2934	$1.19^{+0.54}_{-0.45}$	6.33	0.740	8.67	1.31	$1.19^{+0.09}_{-0.09}$	6.33	0.581	$0.99^{+0.08}_{-0.08}$	6.67	0.217
2941	$0.53^{+0.15}_{-0.15}$	3.67	1.000	0.15	0.11	$0.53^{+0.16}_{-0.14}$	3.67	1.000	$\cdots$ $^{+}_{-}$	$\cdots$	$\cdots$
2943	$1.44^{+0.24}_{-0.24}$	4.00	1.000	9.23	0.11	$1.44^{+0.09}_{-0.08}$	4.00	1.000	$\cdots$ $^{+}_{-}$	$\cdots$	$\cdots$
2946	$2.84^{+0.38}_{-0.38}$	5.67	1.000	1.60	0.35	$2.84^{+0.14}_{-0.16}$	5.67	1.000	$\cdots$ $^{+}_{-}$	$\cdots$	$\cdots$
2954	$3.20^{+0.41}_{-0.41}$	6.33	1.000	0.81	0.17	$3.20^{+0.15}_{-0.16}$	6.33	0.994	$3.38^{+0.03}_{-0.03}$	7.33	0.006
2960	$1.56^{+0.25}_{-0.25}$	6.00	0.996	3.73	1.88	$1.56^{+0.14}_{-0.21}$	6.00	0.990	$1.31^{+0.04}_{-0.04}$	6.33	0.010
2974	$0.15^{+0.11}_{-0.11}$	2.67	1.000	16.16	1.51	$0.15^{+0.07}_{-0.12}$	2.67	1.000	$\cdots$ $^{+}_{-}$	$\cdots$	$\cdots$
2987	$1.63^{+0.26}_{-0.26}$	6.00	1.000	1.93	0.53	$1.63^{+0.17}_{-0.15}$	6.00	1.000	$\cdots$ $^{+}_{-}$	$\cdots$	$\cdots$
2993	$1.90^{+0.28}_{-0.28}$	2.67	1.000	48.12	3.81	$1.90^{+0.13}_{-0.11}$	2.67	1.000	$\cdots$ $^{+}_{-}$	$\cdots$	$\cdots$
2998	$0.55^{+0.15}_{-0.15}$	4.00	1.000	44.10	2.00	$0.55^{+0.08}_{-0.08}$	4.00	1.000	$\cdots$ $^{+}_{-}$	$\cdots$	$\cdots$
3006	$0.56^{+0.15}_{-0.15}$	3.67	1.000	4.54	0.48	$0.56^{+0.11}_{-0.12}$	3.67	1.000	$\cdots$ $^{+}_{-}$	$\cdots$	$\cdots$
3013	$0.53^{+0.15}_{-0.15}$	1.33	1.000	2.83	0.04	$0.53^{+0.07}_{-0.11}$	1.33	1.000	$\cdots$ $^{+}_{-}$	$\cdots$	$\cdots$
3021	$2.94^{+0.39}_{-0.39}$	4.67	1.000	1.59	0.02	$2.94^{+0.09}_{-0.10}$	4.67	1.000	$\cdots$ $^{+}_{-}$	$\cdots$	$\cdots$
3031	$1.39^{+0.23}_{-0.23}$	5.67	1.000	13.10	0.63	$1.39^{+0.11}_{-0.08}$	5.67	1.000	$\cdots$ $^{+}_{-}$	$\cdots$	$\cdots$
3033	$0.87^{+0.72}_{-0.30}$	7.67	0.778	0.65	0.44	$0.87^{+0.30}_{-0.41}$	7.67	0.934	$1.55^{+0.27}_{-0.21}$	7.00	0.066
3048	$0.72^{+0.17}_{-0.17}$	3.33	1.000	5.93	0.19	$0.72^{+0.10}_{-0.09}$	3.33	1.000	$\cdots$ $^{+}_{-}$	$\cdots$	$\cdots$
3052	$2.55^{+0.35}_{-0.35}$	7.33	1.000	3.57	3.07	$2.55^{+0.17}_{-0.11}$	7.33	0.871	$2.41^{+0.03}_{-0.15}$	7.00	0.129
3058	$2.84^{+0.38}_{-0.38}$	6.00	1.000	4.57	0.10	$2.84^{+0.08}_{-0.09}$	6.00	1.000	$\cdots$ $^{+}_{-}$	$\cdots$	$\cdots$
3060	$2.75^{+0.37}_{-0.37}$	8.00	1.000	40.72	12.42	$2.75^{+0.10}_{-0.10}$	8.00	1.000	$\cdots$ $^{+}_{-}$	$\cdots$	$\cdots$
3068	$1.37^{+0.23}_{-0.23}$	5.67	1.000	12.85	2.13	$1.37^{+0.08}_{-0.09}$	5.67	1.000	$\cdots$ $^{+}_{-}$	$\cdots$	$\cdots$
3088	$0.06^{+0.10}_{-0.06}$	2.33	1.000	15.20	1.91	$0.06^{+0.07}_{-0.05}$	2.33	1.000	$\cdots$ $^{+}_{-}$	$\cdots$	$\cdots$
3091	$3.23^{+0.41}_{-0.41}$	6.67	1.000	0.28	0.27	$3.23^{+0.10}_{-0.14}$	6.67	1.000	$\cdots$ $^{+}_{-}$	$\cdots$	$\cdots$
3101	$1.11^{+0.21}_{-0.21}$	3.33	1.000	1.25	0.36	$1.11^{+0.14}_{-0.10}$	3.33	1.000	$\cdots$ $^{+}_{-}$	$\cdots$	$\cdots$
3112	$3.01^{+0.39}_{-0.39}$	7.00	1.000	4.37	2.17	$3.01^{+0.09}_{-0.09}$	7.00	1.000	$\cdots$ $^{+}_{-}$	$\cdots$	$\cdots$
3123	$0.78^{+0.17}_{-0.17}$	5.67	0.979	9.87	0.34	$0.78^{+0.10}_{-0.07}$	5.67	0.979	$1.11^{+0.04}_{-0.04}$	4.00	0.021
3128	$3.25^{+0.42}_{-0.42}$	6.67	1.000	1.29	0.29	$3.25^{+0.09}_{-0.12}$	6.67	0.844	$3.39^{+0.11}_{-0.05}$	7.33	0.156
3136	$0.20^{+0.12}_{-0.12}$	2.67	1.000	1.54	0.03	$0.20^{+0.11}_{-0.08}$	2.67	1.000	$\cdots$ $^{+}_{-}$	$\cdots$	$\cdots$
3143	$0.76^{+0.41}_{-0.17}$	6.00	0.653	7.39	0.24	$0.76^{+0.11}_{-0.08}$	6.00	0.653	$1.13^{+0.08}_{-0.08}$	4.00	0.347
3154	$3.02^{+0.39}_{-0.39}$	5.00	1.000	2.31	0.12	$3.02^{+0.08}_{-0.14}$	5.00	0.776	$3.15^{+0.13}_{-0.05}$	5.33	0.224
3159	$1.00^{+0.20}_{-0.20}$	6.00	1.000	0.29	0.05	$1.00^{+0.17}_{-0.17}$	6.00	1.000	$\cdots$ $^{+}_{-}$	$\cdots$	$\cdots$
3174	$2.99^{+0.39}_{-0.39}$	6.00	1.000	3.51	1.06	$2.99^{+0.09}_{-0.09}$	6.00	1.000	$\cdots$ $^{+}_{-}$	$\cdots$	$\cdots$
3178	$2.55^{+0.35}_{-0.35}$	6.33	1.000	7.62	3.41	$2.55^{+0.11}_{-0.12}$	6.33	1.000	$\cdots$ $^{+}_{-}$	$\cdots$	$\cdots$

Table C.2—Continued

ID[a]	z_b[b]	t_b[c]	ODDS[d]	χ^2_ν[e]	$\chi^2_{\rm mod}$[f]	z_b1[g]	t_b1[c]	ODDS1[h]	z_b2[g]	t_b2[c]	ODDS2[h]
3180	$0.60^{+0.16}_{-0.16}$	5.00	1.000	10.77	3.52	$0.60^{+0.12}_{-0.08}$	5.00	1.000	$\cdots$ $^{+}_{-}$	$\cdots$	$\cdots$
3185	$3.31^{+0.42}_{-0.42}$	6.67	1.000	0.32	0.09	$3.31^{+0.10}_{-0.14}$	6.67	0.946	$3.45^{+0.08}_{-0.04}$	7.33	0.054
3190	$0.59^{+0.16}_{-0.16}$	2.00	1.000	0.49	0.35	$0.59^{+0.09}_{-0.12}$	2.00	1.000	$\cdots$ $^{+}_{-}$	$\cdots$	$\cdots$
3192	$3.12^{+0.40}_{-0.40}$	6.00	1.000	5.88	5.45	$3.12^{+0.21}_{-0.21}$	6.00	1.000	$\cdots$ $^{+}_{-}$	$\cdots$	$\cdots$
3198	$2.72^{+0.37}_{-0.37}$	7.33	1.000	3.84	1.14	$2.72^{+0.15}_{-0.15}$	7.33	1.000	$\cdots$ $^{+}_{-}$	$\cdots$	$\cdots$
3203	$0.20^{+0.12}_{-0.12}$	2.33	1.000	3.40	0.21	$0.20^{+0.07}_{-0.07}$	2.33	1.000	$\cdots$ $^{+}_{-}$	$\cdots$	$\cdots$
3205	$2.57^{+0.35}_{-0.35}$	6.33	1.000	2.10	0.65	$2.57^{+0.16}_{-0.17}$	6.33	1.000	$\cdots$ $^{+}_{-}$	$\cdots$	$\cdots$
3214	$2.83^{+0.38}_{-0.38}$	6.00	1.000	3.16	0.16	$2.83^{+0.09}_{-0.09}$	6.00	1.000	$\cdots$ $^{+}_{-}$	$\cdots$	$\cdots$
3219	$3.00^{+0.39}_{-0.39}$	5.00	1.000	0.43	0.09	$3.00^{+0.28}_{-0.34}$	5.00	1.000	$\cdots$ $^{+}_{-}$	$\cdots$	$\cdots$
3221	$0.97^{+0.19}_{-0.19}$	4.00	1.000	0.43	0.05	$0.97^{+0.12}_{-0.15}$	4.00	1.000	$\cdots$ $^{+}_{-}$	$\cdots$	$\cdots$
3223	$2.47^{+0.34}_{-0.34}$	2.67	0.991	15.81	0.92	$2.47^{+0.24}_{-0.26}$	2.67	0.991	$2.88^{+0.10}_{-0.06}$	3.33	0.009
3247	$0.62^{+0.16}_{-0.16}$	1.67	1.000	4.49	0.01	$0.62^{+0.08}_{-0.08}$	1.67	1.000	$\cdots$ $^{+}_{-}$	$\cdots$	$\cdots$
3248	$2.10^{+0.30}_{-0.30}$	6.33	0.999	2.92	0.58	$2.10^{+0.34}_{-0.21}$	6.33	1.000	$\cdots$ $^{+}_{-}$	$\cdots$	$\cdots$
3257	$1.35^{+0.23}_{-0.23}$	6.00	1.000	7.01	0.97	$1.35^{+0.13}_{-0.09}$	6.00	1.000	$\cdots$ $^{+}_{-}$	$\cdots$	$\cdots$
3259	$1.12^{+0.21}_{-0.21}$	5.00	1.000	2.66	1.55	$1.12^{+0.19}_{-0.10}$	5.00	1.000	$\cdots$ $^{+}_{-}$	$\cdots$	$\cdots$
3268	$0.25^{+0.12}_{-0.12}$	3.67	1.000	3.47	0.09	$0.25^{+0.08}_{-0.07}$	3.67	1.000	$\cdots$ $^{+}_{-}$	$\cdots$	$\cdots$
3274	$0.92^{+0.19}_{-0.19}$	5.67	1.000	3.58	0.51	$0.92^{+0.08}_{-0.11}$	5.67	1.000	$\cdots$ $^{+}_{-}$	$\cdots$	$\cdots$
3280	$1.09^{+0.20}_{-0.21}$	3.67	1.000	2.34	0.19	$1.09^{+0.14}_{-0.10}$	3.67	1.000	$\cdots$ $^{+}_{-}$	$\cdots$	$\cdots$
3288	$0.53^{+0.15}_{-0.15}$	2.33	1.000	16.92	0.15	$0.53^{+0.08}_{-0.07}$	2.33	1.000	$\cdots$ $^{+}_{-}$	$\cdots$	$\cdots$
3299	$0.74^{+0.84}_{-0.17}$	6.00	0.851	5.53	0.36	$0.74^{+0.08}_{-0.07}$	6.00	0.851	$1.55^{+0.07}_{-0.06}$	3.00	0.149
3306	$2.49^{+0.34}_{-0.34}$	6.67	1.000	1.76	1.72	$2.49^{+0.12}_{-0.28}$	6.67	1.000	$\cdots$ $^{+}_{-}$	$\cdots$	$\cdots$
3309	$0.72^{+0.17}_{-0.17}$	5.33	1.000	6.12	0.34	$0.72^{+0.08}_{-0.12}$	5.33	1.000	$\cdots$ $^{+}_{-}$	$\cdots$	$\cdots$
3315	$0.69^{+0.25}_{-0.17}$	6.00	0.926	1.83	0.71	$0.69^{+0.08}_{-0.08}$	6.00	0.926	$0.93^{+0.07}_{-0.07}$	6.00	0.074
3319	$0.75^{+0.17}_{-0.17}$	3.67	1.000	6.26	0.09	$0.75^{+0.08}_{-0.08}$	3.67	1.000	$\cdots$ $^{+}_{-}$	$\cdots$	$\cdots$
3332	$0.13^{+0.11}_{-0.11}$	3.33	1.000	8.04	2.40	$0.13^{+0.09}_{-0.12}$	3.33	1.000	$\cdots$ $^{+}_{-}$	$\cdots$	$\cdots$
3333	$1.08^{+0.36}_{-0.20}$	1.67	0.770	2.05	0.01	$1.08^{+0.11}_{-0.10}$	1.67	0.761	$1.38^{+0.13}_{-0.13}$	1.33	0.239
3345	$3.38^{+0.43}_{-0.43}$	6.00	1.000	0.72	0.72	$3.38^{+0.16}_{-0.18}$	6.00	1.000	$\cdots$ $^{+}_{-}$	$\cdots$	$\cdots$
3347	$3.62^{+0.45}_{-0.45}$	6.67	1.000	0.49	0.70	$3.62^{+0.33}_{-0.18}$	6.67	1.000	$\cdots$ $^{+}_{-}$	$\cdots$	$\cdots$
3349	$0.57^{+0.15}_{-0.15}$	3.33	1.000	8.92	0.08	$0.57^{+0.07}_{-0.08}$	3.33	1.000	$\cdots$ $^{+}_{-}$	$\cdots$	$\cdots$
3351	$2.56^{+0.35}_{-0.35}$	7.67	0.982	0.46	0.35	$2.56^{+0.17}_{-0.53}$	7.67	1.000	$\cdots$ $^{+}_{-}$	$\cdots$	$\cdots$
3354	$2.26^{+0.32}_{-0.32}$	5.67	1.000	5.37	2.28	$2.26^{+0.15}_{-0.13}$	5.67	1.000	$\cdots$ $^{+}_{-}$	$\cdots$	$\cdots$
3357	$0.47^{+0.14}_{-0.14}$	1.00	1.000	1.23	0.13	$0.47^{+0.12}_{-0.08}$	1.00	1.000	$\cdots$ $^{+}_{-}$	$\cdots$	$\cdots$
3372	$0.78^{+0.17}_{-0.17}$	3.33	1.000	25.39	0.74	$0.78^{+0.08}_{-0.08}$	3.33	1.000	$\cdots$ $^{+}_{-}$	$\cdots$	$\cdots$
3373	$0.91^{+0.19}_{-0.19}$	6.33	1.000	8.22	0.50	$0.91^{+0.07}_{-0.07}$	6.33	1.000	$\cdots$ $^{+}_{-}$	$\cdots$	$\cdots$
3376	$0.72^{+0.39}_{-0.17}$	6.33	0.627	2.14	1.64	$0.72^{+0.08}_{-0.08}$	6.33	0.440	$1.05^{+0.12}_{-0.11}$	6.00	0.339
3390	$0.57^{+0.15}_{-0.15}$	3.00	1.000	3.12	0.21	$0.57^{+0.10}_{-0.09}$	3.00	1.000	$\cdots$ $^{+}_{-}$	$\cdots$	$\cdots$

Table C.2—Continued

ID[a]	z_b[b]	t_b[c]	ODDS[d]	χ^2_ν[e]	$\chi^2_{\rm mod}$[f]	z_b1[g]	t_b1[c]	ODDS1[h]	z_b2[g]	t_b2[c]	ODDS2[h]
3416	$3.36^{+0.43}_{-0.43}$	6.33	1.000	11.48	0.21	$3.36^{+0.08}_{-0.08}$	6.33	1.000	$\cdots$ $^{+}_{-}$	$\cdots$	$\cdots$
3418	$3.96^{+0.49}_{-0.49}$	5.67	1.000	0.68	0.73	$3.96^{+0.15}_{-0.13}$	5.67	1.000	$\cdots$ $^{+}_{-}$	$\cdots$	$\cdots$
3424	$0.92^{+0.19}_{-0.19}$	6.00	1.000	5.70	1.03	$0.92^{+0.12}_{-0.09}$	6.00	1.000	$\cdots$ $^{+}_{-}$	$\cdots$	$\cdots$
3425	$2.77^{+0.37}_{-0.37}$	8.00	1.000	3.40	2.72	$2.77^{+0.13}_{-0.17}$	8.00	1.000	$\cdots$ $^{+}_{-}$	$\cdots$	$\cdots$
3436	$0.96^{+0.19}_{-0.25}$	6.67	0.843	0.36	0.21	$0.96^{+0.13}_{-0.08}$	6.67	0.496	$0.78^{+0.10}_{-0.12}$	6.67	0.481
3440	$0.69^{+0.17}_{-0.17}$	5.00	1.000	0.25	0.04	$0.69^{+0.15}_{-0.14}$	5.00	1.000	$\cdots$ $^{+}_{-}$	$\cdots$	$\cdots$
3442	$2.24^{+0.32}_{-0.32}$	6.33	1.000	4.58	1.45	$2.24^{+0.13}_{-0.14}$	6.33	1.000	$\cdots$ $^{+}_{-}$	$\cdots$	$\cdots$
3445	$0.25^{+0.12}_{-0.12}$	3.33	1.000	2.34	0.08	$0.25^{+0.08}_{-0.07}$	3.33	1.000	$\cdots$ $^{+}_{-}$	$\cdots$	$\cdots$
3454	$2.07^{+0.30}_{-0.30}$	2.33	1.000	12.35	3.10	$2.07^{+0.14}_{-0.15}$	2.33	1.000	$\cdots$ $^{+}_{-}$	$\cdots$	$\cdots$
3459	$2.14^{+0.31}_{-0.31}$	6.67	1.000	0.89	0.58	$2.14^{+0.31}_{-0.27}$	6.67	1.000	$\cdots$ $^{+}_{-}$	$\cdots$	$\cdots$
3460	$1.46^{+0.24}_{-0.24}$	6.00	1.000	13.16	0.42	$1.46^{+0.14}_{-0.15}$	6.00	1.000	$\cdots$ $^{+}_{-}$	$\cdots$	$\cdots$
3461	$3.11^{+0.40}_{-0.40}$	3.33	1.000	1.54	0.07	$3.11^{+0.34}_{-0.23}$	3.33	1.000	$\cdots$ $^{+}_{-}$	$\cdots$	$\cdots$
3467	$1.99^{+0.29}_{-0.29}$	5.67	1.000	0.21	0.02	$1.99^{+0.31}_{-0.05}$	5.67	0.620	$1.91^{+0.03}_{-0.22}$	5.67	0.380
3468	$3.01^{+0.39}_{-0.39}$	8.00	1.000	4.57	2.73	$3.01^{+0.13}_{-0.15}$	8.00	1.000	$\cdots$ $^{+}_{-}$	$\cdots$	$\cdots$
3472	$0.88^{+0.18}_{-0.18}$	3.33	1.000	4.61	0.28	$0.88^{+0.12}_{-0.10}$	3.33	1.000	$\cdots$ $^{+}_{-}$	$\cdots$	$\cdots$
3475	$0.22^{+0.12}_{-0.12}$	3.67	1.000	6.55	0.65	$0.22^{+0.08}_{-0.07}$	3.67	1.000	$\cdots$ $^{+}_{-}$	$\cdots$	$\cdots$
3481	$3.00^{+0.39}_{-0.39}$	8.00	1.000	1.23	1.09	$3.00^{+0.16}_{-0.20}$	8.00	0.797	$2.72^{+0.08}_{-0.11}$	7.00	0.203
3483	$2.24^{+0.32}_{-0.32}$	5.33	1.000	6.94	1.25	$2.24^{+0.09}_{-0.10}$	5.33	1.000	$\cdots$ $^{+}_{-}$	$\cdots$	$\cdots$
3484	$0.18^{+0.12}_{-0.12}$	3.33	1.000	2.01	0.03	$0.18^{+0.08}_{-0.07}$	3.33	1.000	$\cdots$ $^{+}_{-}$	$\cdots$	$\cdots$
3492	$0.20^{+0.12}_{-0.12}$	3.33	1.000	11.23	0.31	$0.20^{+0.07}_{-0.08}$	3.33	1.000	$\cdots$ $^{+}_{-}$	$\cdots$	$\cdots$
3504	$0.24^{+0.20}_{-0.12}$	3.00	0.926	2.95	0.16	$0.24^{+0.10}_{-0.15}$	3.00	0.930	$0.42^{+0.08}_{-0.06}$	3.33	0.070
3507	$3.80^{+0.47}_{-0.47}$	5.67	1.000	0.40	0.48	$3.80^{+0.13}_{-0.14}$	5.67	1.000	$\cdots$ $^{+}_{-}$	$\cdots$	$\cdots$
3512	$0.74^{+0.17}_{-0.17}$	3.00	1.000	1.25	0.02	$0.74^{+0.08}_{-0.08}$	3.00	1.000	$\cdots$ $^{+}_{-}$	$\cdots$	$\cdots$
3514	$1.51^{+0.50}_{-1.03}$	7.00	0.715	0.11	0.03	$1.51^{+0.73}_{-0.16}$	7.00	0.886	$0.53^{+0.14}_{-0.14}$	7.33	0.114
3518	$0.61^{+0.16}_{-0.16}$	2.33	1.000	3.75	0.78	$0.61^{+0.10}_{-0.09}$	2.33	1.000	$\cdots$ $^{+}_{-}$	$\cdots$	$\cdots$
3519	$3.33^{+0.42}_{-0.46}$	8.00	0.913	29.46	12.30	$3.33^{+0.14}_{-0.19}$	8.00	0.733	$2.92^{+0.09}_{-0.09}$	7.00	0.267
3521	$3.03^{+0.39}_{-0.39}$	6.33	1.000	2.58	0.43	$3.03^{+0.16}_{-0.17}$	6.33	1.000	$\cdots$ $^{+}_{-}$	$\cdots$	$\cdots$
3523	$1.54^{+0.25}_{-0.25}$	1.33	1.000	20.83	0.28	$1.54^{+0.13}_{-0.14}$	1.33	1.000	$\cdots$ $^{+}_{-}$	$\cdots$	$\cdots$
3527	$2.26^{+0.32}_{-0.32}$	6.33	0.999	2.27	1.64	$2.26^{+0.18}_{-0.19}$	6.33	0.926	$2.04^{+0.03}_{-0.11}$	6.00	0.074
3547	$3.18^{+0.41}_{-0.41}$	7.33	1.000	1.17	0.64	$3.18^{+0.20}_{-0.10}$	7.33	0.571	$3.00^{+0.08}_{-0.19}$	7.00	0.429
3567	$2.95^{+0.39}_{-0.39}$	6.33	1.000	1.03	0.73	$2.95^{+0.23}_{-0.18}$	6.33	1.000	$\cdots$ $^{+}_{-}$	$\cdots$	$\cdots$
3569	$0.60^{+0.16}_{-0.16}$	4.00	1.000	0.98	0.20	$0.60^{+0.10}_{-0.11}$	4.00	1.000	$\cdots$ $^{+}_{-}$	$\cdots$	$\cdots$
3573	$0.42^{+0.14}_{-0.14}$	1.00	1.000	3.65	1.99	$0.42^{+0.15}_{-0.09}$	1.00	1.000	$\cdots$ $^{+}_{-}$	$\cdots$	$\cdots$
3574	$1.79^{+0.27}_{-0.27}$	1.33	1.000	8.78	0.13	$1.79^{+0.14}_{-0.15}$	1.33	1.000	$\cdots$ $^{+}_{-}$	$\cdots$	$\cdots$
3581	$1.88^{+0.28}_{-0.28}$	6.33	1.000	4.08	0.44	$1.88^{+0.14}_{-0.11}$	6.33	1.000	$\cdots$ $^{+}_{-}$	$\cdots$	$\cdots$
3583	$2.08^{+0.30}_{-0.30}$	5.67	1.000	1.49	1.44	$2.08^{+0.25}_{-0.31}$	5.67	1.000	$\cdots$ $^{+}_{-}$	$\cdots$	$\cdots$

Table C.2—Continued

ID[a]	z_b[b]	t_b[c]	ODDS[d]	χ^2_ν[e]	$\chi^2_{\rm mod}$[f]	z_b1[g]	t_b1[c]	ODDS1[h]	z_b2[g]	t_b2[c]	ODDS2[h]
3584	$0.46^{+0.14}_{-0.30}$	4.00	0.829	6.38	3.88	$0.46^{+0.11}_{-0.10}$	4.00	0.829	$0.20^{+0.12}_{-0.08}$	3.00	0.171
3591	$4.12^{+0.50}_{-0.50}$	6.33	1.000	0.49	0.21	$4.12^{+0.12}_{-0.16}$	6.33	1.000	··· + −	···	···
3595	$0.18^{+3.26}_{-0.12}$	3.00	0.532	2.11	0.63	$0.18^{+0.14}_{-0.14}$	3.00	0.534	$3.36^{+0.16}_{-0.20}$	4.67	0.466
3602	$1.44^{+0.24}_{-0.30}$	6.00	0.902	0.10	0.07	$1.44^{+0.22}_{-0.12}$	6.00	0.660	$1.24^{+0.08}_{-0.25}$	6.33	0.340
3605	$2.76^{+0.37}_{-0.37}$	6.00	1.000	1.77	0.16	$2.76^{+0.12}_{-0.14}$	6.00	1.000	··· + −	···	···
3608	$0.86^{+0.35}_{-0.18}$	6.33	0.634	1.19	0.70	$0.86^{+0.16}_{-0.19}$	6.33	0.625	$1.16^{+0.11}_{-0.14}$	6.00	0.375
3610	$0.17^{+0.11}_{-0.12}$	3.00	1.000	10.02	0.13	$0.17^{+0.08}_{-0.09}$	3.00	1.000	··· + −	···	···
3613	$1.06^{+0.20}_{-0.20}$	3.00	1.000	16.90	0.29	$1.06^{+0.08}_{-0.08}$	3.00	1.000	··· + −	···	···
3650	$1.61^{+0.26}_{-0.26}$	1.33	1.000	28.04	0.70	$1.61^{+0.11}_{-0.13}$	1.33	1.000	··· + −	···	···
3655	$1.42^{+0.24}_{-0.24}$	4.00	1.000	7.90	3.15	$1.42^{+0.10}_{-0.16}$	4.00	1.000	··· + −	···	···
3677	$0.59^{+0.16}_{-0.16}$	1.00	1.000	27.36	1.32	$0.59^{+0.07}_{-0.08}$	1.00	1.000	··· + −	···	···
3680	$0.14^{+0.11}_{-0.11}$	3.33	0.993	1.82	0.28	$0.14^{+0.04}_{-0.10}$	3.33	0.600	$0.21^{+0.08}_{-0.03}$	3.67	0.400
3682	$0.90^{+0.19}_{-0.19}$	6.33	0.990	4.68	0.50	$0.90^{+0.12}_{-0.08}$	6.33	0.990	$1.17^{+0.03}_{-0.04}$	6.00	0.010
3688	$0.62^{+0.16}_{-0.16}$	4.33	1.000	5.67	0.12	$0.62^{+0.09}_{-0.09}$	4.33	1.000	··· + −	···	···
3689	$1.51^{+0.25}_{-0.26}$	6.00	0.959	2.52	0.25	$1.51^{+0.11}_{-0.16}$	6.00	0.712	$1.30^{+0.05}_{-0.10}$	6.33	0.288
3690	$2.35^{+0.33}_{-0.33}$	7.00	0.972	1.86	1.38	$2.35^{+0.40}_{-0.46}$	7.00	1.000	··· + −	···	···
3693	$3.16^{+0.41}_{-0.41}$	8.00	1.000	1.05	0.58	$3.16^{+0.15}_{-0.25}$	8.00	0.990	$2.86^{+0.05}_{-0.06}$	7.00	0.010
3701	$2.24^{+0.32}_{-0.32}$	6.67	0.981	0.16	0.04	$2.24^{+0.21}_{-0.35}$	6.67	0.984	$0.10^{+0.06}_{-0.06}$	7.00	0.016
3745	$1.58^{+0.25}_{-0.25}$	4.00	1.000	8.54	0.09	$1.58^{+0.09}_{-0.08}$	4.00	1.000	··· + −	···	···
3752	$2.17^{+0.31}_{-0.31}$	5.00	1.000	8.75	0.98	$2.17^{+0.10}_{-0.09}$	5.00	1.000	··· + −	···	···
3772	$3.19^{+0.41}_{-3.16}$	5.00	0.827	5.97	2.17	$3.19^{+0.17}_{-0.17}$	5.00	0.827	$0.07^{+0.11}_{-0.06}$	3.00	0.173
3777	$1.43^{+0.24}_{-0.24}$	4.33	1.000	2.32	0.49	$1.43^{+0.12}_{-0.16}$	4.33	1.000	··· + −	···	···
3778	$3.78^{+0.47}_{-0.47}$	3.67	1.000	1.19	0.41	$3.78^{+0.17}_{-0.19}$	3.67	1.000	··· + −	···	···
3785	$0.55^{+0.15}_{-0.15}$	3.00	1.000	2.81	0.04	$0.55^{+0.08}_{-0.08}$	3.00	1.000	··· + −	···	···
3799	$1.46^{+0.24}_{-0.24}$	4.00	1.000	5.78	0.37	$1.46^{+0.14}_{-0.09}$	4.00	1.000	··· + −	···	···
3802	$1.39^{+0.23}_{-0.23}$	3.67	1.000	7.86	1.12	$1.39^{+0.10}_{-0.19}$	3.67	1.000	··· + −	···	···
3804	$0.16^{+0.28}_{-0.11}$	4.67	0.872	0.31	0.18	$0.16^{+0.18}_{-0.13}$	4.67	0.898	$0.42^{+0.07}_{-0.07}$	5.67	0.102
3819	$1.63^{+0.26}_{-0.29}$	6.33	0.965	4.83	0.76	$1.63^{+0.15}_{-0.12}$	6.33	0.957	$1.35^{+0.06}_{-0.07}$	6.67	0.043
3822	$0.18^{+0.12}_{-0.12}$	2.33	1.000	2.45	0.59	$0.18^{+0.08}_{-0.07}$	2.33	1.000	··· + −	···	···
3823	$1.50^{+0.25}_{-0.25}$	4.33	1.000	5.20	1.01	$1.50^{+0.11}_{-0.09}$	4.33	1.000	··· + −	···	···
3838	$2.34^{+0.33}_{-0.40}$	6.67	0.937	0.09	0.07	$2.34^{+0.25}_{-0.54}$	6.67	0.997	$0.05^{+0.04}_{-0.04}$	6.67	0.003
3840	$2.84^{+0.44}_{-2.71}$	3.33	0.896	7.09	0.16	$2.84^{+0.24}_{-0.16}$	3.33	0.828	$3.23^{+0.15}_{-0.15}$	5.00	0.140
3844	$2.60^{+0.35}_{-0.35}$	5.00	1.000	9.03	1.36	$2.60^{+0.09}_{-0.08}$	5.00	1.000	··· + −	···	···
3869	$0.20^{+0.12}_{-0.12}$	3.00	1.000	0.18	0.00	$0.20^{+0.07}_{-0.08}$	3.00	1.000	··· + −	···	···
3871	$0.64^{+0.16}_{-0.16}$	4.33	1.000	3.82	0.67	$0.64^{+0.08}_{-0.09}$	4.33	1.000	··· + −	···	···
3878	$1.40^{+0.24}_{-0.24}$	3.67	1.000	6.24	0.66	$1.40^{+0.16}_{-0.18}$	3.67	1.000	··· + −	···	···

Table C.2—Continued

ID[a]	z_b[b]	t_b[c]	ODDS[d]	χ^2_ν[e]	$\chi^2_{\rm mod}$[f]	z_b1[g]	t_b1[c]	ODDS1[h]	z_b2[g]	t_b2[c]	ODDS2[h]
3881	$0.01^{+0.10}_{-0.01}$	4.67	1.000	25.95	9.04	$0.01^{+0.10}_{-0.01}$	4.67	1.000	$\cdots$ $^{+}_{-}$	$\cdots$	$\cdots$
3893	$1.45^{+0.24}_{-0.24}$	4.00	1.000	1.78	0.81	$1.45^{+0.10}_{-0.11}$	4.00	1.000	$\cdots$ $^{+}_{-}$	$\cdots$	$\cdots$
3895	$1.66^{+0.26}_{-0.26}$	6.00	1.000	2.77	0.20	$1.66^{+0.10}_{-0.09}$	6.00	1.000	$\cdots$ $^{+}_{-}$	$\cdots$	$\cdots$
3915	$1.73^{+0.49}_{-0.27}$	4.00	0.877	4.09	0.04	$1.73^{+0.10}_{-0.10}$	4.00	0.877	$2.19^{+0.08}_{-0.12}$	5.33	0.118
3922	$3.43^{+0.43}_{-0.43}$	6.67	1.000	0.28	0.05	$3.43^{+0.11}_{-0.11}$	6.67	1.000	$\cdots$ $^{+}_{-}$	$\cdots$	$\cdots$
3933	$1.28^{+0.22}_{-0.22}$	4.33	1.000	0.90	0.38	$1.28^{+0.12}_{-0.11}$	4.33	1.000	$\cdots$ $^{+}_{-}$	$\cdots$	$\cdots$
3936	$2.51^{+0.34}_{-0.34}$	6.67	1.000	3.01	0.56	$2.51^{+0.16}_{-0.18}$	6.67	1.000	$\cdots$ $^{+}_{-}$	$\cdots$	$\cdots$
3938	$1.27^{+0.32}_{-0.22}$	6.67	0.664	3.73	1.87	$1.27^{+0.10}_{-0.11}$	6.67	0.587	$1.54^{+0.10}_{-0.13}$	6.33	0.413
3939	$2.53^{+0.35}_{-0.35}$	5.67	1.000	12.85	0.57	$2.53^{+0.15}_{-0.13}$	5.67	1.000	$\cdots$ $^{+}_{-}$	$\cdots$	$\cdots$
3940	$0.02^{+0.10}_{-0.02}$	7.67	1.000	14.76	10.59	$0.02^{+0.09}_{-0.01}$	7.67	1.000	$\cdots$ $^{+}_{-}$	$\cdots$	$\cdots$
3967	$2.76^{+0.37}_{-2.63}$	3.67	0.876	0.10	0.03	$2.76^{+0.31}_{-0.34}$	3.67	0.876	$0.21^{+0.12}_{-0.19}$	3.67	0.124
3977	$0.87^{+0.18}_{-0.18}$	5.67	1.000	9.35	0.28	$0.87^{+0.08}_{-0.09}$	5.67	1.000	$\cdots$ $^{+}_{-}$	$\cdots$	$\cdots$
3985	$2.27^{+0.32}_{-0.32}$	5.67	1.000	2.11	0.84	$2.27^{+0.13}_{-0.12}$	5.67	1.000	$\cdots$ $^{+}_{-}$	$\cdots$	$\cdots$
4000	$2.78^{+0.37}_{-0.37}$	6.33	1.000	3.09	0.47	$2.78^{+0.11}_{-0.10}$	6.33	1.000	$\cdots$ $^{+}_{-}$	$\cdots$	$\cdots$
4010	$3.43^{+0.43}_{-0.43}$	4.33	1.000	2.83	0.23	$3.43^{+0.12}_{-0.21}$	4.33	1.000	$\cdots$ $^{+}_{-}$	$\cdots$	$\cdots$
4015	$1.96^{+0.38}_{-1.88}$	6.67	0.836	0.84	0.87	$1.96^{+0.21}_{-0.33}$	6.67	0.699	$2.24^{+0.25}_{-0.07}$	7.00	0.242
4027	$1.37^{+0.23}_{-0.23}$	6.00	1.000	3.26	0.33	$1.37^{+0.18}_{-0.10}$	6.00	1.000	$\cdots$ $^{+}_{-}$	$\cdots$	$\cdots$
4036	$0.04^{+0.10}_{-0.04}$	3.33	0.996	1.61	0.32	$0.04^{+0.14}_{-0.03}$	3.33	1.000	$\cdots$ $^{+}_{-}$	$\cdots$	$\cdots$
4037	$2.83^{+0.38}_{-0.38}$	7.67	1.000	3.22	2.90	$2.83^{+0.28}_{-0.27}$	7.67	1.000	$\cdots$ $^{+}_{-}$	$\cdots$	$\cdots$
4040	$3.05^{+0.40}_{-0.40}$	6.00	1.000	0.63	0.24	$3.05^{+0.09}_{-0.09}$	6.00	1.000	$\cdots$ $^{+}_{-}$	$\cdots$	$\cdots$
4052	$0.87^{+0.19}_{-0.18}$	5.33	0.978	5.42	0.58	$0.87^{+0.12}_{-0.05}$	5.33	0.599	$0.78^{+0.04}_{-0.09}$	5.67	0.337
4058	$2.50^{+0.34}_{-0.34}$	6.67	1.000	1.55	0.12	$2.50^{+0.10}_{-0.10}$	6.67	1.000	$\cdots$ $^{+}_{-}$	$\cdots$	$\cdots$
4061	$3.00^{+0.39}_{-0.39}$	6.67	1.000	7.88	0.86	$3.00^{+0.08}_{-0.09}$	6.67	0.871	$3.14^{+0.09}_{-0.06}$	7.33	0.129
4062	$3.50^{+0.44}_{-0.44}$	6.33	1.000	0.27	0.04	$3.50^{+0.13}_{-0.15}$	6.33	1.000	$\cdots$ $^{+}_{-}$	$\cdots$	$\cdots$
4065	$2.24^{+0.32}_{-0.32}$	6.00	0.989	1.74	0.55	$2.24^{+0.14}_{-0.27}$	6.00	0.730	$2.47^{+0.15}_{-0.09}$	6.33	0.270
4069	$2.02^{+0.30}_{-0.30}$	6.33	1.000	4.54	0.84	$2.02^{+0.25}_{-0.30}$	6.33	1.000	$\cdots$ $^{+}_{-}$	$\cdots$	$\cdots$
4070	$2.58^{+0.35}_{-0.35}$	7.00	1.000	4.39	3.50	$2.58^{+0.09}_{-0.08}$	7.00	0.990	$2.69^{+0.03}_{-0.02}$	7.33	0.010
4084	$1.41^{+0.24}_{-0.24}$	3.33	1.000	7.79	0.02	$1.41^{+0.07}_{-0.08}$	3.33	1.000	$\cdots$ $^{+}_{-}$	$\cdots$	$\cdots$
4087	$2.24^{+0.32}_{-0.32}$	6.33	1.000	2.24	0.68	$2.24^{+0.14}_{-0.23}$	6.33	0.820	$2.44^{+0.12}_{-0.06}$	6.67	0.180
4092	$2.30^{+0.32}_{-0.32}$	5.67	1.000	6.60	1.49	$2.30^{+0.14}_{-0.15}$	5.67	1.000	$\cdots$ $^{+}_{-}$	$\cdots$	$\cdots$
4094	$0.54^{+0.15}_{-0.15}$	5.33	0.998	2.83	1.06	$0.54^{+0.09}_{-0.09}$	5.33	0.913	$0.66^{+0.06}_{-0.03}$	5.67	0.087
4096	$0.55^{+0.15}_{-0.15}$	2.67	1.000	12.84	0.06	$0.55^{+0.08}_{-0.07}$	2.67	1.000	$\cdots$ $^{+}_{-}$	$\cdots$	$\cdots$
4100	$1.65^{+0.26}_{-1.15}$	6.67	0.835	0.38	0.29	$1.65^{+0.39}_{-0.36}$	6.67	0.877	$0.57^{+0.19}_{-0.20}$	7.33	0.112
4126	$0.65^{+0.16}_{-0.16}$	4.33	0.999	10.14	2.65	$0.65^{+0.09}_{-0.18}$	4.33	1.000	$\cdots$ $^{+}_{-}$	$\cdots$	$\cdots$
4136	$0.60^{+0.16}_{-0.16}$	2.00	1.000	1.91	0.58	$0.60^{+0.08}_{-0.10}$	2.00	1.000	$\cdots$ $^{+}_{-}$	$\cdots$	$\cdots$
4137	$2.50^{+0.34}_{-0.34}$	8.00	1.000	10.21	6.33	$2.50^{+0.12}_{-0.13}$	8.00	1.000	$\cdots$ $^{+}_{-}$	$\cdots$	$\cdots$

Table C.2—Continued

ID[a]	z_b[b]	t_b[c]	ODDS[d]	χ^2_ν[e]	$\chi^2_{\rm mod}$[f]	z_b1[g]	t_b1[c]	ODDS1[h]	z_b2[g]	t_b2[c]	ODDS2[h]
4142	$0.65^{+0.16}_{-0.16}$	3.67	1.000	30.46	0.33	$0.65^{+0.08}_{-0.08}$	3.67	1.000	$\cdots$ $^{+}_{-}$	$\cdots$	$\cdots$
4148	$1.06^{+0.20}_{-0.20}$	5.33	1.000	3.03	0.25	$1.06^{+0.18}_{-0.13}$	5.33	1.000	$\cdots$ $^{+}_{-}$	$\cdots$	$\cdots$
4159	$2.19^{+0.31}_{-0.31}$	6.33	1.000	0.51	0.11	$2.19^{+0.26}_{-0.26}$	6.33	1.000	$\cdots$ $^{+}_{-}$	$\cdots$	$\cdots$
4172	$1.49^{+0.24}_{-0.24}$	4.00	1.000	6.51	0.06	$1.49^{+0.08}_{-0.08}$	4.00	1.000	$\cdots$ $^{+}_{-}$	$\cdots$	$\cdots$
4177	$2.80^{+0.37}_{-0.37}$	7.00	1.000	8.07	6.51	$2.80^{+0.12}_{-0.11}$	7.00	0.917	$3.02^{+0.11}_{-0.10}$	7.67	0.083
4178	$2.89^{+0.38}_{-0.38}$	8.00	1.000	3.34	3.30	$2.89^{+0.21}_{-0.28}$	8.00	1.000	$\cdots$ $^{+}_{-}$	$\cdots$	$\cdots$
4183	$2.38^{+0.33}_{-0.33}$	6.67	0.982	7.39	5.25	$2.38^{+0.22}_{-0.42}$	6.67	1.000	$\cdots$ $^{+}_{-}$	$\cdots$	$\cdots$
4184	$2.93^{+0.38}_{-0.38}$	6.00	1.000	0.32	0.31	$2.93^{+0.29}_{-0.15}$	6.00	1.000	$\cdots$ $^{+}_{-}$	$\cdots$	$\cdots$
4188	$0.68^{+0.17}_{-0.17}$	6.00	0.996	1.79	1.17	$0.68^{+0.08}_{-0.19}$	6.00	1.000	$\cdots$ $^{+}_{-}$	$\cdots$	$\cdots$
4193	$2.57^{+0.35}_{-0.35}$	6.33	1.000	1.56	0.11	$2.57^{+0.13}_{-0.14}$	6.33	0.888	$2.35^{+0.08}_{-0.11}$	6.00	0.112
4202	$0.49^{+0.15}_{-0.27}$	2.33	0.490	7.26	0.56	$0.49^{+0.11}_{-0.09}$	2.33	0.469	$0.27^{+0.13}_{-0.10}$	1.33	0.511
4216	$1.21^{+0.22}_{-0.22}$	4.00	1.000	1.94	0.99	$1.21^{+0.11}_{-0.16}$	4.00	1.000	$\cdots$ $^{+}_{-}$	$\cdots$	$\cdots$
4225	$3.53^{+0.44}_{-0.44}$	5.00	1.000	3.15	3.23	$3.53^{+0.13}_{-0.12}$	5.00	1.000	$\cdots$ $^{+}_{-}$	$\cdots$	$\cdots$
4228	$2.70^{+0.36}_{-0.36}$	3.33	1.000	1.84	0.01	$2.70^{+0.16}_{-0.08}$	3.33	1.000	$\cdots$ $^{+}_{-}$	$\cdots$	$\cdots$
4243	$2.00^{+0.29}_{-0.29}$	6.33	1.000	6.24	0.90	$2.00^{+0.11}_{-0.09}$	6.33	0.739	$1.85^{+0.06}_{-0.10}$	6.33	0.237
4245	$1.26^{+0.22}_{-0.22}$	5.33	1.000	1.78	0.04	$1.26^{+0.09}_{-0.10}$	5.33	1.000	$\cdots$ $^{+}_{-}$	$\cdots$	$\cdots$
4253	$0.91^{+0.19}_{-0.19}$	6.00	1.000	15.24	1.00	$0.91^{+0.12}_{-0.10}$	6.00	1.000	$\cdots$ $^{+}_{-}$	$\cdots$	$\cdots$
4254	$3.51^{+0.44}_{-0.44}$	5.33	1.000	3.47	2.21	$3.51^{+0.16}_{-0.20}$	5.33	1.000	$\cdots$ $^{+}_{-}$	$\cdots$	$\cdots$
4258	$0.15^{+0.26}_{-0.11}$	4.33	0.916	1.35	0.19	$0.15^{+0.08}_{-0.10}$	4.33	0.858	$0.27^{+0.05}_{-0.04}$	5.67	0.084
4262	$0.15^{+0.11}_{-0.11}$	3.33	1.000	4.96	0.06	$0.15^{+0.07}_{-0.07}$	3.33	1.000	$\cdots$ $^{+}_{-}$	$\cdots$	$\cdots$
4267	$0.24^{+0.12}_{-0.12}$	4.00	1.000	14.81	0.60	$0.24^{+0.09}_{-0.08}$	4.00	1.000	$\cdots$ $^{+}_{-}$	$\cdots$	$\cdots$
4268	$1.92^{+0.29}_{-0.29}$	6.67	0.998	0.58	0.20	$1.92^{+0.33}_{-0.30}$	6.67	1.000	$\cdots$ $^{+}_{-}$	$\cdots$	$\cdots$
4276	$2.68^{+0.36}_{-0.36}$	6.33	1.000	3.05	0.38	$2.68^{+0.14}_{-0.12}$	6.33	1.000	$\cdots$ $^{+}_{-}$	$\cdots$	$\cdots$
4280	$1.83^{+0.37}_{-0.28}$	6.00	0.850	1.21	0.73	$1.83^{+0.10}_{-0.22}$	6.00	0.451	$2.01^{+0.08}_{-0.08}$	6.00	0.346
4287	$0.98^{+0.26}_{-0.19}$	6.33	0.820	9.05	0.88	$0.98^{+0.13}_{-0.15}$	6.33	0.787	$1.21^{+0.08}_{-0.07}$	6.00	0.213
4289	$2.25^{+0.32}_{-0.32}$	6.33	1.000	0.76	0.39	$2.25^{+0.28}_{-0.31}$	6.33	1.000	$\cdots$ $^{+}_{-}$	$\cdots$	$\cdots$
4301	$1.35^{+0.23}_{-0.23}$	6.00	1.000	1.29	0.37	$1.35^{+0.16}_{-0.12}$	6.00	1.000	$\cdots$ $^{+}_{-}$	$\cdots$	$\cdots$
4302	$3.47^{+0.44}_{-0.44}$	8.00	1.000	5.57	1.37	$3.47^{+0.11}_{-0.11}$	8.00	1.000	$\cdots$ $^{+}_{-}$	$\cdots$	$\cdots$
4315	$0.18^{+0.12}_{-0.12}$	5.67	1.000	11.21	0.41	$0.18^{+0.08}_{-0.07}$	5.67	1.000	$\cdots$ $^{+}_{-}$	$\cdots$	$\cdots$
4316	$3.41^{+0.43}_{-0.43}$	5.33	1.000	0.17	0.08	$3.41^{+0.08}_{-0.09}$	5.33	1.000	$\cdots$ $^{+}_{-}$	$\cdots$	$\cdots$
4320	$0.39^{+0.14}_{-0.14}$	1.00	1.000	23.62	0.12	$0.39^{+0.08}_{-0.08}$	1.00	1.000	$\cdots$ $^{+}_{-}$	$\cdots$	$\cdots$
4321	$1.04^{+0.20}_{-0.20}$	5.67	1.000	3.17	0.20	$1.04^{+0.12}_{-0.10}$	5.67	0.987	$0.87^{+0.04}_{-0.03}$	6.00	0.013
4322	$2.53^{+0.35}_{-0.35}$	7.00	1.000	4.36	2.78	$2.53^{+0.11}_{-0.11}$	7.00	1.000	$\cdots$ $^{+}_{-}$	$\cdots$	$\cdots$
4338	$2.60^{+0.35}_{-0.35}$	6.67	1.000	1.34	0.48	$2.60^{+0.22}_{-0.19}$	6.67	1.000	$\cdots$ $^{+}_{-}$	$\cdots$	$\cdots$
4348	$2.37^{+0.33}_{-0.33}$	2.67	1.000	19.07	0.74	$2.37^{+0.31}_{-0.26}$	2.67	1.000	$\cdots$ $^{+}_{-}$	$\cdots$	$\cdots$
4349	$2.78^{+0.37}_{-0.37}$	6.67	0.994	2.23	1.00	$2.78^{+0.16}_{-0.17}$	6.67	0.887	$3.04^{+0.18}_{-0.10}$	7.33	0.113

Table C.2—Continued

ID[a]	z_b[b]	t_b[c]	ODDS[d]	χ^2_ν[e]	$\chi^2_{\rm mod}$[f]	z_b1[g]	t_b1[c]	ODDS1[h]	z_b2[g]	t_b2[c]	ODDS2[h]
4350	$0.22^{+0.12}_{-0.12}$	3.00	1.000	0.77	0.19	$0.22^{+0.08}_{-0.08}$	3.00	1.000	$\cdots$ $^{+}_{-}$	$\cdots$	$\cdots$
4360	$0.44^{+0.14}_{-0.14}$	3.00	1.000	4.73	0.05	$0.44^{+0.07}_{-0.08}$	3.00	1.000	$\cdots$ $^{+}_{-}$	$\cdots$	$\cdots$
4361	$2.54^{+0.35}_{-0.35}$	7.00	1.000	3.35	1.82	$2.54^{+0.13}_{-0.10}$	7.00	1.000	$\cdots$ $^{+}_{-}$	$\cdots$	$\cdots$
4368	$0.52^{+0.15}_{-0.15}$	3.33	0.999	6.97	0.48	$0.52^{+0.11}_{-0.16}$	3.33	1.000	$\cdots$ $^{+}_{-}$	$\cdots$	$\cdots$
4369	$3.11^{+0.40}_{-0.40}$	6.00	1.000	0.74	0.32	$3.11^{+0.16}_{-0.14}$	6.00	1.000	$\cdots$ $^{+}_{-}$	$\cdots$	$\cdots$
4371	$0.70^{+0.17}_{-0.17}$	6.00	1.000	3.76	0.31	$0.70^{+0.07}_{-0.07}$	6.00	1.000	$\cdots$ $^{+}_{-}$	$\cdots$	$\cdots$
4373	$3.18^{+0.41}_{-0.41}$	6.33	1.000	0.45	0.13	$3.18^{+0.09}_{-0.10}$	6.33	1.000	$\cdots$ $^{+}_{-}$	$\cdots$	$\cdots$
4376	$3.52^{+0.44}_{-3.45}$	4.00	0.970	4.68	2.98	$3.52^{+0.19}_{-0.13}$	4.00	0.970	$0.05^{+0.06}_{-0.04}$	1.00	0.030
4379	$3.01^{+0.39}_{-0.39}$	6.00	1.000	0.60	0.30	$3.01^{+0.21}_{-0.18}$	6.00	1.000	$\cdots$ $^{+}_{-}$	$\cdots$	$\cdots$
4389	$0.55^{+0.15}_{-0.15}$	3.33	1.000	28.76	0.21	$0.55^{+0.08}_{-0.07}$	3.33	1.000	$\cdots$ $^{+}_{-}$	$\cdots$	$\cdots$
4390	$2.15^{+0.31}_{-0.31}$	5.00	1.000	3.09	0.03	$2.15^{+0.10}_{-0.13}$	5.00	1.000	$\cdots$ $^{+}_{-}$	$\cdots$	$\cdots$
4394	$0.51^{+0.15}_{-0.15}$	3.67	1.000	53.40	0.35	$0.51^{+0.08}_{-0.08}$	3.67	1.000	$\cdots$ $^{+}_{-}$	$\cdots$	$\cdots$
4396	$1.26^{+0.22}_{-0.22}$	2.00	1.000	11.91	0.11	$1.26^{+0.08}_{-0.08}$	2.00	1.000	$\cdots$ $^{+}_{-}$	$\cdots$	$\cdots$
4404	$2.60^{+0.35}_{-0.35}$	7.00	1.000	4.50	3.24	$2.60^{+0.08}_{-0.08}$	7.00	1.000	$\cdots$ $^{+}_{-}$	$\cdots$	$\cdots$
4407	$1.16^{+0.21}_{-0.21}$	2.67	1.000	3.06	0.06	$1.16^{+0.11}_{-0.09}$	2.67	1.000	$\cdots$ $^{+}_{-}$	$\cdots$	$\cdots$
4410	$0.29^{+0.13}_{-0.13}$	6.00	0.989	11.05	0.38	$0.29^{+0.06}_{-0.07}$	6.00	0.816	$0.39^{+0.06}_{-0.04}$	5.67	0.184
4411	$3.40^{+0.43}_{-0.43}$	8.00	1.000	1.12	0.42	$3.40^{+0.12}_{-0.20}$	8.00	0.991	$3.16^{+0.04}_{-0.04}$	7.00	0.009
4438	$0.78^{+0.17}_{-0.17}$	3.67	1.000	20.00	0.93	$0.78^{+0.08}_{-0.07}$	3.67	1.000	$\cdots$ $^{+}_{-}$	$\cdots$	$\cdots$
4445	$0.09^{+0.11}_{-0.09}$	5.00	1.000	32.16	2.89	$0.09^{+0.07}_{-0.07}$	5.00	1.000	$\cdots$ $^{+}_{-}$	$\cdots$	$\cdots$
4461	$2.64^{+0.36}_{-0.36}$	5.67	1.000	7.88	0.30	$2.64^{+0.08}_{-0.09}$	5.67	1.000	$\cdots$ $^{+}_{-}$	$\cdots$	$\cdots$
4479	$2.45^{+0.34}_{-0.34}$	7.00	1.000	2.91	2.53	$2.45^{+0.19}_{-0.13}$	7.00	1.000	$\cdots$ $^{+}_{-}$	$\cdots$	$\cdots$
4481	$1.51^{+0.25}_{-0.25}$	4.00	1.000	11.13	3.36	$1.51^{+0.08}_{-0.08}$	4.00	0.919	$1.37^{+0.05}_{-0.06}$	5.33	0.081
4491	$0.74^{+0.17}_{-0.17}$	6.00	1.000	13.74	2.68	$0.74^{+0.12}_{-0.08}$	6.00	1.000	$\cdots$ $^{+}_{-}$	$\cdots$	$\cdots$
4492	$3.04^{+0.40}_{-0.40}$	6.33	1.000	2.94	1.34	$3.04^{+0.14}_{-0.16}$	6.33	1.000	$\cdots$ $^{+}_{-}$	$\cdots$	$\cdots$
4496	$0.76^{+0.17}_{-0.17}$	6.33	1.000	4.54	1.50	$0.76^{+0.09}_{-0.08}$	6.33	1.000	$\cdots$ $^{+}_{-}$	$\cdots$	$\cdots$
4502	$0.69^{+0.17}_{-0.17}$	6.00	1.000	3.01	0.68	$0.69^{+0.07}_{-0.08}$	6.00	1.000	$\cdots$ $^{+}_{-}$	$\cdots$	$\cdots$
4527	$0.56^{+0.15}_{-0.15}$	1.00	1.000	33.61	0.68	$0.56^{+0.07}_{-0.08}$	1.00	1.000	$\cdots$ $^{+}_{-}$	$\cdots$	$\cdots$
4532	$0.23^{+2.85}_{-0.12}$	6.00	0.458	4.32	0.61	$0.23^{+0.08}_{-0.08}$	6.00	0.459	$2.94^{+0.23}_{-0.13}$	6.00	0.541
4545	$1.49^{+0.24}_{-0.24}$	4.00	1.000	3.87	0.93	$1.49^{+0.17}_{-0.20}$	4.00	1.000	$\cdots$ $^{+}_{-}$	$\cdots$	$\cdots$
4547	$3.08^{+0.40}_{-0.40}$	6.00	1.000	1.19	0.40	$3.08^{+0.12}_{-0.12}$	6.00	1.000	$\cdots$ $^{+}_{-}$	$\cdots$	$\cdots$
4563	$2.32^{+0.33}_{-0.32}$	6.33	1.000	0.37	0.02	$2.32^{+0.16}_{-0.12}$	6.33	1.000	$\cdots$ $^{+}_{-}$	$\cdots$	$\cdots$
4578	$1.62^{+0.26}_{-0.26}$	5.67	0.994	2.13	0.47	$1.62^{+0.20}_{-0.25}$	5.67	0.994	$1.26^{+0.04}_{-0.05}$	6.33	0.006
4587	$0.65^{+0.16}_{-0.16}$	1.33	1.000	33.79	0.56	$0.65^{+0.07}_{-0.08}$	1.33	1.000	$\cdots$ $^{+}_{-}$	$\cdots$	$\cdots$
4591	$0.88^{+0.18}_{-0.18}$	4.33	1.000	8.43	0.42	$0.88^{+0.08}_{-0.09}$	4.33	1.000	$\cdots$ $^{+}_{-}$	$\cdots$	$\cdots$
4592	$2.70^{+0.36}_{-0.36}$	6.67	1.000	5.74	5.14	$2.70^{+0.14}_{-0.18}$	6.67	1.000	$\cdots$ $^{+}_{-}$	$\cdots$	$\cdots$
4601	$0.81^{+0.18}_{-0.18}$	6.67	0.984	3.91	2.40	$0.81^{+0.24}_{-0.15}$	6.67	0.992	$1.10^{+0.05}_{-0.05}$	6.33	0.008

Table C.2—Continued

ID[a]	z_b[b]	t_b[c]	ODDS[d]	χ^2_ν[e]	$\chi^2_{\rm mod}$[f]	z_b1[g]	t_b1[c]	ODDS1[h]	z_b2[g]	t_b2[c]	ODDS2[h]
4603	$2.67^{+0.36}_{-0.59}$	6.33	0.952	10.43	10.76	$2.67^{+0.15}_{-0.23}$	6.33	0.952	$2.09^{+0.12}_{-0.12}$	4.00	0.048
4607	$3.53^{+0.44}_{-0.44}$	6.33	1.000	3.51	2.92	$3.53^{+0.13}_{-0.15}$	6.33	1.000	$\cdots\ ^{+}_{-}$	$\cdots$	$\cdots$
4611	$1.14^{+0.21}_{-0.21}$	5.33	1.000	2.15	0.28	$1.14^{+0.15}_{-0.14}$	5.33	1.000	$\cdots\ ^{+}_{-}$	$\cdots$	$\cdots$
4616	$1.47^{+0.24}_{-0.24}$	2.00	1.000	8.98	0.25	$1.47^{+0.09}_{-0.10}$	2.00	1.000	$\cdots\ ^{+}_{-}$	$\cdots$	$\cdots$
4620	$3.06^{+0.40}_{-0.40}$	6.33	1.000	0.58	0.38	$3.06^{+0.19}_{-0.20}$	6.33	1.000	$\cdots\ ^{+}_{-}$	$\cdots$	$\cdots$
4626	$3.31^{+0.42}_{-0.42}$	6.33	1.000	0.97	0.60	$3.31^{+0.12}_{-0.16}$	6.33	1.000	$\cdots\ ^{+}_{-}$	$\cdots$	$\cdots$
4636	$2.88^{+0.38}_{-0.38}$	7.33	1.000	1.14	1.15	$2.88^{+0.04}_{-0.10}$	7.33	0.467	$2.93^{+0.19}_{-0.01}$	7.67	0.498
4638	$1.32^{+0.23}_{-0.23}$	6.00	1.000	1.72	0.44	$1.32^{+0.12}_{-0.08}$	6.00	1.000	$\cdots\ ^{+}_{-}$	$\cdots$	$\cdots$
4641	$2.23^{+0.32}_{-0.34}$	6.33	0.971	0.16	0.03	$2.23^{+0.25}_{-0.43}$	6.33	0.990	$0.03^{+0.05}_{-0.02}$	6.67	0.010
4642	$2.54^{+0.35}_{-0.35}$	5.00	0.976	3.88	0.46	$2.54^{+0.15}_{-0.41}$	5.00	0.981	$0.03^{+0.05}_{-0.02}$	4.00	0.019
4648	$3.42^{+0.43}_{-0.43}$	4.33	1.000	1.69	0.20	$3.42^{+0.21}_{-0.43}$	4.33	0.950	$3.75^{+0.10}_{-0.12}$	6.00	0.050
4651	$1.66^{+0.26}_{-0.26}$	6.00	1.000	1.17	0.06	$1.66^{+0.10}_{-0.10}$	6.00	1.000	$\cdots\ ^{+}_{-}$	$\cdots$	$\cdots$
4657	$1.61^{+0.26}_{-0.26}$	3.33	1.000	9.52	1.52	$1.61^{+0.11}_{-0.09}$	3.33	1.000	$\cdots\ ^{+}_{-}$	$\cdots$	$\cdots$
4660	$2.71^{+0.36}_{-0.36}$	6.67	1.000	5.59	2.68	$2.71^{+0.14}_{-0.18}$	6.67	1.000	$\cdots\ ^{+}_{-}$	$\cdots$	$\cdots$
4661	$3.20^{+0.41}_{-0.41}$	4.33	1.000	1.67	1.16	$3.20^{+0.23}_{-0.19}$	4.33	1.000	$\cdots\ ^{+}_{-}$	$\cdots$	$\cdots$
4662	$1.20^{+0.44}_{-0.22}$	6.33	0.500	16.33	2.11	$1.20^{+0.10}_{-0.09}$	6.33	0.483	$1.48^{+0.08}_{-0.10}$	6.00	0.414
4668	$2.66^{+0.36}_{-2.64}$	4.67	0.865	6.38	0.93	$2.66^{+0.29}_{-0.33}$	4.67	0.856	$0.05^{+0.10}_{-0.04}$	3.67	0.127
4673	$3.30^{+0.42}_{-0.42}$	3.67	0.978	12.41	1.94	$3.30^{+0.17}_{-0.18}$	3.67	0.978	$0.06^{+0.05}_{-0.05}$	1.67	0.014
4674	$3.13^{+0.40}_{-0.41}$	6.33	1.000	2.56	0.61	$3.13^{+0.08}_{-0.09}$	6.33	1.000	$\cdots\ ^{+}_{-}$	$\cdots$	$\cdots$
4678	$4.31^{+0.52}_{-0.52}$	6.33	1.000	0.30	0.14	$4.31^{+0.09}_{-0.11}$	6.33	1.000	$\cdots\ ^{+}_{-}$	$\cdots$	$\cdots$
4686	$2.17^{+0.35}_{-0.31}$	7.33	0.931	5.27	3.75	$2.17^{+0.18}_{-0.18}$	7.33	0.603	$2.46^{+0.14}_{-0.11}$	8.00	0.397
4699	$2.34^{+0.33}_{-0.33}$	7.00	0.995	5.33	5.23	$2.34^{+0.21}_{-0.08}$	7.00	0.510	$2.23^{+0.03}_{-0.26}$	6.67	0.490
4701	$0.74^{+0.17}_{-0.17}$	5.00	1.000	10.08	1.20	$0.74^{+0.09}_{-0.09}$	5.00	1.000	$\cdots\ ^{+}_{-}$	$\cdots$	$\cdots$
4714	$2.61^{+0.35}_{-0.35}$	5.00	1.000	11.56	1.70	$2.61^{+0.08}_{-0.09}$	5.00	1.000	$\cdots\ ^{+}_{-}$	$\cdots$	$\cdots$
4717	$0.11^{+0.11}_{-0.11}$	3.00	1.000	3.50	0.17	$0.11^{+0.11}_{-0.08}$	3.00	1.000	$\cdots\ ^{+}_{-}$	$\cdots$	$\cdots$
4764	$2.09^{+0.30}_{-0.30}$	5.67	1.000	2.06	1.44	$2.09^{+0.25}_{-0.24}$	5.67	1.000	$\cdots\ ^{+}_{-}$	$\cdots$	$\cdots$
4766	$2.98^{+0.39}_{-0.39}$	8.00	1.000	19.84	4.48	$2.98^{+0.09}_{-0.16}$	8.00	1.000	$\cdots\ ^{+}_{-}$	$\cdots$	$\cdots$
4767	$0.53^{+0.15}_{-0.15}$	2.67	1.000	14.46	0.89	$0.53^{+0.08}_{-0.08}$	2.67	1.000	$\cdots\ ^{+}_{-}$	$\cdots$	$\cdots$
4774	$2.66^{+0.36}_{-0.36}$	7.00	1.000	1.00	1.05	$2.66^{+0.11}_{-0.10}$	7.00	1.000	$\cdots\ ^{+}_{-}$	$\cdots$	$\cdots$
4779	$2.53^{+0.35}_{-0.35}$	6.33	0.996	0.24	0.04	$2.53^{+0.18}_{-0.37}$	6.33	0.997	$0.05^{+0.03}_{-0.03}$	6.33	0.003
4801	$1.39^{+0.23}_{-0.23}$	3.00	1.000	1.89	0.05	$1.39^{+0.08}_{-0.08}$	3.00	1.000	$\cdots\ ^{+}_{-}$	$\cdots$	$\cdots$
4805	$0.53^{+0.15}_{-0.15}$	2.00	1.000	2.48	0.14	$0.53^{+0.08}_{-0.11}$	2.00	1.000	$\cdots\ ^{+}_{-}$	$\cdots$	$\cdots$
4807	$2.38^{+0.33}_{-0.33}$	7.00	1.000	1.00	0.26	$2.38^{+0.13}_{-0.26}$	7.00	1.000	$\cdots\ ^{+}_{-}$	$\cdots$	$\cdots$
4813	$2.85^{+0.38}_{-0.38}$	7.00	0.990	2.65	0.64	$2.85^{+0.10}_{-0.11}$	7.00	0.660	$3.04^{+0.08}_{-0.09}$	7.33	0.208
4814	$3.12^{+0.40}_{-0.40}$	6.33	1.000	0.79	0.16	$3.12^{+0.19}_{-0.21}$	6.33	1.000	$\cdots\ ^{+}_{-}$	$\cdots$	$\cdots$
4816	$1.41^{+0.24}_{-0.24}$	2.67	1.000	12.77	0.40	$1.41^{+0.08}_{-0.08}$	2.67	1.000	$\cdots\ ^{+}_{-}$	$\cdots$	$\cdots$

Table C.2—Continued

ID[a]	z_b[b]	t_b[c]	ODDS[d]	χ^2_ν[e]	$\chi^2_{\rm mod}$[f]	z_b1[g]	t_b1[c]	ODDS1[h]	z_b2[g]	t_b2[c]	ODDS2[h]
4825	$0.24^{+0.12}_{-0.12}$	3.00	1.000	4.05	0.03	$0.24^{+0.07}_{-0.08}$	3.00	1.000	$\cdots$ $^{+}_{-}$	$\cdots$	$\cdots$
4830	$3.40^{+0.43}_{-0.43}$	6.00	1.000	0.79	0.38	$3.40^{+0.11}_{-0.12}$	6.00	1.000	$\cdots$ $^{+}_{-}$	$\cdots$	$\cdots$
4835	$1.36^{+0.23}_{-0.23}$	3.33	1.000	12.60	1.47	$1.36^{+0.09}_{-0.08}$	3.33	1.000	$\cdots$ $^{+}_{-}$	$\cdots$	$\cdots$
4838	$2.96^{+0.39}_{-0.39}$	4.67	1.000	5.51	0.77	$2.96^{+0.09}_{-0.08}$	4.67	1.000	$\cdots$ $^{+}_{-}$	$\cdots$	$\cdots$
4841	$1.17^{+0.21}_{-0.21}$	4.00	1.000	3.21	0.76	$1.17^{+0.11}_{-0.10}$	4.00	1.000	$\cdots$ $^{+}_{-}$	$\cdots$	$\cdots$
4849	$1.49^{+0.24}_{-0.44}$	5.33	0.680	3.22	2.66	$1.49^{+0.20}_{-0.13}$	5.33	0.680	$1.11^{+0.13}_{-0.10}$	6.33	0.320
4860	$3.55^{+0.45}_{-0.45}$	5.33	1.000	0.94	0.52	$3.55^{+0.11}_{-0.12}$	5.33	1.000	$\cdots$ $^{+}_{-}$	$\cdots$	$\cdots$
4874	$0.03^{+0.10}_{-0.03}$	4.67	1.000	7.17	2.63	$0.03^{+0.11}_{-0.02}$	4.67	1.000	$\cdots$ $^{+}_{-}$	$\cdots$	$\cdots$
4878	$0.18^{+0.12}_{-0.12}$	4.33	1.000	0.55	0.02	$0.18^{+0.10}_{-0.08}$	4.33	1.000	$\cdots$ $^{+}_{-}$	$\cdots$	$\cdots$
4880	$1.52^{+0.25}_{-0.36}$	5.67	0.896	1.75	0.08	$1.52^{+0.20}_{-0.12}$	5.67	0.894	$1.20^{+0.10}_{-0.07}$	6.33	0.091
4907	$2.60^{+0.35}_{-0.35}$	6.67	1.000	0.89	0.14	$2.60^{+0.13}_{-0.15}$	6.67	1.000	$\cdots$ $^{+}_{-}$	$\cdots$	$\cdots$
4908	$2.58^{+0.35}_{-0.35}$	6.33	1.000	3.64	1.37	$2.58^{+0.12}_{-0.16}$	6.33	1.000	$\cdots$ $^{+}_{-}$	$\cdots$	$\cdots$
4913	$0.47^{+0.14}_{-0.14}$	1.00	1.000	2.23	0.73	$0.47^{+0.11}_{-0.08}$	1.00	1.000	$\cdots$ $^{+}_{-}$	$\cdots$	$\cdots$
4927	$3.48^{+0.44}_{-0.44}$	6.33	1.000	0.73	0.05	$3.48^{+0.09}_{-0.09}$	6.33	1.000	$\cdots$ $^{+}_{-}$	$\cdots$	$\cdots$
4929	$0.45^{+0.14}_{-0.14}$	2.33	1.000	43.88	1.91	$0.45^{+0.08}_{-0.07}$	2.33	1.000	$\cdots$ $^{+}_{-}$	$\cdots$	$\cdots$
4930	$2.05^{+0.30}_{-0.36}$	6.67	0.959	1.40	1.17	$2.05^{+0.38}_{-0.47}$	6.67	0.985	$0.07^{+0.07}_{-0.06}$	7.00	0.015
4947	$0.27^{+0.12}_{-0.12}$	4.00	1.000	1.09	0.03	$0.27^{+0.08}_{-0.08}$	4.00	1.000	$\cdots$ $^{+}_{-}$	$\cdots$	$\cdots$
4950	$1.09^{+0.20}_{-0.21}$	2.33	1.000	14.77	0.02	$1.09^{+0.08}_{-0.07}$	2.33	1.000	$\cdots$ $^{+}_{-}$	$\cdots$	$\cdots$
4983	$1.83^{+0.38}_{-0.28}$	6.33	0.907	2.39	1.04	$1.83^{+0.09}_{-0.22}$	6.33	0.469	$2.00^{+0.33}_{-0.08}$	6.33	0.531
4999	$1.36^{+0.23}_{-0.23}$	6.00	1.000	8.29	1.32	$1.36^{+0.08}_{-0.09}$	6.00	1.000	$\cdots$ $^{+}_{-}$	$\cdots$	$\cdots$
5005	$1.49^{+0.24}_{-0.24}$	3.67	1.000	1.55	0.77	$1.49^{+0.09}_{-0.09}$	3.67	0.753	$1.33^{+0.07}_{-0.08}$	5.00	0.247
5006	$3.45^{+0.44}_{-0.44}$	7.33	1.000	2.07	1.89	$3.45^{+0.14}_{-0.08}$	7.33	0.924	$3.32^{+0.05}_{-0.06}$	7.00	0.076
5010	$0.70^{+0.17}_{-0.17}$	5.33	1.000	3.34	0.12	$0.70^{+0.08}_{-0.07}$	5.33	1.000	$\cdots$ $^{+}_{-}$	$\cdots$	$\cdots$
5022	$0.43^{+0.14}_{-0.19}$	3.33	0.934	13.23	0.16	$0.43^{+0.08}_{-0.07}$	3.33	0.918	$0.27^{+0.05}_{-0.06}$	3.00	0.082
5037	$2.14^{+0.31}_{-0.38}$	6.00	0.919	4.38	2.01	$2.14^{+0.32}_{-0.24}$	6.00	0.877	$1.80^{+0.10}_{-0.11}$	6.00	0.123
5052	$0.56^{+0.15}_{-0.15}$	2.67	1.000	3.93	0.16	$0.56^{+0.12}_{-0.12}$	2.67	1.000	$\cdots$ $^{+}_{-}$	$\cdots$	$\cdots$
5053	$2.14^{+0.31}_{-0.31}$	5.33	0.995	4.48	0.59	$2.14^{+0.14}_{-0.19}$	5.33	0.995	$0.09^{+0.03}_{-0.02}$	6.33	0.005
5056	$1.60^{+0.25}_{-0.25}$	1.33	1.000	17.29	0.87	$1.60^{+0.13}_{-0.12}$	1.33	1.000	$\cdots$ $^{+}_{-}$	$\cdots$	$\cdots$
5060	$1.63^{+0.26}_{-0.26}$	6.00	1.000	3.84	0.67	$1.63^{+0.12}_{-0.13}$	6.00	1.000	$\cdots$ $^{+}_{-}$	$\cdots$	$\cdots$
5063	$4.32^{+0.52}_{-0.52}$	5.33	1.000	0.07	0.01	$4.32^{+0.09}_{-0.09}$	5.33	1.000	$\cdots$ $^{+}_{-}$	$\cdots$	$\cdots$
5089	$2.19^{+0.31}_{-0.31}$	5.33	1.000	2.77	1.64	$2.19^{+0.12}_{-0.20}$	5.33	1.000	$\cdots$ $^{+}_{-}$	$\cdots$	$\cdots$
5093	$0.44^{+0.14}_{-0.34}$	5.67	0.792	1.65	0.46	$0.44^{+0.07}_{-0.08}$	5.67	0.792	$0.14^{+0.08}_{-0.10}$	5.00	0.180
5098	$3.15^{+0.41}_{-0.41}$	6.33	1.000	1.23	0.70	$3.15^{+0.09}_{-0.10}$	6.33	1.000	$\cdots$ $^{+}_{-}$	$\cdots$	$\cdots$
5102	$0.04^{+0.59}_{-0.04}$	2.33	0.573	7.48	0.78	$0.04^{+0.10}_{-0.03}$	2.33	0.573	$0.50^{+0.22}_{-0.09}$	4.67	0.427
5106	$3.21^{+0.41}_{-0.41}$	5.00	0.996	1.93	0.18	$3.21^{+0.19}_{-0.47}$	5.00	1.000	$\cdots$ $^{+}_{-}$	$\cdots$	$\cdots$
5107	$3.52^{+0.44}_{-0.44}$	6.33	1.000	1.00	0.26	$3.52^{+0.12}_{-0.12}$	6.33	1.000	$\cdots$ $^{+}_{-}$	$\cdots$	$\cdots$

Table C.2—Continued

ID[a]	z_b[b]	t_b[c]	ODDS[d]	χ^2_ν[e]	$\chi^2_{\rm mod}$[f]	z_b1[g]	t_b1[c]	ODDS1[h]	z_b2[g]	t_b2[c]	ODDS2[h]
5109	$2.95^{+0.39}_{-0.39}$	5.00	1.000	4.92	2.10	$2.95^{+0.13}_{-0.14}$	5.00	1.000	$\cdots\ ^{+}_{-}$	···	···
5111	$0.73^{+0.17}_{-0.17}$	5.00	1.000	1.81	0.65	$0.73^{+0.12}_{-0.12}$	5.00	1.000	$\cdots\ ^{+}_{-}$	···	···
5115	$1.27^{+0.22}_{-0.22}$	5.67	1.000	7.49	1.10	$1.27^{+0.13}_{-0.10}$	5.67	0.960	$1.42^{+0.07}_{-0.02}$	4.00	0.040
5120	$2.01^{+0.30}_{-0.29}$	6.67	0.979	2.81	1.42	$2.01^{+0.24}_{-0.39}$	6.67	0.989	$0.06^{+0.05}_{-0.05}$	7.00	0.011
5134	$0.53^{+2.88}_{-0.15}$	4.00	0.470	5.23	1.79	$0.53^{+0.13}_{-0.13}$	4.00	0.470	$3.34^{+0.14}_{-0.20}$	5.00	0.505
5136	$2.91^{+0.38}_{-0.38}$	5.33	1.000	17.90	7.58	$2.91^{+0.08}_{-0.10}$	5.33	1.000	$\cdots\ ^{+}_{-}$	···	···
5159	$1.86^{+0.28}_{-0.28}$	6.00	1.000	3.13	0.51	$1.86^{+0.17}_{-0.09}$	6.00	1.000	$\cdots\ ^{+}_{-}$	···	···
5177	$0.47^{+0.14}_{-0.14}$	1.67	1.000	21.89	0.01	$0.47^{+0.07}_{-0.07}$	1.67	1.000	$\cdots\ ^{+}_{-}$	···	···
5178	$0.59^{+0.16}_{-0.16}$	6.00	1.000	3.48	0.96	$0.59^{+0.10}_{-0.13}$	6.00	1.000	$\cdots\ ^{+}_{-}$	···	···
5182	$2.58^{+0.35}_{-0.35}$	8.00	0.988	10.76	6.81	$2.58^{+0.14}_{-0.20}$	8.00	0.983	$2.16^{+0.12}_{-0.06}$	7.00	0.017
5187	$0.76^{+0.17}_{-0.17}$	3.00	1.000	9.01	0.05	$0.76^{+0.08}_{-0.08}$	3.00	1.000	$\cdots\ ^{+}_{-}$	···	···
5190	$1.35^{+0.23}_{-0.23}$	3.67	1.000	14.52	1.93	$1.35^{+0.08}_{-0.08}$	3.67	1.000	$\cdots\ ^{+}_{-}$	···	···
5196	$1.78^{+0.27}_{-0.27}$	6.00	0.992	3.76	1.78	$1.78^{+0.18}_{-0.16}$	6.00	0.968	$2.01^{+0.09}_{-0.05}$	6.00	0.026
5200	$1.98^{+0.29}_{-0.29}$	6.67	0.983	1.92	0.83	$1.98^{+0.23}_{-0.36}$	6.67	0.991	$0.07^{+0.04}_{-0.06}$	7.00	0.009
5201	$1.05^{+0.21}_{-0.20}$	6.33	0.978	2.46	0.37	$1.05^{+0.14}_{-0.13}$	6.33	0.913	$1.25^{+0.07}_{-0.06}$	6.00	0.087
5205	$3.13^{+0.40}_{-0.41}$	7.67	1.000	4.86	2.57	$3.13^{+0.13}_{-0.19}$	7.67	0.988	$2.83^{+0.05}_{-0.05}$	7.00	0.012
5212	$0.19^{+0.12}_{-0.12}$	2.67	1.000	1.01	0.10	$0.19^{+0.13}_{-0.12}$	2.67	1.000	$\cdots\ ^{+}_{-}$	···	···
5216	$1.11^{+0.21}_{-0.21}$	5.67	1.000	8.27	0.41	$1.11^{+0.08}_{-0.09}$	5.67	1.000	$\cdots\ ^{+}_{-}$	···	···
5231	$2.52^{+0.35}_{-0.35}$	6.67	1.000	2.74	1.39	$2.52^{+0.13}_{-0.12}$	6.67	1.000	$\cdots\ ^{+}_{-}$	···	···
5249	$2.73^{+0.37}_{-0.37}$	5.67	1.000	7.09	2.11	$2.73^{+0.22}_{-0.20}$	5.67	1.000	$\cdots\ ^{+}_{-}$	···	···
5251	$2.57^{+0.35}_{-0.35}$	6.67	1.000	2.62	2.95	$2.57^{+0.09}_{-0.08}$	6.67	1.000	$\cdots\ ^{+}_{-}$	···	···
5253	$0.54^{+1.16}_{-0.27}$	7.67	0.711	1.37	1.17	$0.54^{+0.34}_{-0.36}$	7.67	0.885	$1.58^{+0.27}_{-0.19}$	7.33	0.115
5254	$2.33^{+0.33}_{-2.18}$	7.00	0.922	0.58	0.28	$2.33^{+0.15}_{-0.20}$	7.00	0.762	$2.06^{+0.07}_{-0.23}$	6.67	0.176
5261	$2.54^{+0.35}_{-0.35}$	6.67	0.982	6.66	5.18	$2.54^{+0.19}_{-0.46}$	6.67	1.000	$\cdots\ ^{+}_{-}$	···	···
5263	$0.10^{+0.11}_{-0.10}$	3.67	0.981	1.64	0.22	$0.10^{+0.16}_{-0.09}$	3.67	1.000	$\cdots\ ^{+}_{-}$	···	···
5267	$0.23^{+0.12}_{-0.12}$	4.67	1.000	0.41	0.07	$0.23^{+0.09}_{-0.12}$	4.67	1.000	$\cdots\ ^{+}_{-}$	···	···
5268	$0.47^{+0.14}_{-0.14}$	5.33	1.000	14.38	0.19	$0.47^{+0.08}_{-0.07}$	5.33	1.000	$\cdots\ ^{+}_{-}$	···	···
5275	$3.28^{+0.42}_{-0.42}$	5.33	1.000	0.46	0.44	$3.28^{+0.18}_{-0.20}$	5.33	1.000	$\cdots\ ^{+}_{-}$	···	···
5276	$0.66^{+0.16}_{-0.16}$	6.33	1.000	1.08	0.37	$0.66^{+0.07}_{-0.07}$	6.33	1.000	$\cdots\ ^{+}_{-}$	···	···
5286	$2.93^{+0.38}_{-0.38}$	5.00	1.000	5.29	2.18	$2.93^{+0.08}_{-0.10}$	5.00	1.000	$\cdots\ ^{+}_{-}$	···	···
5292	$0.91^{+0.19}_{-0.19}$	6.33	0.975	4.28	1.06	$0.91^{+0.08}_{-0.09}$	6.33	0.973	$0.70^{+0.04}_{-0.04}$	6.33	0.027
5304	$2.62^{+0.36}_{-0.35}$	6.33	1.000	2.09	0.39	$2.62^{+0.10}_{-0.10}$	6.33	1.000	$\cdots\ ^{+}_{-}$	···	···
5330	$0.64^{+1.10}_{-0.16}$	7.00	0.957	2.67	3.33	$0.64^{+0.16}_{-0.16}$	7.00	0.957	$1.75^{+0.11}_{-0.10}$	6.33	0.043
5331	$3.55^{+0.45}_{-0.45}$	5.33	1.000	0.62	0.51	$3.55^{+0.19}_{-0.31}$	5.33	1.000	$\cdots\ ^{+}_{-}$	···	···
5341	$0.55^{+0.15}_{-0.15}$	1.67	0.987	4.18	0.82	$0.55^{+0.14}_{-0.04}$	1.67	0.685	$0.49^{+0.02}_{-0.15}$	1.33	0.315
5346	$3.37^{+0.43}_{-0.43}$	6.33	1.000	2.71	0.87	$3.37^{+0.12}_{-0.12}$	6.33	1.000	$\cdots\ ^{+}_{-}$	···	···

Table C.2—Continued

ID[a]	z_b[b]	t_b[c]	ODDS[d]	χ^2_ν[e]	$\chi^2_{\rm mod}$[f]	z_b1[g]	t_b1[c]	ODDS1[h]	z_b2[g]	t_b2[c]	ODDS2[h]
5348	$3.14^{+0.41}_{-0.41}$	6.33	1.000	0.94	0.47	$3.14^{+0.15}_{-0.20}$	6.33	1.000	··· $^{+}_{-}$	···	···
5358	$2.16^{+0.31}_{-0.50}$	5.00	0.539	6.95	2.71	$2.16^{+0.15}_{-0.16}$	5.00	0.536	$1.74^{+0.15}_{-0.13}$	3.67	0.464
5365	$1.66^{+0.26}_{-0.26}$	3.33	1.000	18.50	0.06	$1.66^{+0.09}_{-0.08}$	3.33	1.000	··· $^{+}_{-}$	···	···
5367	$0.22^{+0.12}_{-0.13}$	5.67	0.974	1.17	0.81	$0.22^{+0.09}_{-0.20}$	5.67	1.000	··· $^{+}_{-}$	···	···
5377	$1.55^{+0.25}_{-0.25}$	6.33	0.995	2.93	1.09	$1.55^{+0.14}_{-0.22}$	6.33	0.731	$1.74^{+0.10}_{-0.05}$	6.00	0.269
5380	$0.12^{+0.11}_{-0.11}$	3.67	0.982	4.09	1.78	$0.12^{+0.04}_{-0.11}$	3.67	0.527	$0.19^{+0.08}_{-0.03}$	4.00	0.473
5388	$1.28^{+0.22}_{-0.22}$	4.67	1.000	4.91	0.97	$1.28^{+0.07}_{-0.08}$	4.67	0.908	$1.42^{+0.06}_{-0.06}$	3.67	0.092
5399	$0.24^{+0.12}_{-0.13}$	5.33	0.985	9.95	1.36	$0.24^{+0.07}_{-0.04}$	5.33	0.567	$0.16^{+0.04}_{-0.08}$	5.00	0.433
5405	$1.08^{+0.20}_{-0.20}$	3.33	1.000	2.65	0.24	$1.08^{+0.09}_{-0.08}$	3.33	1.000	··· $^{+}_{-}$	···	···
5408	$1.51^{+0.25}_{-0.25}$	3.33	1.000	5.26	0.58	$1.51^{+0.14}_{-0.13}$	3.33	1.000	··· $^{+}_{-}$	···	···
5411	$2.73^{+0.37}_{-0.37}$	6.33	1.000	0.73	0.09	$2.73^{+0.11}_{-0.12}$	6.33	1.000	··· $^{+}_{-}$	···	···
5415	$0.49^{+0.15}_{-0.15}$	1.33	1.000	3.14	0.10	$0.49^{+0.11}_{-0.14}$	1.33	1.000	··· $^{+}_{-}$	···	···
5417	$1.11^{+0.21}_{-0.21}$	3.00	1.000	40.31	1.59	$1.11^{+0.07}_{-0.08}$	3.00	1.000	··· $^{+}_{-}$	···	···
5431	$0.13^{+0.39}_{-0.11}$	2.33	0.617	3.30	0.31	$0.13^{+0.21}_{-0.12}$	2.33	0.660	$0.47^{+0.10}_{-0.12}$	3.67	0.340
5435	$0.22^{+0.12}_{-0.12}$	5.67	1.000	14.88	2.47	$0.22^{+0.07}_{-0.07}$	5.67	1.000	··· $^{+}_{-}$	···	···
5443	$3.42^{+0.43}_{-0.43}$	8.00	1.000	2.96	0.71	$3.42^{+0.11}_{-0.15}$	8.00	1.000	··· $^{+}_{-}$	···	···
5456	$3.44^{+0.43}_{-0.43}$	5.67	1.000	4.83	1.55	$3.44^{+0.12}_{-0.15}$	5.67	1.000	··· $^{+}_{-}$	···	···
5473	$2.96^{+0.39}_{-0.39}$	5.67	1.000	1.06	0.35	$2.96^{+0.11}_{-0.09}$	5.67	1.000	··· $^{+}_{-}$	···	···
5491	$0.17^{+0.11}_{-0.12}$	6.67	1.000	44.67	1.94	$0.17^{+0.08}_{-0.07}$	6.67	1.000	··· $^{+}_{-}$	···	···
5496	$1.77^{+0.27}_{-1.71}$	6.00	0.456	1.47	2.09	$1.77^{+0.31}_{-0.20}$	6.00	0.420	$1.40^{+0.17}_{-0.14}$	6.33	0.289
5497	$0.71^{+0.17}_{-0.17}$	6.00	1.000	22.12	1.32	$0.71^{+0.07}_{-0.07}$	6.00	1.000	··· $^{+}_{-}$	···	···
5501	$0.01^{+0.10}_{-0.01}$	2.67	1.000	41.71	9.66	$0.01^{+0.10}_{-0.01}$	2.67	1.000	··· $^{+}_{-}$	···	···
5526	$0.48^{+0.15}_{-0.14}$	1.00	1.000	4.79	0.05	$0.48^{+0.04}_{-0.08}$	1.00	0.592	$0.55^{+0.07}_{-0.03}$	1.33	0.408
5529	$1.33^{+0.23}_{-0.23}$	1.67	1.000	7.01	0.04	$1.33^{+0.11}_{-0.13}$	1.67	1.000	··· $^{+}_{-}$	···	···
5533	$3.04^{+0.40}_{-0.40}$	6.33	1.000	2.61	1.79	$3.04^{+0.21}_{-0.19}$	6.33	1.000	··· $^{+}_{-}$	···	···
5536	$1.72^{+0.48}_{-0.27}$	6.33	0.853	1.51	1.24	$1.72^{+0.25}_{-0.16}$	6.33	0.830	$2.00^{+0.08}_{-0.03}$	6.00	0.072
5540	$0.17^{+0.11}_{-0.12}$	3.33	1.000	2.67	0.10	$0.17^{+0.08}_{-0.07}$	3.33	1.000	··· $^{+}_{-}$	···	···
5545	$2.30^{+0.32}_{-0.32}$	6.00	1.000	2.72	0.85	$2.30^{+0.27}_{-0.24}$	6.00	1.000	··· $^{+}_{-}$	···	···
5548	$3.58^{+0.45}_{-0.45}$	6.33	1.000	0.74	0.08	$3.58^{+0.10}_{-0.10}$	6.33	1.000	··· $^{+}_{-}$	···	···
5569	$0.55^{+0.15}_{-0.15}$	5.00	1.000	21.69	1.31	$0.55^{+0.08}_{-0.08}$	5.00	1.000	··· $^{+}_{-}$	···	···
5579	$3.06^{+0.40}_{-0.40}$	6.00	1.000	1.73	1.17	$3.06^{+0.12}_{-0.12}$	6.00	1.000	··· $^{+}_{-}$	···	···
5605	$1.86^{+0.28}_{-1.25}$	6.00	0.944	3.16	0.58	$1.86^{+0.16}_{-0.17}$	6.00	0.944	$0.62^{+0.09}_{-0.09}$	7.00	0.056
5606	$0.16^{+0.11}_{-0.11}$	2.67	1.000	2.39	0.05	$0.16^{+0.07}_{-0.07}$	2.67	1.000	··· $^{+}_{-}$	···	···
5614	$1.57^{+0.25}_{-0.25}$	4.00	1.000	15.54	1.55	$1.57^{+0.09}_{-0.10}$	4.00	1.000	··· $^{+}_{-}$	···	···
5615	$1.06^{+0.20}_{-0.20}$	2.67	1.000	4.43	0.04	$1.06^{+0.09}_{-0.09}$	2.67	1.000	··· $^{+}_{-}$	···	···
5620	$0.21^{+0.12}_{-0.12}$	6.33	1.000	13.36	0.75	$0.21^{+0.07}_{-0.07}$	6.33	1.000	··· $^{+}_{-}$	···	···

Table C.2—Continued

ID[a]	z_b[b]	t_b[c]	ODDS[d]	χ^2_ν[e]	$\chi^2_{\rm mod}$[f]	z_b1[g]	t_b1[c]	ODDS1[h]	z_b2[g]	t_b2[c]	ODDS2[h]
5626	$0.21^{+2.15}_{-0.12}$	6.00	0.759	0.73	0.57	$0.21^{+0.08}_{-0.11}$	6.00	0.759	$2.27^{+0.17}_{-0.18}$	4.00	0.233
5627	$1.88^{+0.36}_{-0.28}$	5.33	0.927	0.29	0.02	$1.88^{+0.52}_{-0.37}$	5.33	1.000	··· $^{+}_{-}$	···	···
5628	$2.73^{+0.37}_{-0.37}$	7.33	1.000	6.32	4.69	$2.73^{+0.25}_{-0.05}$	7.33	0.647	$2.64^{+0.04}_{-0.13}$	7.00	0.353
5634	$0.43^{+0.14}_{-0.30}$	6.00	0.844	0.44	0.16	$0.43^{+0.09}_{-0.07}$	6.00	0.844	$0.18^{+0.09}_{-0.09}$	5.33	0.156
5649	$2.54^{+0.35}_{-0.35}$	7.00	1.000	1.35	0.82	$2.54^{+0.11}_{-0.18}$	7.00	0.989	$2.67^{+0.04}_{-0.02}$	7.33	0.011
5658	$1.07^{+0.20}_{-0.20}$	3.33	1.000	11.36	0.69	$1.07^{+0.07}_{-0.08}$	3.33	1.000	··· $^{+}_{-}$	···	···
5661	$1.33^{+0.23}_{-0.23}$	6.67	1.000	2.26	0.54	$1.33^{+0.10}_{-0.09}$	6.67	0.995	$1.15^{+0.02}_{-0.02}$	7.00	0.005
5662	$2.15^{+0.41}_{-0.31}$	6.33	0.822	5.85	3.03	$2.15^{+0.22}_{-0.23}$	6.33	0.686	$2.49^{+0.16}_{-0.12}$	6.67	0.314
5670	$0.09^{+0.11}_{-0.09}$	2.33	1.000	7.50	0.03	$0.09^{+0.08}_{-0.08}$	2.33	1.000	··· $^{+}_{-}$	···	···
5679	$3.33^{+0.42}_{-0.42}$	6.00	1.000	8.07	0.39	$3.33^{+0.11}_{-0.11}$	6.00	1.000	··· $^{+}_{-}$	···	···
5683	$3.00^{+0.39}_{-0.39}$	6.33	1.000	2.87	0.16	$3.00^{+0.08}_{-0.08}$	6.33	1.000	··· $^{+}_{-}$	···	···
5685	$0.55^{+0.15}_{-0.15}$	5.33	1.000	3.72	0.21	$0.55^{+0.10}_{-0.09}$	5.33	1.000	··· $^{+}_{-}$	···	···
5686	$1.53^{+0.25}_{-0.25}$	3.00	1.000	2.03	0.23	$1.53^{+0.11}_{-0.10}$	3.00	1.000	··· $^{+}_{-}$	···	···
5687	$0.56^{+0.15}_{-0.15}$	3.67	1.000	1.48	0.14	$0.56^{+0.13}_{-0.12}$	3.67	1.000	··· $^{+}_{-}$	···	···
5688	$0.42^{+0.14}_{-0.31}$	5.67	0.467	1.15	1.07	$0.42^{+0.08}_{-0.07}$	5.67	0.450	$0.24^{+0.08}_{-0.17}$	5.33	0.550
5694	$1.21^{+0.22}_{-0.22}$	5.67	1.000	12.18	1.58	$1.21^{+0.09}_{-0.10}$	5.67	1.000	··· $^{+}_{-}$	···	···
5697	$1.52^{+0.25}_{-0.26}$	6.00	0.947	4.31	0.24	$1.52^{+0.09}_{-0.15}$	6.00	0.642	$1.30^{+0.07}_{-0.08}$	6.33	0.358
5701	$2.82^{+0.37}_{-0.37}$	5.67	1.000	3.55	0.12	$2.82^{+0.10}_{-0.09}$	5.67	1.000	··· $^{+}_{-}$	···	···
5707	$0.93^{+0.19}_{-0.19}$	5.67	0.995	1.30	0.15	$0.93^{+0.13}_{-0.19}$	5.67	0.966	$1.09^{+0.07}_{-0.03}$	4.00	0.034
5709	$1.35^{+0.23}_{-0.23}$	6.33	0.998	1.92	0.98	$1.35^{+0.11}_{-0.13}$	6.33	0.997	$1.11^{+0.02}_{-0.02}$	6.67	0.003
5716	$3.09^{+0.40}_{-0.40}$	6.33	1.000	1.24	0.12	$3.09^{+0.13}_{-0.11}$	6.33	1.000	··· $^{+}_{-}$	···	···
5726	$0.48^{+0.18}_{-0.14}$	5.67	0.951	2.56	0.26	$0.48^{+0.13}_{-0.09}$	5.67	0.933	$0.66^{+0.05}_{-0.05}$	6.00	0.067
5735	$2.45^{+0.34}_{-0.37}$	6.33	0.949	3.81	1.60	$2.45^{+0.15}_{-0.15}$	6.33	0.589	$2.18^{+0.12}_{-0.18}$	6.00	0.411
5748	$1.97^{+0.29}_{-0.29}$	5.33	1.000	3.93	2.38	$1.97^{+0.21}_{-0.22}$	5.33	1.000	··· $^{+}_{-}$	···	···
5750	$2.76^{+0.37}_{-0.37}$	7.67	1.000	0.68	0.17	$2.76^{+0.12}_{-0.16}$	7.67	1.000	··· $^{+}_{-}$	···	···
5753	$0.91^{+0.27}_{-0.19}$	6.33	0.851	3.27	0.51	$0.91^{+0.08}_{-0.13}$	6.33	0.830	$1.14^{+0.09}_{-0.08}$	6.00	0.170
5766	$2.21^{+0.33}_{-0.32}$	6.00	0.974	2.84	0.73	$2.21^{+0.17}_{-0.34}$	6.00	0.798	$2.46^{+0.16}_{-0.08}$	6.33	0.202
5771	$0.09^{+0.11}_{-0.09}$	3.67	0.991	2.07	1.44	$0.09^{+0.16}_{-0.08}$	3.67	1.000	··· $^{+}_{-}$	···	···
5778	$0.05^{+0.51}_{-0.05}$	2.33	0.914	7.91	1.25	$0.05^{+0.15}_{-0.04}$	2.33	0.922	$0.52^{+0.12}_{-0.08}$	4.33	0.078
5787	$1.81^{+0.28}_{-0.27}$	5.67	1.000	4.57	0.23	$1.81^{+0.15}_{-0.11}$	5.67	0.964	$1.99^{+0.07}_{-0.03}$	5.67	0.036
5805	$1.41^{+0.24}_{-0.24}$	3.00	1.000	11.65	0.03	$1.41^{+0.08}_{-0.07}$	3.00	1.000	··· $^{+}_{-}$	···	···
5808	$3.31^{+0.42}_{-0.42}$	5.67	1.000	0.46	0.12	$3.31^{+0.15}_{-0.17}$	5.67	1.000	··· $^{+}_{-}$	···	···
5812	$1.27^{+0.22}_{-0.22}$	5.33	1.000	0.44	0.02	$1.27^{+0.08}_{-0.09}$	5.33	0.949	$1.37^{+0.06}_{-0.02}$	4.67	0.051
5815	$0.81^{+0.18}_{-0.18}$	3.67	1.000	9.19	0.67	$0.81^{+0.13}_{-0.11}$	3.67	1.000	··· $^{+}_{-}$	···	···
5827	$1.66^{+0.26}_{-0.26}$	2.67	1.000	25.97	1.37	$1.66^{+0.09}_{-0.08}$	2.67	1.000	··· $^{+}_{-}$	···	···
5831	$2.17^{+0.31}_{-0.31}$	6.00	1.000	2.58	0.66	$2.17^{+0.12}_{-0.11}$	6.00	0.865	$2.05^{+0.01}_{-0.11}$	6.00	0.135

Table C.2—Continued

ID[a]	z_b[b]	t_b[c]	ODDS[d]	χ^2_ν[e]	$\chi^2_{\rm mod}$[f]	z_b1[g]	t_b1[c]	ODDS1[h]	z_b2[g]	t_b2[c]	ODDS2[h]
5837	$2.28^{+0.32}_{-0.32}$	6.00	1.000	2.40	1.13	$2.28^{+0.31}_{-0.27}$	6.00	1.000	$\cdots$ $^{+}_{-}$	$\cdots$	$\cdots$
5839	$2.95^{+0.39}_{-0.39}$	7.33	1.000	5.78	2.51	$2.95^{+0.06}_{-0.16}$	7.33	0.386	$3.06^{+0.05}_{-0.05}$	7.67	0.291
5843	$2.23^{+0.32}_{-0.32}$	6.00	0.997	4.18	0.91	$2.23^{+0.15}_{-0.18}$	6.00	0.858	$2.48^{+0.10}_{-0.10}$	6.33	0.142
5849	$2.66^{+0.36}_{-0.36}$	7.67	1.000	0.82	0.84	$2.66^{+0.16}_{-0.28}$	7.67	1.000	$\cdots$ $^{+}_{-}$	$\cdots$	$\cdots$
5856	$3.36^{+0.43}_{-0.43}$	6.33	1.000	1.49	0.87	$3.36^{+0.08}_{-0.09}$	6.33	1.000	$\cdots$ $^{+}_{-}$	$\cdots$	$\cdots$
5860	$2.44^{+0.34}_{-0.34}$	7.00	1.000	4.13	2.35	$2.44^{+0.08}_{-0.08}$	7.00	1.000	$\cdots$ $^{+}_{-}$	$\cdots$	$\cdots$
5867	$3.35^{+0.43}_{-0.43}$	6.00	1.000	1.02	0.29	$3.35^{+0.15}_{-0.16}$	6.00	1.000	$\cdots$ $^{+}_{-}$	$\cdots$	$\cdots$
5877	$0.64^{+0.16}_{-0.16}$	2.33	0.999	2.47	0.43	$0.64^{+0.10}_{-0.18}$	2.33	1.000	$\cdots$ $^{+}_{-}$	$\cdots$	$\cdots$
5878	$2.50^{+0.34}_{-0.39}$	5.33	0.904	14.42	1.44	$2.50^{+0.10}_{-0.09}$	5.33	0.758	$2.16^{+0.10}_{-0.08}$	4.67	0.242
5887	$2.76^{+0.37}_{-0.37}$	7.00	1.000	0.43	0.49	$2.76^{+0.06}_{-0.16}$	7.00	0.435	$2.89^{+0.25}_{-0.07}$	7.33	0.565
5888	$3.00^{+0.39}_{-0.39}$	4.67	0.996	1.39	1.46	$3.00^{+0.29}_{-0.45}$	4.67	1.000	$\cdots$ $^{+}_{-}$	$\cdots$	$\cdots$
5894	$2.25^{+0.32}_{-0.32}$	6.67	0.994	1.18	0.88	$2.25^{+0.13}_{-0.15}$	6.67	0.739	$2.03^{+0.07}_{-0.15}$	6.33	0.261
5896	$2.01^{+0.30}_{-0.29}$	7.00	1.000	4.73	4.19	$2.01^{+0.15}_{-0.12}$	7.00	1.000	$\cdots$ $^{+}_{-}$	$\cdots$	$\cdots$
5898	$1.66^{+0.26}_{-0.26}$	6.00	1.000	2.98	0.15	$1.66^{+0.09}_{-0.09}$	6.00	1.000	$\cdots$ $^{+}_{-}$	$\cdots$	$\cdots$
5916	$2.55^{+0.35}_{-0.35}$	7.33	0.996	1.03	1.08	$2.55^{+0.19}_{-0.09}$	7.33	0.603	$2.39^{+0.07}_{-0.25}$	7.00	0.397
5920	$2.55^{+0.35}_{-0.35}$	6.67	0.984	6.52	5.24	$2.55^{+0.13}_{-0.26}$	6.67	0.973	$2.19^{+0.10}_{-0.08}$	6.00	0.027
5922	$1.02^{+0.20}_{-0.20}$	3.67	1.000	1.81	0.03	$1.02^{+0.08}_{-0.08}$	3.67	1.000	$\cdots$ $^{+}_{-}$	$\cdots$	$\cdots$
5932	$3.49^{+0.44}_{-0.44}$	5.33	0.989	4.09	5.36	$3.49^{+0.15}_{-0.25}$	5.33	0.987	$2.96^{+0.05}_{-0.04}$	3.33	0.007
5933	$0.25^{+0.12}_{-0.12}$	3.67	1.000	5.06	0.25	$0.25^{+0.09}_{-0.08}$	3.67	1.000	$\cdots$ $^{+}_{-}$	$\cdots$	$\cdots$
5946	$2.77^{+0.37}_{-0.37}$	4.67	1.000	6.04	0.04	$2.77^{+0.08}_{-0.10}$	4.67	1.000	$\cdots$ $^{+}_{-}$	$\cdots$	$\cdots$
5952	$3.13^{+0.40}_{-0.41}$	5.33	1.000	0.61	0.56	$3.13^{+0.25}_{-0.28}$	5.33	1.000	$\cdots$ $^{+}_{-}$	$\cdots$	$\cdots$
5959	$0.71^{+0.17}_{-0.17}$	6.33	1.000	18.70	2.91	$0.71^{+0.07}_{-0.07}$	6.33	1.000	$\cdots$ $^{+}_{-}$	$\cdots$	$\cdots$
5962	$1.03^{+0.20}_{-0.20}$	2.00	1.000	19.88	0.03	$1.03^{+0.08}_{-0.12}$	2.00	1.000	$\cdots$ $^{+}_{-}$	$\cdots$	$\cdots$
5975	$1.60^{+0.25}_{-0.25}$	4.00	1.000	7.59	1.16	$1.60^{+0.08}_{-0.09}$	4.00	1.000	$\cdots$ $^{+}_{-}$	$\cdots$	$\cdots$
5989	$1.12^{+0.21}_{-0.21}$	3.67	1.000	10.73	0.26	$1.12^{+0.12}_{-0.07}$	3.67	1.000	$\cdots$ $^{+}_{-}$	$\cdots$	$\cdots$
5995	$0.71^{+0.17}_{-0.17}$	6.33	1.000	13.56	0.96	$0.71^{+0.07}_{-0.07}$	6.33	1.000	$\cdots$ $^{+}_{-}$	$\cdots$	$\cdots$
5999	$0.70^{+0.17}_{-0.17}$	5.67	1.000	3.20	0.13	$0.70^{+0.07}_{-0.07}$	5.67	1.000	$\cdots$ $^{+}_{-}$	$\cdots$	$\cdots$
6009	$0.13^{+0.11}_{-0.11}$	5.00	1.000	5.66	0.24	$0.13^{+0.07}_{-0.08}$	5.00	1.000	$\cdots$ $^{+}_{-}$	$\cdots$	$\cdots$
6017	$0.92^{+0.19}_{-0.19}$	6.33	1.000	5.90	2.95	$0.92^{+0.10}_{-0.16}$	6.33	1.000	$\cdots$ $^{+}_{-}$	$\cdots$	$\cdots$
6018	$0.56^{+0.15}_{-0.15}$	2.33	1.000	11.21	0.23	$0.56^{+0.09}_{-0.08}$	2.33	1.000	$\cdots$ $^{+}_{-}$	$\cdots$	$\cdots$
6027	$1.08^{+0.20}_{-0.20}$	1.33	1.000	18.93	1.98	$1.08^{+0.10}_{-0.09}$	1.33	1.000	$\cdots$ $^{+}_{-}$	$\cdots$	$\cdots$
6038	$0.55^{+0.15}_{-0.15}$	1.33	1.000	17.39	2.59	$0.55^{+0.08}_{-0.07}$	1.33	1.000	$\cdots$ $^{+}_{-}$	$\cdots$	$\cdots$
6047	$0.54^{+0.15}_{-0.15}$	2.33	1.000	2.29	0.06	$0.54^{+0.11}_{-0.09}$	2.33	1.000	$\cdots$ $^{+}_{-}$	$\cdots$	$\cdots$
6051	$0.59^{+0.16}_{-0.16}$	5.33	1.000	3.26	0.08	$0.59^{+0.09}_{-0.10}$	5.33	1.000	$\cdots$ $^{+}_{-}$	$\cdots$	$\cdots$
6056	$0.67^{+0.16}_{-0.16}$	6.33	1.000	5.89	0.67	$0.67^{+0.07}_{-0.07}$	6.33	1.000	$\cdots$ $^{+}_{-}$	$\cdots$	$\cdots$
6060	$0.24^{+0.27}_{-0.12}$	5.00	0.610	10.42	0.24	$0.24^{+0.08}_{-0.07}$	5.00	0.610	$0.48^{+0.07}_{-0.08}$	4.00	0.390

Table C.2—Continued

ID[a]	z_b[b]	t_b[c]	ODDS[d]	χ^2_ν[e]	$\chi^2_{\rm mod}$[f]	z_b1[g]	t_b1[c]	ODDS1[h]	z_b2[g]	t_b2[c]	ODDS2[h]
6066	$4.16^{+0.51}_{-0.51}$	6.00	1.000	8.69	1.17	$4.16^{+0.06}_{-0.14}$	6.00	0.558	$4.27^{+0.11}_{-0.05}$	6.67	0.442
6076	$0.92^{+0.19}_{-0.19}$	5.67	1.000	1.40	0.12	$0.92^{+0.11}_{-0.10}$	5.67	1.000	$\cdots$ $^{+}_{-}$	$\cdots$	$\cdots$
6079	$1.28^{+0.22}_{-0.22}$	2.67	1.000	4.56	0.26	$1.28^{+0.08}_{-0.08}$	2.67	1.000	$\cdots$ $^{+}_{-}$	$\cdots$	$\cdots$
6082	$0.23^{+0.12}_{-0.12}$	6.00	1.000	29.92	1.38	$0.23^{+0.07}_{-0.07}$	6.00	1.000	$\cdots$ $^{+}_{-}$	$\cdots$	$\cdots$
6090	$1.75^{+0.56}_{-0.27}$	4.00	0.553	5.51	0.28	$1.75^{+0.17}_{-0.13}$	4.00	0.524	$2.23^{+0.22}_{-0.15}$	5.67	0.425
6103	$2.99^{+0.39}_{-0.39}$	7.00	1.000	0.03	0.07	$2.99^{+0.12}_{-0.19}$	7.00	0.792	$3.18^{+0.17}_{-0.07}$	7.33	0.208
6108	$1.06^{+0.20}_{-0.20}$	2.33	1.000	1.27	0.04	$1.06^{+0.10}_{-0.10}$	2.33	1.000	$\cdots$ $^{+}_{-}$	$\cdots$	$\cdots$
6110	$3.01^{+0.39}_{-0.39}$	6.67	1.000	1.25	1.35	$3.01^{+0.23}_{-0.19}$	6.67	1.000	$\cdots$ $^{+}_{-}$	$\cdots$	$\cdots$
6112	$0.89^{+0.65}_{-0.21}$	6.33	0.668	0.83	0.38	$0.89^{+0.04}_{-0.11}$	6.33	0.282	$0.96^{+0.09}_{-0.03}$	6.33	0.245
6119	$1.77^{+0.27}_{-0.27}$	6.00	1.000	3.59	1.55	$1.77^{+0.15}_{-0.08}$	6.00	1.000	$\cdots$ $^{+}_{-}$	$\cdots$	$\cdots$
6123	$3.01^{+0.39}_{-0.39}$	6.33	1.000	2.17	1.57	$3.01^{+0.21}_{-0.17}$	6.33	1.000	$\cdots$ $^{+}_{-}$	$\cdots$	$\cdots$
6128	$2.72^{+0.37}_{-0.37}$	7.33	1.000	19.66	6.04	$2.72^{+0.16}_{-0.14}$	7.33	1.000	$\cdots$ $^{+}_{-}$	$\cdots$	$\cdots$
6133	$2.28^{+0.32}_{-0.32}$	4.00	1.000	14.93	0.08	$2.28^{+0.10}_{-0.10}$	4.00	1.000	$\cdots$ $^{+}_{-}$	$\cdots$	$\cdots$
6139	$4.56^{+0.55}_{-0.55}$	7.00	1.000	0.41	0.36	$4.56^{+0.13}_{-0.09}$	7.00	1.000	$\cdots$ $^{+}_{-}$	$\cdots$	$\cdots$
6143	$0.92^{+0.19}_{-0.19}$	3.33	1.000	4.70	0.49	$0.92^{+0.13}_{-0.16}$	3.33	1.000	$\cdots$ $^{+}_{-}$	$\cdots$	$\cdots$
6151	$1.04^{+0.20}_{-0.20}$	6.67	1.000	1.20	0.37	$1.04^{+0.12}_{-0.10}$	6.67	1.000	$\cdots$ $^{+}_{-}$	$\cdots$	$\cdots$
6162	$0.13^{+0.11}_{-0.11}$	5.00	1.000	8.00	0.80	$0.13^{+0.08}_{-0.12}$	5.00	1.000	$\cdots$ $^{+}_{-}$	$\cdots$	$\cdots$
6187	$0.92^{+0.19}_{-0.19}$	6.00	1.000	7.42	0.41	$0.92^{+0.08}_{-0.07}$	6.00	1.000	$\cdots$ $^{+}_{-}$	$\cdots$	$\cdots$
6188	$1.03^{+0.20}_{-0.20}$	1.00	1.000	30.24	2.47	$1.03^{+0.07}_{-0.08}$	1.00	0.861	$1.13^{+0.06}_{-0.03}$	1.33	0.139
6190	$0.64^{+0.16}_{-0.16}$	3.67	1.000	2.10	0.50	$0.64^{+0.11}_{-0.11}$	3.67	1.000	$\cdots$ $^{+}_{-}$	$\cdots$	$\cdots$
6196	$0.89^{+0.19}_{-0.19}$	4.33	1.000	5.81	0.42	$0.89^{+0.14}_{-0.07}$	4.33	0.890	$0.78^{+0.04}_{-0.07}$	5.33	0.110
6197	$0.54^{+0.15}_{-0.15}$	3.67	1.000	0.35	0.18	$0.54^{+0.11}_{-0.11}$	3.67	1.000	$\cdots$ $^{+}_{-}$	$\cdots$	$\cdots$
6201	$1.15^{+0.21}_{-0.21}$	5.67	1.000	2.40	0.25	$1.15^{+0.12}_{-0.13}$	5.67	1.000	$\cdots$ $^{+}_{-}$	$\cdots$	$\cdots$
6203	$2.77^{+0.37}_{-0.37}$	6.67	1.000	3.57	0.60	$2.77^{+0.07}_{-0.08}$	6.67	1.000	$\cdots$ $^{+}_{-}$	$\cdots$	$\cdots$
6206	$0.87^{+0.18}_{-0.18}$	1.33	1.000	28.97	0.20	$0.87^{+0.08}_{-0.07}$	1.33	1.000	$\cdots$ $^{+}_{-}$	$\cdots$	$\cdots$
6227	$2.99^{+0.39}_{-0.39}$	5.33	1.000	1.65	0.05	$2.99^{+0.14}_{-0.09}$	5.33	1.000	$\cdots$ $^{+}_{-}$	$\cdots$	$\cdots$
6250	$2.80^{+0.37}_{-0.37}$	5.67	1.000	3.03	0.04	$2.80^{+0.07}_{-0.09}$	5.67	1.000	$\cdots$ $^{+}_{-}$	$\cdots$	$\cdots$
6260	$3.88^{+0.48}_{-0.48}$	6.00	1.000	0.27	0.24	$3.88^{+0.17}_{-0.13}$	6.00	1.000	$\cdots$ $^{+}_{-}$	$\cdots$	$\cdots$
6274	$3.48^{+0.44}_{-0.44}$	5.67	1.000	0.04	0.00	$3.48^{+0.17}_{-0.20}$	5.67	1.000	$\cdots$ $^{+}_{-}$	$\cdots$	$\cdots$
6278	$0.72^{+0.17}_{-0.17}$	5.33	1.000	9.35	0.57	$0.72^{+0.09}_{-0.08}$	5.33	1.000	$\cdots$ $^{+}_{-}$	$\cdots$	$\cdots$
6288	$0.22^{+0.12}_{-0.12}$	4.00	1.000	2.00	0.42	$0.22^{+0.07}_{-0.08}$	4.00	1.000	$\cdots$ $^{+}_{-}$	$\cdots$	$\cdots$
6289	$3.05^{+0.40}_{-0.40}$	8.00	0.998	2.86	1.14	$3.05^{+0.13}_{-0.19}$	8.00	0.665	$2.73^{+0.13}_{-0.10}$	7.00	0.335
6290	$1.37^{+0.23}_{-0.23}$	4.00	1.000	3.03	1.36	$1.37^{+0.11}_{-0.16}$	4.00	1.000	$\cdots$ $^{+}_{-}$	$\cdots$	$\cdots$
6317	$1.29^{+0.22}_{-0.22}$	4.00	1.000	5.33	1.45	$1.29^{+0.14}_{-0.14}$	4.00	1.000	$\cdots$ $^{+}_{-}$	$\cdots$	$\cdots$
6322	$2.46^{+0.34}_{-0.34}$	6.33	1.000	0.44	0.23	$2.46^{+0.14}_{-0.24}$	6.33	1.000	$\cdots$ $^{+}_{-}$	$\cdots$	$\cdots$
6335	$2.66^{+0.36}_{-0.36}$	7.33	1.000	5.07	1.06	$2.66^{+0.14}_{-0.09}$	7.33	1.000	$\cdots$ $^{+}_{-}$	$\cdots$	$\cdots$

Table C.2—Continued

ID[a]	z_b[b]	t_b[c]	ODDS[d]	χ^2_ν[e]	$\chi^2_{\rm mod}$[f]	z_b1[g]	t_b1[c]	ODDS1[h]	z_b2[g]	t_b2[c]	ODDS2[h]
6352	$2.72^{+0.37}_{-0.37}$	7.33	1.000	7.94	8.51	$2.72^{+0.17}_{-0.08}$	7.33	0.644	$2.58^{+0.06}_{-0.16}$	7.00	0.356
6377	$2.27^{+0.32}_{-0.32}$	6.33	1.000	1.10	0.43	$2.27^{+0.24}_{-0.25}$	6.33	1.000	$\cdots^{+}_{-}$	$\cdots$	$\cdots$
6386	$0.62^{+0.16}_{-0.16}$	3.33	0.995	8.86	1.70	$0.62^{+0.14}_{-0.19}$	3.33	1.000	$\cdots^{+}_{-}$	$\cdots$	$\cdots$
6391	$1.63^{+0.26}_{-0.37}$	6.00	0.886	0.63	0.06	$1.63^{+0.15}_{-0.11}$	6.00	0.649	$1.39^{+0.13}_{-0.11}$	6.33	0.326
6394	$1.65^{+0.26}_{-0.26}$	3.67	1.000	10.02	0.47	$1.65^{+0.10}_{-0.10}$	3.67	1.000	$\cdots^{+}_{-}$	$\cdots$	$\cdots$
6396	$2.64^{+0.36}_{-0.36}$	7.00	1.000	3.29	2.77	$2.64^{+0.11}_{-0.10}$	7.00	1.000	$\cdots^{+}_{-}$	$\cdots$	$\cdots$
6399	$1.98^{+0.29}_{-0.29}$	2.00	1.000	15.35	0.01	$1.98^{+0.12}_{-0.11}$	2.00	1.000	$\cdots^{+}_{-}$	$\cdots$	$\cdots$
6411	$2.46^{+0.34}_{-0.34}$	7.00	1.000	2.44	1.27	$2.46^{+0.12}_{-0.24}$	7.00	1.000	$\cdots^{+}_{-}$	$\cdots$	$\cdots$
6438	$2.60^{+0.35}_{-0.35}$	5.67	1.000	9.35	1.14	$2.60^{+0.08}_{-0.10}$	5.67	1.000	$\cdots^{+}_{-}$	$\cdots$	$\cdots$
6451	$3.61^{+0.45}_{-0.45}$	6.67	1.000	1.93	1.14	$3.61^{+0.10}_{-0.09}$	6.67	1.000	$\cdots^{+}_{-}$	$\cdots$	$\cdots$
6462	$1.64^{+0.26}_{-0.26}$	3.33	1.000	24.40	3.10	$1.64^{+0.08}_{-0.14}$	3.33	1.000	$\cdots^{+}_{-}$	$\cdots$	$\cdots$
6478	$3.33^{+0.42}_{-0.42}$	6.67	1.000	0.53	0.10	$3.33^{+0.09}_{-0.10}$	6.67	0.947	$3.46^{+0.07}_{-0.04}$	7.33	0.053
6487	$3.08^{+0.40}_{-0.40}$	6.00	1.000	0.18	0.07	$3.08^{+0.05}_{-0.20}$	6.00	0.500	$3.17^{+0.19}_{-0.04}$	6.33	0.500
6488	$3.08^{+0.40}_{-0.40}$	5.67	1.000	1.72	0.14	$3.08^{+0.16}_{-0.16}$	5.67	1.000	$\cdots^{+}_{-}$	$\cdots$	$\cdots$
6490	$2.20^{+0.31}_{-0.39}$	6.00	0.930	2.34	0.76	$2.20^{+0.14}_{-0.12}$	6.00	0.681	$2.03^{+0.05}_{-0.12}$	5.67	0.237
6498	$2.48^{+0.34}_{-0.34}$	8.00	0.986	1.53	2.67	$2.48^{+0.16}_{-0.45}$	8.00	1.000	$\cdots^{+}_{-}$	$\cdots$	$\cdots$
6499	$1.80^{+0.27}_{-0.27}$	6.00	1.000	4.97	1.17	$1.80^{+0.24}_{-0.15}$	6.00	1.000	$\cdots^{+}_{-}$	$\cdots$	$\cdots$
6502	$2.70^{+0.40}_{-0.36}$	7.00	0.939	1.76	2.37	$2.70^{+0.16}_{-0.14}$	7.00	0.593	$3.02^{+0.15}_{-0.16}$	8.00	0.407
6504	$3.17^{+0.41}_{-0.41}$	6.00	1.000	0.88	0.10	$3.17^{+0.14}_{-0.16}$	6.00	1.000	$\cdots^{+}_{-}$	$\cdots$	$\cdots$
6506	$0.18^{+0.12}_{-0.12}$	4.00	1.000	14.45	1.10	$0.18^{+0.08}_{-0.07}$	4.00	1.000	$\cdots^{+}_{-}$	$\cdots$	$\cdots$
6508	$3.21^{+0.41}_{-0.41}$	6.00	1.000	0.83	0.96	$3.21^{+0.19}_{-0.21}$	6.00	1.000	$\cdots^{+}_{-}$	$\cdots$	$\cdots$
6518	$1.76^{+0.27}_{-0.27}$	6.33	0.987	1.11	0.58	$1.76^{+0.40}_{-0.19}$	6.33	1.000	$\cdots^{+}_{-}$	$\cdots$	$\cdots$
6519	$0.93^{+0.19}_{-0.19}$	1.33	1.000	3.64	0.01	$0.93^{+0.09}_{-0.11}$	1.33	1.000	$\cdots^{+}_{-}$	$\cdots$	$\cdots$
6520	$2.62^{+0.36}_{-0.35}$	7.00	1.000	5.38	6.10	$2.62^{+0.23}_{-0.14}$	7.00	1.000	$\cdots^{+}_{-}$	$\cdots$	$\cdots$
6523	$1.28^{+0.22}_{-0.22}$	1.33	1.000	11.61	1.63	$1.28^{+0.12}_{-0.15}$	1.33	1.000	$\cdots^{+}_{-}$	$\cdots$	$\cdots$
6527	$3.13^{+0.40}_{-0.41}$	6.33	1.000	1.38	0.97	$3.13^{+0.17}_{-0.24}$	6.33	1.000	$\cdots^{+}_{-}$	$\cdots$	$\cdots$
6533	$3.26^{+0.42}_{-0.42}$	6.33	1.000	0.40	0.06	$3.26^{+0.12}_{-0.21}$	6.33	1.000	$\cdots^{+}_{-}$	$\cdots$	$\cdots$
6539	$3.05^{+0.40}_{-0.40}$	5.67	1.000	13.65	0.81	$3.05^{+0.12}_{-0.14}$	5.67	1.000	$\cdots^{+}_{-}$	$\cdots$	$\cdots$
6542	$2.74^{+0.37}_{-0.37}$	5.33	1.000	8.08	0.24	$2.74^{+0.09}_{-0.09}$	5.33	1.000	$\cdots^{+}_{-}$	$\cdots$	$\cdots$
6543	$3.99^{+0.49}_{-0.49}$	5.67	1.000	0.07	0.00	$3.99^{+0.11}_{-0.12}$	5.67	1.000	$\cdots^{+}_{-}$	$\cdots$	$\cdots$
6554	$3.21^{+0.41}_{-0.41}$	6.33	1.000	0.96	0.24	$3.21^{+0.15}_{-0.20}$	6.33	1.000	$\cdots^{+}_{-}$	$\cdots$	$\cdots$
6558	$1.59^{+0.25}_{-0.25}$	4.33	1.000	4.83	0.08	$1.59^{+0.11}_{-0.10}$	4.33	1.000	$\cdots^{+}_{-}$	$\cdots$	$\cdots$
6576	$2.00^{+0.29}_{-1.91}$	7.33	0.959	2.53	2.79	$2.00^{+0.38}_{-0.36}$	7.33	0.970	$0.07^{+0.08}_{-0.06}$	7.33	0.030
6595	$2.85^{+0.38}_{-0.38}$	6.33	1.000	1.65	0.85	$2.85^{+0.27}_{-0.22}$	6.33	1.000	$\cdots^{+}_{-}$	$\cdots$	$\cdots$
6607	$2.46^{+0.34}_{-0.34}$	6.67	1.000	2.88	2.92	$2.46^{+0.08}_{-0.09}$	6.67	1.000	$\cdots^{+}_{-}$	$\cdots$	$\cdots$
6614	$1.63^{+0.26}_{-0.30}$	6.00	0.966	4.54	0.89	$1.63^{+0.18}_{-0.30}$	6.00	0.980	$1.31^{+0.02}_{-0.10}$	6.67	0.020

Table C.2—Continued

ID[a]	z_b[b]	t_b[c]	ODDS[d]	χ^2_ν[e]	$\chi^2_{\rm mod}$[f]	z_b1[g]	t_b1[c]	ODDS1[h]	z_b2[g]	t_b2[c]	ODDS2[h]
6627	$0.91^{+0.23}_{-0.19}$	6.33	0.895	6.15	1.02	$0.91^{+0.07}_{-0.08}$	6.33	0.841	$1.11^{+0.07}_{-0.06}$	6.00	0.159
6642	$2.54^{+0.35}_{-0.35}$	6.67	1.000	5.22	3.39	$2.54^{+0.08}_{-0.08}$	6.67	1.000	$\cdots\ ^{+}_{-}$	$\cdots$	$\cdots$
6645	$1.52^{+0.25}_{-0.25}$	4.00	1.000	4.49	0.05	$1.52^{+0.09}_{-0.08}$	4.00	1.000	$\cdots\ ^{+}_{-}$	$\cdots$	$\cdots$
6648	$1.16^{+0.21}_{-0.26}$	6.33	0.929	3.22	0.67	$1.16^{+0.12}_{-0.13}$	6.33	0.877	$0.94^{+0.09}_{-0.13}$	6.67	0.116
6649	$0.09^{+0.13}_{-0.09}$	3.00	0.953	3.99	0.52	$0.09^{+0.19}_{-0.08}$	3.00	1.000	$\cdots\ ^{+}_{-}$	$\cdots$	$\cdots$
6658	$1.86^{+0.28}_{-0.28}$	7.00	0.978	3.27	2.87	$1.86^{+0.38}_{-0.05}$	7.00	0.522	$1.77^{+0.04}_{-0.28}$	7.00	0.471
6670	$0.60^{+0.16}_{-0.16}$	3.67	1.000	7.49	2.60	$0.60^{+0.09}_{-0.09}$	3.67	1.000	$\cdots\ ^{+}_{-}$	$\cdots$	$\cdots$
6671	$2.54^{+0.35}_{-0.35}$	6.67	1.000	2.70	3.10	$2.54^{+0.18}_{-0.35}$	6.67	1.000	$\cdots\ ^{+}_{-}$	$\cdots$	$\cdots$
6673	$1.33^{+0.23}_{-0.23}$	4.00	1.000	4.34	0.34	$1.33^{+0.13}_{-0.12}$	4.00	1.000	$\cdots\ ^{+}_{-}$	$\cdots$	$\cdots$
6675	$2.85^{+0.38}_{-0.38}$	5.00	1.000	1.80	0.86	$2.85^{+0.09}_{-0.12}$	5.00	1.000	$\cdots\ ^{+}_{-}$	$\cdots$	$\cdots$
6680	$2.01^{+0.30}_{-0.29}$	5.67	1.000	7.10	0.13	$2.01^{+0.07}_{-0.30}$	5.67	0.790	$2.13^{+0.10}_{-0.05}$	5.67	0.210
6695	$3.06^{+0.40}_{-0.40}$	7.00	1.000	0.08	0.08	$3.06^{+0.10}_{-0.21}$	7.00	0.529	$3.28^{+0.15}_{-0.12}$	7.67	0.471
6700	$0.13^{+0.11}_{-0.11}$	3.00	1.000	5.31	0.25	$0.13^{+0.07}_{-0.08}$	3.00	1.000	$\cdots\ ^{+}_{-}$	$\cdots$	$\cdots$
6701	$3.22^{+0.41}_{-0.41}$	6.00	1.000	0.23	0.08	$3.22^{+0.15}_{-0.13}$	6.00	1.000	$\cdots\ ^{+}_{-}$	$\cdots$	$\cdots$
6710	$0.90^{+0.19}_{-0.19}$	5.67	1.000	5.78	0.23	$0.90^{+0.08}_{-0.08}$	5.67	1.000	$\cdots\ ^{+}_{-}$	$\cdots$	$\cdots$
6715	$2.14^{+0.31}_{-0.36}$	6.67	0.960	0.48	0.31	$2.14^{+0.36}_{-0.44}$	6.67	0.982	$0.06^{+0.08}_{-0.05}$	7.00	0.018
6722	$3.46^{+0.44}_{-0.44}$	8.00	1.000	3.17	1.34	$3.46^{+0.14}_{-0.18}$	8.00	1.000	$\cdots\ ^{+}_{-}$	$\cdots$	$\cdots$
6732	$3.30^{+0.42}_{-0.42}$	7.00	1.000	18.74	7.47	$3.30^{+0.08}_{-0.07}$	7.00	0.945	$3.51^{+0.05}_{-0.06}$	8.00	0.046
6747	$0.56^{+0.15}_{-0.15}$	1.00	1.000	4.14	0.62	$0.56^{+0.07}_{-0.07}$	1.00	1.000	$\cdots\ ^{+}_{-}$	$\cdots$	$\cdots$
6749	$1.44^{+0.24}_{-0.24}$	5.67	0.999	0.43	0.15	$1.44^{+0.19}_{-0.15}$	5.67	0.996	$1.22^{+0.03}_{-0.03}$	6.33	0.004
6754	$1.21^{+0.22}_{-0.22}$	6.00	1.000	6.45	0.29	$1.21^{+0.08}_{-0.08}$	6.00	1.000	$\cdots\ ^{+}_{-}$	$\cdots$	$\cdots$
6776	$0.11^{+0.38}_{-0.11}$	5.00	0.586	1.11	0.48	$0.11^{+0.11}_{-0.10}$	5.00	0.582	$0.44^{+0.11}_{-0.10}$	5.33	0.371
6778	$0.56^{+0.15}_{-0.15}$	2.33	0.987	9.68	0.41	$0.56^{+0.09}_{-0.10}$	2.33	0.987	$0.34^{+0.03}_{-0.04}$	1.33	0.013
6781	$0.48^{+0.20}_{-0.14}$	6.00	0.841	1.43	0.45	$0.48^{+0.11}_{-0.09}$	6.00	0.747	$0.65^{+0.07}_{-0.06}$	6.00	0.253
6782	$1.57^{+0.25}_{-0.25}$	6.00	1.000	1.36	0.09	$1.57^{+0.10}_{-0.09}$	6.00	1.000	$\cdots\ ^{+}_{-}$	$\cdots$	$\cdots$
6785	$1.37^{+0.23}_{-0.23}$	3.33	1.000	6.32	0.02	$1.37^{+0.08}_{-0.07}$	3.33	1.000	$\cdots\ ^{+}_{-}$	$\cdots$	$\cdots$
6808	$3.50^{+0.44}_{-0.44}$	6.33	1.000	2.33	1.28	$3.50^{+0.15}_{-0.15}$	6.33	1.000	$\cdots\ ^{+}_{-}$	$\cdots$	$\cdots$
6820	$3.67^{+0.46}_{-0.46}$	8.00	1.000	0.94	0.75	$3.67^{+0.14}_{-0.21}$	8.00	1.000	$\cdots\ ^{+}_{-}$	$\cdots$	$\cdots$
6821	$1.12^{+0.21}_{-0.21}$	4.33	1.000	12.81	1.24	$1.12^{+0.08}_{-0.07}$	4.33	1.000	$\cdots\ ^{+}_{-}$	$\cdots$	$\cdots$
6827	$3.31^{+0.42}_{-0.42}$	5.67	1.000	0.23	0.19	$3.31^{+0.14}_{-0.17}$	5.67	1.000	$\cdots\ ^{+}_{-}$	$\cdots$	$\cdots$
6834	$0.01^{+2.66}_{-0.01}$	4.67	0.855	29.41	17.72	$0.01^{+2.66}_{-0.01}$	4.67	0.855	$2.65^{+0.05}_{-0.06}$	5.00	1.000
6837	$2.73^{+0.37}_{-0.37}$	6.33	1.000	2.57	0.29	$2.73^{+0.11}_{-0.11}$	6.33	1.000	$\cdots\ ^{+}_{-}$	$\cdots$	$\cdots$
6839	$3.11^{+0.40}_{-0.40}$	6.33	1.000	0.44	0.07	$3.11^{+0.11}_{-0.13}$	6.33	1.000	$\cdots\ ^{+}_{-}$	$\cdots$	$\cdots$
6846	$0.73^{+0.36}_{-0.17}$	6.33	0.953	15.89	2.40	$0.73^{+0.08}_{-0.07}$	6.33	0.954	$1.09^{+0.05}_{-0.05}$	5.67	0.046
6853	$0.70^{+0.17}_{-0.17}$	5.33	1.000	9.27	1.02	$0.70^{+0.07}_{-0.07}$	5.33	1.000	$\cdots\ ^{+}_{-}$	$\cdots$	$\cdots$
6854	$2.26^{+0.32}_{-0.32}$	6.33	1.000	3.11	1.52	$2.26^{+0.21}_{-0.29}$	6.33	1.000	$\cdots\ ^{+}_{-}$	$\cdots$	$\cdots$

Table C.2—Continued

ID[a]	z_b[b]	t_b[c]	ODDS[d]	χ^2_ν[e]	$\chi^2_{\rm mod}$[f]	z_b1[g]	t_b1[c]	ODDS1[h]	z_b2[g]	t_b2[c]	ODDS2[h]
6862	$0.51^{+0.15}_{-0.15}$	2.33	1.000	89.64	1.38	$0.51^{+0.08}_{-0.07}$	2.33	1.000	$\cdots$ $^{+}_{-}$	$\cdots$	$\cdots$
6870	$1.26^{+0.22}_{-0.22}$	4.33	0.995	1.14	0.16	$1.26^{+0.07}_{-0.12}$	4.33	0.613	$1.37^{+0.16}_{-0.04}$	3.67	0.387
6874	$1.82^{+0.28}_{-0.28}$	3.33	1.000	5.68	0.91	$1.82^{+0.20}_{-0.15}$	3.33	1.000	$\cdots$ $^{+}_{-}$	$\cdots$	$\cdots$
6893	$0.07^{+0.10}_{-0.07}$	3.00	1.000	4.47	0.24	$0.07^{+0.08}_{-0.06}$	3.00	1.000	$\cdots$ $^{+}_{-}$	$\cdots$	$\cdots$
6894	$1.19^{+0.21}_{-0.22}$	5.67	0.997	3.47	0.34	$1.19^{+0.14}_{-0.11}$	5.67	0.985	$1.37^{+0.04}_{-0.04}$	4.67	0.012
6912	$3.25^{+0.42}_{-0.42}$	5.33	1.000	2.35	0.89	$3.25^{+0.21}_{-0.21}$	5.33	1.000	$\cdots$ $^{+}_{-}$	$\cdots$	$\cdots$
6919	$2.91^{+0.38}_{-0.38}$	6.33	1.000	0.93	0.56	$2.91^{+0.24}_{-0.17}$	6.33	1.000	$\cdots$ $^{+}_{-}$	$\cdots$	$\cdots$
6922	$1.33^{+0.23}_{-0.23}$	3.33	1.000	1.67	0.09	$1.33^{+0.09}_{-0.08}$	3.33	1.000	$\cdots$ $^{+}_{-}$	$\cdots$	$\cdots$
6933	$0.58^{+0.16}_{-0.15}$	5.00	1.000	6.27	0.05	$0.58^{+0.08}_{-0.08}$	5.00	1.000	$\cdots$ $^{+}_{-}$	$\cdots$	$\cdots$
6937	$2.91^{+0.38}_{-0.38}$	6.00	1.000	3.01	1.61	$2.91^{+0.23}_{-0.17}$	6.00	1.000	$\cdots$ $^{+}_{-}$	$\cdots$	$\cdots$
6939	$1.20^{+0.22}_{-0.41}$	6.00	0.897	7.55	0.38	$1.20^{+0.09}_{-0.08}$	6.00	0.897	$0.84^{+0.06}_{-0.09}$	6.33	0.103
6941	$2.45^{+0.34}_{-0.34}$	6.67	1.000	1.48	0.74	$2.45^{+0.09}_{-0.10}$	6.67	1.000	$\cdots$ $^{+}_{-}$	$\cdots$	$\cdots$
6953	$0.74^{+0.17}_{-0.17}$	6.00	1.000	2.21	0.63	$0.74^{+0.08}_{-0.07}$	6.00	1.000	$\cdots$ $^{+}_{-}$	$\cdots$	$\cdots$
6957	$1.56^{+0.25}_{-0.25}$	4.00	1.000	12.65	1.88	$1.56^{+0.09}_{-0.08}$	4.00	1.000	$\cdots$ $^{+}_{-}$	$\cdots$	$\cdots$
6959	$0.28^{+0.12}_{-0.12}$	3.67	1.000	16.35	5.43	$0.28^{+0.08}_{-0.08}$	3.67	1.000	$\cdots$ $^{+}_{-}$	$\cdots$	$\cdots$
6967	$2.02^{+0.30}_{-2.01}$	6.67	0.800	1.35	0.38	$2.02^{+0.25}_{-0.29}$	6.67	0.800	$0.04^{+0.10}_{-0.03}$	7.00	0.200
6974	$0.50^{+0.15}_{-0.15}$	5.67	1.000	17.02	0.38	$0.50^{+0.11}_{-0.08}$	5.67	1.000	$\cdots$ $^{+}_{-}$	$\cdots$	$\cdots$
6993	$0.57^{+0.15}_{-0.18}$	7.33	0.964	1.31	0.75	$0.57^{+0.18}_{-0.27}$	7.33	1.000	$\cdots$ $^{+}_{-}$	$\cdots$	$\cdots$
6997	$0.63^{+0.16}_{-0.16}$	3.67	1.000	5.08	0.13	$0.63^{+0.08}_{-0.08}$	3.67	1.000	$\cdots$ $^{+}_{-}$	$\cdots$	$\cdots$
6999	$3.09^{+0.40}_{-0.40}$	6.33	1.000	0.68	0.36	$3.09^{+0.13}_{-0.13}$	6.33	1.000	$\cdots$ $^{+}_{-}$	$\cdots$	$\cdots$
7012	$2.14^{+0.31}_{-0.31}$	5.00	1.000	8.12	3.42	$2.14^{+0.11}_{-0.11}$	5.00	1.000	$\cdots$ $^{+}_{-}$	$\cdots$	$\cdots$
7022	$1.66^{+0.26}_{-0.26}$	3.67	1.000	5.74	0.05	$1.66^{+0.10}_{-0.09}$	3.67	1.000	$\cdots$ $^{+}_{-}$	$\cdots$	$\cdots$
7025	$3.40^{+0.43}_{-0.43}$	8.00	1.000	11.21	0.97	$3.40^{+0.08}_{-0.07}$	8.00	1.000	$\cdots$ $^{+}_{-}$	$\cdots$	$\cdots$
7028	$1.56^{+0.25}_{-0.25}$	4.00	1.000	9.85	2.67	$1.56^{+0.13}_{-0.14}$	4.00	1.000	$\cdots$ $^{+}_{-}$	$\cdots$	$\cdots$
7036	$1.40^{+0.24}_{-0.24}$	4.00	1.000	2.65	0.02	$1.40^{+0.07}_{-0.08}$	4.00	1.000	$\cdots$ $^{+}_{-}$	$\cdots$	$\cdots$
7037	$0.01^{+0.10}_{-0.01}$	5.00	0.993	30.47	20.03	$0.01^{+0.10}_{-0.01}$	5.00	0.993	$2.70^{+0.02}_{-0.01}$	5.00	1.000
7046	$0.55^{+0.15}_{-0.15}$	5.33	1.000	1.45	0.28	$0.55^{+0.14}_{-0.12}$	5.33	1.000	$\cdots$ $^{+}_{-}$	$\cdots$	$\cdots$
7067	$1.51^{+0.25}_{-0.25}$	3.33	1.000	2.97	0.02	$1.51^{+0.09}_{-0.08}$	3.33	1.000	$\cdots$ $^{+}_{-}$	$\cdots$	$\cdots$
7071	$0.71^{+0.17}_{-0.17}$	5.33	1.000	9.53	0.65	$0.71^{+0.08}_{-0.07}$	5.33	1.000	$\cdots$ $^{+}_{-}$	$\cdots$	$\cdots$
7072	$2.10^{+0.30}_{-0.30}$	7.00	0.998	2.54	2.80	$2.10^{+0.26}_{-0.34}$	7.00	1.000	$\cdots$ $^{+}_{-}$	$\cdots$	$\cdots$
7076	$0.14^{+0.11}_{-0.11}$	6.00	1.000	2.38	2.00	$0.14^{+0.13}_{-0.10}$	6.00	1.000	$\cdots$ $^{+}_{-}$	$\cdots$	$\cdots$
7086	$0.68^{+0.17}_{-0.17}$	3.67	1.000	0.20	0.10	$0.68^{+0.08}_{-0.09}$	3.67	1.000	$\cdots$ $^{+}_{-}$	$\cdots$	$\cdots$
7104	$1.88^{+0.28}_{-1.81}$	6.67	0.842	0.50	0.07	$1.88^{+0.23}_{-0.24}$	6.67	0.842	$0.10^{+0.08}_{-0.07}$	7.00	0.158
7112	$1.12^{+0.21}_{-0.21}$	2.67	1.000	38.05	1.02	$1.12^{+0.08}_{-0.08}$	2.67	1.000	$\cdots$ $^{+}_{-}$	$\cdots$	$\cdots$
7121	$0.70^{+0.17}_{-0.17}$	2.00	1.000	10.04	0.53	$0.70^{+0.07}_{-0.08}$	2.00	1.000	$\cdots$ $^{+}_{-}$	$\cdots$	$\cdots$
7129	$1.34^{+0.23}_{-0.23}$	4.00	1.000	4.60	0.78	$1.34^{+0.12}_{-0.10}$	4.00	1.000	$\cdots$ $^{+}_{-}$	$\cdots$	$\cdots$

Table C.2—Continued

ID[a]	z_b[b]	t_b[c]	ODDS[d]	χ^2_ν[e]	$\chi^2_{\rm mod}$[f]	z_b1[g]	t_b1[c]	ODDS1[h]	z_b2[g]	t_b2[c]	ODDS2[h]
7131	$1.44^{+0.24}_{-0.24}$	2.33	1.000	31.24	0.04	$1.44^{+0.08}_{-0.08}$	2.33	1.000	$\cdots$ $^{+}_{-}$	$\cdots$	$\cdots$
7146	$2.65^{+0.36}_{-0.36}$	6.33	1.000	10.78	0.28	$2.65^{+0.08}_{-0.08}$	6.33	1.000	$\cdots$ $^{+}_{-}$	$\cdots$	$\cdots$
7148	$0.49^{+0.15}_{-0.28}$	4.00	0.858	3.31	0.42	$0.49^{+0.10}_{-0.10}$	4.00	0.858	$0.24^{+0.06}_{-0.07}$	5.00	0.142
7151	$3.35^{+0.43}_{-0.43}$	6.00	1.000	0.19	0.03	$3.35^{+0.15}_{-0.18}$	6.00	1.000	$\cdots$ $^{+}_{-}$	$\cdots$	$\cdots$
7172	$1.84^{+0.28}_{-0.28}$	1.33	0.998	3.63	0.32	$1.84^{+0.17}_{-0.20}$	1.33	0.991	$1.59^{+0.05}_{-0.05}$	1.67	0.009
7185	$0.70^{+0.17}_{-0.18}$	5.33	0.971	3.58	0.68	$0.70^{+0.08}_{-0.08}$	5.33	0.888	$0.59^{+0.03}_{-0.12}$	5.00	0.112
7188	$0.69^{+0.17}_{-0.22}$	6.00	0.937	2.74	1.46	$0.69^{+0.08}_{-0.09}$	6.00	0.913	$0.50^{+0.10}_{-0.07}$	5.33	0.087
7189	$3.02^{+0.39}_{-0.39}$	6.00	1.000	3.06	0.19	$3.02^{+0.15}_{-0.13}$	6.00	1.000	$\cdots$ $^{+}_{-}$	$\cdots$	$\cdots$
7193	$1.47^{+0.24}_{-0.24}$	3.67	1.000	1.67	0.09	$1.47^{+0.14}_{-0.04}$	3.67	0.539	$1.40^{+0.03}_{-0.16}$	4.33	0.461
7194	$1.53^{+0.31}_{-0.97}$	7.33	0.906	0.19	0.04	$1.53^{+0.46}_{-0.32}$	7.33	0.965	$0.54^{+0.11}_{-0.13}$	7.67	0.035
7199	$1.59^{+0.25}_{-0.25}$	6.00	1.000	9.19	2.32	$1.59^{+0.13}_{-0.11}$	6.00	1.000	$\cdots$ $^{+}_{-}$	$\cdots$	$\cdots$
7203	$0.49^{+0.15}_{-0.15}$	4.00	1.000	11.36	1.17	$0.49^{+0.08}_{-0.09}$	4.00	1.000	$\cdots$ $^{+}_{-}$	$\cdots$	$\cdots$
7209	$2.70^{+0.36}_{-0.36}$	7.67	1.000	12.06	10.52	$2.70^{+0.14}_{-0.24}$	7.67	1.000	$\cdots$ $^{+}_{-}$	$\cdots$	$\cdots$
7219	$2.03^{+0.30}_{-0.30}$	6.33	0.980	0.98	0.60	$2.03^{+0.41}_{-0.30}$	6.33	1.000	$\cdots$ $^{+}_{-}$	$\cdots$	$\cdots$
7227	$1.74^{+0.27}_{-0.27}$	5.33	1.000	6.91	0.76	$1.74^{+0.09}_{-0.07}$	5.33	0.510	$1.61^{+0.06}_{-0.11}$	5.33	0.491
7230	$2.53^{+0.35}_{-0.35}$	6.67	1.000	4.82	2.43	$2.53^{+0.08}_{-0.13}$	6.67	1.000	$\cdots$ $^{+}_{-}$	$\cdots$	$\cdots$
7234	$1.56^{+0.25}_{-0.25}$	4.33	1.000	6.22	0.07	$1.56^{+0.09}_{-0.09}$	4.33	1.000	$\cdots$ $^{+}_{-}$	$\cdots$	$\cdots$
7244	$3.00^{+0.39}_{-0.39}$	5.00	1.000	6.10	1.35	$3.00^{+0.16}_{-0.11}$	5.00	1.000	$\cdots$ $^{+}_{-}$	$\cdots$	$\cdots$
7246	$2.60^{+0.35}_{-0.35}$	4.00	1.000	0.31	0.03	$2.60^{+0.34}_{-0.26}$	4.00	1.000	$\cdots$ $^{+}_{-}$	$\cdots$	$\cdots$
7268	$0.93^{+0.19}_{-0.19}$	6.00	1.000	1.72	0.18	$0.93^{+0.11}_{-0.08}$	6.00	1.000	$\cdots$ $^{+}_{-}$	$\cdots$	$\cdots$
7269	$0.62^{+0.16}_{-0.16}$	3.33	1.000	23.51	0.08	$0.62^{+0.08}_{-0.08}$	3.33	1.000	$\cdots$ $^{+}_{-}$	$\cdots$	$\cdots$
7274	$3.48^{+0.44}_{-0.44}$	5.00	1.000	2.20	0.08	$3.48^{+0.12}_{-0.14}$	5.00	0.851	$3.18^{+0.16}_{-0.14}$	4.00	0.149
7290	$1.60^{+0.25}_{-0.25}$	6.00	1.000	2.86	0.49	$1.60^{+0.15}_{-0.20}$	6.00	1.000	$\cdots$ $^{+}_{-}$	$\cdots$	$\cdots$
7312	$2.76^{+0.37}_{-0.37}$	7.67	1.000	0.24	0.37	$2.76^{+0.20}_{-0.28}$	7.67	1.000	$\cdots$ $^{+}_{-}$	$\cdots$	$\cdots$
7313	$2.62^{+0.36}_{-0.35}$	6.67	1.000	7.14	4.90	$2.62^{+0.10}_{-0.10}$	6.67	1.000	$\cdots$ $^{+}_{-}$	$\cdots$	$\cdots$
7316	$0.25^{+0.20}_{-0.12}$	3.00	0.903	2.26	0.11	$0.25^{+0.10}_{-0.14}$	3.00	0.895	$0.42^{+0.09}_{-0.07}$	3.33	0.105
7318	$1.77^{+0.27}_{-0.27}$	6.00	0.999	0.14	0.03	$1.77^{+0.31}_{-0.19}$	6.00	1.000	$\cdots$ $^{+}_{-}$	$\cdots$	$\cdots$
7326	$0.16^{+3.25}_{-0.11}$	2.00	0.697	1.39	0.18	$0.16^{+0.26}_{-0.15}$	2.00	0.773	$2.24^{+0.21}_{-0.19}$	2.00	0.133
7328	$1.22^{+0.22}_{-0.22}$	1.00	1.000	6.49	1.02	$1.22^{+0.07}_{-0.07}$	1.00	1.000	$\cdots$ $^{+}_{-}$	$\cdots$	$\cdots$
7330	$1.78^{+0.27}_{-0.27}$	6.00	1.000	0.49	0.05	$1.78^{+0.23}_{-0.13}$	6.00	1.000	$\cdots$ $^{+}_{-}$	$\cdots$	$\cdots$
7338	$3.80^{+0.47}_{-0.47}$	6.67	1.000	0.49	0.25	$3.80^{+0.09}_{-0.20}$	6.67	0.560	$3.96^{+0.17}_{-0.07}$	7.33	0.440
7347	$2.44^{+0.34}_{-0.38}$	7.33	0.951	0.44	0.18	$2.44^{+0.19}_{-0.11}$	7.33	0.632	$2.24^{+0.09}_{-0.26}$	7.00	0.368
7370	$1.63^{+0.26}_{-0.26}$	4.00	1.000	3.04	0.03	$1.63^{+0.09}_{-0.11}$	4.00	1.000	$\cdots$ $^{+}_{-}$	$\cdots$	$\cdots$
7375	$3.17^{+0.41}_{-0.41}$	8.00	1.000	5.78	1.98	$3.17^{+0.08}_{-0.13}$	8.00	1.000	$\cdots$ $^{+}_{-}$	$\cdots$	$\cdots$
7392	$0.79^{+0.17}_{-0.18}$	5.00	1.000	1.21	0.05	$0.79^{+0.09}_{-0.09}$	5.00	1.000	$\cdots$ $^{+}_{-}$	$\cdots$	$\cdots$
7394	$1.35^{+0.23}_{-0.23}$	5.67	1.000	3.98	0.35	$1.35^{+0.09}_{-0.08}$	5.67	1.000	$\cdots$ $^{+}_{-}$	$\cdots$	$\cdots$

Table C.2—Continued

ID[a]	z_b[b]	t_b[c]	ODDS[d]	χ^2_ν[e]	$\chi^2_{\rm mod}$[f]	z_b1[g]	t_b1[c]	ODDS1[h]	z_b2[g]	t_b2[c]	ODDS2[h]
7398	$0.59^{+0.16}_{-0.16}$	6.67	1.000	26.09	1.43	$0.59^{+0.08}_{-0.08}$	6.67	1.000	$\cdots$ $^{+}_{-}$	$\cdots$	$\cdots$
7400	$3.61^{+0.45}_{-0.45}$	6.67	1.000	0.38	0.45	$3.61^{+0.17}_{-0.14}$	6.67	1.000	$\cdots$ $^{+}_{-}$	$\cdots$	$\cdots$
7406	$0.97^{+0.19}_{-0.19}$	1.67	1.000	10.02	0.64	$0.97^{+0.10}_{-0.08}$	1.67	1.000	$\cdots$ $^{+}_{-}$	$\cdots$	$\cdots$
7423	$2.76^{+0.37}_{-0.37}$	8.00	1.000	2.97	2.38	$2.76^{+0.11}_{-0.15}$	8.00	1.000	$\cdots$ $^{+}_{-}$	$\cdots$	$\cdots$
7428	$3.24^{+0.42}_{-0.46}$	5.33	0.956	2.53	0.82	$3.24^{+0.17}_{-0.16}$	5.33	0.837	$2.86^{+0.15}_{-0.12}$	4.00	0.130
7432	$1.84^{+0.28}_{-0.28}$	2.67	1.000	70.07	6.36	$1.84^{+0.11}_{-0.10}$	2.67	1.000	$\cdots$ $^{+}_{-}$	$\cdots$	$\cdots$
7452	$0.56^{+0.15}_{-0.15}$	4.67	1.000	2.81	0.04	$0.56^{+0.09}_{-0.08}$	4.67	1.000	$\cdots$ $^{+}_{-}$	$\cdots$	$\cdots$
7459	$0.59^{+0.16}_{-0.16}$	3.00	1.000	2.29	0.20	$0.59^{+0.05}_{-0.09}$	3.00	0.634	$0.65^{+0.09}_{-0.01}$	3.33	0.366
7469	$3.60^{+0.45}_{-0.45}$	6.33	1.000	0.71	0.19	$3.60^{+0.13}_{-0.13}$	6.33	1.000	$\cdots$ $^{+}_{-}$	$\cdots$	$\cdots$
7471	$2.53^{+0.35}_{-0.35}$	6.67	1.000	5.07	3.00	$2.53^{+0.12}_{-0.16}$	6.67	1.000	$\cdots$ $^{+}_{-}$	$\cdots$	$\cdots$
7478	$3.60^{+0.45}_{-0.45}$	6.00	1.000	0.46	0.34	$3.60^{+0.14}_{-0.16}$	6.00	1.000	$\cdots$ $^{+}_{-}$	$\cdots$	$\cdots$
7490	$0.71^{+0.17}_{-0.17}$	6.00	1.000	4.91	0.54	$0.71^{+0.07}_{-0.07}$	6.00	1.000	$\cdots$ $^{+}_{-}$	$\cdots$	$\cdots$
7492	$1.72^{+0.30}_{-0.27}$	6.00	0.969	2.02	0.24	$1.72^{+0.24}_{-0.29}$	6.00	0.963	$2.00^{+0.09}_{-0.04}$	6.00	0.020
7495	$0.12^{+0.11}_{-0.11}$	3.00	1.000	2.41	0.08	$0.12^{+0.07}_{-0.08}$	3.00	1.000	$\cdots$ $^{+}_{-}$	$\cdots$	$\cdots$
7506	$1.15^{+0.21}_{-0.21}$	3.67	1.000	2.40	0.34	$1.15^{+0.15}_{-0.10}$	3.67	1.000	$\cdots$ $^{+}_{-}$	$\cdots$	$\cdots$
7526	$2.49^{+0.34}_{-0.34}$	6.33	1.000	8.76	1.32	$2.49^{+0.08}_{-0.08}$	6.33	0.496	$2.26^{+0.11}_{-0.11}$	6.00	0.504
7529	$2.64^{+0.36}_{-0.36}$	4.33	1.000	0.48	0.03	$2.64^{+0.16}_{-0.25}$	4.33	1.000	$\cdots$ $^{+}_{-}$	$\cdots$	$\cdots$
7534	$2.99^{+0.39}_{-0.39}$	6.67	1.000	2.44	2.96	$2.99^{+0.28}_{-0.16}$	6.67	1.000	$\cdots$ $^{+}_{-}$	$\cdots$	$\cdots$
7555	$0.47^{+0.14}_{-0.14}$	3.67	1.000	0.17	0.01	$0.47^{+0.10}_{-0.08}$	3.67	1.000	$\cdots$ $^{+}_{-}$	$\cdots$	$\cdots$
7556	$0.53^{+0.15}_{-0.15}$	3.00	1.000	20.78	0.06	$0.53^{+0.07}_{-0.08}$	3.00	1.000	$\cdots$ $^{+}_{-}$	$\cdots$	$\cdots$
7559	$0.85^{+0.18}_{-0.18}$	3.67	1.000	14.85	0.34	$0.85^{+0.08}_{-0.08}$	3.67	1.000	$\cdots$ $^{+}_{-}$	$\cdots$	$\cdots$
7587	$2.63^{+0.36}_{-0.36}$	5.00	0.982	1.35	0.02	$2.63^{+0.10}_{-0.12}$	5.00	0.982	$0.05^{+0.04}_{-0.04}$	4.00	0.018
7593	$1.02^{+0.20}_{-0.20}$	3.67	1.000	8.27	4.98	$1.02^{+0.09}_{-0.10}$	3.67	1.000	$\cdots$ $^{+}_{-}$	$\cdots$	$\cdots$
7600	$3.25^{+0.42}_{-0.42}$	5.33	1.000	0.90	0.03	$3.25^{+0.08}_{-0.09}$	5.33	1.000	$\cdots$ $^{+}_{-}$	$\cdots$	$\cdots$
7608	$2.11^{+0.31}_{-0.30}$	7.00	1.000	3.63	2.19	$2.11^{+0.14}_{-0.15}$	7.00	1.000	$\cdots$ $^{+}_{-}$	$\cdots$	$\cdots$
7610	$2.75^{+0.37}_{-0.37}$	6.67	1.000	3.44	1.84	$2.75^{+0.14}_{-0.13}$	6.67	0.993	$3.00^{+0.04}_{-0.04}$	7.33	0.007
7613	$2.22^{+0.32}_{-0.32}$	7.00	0.983	0.23	0.12	$2.22^{+0.16}_{-0.42}$	7.00	0.970	$2.41^{+0.10}_{-0.03}$	7.33	0.025
7617	$3.12^{+0.40}_{-0.40}$	6.67	1.000	0.48	0.11	$3.12^{+0.09}_{-0.13}$	6.67	0.576	$3.29^{+0.15}_{-0.08}$	7.33	0.424
7633	$3.02^{+0.39}_{-0.39}$	6.67	1.000	1.16	0.24	$3.02^{+0.15}_{-0.17}$	6.67	1.000	$\cdots$ $^{+}_{-}$	$\cdots$	$\cdots$
7647	$1.62^{+0.26}_{-0.26}$	3.33	1.000	16.88	0.10	$1.62^{+0.09}_{-0.09}$	3.33	1.000	$\cdots$ $^{+}_{-}$	$\cdots$	$\cdots$
7658	$3.04^{+0.40}_{-0.40}$	6.00	1.000	0.60	0.08	$3.04^{+0.23}_{-0.16}$	6.00	1.000	$\cdots$ $^{+}_{-}$	$\cdots$	$\cdots$
7664	$0.72^{+0.17}_{-0.17}$	5.00	1.000	14.96	1.13	$0.72^{+0.08}_{-0.08}$	5.00	1.000	$\cdots$ $^{+}_{-}$	$\cdots$	$\cdots$
7669	$2.67^{+0.36}_{-0.36}$	7.00	1.000	5.28	2.99	$2.67^{+0.11}_{-0.14}$	7.00	1.000	$\cdots$ $^{+}_{-}$	$\cdots$	$\cdots$
7671	$3.90^{+0.48}_{-0.48}$	6.33	1.000	4.16	4.83	$3.90^{+0.16}_{-0.19}$	6.33	1.000	$\cdots$ $^{+}_{-}$	$\cdots$	$\cdots$
7675	$3.56^{+0.45}_{-0.45}$	4.00	1.000	1.39	1.45	$3.56^{+0.26}_{-0.27}$	4.00	1.000	$\cdots$ $^{+}_{-}$	$\cdots$	$\cdots$
7678	$0.70^{+0.17}_{-0.17}$	6.00	1.000	15.16	0.78	$0.70^{+0.07}_{-0.07}$	6.00	1.000	$\cdots$ $^{+}_{-}$	$\cdots$	$\cdots$

Table C.2—Continued

ID[a]	z_b[b]	t_b[c]	ODDS[d]	χ^2_ν[e]	$\chi^2_{\rm mod}$[f]	z_b1[g]	t_b1[c]	ODDS1[h]	z_b2[g]	t_b2[c]	ODDS2[h]
7681	$2.22^{+0.32}_{-0.32}$	5.67	1.000	1.89	0.28	$2.22^{+0.11}_{-0.12}$	5.67	1.000	$\cdots\ ^{+}_{-}$	···	···
7687	$0.21^{+0.12}_{-0.12}$	6.00	1.000	2.84	0.10	$0.21^{+0.07}_{-0.08}$	6.00	1.000	$\cdots\ ^{+}_{-}$	···	···
7688	$2.58^{+0.35}_{-0.35}$	3.33	1.000	2.83	0.01	$2.58^{+0.07}_{-0.08}$	3.33	1.000	$\cdots\ ^{+}_{-}$	···	···
7705	$1.32^{+0.23}_{-0.23}$	6.00	1.000	8.03	0.22	$1.32^{+0.09}_{-0.07}$	6.00	1.000	$\cdots\ ^{+}_{-}$	···	···
7710	$3.52^{+0.44}_{-0.44}$	7.67	1.000	2.14	2.93	$3.52^{+0.15}_{-0.10}$	7.67	0.636	$3.35^{+0.07}_{-0.16}$	7.00	0.364
7711	$2.21^{+0.32}_{-0.32}$	5.33	1.000	4.74	0.14	$2.21^{+0.11}_{-0.12}$	5.33	1.000	$\cdots\ ^{+}_{-}$	···	···
7712	$2.79^{+0.37}_{-0.37}$	3.33	1.000	0.34	0.01	$2.79^{+0.17}_{-0.11}$	3.33	1.000	$\cdots\ ^{+}_{-}$	···	···
7720	$2.72^{+0.37}_{-0.37}$	7.00	0.999	2.61	3.09	$2.72^{+0.19}_{-0.17}$	7.00	0.958	$3.01^{+0.10}_{-0.10}$	7.67	0.042
7725	$1.30^{+0.23}_{-0.22}$	3.33	1.000	5.61	0.02	$1.30^{+0.08}_{-0.07}$	3.33	1.000	$\cdots\ ^{+}_{-}$	···	···
7737	$0.45^{+0.14}_{-0.14}$	3.33	1.000	15.83	0.15	$0.45^{+0.08}_{-0.08}$	3.33	1.000	$\cdots\ ^{+}_{-}$	···	···
7738	$3.13^{+0.40}_{-0.41}$	8.00	1.000	1.47	0.63	$3.13^{+0.15}_{-0.34}$	8.00	1.000	$\cdots\ ^{+}_{-}$	···	···
7743	$0.58^{+0.16}_{-0.15}$	5.33	1.000	1.35	0.30	$0.58^{+0.11}_{-0.09}$	5.33	1.000	$\cdots\ ^{+}_{-}$	···	···
7750	$0.93^{+0.19}_{-0.19}$	1.00	1.000	2.57	0.08	$0.93^{+0.09}_{-0.08}$	1.00	1.000	$\cdots\ ^{+}_{-}$	···	···
7756	$1.46^{+0.24}_{-0.24}$	3.00	1.000	1.59	0.01	$1.46^{+0.09}_{-0.09}$	3.00	1.000	$\cdots\ ^{+}_{-}$	···	···
7758	$2.75^{+0.37}_{-0.37}$	7.00	1.000	4.02	3.63	$2.75^{+0.17}_{-0.12}$	7.00	0.960	$3.01^{+0.09}_{-0.09}$	7.67	0.040
7760	$2.53^{+0.35}_{-0.35}$	7.00	1.000	3.81	4.88	$2.53^{+0.08}_{-0.09}$	7.00	1.000	$\cdots\ ^{+}_{-}$	···	···
7762	$2.57^{+0.35}_{-0.35}$	8.00	1.000	29.58	4.14	$2.57^{+0.08}_{-0.09}$	8.00	1.000	$\cdots\ ^{+}_{-}$	···	···
7775	$0.51^{+0.15}_{-0.15}$	1.67	1.000	7.26	0.02	$0.51^{+0.08}_{-0.07}$	1.67	1.000	$\cdots\ ^{+}_{-}$	···	···
7780	$0.55^{+0.15}_{-0.15}$	2.33	1.000	7.51	0.05	$0.55^{+0.08}_{-0.08}$	2.33	1.000	$\cdots\ ^{+}_{-}$	···	···
7786	$2.73^{+0.37}_{-0.37}$	5.00	1.000	4.46	0.33	$2.73^{+0.07}_{-0.08}$	5.00	1.000	$\cdots\ ^{+}_{-}$	···	···
7815	$3.49^{+0.44}_{-0.44}$	5.33	1.000	0.05	0.01	$3.49^{+0.14}_{-0.19}$	5.33	1.000	$\cdots\ ^{+}_{-}$	···	···
7827	$1.08^{+0.20}_{-0.20}$	2.00	1.000	2.41	1.13	$1.08^{+0.09}_{-0.09}$	2.00	1.000	$\cdots\ ^{+}_{-}$	···	···
7845	$2.16^{+0.31}_{-0.31}$	5.33	1.000	2.24	1.21	$2.16^{+0.13}_{-0.18}$	5.33	1.000	$\cdots\ ^{+}_{-}$	···	···
7847	$0.31^{+0.13}_{-0.13}$	1.33	1.000	10.36	0.02	$0.31^{+0.07}_{-0.07}$	1.33	1.000	$\cdots\ ^{+}_{-}$	···	···
7862	$3.53^{+0.44}_{-0.44}$	6.00	1.000	0.76	0.13	$3.53^{+0.14}_{-0.17}$	6.00	1.000	$\cdots\ ^{+}_{-}$	···	···
7868	$3.24^{+0.42}_{-0.42}$	6.33	1.000	1.54	0.46	$3.24^{+0.13}_{-0.13}$	6.33	1.000	$\cdots\ ^{+}_{-}$	···	···
7874	$3.19^{+0.41}_{-0.41}$	6.67	1.000	0.80	0.57	$3.19^{+0.12}_{-0.16}$	6.67	0.997	$3.36^{+0.02}_{-0.02}$	7.33	0.003
7879	$0.15^{+3.13}_{-0.11}$	3.00	0.904	1.50	0.33	$0.15^{+0.20}_{-0.11}$	3.00	0.925	$3.30^{+0.10}_{-0.14}$	5.00	0.050
7900	$2.61^{+0.35}_{-0.35}$	6.33	1.000	2.29	1.08	$2.61^{+0.11}_{-0.10}$	6.33	1.000	$\cdots\ ^{+}_{-}$	···	···
7905	$0.71^{+0.37}_{-0.17}$	6.33	0.722	9.02	0.67	$0.71^{+0.07}_{-0.07}$	6.33	0.665	$1.04^{+0.09}_{-0.10}$	6.00	0.244
7907	$3.10^{+0.40}_{-0.40}$	6.00	1.000	2.54	2.03	$3.10^{+0.12}_{-0.12}$	6.00	1.000	$\cdots\ ^{+}_{-}$	···	···
7909	$2.54^{+0.35}_{-0.35}$	6.67	1.000	2.47	0.69	$2.54^{+0.11}_{-0.11}$	6.67	1.000	$\cdots\ ^{+}_{-}$	···	···
7938	$2.00^{+0.29}_{-0.29}$	6.67	1.000	2.32	1.68	$2.00^{+0.21}_{-0.22}$	6.67	1.000	$\cdots\ ^{+}_{-}$	···	···
7953	$0.07^{+2.24}_{-0.07}$	6.67	0.969	3.12	3.10	$0.07^{+0.07}_{-0.06}$	6.67	0.969	$2.34^{+0.04}_{-0.05}$	6.33	0.031
7957	$3.54^{+0.44}_{-0.44}$	5.33	1.000	1.24	0.04	$3.54^{+0.11}_{-0.13}$	5.33	1.000	$\cdots\ ^{+}_{-}$	···	···
7962	$1.40^{+0.24}_{-0.24}$	3.67	1.000	12.81	1.97	$1.40^{+0.19}_{-0.16}$	3.67	1.000	$\cdots\ ^{+}_{-}$	···	···

Table C.2—Continued

ID[a]	z_b[b]	t_b[c]	ODDS[d]	χ^2_ν[e]	$\chi^2_{\rm mod}$[f]	z_b1[g]	t_b1[c]	ODDS1[h]	z_b2[g]	t_b2[c]	ODDS2[h]
7966	$0.62^{+0.16}_{-0.16}$	5.00	1.000	3.78	0.28	$0.62^{+0.11}_{-0.11}$	5.00	1.000	$\cdots$ $^{+}_{-}$	$\cdots$	$\cdots$
7974	$1.36^{+0.23}_{-0.23}$	5.67	1.000	27.03	2.81	$1.36^{+0.07}_{-0.08}$	5.67	1.000	$\cdots$ $^{+}_{-}$	$\cdots$	$\cdots$
7983	$2.42^{+0.34}_{-0.34}$	6.67	1.000	2.83	0.27	$2.42^{+0.08}_{-0.09}$	6.67	0.688	$2.25^{+0.08}_{-0.11}$	6.33	0.312
7986	$2.62^{+0.36}_{-0.35}$	8.00	1.000	18.69	13.41	$2.62^{+0.14}_{-0.17}$	8.00	1.000	$\cdots$ $^{+}_{-}$	$\cdots$	$\cdots$
7994	$2.89^{+0.41}_{-0.38}$	6.67	0.947	1.82	1.79	$2.89^{+0.19}_{-0.18}$	6.67	0.625	$3.24^{+0.13}_{-0.16}$	7.67	0.375
7995	$1.37^{+0.23}_{-0.23}$	3.00	1.000	6.57	0.01	$1.37^{+0.08}_{-0.07}$	3.00	1.000	$\cdots$ $^{+}_{-}$	$\cdots$	$\cdots$
7998	$2.75^{+0.37}_{-0.37}$	6.67	1.000	2.29	1.34	$2.75^{+0.14}_{-0.14}$	6.67	1.000	$\cdots$ $^{+}_{-}$	$\cdots$	$\cdots$
8003	$3.01^{+0.39}_{-0.39}$	8.00	1.000	0.52	0.61	$3.01^{+0.16}_{-0.23}$	8.00	0.958	$2.74^{+0.04}_{-0.09}$	7.00	0.042
8006	$1.53^{+0.25}_{-0.25}$	7.00	0.975	1.03	1.25	$1.53^{+0.34}_{-0.16}$	7.00	0.989	$0.53^{+0.07}_{-0.06}$	7.33	0.011
8015	$0.21^{+0.12}_{-0.12}$	2.33	1.000	1.11	0.01	$0.21^{+0.07}_{-0.07}$	2.33	1.000	$\cdots$ $^{+}_{-}$	$\cdots$	$\cdots$
8017	$3.53^{+0.44}_{-0.44}$	5.33	1.000	2.21	1.77	$3.53^{+0.11}_{-0.11}$	5.33	1.000	$\cdots$ $^{+}_{-}$	$\cdots$	$\cdots$
8022	$3.71^{+0.46}_{-0.46}$	5.33	1.000	0.40	0.02	$3.71^{+0.10}_{-0.22}$	5.33	1.000	$\cdots$ $^{+}_{-}$	$\cdots$	$\cdots$
8024	$3.03^{+0.39}_{-0.39}$	6.67	1.000	0.35	0.09	$3.03^{+0.14}_{-0.14}$	6.67	0.959	$3.22^{+0.09}_{-0.05}$	7.33	0.041
8026	$0.53^{+0.15}_{-0.15}$	4.00	1.000	18.01	0.76	$0.53^{+0.08}_{-0.08}$	4.00	1.000	$\cdots$ $^{+}_{-}$	$\cdots$	$\cdots$
8037	$0.49^{+0.15}_{-0.15}$	4.67	1.000	1.04	0.68	$0.49^{+0.12}_{-0.10}$	4.67	1.000	$\cdots$ $^{+}_{-}$	$\cdots$	$\cdots$
8038	$0.15^{+0.11}_{-0.11}$	5.33	1.000	3.06	0.09	$0.15^{+0.08}_{-0.08}$	5.33	1.000	$\cdots$ $^{+}_{-}$	$\cdots$	$\cdots$
8040	$0.21^{+0.12}_{-0.12}$	4.00	1.000	12.73	1.29	$0.21^{+0.07}_{-0.07}$	4.00	1.000	$\cdots$ $^{+}_{-}$	$\cdots$	$\cdots$
8042	$3.12^{+0.40}_{-0.40}$	6.67	1.000	0.55	0.33	$3.12^{+0.12}_{-0.14}$	6.67	1.000	$\cdots$ $^{+}_{-}$	$\cdots$	$\cdots$
8049	$0.20^{+0.12}_{-0.12}$	2.67	1.000	18.28	0.76	$0.20^{+0.02}_{-0.08}$	2.67	0.437	$0.25^{+0.07}_{-0.03}$	3.00	0.563
8051	$1.11^{+0.21}_{-0.21}$	3.67	1.000	2.83	1.80	$1.11^{+0.08}_{-0.08}$	3.67	1.000	$\cdots$ $^{+}_{-}$	$\cdots$	$\cdots$
8053	$2.59^{+0.35}_{-0.35}$	6.67	1.000	1.19	1.00	$2.59^{+0.21}_{-0.19}$	6.67	1.000	$\cdots$ $^{+}_{-}$	$\cdots$	$\cdots$
8062	$3.91^{+0.48}_{-0.48}$	6.00	1.000	1.08	0.90	$3.91^{+0.15}_{-0.12}$	6.00	1.000	$\cdots$ $^{+}_{-}$	$\cdots$	$\cdots$
8069	$0.66^{+0.16}_{-0.16}$	3.67	1.000	27.44	1.13	$0.66^{+0.07}_{-0.10}$	3.67	1.000	$\cdots$ $^{+}_{-}$	$\cdots$	$\cdots$
8071	$3.01^{+0.39}_{-0.76}$	4.67	0.625	21.20	8.08	$3.01^{+0.12}_{-0.12}$	4.67	0.625	$2.35^{+0.18}_{-0.16}$	2.67	0.375
8082	$1.15^{+0.21}_{-0.21}$	1.00	1.000	0.76	0.31	$1.15^{+0.08}_{-0.11}$	1.00	1.000	$\cdots$ $^{+}_{-}$	$\cdots$	$\cdots$
8084	$0.59^{+0.16}_{-0.16}$	4.00	1.000	0.83	0.67	$0.59^{+0.11}_{-0.13}$	4.00	1.000	$\cdots$ $^{+}_{-}$	$\cdots$	$\cdots$
8092	$3.76^{+0.47}_{-0.47}$	5.33	1.000	0.07	0.00	$3.76^{+0.10}_{-0.12}$	5.33	1.000	$\cdots$ $^{+}_{-}$	$\cdots$	$\cdots$
8105	$3.43^{+0.43}_{-0.43}$	5.33	1.000	1.98	0.32	$3.43^{+0.10}_{-0.17}$	5.33	1.000	$\cdots$ $^{+}_{-}$	$\cdots$	$\cdots$
8125	$0.77^{+0.43}_{-0.17}$	6.33	0.748	20.97	2.41	$0.77^{+0.08}_{-0.08}$	6.33	0.747	$1.17^{+0.07}_{-0.07}$	5.67	0.253
8126	$3.14^{+0.41}_{-0.41}$	5.33	1.000	0.74	0.14	$3.14^{+0.24}_{-0.31}$	5.33	1.000	$\cdots$ $^{+}_{-}$	$\cdots$	$\cdots$
8138	$0.67^{+0.16}_{-0.16}$	5.00	1.000	1.26	0.02	$0.67^{+0.09}_{-0.09}$	5.00	1.000	$\cdots$ $^{+}_{-}$	$\cdots$	$\cdots$
8150	$1.75^{+0.27}_{-0.27}$	6.33	1.000	4.56	0.58	$1.75^{+0.09}_{-0.12}$	6.33	1.000	$\cdots$ $^{+}_{-}$	$\cdots$	$\cdots$
8156	$2.30^{+0.32}_{-0.32}$	6.33	1.000	0.02	0.00	$2.30^{+0.09}_{-0.09}$	6.33	1.000	$\cdots$ $^{+}_{-}$	$\cdots$	$\cdots$
8161	$2.14^{+0.31}_{-0.54}$	5.33	0.691	3.40	1.93	$2.14^{+0.15}_{-0.28}$	5.33	0.686	$1.70^{+0.16}_{-0.17}$	4.00	0.314
8171	$2.49^{+0.34}_{-0.34}$	6.67	1.000	2.73	1.25	$2.49^{+0.10}_{-0.21}$	6.67	1.000	$\cdots$ $^{+}_{-}$	$\cdots$	$\cdots$
8177	$2.80^{+0.37}_{-0.37}$	6.33	1.000	0.03	0.02	$2.80^{+0.15}_{-0.17}$	6.33	1.000	$\cdots$ $^{+}_{-}$	$\cdots$	$\cdots$

Table C.2—Continued

ID[a]	z_b[b]	t_b[c]	ODDS[d]	χ^2_ν[e]	$\chi^2_{\rm mod}$[f]	z_b1[g]	t_b1[c]	ODDS1[h]	z_b2[g]	t_b2[c]	ODDS2[h]
8181	$3.07^{+0.40}_{-0.40}$	4.33	1.000	3.08	0.06	$3.07^{+0.18}_{-0.11}$	4.33	1.000	$\cdots$ $^{+}_{-}$	$\cdots$	$\cdots$
8182	$3.13^{+0.40}_{-0.41}$	8.00	1.000	2.13	2.64	$3.13^{+0.17}_{-0.23}$	8.00	0.950	$2.86^{+0.04}_{-0.11}$	7.00	0.050
8196	$2.64^{+0.36}_{-0.36}$	7.00	1.000	4.16	2.57	$2.64^{+0.17}_{-0.13}$	7.00	1.000	$\cdots$ $^{+}_{-}$	$\cdots$	$\cdots$
8198	$2.83^{+0.38}_{-0.38}$	6.00	0.995	1.80	0.49	$2.83^{+0.21}_{-0.17}$	6.00	0.995	$0.22^{+0.03}_{-0.03}$	6.00	0.005
8207	$3.81^{+0.47}_{-0.47}$	4.33	1.000	1.06	0.54	$3.81^{+0.10}_{-0.15}$	4.33	0.786	$3.95^{+0.09}_{-0.04}$	5.33	0.214
8217	$3.36^{+0.43}_{-0.43}$	6.67	1.000	10.69	1.53	$3.36^{+0.09}_{-0.10}$	6.67	1.000	$\cdots$ $^{+}_{-}$	$\cdots$	$\cdots$
8230	$3.60^{+0.45}_{-0.45}$	8.00	1.000	4.64	0.72	$3.60^{+0.08}_{-0.08}$	8.00	1.000	$\cdots$ $^{+}_{-}$	$\cdots$	$\cdots$
8238	$1.21^{+0.22}_{-0.22}$	1.33	1.000	9.94	2.14	$1.21^{+0.11}_{-0.15}$	1.33	1.000	$\cdots$ $^{+}_{-}$	$\cdots$	$\cdots$
8242	$0.11^{+0.11}_{-0.11}$	5.67	0.983	2.76	0.40	$0.11^{+0.16}_{-0.09}$	5.67	0.991	$0.42^{+0.03}_{-0.03}$	6.33	0.009
8255	$1.19^{+0.21}_{-0.22}$	4.00	1.000	2.40	0.07	$1.19^{+0.08}_{-0.08}$	4.00	1.000	$\cdots$ $^{+}_{-}$	$\cdots$	$\cdots$
8257	$0.49^{+0.15}_{-0.15}$	3.00	1.000	55.24	1.84	$0.49^{+0.07}_{-0.08}$	3.00	1.000	$\cdots$ $^{+}_{-}$	$\cdots$	$\cdots$
8259	$0.62^{+0.16}_{-0.16}$	3.67	1.000	0.80	0.58	$0.62^{+0.11}_{-0.15}$	3.67	1.000	$\cdots$ $^{+}_{-}$	$\cdots$	$\cdots$
8261	$1.36^{+0.23}_{-0.23}$	1.33	1.000	17.88	0.00	$1.36^{+0.09}_{-0.08}$	1.33	1.000	$\cdots$ $^{+}_{-}$	$\cdots$	$\cdots$
8262	$2.21^{+0.32}_{-0.32}$	6.00	1.000	3.96	1.56	$2.21^{+0.10}_{-0.11}$	6.00	1.000	$\cdots$ $^{+}_{-}$	$\cdots$	$\cdots$
8270	$1.53^{+0.25}_{-0.25}$	5.33	1.000	2.90	0.04	$1.53^{+0.10}_{-0.09}$	5.33	1.000	$\cdots$ $^{+}_{-}$	$\cdots$	$\cdots$
8275	$0.69^{+0.17}_{-0.17}$	3.67	1.000	17.46	0.12	$0.69^{+0.07}_{-0.07}$	3.67	1.000	$\cdots$ $^{+}_{-}$	$\cdots$	$\cdots$
8283	$2.11^{+0.31}_{-0.30}$	2.33	1.000	42.17	3.46	$2.11^{+0.13}_{-0.13}$	2.33	1.000	$\cdots$ $^{+}_{-}$	$\cdots$	$\cdots$
8293	$2.03^{+0.30}_{-1.99}$	6.00	0.963	0.85	0.04	$2.03^{+0.06}_{-0.21}$	6.00	0.582	$2.12^{+0.25}_{-0.03}$	6.00	0.385
8294	$1.21^{+0.22}_{-0.42}$	6.00	0.834	4.92	0.63	$1.21^{+0.11}_{-0.11}$	6.00	0.834	$0.85^{+0.14}_{-0.12}$	6.33	0.166
8304	$3.34^{+0.43}_{-0.42}$	8.00	1.000	2.35	1.47	$3.34^{+0.13}_{-0.24}$	8.00	0.994	$3.06^{+0.04}_{-0.04}$	7.00	0.006
8311	$2.72^{+0.37}_{-0.37}$	6.00	1.000	1.27	0.07	$2.72^{+0.10}_{-0.09}$	6.00	1.000	$\cdots$ $^{+}_{-}$	$\cdots$	$\cdots$
8314	$0.84^{+0.18}_{-0.18}$	2.00	1.000	28.62	0.21	$0.84^{+0.07}_{-0.08}$	2.00	1.000	$\cdots$ $^{+}_{-}$	$\cdots$	$\cdots$
8316	$0.57^{+0.15}_{-0.15}$	1.33	1.000	59.69	0.82	$0.57^{+0.07}_{-0.07}$	1.33	1.000	$\cdots$ $^{+}_{-}$	$\cdots$	$\cdots$
8327	$2.89^{+0.38}_{-0.38}$	5.00	0.994	4.38	3.75	$2.89^{+0.21}_{-0.18}$	5.00	0.994	$2.20^{+0.05}_{-0.04}$	3.00	0.006
8337	$2.60^{+0.35}_{-0.35}$	6.67	1.000	2.44	2.56	$2.60^{+0.15}_{-0.16}$	6.67	1.000	$\cdots$ $^{+}_{-}$	$\cdots$	$\cdots$
8351	$1.44^{+0.24}_{-0.43}$	5.33	0.837	14.77	1.16	$1.44^{+0.12}_{-0.10}$	5.33	0.684	$1.21^{+0.09}_{-0.09}$	6.00	0.257
8354	$2.95^{+0.39}_{-0.39}$	6.00	1.000	2.74	0.54	$2.95^{+0.14}_{-0.11}$	6.00	1.000	$\cdots$ $^{+}_{-}$	$\cdots$	$\cdots$
8355	$2.15^{+0.31}_{-0.46}$	6.33	0.779	2.48	1.41	$2.15^{+0.20}_{-0.24}$	6.33	0.708	$1.81^{+0.10}_{-0.22}$	6.00	0.292
8363	$1.64^{+0.26}_{-0.26}$	1.67	1.000	3.03	0.35	$1.64^{+0.13}_{-0.13}$	1.67	1.000	$\cdots$ $^{+}_{-}$	$\cdots$	$\cdots$
8372	$0.43^{+0.14}_{-0.24}$	3.33	0.583	27.71	0.12	$0.43^{+0.07}_{-0.07}$	3.33	0.574	$0.24^{+0.07}_{-0.10}$	3.00	0.426
8374	$1.18^{+0.21}_{-0.33}$	4.00	0.957	5.53	0.27	$1.18^{+0.08}_{-0.09}$	4.00	0.872	$1.05^{+0.04}_{-0.07}$	5.33	0.085
8387	$3.01^{+0.39}_{-0.39}$	7.00	1.000	0.64	0.38	$3.01^{+0.11}_{-0.17}$	7.00	0.697	$3.20^{+0.18}_{-0.08}$	7.33	0.303
8392	$1.34^{+0.23}_{-0.23}$	4.00	1.000	1.69	0.06	$1.34^{+0.14}_{-0.15}$	4.00	1.000	$\cdots$ $^{+}_{-}$	$\cdots$	$\cdots$
8398	$0.90^{+0.28}_{-0.19}$	6.33	0.737	2.89	2.43	$0.90^{+0.10}_{-0.14}$	6.33	0.625	$1.12^{+0.11}_{-0.12}$	6.00	0.354
8409	$2.93^{+0.38}_{-0.38}$	5.00	1.000	4.51	2.31	$2.93^{+0.10}_{-0.11}$	5.00	1.000	$\cdots$ $^{+}_{-}$	$\cdots$	$\cdots$
8419	$3.73^{+0.46}_{-0.46}$	6.33	1.000	0.04	0.01	$3.73^{+0.15}_{-0.13}$	6.33	1.000	$\cdots$ $^{+}_{-}$	$\cdots$	$\cdots$

Table C.2—Continued

ID[a]	z_b[b]	t_b[c]	ODDS[d]	χ^2_ν[e]	$\chi^2_{\rm mod}$[f]	z_b1[g]	t_b1[c]	ODDS1[h]	z_b2[g]	t_b2[c]	ODDS2[h]
8428	$0.55^{+1.09}_{-0.15}$	7.33	0.797	0.90	1.38	$0.55^{+0.19}_{-0.21}$	7.33	0.806	$1.54^{+0.22}_{-0.14}$	7.00	0.194
8446	$2.76^{+0.37}_{-0.37}$	6.67	1.000	4.75	3.43	$2.76^{+0.21}_{-0.13}$	6.67	1.000	$\cdots\ ^{+}_{-}$	$\cdots$	$\cdots$
8449	$3.45^{+0.44}_{-0.44}$	6.67	1.000	1.26	1.51	$3.45^{+0.23}_{-0.15}$	6.67	1.000	$\cdots\ ^{+}_{-}$	$\cdots$	$\cdots$
8454	$0.44^{+0.14}_{-0.14}$	3.67	1.000	4.62	0.11	$0.44^{+0.08}_{-0.07}$	3.67	1.000	$\cdots\ ^{+}_{-}$	$\cdots$	$\cdots$
8461	$1.51^{+0.25}_{-0.25}$	3.00	1.000	1.62	0.00	$1.51^{+0.08}_{-0.08}$	3.00	1.000	$\cdots\ ^{+}_{-}$	$\cdots$	$\cdots$
8467	$2.54^{+0.35}_{-0.35}$	6.33	1.000	0.60	0.12	$2.54^{+0.15}_{-0.18}$	6.33	0.979	$2.32^{+0.04}_{-0.08}$	6.00	0.021
8486	$2.45^{+0.34}_{-0.34}$	7.00	1.000	3.05	0.98	$2.45^{+0.11}_{-0.21}$	7.00	1.000	$\cdots\ ^{+}_{-}$	$\cdots$	$\cdots$
8491	$2.02^{+0.48}_{-0.30}$	6.67	0.813	0.91	0.18	$2.02^{+0.13}_{-0.36}$	6.67	0.525	$2.25^{+0.12}_{-0.10}$	7.00	0.330
8501	$1.34^{+0.23}_{-0.23}$	6.00	1.000	5.69	0.88	$1.34^{+0.11}_{-0.09}$	6.00	1.000	$\cdots\ ^{+}_{-}$	$\cdots$	$\cdots$
8504	$1.69^{+0.30}_{-0.26}$	6.33	0.968	3.40	3.62	$1.69^{+0.45}_{-0.19}$	6.33	1.000	$\cdots\ ^{+}_{-}$	$\cdots$	$\cdots$
8520	$2.69^{+0.36}_{-0.36}$	7.00	1.000	0.17	0.08	$2.69^{+0.19}_{-0.14}$	7.00	1.000	$\cdots\ ^{+}_{-}$	$\cdots$	$\cdots$
8523	$0.48^{+0.15}_{-0.14}$	6.33	1.000	2.36	0.29	$0.48^{+0.08}_{-0.08}$	6.33	1.000	$\cdots\ ^{+}_{-}$	$\cdots$	$\cdots$
8530	$0.14^{+3.21}_{-0.11}$	3.33	0.735	3.14	1.13	$0.14^{+0.18}_{-0.13}$	3.33	0.753	$3.26^{+0.19}_{-0.20}$	5.33	0.247
8551	$0.86^{+0.18}_{-0.18}$	3.33	1.000	30.40	1.22	$0.86^{+0.08}_{-0.08}$	3.33	1.000	$\cdots\ ^{+}_{-}$	$\cdots$	$\cdots$
8553	$1.70^{+0.26}_{-0.27}$	3.67	1.000	1.58	0.09	$1.70^{+0.17}_{-0.14}$	3.67	1.000	$\cdots\ ^{+}_{-}$	$\cdots$	$\cdots$
8555	$2.72^{+0.37}_{-0.37}$	7.00	1.000	14.47	4.66	$2.72^{+0.09}_{-0.09}$	7.00	1.000	$\cdots\ ^{+}_{-}$	$\cdots$	$\cdots$
8561	$2.68^{+0.36}_{-0.36}$	6.67	1.000	3.16	2.03	$2.68^{+0.08}_{-0.09}$	6.67	1.000	$\cdots\ ^{+}_{-}$	$\cdots$	$\cdots$
8576	$0.53^{+0.15}_{-0.15}$	1.33	1.000	17.21	0.02	$0.53^{+0.07}_{-0.07}$	1.33	1.000	$\cdots\ ^{+}_{-}$	$\cdots$	$\cdots$
8577	$1.36^{+0.23}_{-0.23}$	5.67	1.000	4.31	0.41	$1.36^{+0.09}_{-0.10}$	5.67	0.824	$1.50^{+0.10}_{-0.05}$	4.00	0.176
8580	$3.44^{+0.43}_{-0.43}$	6.33	1.000	1.87	0.84	$3.44^{+0.10}_{-0.10}$	6.33	1.000	$\cdots\ ^{+}_{-}$	$\cdots$	$\cdots$
8585	$1.45^{+0.24}_{-0.24}$	3.00	1.000	4.43	0.01	$1.45^{+0.07}_{-0.08}$	3.00	1.000	$\cdots\ ^{+}_{-}$	$\cdots$	$\cdots$
8597	$1.58^{+0.25}_{-0.30}$	6.00	0.955	2.24	1.42	$1.58^{+0.16}_{-0.19}$	6.00	0.938	$1.30^{+0.09}_{-0.08}$	6.33	0.062
8603	$2.15^{+0.31}_{-0.31}$	5.33	1.000	8.03	1.56	$2.15^{+0.10}_{-0.16}$	5.33	1.000	$\cdots\ ^{+}_{-}$	$\cdots$	$\cdots$
8614	$2.74^{+0.37}_{-0.37}$	6.33	1.000	2.93	0.04	$2.74^{+0.07}_{-0.07}$	6.33	1.000	$\cdots\ ^{+}_{-}$	$\cdots$	$\cdots$
8624	$0.70^{+0.17}_{-0.17}$	3.33	1.000	10.69	0.19	$0.70^{+0.08}_{-0.08}$	3.33	1.000	$\cdots\ ^{+}_{-}$	$\cdots$	$\cdots$
8626	$1.85^{+0.28}_{-0.28}$	6.33	0.988	3.39	2.82	$1.85^{+0.38}_{-0.34}$	6.33	1.000	$\cdots\ ^{+}_{-}$	$\cdots$	$\cdots$
8629	$0.60^{+0.16}_{-0.16}$	4.33	1.000	3.19	0.78	$0.60^{+0.09}_{-0.09}$	4.33	1.000	$\cdots\ ^{+}_{-}$	$\cdots$	$\cdots$
8637	$2.41^{+0.33}_{-0.33}$	6.67	1.000	0.75	0.07	$2.41^{+0.11}_{-0.18}$	6.67	1.000	$\cdots\ ^{+}_{-}$	$\cdots$	$\cdots$
8650	$2.91^{+0.38}_{-0.38}$	6.33	1.000	1.85	1.80	$2.91^{+0.22}_{-0.17}$	6.33	1.000	$\cdots\ ^{+}_{-}$	$\cdots$	$\cdots$
8653	$1.33^{+0.23}_{-0.23}$	6.00	1.000	21.83	0.64	$1.33^{+0.08}_{-0.08}$	6.00	1.000	$\cdots\ ^{+}_{-}$	$\cdots$	$\cdots$
8671	$3.17^{+0.41}_{-0.41}$	5.33	1.000	0.04	0.01	$3.17^{+0.19}_{-0.34}$	5.33	1.000	$\cdots\ ^{+}_{-}$	$\cdots$	$\cdots$
8680	$1.06^{+0.20}_{-0.20}$	3.33	1.000	21.34	0.69	$1.06^{+0.08}_{-0.08}$	3.33	1.000	$\cdots\ ^{+}_{-}$	$\cdots$	$\cdots$
8686	$1.78^{+0.27}_{-0.27}$	2.00	1.000	23.75	4.76	$1.78^{+0.10}_{-0.10}$	2.00	1.000	$\cdots\ ^{+}_{-}$	$\cdots$	$\cdots$
8687	$1.76^{+0.68}_{-0.27}$	3.67	0.705	3.43	1.46	$1.76^{+0.16}_{-0.32}$	3.67	0.514	$2.01^{+0.73}_{-0.09}$	3.67	0.486
8693	$0.43^{+0.14}_{-0.14}$	3.67	1.000	9.21	0.09	$0.43^{+0.07}_{-0.07}$	3.67	1.000	$\cdots\ ^{+}_{-}$	$\cdots$	$\cdots$
8698	$2.73^{+0.38}_{-0.37}$	4.00	0.969	1.67	0.08	$2.73^{+0.17}_{-0.31}$	4.00	0.636	$3.00^{+0.25}_{-0.10}$	5.33	0.363

Table C.2—Continued

ID[a]	z_b[b]	t_b[c]	ODDS[d]	χ^2_ν[e]	$\chi^2_{\rm mod}$[f]	z_b1[g]	t_b1[c]	ODDS1[h]	z_b2[g]	t_b2[c]	ODDS2[h]
8702	$1.82^{+0.42}_{-0.28}$	6.33	0.795	0.87	0.34	$1.82^{+0.08}_{-0.23}$	6.33	0.374	$1.99^{+0.37}_{-0.09}$	6.33	0.605
8705	$2.65^{+0.36}_{-0.36}$	7.00	1.000	1.43	0.89	$2.65^{+0.27}_{-0.14}$	7.00	1.000	··· $^{+}_{-}$	···	···
8710	$1.73^{+0.50}_{-0.27}$	4.00	0.838	5.21	0.82	$1.73^{+0.20}_{-0.17}$	4.00	0.820	$2.17^{+0.17}_{-0.09}$	5.67	0.130
8721	$3.40^{+0.43}_{-0.43}$	8.00	1.000	0.38	0.34	$3.40^{+0.15}_{-0.18}$	8.00	0.927	$3.19^{+0.03}_{-0.16}$	7.00	0.073
8731	$2.13^{+0.31}_{-2.10}$	6.67	0.872	0.14	0.17	$2.13^{+0.32}_{-0.57}$	6.67	0.922	$0.05^{+0.10}_{-0.04}$	7.00	0.078
8740	$1.47^{+0.24}_{-0.24}$	4.33	1.000	4.32	0.41	$1.47^{+0.17}_{-0.18}$	4.33	1.000	··· $^{+}_{-}$	···	···
8741	$2.99^{+0.39}_{-0.39}$	8.00	1.000	11.01	4.32	$2.99^{+0.09}_{-0.14}$	8.00	0.886	$2.82^{+0.03}_{-0.07}$	7.33	0.085
8744	$0.73^{+0.17}_{-0.17}$	6.67	1.000	4.86	1.13	$0.73^{+0.10}_{-0.07}$	6.67	1.000	··· $^{+}_{-}$	···	···
8749	$0.75^{+0.17}_{-0.17}$	2.33	0.980	60.04	0.59	$0.75^{+0.10}_{-0.08}$	2.33	0.980	$1.87^{+0.04}_{-0.04}$	1.33	0.020
8750	$2.99^{+0.39}_{-0.39}$	6.00	1.000	0.78	0.11	$2.99^{+0.21}_{-0.14}$	6.00	1.000	··· $^{+}_{-}$	···	···
8757	$2.89^{+0.38}_{-0.38}$	6.33	1.000	4.03	0.33	$2.89^{+0.05}_{-0.10}$	6.33	0.607	$2.97^{+0.10}_{-0.03}$	6.67	0.393
8759	$3.23^{+0.41}_{-0.41}$	7.00	1.000	0.10	0.01	$3.23^{+0.08}_{-0.08}$	7.00	0.743	$3.37^{+0.12}_{-0.06}$	7.33	0.257
8765	$1.56^{+0.25}_{-0.25}$	6.00	1.000	5.74	0.67	$1.56^{+0.08}_{-0.08}$	6.00	1.000	··· $^{+}_{-}$	···	···
8768	$2.74^{+0.37}_{-0.37}$	6.33	1.000	5.86	4.20	$2.74^{+0.16}_{-0.16}$	6.33	1.000	··· $^{+}_{-}$	···	···
8782	$0.10^{+0.11}_{-0.10}$	3.00	1.000	16.32	0.80	$0.10^{+0.07}_{-0.07}$	3.00	1.000	··· $^{+}_{-}$	···	···
8801	$1.41^{+0.24}_{-0.24}$	4.00	1.000	3.94	0.51	$1.41^{+0.09}_{-0.09}$	4.00	0.994	$1.31^{+0.01}_{-0.03}$	5.33	0.006
8805	$1.70^{+0.57}_{-1.52}$	7.00	0.566	0.49	0.47	$1.70^{+0.43}_{-0.28}$	7.00	0.580	$0.47^{+0.22}_{-0.20}$	7.33	0.339
8810	$0.70^{+0.17}_{-0.17}$	3.67	1.000	23.84	2.27	$0.70^{+0.07}_{-0.07}$	3.67	1.000	··· $^{+}_{-}$	···	···
8812	$3.36^{+0.43}_{-0.43}$	5.67	1.000	3.53	0.54	$3.36^{+0.14}_{-0.16}$	5.67	1.000	··· $^{+}_{-}$	···	···
8816	$2.40^{+0.33}_{-0.33}$	6.67	0.993	2.35	1.59	$2.40^{+0.18}_{-0.41}$	6.67	1.000	··· $^{+}_{-}$	···	···
8822	$1.95^{+0.50}_{-0.29}$	3.67	0.953	4.09	0.62	$1.95^{+0.43}_{-0.27}$	3.67	0.969	$2.52^{+0.12}_{-0.14}$	5.00	0.031
8841	$2.73^{+0.37}_{-0.37}$	8.00	1.000	0.66	0.38	$2.73^{+0.14}_{-0.19}$	8.00	1.000	··· $^{+}_{-}$	···	···
8844	$3.53^{+0.44}_{-0.44}$	4.67	1.000	0.48	0.21	$3.53^{+0.16}_{-0.21}$	4.67	0.970	$3.71^{+0.09}_{-0.02}$	5.33	0.030
8852	$1.96^{+0.41}_{-0.29}$	7.67	0.819	0.52	0.49	$1.96^{+0.18}_{-0.43}$	7.67	0.627	$2.26^{+0.23}_{-0.12}$	8.00	0.373
8872	$1.43^{+0.24}_{-0.24}$	4.00	1.000	3.11	0.65	$1.43^{+0.13}_{-0.19}$	4.00	1.000	··· $^{+}_{-}$	···	···
8880	$1.04^{+0.20}_{-0.20}$	3.00	1.000	17.46	0.13	$1.04^{+0.09}_{-0.08}$	3.00	1.000	··· $^{+}_{-}$	···	···
8893	$2.15^{+0.31}_{-0.45}$	6.00	0.843	2.73	0.91	$2.15^{+0.34}_{-0.08}$	6.00	0.546	$2.03^{+0.04}_{-0.12}$	6.00	0.243
8918	$2.25^{+0.32}_{-0.32}$	5.67	1.000	3.10	1.00	$2.25^{+0.13}_{-0.13}$	5.67	1.000	··· $^{+}_{-}$	···	···
8924	$1.75^{+0.27}_{-0.27}$	4.00	1.000	9.60	0.92	$1.75^{+0.24}_{-0.17}$	4.00	1.000	··· $^{+}_{-}$	···	···
8930	$1.28^{+0.22}_{-0.22}$	5.67	1.000	0.64	0.57	$1.28^{+0.16}_{-0.13}$	5.67	1.000	··· $^{+}_{-}$	···	···
8941	$1.34^{+0.23}_{-0.23}$	6.33	1.000	3.43	0.26	$1.34^{+0.11}_{-0.09}$	6.33	0.972	$1.23^{+0.02}_{-0.05}$	6.67	0.028
8942	$1.40^{+0.24}_{-0.24}$	7.00	0.995	0.78	0.61	$1.40^{+0.20}_{-0.12}$	7.00	0.995	$1.98^{+0.03}_{-0.03}$	7.00	0.005
8948	$3.38^{+0.43}_{-0.43}$	6.33	1.000	2.04	1.38	$3.38^{+0.19}_{-0.34}$	6.33	1.000	··· $^{+}_{-}$	···	···
8950	$2.83^{+0.38}_{-0.38}$	5.67	1.000	1.92	0.02	$2.83^{+0.08}_{-0.08}$	5.67	1.000	··· $^{+}_{-}$	···	···
8954	$0.08^{+3.10}_{-0.08}$	2.00	0.648	4.48	2.75	$0.08^{+0.10}_{-0.07}$	2.00	0.648	$3.06^{+0.21}_{-0.15}$	3.33	0.352
8964	$3.37^{+0.43}_{-0.43}$	6.33	1.000	2.66	2.38	$3.37^{+0.11}_{-0.15}$	6.33	1.000	··· $^{+}_{-}$	···	···

Table C.2—Continued

ID[a]	z_b[b]	t_b[c]	ODDS[d]	χ^2_ν[e]	$\chi^2_{\rm mod}$[f]	z_b1[g]	t_b1[c]	ODDS1[h]	z_b2[g]	t_b2[c]	ODDS2[h]
8972	$1.46^{+0.24}_{-0.24}$	4.00	1.000	3.92	0.38	$1.46^{+0.11}_{-0.11}$	4.00	1.000	$\cdots$ $^{+}_{-}$	$\cdots$	$\cdots$
8994	$2.04^{+0.30}_{-0.30}$	2.00	0.987	5.61	0.30	$2.04^{+0.12}_{-0.16}$	2.00	0.665	$2.24^{+0.17}_{-0.08}$	1.67	0.335
8997	$1.13^{+0.21}_{-0.21}$	4.00	1.000	1.40	0.18	$1.13^{+0.12}_{-0.13}$	4.00	1.000	$\cdots$ $^{+}_{-}$	$\cdots$	$\cdots$
9000	$2.64^{+0.36}_{-0.36}$	5.67	1.000	7.50	0.09	$2.64^{+0.08}_{-0.08}$	5.67	1.000	$\cdots$ $^{+}_{-}$	$\cdots$	$\cdots$
9006	$1.39^{+0.36}_{-1.37}$	6.67	0.647	2.46	3.16	$1.39^{+0.15}_{-0.13}$	6.67	0.527	$1.65^{+0.21}_{-0.11}$	6.33	0.342
9018	$1.19^{+0.21}_{-0.46}$	5.67	0.546	11.08	1.68	$1.19^{+0.08}_{-0.07}$	5.67	0.546	$0.78^{+0.08}_{-0.08}$	6.33	0.454
9019	$2.17^{+0.37}_{-0.31}$	7.00	0.946	3.37	3.41	$2.17^{+0.24}_{-0.26}$	7.00	0.884	$2.48^{+0.18}_{-0.07}$	7.33	0.116
9024	$1.76^{+0.27}_{-0.59}$	6.33	0.760	3.94	1.88	$1.76^{+0.19}_{-0.06}$	6.33	0.347	$1.64^{+0.06}_{-0.26}$	6.33	0.472
9034	$1.15^{+0.21}_{-0.21}$	4.00	1.000	1.13	0.88	$1.15^{+0.10}_{-0.11}$	4.00	1.000	$\cdots$ $^{+}_{-}$	$\cdots$	$\cdots$
9074	$1.03^{+0.20}_{-0.20}$	1.00	1.000	8.74	0.34	$1.03^{+0.11}_{-0.09}$	1.00	1.000	$\cdots$ $^{+}_{-}$	$\cdots$	$\cdots$
9088	$0.48^{+0.15}_{-0.14}$	5.67	1.000	5.17	0.14	$0.48^{+0.10}_{-0.08}$	5.67	1.000	$\cdots$ $^{+}_{-}$	$\cdots$	$\cdots$
9090	$0.24^{+0.12}_{-0.12}$	3.67	0.994	5.87	0.13	$0.24^{+0.07}_{-0.04}$	3.67	0.558	$0.17^{+0.03}_{-0.08}$	3.33	0.442
9092	$3.21^{+0.41}_{-0.41}$	8.00	1.000	0.23	0.09	$3.21^{+0.11}_{-0.19}$	8.00	1.000	$\cdots$ $^{+}_{-}$	$\cdots$	$\cdots$
9097	$2.47^{+0.34}_{-0.37}$	6.33	0.967	1.21	0.65	$2.47^{+0.18}_{-0.12}$	6.33	0.524	$2.24^{+0.11}_{-0.28}$	6.00	0.476
9102	$1.43^{+0.24}_{-0.24}$	2.33	1.000	8.11	3.43	$1.43^{+0.09}_{-0.08}$	2.33	1.000	$\cdots$ $^{+}_{-}$	$\cdots$	$\cdots$
9110	$2.31^{+0.32}_{-0.32}$	6.33	0.995	0.62	0.34	$2.31^{+0.21}_{-0.38}$	6.33	0.999	$0.05^{+0.01}_{-0.02}$	6.67	0.001
9112	$0.45^{+0.14}_{-0.14}$	6.00	1.000	2.07	0.61	$0.45^{+0.15}_{-0.07}$	6.00	1.000	$\cdots$ $^{+}_{-}$	$\cdots$	$\cdots$
9113	$1.68^{+0.59}_{-0.26}$	4.33	0.577	1.17	0.11	$1.68^{+0.21}_{-0.19}$	4.33	0.563	$2.18^{+0.19}_{-0.09}$	5.00	0.289
9123	$2.31^{+0.32}_{-0.32}$	5.33	1.000	4.86	0.05	$2.31^{+0.11}_{-0.12}$	5.33	1.000	$\cdots$ $^{+}_{-}$	$\cdots$	$\cdots$
9125	$1.32^{+0.23}_{-0.23}$	3.00	1.000	4.96	1.76	$1.32^{+0.07}_{-0.08}$	3.00	1.000	$\cdots$ $^{+}_{-}$	$\cdots$	$\cdots$
9135	$1.66^{+0.26}_{-0.26}$	6.00	1.000	5.41	1.27	$1.66^{+0.15}_{-0.12}$	6.00	1.000	$\cdots$ $^{+}_{-}$	$\cdots$	$\cdots$
9139	$2.33^{+0.33}_{-0.33}$	6.67	1.000	1.88	0.24	$2.33^{+0.17}_{-0.11}$	6.67	1.000	$\cdots$ $^{+}_{-}$	$\cdots$	$\cdots$
9159	$1.92^{+0.29}_{-0.29}$	3.33	1.000	19.27	1.27	$1.92^{+0.16}_{-0.15}$	3.33	1.000	$\cdots$ $^{+}_{-}$	$\cdots$	$\cdots$
9171	$0.68^{+0.17}_{-0.17}$	4.33	1.000	5.59	1.74	$0.68^{+0.07}_{-0.09}$	4.33	1.000	$\cdots$ $^{+}_{-}$	$\cdots$	$\cdots$
9179	$0.27^{+0.12}_{-0.14}$	3.33	0.964	1.56	0.19	$0.27^{+0.12}_{-0.05}$	3.33	0.617	$0.19^{+0.03}_{-0.10}$	3.00	0.383
9182	$3.15^{+0.41}_{-0.41}$	7.67	1.000	0.37	0.16	$3.15^{+0.15}_{-0.22}$	7.67	0.936	$2.86^{+0.07}_{-0.10}$	7.00	0.064
9183	$0.95^{+0.19}_{-0.19}$	6.33	1.000	9.78	0.49	$0.95^{+0.08}_{-0.03}$	6.33	0.542	$0.89^{+0.03}_{-0.09}$	6.33	0.458
9185	$3.48^{+0.44}_{-0.44}$	5.33	1.000	1.42	1.62	$3.48^{+0.13}_{-0.12}$	5.33	1.000	$\cdots$ $^{+}_{-}$	$\cdots$	$\cdots$
9194	$0.66^{+0.16}_{-0.16}$	5.00	1.000	0.88	0.03	$0.66^{+0.09}_{-0.11}$	5.00	1.000	$\cdots$ $^{+}_{-}$	$\cdots$	$\cdots$
9204	$0.20^{+0.12}_{-0.12}$	3.00	1.000	4.22	0.07	$0.20^{+0.07}_{-0.07}$	3.00	1.000	$\cdots$ $^{+}_{-}$	$\cdots$	$\cdots$
9211	$2.76^{+0.37}_{-0.37}$	6.33	0.994	2.14	0.97	$2.76^{+0.20}_{-0.16}$	6.33	0.966	$3.09^{+0.11}_{-0.13}$	7.33	0.034
9215	$3.66^{+0.46}_{-0.46}$	5.67	1.000	2.51	0.34	$3.66^{+0.12}_{-0.21}$	5.67	1.000	$\cdots$ $^{+}_{-}$	$\cdots$	$\cdots$
9225	$1.24^{+0.23}_{-0.47}$	5.67	0.913	0.50	0.16	$1.24^{+0.09}_{-0.18}$	5.67	0.721	$1.40^{+0.16}_{-0.07}$	4.67	0.217
9227	$3.45^{+0.44}_{-0.44}$	6.33	1.000	0.30	0.21	$3.45^{+0.15}_{-0.18}$	6.33	1.000	$\cdots$ $^{+}_{-}$	$\cdots$	$\cdots$
9230	$0.04^{+0.10}_{-0.04}$	2.33	1.000	32.10	6.01	$0.04^{+0.07}_{-0.03}$	2.33	1.000	$\cdots$ $^{+}_{-}$	$\cdots$	$\cdots$
9235	$0.70^{+0.17}_{-0.17}$	6.00	1.000	11.98	1.04	$0.70^{+0.07}_{-0.07}$	6.00	1.000	$\cdots$ $^{+}_{-}$	$\cdots$	$\cdots$

Table C.2—Continued

ID[a]	z_b[b]	t_b[c]	ODDS[d]	χ^2_ν[e]	$\chi^2_{\rm mod}$[f]	z_b1[g]	t_b1[c]	ODDS1[h]	z_b2[g]	t_b2[c]	ODDS2[h]
9244	$0.67^{+0.16}_{-0.16}$	4.00	1.000	2.33	0.28	$0.67^{+0.07}_{-0.10}$	4.00	1.000	$\cdots$ $^{+}_{-}$	$\cdots$	$\cdots$
9253	$0.52^{+0.15}_{-0.15}$	3.00	1.000	55.09	0.16	$0.52^{+0.08}_{-0.07}$	3.00	1.000	$\cdots$ $^{+}_{-}$	$\cdots$	$\cdots$
9264	$1.00^{+0.20}_{-0.20}$	1.00	1.000	78.07	0.02	$1.00^{+0.08}_{-0.09}$	1.00	1.000	$\cdots$ $^{+}_{-}$	$\cdots$	$\cdots$
9269	$0.50^{+0.15}_{-0.15}$	2.33	1.000	2.10	0.03	$0.50^{+0.08}_{-0.08}$	2.33	1.000	$\cdots$ $^{+}_{-}$	$\cdots$	$\cdots$
9273	$0.92^{+0.21}_{-0.19}$	6.33	0.966	1.23	0.13	$0.92^{+0.08}_{-0.10}$	6.33	0.959	$1.14^{+0.06}_{-0.06}$	6.00	0.041
9289	$2.87^{+0.38}_{-0.38}$	4.67	0.984	1.18	0.29	$2.87^{+0.30}_{-0.48}$	4.67	0.990	$0.11^{+0.08}_{-0.07}$	3.67	0.010
9299	$3.32^{+0.42}_{-0.42}$	8.00	1.000	0.58	0.03	$3.32^{+0.08}_{-0.15}$	8.00	1.000	$\cdots$ $^{+}_{-}$	$\cdots$	$\cdots$
9304	$3.28^{+0.42}_{-0.42}$	8.00	0.999	3.09	1.64	$3.28^{+0.14}_{-0.22}$	8.00	0.907	$2.93^{+0.13}_{-0.08}$	7.00	0.093
9305	$2.24^{+0.32}_{-0.32}$	6.67	0.981	3.39	1.14	$2.24^{+0.16}_{-0.11}$	6.67	0.699	$2.06^{+0.07}_{-0.15}$	6.67	0.283
9308	$2.41^{+0.33}_{-0.33}$	6.33	1.000	2.37	0.66	$2.41^{+0.13}_{-0.08}$	6.33	0.720	$2.28^{+0.05}_{-0.12}$	6.00	0.280
9312	$3.10^{+0.40}_{-0.40}$	6.00	1.000	0.83	0.05	$3.10^{+0.13}_{-0.12}$	6.00	1.000	$\cdots$ $^{+}_{-}$	$\cdots$	$\cdots$
9328	$2.46^{+0.55}_{-2.24}$	4.00	0.803	1.37	0.19	$2.46^{+0.26}_{-0.29}$	4.00	0.792	$2.92^{+0.21}_{-0.20}$	5.67	0.176
9330	$3.30^{+0.42}_{-0.42}$	5.67	1.000	1.06	0.23	$3.30^{+0.16}_{-0.22}$	5.67	1.000	$\cdots$ $^{+}_{-}$	$\cdots$	$\cdots$
9332	$1.57^{+0.25}_{-0.25}$	3.67	1.000	1.98	0.01	$1.57^{+0.08}_{-0.09}$	3.67	1.000	$\cdots$ $^{+}_{-}$	$\cdots$	$\cdots$
9341	$1.04^{+0.20}_{-0.20}$	4.33	1.000	15.07	1.79	$1.04^{+0.08}_{-0.08}$	4.33	1.000	$\cdots$ $^{+}_{-}$	$\cdots$	$\cdots$
9347	$2.46^{+0.34}_{-0.34}$	6.67	1.000	1.91	0.06	$2.46^{+0.11}_{-0.08}$	6.67	1.000	$\cdots$ $^{+}_{-}$	$\cdots$	$\cdots$
9348	$0.44^{+0.14}_{-0.14}$	6.00	1.000	8.25	0.31	$0.44^{+0.08}_{-0.07}$	6.00	1.000	$\cdots$ $^{+}_{-}$	$\cdots$	$\cdots$
9349	$0.24^{+0.16}_{-0.12}$	3.33	0.948	2.15	0.51	$0.24^{+0.22}_{-0.16}$	3.33	1.000	$\cdots$ $^{+}_{-}$	$\cdots$	$\cdots$
9356	$0.91^{+0.19}_{-0.19}$	6.00	1.000	2.55	0.33	$0.91^{+0.12}_{-0.09}$	6.00	1.000	$\cdots$ $^{+}_{-}$	$\cdots$	$\cdots$
9360	$0.92^{+0.19}_{-0.19}$	5.67	0.978	2.48	0.22	$0.92^{+0.10}_{-0.10}$	5.67	0.844	$1.09^{+0.07}_{-0.07}$	4.00	0.156
9361	$0.73^{+0.17}_{-0.17}$	5.33	0.985	3.49	0.37	$0.73^{+0.08}_{-0.08}$	5.33	0.986	$0.49^{+0.04}_{-0.03}$	5.00	0.014
9368	$3.55^{+0.45}_{-0.45}$	6.67	1.000	0.55	0.41	$3.55^{+0.13}_{-0.18}$	6.67	0.702	$3.78^{+0.16}_{-0.10}$	7.67	0.298
9371	$1.02^{+0.20}_{-0.20}$	3.67	1.000	3.96	0.13	$1.02^{+0.08}_{-0.09}$	3.67	1.000	$\cdots$ $^{+}_{-}$	$\cdots$	$\cdots$
9372	$0.75^{+0.17}_{-0.17}$	5.00	1.000	3.18	1.17	$0.75^{+0.11}_{-0.10}$	5.00	1.000	$\cdots$ $^{+}_{-}$	$\cdots$	$\cdots$
9385	$2.67^{+0.36}_{-0.36}$	6.33	1.000	0.49	0.19	$2.67^{+0.16}_{-0.18}$	6.33	1.000	$\cdots$ $^{+}_{-}$	$\cdots$	$\cdots$
9393	$2.58^{+0.35}_{-0.35}$	7.00	1.000	9.96	5.24	$2.58^{+0.13}_{-0.16}$	7.00	1.000	$\cdots$ $^{+}_{-}$	$\cdots$	$\cdots$
9394	$2.79^{+0.37}_{-0.37}$	5.67	1.000	1.64	0.04	$2.79^{+0.09}_{-0.09}$	5.67	1.000	$\cdots$ $^{+}_{-}$	$\cdots$	$\cdots$
9396	$2.48^{+0.34}_{-0.34}$	6.33	1.000	4.07	0.10	$2.48^{+0.08}_{-0.09}$	6.33	0.904	$2.25^{+0.08}_{-0.07}$	6.00	0.096
9397	$0.42^{+0.14}_{-0.14}$	6.67	1.000	30.52	8.86	$0.42^{+0.07}_{-0.07}$	6.67	1.000	$\cdots$ $^{+}_{-}$	$\cdots$	$\cdots$
9402	$1.03^{+0.20}_{-0.20}$	4.00	1.000	10.91	0.16	$1.03^{+0.08}_{-0.08}$	4.00	1.000	$\cdots$ $^{+}_{-}$	$\cdots$	$\cdots$
9409	$3.77^{+0.47}_{-0.47}$	5.33	1.000	3.43	0.11	$3.77^{+0.08}_{-0.08}$	5.33	1.000	$\cdots$ $^{+}_{-}$	$\cdots$	$\cdots$
9414	$1.21^{+0.26}_{-0.22}$	6.67	0.953	1.07	1.12	$1.21^{+0.11}_{-0.16}$	6.67	0.834	$1.38^{+0.18}_{-0.06}$	6.33	0.166
9419	$3.10^{+0.40}_{-0.40}$	8.00	1.000	0.33	0.30	$3.10^{+0.14}_{-0.24}$	8.00	0.991	$2.82^{+0.04}_{-0.05}$	7.00	0.009
9425	$2.18^{+0.31}_{-0.31}$	5.33	1.000	0.99	0.04	$2.18^{+0.17}_{-0.21}$	5.33	1.000	$\cdots$ $^{+}_{-}$	$\cdots$	$\cdots$
9432	$2.62^{+0.36}_{-0.35}$	7.00	1.000	23.04	2.98	$2.62^{+0.08}_{-0.07}$	7.00	1.000	$\cdots$ $^{+}_{-}$	$\cdots$	$\cdots$
9437	$0.70^{+0.17}_{-0.17}$	6.00	1.000	1.50	0.02	$0.70^{+0.07}_{-0.07}$	6.00	1.000	$\cdots$ $^{+}_{-}$	$\cdots$	$\cdots$

Table C.2—Continued

ID[a]	z_b[b]	t_b[c]	ODDS[d]	χ^2_ν[e]	$\chi^2_{\rm mod}$[f]	z_b1[g]	t_b1[c]	ODDS1[h]	z_b2[g]	t_b2[c]	ODDS2[h]
9444	$1.82^{+0.28}_{-0.28}$	1.33	1.000	22.47	0.01	$1.82^{+0.08}_{-0.08}$	1.33	1.000	$\cdots$ $^{+}_{-}$	$\cdots$	$\cdots$
9452	$2.52^{+0.35}_{-0.35}$	6.67	1.000	1.13	0.13	$2.52^{+0.09}_{-0.10}$	6.67	1.000	$\cdots$ $^{+}_{-}$	$\cdots$	$\cdots$
9455	$0.47^{+0.14}_{-0.14}$	3.67	1.000	16.48	0.10	$0.47^{+0.08}_{-0.07}$	3.67	1.000	$\cdots$ $^{+}_{-}$	$\cdots$	$\cdots$
9474	$1.04^{+0.20}_{-0.20}$	3.33	1.000	4.19	0.05	$1.04^{+0.08}_{-0.07}$	3.33	1.000	$\cdots$ $^{+}_{-}$	$\cdots$	$\cdots$
9487	$3.80^{+0.47}_{-0.47}$	7.67	1.000	4.01	1.29	$3.80^{+0.13}_{-0.09}$	7.67	0.709	$3.65^{+0.06}_{-0.10}$	7.00	0.291
9505	$2.96^{+0.39}_{-0.39}$	8.00	1.000	2.79	2.13	$2.96^{+0.13}_{-0.22}$	8.00	1.000	$\cdots$ $^{+}_{-}$	$\cdots$	$\cdots$
9532	$0.72^{+0.17}_{-0.17}$	2.33	1.000	7.10	0.03	$0.72^{+0.07}_{-0.08}$	2.33	1.000	$\cdots$ $^{+}_{-}$	$\cdots$	$\cdots$
9543	$3.27^{+0.42}_{-0.42}$	5.33	1.000	1.25	0.02	$3.27^{+0.08}_{-0.09}$	5.33	1.000	$\cdots$ $^{+}_{-}$	$\cdots$	$\cdots$
9570	$2.66^{+0.36}_{-0.36}$	8.00	1.000	5.52	2.97	$2.66^{+0.13}_{-0.22}$	8.00	1.000	$\cdots$ $^{+}_{-}$	$\cdots$	$\cdots$
9585	$0.86^{+0.19}_{-0.18}$	5.33	0.976	0.43	0.12	$0.86^{+0.27}_{-0.18}$	5.33	1.000	$\cdots$ $^{+}_{-}$	$\cdots$	$\cdots$
9588	$0.99^{+0.19}_{-0.19}$	2.67	1.000	3.68	0.05	$0.99^{+0.08}_{-0.09}$	2.67	1.000	$\cdots$ $^{+}_{-}$	$\cdots$	$\cdots$
9593	$2.46^{+0.34}_{-0.36}$	8.00	0.964	1.18	0.80	$2.46^{+0.13}_{-0.46}$	8.00	1.000	$\cdots$ $^{+}_{-}$	$\cdots$	$\cdots$
9598	$0.61^{+0.16}_{-0.16}$	4.67	1.000	0.22	0.10	$0.61^{+0.14}_{-0.15}$	4.67	1.000	$\cdots$ $^{+}_{-}$	$\cdots$	$\cdots$
9599	$0.15^{+0.11}_{-0.11}$	3.33	1.000	0.61	0.03	$0.15^{+0.11}_{-0.10}$	3.33	1.000	$\cdots$ $^{+}_{-}$	$\cdots$	$\cdots$
9609	$0.76^{+0.17}_{-0.17}$	5.00	1.000	3.27	0.12	$0.76^{+0.10}_{-0.10}$	5.00	1.000	$\cdots$ $^{+}_{-}$	$\cdots$	$\cdots$
9617	$2.52^{+0.35}_{-0.35}$	6.00	1.000	2.19	0.12	$2.52^{+0.19}_{-0.17}$	6.00	1.000	$\cdots$ $^{+}_{-}$	$\cdots$	$\cdots$
9624	$1.60^{+0.29}_{-1.06}$	7.33	0.921	0.00	0.00	$1.60^{+0.45}_{-0.28}$	7.33	0.959	$0.54^{+0.13}_{-0.16}$	7.67	0.041
9640	$2.51^{+0.34}_{-0.34}$	6.67	1.000	2.57	0.26	$2.51^{+0.09}_{-0.11}$	6.67	1.000	$\cdots$ $^{+}_{-}$	$\cdots$	$\cdots$
9649	$0.88^{+0.18}_{-0.18}$	5.00	1.000	7.60	0.16	$0.88^{+0.09}_{-0.09}$	5.00	0.928	$1.02^{+0.05}_{-0.05}$	3.67	0.072
9672	$0.91^{+0.19}_{-0.19}$	5.67	1.000	10.61	0.40	$0.91^{+0.08}_{-0.07}$	5.67	1.000	$\cdots$ $^{+}_{-}$	$\cdots$	$\cdots$
9674	$1.55^{+0.25}_{-0.25}$	5.33	1.000	3.23	0.06	$1.55^{+0.18}_{-0.15}$	5.33	1.000	$\cdots$ $^{+}_{-}$	$\cdots$	$\cdots$
9675	$1.22^{+0.22}_{-0.37}$	6.00	0.920	1.43	0.15	$1.22^{+0.10}_{-0.12}$	6.00	0.919	$0.95^{+0.07}_{-0.05}$	6.33	0.043
9676	$3.29^{+0.42}_{-0.42}$	6.33	1.000	0.07	0.01	$3.29^{+0.11}_{-0.12}$	6.33	1.000	$\cdots$ $^{+}_{-}$	$\cdots$	$\cdots$
9678	$2.15^{+0.37}_{-0.31}$	6.00	0.909	1.18	0.32	$2.15^{+0.10}_{-0.27}$	6.00	0.495	$2.33^{+0.28}_{-0.08}$	6.33	0.497
9689	$0.63^{+0.16}_{-0.16}$	3.67	1.000	1.09	0.11	$0.63^{+0.08}_{-0.10}$	3.67	1.000	$\cdots$ $^{+}_{-}$	$\cdots$	$\cdots$
9706	$2.77^{+0.37}_{-0.37}$	5.33	1.000	1.83	0.05	$2.77^{+0.09}_{-0.10}$	5.33	1.000	$\cdots$ $^{+}_{-}$	$\cdots$	$\cdots$
9711	$3.48^{+0.44}_{-0.44}$	7.33	1.000	0.18	0.13	$3.48^{+0.16}_{-0.09}$	7.33	0.604	$3.33^{+0.06}_{-0.16}$	7.00	0.396
9712	$0.90^{+0.19}_{-0.19}$	3.33	1.000	11.87	0.12	$0.90^{+0.08}_{-0.08}$	3.33	1.000	$\cdots$ $^{+}_{-}$	$\cdots$	$\cdots$
9713	$0.72^{+0.17}_{-0.17}$	5.67	1.000	3.55	0.35	$0.72^{+0.08}_{-0.08}$	5.67	1.000	$\cdots$ $^{+}_{-}$	$\cdots$	$\cdots$
9724	$0.70^{+0.17}_{-0.17}$	6.00	1.000	16.66	1.09	$0.70^{+0.07}_{-0.07}$	6.00	1.000	$\cdots$ $^{+}_{-}$	$\cdots$	$\cdots$
9731	$1.10^{+0.47}_{-0.38}$	5.67	0.660	1.88	1.01	$1.10^{+0.19}_{-0.17}$	5.67	0.653	$0.77^{+0.16}_{-0.10}$	6.33	0.215
9759	$1.39^{+0.23}_{-0.23}$	3.67	1.000	1.52	0.01	$1.39^{+0.08}_{-0.07}$	3.67	0.918	$1.30^{+0.02}_{-0.06}$	4.33	0.082
9765	$1.45^{+0.24}_{-0.24}$	3.00	1.000	30.97	0.11	$1.45^{+0.09}_{-0.08}$	3.00	1.000	$\cdots$ $^{+}_{-}$	$\cdots$	$\cdots$
9778	$0.30^{+0.13}_{-0.13}$	1.67	1.000	12.20	0.07	$0.30^{+0.08}_{-0.08}$	1.67	1.000	$\cdots$ $^{+}_{-}$	$\cdots$	$\cdots$
9783	$1.36^{+0.23}_{-0.23}$	5.33	1.000	0.74	0.05	$1.36^{+0.07}_{-0.11}$	5.33	0.810	$1.47^{+0.09}_{-0.04}$	4.00	0.190
9787	$2.14^{+0.31}_{-0.51}$	5.67	0.634	2.19	0.27	$2.14^{+0.15}_{-0.07}$	5.67	0.340	$1.72^{+0.19}_{-0.17}$	5.67	0.438

Table C.2—Continued

ID[a]	z_b[b]	t_b[c]	ODDS[d]	χ^2_ν[e]	$\chi^2_{\rm mod}$[f]	z_b1[g]	t_b1[c]	ODDS1[h]	z_b2[g]	t_b2[c]	ODDS2[h]
9806	$2.58^{+0.35}_{-0.35}$	6.67	1.000	0.44	0.03	$2.58^{+0.09}_{-0.08}$	6.67	1.000	$\cdots\ ^{+}_{-}$	...	...
9807	$0.64^{+0.16}_{-0.16}$	2.67	1.000	3.49	0.05	$0.64^{+0.08}_{-0.08}$	2.67	1.000	$\cdots\ ^{+}_{-}$	...	...
9834	$0.38^{+0.13}_{-0.13}$	2.33	1.000	5.79	0.22	$0.38^{+0.08}_{-0.08}$	2.33	1.000	$\cdots\ ^{+}_{-}$	...	...
9837	$1.13^{+0.21}_{-0.38}$	4.00	0.790	2.83	0.09	$1.13^{+0.09}_{-0.08}$	4.00	0.716	$0.80^{+0.10}_{-0.10}$	5.67	0.210
9839	$2.49^{+0.34}_{-0.34}$	6.33	1.000	0.43	0.01	$2.49^{+0.09}_{-0.09}$	6.33	1.000	$\cdots\ ^{+}_{-}$	...	...
9847	$0.17^{+0.11}_{-0.14}$	2.00	0.947	1.90	0.08	$0.17^{+0.07}_{-0.06}$	2.00	0.739	$0.08^{+0.03}_{-0.07}$	1.33	0.261
9848	$0.78^{+0.42}_{-0.17}$	6.33	0.872	2.40	0.56	$0.78^{+0.14}_{-0.11}$	6.33	0.872	$1.17^{+0.08}_{-0.12}$	5.67	0.128
9859	$0.94^{+0.19}_{-0.25}$	6.00	0.943	1.93	0.46	$0.94^{+0.17}_{-0.10}$	6.00	0.943	$0.70^{+0.05}_{-0.05}$	6.33	0.057
9889	$1.27^{+0.22}_{-0.22}$	6.00	1.000	0.99	0.31	$1.27^{+0.18}_{-0.11}$	6.00	1.000	$\cdots\ ^{+}_{-}$	...	...
9895	$0.97^{+0.19}_{-0.19}$	4.00	1.000	9.01	0.12	$0.97^{+0.08}_{-0.12}$	4.00	1.000	$\cdots\ ^{+}_{-}$	...	...
9903	$1.02^{+0.20}_{-0.20}$	4.00	1.000	3.38	0.13	$1.02^{+0.09}_{-0.08}$	4.00	1.000	$\cdots\ ^{+}_{-}$	...	...
9925	$2.17^{+0.31}_{-0.31}$	5.67	1.000	1.49	0.10	$2.17^{+0.16}_{-0.18}$	5.67	1.000	$\cdots\ ^{+}_{-}$	...	...
9927	$1.53^{+0.25}_{-0.33}$	6.33	0.935	0.19	0.05	$1.53^{+0.35}_{-0.21}$	6.33	0.944	$1.21^{+0.11}_{-0.12}$	6.67	0.056
9944	$1.60^{+0.25}_{-1.14}$	7.00	0.817	0.48	0.34	$1.60^{+0.37}_{-0.20}$	7.00	0.832	$0.54^{+0.15}_{-0.15}$	7.33	0.156
9947	$1.10^{+0.21}_{-0.21}$	2.67	1.000	4.19	0.08	$1.10^{+0.10}_{-0.10}$	2.67	1.000	$\cdots\ ^{+}_{-}$	...	...
9959	$0.33^{+0.13}_{-0.13}$	1.00	0.994	0.00	0.01	$0.33^{+0.06}_{-0.08}$	1.00	0.804	$0.40^{+0.11}_{-0.01}$	1.33	0.196
9962	$0.77^{+0.17}_{-0.17}$	3.33	1.000	9.99	0.08	$0.77^{+0.08}_{-0.08}$	3.33	1.000	$\cdots\ ^{+}_{-}$	...	...
9964	$0.10^{+0.54}_{-0.10}$	6.00	0.850	1.68	0.69	$0.10^{+0.08}_{-0.08}$	6.00	0.850	$0.52^{+0.16}_{-0.09}$	6.67	0.133
9972	$2.67^{+0.36}_{-0.52}$	5.67	0.814	7.76	0.26	$2.67^{+0.11}_{-0.12}$	5.67	0.814	$2.20^{+0.11}_{-0.10}$	4.00	0.186
9974	$0.88^{+0.18}_{-0.18}$	6.00	1.000	13.52	0.46	$0.88^{+0.09}_{-0.08}$	6.00	1.000	$\cdots\ ^{+}_{-}$	...	...
9980	$1.05^{+0.20}_{-0.20}$	7.33	1.000	0.88	0.80	$1.05^{+0.14}_{-0.11}$	7.33	1.000	$\cdots\ ^{+}_{-}$	...	...
9983	$4.72^{+0.56}_{-0.56}$	6.00	1.000	0.69	0.04	$4.72^{+0.09}_{-0.11}$	6.00	1.000	$\cdots\ ^{+}_{-}$	...	...
9990	$3.34^{+0.43}_{-0.42}$	8.00	1.000	0.12	0.08	$3.34^{+0.13}_{-0.17}$	8.00	0.909	$3.11^{+0.06}_{-0.15}$	7.00	0.091
9999	$2.01^{+0.30}_{-0.29}$	6.33	0.994	0.29	0.06	$2.01^{+0.34}_{-0.35}$	6.33	1.000	$\cdots\ ^{+}_{-}$	...	...
10004	$2.77^{+0.37}_{-0.37}$	7.67	1.000	9.22	8.64	$2.77^{+0.15}_{-0.25}$	7.67	1.000	$\cdots\ ^{+}_{-}$	...	...
10016	$2.99^{+0.39}_{-0.39}$	8.00	1.000	0.21	0.05	$2.99^{+0.14}_{-0.19}$	8.00	0.979	$2.75^{+0.05}_{-0.05}$	7.00	0.021
10018	$3.02^{+0.39}_{-0.39}$	8.00	1.000	0.36	0.52	$3.02^{+0.17}_{-0.22}$	8.00	0.956	$2.76^{+0.04}_{-0.10}$	7.00	0.044
10020	$1.03^{+0.20}_{-0.20}$	3.67	1.000	0.20	0.01	$1.03^{+0.08}_{-0.14}$	3.67	1.000	$\cdots\ ^{+}_{-}$	...	...
10021	$2.36^{+0.33}_{-0.33}$	7.00	1.000	2.97	0.72	$2.36^{+0.09}_{-0.18}$	7.00	1.000	$\cdots\ ^{+}_{-}$	...	...
10025	$0.06^{+0.10}_{-0.06}$	3.00	0.983	1.49	0.02	$0.06^{+0.08}_{-0.05}$	3.00	0.983	$2.61^{+0.03}_{-0.04}$	3.33	0.017
10035	$1.22^{+0.22}_{-0.22}$	4.00	1.000	2.56	0.25	$1.22^{+0.11}_{-0.11}$	4.00	0.996	$1.42^{+0.02}_{-0.02}$	3.33	0.004
10042	$0.79^{+1.35}_{-0.18}$	6.67	0.613	4.80	5.06	$0.79^{+0.20}_{-0.12}$	6.67	0.614	$1.51^{+0.21}_{-0.11}$	5.00	0.280
10043	$0.68^{+0.17}_{-0.23}$	5.67	0.703	3.95	0.36	$0.68^{+0.08}_{-0.08}$	5.67	0.498	$0.50^{+0.10}_{-0.09}$	5.33	0.502
20037	$1.24^{+0.22}_{-0.22}$	3.00	1.000	7.32	0.60	$1.24^{+0.09}_{-0.09}$	3.00	1.000	$\cdots\ ^{+}_{-}$	...	...
20061	$1.24^{+0.22}_{-0.22}$	4.00	1.000	28.42	11.88	$1.24^{+0.08}_{-0.08}$	4.00	1.000	$\cdots\ ^{+}_{-}$	...	...
40448	$2.52^{+0.35}_{-0.35}$	5.67	1.000	1.01	0.36	$2.52^{+0.17}_{-0.29}$	5.67	1.000	$\cdots\ ^{+}_{-}$	...	...

Table C.2—Continued

ID[a]	z_b[b]	t_b[c]	ODDS[d]	χ^2_ν[e]	$\chi^2_{\rm mod}$[f]	z_b1[g]	t_b1[c]	ODDS1[h]	z_b2[g]	t_b2[c]	ODDS2[h]
50139	$2.65^{+0.36}_{-0.36}$	5.00	1.000	4.24	0.09	$2.65^{+0.12}_{-0.10}$	5.00	1.000	$\cdots\ ^{+}_{-}$	...	...
50721	$1.57^{+0.25}_{-0.25}$	6.00	1.000	2.35	0.53	$1.57^{+0.14}_{-0.18}$	6.00	1.000	$\cdots\ ^{+}_{-}$	...	...
50947	$3.01^{+0.39}_{-0.39}$	4.67	0.992	1.32	0.13	$3.01^{+0.11}_{-0.20}$	4.67	0.632	$3.26^{+0.22}_{-0.14}$	5.33	0.368
51093	$2.70^{+0.36}_{-0.36}$	8.00	1.000	0.67	1.22	$2.70^{+0.21}_{-0.35}$	8.00	1.000	$\cdots\ ^{+}_{-}$	...	...
51179	$2.97^{+0.39}_{-0.39}$	4.67	1.000	1.78	0.10	$2.97^{+0.12}_{-0.15}$	4.67	1.000	$\cdots\ ^{+}_{-}$	...	...
51644	$0.51^{+0.15}_{-0.15}$	3.33	1.000	25.53	0.33	$0.51^{+0.08}_{-0.09}$	3.33	1.000	$\cdots\ ^{+}_{-}$	...	...
51711	$3.12^{+0.40}_{-0.40}$	3.67	0.997	9.09	0.35	$3.12^{+0.21}_{-0.18}$	3.67	0.997	$0.05^{+0.03}_{-0.02}$	2.00	0.003
52596	$0.02^{+2.12}_{-0.02}$	7.00	0.618	11.03	1.85	$0.02^{+0.09}_{-0.01}$	7.00	0.618	$1.31^{+0.07}_{-0.08}$	7.00	0.210
52761	$0.67^{+0.16}_{-0.16}$	5.33	1.000	3.50	0.77	$0.67^{+0.09}_{-0.12}$	5.33	1.000	$\cdots\ ^{+}_{-}$	...	...
52786	$3.02^{+0.39}_{-0.39}$	6.67	1.000	1.21	0.51	$3.02^{+0.31}_{-0.15}$	6.67	1.000	$\cdots\ ^{+}_{-}$	...	...
52950	$2.40^{+0.33}_{-0.33}$	6.33	1.000	0.43	0.04	$2.40^{+0.14}_{-0.14}$	6.33	1.000	$\cdots\ ^{+}_{-}$	...	...
52966	$0.46^{+0.14}_{-0.14}$	3.33	1.000	0.75	0.02	$0.46^{+0.09}_{-0.08}$	3.33	1.000	$\cdots\ ^{+}_{-}$	...	...
53090	$3.53^{+0.44}_{-0.44}$	6.00	1.000	0.21	0.02	$3.53^{+0.14}_{-0.14}$	6.00	1.000	$\cdots\ ^{+}_{-}$	...	...
53163	$0.17^{+0.11}_{-0.12}$	2.33	1.000	0.35	0.00	$0.17^{+0.07}_{-0.07}$	2.33	1.000	$\cdots\ ^{+}_{-}$	...	...
53335	$2.62^{+0.36}_{-0.35}$	6.33	1.000	9.01	0.33	$2.62^{+0.08}_{-0.09}$	6.33	1.000	$\cdots\ ^{+}_{-}$	...	...
53380	$0.53^{+0.15}_{-0.15}$	1.00	1.000	27.36	0.05	$0.53^{+0.07}_{-0.07}$	1.00	1.000	$\cdots\ ^{+}_{-}$	...	...
53540	$0.17^{+0.27}_{-0.12}$	5.33	0.905	2.23	0.38	$0.17^{+0.11}_{-0.10}$	5.33	0.905	$0.43^{+0.06}_{-0.06}$	6.00	0.095
53790	$2.35^{+0.33}_{-0.33}$	6.67	1.000	0.37	0.05	$2.35^{+0.14}_{-0.16}$	6.67	1.000	$\cdots\ ^{+}_{-}$	...	...
53972	$3.09^{+0.40}_{-0.40}$	5.67	1.000	1.59	0.10	$3.09^{+0.14}_{-0.14}$	5.67	1.000	$\cdots\ ^{+}_{-}$	...	...
54717	$2.42^{+0.34}_{-0.34}$	7.00	1.000	1.45	0.99	$2.42^{+0.07}_{-0.25}$	7.00	0.568	$2.54^{+0.17}_{-0.05}$	7.33	0.432
54735	$2.69^{+0.36}_{-0.36}$	6.00	1.000	25.76	0.40	$2.69^{+0.08}_{-0.08}$	6.00	1.000	$\cdots\ ^{+}_{-}$	...	...
54801	$1.67^{+0.26}_{-1.19}$	7.00	0.782	0.62	0.33	$1.67^{+0.36}_{-0.23}$	7.00	0.788	$0.57^{+0.18}_{-0.18}$	7.33	0.203
55351	$3.97^{+0.49}_{-0.49}$	7.67	1.000	6.99	2.22	$3.97^{+0.13}_{-0.12}$	7.67	0.875	$3.80^{+0.05}_{-0.13}$	6.67	0.125
55406	$3.82^{+0.47}_{-0.47}$	5.67	1.000	0.52	0.05	$3.82^{+0.11}_{-0.13}$	5.67	0.929	$3.59^{+0.10}_{-0.12}$	4.33	0.071
55515	$2.50^{+0.34}_{-0.53}$	6.67	0.864	0.79	0.41	$2.50^{+0.27}_{-0.67}$	6.67	0.995	$0.08^{+0.07}_{-0.04}$	6.67	0.005
55812	$2.86^{+0.38}_{-0.38}$	8.00	1.000	0.71	0.45	$2.86^{+0.15}_{-0.17}$	8.00	1.000	$\cdots\ ^{+}_{-}$	...	...
55969	$0.43^{+0.14}_{-0.14}$	3.00	0.997	0.48	0.04	$0.43^{+0.12}_{-0.17}$	3.00	1.000	$\cdots\ ^{+}_{-}$	...	...
56017	$2.64^{+0.36}_{-0.36}$	8.00	1.000	0.23	0.13	$2.64^{+0.10}_{-0.13}$	8.00	1.000	$\cdots\ ^{+}_{-}$	...	...
56215	$3.34^{+0.43}_{-0.44}$	7.67	0.962	3.44	1.59	$3.34^{+0.12}_{-0.18}$	7.67	0.625	$2.96^{+0.20}_{-0.11}$	6.33	0.375
56333	$2.94^{+0.39}_{-0.39}$	7.33	0.999	21.00	20.18	$2.94^{+0.18}_{-0.13}$	7.33	0.814	$3.15^{+0.20}_{-0.03}$	8.00	0.186
56463	$0.91^{+0.19}_{-0.19}$	1.00	0.987	0.93	0.00	$0.91^{+0.08}_{-0.07}$	1.00	0.987	$1.22^{+0.03}_{-0.03}$	1.00	0.013
56611	$2.20^{+0.31}_{-2.18}$	6.00	0.798	0.14	0.04	$2.20^{+0.10}_{-0.27}$	6.00	0.708	$0.06^{+0.07}_{-0.05}$	6.67	0.202
56612	$1.11^{+0.21}_{-0.34}$	6.00	0.676	13.25	0.49	$1.11^{+0.08}_{-0.10}$	6.00	0.676	$0.83^{+0.08}_{-0.11}$	6.33	0.324
56987	$2.86^{+0.38}_{-0.38}$	6.33	1.000	3.03	0.33	$2.86^{+0.13}_{-0.11}$	6.33	1.000	$\cdots\ ^{+}_{-}$	...	...
57116	$2.83^{+0.38}_{-0.38}$	5.00	0.998	1.36	0.40	$2.83^{+0.34}_{-0.34}$	5.00	0.998	$0.07^{+0.02}_{-0.03}$	3.67	0.002
57353	$2.92^{+0.40}_{-0.38}$	7.00	0.974	2.96	1.18	$2.92^{+0.12}_{-0.10}$	7.00	0.898	$3.30^{+0.08}_{-0.16}$	8.00	0.102

Table C.2—Continued

ID[a]	z_b[b]	t_b[c]	ODDS[d]	χ^2_ν[e]	$\chi^2_{\rm mod}$[f]	z_b1[g]	t_b1[c]	ODDS1[h]	z_b2[g]	t_b2[c]	ODDS2[h]
57577	$0.58^{+0.16}_{-0.15}$	3.33	1.000	17.07	0.16	$0.58^{+0.09}_{-0.08}$	3.33	1.000	$\cdots$ $^{+}_{-}$	$\cdots$	$\cdots$
57616	$1.41^{+0.24}_{-0.24}$	4.00	1.000	7.11	0.17	$1.41^{+0.09}_{-0.09}$	4.00	1.000	$\cdots$ $^{+}_{-}$	$\cdots$	$\cdots$
57909	$3.37^{+0.43}_{-0.43}$	7.67	0.981	0.06	0.13	$3.37^{+0.21}_{-0.53}$	7.67	1.000	$\cdots$ $^{+}_{-}$	$\cdots$	$\cdots$
58328	$2.46^{+0.34}_{-0.40}$	8.00	0.891	3.24	2.60	$2.46^{+0.13}_{-0.13}$	8.00	0.509	$2.16^{+0.17}_{-0.18}$	7.33	0.491
58728	$1.46^{+0.24}_{-0.24}$	4.00	1.000	4.26	0.03	$1.46^{+0.08}_{-0.08}$	4.00	1.000	$\cdots$ $^{+}_{-}$	$\cdots$	$\cdots$
58772	$0.30^{+0.13}_{-0.13}$	3.33	0.981	4.23	0.13	$0.30^{+0.10}_{-0.06}$	3.33	0.740	$0.21^{+0.03}_{-0.07}$	3.00	0.260
58779	$3.04^{+0.40}_{-0.40}$	6.33	1.000	3.21	0.54	$3.04^{+0.15}_{-0.14}$	6.33	1.000	$\cdots$ $^{+}_{-}$	$\cdots$	$\cdots$
58909	$3.38^{+0.43}_{-0.43}$	5.33	0.995	0.30	0.05	$3.38^{+0.19}_{-0.48}$	5.33	1.000	$\cdots$ $^{+}_{-}$	$\cdots$	$\cdots$
59220	$0.89^{+0.19}_{-0.19}$	5.00	1.000	3.56	0.11	$0.89^{+0.15}_{-0.11}$	5.00	1.000	$\cdots$ $^{+}_{-}$	$\cdots$	$\cdots$
59307	$2.16^{+0.31}_{-0.31}$	4.33	1.000	1.62	0.02	$2.16^{+0.17}_{-0.14}$	4.33	1.000	$\cdots$ $^{+}_{-}$	$\cdots$	$\cdots$
59352	$2.34^{+0.33}_{-0.33}$	6.67	0.986	0.20	0.06	$2.34^{+0.16}_{-0.41}$	6.67	1.000	$\cdots$ $^{+}_{-}$	$\cdots$	$\cdots$
59855	$3.87^{+0.48}_{-0.48}$	4.00	1.000	1.29	0.30	$3.87^{+0.22}_{-0.12}$	4.00	0.644	$3.69^{+0.06}_{-0.20}$	3.33	0.333
59970	$2.59^{+0.35}_{-0.35}$	7.00	1.000	0.86	0.93	$2.59^{+0.25}_{-0.17}$	7.00	1.000	$\cdots$ $^{+}_{-}$	$\cdots$	$\cdots$
60088	$2.42^{+0.34}_{-0.56}$	7.00	0.872	1.92	2.75	$2.42^{+0.34}_{-0.11}$	7.00	0.476	$2.24^{+0.07}_{-0.59}$	6.67	0.512
60146	$1.40^{+0.24}_{-0.24}$	3.00	1.000	41.85	0.12	$1.40^{+0.08}_{-0.07}$	3.00	1.000	$\cdots$ $^{+}_{-}$	$\cdots$	$\cdots$
60162	$1.19^{+0.21}_{-0.33}$	6.00	0.736	14.64	0.39	$1.19^{+0.08}_{-0.07}$	6.00	0.736	$0.91^{+0.07}_{-0.09}$	6.33	0.264
60302	$3.02^{+0.39}_{-0.39}$	5.33	1.000	0.60	0.17	$3.02^{+0.26}_{-0.29}$	5.33	1.000	$\cdots$ $^{+}_{-}$	$\cdots$	$\cdots$
60303	$1.04^{+0.20}_{-0.20}$	3.67	1.000	7.23	0.10	$1.04^{+0.09}_{-0.08}$	3.67	1.000	$\cdots$ $^{+}_{-}$	$\cdots$	$\cdots$

Note. — See notes from Table 2.2.

Table C.3. Catalog of Galaxies with Reliable Spectroscopic Redshifts in the UDF

ID[a]	Survey	$z_{\rm spec}$	z_b[b]	$\chi^2_{\rm mod}$[c]	ODDS[d]	V (mag)	$u-V$ (mag)	$u-B$ (mag)	$V-z'$ (mag)
3088	FORS2	0.13	$0.06^{+0.10}_{-0.06}$	1.91	1.00	22.85±0.00	1.99±0.01	1.16±0.01	0.48±0.00
5670	VVDS	0.13	$0.09^{+0.11}_{-0.09}$	0.03	1.00	21.23±0.00	2.00±0.00	1.12±0.00	0.54±0.00
1971	VVDS	0.15	$0.03^{+0.10}_{-0.03}$	0.07	1.00	20.46±0.00	1.48±0.00	0.82±0.00	0.37±0.00
2974	VIMOS	0.15	$0.15^{+0.11}_{-0.11}$	1.51	1.00	24.08±0.01	1.97±0.03	0.99±0.03	0.49±0.01
5620	VVDS	0.21	$0.21^{+0.12}_{-0.12}$	0.75	1.00	23.42±0.00	0.88±0.01	0.43±0.01	0.01±0.00
3822	VIMOS	0.21	$0.18^{+0.12}_{-0.12}$	0.59	1.00	19.14±0.00	1.91±0.00	0.87±0.00	0.70±0.00
1000	FORS2	0.21	$0.21^{+0.12}_{-0.13}$	1.08	0.97	23.39±0.00	0.93±0.01	0.46±0.01	-0.01±0.01
5606	VVDS	0.23	$0.16^{+0.11}_{-0.11}$	0.05	1.00	21.14±0.00	1.79±0.00	0.82±0.00	0.55±0.00
5491	VIMOS	0.23	$0.17^{+0.11}_{-0.12}$	1.94	1.00	22.24±0.00	0.64±0.00	0.30±0.00	-0.15±0.00
7847	VVDS	0.33	$0.31^{+0.13}_{-0.13}$	0.02	1.00	22.00±0.00	2.97±0.01	1.36±0.01	1.10±0.00
3492	VVDS	0.34	$0.20^{+0.12}_{-0.12}$	0.31	1.00	20.83±0.00	1.48±0.00	0.56±0.00	0.43±0.00
3268	VVDS	0.35	$0.25^{+0.12}_{-0.12}$	0.09	1.00	22.11±0.00	1.36±0.00	0.51±0.01	0.46±0.00
4267	VVDS	0.35	$0.24^{+0.12}_{-0.12}$	0.60	1.00	24.63±0.01	1.19±0.03	0.35±0.03	0.20±0.01
8585	VVDS	0.38	$1.45^{+0.24}_{-0.24}$	0.01	1.00	22.07±0.00	0.70±0.00	0.41±0.00	0.96±0.00
900	Szokoly	0.41	$0.40^{+0.14}_{-0.14}$	0.08	1.00	21.07±0.00	1.94±0.00	0.72±0.00	1.01±0.00
4929	Szokoly	0.44	$0.45^{+0.14}_{-0.14}$	1.91	1.00	21.53±0.00	1.96±0.00	0.77±0.00	1.10±0.00
4445	Szokoly	0.46	$0.09^{+0.11}_{-0.09}$	2.89	1.00	21.50±0.00	0.77±0.00	0.31±0.00	0.58±0.00
5177	VIMOS	0.53	$0.47^{+0.14}_{-0.14}$	0.01	1.00	23.32±0.00	2.39±0.02	0.96±0.03	1.26±0.00
2107	VVDS	0.53	$0.47^{+0.14}_{-0.14}$	0.01	1.00	22.76±0.00	2.71±0.02	1.09±0.02	1.40±0.00
1960	FORS2	0.61	$0.45^{+0.14}_{-0.14}$	0.09	1.00	22.51±0.00	2.34±0.01	0.99±0.01	1.25±0.00
6747	VVDS	0.62	$0.56^{+0.15}_{-0.15}$	0.62	1.00	22.95±0.00	3.98±0.08	1.91±0.09	1.73±0.00
4094	FORS2	0.66	$0.54^{+0.15}_{-0.15}$	1.06	1.00	25.13±0.01	0.65±0.03	0.20±0.04	0.61±0.01
1375	FORS2	0.66	$0.55^{+0.15}_{-0.15}$	0.14	1.00	23.64±0.00	1.09±0.01	0.46±0.01	0.75±0.00
2387	FORS2	0.67	$0.62^{+0.16}_{-0.16}$	0.17	1.00	22.14±0.00	4.17±0.05	1.82±0.06	1.83±0.00
968	FORS2	0.67	$0.50^{+0.15}_{-0.15}$	0.27	1.00	21.56±0.00	1.10±0.00	0.50±0.00	0.72±0.00
2607	VVDS	0.67	$0.60^{+0.16}_{-0.16}$	0.08	1.00	21.94±0.00	1.97±0.01	0.84±0.01	1.28±0.00
662	VVDS	0.67	$0.53^{+0.15}_{-0.15}$	0.18	1.00	22.56±0.00	1.02±0.00	0.42±0.01	0.71±0.00
53380	VVDS	0.67	$0.53^{+0.15}_{-0.15}$	0.05	1.00	23.87±0.01	3.05±0.07	1.42±0.08	1.68±0.01
3349	VIMOS	0.67	$0.57^{+0.15}_{-0.15}$	0.08	1.00	24.20±0.01	1.15±0.02	0.39±0.02	0.91±0.01
8	VIMOS	0.67	$0.52^{+0.15}_{-0.15}$	0.01	1.00	22.58±0.00	3.60±0.04	1.78±0.05	1.66±0.00
355	VIMOS	0.67	$0.52^{+0.15}_{-0.15}$	0.10	1.00	23.69±0.00	1.46±0.02	0.65±0.02	0.97±0.00
9244	VIMOS	0.69	$0.67^{+0.16}_{-0.16}$	0.28	1.00	24.33±0.01	0.67±0.01	0.16±0.02	0.78±0.01
4389	VIMOS	0.71	$0.55^{+0.15}_{-0.15}$	0.21	1.00	23.93±0.00	1.29±0.01	0.52±0.02	0.94±0.00

Table C.3—Continued

ID[a]	Survey	$z_{\rm spec}$	z_b[b]	$\chi^2_{\rm mod}$[c]	ODDS[d]	V (mag)	$u-V$ (mag)	$u-B$ (mag)	$V-z'$ (mag)
1025	FORS2	0.73	$1.09^{+0.20}_{-0.21}$	0.10	1.00	25.85±0.01	0.38±0.04	-0.13±0.04	1.34±0.01
6933	FORS2	0.74	$0.58^{+0.16}_{-0.15}$	0.05	1.00	23.67±0.00	0.89±0.01	0.38±0.01	0.77±0.01
1041	VIMOS	0.74	$0.56^{+0.15}_{-0.15}$	3.54	1.00	24.35±0.00	1.44±0.02	0.71±0.03	1.05±0.01
8810	FORS2	0.74	$0.70^{+0.17}_{-0.17}$	2.27	1.00	23.10±0.00	0.92±0.01	0.36±0.01	0.99±0.00
4142	VIMOS	0.74	$0.65^{+0.16}_{-0.16}$	0.33	1.00	22.32±0.00	1.04±0.00	0.44±0.00	0.88±0.00
2525	VIMOS	0.74	$0.63^{+0.16}_{-0.16}$	0.13	1.00	23.52±0.00	1.18±0.01	0.49±0.01	1.02±0.00
8275	Szokoly	0.76	$0.69^{+0.17}_{-0.17}$	0.12	1.00	22.13±0.00	0.89±0.00	0.38±0.00	0.94±0.00
6953	FORS2	0.76	$0.74^{+0.17}_{-0.17}$	0.63	1.00	25.17±0.01	0.47±0.02	0.14±0.02	0.82±0.01
2215	FORS2	0.90	$0.70^{+0.17}_{-0.17}$	0.34	1.00	25.33±0.01	0.42±0.02	0.28±0.03	0.78±0.01
9712	VIMOS	0.91	$0.90^{+0.19}_{-0.19}$	0.12	1.00	24.61±0.01	0.65±0.01	0.35±0.02	1.17±0.01
5187	VIMOS	0.95	$0.76^{+0.17}_{-0.17}$	0.05	1.00	24.55±0.00	0.88±0.02	0.25±0.02	1.20±0.01
6206	FORS2	0.95	$0.87^{+0.18}_{-0.18}$	0.20	1.00	23.40±0.00	2.14±0.02	0.84±0.03	2.20±0.00
9402	VIMOS	0.95	$1.03^{+0.20}_{-0.20}$	0.16	1.00	24.29±0.01	0.46±0.01	0.37±0.01	0.95±0.01
901	VIMOS	0.96	$0.75^{+0.17}_{-0.17}$	0.67	1.00	24.05±0.00	0.66±0.01	0.27±0.01	0.97±0.00
153	FORS2	0.98	$0.88^{+0.18}_{-0.18}$	0.01	1.00	22.85±0.00	4.81±0.18	2.59±0.19	2.28±0.00
3372	VVDS	1.00	$0.78^{+0.17}_{-0.17}$	0.74	1.00	22.32±0.00	0.90±0.00	0.36±0.00	1.09±0.00
7328	FORS2	1.04	$1.22^{+0.22}_{-0.22}$	1.02	1.00	25.98±0.02	2.81±0.36	1.03±0.39	2.56±0.02
8680	FORS2	1.09	$1.06^{+0.20}_{-0.20}$	0.69	1.00	24.62±0.00	0.82±0.02	0.48±0.02	1.12±0.01
8261	FORS2	1.09	$1.36^{+0.23}_{-0.23}$	0.00	1.00	24.65±0.01	1.56±0.04	0.46±0.05	1.98±0.01
5417	VVDS	1.10	$1.11^{+0.21}_{-0.21}$	1.59	1.00	22.57±0.00	0.91±0.00	0.45±0.01	1.13±0.00
5694	FORS2	1.10	$1.21^{+0.22}_{-0.22}$	1.58	1.00	24.35±0.01	0.34±0.01	0.26±0.01	0.75±0.01
5658	FORS2	1.10	$1.07^{+0.20}_{-0.20}$	0.69	1.00	24.56±0.01	0.69±0.02	0.33±0.02	1.18±0.01
9264	FORS2	1.10	$1.00^{+0.20}_{-0.20}$	0.02	1.00	23.41±0.01	5.12±0.39	3.28±0.39	2.58±0.01
5405	FORS2	1.10	$1.08^{+0.20}_{-0.20}$	0.24	1.00	25.73±0.01	0.65±0.04	0.38±0.04	1.18±0.02
3613	FORS2	1.10	$1.06^{+0.20}_{-0.20}$	0.29	1.00	23.29±0.00	0.82±0.01	0.37±0.01	1.21±0.00
5962	FORS2	1.10	$1.03^{+0.20}_{-0.20}$	0.03	1.00	25.59±0.02	1.34±0.07	0.02±0.10	1.78±0.02
8749	FORS2	1.10	$0.75^{+0.17}_{-0.17}$	0.59	0.98	24.21±0.00	1.42±0.02	0.49±0.02	1.50±0.00
5989	FORS2	1.13	$1.12^{+0.21}_{-0.21}$	0.26	1.00	24.55±0.01	0.63±0.01	0.42±0.02	1.03±0.01
224	FORS2	1.14	$1.62^{+0.26}_{-0.26}$	0.06	1.00	24.26±0.00	0.31±0.01	0.28±0.01	0.40±0.01
2414	FORS2	1.19	$0.94^{+0.19}_{-0.19}$	0.00	1.00	25.67±0.02	3.13±0.36	1.61±0.38	2.46±0.02
20037	FORS2	1.22	$1.24^{+0.22}_{-0.22}$	0.60	1.00	25.05±0.01	0.69±0.02	0.27±0.03	1.14±0.01
9397	Szokoly	1.22	$0.42^{+0.14}_{-0.14}$	8.86	1.00	21.16±0.00	0.04±0.00	-0.21±0.00	0.16±0.00
4816	FORS2	1.22	$1.41^{+0.24}_{-0.24}$	0.40	1.00	24.51±0.01	0.98±0.02	0.57±0.02	1.09±0.01
3299	FORS2	1.22	$0.74^{+0.84}_{-0.17}$	0.36	0.85	25.37±0.01	0.61±0.03	0.30±0.03	0.83±0.01
4396	FORS2	1.22	$1.26^{+0.22}_{-0.22}$	0.11	1.00	25.34±0.02	0.88±0.04	0.46±0.05	1.77±0.02

Table C.3—Continued

ID[a]	Survey	$z_{\rm spec}$	z_b[b]	$\chi^2_{\rm mod}$[c]	ODDS[d]	V (mag)	$u-V$ (mag)	$u-B$ (mag)	$V-z'$ (mag)
1266	FORS2	1.25	$1.40^{+0.24}_{-0.24}$	0.01	1.00	24.25±0.00	0.88±0.01	0.46±0.01	1.27±0.00
7995	FORS2	1.29	$1.37^{+0.23}_{-0.23}$	0.01	1.00	23.58±0.00	0.79±0.01	0.50±0.01	1.05±0.00
9125	VIMOS	1.29	$1.32^{+0.23}_{-0.23}$	1.76	1.00	23.79±0.00	0.81±0.01	0.52±0.01	1.12±0.00
6079	FORS2	1.30	$1.28^{+0.22}_{-0.22}$	0.26	1.00	25.33±0.01	0.92±0.03	0.52±0.03	1.24±0.01
58728	FORS2	1.31	$1.46^{+0.24}_{-0.24}$	0.03	1.00	24.85±0.01	0.46±0.02	0.36±0.02	0.63±0.01
7974	FORS2	1.31	$1.36^{+0.23}_{-0.23}$	2.81	1.00	24.45±0.01	0.46±0.01	0.38±0.01	0.56±0.01
797	VIMOS	1.31	$1.53^{+0.25}_{-0.25}$	0.01	1.00	22.18±0.00	0.63±0.00	0.44±0.00	0.61±0.00
6188	FORS2	1.31	$1.03^{+0.20}_{-0.20}$	2.47	1.00	25.34±0.02	3.34±0.37	2.11±0.38	2.28±0.02
5190	FORS2	1.32	$1.35^{+0.23}_{-0.23}$	1.93	1.00	23.97±0.00	0.70±0.01	0.51±0.01	0.83±0.00
7725	FORS2	1.32	$1.30^{+0.23}_{-0.22}$	0.02	1.00	24.11±0.00	0.72±0.01	0.48±0.01	1.00±0.01
6027	FORS2	1.32	$1.08^{+0.20}_{-0.20}$	1.98	1.00	24.84±0.01	2.23±0.08	1.06±0.10	2.16±0.01
4835	FORS2	1.32	$1.36^{+0.23}_{-0.23}$	1.47	1.00	25.49±0.01	0.92±0.04	0.65±0.04	0.90±0.01
4801	FORS2	1.32	$1.39^{+0.23}_{-0.23}$	0.05	1.00	24.22±0.01	0.65±0.01	0.38±0.02	1.03±0.01
1666	FORS2	1.32	$1.35^{+0.23}_{-0.23}$	0.88	1.00	23.81±0.00	0.40±0.01	0.33±0.01	0.56±0.01
2201	FORS2	1.38	$1.41^{+0.24}_{-0.24}$	0.00	1.00	24.78±0.00	0.64±0.02	0.44±0.02	0.87±0.01
8765	FORS2	1.41	$1.56^{+0.25}_{-0.25}$	0.67	1.00	25.09±0.01	0.32±0.02	0.27±0.02	0.45±0.01
8461	FORS2	1.43	$1.51^{+0.25}_{-0.25}$	0.00	1.00	24.10±0.00	0.85±0.01	0.56±0.01	0.89±0.01
4616	FORS2	1.43	$1.47^{+0.24}_{-0.24}$	0.25	1.00	25.80±0.02	1.47±0.09	1.09±0.10	1.52±0.02
3574	FORS2	1.54	$1.79^{+0.27}_{-0.27}$	0.13	1.00	27.02±0.04	1.94±0.36	0.06±0.46	1.60±0.04
4950	FORS2	1.55	$1.09^{+0.20}_{-0.21}$	0.02	1.00	24.73±0.01	1.13±0.03	0.65±0.03	1.61±0.01
6462	FORS2	1.57	$1.64^{+0.26}_{-0.26}$	3.10	1.00	23.95±0.00	0.69±0.01	0.50±0.01	0.61±0.01
5365	FORS2	1.61	$1.66^{+0.26}_{-0.26}$	0.06	1.00	24.46±0.01	0.87±0.02	0.66±0.02	0.60±0.01
3752	FORS2	1.61	$2.17^{+0.31}_{-0.31}$	0.98	1.00	24.80±0.01	0.81±0.02	0.64±0.02	0.43±0.01
6834	FORS2	1.99	$0.01^{+2.66}_{-0.01}$	17.72	0.86	24.46±0.01	1.27±0.02	0.97±0.02	0.50±0.01
2993	VIMOS	2.00	$1.90^{+0.28}_{-0.28}$	3.81	1.00	23.80±0.00	1.49±0.02	1.04±0.02	0.71±0.01
830	VIMOS	2.44	$2.69^{+0.36}_{-0.36}$	0.20	1.00	24.80±0.00	1.25±0.02	0.87±0.03	0.05±0.01
2240	VIMOS	2.62	$2.61^{+0.35}_{-0.35}$	0.40	1.00	24.52±0.00	1.27±0.02	1.17±0.02	-0.04±0.01
97	VIMOS	2.69	$2.87^{+0.38}_{-0.38}$	0.13	1.00	25.02±0.01	2.01±0.06	1.48±0.07	0.08±0.01
865	Szokoly	3.06	$3.68^{+0.46}_{-0.46}$	21.40	1.00	25.30±0.01	3.56±0.36	1.70±0.38	0.91±0.02
6732	FORS2	3.19	$3.30^{+0.42}_{-0.42}$	7.47	1.00	24.58±0.00	4.36±0.37	3.26±0.37	-0.02±0.01
9409	FORS2	3.80	$3.77^{+0.47}_{-0.47}$	0.11	1.00	25.20±0.01	2.78±0.22	0.83±0.22	0.57±0.01
9983	FORS2	4.77	$4.72^{+0.56}_{-0.56}$	0.04	1.00	27.26±0.04	1.51±0.32	-0.82±0.54	1.90±0.05

Note. — See notes from Table 2.3.

Table C.4. Catalog of Candidate z∼3 LBGs in the UDF

ID[a]	z_b[b]	$\chi^2_{\rm mod}$[c]	ODDS[d]	Type[e]	V (mag)	$u-V$ (mag)	$u-B$ (mag)	$V-z'$ (mag)
22	$3.23^{+0.41}_{-0.41}$	0.44	1.00	2	27.38±0.03	1.53±0.36	0.96±0.36	0.49±0.04
76	$2.62^{+0.36}_{-0.35}$	0.52	1.00	2	26.47±0.02	1.39±0.16	1.19±0.16	0.11±0.03
84	$3.11^{+0.40}_{-0.40}$	0.01	1.00	1	26.56±0.02	2.40±0.35	1.69±0.35	0.03±0.04
97	$2.87^{+0.38}_{-0.38}$	0.13	1.00	1	25.02±0.01	2.01±0.06	1.48±0.07	0.08±0.01
99	$2.81^{+0.37}_{-0.37}$	0.32	1.00	2	24.74±0.01	1.96±0.07	1.51±0.08	0.52±0.01
101	$2.66^{+0.36}_{-0.36}$	0.17	1.00	2	27.38±0.02	1.45±0.32	1.09±0.32	0.09±0.05
131	$3.06^{+0.40}_{-0.40}$	0.21	1.00	1	26.95±0.02	2.02±0.35	1.43±0.36	0.03±0.05
209	$2.67^{+0.36}_{-0.36}$	9.03	1.00	3	26.92±0.02	1.27±0.34	1.26±0.34	-0.31±0.05
213	$3.14^{+0.41}_{-0.41}$	0.18	1.00	2	26.91±0.02	1.95±0.34	1.19±0.35	0.56±0.04
230	$3.70^{+0.46}_{-0.46}$	0.00	1.00	3	25.68±0.01	3.08±0.35	1.29±0.36	0.44±0.02
252	$3.31^{+0.42}_{-0.42}$	1.35	1.00	2	27.46±0.03	1.35±0.33	0.62±0.34	-0.28±0.08
268	$3.11^{+0.40}_{-0.40}$	2.15	1.00	1	26.81±0.03	1.76±0.29	1.49±0.29	0.09±0.05
296	$2.75^{+0.37}_{-0.37}$	1.12	1.00	1	26.93±0.02	1.36±0.23	1.19±0.23	-0.42±0.06
310	$2.71^{+0.36}_{-0.36}$	0.10	1.00	2	25.21±0.01	1.34±0.04	0.90±0.04	0.14±0.01
313	$3.13^{+0.40}_{-0.41}$	0.02	1.00	1	27.16±0.02	1.78±0.34	1.04±0.34	0.02±0.05
357	$2.66^{+0.36}_{-0.36}$	0.14	1.00	2	25.50±0.01	1.27±0.07	0.88±0.07	0.08±0.01
359	$3.45^{+0.44}_{-0.44}$	0.03	1.00	1	26.55±0.02	2.40±0.35	1.17±0.36	0.26±0.03
379	$3.10^{+0.40}_{-0.40}$	0.36	1.00	1	27.19±0.02	1.76±0.34	1.40±0.34	-0.07±0.05
381	$3.05^{+0.40}_{-0.40}$	2.06	0.99	1	27.21±0.03	1.76±0.36	1.60±0.36	-0.00±0.06
388	$2.63^{+0.36}_{-0.36}$	2.61	1.00	2	26.70±0.02	0.56±0.11	0.34±0.11	-0.29±0.06
405	$3.05^{+0.40}_{-0.40}$	0.51	1.00	1	26.83±0.02	2.17±0.35	1.81±0.35	-0.20±0.04
409	$3.42^{+0.43}_{-0.43}$	0.22	1.00	2	27.00±0.02	1.89±0.34	0.61±0.35	0.03±0.04
500	$2.99^{+0.39}_{-0.39}$	1.65	1.00	1	27.22±0.02	1.76±0.35	1.54±0.35	-0.23±0.05
513	$3.29^{+0.42}_{-0.42}$	0.30	1.00	2	26.92±0.03	1.89±0.33	1.31±0.33	0.83±0.04
522	$3.09^{+0.40}_{-0.40}$	0.22	1.00	1	27.14±0.03	1.66±0.32	1.29±0.32	-0.14±0.07
529	$3.29^{+0.42}_{-0.42}$	0.01	1.00	2	27.39±0.02	0.96±0.34	-0.01±0.35	0.10±0.05
599	$2.87^{+0.38}_{-0.38}$	0.58	1.00	2	26.97±0.02	1.99±0.35	1.51±0.35	0.25±0.04
604	$3.13^{+0.40}_{-0.41}$	0.46	1.00	1	26.83±0.02	1.98±0.34	1.24±0.34	0.10±0.03
607	$2.74^{+0.37}_{-0.37}$	1.65	1.00	1	26.96±0.02	1.50±0.23	1.39±0.24	-0.27±0.06
637	$3.31^{+0.42}_{-0.42}$	0.09	1.00	1	24.84±0.00	3.42±0.19	2.42±0.19	0.23±0.01
643	$2.61^{+0.35}_{-0.35}$	0.62	1.00	2	26.72±0.01	1.03±0.11	0.80±0.12	-0.16±0.04
674	$2.81^{+0.37}_{-0.37}$	0.18	1.00	1	26.43±0.02	2.31±0.29	1.90±0.29	-0.05±0.04
702	$2.95^{+0.39}_{-0.39}$	0.05	1.00	1	25.84±0.01	2.55±0.21	1.58±0.21	0.30±0.02
711	$2.57^{+0.35}_{-0.35}$	0.23	1.00	2	26.16±0.01	1.16±0.08	1.02±0.08	-0.01±0.02
732	$2.98^{+0.39}_{-0.39}$	2.12	1.00	1	27.18±0.02	1.80±0.35	1.62±0.35	-0.16±0.05
741	$3.55^{+0.45}_{-0.45}$	3.27	1.00	3	25.89±0.01	2.97±0.35	1.43±0.35	0.53±0.02
769	$2.73^{+0.37}_{-0.37}$	0.01	1.00	2	23.81±0.00	1.52±0.02	0.96±0.02	0.34±0.01
784	$2.53^{+0.35}_{-0.35}$	0.76	1.00	2	26.34±0.02	1.03±0.11	0.95±0.11	0.10±0.04
791	$2.82^{+0.37}_{-0.37}$	0.06	1.00	2	25.38±0.01	1.91±0.10	1.38±0.10	0.20±0.01
830	$2.69^{+0.36}_{-0.36}$	0.20	1.00	2	24.80±0.00	1.25±0.02	0.87±0.03	0.05±0.01
841	$2.53^{+0.35}_{-0.35}$	0.15	1.00	2	26.38±0.01	0.96±0.09	0.83±0.09	-0.12±0.03
862	$3.18^{+0.41}_{-0.41}$	4.12	1.00	3	27.16±0.02	1.87±0.36	1.12±0.37	-0.44±0.05
881	$3.22^{+0.41}_{-0.41}$	0.05	1.00	2	25.64±0.01	3.15±0.34	2.20±0.35	0.69±0.02
906	$2.68^{+0.36}_{-0.36}$	12.26	1.00	3	27.52±0.02	1.50±0.36	1.60±0.36	-0.14±0.05
926	$2.61^{+0.35}_{-0.35}$	0.29	1.00	2	26.73±0.02	0.71±0.10	0.69±0.10	-0.22±0.04
951	$3.03^{+0.39}_{-0.39}$	0.19	1.00	2	27.49±0.03	1.41±0.34	0.82±0.35	0.20±0.05
955	$2.88^{+0.38}_{-0.38}$	0.26	1.00	1	26.00±0.01	2.30±0.23	1.82±0.23	0.11±0.02
1044	$2.56^{+0.35}_{-0.35}$	12.49	0.99	3	27.25±0.02	1.06±0.35	1.17±0.35	-0.17±0.05
1049	$2.67^{+0.36}_{-0.36}$	0.02	1.00	2	24.95±0.01	1.58±0.04	0.67±0.04	0.34±0.01
1058	$2.86^{+0.38}_{-0.38}$	4.61	1.00	3	26.89±0.02	1.95±0.36	1.80±0.36	-0.22±0.04
1091	$2.55^{+0.35}_{-0.35}$	1.65	1.00	1	26.91±0.02	1.34±0.19	1.24±0.20	-0.14±0.04
1095	$3.15^{+0.41}_{-0.41}$	0.43	1.00	2	26.81±0.02	2.15±0.36	1.09±0.37	0.47±0.03
1107	$3.36^{+0.43}_{-0.43}$	0.10	1.00	2	27.41±0.02	1.61±0.36	0.56±0.37	0.29±0.04
1112	$3.04^{+0.40}_{-0.40}$	1.43	1.00	1	24.51±0.01	2.99±0.13	2.07±0.14	0.17±0.02
1120	$3.29^{+0.42}_{-0.42}$	0.65	1.00	1	26.61±0.02	2.29±0.34	1.32±0.34	0.10±0.04
1174	$2.97^{+0.39}_{-0.39}$	1.10	1.00	1	27.57±0.02	1.40±0.35	0.98±0.36	-0.30±0.06

Table C.4—Continued

ID[a]	z_b[b]	$\chi^2_{\rm mod}$[c]	ODDS[d]	Type[e]	V (mag)	$u-V$ (mag)	$u-B$ (mag)	$V-z'$ (mag)
1189	$2.77^{+0.37}_{-0.37}$	0.05	1.00	2	24.87±0.00	1.47±0.03	0.93±0.03	0.23±0.01
1217	$2.75^{+0.37}_{-0.37}$	0.52	1.00	1	26.53±0.01	2.28±0.30	1.94±0.30	0.01±0.02
1242	$2.83^{+0.38}_{-0.38}$	0.46	1.00	2	25.44±0.01	1.83±0.09	1.29±0.09	0.24±0.02
1253	$3.42^{+0.43}_{-0.43}$	0.02	1.00	2	27.01±0.02	1.82±0.33	0.61±0.34	0.18±0.04
1265	$3.00^{+0.39}_{-0.39}$	0.24	1.00	1	27.20±0.02	1.74±0.34	1.10±0.35	-0.05±0.05
1273	$3.03^{+0.39}_{-0.39}$	0.16	1.00	1	26.24±0.01	2.79±0.37	2.20±0.37	0.02±0.02
1354	$3.05^{+0.40}_{-0.40}$	1.54	1.00	1	26.23±0.01	2.68±0.35	2.01±0.35	0.00±0.03
1383	$3.21^{+0.41}_{-0.41}$	0.02	1.00	1	26.55±0.02	2.39±0.35	1.52±0.35	0.25±0.03
1386	$3.08^{+0.40}_{-0.40}$	0.08	1.00	1	26.41±0.01	2.53±0.35	1.76±0.35	0.19±0.03
1396	$3.07^{+0.40}_{-0.40}$	0.11	1.00	1	26.03±0.01	2.44±0.32	1.81±0.32	0.06±0.03
1414	$2.86^{+0.38}_{-0.38}$	0.97	1.00	1	27.19±0.02	1.82±0.37	1.32±0.37	-0.03±0.05
1416	$2.53^{+0.35}_{-0.35}$	1.30	1.00	2	24.74±0.00	0.89±0.02	0.69±0.02	0.12±0.01
1421	$2.55^{+0.35}_{-0.35}$	1.17	1.00	2	24.38±0.00	1.08±0.02	0.80±0.02	0.30±0.01
1440	$3.31^{+0.42}_{-0.42}$	0.01	1.00	1	26.84±0.02	1.91±0.34	0.92±0.35	0.18±0.04
1454	$2.70^{+0.36}_{-0.36}$	0.76	1.00	1	25.14±0.01	1.46±0.04	1.13±0.04	-0.03±0.01
1559	$3.01^{+0.39}_{-0.39}$	0.13	1.00	1	26.29±0.01	2.49±0.34	1.94±0.34	0.03±0.03
1564	$3.34^{+0.43}_{-0.42}$	0.14	1.00	1	24.85±0.00	4.09±0.36	3.05±0.36	0.23±0.01
1683	$2.52^{+0.35}_{-0.35}$	0.09	1.00	2	26.76±0.02	0.61±0.08	0.61±0.08	-0.21±0.04
1738	$2.67^{+0.36}_{-0.36}$	2.36	1.00	1	26.27±0.01	1.05±0.08	1.02±0.08	-0.30±0.03
1739	$2.51^{+0.34}_{-0.34}$	0.79	1.00	2	25.88±0.01	0.94±0.05	0.77±0.05	0.09±0.02
1753	$3.44^{+0.43}_{-0.43}$	0.26	1.00	2	27.47±0.03	1.02±0.35	-0.37±0.38	0.58±0.04
1809	$3.60^{+0.45}_{-0.45}$	0.03	1.00	3	25.55±0.01	3.35±0.36	1.79±0.36	0.41±0.02
1849	$2.58^{+0.35}_{-0.35}$	0.05	1.00	2	26.22±0.01	1.09±0.10	0.84±0.10	-0.00±0.03
1880	$3.31^{+0.42}_{-0.42}$	0.23	1.00	1	26.04±0.01	2.31±0.28	1.36±0.28	0.20±0.02
1888	$3.07^{+0.40}_{-0.40}$	0.18	1.00	1	26.99±0.02	1.58±0.34	0.85±0.34	-0.03±0.05
2012	$2.98^{+0.39}_{-0.39}$	1.02	1.00	1	24.39±0.00	2.52±0.07	1.67±0.07	0.21±0.01
2044	$2.51^{+0.34}_{-0.34}$	0.61	1.00	2	27.06±0.02	0.98±0.15	0.77±0.16	0.11±0.04
2045	$2.58^{+0.35}_{-0.35}$	0.20	1.00	2	26.10±0.01	1.12±0.08	0.91±0.09	0.08±0.02
2093	$3.06^{+0.40}_{-0.40}$	1.20	1.00	2	27.19±0.02	1.12±0.32	0.36±0.33	-0.08±0.05
2102	$3.04^{+0.40}_{-0.40}$	0.87	1.00	1	27.09±0.02	1.80±0.33	1.52±0.33	-0.20±0.06
2189	$2.83^{+0.38}_{-0.38}$	0.20	1.00	1	25.31±0.01	2.03±0.08	1.60±0.08	0.05±0.01
2228	$2.89^{+0.38}_{-0.38}$	0.66	1.00	1	27.05±0.03	1.75±0.34	1.27±0.35	-0.08±0.06
2240	$2.61^{+0.35}_{-0.35}$	0.40	1.00	1	24.52±0.00	1.27±0.02	1.17±0.02	-0.04±0.01
2248	$2.52^{+0.35}_{-0.35}$	1.07	1.00	2	25.88±0.01	0.61±0.04	0.57±0.05	-0.22±0.02
2350	$3.09^{+0.40}_{-0.40}$	0.34	1.00	1	26.29±0.02	2.45±0.34	1.89±0.34	0.26±0.03
2445	$2.57^{+0.35}_{-0.35}$	0.27	1.00	2	25.91±0.01	1.33±0.10	0.61±0.11	0.28±0.03
2463	$2.89^{+0.38}_{-0.38}$	0.39	1.00	1	24.91±0.01	1.96±0.05	1.35±0.05	0.13±0.01
2468	$2.88^{+0.38}_{-0.38}$	1.43	1.00	1	26.99±0.02	1.65±0.33	1.14±0.33	-0.06±0.05
2516	$2.93^{+0.41}_{-0.38}$	1.00	0.93	3	26.30±0.01	2.01±0.20	1.39±0.20	-0.11±0.03
2538	$2.56^{+0.35}_{-0.35}$	0.62	1.00	2	26.55±0.02	0.91±0.09	0.62±0.10	-0.05±0.04
2540	$3.10^{+0.40}_{-0.40}$	0.58	1.00	1	27.30±0.03	1.57±0.33	0.95±0.34	0.02±0.07
2547	$3.18^{+0.41}_{-0.41}$	0.32	1.00	1	27.06±0.02	1.90±0.35	1.47±0.35	-0.11±0.05
2558	$3.02^{+0.39}_{-0.39}$	0.02	1.00	1	24.54±0.00	2.69±0.10	1.90±0.10	0.13±0.01
2566	$3.48^{+0.44}_{-0.44}$	0.03	1.00	2	26.83±0.02	2.11±0.34	0.84±0.36	0.56±0.03
2581	$3.40^{+0.43}_{-0.43}$	2.24	1.00	2	26.92±0.02	2.05±0.35	1.01±0.36	0.43±0.03
2595	$2.97^{+0.39}_{-0.39}$	1.41	1.00	1	27.37±0.02	1.60±0.35	1.37±0.35	-0.17±0.05
2611	$3.23^{+0.41}_{-0.41}$	0.70	1.00	1	27.27±0.03	1.54±0.34	1.07±0.34	-0.06±0.06
2688	$3.28^{+0.42}_{-0.42}$	0.03	1.00	2	27.24±0.02	1.69±0.35	0.75±0.35	0.09±0.05
2728	$3.17^{+0.41}_{-0.41}$	0.09	1.00	1	26.46±0.02	2.49±0.35	1.74±0.36	0.09±0.03
2734	$3.03^{+0.39}_{-0.39}$	1.02	1.00	1	26.80±0.01	1.78±0.35	1.42±0.35	-0.17±0.04
2750	$3.64^{+0.45}_{-0.46}$	0.82	1.00	3	26.40±0.02	2.50±0.34	0.93±0.36	0.34±0.03
2813	$2.67^{+0.36}_{-0.36}$	0.01	1.00	2	25.26±0.01	1.74±0.06	0.88±0.07	0.39±0.01
2826	$2.53^{+0.35}_{-0.35}$	1.30	1.00	1	27.41±0.02	1.36±0.28	1.31±0.28	-0.03±0.05
2837	$3.38^{+0.43}_{-0.43}$	1.10	1.00	2	26.89±0.02	1.94±0.34	0.94±0.35	0.52±0.04
2872	$3.01^{+0.39}_{-0.39}$	0.46	1.00	1	25.91±0.01	2.44±0.20	1.78±0.20	-0.01±0.02
2873	$3.46^{+0.44}_{-0.44}$	0.17	1.00	1	26.22±0.02	2.62±0.33	1.45±0.34	0.40±0.03

Table C.4—Continued

ID[a]	z_b[b]	$\chi^2_{\rm mod}$[c]	ODDS[d]	Type[e]	V (mag)	$u-V$ (mag)	$u-B$ (mag)	$V-z'$ (mag)
2882	$2.94^{+0.39}_{-0.39}$	0.48	1.00	1	26.41±0.01	1.94±0.20	1.38±0.20	0.03±0.03
2946	$2.84^{+0.38}_{-0.38}$	0.35	1.00	1	26.72±0.02	1.95±0.27	1.43±0.27	0.17±0.03
2954	$3.20^{+0.41}_{-0.41}$	0.17	1.00	1	26.37±0.02	2.40±0.34	1.57±0.35	0.03±0.03
3021	$2.94^{+0.39}_{-0.39}$	0.02	1.00	1	25.19±0.01	2.39±0.11	1.52±0.11	0.35±0.02
3052	$2.55^{+0.35}_{-0.35}$	3.07	1.00	2	26.97±0.02	0.92±0.14	0.94±0.14	-0.18±0.04
3058	$2.84^{+0.38}_{-0.38}$	0.10	1.00	1	25.24±0.01	1.81±0.07	1.29±0.07	0.09±0.01
3060	$2.75^{+0.37}_{-0.37}$	12.42	1.00	3	26.48±0.01	2.38±0.35	2.51±0.35	-0.26±0.04
3091	$3.23^{+0.41}_{-0.41}$	0.27	1.00	1	26.25±0.01	2.38±0.34	1.50±0.35	0.05±0.03
3112	$3.01^{+0.39}_{-0.39}$	2.17	1.00	1	25.76±0.01	3.22±0.36	2.69±0.36	-0.00±0.02
3128	$3.25^{+0.42}_{-0.42}$	0.29	1.00	1	26.72±0.01	2.25±0.36	1.36±0.36	-0.00±0.03
3154	$3.02^{+0.39}_{-0.39}$	0.12	1.00	1	26.33±0.02	2.51±0.32	1.64±0.33	0.34±0.03
3174	$2.99^{+0.39}_{-0.39}$	1.06	1.00	1	25.37±0.01	2.80±0.17	2.17±0.17	0.14±0.01
3178	$2.55^{+0.35}_{-0.35}$	3.41	1.00	2	26.23±0.02	1.33±0.13	1.22±0.14	0.08±0.04
3185	$3.31^{+0.42}_{-0.42}$	0.09	1.00	1	26.70±0.01	2.18±0.35	1.18±0.36	0.05±0.03
3198	$2.72^{+0.37}_{-0.37}$	1.14	1.00	1	26.88±0.02	1.75±0.27	1.64±0.27	-0.13±0.04
3205	$2.57^{+0.35}_{-0.35}$	0.65	1.00	1	27.12±0.02	1.63±0.29	1.43±0.29	0.06±0.04
3214	$2.83^{+0.38}_{-0.38}$	0.16	1.00	1	25.54±0.01	1.77±0.08	1.21±0.08	0.05±0.02
3219	$3.00^{+0.39}_{-0.39}$	0.09	1.00	2	27.27±0.03	1.64±0.34	0.95±0.35	0.33±0.05
3345	$3.38^{+0.43}_{-0.43}$	0.72	1.00	2	27.00±0.02	1.91±0.35	0.89±0.36	0.27±0.04
3416	$3.36^{+0.43}_{-0.43}$	0.21	1.00	1	25.05±0.01	2.87±0.14	1.81±0.14	0.22±0.01
3425	$2.77^{+0.37}_{-0.37}$	2.72	1.00	2	27.24±0.02	0.90±0.17	0.62±0.17	-0.36±0.06
3461	$3.11^{+0.40}_{-0.40}$	0.07	1.00	2	27.10±0.03	1.86±0.35	1.07±0.35	0.59±0.04
3468	$3.01^{+0.39}_{-0.39}$	2.73	1.00	1	26.56±0.02	2.25±0.36	2.02±0.36	-0.15±0.05
3481	$3.00^{+0.39}_{-0.39}$	1.09	1.00	1	27.39±0.02	1.54±0.34	1.29±0.35	-0.10±0.05
3521	$3.03^{+0.39}_{-0.39}$	0.43	1.00	1	27.16±0.02	1.85±0.36	1.33±0.37	-0.01±0.05
3547	$3.18^{+0.41}_{-0.41}$	0.64	1.00	1	27.06±0.03	1.92±0.36	1.43±0.37	-0.07±0.06
3567	$2.95^{+0.39}_{-0.39}$	0.73	1.00	1	27.48±0.03	1.47±0.35	0.84±0.35	-0.05±0.06
3605	$2.76^{+0.37}_{-0.37}$	0.16	1.00	2	26.42±0.02	1.35±0.12	0.83±0.13	0.04±0.03
3693	$3.16^{+0.41}_{-0.41}$	0.58	1.00	1	26.95±0.02	1.77±0.35	1.35±0.35	-0.19±0.06
3844	$2.60^{+0.35}_{-0.35}$	1.36	1.00	2	24.69±0.01	1.23±0.03	0.89±0.03	0.35±0.01
3922	$3.43^{+0.43}_{-0.43}$	0.05	1.00	1	26.39±0.01	2.53±0.36	1.27±0.36	0.11±0.03
3936	$2.51^{+0.34}_{-0.34}$	0.56	1.00	2	26.92±0.02	1.01±0.18	0.86±0.18	-0.01±0.04
3939	$2.53^{+0.35}_{-0.35}$	0.57	1.00	2	26.07±0.01	1.31±0.09	1.15±0.09	0.20±0.03
4000	$2.78^{+0.37}_{-0.37}$	0.47	1.00	1	26.20±0.01	1.79±0.15	1.39±0.15	0.09±0.03
4010	$3.43^{+0.43}_{-0.43}$	0.23	1.00	2	26.03±0.01	2.83±0.35	1.58±0.36	0.57±0.02
4037	$2.83^{+0.38}_{-0.38}$	2.90	1.00	1	27.40±0.02	1.53±0.34	1.36±0.35	-0.23±0.06
4040	$3.05^{+0.40}_{-0.40}$	0.24	1.00	1	25.38±0.01	3.16±0.25	2.44±0.26	0.12±0.02
4058	$2.50^{+0.34}_{-0.34}$	0.12	1.00	2	25.69±0.01	0.87±0.05	0.79±0.05	-0.04±0.02
4061	$3.00^{+0.39}_{-0.39}$	0.86	1.00	1	26.11±0.01	2.84±0.36	2.43±0.36	0.09±0.02
4062	$3.50^{+0.44}_{-0.44}$	0.04	1.00	2	27.03±0.02	1.95±0.36	0.61±0.37	0.25±0.03
4070	$2.58^{+0.35}_{-0.35}$	3.50	1.00	1	25.77±0.01	1.20±0.06	1.06±0.06	-0.16±0.02
4177	$2.80^{+0.37}_{-0.37}$	6.51	1.00	3	26.26±0.02	2.07±0.28	1.80±0.28	-0.09±0.05
4178	$2.89^{+0.38}_{-0.38}$	3.30	1.00	1	27.22±0.02	1.72±0.35	1.53±0.36	-0.27±0.05
4184	$2.93^{+0.38}_{-0.38}$	0.31	1.00	2	27.16±0.02	1.28±0.35	0.60±0.35	0.11±0.04
4193	$2.57^{+0.35}_{-0.35}$	0.11	1.00	2	26.90±0.02	0.94±0.12	0.68±0.13	0.02±0.03
4225	$3.53^{+0.44}_{-0.44}$	3.23	1.00	3	25.81±0.01	2.98±0.34	1.53±0.35	0.46±0.02
4228	$2.70^{+0.36}_{-0.36}$	0.01	1.00	2	25.06±0.01	1.84±0.06	1.12±0.07	0.43±0.01
4276	$2.68^{+0.36}_{-0.36}$	0.38	1.00	2	26.43±0.01	1.12±0.14	0.72±0.14	-0.09±0.03
4302	$3.47^{+0.44}_{-0.44}$	1.37	1.00	2	27.06±0.02	1.84±0.35	0.73±0.36	-0.25±0.04
4316	$3.41^{+0.43}_{-0.43}$	0.08	1.00	1	25.21±0.01	3.62±0.36	2.51±0.36	0.34±0.01
4322	$2.53^{+0.35}_{-0.35}$	2.78	1.00	1	26.80±0.02	1.36±0.17	1.33±0.17	-0.08±0.04
4338	$2.60^{+0.35}_{-0.35}$	0.48	1.00	1	27.26±0.03	1.38±0.28	1.14±0.28	-0.03±0.06
4349	$2.78^{+0.37}_{-0.37}$	1.00	0.99	1	27.21±0.03	1.35±0.29	1.07±0.30	-0.06±0.07
4361	$2.54^{+0.35}_{-0.35}$	1.82	1.00	1	26.63±0.01	1.27±0.13	1.21±0.14	-0.14±0.03
4369	$3.11^{+0.40}_{-0.40}$	0.32	1.00	1	26.64±0.02	2.18±0.32	1.46±0.33	0.13±0.04
4373	$3.18^{+0.41}_{-0.41}$	0.13	1.00	1	25.81±0.01	2.74±0.36	1.95±0.36	0.11±0.02

Table C.4—Continued

ID[a]	z_b[b]	$\chi^2_{\rm mod}$[c]	ODDS[d]	Type[e]	V (mag)	$u-V$ (mag)	$u-B$ (mag)	$V-z'$ (mag)
4379	$3.01^{+0.39}_{-0.39}$	0.30	1.00	1	27.30±0.02	1.66±0.35	1.00±0.36	0.11±0.05
4404	$2.60^{+0.35}_{-0.35}$	3.24	1.00	1	25.69±0.01	1.30±0.07	1.18±0.07	-0.11±0.02
4411	$3.40^{+0.43}_{-0.43}$	0.42	1.00	1	26.92±0.02	2.04±0.37	1.13±0.37	-0.16±0.05
4461	$2.64^{+0.36}_{-0.36}$	0.30	1.00	2	25.26±0.01	1.24±0.04	0.91±0.04	0.14±0.01
4492	$3.04^{+0.40}_{-0.40}$	1.34	1.00	1	27.03±0.02	1.94±0.36	1.37±0.37	-0.01±0.04
4547	$3.08^{+0.40}_{-0.40}$	0.40	1.00	1	26.27±0.01	2.66±0.35	1.97±0.35	0.15±0.03
4592	$2.70^{+0.36}_{-0.36}$	5.14	1.00	3	27.52±0.03	1.45±0.36	1.25±0.36	-0.12±0.06
4603	$2.67^{+0.36}_{-0.59}$	10.76	0.95	3	26.74±0.02	1.87±0.28	1.58±0.28	-0.10±0.06
4607	$3.53^{+0.44}_{-0.44}$	2.92	1.00	3	26.64±0.02	2.35±0.36	0.89±0.37	0.31±0.03
4620	$3.06^{+0.40}_{-0.40}$	0.38	1.00	1	27.31±0.02	1.52±0.33	0.85±0.33	0.02±0.05
4626	$3.31^{+0.42}_{-0.42}$	0.60	1.00	1	26.69±0.02	2.27±0.36	1.32±0.36	0.20±0.03
4636	$2.88^{+0.38}_{-0.38}$	1.15	1.00	1	26.74±0.01	2.15±0.33	1.78±0.34	-0.22±0.04
4648	$3.42^{+0.43}_{-0.43}$	0.20	1.00	2	26.64±0.03	1.74±0.32	0.47±0.35	0.53±0.04
4660	$2.71^{+0.36}_{-0.36}$	2.68	1.00	2	27.37±0.03	1.51±0.34	1.38±0.34	0.12±0.06
4661	$3.20^{+0.41}_{-0.41}$	1.16	1.00	2	26.69±0.02	2.26±0.36	1.33±0.36	0.50±0.03
4674	$3.13^{+0.40}_{-0.41}$	0.61	1.00	1	25.32±0.01	3.52±0.34	2.79±0.35	0.14±0.01
4714	$2.61^{+0.35}_{-0.35}$	1.70	1.00	2	25.22±0.01	1.33±0.04	1.00±0.04	0.31±0.01
4766	$2.98^{+0.39}_{-0.39}$	4.48	1.00	3	26.25±0.01	2.77±0.37	2.66±0.37	-0.25±0.03
4774	$2.66^{+0.36}_{-0.36}$	1.05	1.00	1	26.68±0.01	1.59±0.18	1.38±0.18	-0.09±0.03
4779	$2.53^{+0.35}_{-0.35}$	0.04	1.00	2	27.05±0.02	0.95±0.15	0.71±0.15	0.07±0.05
4813	$2.85^{+0.38}_{-0.38}$	0.64	0.99	1	25.91±0.01	2.18±0.22	1.69±0.22	-0.14±0.03
4814	$3.12^{+0.40}_{-0.40}$	0.16	1.00	2	27.28±0.03	1.20±0.35	0.51±0.36	0.01±0.06
4830	$3.40^{+0.43}_{-0.43}$	0.38	1.00	1	26.70±0.01	2.28±0.36	1.21±0.36	0.23±0.03
4838	$2.96^{+0.39}_{-0.39}$	0.77	1.00	1	25.04±0.01	2.72±0.14	1.86±0.14	0.38±0.01
4860	$3.55^{+0.45}_{-0.45}$	0.52	1.00	3	25.69±0.01	2.90±0.33	1.57±0.34	0.43±0.02
4907	$2.60^{+0.35}_{-0.35}$	0.14	1.00	2	26.52±0.02	1.13±0.12	0.90±0.13	-0.00±0.04
4908	$2.58^{+0.35}_{-0.35}$	1.37	1.00	1	26.37±0.01	1.72±0.27	1.50±0.28	0.10±0.03
4927	$3.48^{+0.44}_{-0.44}$	0.05	1.00	1	25.64±0.01	3.32±0.36	2.04±0.37	0.25±0.02
5006	$3.45^{+0.44}_{-0.44}$	1.89	1.00	1	26.22±0.01	2.76±0.36	1.67±0.36	-0.04±0.02
5098	$3.15^{+0.41}_{-0.41}$	0.70	1.00	1	25.60±0.01	3.35±0.36	2.56±0.36	0.05±0.02
5106	$3.21^{+0.41}_{-0.41}$	0.18	1.00	2	27.48±0.03	1.45±0.36	0.79±0.37	0.41±0.05
5109	$2.95^{+0.39}_{-0.39}$	2.10	1.00	2	26.69±0.02	2.26±0.35	1.49±0.35	0.41±0.03
5136	$2.91^{+0.38}_{-0.38}$	7.58	1.00	3	25.17±0.01	2.45±0.13	1.66±0.13	0.25±0.02
5205	$3.13^{+0.40}_{-0.41}$	2.57	1.00	1	26.73±0.02	2.21±0.35	1.87±0.35	-0.16±0.04
5231	$2.52^{+0.35}_{-0.35}$	1.39	1.00	2	26.28±0.01	0.95±0.10	0.79±0.10	-0.13±0.03
5249	$2.73^{+0.37}_{-0.37}$	2.11	1.00	1	27.19±0.02	1.78±0.35	1.48±0.35	0.16±0.05
5251	$2.57^{+0.35}_{-0.35}$	2.95	1.00	2	25.91±0.01	1.10±0.06	0.91±0.06	-0.05±0.02
5275	$3.28^{+0.42}_{-0.42}$	0.44	1.00	2	27.21±0.02	1.72±0.34	0.84±0.35	0.28±0.04
5286	$2.93^{+0.38}_{-0.38}$	2.18	1.00	1	25.56±0.01	2.40±0.17	1.57±0.17	0.30±0.02
5304	$2.62^{+0.36}_{-0.35}$	0.39	1.00	2	26.11±0.01	1.10±0.08	0.74±0.08	-0.05±0.03
5346	$3.37^{+0.43}_{-0.43}$	0.87	1.00	1	27.07±0.02	1.91±0.36	0.85±0.37	0.06±0.04
5348	$3.14^{+0.41}_{-0.41}$	0.47	1.00	1	26.75±0.02	1.66±0.35	0.85±0.35	0.02±0.03
5411	$2.73^{+0.37}_{-0.37}$	0.09	1.00	1	26.31±0.02	1.53±0.14	1.14±0.14	-0.00±0.04
5443	$3.42^{+0.43}_{-0.43}$	0.71	1.00	1	26.84±0.01	2.10±0.35	1.13±0.35	-0.16±0.04
5456	$3.44^{+0.43}_{-0.43}$	1.55	1.00	2	26.44±0.02	1.94±0.21	0.81±0.22	0.32±0.03
5473	$2.96^{+0.39}_{-0.39}$	0.35	1.00	1	25.83±0.01	2.55±0.29	1.78±0.29	0.15±0.02
5533	$3.04^{+0.40}_{-0.40}$	1.79	1.00	1	27.15±0.03	1.69±0.33	0.99±0.34	-0.11±0.06
5548	$3.58^{+0.45}_{-0.45}$	0.08	1.00	3	26.36±0.01	2.56±0.36	1.01±0.36	0.25±0.02
5579	$3.06^{+0.40}_{-0.40}$	1.17	1.00	1	26.27±0.01	2.64±0.36	1.93±0.36	0.15±0.02
5628	$2.73^{+0.37}_{-0.37}$	4.69	1.00	3	27.22±0.03	1.58±0.33	1.54±0.33	-0.17±0.07
5649	$2.54^{+0.35}_{-0.35}$	0.82	1.00	2	26.15±0.01	0.72±0.10	0.55±0.10	-0.14±0.02
5662	$2.15^{+0.41}_{-0.31}$	3.03	0.82	3	27.35±0.03	1.35±0.29	1.36±0.29	-0.05±0.07
5679	$3.33^{+0.42}_{-0.42}$	0.39	1.00	1	25.61±0.01	2.33±0.15	1.30±0.16	0.22±0.02
5683	$3.00^{+0.39}_{-0.39}$	0.16	1.00	1	24.44±0.01	3.09±0.11	2.49±0.11	0.05±0.01
5701	$2.82^{+0.37}_{-0.37}$	0.12	1.00	2	25.70±0.01	1.53±0.08	0.94±0.08	0.12±0.02
5716	$3.09^{+0.40}_{-0.40}$	0.12	1.00	1	26.39±0.01	2.50±0.36	1.83±0.36	0.04±0.03

Table C.4—Continued

ID[a]	z_b[b]	$\chi^2_{\rm mod}$[c]	ODDS[d]	Type[e]	V (mag)	$u-V$ (mag)	$u-B$ (mag)	$V-z'$ (mag)
5750	$2.76^{+0.37}_{-0.37}$	0.17	1.00	1	26.68±0.01	1.29±0.14	1.12±0.14	-0.25±0.03
5808	$3.31^{+0.42}_{-0.42}$	0.12	1.00	1	26.25±0.02	2.63±0.35	1.63±0.35	0.27±0.03
5839	$2.95^{+0.39}_{-0.39}$	2.51	1.00	2	27.58±0.03	1.33±0.37	0.63±0.37	-0.50±0.08
5849	$2.66^{+0.36}_{-0.36}$	0.84	1.00	1	27.40±0.03	1.08±0.23	1.03±0.23	-0.31±0.08
5856	$3.36^{+0.43}_{-0.43}$	0.87	1.00	1	25.97±0.01	3.01±0.36	1.98±0.36	0.16±0.02
5867	$3.35^{+0.43}_{-0.43}$	0.29	1.00	1	26.48±0.02	2.35±0.32	1.23±0.33	0.15±0.04
5887	$2.76^{+0.37}_{-0.37}$	0.49	1.00	1	27.14±0.02	1.45±0.25	1.07±0.26	-0.15±0.05
5888	$3.00^{+0.39}_{-0.39}$	1.46	1.00	2	27.42±0.03	1.51±0.36	0.74±0.37	0.37±0.06
5916	$2.55^{+0.35}_{-0.35}$	1.08	1.00	2	27.30±0.02	0.43±0.12	0.33±0.12	-0.23±0.06
5920	$2.55^{+0.35}_{-0.35}$	5.24	0.98	3	27.05±0.02	1.71±0.30	1.64±0.30	0.00±0.05
5932	$3.49^{+0.44}_{-0.44}$	5.36	0.99	3	26.52±0.02	2.38±0.34	1.08±0.35	0.36±0.03
5946	$2.77^{+0.37}_{-0.37}$	0.04	1.00	2	23.04±0.00	1.73±0.01	1.15±0.02	0.30±0.01
5952	$3.13^{+0.40}_{-0.41}$	0.56	1.00	2	27.39±0.03	1.47±0.33	0.70±0.34	0.29±0.06
6103	$2.99^{+0.39}_{-0.39}$	0.07	1.00	1	26.72±0.01	1.47±0.35	0.87±0.35	-0.03±0.03
6110	$3.01^{+0.39}_{-0.39}$	1.35	1.00	1	27.13±0.03	1.72±0.32	1.12±0.33	-0.04±0.06
6123	$3.01^{+0.39}_{-0.39}$	1.57	1.00	1	27.09±0.02	1.69±0.32	0.95±0.32	-0.07±0.05
6128	$2.72^{+0.37}_{-0.37}$	6.04	1.00	3	26.76±0.01	2.22±0.36	2.23±0.36	-0.21±0.04
6203	$2.77^{+0.37}_{-0.37}$	0.60	1.00	1	24.51±0.00	1.72±0.03	1.30±0.03	-0.06±0.01
6227	$2.99^{+0.39}_{-0.39}$	0.05	1.00	1	25.69±0.01	2.26±0.18	1.44±0.18	0.18±0.02
6250	$2.80^{+0.37}_{-0.37}$	0.04	1.00	2	24.85±0.00	1.53±0.03	0.97±0.04	0.16±0.01
6274	$3.48^{+0.44}_{-0.44}$	0.00	1.00	2	26.06±0.03	2.11±0.26	0.84±0.29	0.31±0.05
6289	$3.05^{+0.40}_{-0.40}$	1.14	1.00	1	27.04±0.02	1.92±0.36	1.68±0.36	-0.07±0.04
6335	$2.66^{+0.36}_{-0.36}$	1.06	1.00	1	25.98±0.01	1.25±0.08	1.20±0.08	-0.16±0.02
6352	$2.72^{+0.37}_{-0.37}$	8.51	1.00	3	26.97±0.02	1.72±0.31	1.55±0.32	-0.17±0.05
6396	$2.64^{+0.36}_{-0.36}$	2.77	1.00	1	26.54±0.02	1.60±0.17	1.44±0.17	-0.17±0.04
6438	$2.60^{+0.35}_{-0.35}$	1.14	1.00	2	25.29±0.01	1.19±0.04	0.91±0.04	0.17±0.02
6478	$3.33^{+0.42}_{-0.42}$	0.10	1.00	1	25.75±0.01	2.72±0.33	1.67±0.34	0.05±0.02
6487	$3.08^{+0.40}_{-0.40}$	0.07	1.00	2	27.13±0.02	1.65±0.36	0.83±0.36	0.14±0.04
6488	$3.08^{+0.40}_{-0.40}$	0.14	1.00	2	26.93±0.02	1.97±0.33	1.39±0.34	0.23±0.04
6502	$2.70^{+0.40}_{-0.36}$	2.37	0.94	3	27.47±0.03	1.39±0.35	1.18±0.35	-0.14±0.06
6504	$3.17^{+0.41}_{-0.41}$	0.10	1.00	1	26.73±0.01	2.25±0.36	1.46±0.36	0.09±0.03
6508	$3.21^{+0.41}_{-0.41}$	0.96	1.00	2	27.52±0.02	1.44±0.35	0.62±0.35	0.20±0.05
6520	$2.62^{+0.36}_{-0.35}$	6.10	1.00	3	27.47±0.03	1.42±0.33	1.44±0.33	-0.08±0.07
6527	$3.13^{+0.40}_{-0.41}$	0.97	1.00	1	26.98±0.02	1.99±0.36	1.16±0.36	0.03±0.04
6533	$3.26^{+0.42}_{-0.42}$	0.06	1.00	1	26.40±0.01	2.57±0.37	1.65±0.37	0.15±0.03
6539	$3.05^{+0.40}_{-0.40}$	0.81	1.00	1	26.63±0.02	2.33±0.35	2.00±0.35	0.22±0.04
6542	$2.74^{+0.37}_{-0.37}$	0.24	1.00	2	25.74±0.01	1.80±0.10	1.38±0.10	0.20±0.02
6554	$3.21^{+0.41}_{-0.41}$	0.24	1.00	1	26.77±0.02	1.87±0.35	1.04±0.35	0.04±0.04
6595	$2.85^{+0.38}_{-0.38}$	0.85	1.00	2	27.53±0.02	1.45±0.35	0.99±0.36	0.08±0.05
6642	$2.54^{+0.35}_{-0.35}$	3.39	1.00	2	25.68±0.01	1.03±0.05	0.91±0.05	-0.05±0.02
6671	$2.54^{+0.35}_{-0.35}$	3.10	1.00	1	27.19±0.03	1.38±0.32	1.21±0.32	-0.09±0.06
6675	$2.85^{+0.38}_{-0.38}$	0.86	1.00	2	25.84±0.01	1.79±0.11	1.08±0.11	0.28±0.02
6695	$3.06^{+0.40}_{-0.40}$	0.08	1.00	1	27.10±0.02	1.88±0.36	1.23±0.36	-0.03±0.05
6701	$3.22^{+0.41}_{-0.41}$	0.08	1.00	1	26.42±0.01	2.51±0.36	1.61±0.36	0.17±0.02
6722	$3.46^{+0.44}_{-0.44}$	1.34	1.00	2	27.31±0.02	1.65±0.35	0.51±0.37	-0.23±0.06
6732	$3.30^{+0.42}_{-0.42}$	7.47	1.00	3	24.58±0.00	4.36±0.37	3.26±0.37	-0.02±0.01
6808	$3.50^{+0.44}_{-0.44}$	1.28	1.00	2	27.27±0.03	1.58±0.34	0.12±0.36	0.07±0.05
6827	$3.31^{+0.42}_{-0.42}$	0.19	1.00	1	26.60±0.02	2.31±0.35	1.33±0.35	0.25±0.03
6837	$2.73^{+0.37}_{-0.37}$	0.29	1.00	1	26.19±0.01	1.50±0.11	1.11±0.12	-0.06±0.03
6839	$3.11^{+0.40}_{-0.40}$	0.07	1.00	1	26.60±0.01	2.38±0.36	1.68±0.36	0.08±0.03
6912	$3.25^{+0.42}_{-0.42}$	0.89	1.00	2	27.06±0.03	1.79±0.33	1.10±0.34	0.39±0.05
6919	$2.91^{+0.38}_{-0.38}$	0.56	1.00	1	27.36±0.03	1.51±0.32	0.95±0.33	0.01±0.06
6937	$2.91^{+0.38}_{-0.38}$	1.61	1.00	1	27.05±0.02	1.92±0.36	1.39±0.36	0.10±0.05
6999	$3.09^{+0.40}_{-0.40}$	0.36	1.00	1	26.36±0.02	2.52±0.34	1.84±0.34	0.10±0.03
7025	$3.40^{+0.43}_{-0.43}$	0.97	1.00	1	25.22±0.00	3.80±0.37	2.89±0.37	-0.22±0.01
7146	$2.65^{+0.36}_{-0.36}$	0.28	1.00	2	25.12±0.01	1.18±0.03	0.90±0.03	0.13±0.01

Table C.4—Continued

ID[a]	z_b[b]	$\chi^2_{\rm mod}$[c]	ODDS[d]	Type[e]	V (mag)	$u-V$ (mag)	$u-B$ (mag)	$V-z'$ (mag)
7151	$3.35^{+0.43}_{-0.43}$	0.03	1.00	2	27.02±0.02	1.78±0.35	0.77±0.36	0.22±0.04
7189	$3.02^{+0.39}_{-0.39}$	0.19	1.00	1	26.15±0.01	2.61±0.34	1.95±0.34	0.16±0.02
7209	$2.70^{+0.36}_{-0.36}$	10.52	1.00	3	27.18±0.02	1.68±0.35	1.68±0.35	-0.22±0.05
7230	$2.53^{+0.35}_{-0.35}$	2.43	1.00	2	25.43±0.01	0.84±0.03	0.61±0.03	-0.08±0.02
7244	$3.00^{+0.39}_{-0.39}$	1.35	1.00	1	25.98±0.01	2.93±0.35	2.19±0.35	0.31±0.02
7246	$2.60^{+0.35}_{-0.35}$	0.03	1.00	2	27.04±0.02	1.64±0.27	1.02±0.28	0.25±0.04
7274	$3.48^{+0.44}_{-0.44}$	0.08	1.00	2	26.42±0.01	2.11±0.36	0.91±0.36	0.45±0.02
7312	$2.76^{+0.37}_{-0.37}$	0.37	1.00	1	27.42±0.03	1.44±0.33	1.26±0.33	-0.30±0.09
7313	$2.62^{+0.36}_{-0.35}$	4.90	1.00	3	26.15±0.01	1.19±0.08	0.86±0.08	-0.20±0.03
7375	$3.17^{+0.41}_{-0.41}$	1.98	1.00	1	25.63±0.01	2.84±0.36	2.32±0.36	-0.24±0.02
7423	$2.76^{+0.37}_{-0.37}$	2.38	1.00	1	26.86±0.01	1.28±0.21	1.09±0.22	-0.26±0.04
7471	$2.53^{+0.35}_{-0.35}$	3.00	1.00	2	26.85±0.02	1.29±0.17	1.25±0.17	0.04±0.04
7529	$2.64^{+0.36}_{-0.36}$	0.03	1.00	2	26.41±0.01	1.58±0.15	1.02±0.16	0.29±0.03
7534	$2.99^{+0.39}_{-0.39}$	2.96	1.00	1	26.65±0.02	2.15±0.32	1.57±0.33	-0.05±0.05
7600	$3.25^{+0.42}_{-0.42}$	0.03	1.00	1	25.14±0.01	3.87±0.37	2.97±0.37	0.32±0.01
7610	$2.75^{+0.37}_{-0.37}$	1.84	1.00	1	27.21±0.02	1.72±0.35	1.39±0.35	-0.01±0.04
7617	$3.12^{+0.40}_{-0.40}$	0.11	1.00	1	26.09±0.01	2.79±0.34	2.07±0.34	-0.01±0.03
7633	$3.02^{+0.39}_{-0.39}$	0.24	1.00	1	26.92±0.02	1.80±0.33	1.27±0.33	0.06±0.04
7658	$3.04^{+0.40}_{-0.40}$	0.08	1.00	1	26.87±0.02	1.99±0.33	1.22±0.33	0.13±0.04
7669	$2.67^{+0.36}_{-0.36}$	2.99	1.00	1	27.17±0.02	1.64±0.34	1.53±0.34	0.01±0.05
7688	$2.58^{+0.35}_{-0.35}$	0.01	1.00	2	21.72±0.00	1.54±0.00	0.76±0.00	0.33±0.00
7712	$2.79^{+0.37}_{-0.37}$	0.01	1.00	2	26.00±0.01	1.90±0.14	1.02±0.15	0.42±0.02
7720	$2.72^{+0.37}_{-0.37}$	3.09	1.00	1	27.41±0.02	1.40±0.34	1.14±0.34	-0.08±0.05
7738	$3.13^{+0.40}_{-0.41}$	0.63	1.00	1	27.29±0.02	1.62±0.35	1.10±0.35	-0.27±0.05
7758	$2.75^{+0.37}_{-0.37}$	3.63	1.00	1	27.06±0.02	1.91±0.36	1.63±0.36	-0.15±0.05
7786	$2.73^{+0.37}_{-0.37}$	0.33	1.00	2	23.97±0.00	1.53±0.02	1.02±0.02	0.29±0.01
7815	$3.49^{+0.44}_{-0.44}$	0.01	1.00	2	26.73±0.02	2.19±0.35	0.97±0.36	0.39±0.03
7868	$3.24^{+0.42}_{-0.42}$	0.46	1.00	1	26.77±0.02	2.19±0.35	1.31±0.36	0.03±0.03
7874	$3.19^{+0.41}_{-0.41}$	0.57	1.00	1	26.72±0.01	2.27±0.36	1.43±0.36	0.00±0.03
7900	$2.61^{+0.35}_{-0.35}$	1.08	1.00	2	26.29±0.01	1.26±0.10	1.01±0.11	0.09±0.03
7907	$3.10^{+0.40}_{-0.40}$	2.03	1.00	1	25.78±0.01	2.87±0.32	2.11±0.33	0.17±0.03
7909	$2.54^{+0.35}_{-0.35}$	0.69	1.00	2	26.58±0.01	1.23±0.14	1.13±0.14	-0.01±0.03
7957	$3.54^{+0.44}_{-0.44}$	0.04	1.00	3	25.85±0.01	2.87±0.34	1.55±0.35	0.42±0.02
7986	$2.62^{+0.36}_{-0.35}$	13.41	1.00	3	27.47±0.02	1.49±0.36	1.67±0.36	-0.25±0.07
7998	$2.75^{+0.37}_{-0.37}$	1.34	1.00	1	27.23±0.02	1.63±0.35	1.30±0.35	0.02±0.04
8003	$3.01^{+0.39}_{-0.39}$	0.61	1.00	1	27.46±0.02	1.46±0.35	1.17±0.35	-0.19±0.05
8017	$3.53^{+0.44}_{-0.44}$	1.77	1.00	3	26.03±0.01	2.63±0.34	1.24±0.35	0.39±0.02
8024	$3.03^{+0.39}_{-0.39}$	0.09	1.00	1	26.44±0.01	2.39±0.35	1.78±0.35	0.02±0.03
8042	$3.12^{+0.40}_{-0.40}$	0.33	1.00	1	26.44±0.02	2.39±0.34	1.68±0.34	0.07±0.03
8053	$2.59^{+0.35}_{-0.35}$	1.00	1.00	1	27.39±0.02	1.39±0.30	1.16±0.30	-0.09±0.05
8105	$3.43^{+0.43}_{-0.43}$	0.32	1.00	1	25.78±0.01	3.01±0.35	1.91±0.35	0.42±0.01
8126	$3.14^{+0.41}_{-0.41}$	0.14	1.00	2	26.98±0.03	1.61±0.29	0.70±0.30	0.25±0.05
8177	$2.80^{+0.37}_{-0.37}$	0.02	1.00	1	27.08±0.02	1.67±0.29	1.17±0.29	0.02±0.04
8181	$3.07^{+0.40}_{-0.40}$	0.06	1.00	1	25.74±0.01	3.05±0.33	2.11±0.33	0.40±0.02
8182	$3.13^{+0.40}_{-0.41}$	2.64	1.00	1	27.28±0.03	1.57±0.32	1.11±0.32	-0.26±0.07
8196	$2.64^{+0.36}_{-0.36}$	2.57	1.00	1	27.39±0.02	1.56±0.35	1.49±0.35	-0.05±0.06
8198	$2.83^{+0.38}_{-0.38}$	0.49	0.99	2	27.04±0.02	1.23±0.20	0.63±0.21	0.02±0.04
8217	$3.36^{+0.43}_{-0.43}$	1.53	1.00	1	25.40±0.01	3.00±0.24	1.91±0.24	0.23±0.02
8230	$3.60^{+0.45}_{-0.45}$	0.72	1.00	3	25.65±0.01	3.07±0.35	1.64±0.35	-0.13±0.02
8304	$3.34^{+0.43}_{-0.42}$	1.47	1.00	1	27.27±0.02	1.69±0.35	0.87±0.35	-0.29±0.06
8311	$2.72^{+0.37}_{-0.37}$	0.07	1.00	2	25.88±0.01	1.50±0.08	1.07±0.09	0.13±0.02
8327	$2.89^{+0.38}_{-0.38}$	3.75	0.99	2	27.23±0.03	1.75±0.36	0.94±0.37	0.29±0.05
8337	$2.60^{+0.35}_{-0.35}$	2.56	1.00	2	27.01±0.03	1.29±0.20	1.15±0.21	-0.00±0.06
8354	$2.95^{+0.39}_{-0.39}$	0.54	1.00	2	26.70±0.02	1.56±0.19	0.74±0.19	0.05±0.03
8387	$3.01^{+0.39}_{-0.39}$	0.38	1.00	1	27.02±0.02	1.95±0.35	1.32±0.35	-0.10±0.04
8409	$2.93^{+0.38}_{-0.38}$	2.31	1.00	1	25.67±0.01	2.55±0.21	1.78±0.21	0.37±0.02

Table C.4—Continued

ID[a]	z_b[b]	$\chi^2_{\rm mod}$[c]	ODDS[d]	Type[e]	V (mag)	$u-V$ (mag)	$u-B$ (mag)	$V-z'$ (mag)
8446	$2.76^{+0.37}_{-0.37}$	3.43	1.00	1	26.70±0.02	1.85±0.25	1.44±0.25	-0.22±0.05
8449	$3.45^{+0.44}_{-0.44}$	1.51	1.00	2	27.30±0.02	1.64±0.34	0.26±0.36	0.11±0.05
8467	$2.54^{+0.35}_{-0.35}$	0.12	1.00	2	26.99±0.02	1.08±0.15	0.87±0.16	0.07±0.04
8520	$2.69^{+0.36}_{-0.36}$	0.08	1.00	1	26.87±0.01	1.53±0.24	1.25±0.24	-0.09±0.03
8555	$2.72^{+0.37}_{-0.37}$	4.66	1.00	3	26.50±0.02	2.41±0.34	2.31±0.34	-0.01±0.04
8561	$2.68^{+0.36}_{-0.36}$	2.03	1.00	1	25.85±0.01	1.47±0.08	1.21±0.08	-0.00±0.02
8580	$3.44^{+0.43}_{-0.43}$	0.84	1.00	1	26.21±0.01	2.16±0.35	1.01±0.35	0.24±0.02
8614	$2.74^{+0.37}_{-0.37}$	0.04	1.00	1	23.93±0.00	1.56±0.02	1.18±0.02	0.05±0.01
8650	$2.91^{+0.38}_{-0.38}$	1.80	1.00	1	27.18±0.02	1.71±0.35	1.10±0.35	-0.02±0.05
8671	$3.17^{+0.41}_{-0.41}$	0.01	1.00	2	27.16±0.02	1.72±0.36	0.89±0.37	0.28±0.04
8705	$2.65^{+0.36}_{-0.36}$	0.89	1.00	1	27.16±0.02	1.59±0.29	1.40±0.30	-0.20±0.06
8721	$3.40^{+0.43}_{-0.43}$	0.34	1.00	2	27.44±0.03	1.46±0.33	0.62±0.34	-0.14±0.06
8741	$2.99^{+0.39}_{-0.39}$	4.32	1.00	3	26.46±0.01	2.37±0.35	2.20±0.35	-0.15±0.04
8750	$2.99^{+0.39}_{-0.39}$	0.11	1.00	1	26.49±0.02	2.30±0.34	1.60±0.34	0.05±0.03
8757	$2.89^{+0.38}_{-0.38}$	0.33	1.00	1	25.98±0.01	2.88±0.34	2.38±0.34	0.05±0.02
8759	$3.23^{+0.41}_{-0.41}$	0.01	1.00	1	25.74±0.01	3.23±0.36	2.34±0.36	0.01±0.02
8768	$2.74^{+0.37}_{-0.37}$	4.20	1.00	3	27.10±0.03	1.58±0.30	1.31±0.31	0.04±0.06
8812	$3.36^{+0.43}_{-0.43}$	0.54	1.00	2	26.52±0.02	1.78±0.22	0.77±0.23	0.30±0.03
8841	$2.73^{+0.37}_{-0.37}$	0.38	1.00	1	27.25±0.02	1.06±0.20	0.90±0.20	-0.21±0.06
8948	$3.38^{+0.43}_{-0.43}$	1.38	1.00	2	27.41±0.03	1.54±0.34	0.29±0.37	0.17±0.06
8950	$2.83^{+0.38}_{-0.38}$	0.02	1.00	2	24.54±0.00	1.75±0.03	1.19±0.03	0.17±0.01
8964	$3.37^{+0.43}_{-0.43}$	2.38	1.00	1	26.06±0.01	2.83±0.35	1.73±0.35	0.20±0.02
9000	$2.64^{+0.36}_{-0.36}$	0.09	1.00	2	24.66±0.00	1.25±0.03	0.90±0.03	0.15±0.01
9019	$2.17^{+0.37}_{-0.31}$	3.41	0.95	3	27.36±0.02	1.06±0.27	1.12±0.27	-0.14±0.05
9092	$3.21^{+0.41}_{-0.41}$	0.09	1.00	1	26.44±0.01	2.48±0.35	1.95±0.35	-0.15±0.03
9182	$3.15^{+0.41}_{-0.41}$	0.16	1.00	1	27.18±0.02	1.79±0.35	1.35±0.35	-0.08±0.05
9185	$3.48^{+0.44}_{-0.44}$	1.62	1.00	1	26.51±0.01	2.45±0.35	1.25±0.36	0.37±0.02
9211	$2.76^{+0.37}_{-0.37}$	0.97	0.99	2	27.45±0.02	1.37±0.35	1.01±0.35	0.03±0.05
9227	$3.45^{+0.44}_{-0.44}$	0.21	1.00	2	27.19±0.02	1.19±0.33	-0.06±0.35	0.24±0.04
9299	$3.32^{+0.42}_{-0.42}$	0.03	1.00	1	24.93±0.00	4.00±0.36	3.32±0.36	-0.11±0.01
9304	$3.28^{+0.42}_{-0.42}$	1.64	1.00	1	27.37±0.02	1.58±0.34	0.81±0.35	-0.31±0.06
9312	$3.10^{+0.40}_{-0.40}$	0.05	1.00	1	26.13±0.01	2.81±0.35	2.09±0.35	0.16±0.02
9330	$3.30^{+0.42}_{-0.42}$	0.23	1.00	2	27.15±0.03	1.60±0.34	0.73±0.35	0.18±0.05
9385	$2.67^{+0.36}_{-0.36}$	0.19	1.00	1	26.99±0.02	1.53±0.25	1.25±0.25	0.05±0.05
9394	$2.79^{+0.37}_{-0.37}$	0.04	1.00	2	25.75±0.01	1.68±0.09	1.16±0.09	0.13±0.02
9419	$3.10^{+0.40}_{-0.40}$	0.30	1.00	1	27.14±0.02	1.81±0.35	1.40±0.35	-0.21±0.05
9432	$2.62^{+0.36}_{-0.35}$	2.98	1.00	1	25.51±0.01	1.58±0.07	1.58±0.07	0.03±0.02
9452	$2.52^{+0.35}_{-0.35}$	0.13	1.00	2	25.85±0.01	0.83±0.05	0.61±0.05	-0.09±0.03
9505	$2.96^{+0.39}_{-0.39}$	2.13	1.00	1	27.04±0.02	1.91±0.35	1.68±0.35	-0.26±0.05
9543	$3.27^{+0.42}_{-0.42}$	0.02	1.00	1	24.64±0.00	4.25±0.36	3.31±0.36	0.30±0.01
9570	$2.66^{+0.36}_{-0.36}$	2.97	1.00	1	27.19±0.02	1.46±0.27	1.54±0.27	-0.09±0.06
9617	$2.52^{+0.35}_{-0.35}$	0.12	1.00	2	26.33±0.01	1.06±0.09	0.74±0.09	0.09±0.02
9640	$2.51^{+0.34}_{-0.34}$	0.26	1.00	2	26.09±0.01	0.89±0.06	0.75±0.06	0.03±0.02
9676	$3.29^{+0.42}_{-0.42}$	0.01	1.00	1	26.11±0.01	2.71±0.35	1.74±0.36	0.12±0.03
9706	$2.77^{+0.37}_{-0.37}$	0.05	1.00	2	25.62±0.01	1.53±0.07	1.02±0.08	0.21±0.02
9711	$3.48^{+0.44}_{-0.44}$	0.13	1.00	2	27.23±0.02	1.66±0.34	0.60±0.35	0.00±0.05
9806	$2.58^{+0.35}_{-0.35}$	0.03	1.00	2	26.07±0.01	1.09±0.07	0.88±0.07	-0.05±0.02
9990	$3.34^{+0.43}_{-0.42}$	0.08	1.00	1	27.10±0.02	1.85±0.34	1.09±0.34	-0.11±0.05
10004	$2.77^{+0.37}_{-0.37}$	8.64	1.00	3	27.17±0.02	1.76±0.34	1.78±0.34	-0.10±0.06
10016	$2.99^{+0.39}_{-0.39}$	0.05	1.00	1	26.56±0.01	2.30±0.32	1.95±0.32	-0.19±0.04
10018	$3.02^{+0.39}_{-0.39}$	0.52	1.00	1	27.21±0.03	1.45±0.32	1.14±0.32	-0.17±0.06
40448	$2.52^{+0.35}_{-0.35}$	0.36	1.00	2	26.72±0.02	1.07±0.18	0.75±0.18	0.09±0.05
50139	$2.65^{+0.36}_{-0.36}$	0.09	1.00	2	25.83±0.01	1.44±0.08	1.08±0.08	0.33±0.02
50947	$3.01^{+0.39}_{-0.39}$	0.13	0.99	2	26.24±0.03	1.93±0.31	0.93±0.33	0.34±0.04
51093	$2.70^{+0.36}_{-0.36}$	1.22	1.00	1	27.43±0.05	1.30±0.31	1.30±0.31	-0.18±0.11
51179	$2.97^{+0.39}_{-0.39}$	0.10	1.00	1	25.61±0.02	2.79±0.32	2.05±0.32	0.42±0.03

Table C.4—Continued

ID[a]	z_b[b]	$\chi^2_{\rm mod}$[c]	ODDS[d]	Type[e]	V (mag)	$u-V$ (mag)	$u-B$ (mag)	$V-z'$ (mag)
51711	$3.12^{+0.40}_{-0.40}$	0.35	1.00	2	26.43±0.02	2.42±0.33	1.92±0.33	0.65±0.03
52786	$3.02^{+0.39}_{-0.39}$	0.51	1.00	1	26.53±0.02	2.28±0.33	1.77±0.34	0.10±0.05
53335	$2.62^{+0.36}_{-0.35}$	0.33	1.00	2	25.60±0.01	1.15±0.05	0.95±0.05	0.13±0.02
53972	$3.09^{+0.40}_{-0.40}$	0.10	1.00	1	26.14±0.01	2.80±0.36	2.01±0.36	0.21±0.02
54735	$2.69^{+0.36}_{-0.36}$	0.40	1.00	2	22.11±0.00	1.21±0.00	0.78±0.00	0.08±0.00
55812	$2.86^{+0.38}_{-0.38}$	0.45	1.00	1	26.81±0.02	1.68±0.28	1.35±0.28	-0.35±0.07
56017	$2.64^{+0.36}_{-0.36}$	0.13	1.00	2	26.33±0.01	0.78±0.07	0.74±0.07	-0.28±0.04
56215	$3.34^{+0.43}_{-0.44}$	1.59	0.96	3	26.10±0.02	2.22±0.23	1.51±0.24	-0.10±0.04
56987	$2.86^{+0.38}_{-0.38}$	0.33	1.00	1	26.05±0.02	2.44±0.24	2.02±0.24	0.09±0.04
57116	$2.83^{+0.38}_{-0.38}$	0.40	1.00	2	26.93±0.04	1.26±0.30	0.77±0.31	0.36±0.06
57353	$2.92^{+0.40}_{-0.38}$	1.18	0.97	3	25.86±0.02	2.40±0.23	1.66±0.24	-0.18±0.04
58779	$3.04^{+0.40}_{-0.40}$	0.54	1.00	1	26.74±0.02	2.03±0.35	1.54±0.35	0.07±0.04
58909	$3.38^{+0.43}_{-0.43}$	0.05	1.00	2	27.31±0.03	1.59±0.35	0.58±0.36	0.32±0.05
59970	$2.59^{+0.35}_{-0.35}$	0.93	1.00	2	27.01±0.04	1.23±0.19	1.21±0.20	0.02±0.08
60302	$3.02^{+0.39}_{-0.39}$	0.17	1.00	2	27.15±0.03	1.70±0.33	1.01±0.34	0.29±0.05

Note. — See notes from Table 2.4.

Table C.5. Properties of LBGs included in image stack

ID[a]	z_{phot}[b]	V mag	$u-V$ mag	$B-V$ mag	$V-z'$ mag	FWHM arcsec	Ellipticity
84	$3.11^{+0.40}_{-0.40}$	26.56±0.02	2.40±0.35	0.70±0.05	0.03±0.04	0.24	0.18
862	$3.18^{+0.41}_{-0.41}$	27.16±0.02	1.87±0.36	0.74±0.05	-0.44±0.05	0.12	0.14
906	$2.68^{+0.36}_{-0.36}$	27.52±0.02	1.50±0.36	-0.10±0.04	-0.14±0.05	0.10	0.04
1217	$2.75^{+0.37}_{-0.37}$	26.53±0.01	2.28±0.30	0.34±0.02	0.01±0.02	0.14	0.23
1273	$3.03^{+0.39}_{-0.39}$	26.24±0.01	2.79±0.37	0.58±0.03	0.02±0.02	0.12	0.12
1414	$2.86^{+0.38}_{-0.38}$	27.19±0.02	1.82±0.37	0.49±0.06	-0.03±0.05	0.10	0.13
1738	$2.67^{+0.36}_{-0.36}$	26.27±0.01	1.05±0.08	0.03±0.02	-0.30±0.03	0.16	0.15
1753	$3.44^{+0.43}_{-0.43}$	27.47±0.03	1.02±0.35	1.39±0.14	0.58±0.04	0.18	0.12
2581	$3.40^{+0.43}_{-0.43}$	26.92±0.02	2.05±0.35	1.04±0.07	0.43±0.03	0.18	0.24
2595	$2.97^{+0.39}_{-0.39}$	27.37±0.02	1.60±0.35	0.22±0.04	-0.17±0.05	0.13	0.05
2946	$2.84^{+0.38}_{-0.38}$	26.72±0.02	1.95±0.27	0.52±0.04	0.17±0.03	0.18	0.15
3052	$2.55^{+0.35}_{-0.35}$	26.97±0.02	0.92±0.14	-0.02±0.03	-0.18±0.04	0.20	0.16
3112	$3.01^{+0.39}_{-0.39}$	25.76±0.01	3.22±0.36	0.54±0.02	-0.00±0.02	0.20	0.17
3128	$3.25^{+0.42}_{-0.42}$	26.72±0.01	2.25±0.36	0.90±0.05	-0.00±0.03	0.22	0.25
3174	$2.99^{+0.39}_{-0.39}$	25.37±0.01	2.80±0.17	0.63±0.02	0.14±0.01	0.22	0.08
3198	$2.72^{+0.37}_{-0.37}$	26.88±0.02	1.75±0.27	0.11±0.03	-0.13±0.04	0.15	0.18
3219	$3.00^{+0.39}_{-0.39}$	27.27±0.03	1.64±0.34	0.69±0.07	0.33±0.05	0.24	0.20
3416	$3.36^{+0.43}_{-0.43}$	25.05±0.01	2.87±0.14	1.06±0.02	0.22±0.01	0.16	0.16
3481	$3.00^{+0.39}_{-0.39}$	27.39±0.02	1.54±0.34	0.25±0.05	-0.10±0.05	0.16	0.23
3922	$3.43^{+0.43}_{-0.43}$	26.39±0.01	2.53±0.36	1.26±0.07	0.11±0.03	0.16	0.07
4193	$2.57^{+0.35}_{-0.35}$	26.90±0.02	0.94±0.12	0.26±0.03	0.02±0.03	0.17	0.23
4302	$3.47^{+0.44}_{-0.44}$	27.06±0.02	1.84±0.35	1.12±0.06	-0.25±0.04	0.12	0.10
4636	$2.88^{+0.38}_{-0.38}$	26.74±0.01	2.15±0.33	0.37±0.03	-0.22±0.04	0.20	0.22
4766	$2.98^{+0.39}_{-0.39}$	26.25±0.01	2.77±0.37	0.11±0.02	-0.25±0.03	0.14	0.12
4774	$2.66^{+0.36}_{-0.36}$	26.68±0.01	1.59±0.18	0.22±0.03	-0.09±0.03	0.12	0.05
4830	$3.40^{+0.43}_{-0.43}$	26.70±0.01	2.28±0.36	1.08±0.06	0.23±0.03	0.21	0.22
5006	$3.45^{+0.44}_{-0.44}$	26.22±0.01	2.76±0.36	1.09±0.04	-0.04±0.02	0.17	0.16
5275	$3.28^{+0.42}_{-0.42}$	27.21±0.02	1.72±0.34	0.88±0.08	0.28±0.04	0.13	0.15
5346	$3.37^{+0.43}_{-0.43}$	27.07±0.02	1.91±0.36	1.06±0.07	0.06±0.04	0.13	0.15
5750	$2.76^{+0.37}_{-0.37}$	26.68±0.01	1.29±0.14	0.17±0.02	-0.25±0.03	0.12	0.18
5856	$3.36^{+0.43}_{-0.43}$	25.97±0.01	3.01±0.36	1.03±0.03	0.16±0.02	0.18	0.16
5916	$2.55^{+0.35}_{-0.35}$	27.30±0.02	0.43±0.12	0.11±0.04	-0.23±0.06	0.21	0.16
6352	$2.72^{+0.37}_{-0.37}$	26.97±0.02	1.72±0.31	0.17±0.04	-0.17±0.05	0.14	0.12
6504	$3.17^{+0.41}_{-0.41}$	26.73±0.01	2.25±0.36	0.79±0.04	0.09±0.03	0.20	0.19
6508	$3.21^{+0.41}_{-0.41}$	27.52±0.02	1.44±0.35	0.82±0.08	0.20±0.05	0.17	0.14
6595	$2.85^{+0.38}_{-0.38}$	27.53±0.02	1.45±0.35	0.46±0.06	0.08±0.05	0.15	0.12
7025	$3.40^{+0.43}_{-0.43}$	25.22±0.00	3.80±0.37	0.91±0.02	-0.22±0.01	0.13	0.22
7610	$2.75^{+0.37}_{-0.37}$	27.21±0.02	1.72±0.35	0.33±0.04	-0.01±0.04	0.22	0.17
7738	$3.13^{+0.40}_{-0.41}$	27.29±0.02	1.62±0.35	0.52±0.05	-0.27±0.05	0.12	0.13
7758	$2.75^{+0.37}_{-0.37}$	27.06±0.02	1.91±0.36	0.28±0.05	-0.15±0.05	0.15	0.15
7874	$3.19^{+0.41}_{-0.41}$	26.72±0.01	2.27±0.36	0.84±0.05	0.00±0.03	0.23	0.13
7986	$2.62^{+0.36}_{-0.35}$	27.47±0.02	1.49±0.36	-0.18±0.04	-0.25±0.07	0.13	0.25
8387	$3.01^{+0.39}_{-0.39}$	27.02±0.02	1.95±0.35	0.63±0.05	-0.10±0.04	0.18	0.22
9394	$2.79^{+0.37}_{-0.37}$	25.75±0.01	1.68±0.09	0.52±0.02	0.13±0.02	0.18	0.21
9570	$2.66^{+0.36}_{-0.36}$	27.19±0.02	1.46±0.27	-0.08±0.04	-0.09±0.06	0.11	0.09
9806	$2.58^{+0.35}_{-0.35}$	26.07±0.01	1.09±0.07	0.20±0.02	-0.05±0.02	0.14	0.01
56017	$2.64^{+0.36}_{-0.36}$	26.33±0.01	0.78±0.07	0.05±0.02	-0.28±0.04	0.16	0.22
60302	$3.02^{+0.39}_{-0.39}$	27.15±0.03	1.70±0.33	0.70±0.08	0.29±0.05	0.14	0.11

Note. — See notes from Table 3.1.

Table C.6. Journal of Observations

QSO	R.A. (J2000)	Dec. (J2000)	r (AB)	i (AB)	z_{em}	z_{abs}	Date (UT)	Instr.	Slit (arcsec)	t_{exp} (s)	S/N pixel^{-1}
(1)	(2)	(3)	(4)	(5)	(6)	(7)	(8)	(9)	(10)	(11)	(12)
J0040−0915	00 40 54.7	−09 15 27	20.48	19.18	4.98	4.74	2010 Jan 20	ESI	0.50	2280	17
J0210−0018	02 10 43.2	−00 18 18	20.48	19.20	4.72	4.57[a]	2010 Jan 20	ESI	0.50	2880	11
J0331−0741	03 31 19.7	−07 41 43	20.56	19.12	4.71	4.19[a]	2010 Jan 20	ESI	0.75	4320	21
J0747+4434	07 47 49.7	+44 34 17	19.62	17.35	4.43	4.02	2009 Mar 22	ESI	0.75	3600	15
J0759+1800	07 59 07.6	+18 00 55	21.06	19.16	4.86	4.66	2010 Jan 20	ESI	0.75	4320	20
J0813+3508	08 13 33.3	+35 08 11	20.81	19.13	4.92	4.30[a]	2010 Apr 21	ESI	0.75	1400	16
J0817+1351	08 17 40.5	+13 51 35	19.86	19.22	4.39	4.26,3.49	2010 Jan 20	ESI	0.75	3600	18
J0825+3544	08 25 40.1	+35 44 14	18.45	18.38	3.85	3.66	2008 Mar 05	ESI	0.75	2700	40
							2008 Mar 25	HIRESr	0.86	10800	20
J0825+5127	08 25 35.2	+51 27 06	18.18	17.93	3.51	3.21,3.32	2008 Mar 05	ESI	0.75	2700	28
J0831+4046	08 31 22.6	+40 46 23	20.30	19.06	4.89	4.34	2010 Apr 20	ESI	0.75	2100	21
J0834+2140	08 34 29.4	+21 40 25	20.56	19.42	4.50	4.39,4.46,3.71	2010 Apr 20	ESI	0.75	5400	21
J0839+3524	08 39 20.5	+35 24 59	20.95	19.54	4.78	4.28	2010 Apr 21	ESI	0.75	2800	18
J0909+3303	09 09 40.7	+33 03 48	18.56	18.46	3.78	3.66	2008 Mar 05	ESI	0.75	2700	30
J1004+4347	10 04 16.1	+43 47 39	20.99	19.36	4.87	4.46	2010 Apr 20	ESI	0.75	4200	21
J1013+4240	10 13 36.3	+42 40 27	21.14	19.87	5.04	4.80	2010 Apr 21	ESI	0.75	5400	21
J1017+6116	10 17 25.9	+61 16 28	18.09	19.10	2.81	2.77	2008 Mar 05	ESI	0.75	1800	30
J1042+3107	10 42 42.4	+31 07 13	20.40	19.00	4.69	4.09	2010 Apr 20	ESI	0.75	3300	27
J1051+3107	10 51 22.5	+31 07 49	19.12	18.54	4.25	4.14	2010 Jan 20	ESI	0.75	2400	29
J1051+3545	10 51 23.0	+35 45 34	20.28	18.45	4.90	3.90,4.35,4.82	2009 Mar 22	ESI	0.75	4800	35
							2010 Apr 04	HIRESr	0.86	7800	12
J1100+1122	11 00 45.2	+11 22 39	20.79	18.85	4.71	3.76,4.40	2009 Mar 22	ESI	0.75	3600	25
J1101+0531	11 01 34.4	+05 31 34	20.92	19.26	4.99	4.34	2010 Apr 21	ESI	0.75	2700	23
J1111+3509	11 11 26.7	+35 09 21	20.00	19.55	4.12	4.05	2010 Apr 20	ESI	0.75	4200	15
J1146+4037	11 46 57.8	+40 37 09	21.00	19.40	4.99	4.85[a]	2010 Jan 20	ESI	0.75	2400	19
J1155+3510	11 55 26.3	+35 10 53	18.16	17.99	2.84	2.76	2008 Mar 05	ESI	0.75	2700	36
J1200+4015	12 00 39.8	+40 15 56	18.32	18.21	3.36	3.22	2008 Mar 05	ESI	0.75	2700	40
							2008 Mar 24	HIRESr	0.86	10800	22
J1200+4618	12 00 36.7	+46 18 50	20.98	19.29	4.73	4.48	2010 Apr 21	ESI	0.75	2700	23
J1201+2117	12 01 10.3	+21 17 59	20.43	18.73	4.58	3.70,3.80,4.16	2010 Jan 20	ESI	0.75	2400	27
J1202+3235	12 02 07.7	+32 35 38	20.60	19.23	5.29	4.80,5.06	2009 Mar 22	ESI	0.75	3600	28
							2010 Apr 04	HIRESr	0.86	14400	18
J1204−0021	12 04 41.7	−00 21 50	20.69	19.27	5.03	4.67[a]	2010 Apr 20	ESI	0.75	1200	16
J1220+4442	12 20 42.0	+44 42 18	20.84	19.70	4.66	4.57[a]	2010 Apr 21	ESI	0.75	4000	14

Table C.6—Continued

QSO	R.A. (J2000)	Dec. (J2000)	r (AB)	i (AB)	z_{em}	z_{abs}	Date (UT)	Instr.	Slit (arcsec)	t_{exp} (s)	S/N pixel^{-1}
(1)	(2)	(3)	(4)	(5)	(6)	(7)	(8)	(9)	(10)	(11)	(12)
J1238+3437	12 38 40.9	+34 37 03	18.51	18.37	2.57	2.47	2008 Mar 05	ESI	0.75	1800	30
J1241+4617	12 41 38.3	+46 17 17	18.54	18.50	2.77	2.67	2008 Mar 05	ESI	0.75	1800	24
J1248+3110	12 48 20.2	+31 10 43	19.89	19.27	4.36	3.70,4.07[a]	2010 Apr 21	ESI	0.75	3300	25
J1253+1046	12 53 53.4	+10 46 03	21.01	19.42	4.91	4.60,4.793[a]	2010 Jan 20	ESI	0.75	2400	20
J1257−0111	12 57 59.2	−01 11 30	18.87	18.54	4.11	4.02	2010 Jan 20	ESI	0.75	2400	31
J1302+5505	13 02 15.7	+55 05 53	19.81	19.13	4.44	3.75,4.01,4.13[a]	2009 Mar 22	ESI	0.75	3600	25
J1304+1202	13 04 26.2	+12 02 46	18.00	17.95	2.98	2.91,2.93	2008 Mar 05	ESI	0.75	1800	36
							2008 Mar 24	HIRESr	0.86	10800	18
J1312+2307	13 12 34.1	+23 07 16	20.78	19.38	5.00	4.62[a]	2010 Apr 20	ESI	0.75	1500	21
J1353+5328	13 53 17.1	+53 28 26	18.10	18.22	2.92	2.83	2008 Mar 05	ESI	0.75	1800	24
							2008 Mar 25	HIRESr	0.86	8400	15
J1412+0624	14 12 10.0	+06 24 07	20.24	19.43	4.42	4.11	2010 Apr 21	ESI	0.75	4500	26
J1438+4314	14 38 35.9	+43 14 59	18.94	17.63	4.61	4.40	2009 Mar 22	ESI	0.75	900	28
							2010 Apr 04	HIRESr	0.86	10800	33
J1446−0101	14 46 17.4	−01 01 31	19.59	19.07	4.15	3.71,4.086[a]	2010 Jan 20	ESI	0.75	1800	17
J1507+4406	15 07 26.3	+44 06 49	17.84	17.70	3.11	3.06	2008 Mar 05	ESI	0.75	1800	26
J1513+1058	15 13 20.9	+10 58 07	20.54	19.39	4.62	4.45[a]	2010 Apr 20	ESI	0.75	1600	11
J1541+3153	15 41 53.5	+31 53 29	17.51	17.42	2.55	2.44	2008 Mar 05	ESI	0.75	1800	30
							2008 Mar 25	HIRESr	0.86	4800	20
J1607+1604	16 07 34.2	+16 04 17	20.64	19.24	4.80	4.47	2010 Apr 21	ESI	0.75	3600	24
J1626+2751	16 26 26.5	+27 51 32	21.65	19.31	5.19	4.31,4.50,5.08,5.18	2009 Mar 22	ESI	0.75	5400	30
J1654+2227	16 54 36.8	+22 27 33	19.90	18.34	4.68	4.00,4.10	2009 Mar 22	ESI	0.75	3600	28
J1659+2709	16 59 02.1	+27 09 35	21.15	19.49	5.32	5.19[a]	2010 Apr 20	ESI	0.75	2300	23
J2252+1425	22 52 46.4	+14 25 26	21.17	19.80	4.91	4.75	2010 Aug 10	ESI	0.75	9000	15

Note. — See notes from Table 4.1.

Table C.7. New DLA metallicities

QSO (1)	z_{abs} (2)	log$N_{\rm HI}$ (3)	f_α[a] (4)	[α/H] (5)	$f_{\rm Fe}$[b] (6)	[Fe/H] (7)	$f_{\rm mtl}$[c] (8)	[M/H] (9)
J0040−0915	4.7395	20.30±0.15	1	-1.74±0.03	6	-2.04±0.09	1	-1.74±0.15
J0747+4434	4.0197	20.95±0.15	3	-1.38±0.00	1	-2.72±0.14	2	-2.32±0.25
J0759+1800	4.6577	20.85±0.15	4	-1.60±0.04	1	-2.03±0.03	1	-1.60±0.16
J0817+1351	3.4901	20.70±0.15	1	-1.14±0.10	3	-0.98±0.00	1	-1.14±0.18
J0817+1351	4.2583	21.30±0.15	4	-1.36±0.05	4	-1.52±0.04	1	-1.36±0.16
J0825+3544	3.2073	20.30±0.10	2	-1.83±0.02	1	-1.98±0.03	2	-1.58±0.13
J0825+3544	3.6567	21.25±0.10	1	-1.82±0.10	4	-1.95±0.04	1	-1.82±0.14
J0825+5127	3.3180	20.85±0.10	1	-1.67±0.10	1	-2.07±0.01	1	-1.67±0.14
J0831+4046	4.3440	20.75±0.15	1	-2.36±0.03	1	-2.41±0.07	1	-2.36±0.15
J0834+2140	3.7102	20.85±0.10	1	-1.65±0.14	1	-1.86±0.02	1	-1.65±0.17
J0834+2140	4.3900	21.00±0.20	4	-1.30±0.04	1	-1.69±0.02	1	-1.30±0.20
J0834+2140	4.4610	20.30±0.15	1	-1.86±0.04	1	-1.92±0.07	1	-1.86±0.16
J0839+3524	4.2800	20.30±0.15	1	-1.42±0.02	1	-1.45±0.04	1	-1.42±0.15
J0909+3303	3.6584	20.55±0.10	4	-1.09±0.04	4	-1.30±0.13	1	-1.09±0.11
J1004+4347	4.4596	20.70±0.15	1	-2.07±0.03	6	-2.15±0.02	1	-2.07±0.15
J1013+4240	4.7979	20.60±0.15	1	-1.98±0.02	0	···	1	-1.98±0.15
J1017+6116	2.7684	20.60±0.10	1	-2.17±0.03	1	-2.29±0.05	1	-2.17±0.11
J1042+3107	4.0865	20.75±0.10	1	-1.95±0.01	1	-1.98±0.03	1	-1.95±0.10
J1051+3107	4.1391	20.70±0.20	1	-2.04±0.02	1	-2.42±0.09	1	-2.04±0.20
J1051+3545	4.3498	20.45±0.10	1	-1.77±0.02	1	-2.17±0.05	1	-1.77±0.10
J1051+3545	4.8206	20.35±0.10	1	-2.28±0.02	0	···	1	-2.28±0.10
J1100+1122	3.7564	21.09±0.15	1	-2.29±0.01	6	-2.56±0.01	1	-2.29±0.15
J1101+0531	4.3446	21.30±0.10	1	-1.16±0.06	4	-1.66±0.10	1	-1.16±0.12
J1111+3509	4.0520	20.80±0.15	1	-1.95±0.05	1	-2.12±0.05	1	-1.95±0.16
J1155+3510	2.7582	21.00±0.10	1	-1.38±0.03	4	-1.61±0.04	1	-1.38±0.10
J1200+4015	3.2200	20.85±0.10	4	-0.64±0.01	1	-0.99±0.04	1	-0.64±0.10
J1200+4618	4.4765	20.50±0.15	2	-1.56±0.01	1	-1.68±0.02	2	-1.28±0.12
J1201+2117	3.8000	21.35±0.15	1	-0.80±0.01	4	-1.01±0.01	1	-0.80±0.15
J1201+2117	4.1580	20.60±0.15	1	-2.72±0.05	6	-3.04±0.06	1	-2.72±0.16
J1202+3235	4.7955	21.10±0.15	2	-2.80±0.29	1	-2.65±0.03	2	-2.26±0.13
J1202+3235	5.0645	20.30±0.15	1	-2.73±0.05	0	···	1	-2.73±0.16
J1238+3437	2.4714	20.80±0.10	2	-2.03±0.02	1	-2.19±0.03	2	-1.79±0.13
J1241+4617	2.6674	20.70±0.10	4	-1.59±0.06	1	-2.13±0.04	1	-1.59±0.12
J1248+3110	3.6973	20.60±0.10	2	-1.89±0.02	1	-1.93±0.03	2	-1.53±0.13
J1253+1046	4.6001	20.30±0.15	2	-1.59±0.02	1	-1.54±0.03	2	-1.14±0.13
J1257−0111	4.0208	20.30±0.10	1	-1.56±0.02	1	-2.10±0.07	1	-1.56±0.10
J1304+1202	2.9133	20.55±0.15	4	-1.75±0.07	1	-2.34±0.05	1	-1.75±0.17
J1304+1202	2.9289	20.30±0.15	4	-1.54±0.04	1	-1.90±0.03	1	-1.54±0.16
J1353+5328	2.8349	20.80±0.10	1	-1.50±0.07	1	-1.54±0.11	1	-1.50±0.12
J1412+0624	4.1095	20.40±0.15	2	-1.80±0.02	1	-2.02±0.08	2	-1.62±0.17
J1438+4314	4.3990	20.89±0.15	4	-1.19±0.01	1	-1.92±0.00	1	-1.19±0.15
J1507+4406	3.0644	20.75±0.10	1	-2.09±0.02	1	-2.17±0.03	1	-2.09±0.10
J1541+3153	2.4435	20.95±0.10	1	-1.49±0.04	5	-2.18±0.14	1	-1.49±0.11
J1607+1604	4.4740	20.30±0.15	1	-1.87±0.02	1	-2.02±0.06	1	-1.87±0.15
J1626+2751	4.3110	21.34±0.15	2	-1.74±0.05	4	-1.67±0.06	2	-1.27±0.16
J1626+2751	4.4968	21.39±0.15	1	-2.54±0.01	1	-2.75±0.02	1	-2.54±0.15
J1626+2751[d]	5.1791	20.94±0.15	4	-1.47±0.02	4	-1.33±0.09	1	-1.47±0.15
J1654+2227	4.0023	20.60±0.15	0	···	1	-2.14±0.03	2	-1.74±0.13
J2252+1425	4.7475	20.60±0.15	0	···	1	-2.07±0.11	2	-1.67±0.21

Note. — See notes from Table 4.2.

Table C.8. List of Observations

Date	Frames[a] (Obs.)	Frames[b] (Used)	Num. Stars[c] (Initial)	Num. Stars[d] (Final)	SNR[e]	Strehl
1995 Jun 10	1200	425	54	66	10.3	0.08
1995 Jun 11	2700	1604	95	110	15.0	0.06
1995 Jun 12	2100	1082	107	108	12.0	0.04
1996 Jun 26	4200	585	116	119	19.8	0.04
1996 Jun 27	2300	1260	117	121	20.5	0.04
1997 May 14	3600	1851	63	82	16.7	0.06
1998 Apr 02	2660	1649	119	121	16.3	0.05
1998 May 14	4560	1748	96	114	16.7	0.04
1998 May 15	7030	1953	41	55	9.9	0.06
1998 Jul 04	2280	943	108	114	17.8	0.08
1998 Aug 04	6270	1469	87	107	15.5	0.05
1998 Aug 05	5700	1592	94	103	17.3	0.07
1998 Oct 09	2660	1188	83	99	17.1	0.08
1998 Oct 11	570	450	79	96	15.0	0.05
1999 May 02	7030	1589	115	116	19.9	0.09
1999 May 03	2090	1264	103	114	16.0	0.07
1999 Jul 24	5510	2239	113	119	18.5	0.11
1999 Jul 25	950	788	102	114	15.0	0.06
2000 Apr 21	3040	947	90	112	18.5	0.04
2000 May 19	9880	1970	64	91	10.2	0.09
2000 May 20	7600	2146	81	97	16.5	0.10
2000 Jul 19	8740	1939	111	116	17.1	0.07
2000 Jul 20	3420	1454	111	119	19.8	0.09
2000 Oct 18	2280	1807	82	107	15.1	0.05
2001 May 08	1520	889	111	124	20.1	0.04
2001 May 09	6270	1990	76	100	13.1	0.08
2001 Jul 28	4180	1752	99	104	20.0	0.13
2001 Jul 29	6080	1751	105	115	19.0	0.07
2002 Apr 23	7410	1669	117	119	17.2	0.05
2002 Apr 24	7790	1882	104	113	19.6	0.06
2002 May 23	1900	1249	66	84	18.3	0.07
2002 May 24	2660	1537	85	100	17.7	0.09
2002 May 28	2850	1866	59	80	13.2	0.06
2002 May 29	3420	1552	86	104	16.8	0.07
2002 Jun 01	5510	1992	43	53	7.7	0.09
2002 Jul 19	4370	1115	41	57	7.0	0.07
2002 Jul 20	3990	1355	51	64	11.0	0.06
2003 Apr 21	5130	1799	93	107	19.1	0.04
2003 Apr 23	5320	1970	69	87	13.2	0.05
2003 Jul 22	5130	1718	70	94	16.6	0.08
2003 Sep 07	4560	1795	108	112	16.3	0.07
2003 Sep 08	4370	1223	97	110	12.3	0.07
2004 Apr 29	6840	1181	53	68	14.5	0.11
2004 Apr 30	4180	1203	98	105	16.6	0.05
2004 Jul 25	5320	2007	98	110	18.1	0.08
2004 Jul 26	8550	2309	33	38	6.7	0.08
2004 Aug 29	3230	1328	120	122	21.0	0.10
2005 Apr 24	7410	2195	51	60	11.6	0.07
2005 Apr 25	9500	2035	116	116	20.8	0.05
2005 Jul 26	6650	1497	98	113	19.0	0.06

Note. — See notes from Table 5.1.

Table C.9. List of Variable Stars

Star ID	Other ID	K[a] (mag)	Int. Var. (mag)	p (arcsec)	ΔR.A. (arcsec)	ΔDec. (arcsec)	Probability	Nights (days)	Type
IRS16SW	E23	10.06±0.19	0.17	1.41	1.04	-0.95	2.3E-23	50	Ofpe/WN9[h]
IRS16NW	E19	10.09±0.09	0.07	1.21	-0.01	1.21	3.3E-05	49	Ofpe/WN9[g]
IRS29N	E31	10.33±0.20	0.18	2.15	-1.63	1.40	1.1E-15	35	WC9[g]
IRS16CC	E27	10.60±0.05	0.01	2.07	1.99	0.57	3.0E-01	50	O9.5-B0.5 I[ci]
S2-11	GEN+2.03-0.63	11.99±0.13	0.11	2.07	1.99	-0.58	4.9E-19	49	Late[g]
S2-4	E28:GEN+1.46-1.49	12.26±0.17	0.15	2.05	1.45	-1.45	6.1E-14	47	B0-0.5 I[g]
S1-1	GEN+1.01+0.02	13.00±0.11	0.08	0.98	0.98	0.05	3.6E-04	49	Early[f]
S2-36	···	13.28±0.13	0.12	2.08	2.04	0.43	3.7E-09	48	Early[f]
S1-21	E24:W7	13.33±0.17	0.15	1.69	-1.69	0.13	4.2E-06	42	O9-9.5 III?[g]
S1-12	E21:W13	13.82±0.18	0.17	1.31	-0.85	-1.00	4.2E-07	45	OB I?[c]
S2-7	E29:GEN+1.06+1.81	14.06±0.25	0.21	2.09	0.97	1.85	4.2E-10	45	O9-B0[c]
S0-32	···	14.18±0.20	0.15	0.81	0.26	0.77	6.3E-04	49	Early[f]
S2-58	···	14.21±0.14	0.10	2.45	2.17	-1.14	6.8E-04	47	Early[f]
S1-45	···	15.41±0.55	0.28	1.63	-1.28	1.00	6.1E-06	41	Early[f]
S2-65	···	15.83±0.49	0.29	2.57	2.37	-1.00	2.5E-04	29	···
S0-34	···	15.85±0.40	0.31	0.83	0.32	-0.77	4.1E-06	26	···

Note. — See notes from Table 5.2.

Table C.10. List of Non-variable Stars

Star ID	Other ID	K (mag)	p (arcsec)	ΔR.A. (arcsec)	ΔDec. (arcsec)	Nights (days)	Type
IRS16NE	E39	9.00±0.05	3.06	2.85	1.10	35	Ofpe/WN9[g]
IRS16C	E20	9.83±0.05	1.23	1.13	0.50	50	Ofpe/WN9[ġ]
S2-17	E34:GEN+1.27-1.87	10.90±0.07	2.23	1.27	-1.84	35	B0.5-1 I[g]
IRS16SW-E	E32:16SE1	11.00±0.08	2.15	1.85	-1.11	50	WC8/9[g]
IRS29S	···	11.31±0.06	2.08	-1.86	0.93	30	K3 III[d]
S1-24	E26:GEN+0.76-1.55	11.64±0.07	1.72	0.73	-1.55	45	O8-9.5 I[g]
S2-16	E35:29NE1	11.85±0.08	2.29	-1.01	2.05	33	WC8/9[g]
S1-23	GEN-0.90-1.46	11.86±0.09	1.73	-0.92	-1.46	33	Late[g]
S3-2	GEN+3.07+0.56	12.00±0.11	3.09	3.03	0.60	31	Early[f]
S2-6	E30:GEN+1.60-1.36	12.06±0.08	2.07	1.59	-1.31	50	O8.5-9.5 I[c]
S1-3	E15:GEN+0.57+0.84	12.10±0.06	0.99	0.46	0.88	50	Early[ħ]
S3-5	E40:16SE	12.15±0.09	3.16	2.95	-1.13	21	WN5/6[g]
S2-8	W2	12.24±0.08	2.16	-1.99	0.84	23	Early[f]
S1-17	GEN+0.55-1.45	12.51±0.08	1.52	0.50	-1.44	49	Late[g]
S1-4	GEN+0.77-0.71	12.53±0.07	1.02	0.77	-0.66	50	Early[f]
S2-19	E36:GEN+0.53+2.27	12.62±0.11	2.34	0.42	2.30	33	O9-B0 I?[g]
S1-20	GEN+0.41+1.59	12.70±0.11	1.66	0.37	1.61	49	Late[g]
S1-22	E25:W14	12.72±0.08	1.72	-1.65	-0.51	42	O8.5-9.5 I?[g]
S1-5	GEN+0.43-0.96	12.78±0.04	0.98	0.37	-0.91	50	Late[g]
S1-14	E22:W10	12.82±0.07	1.40	-1.37	-0.30	46	O8-9.5 III/I[g]
S3-6	GEN+3.26+0.08	12.82±0.05	3.22	3.22	0.09	17	Late[g]
S2-22	GEN+2.37-0.29	12.92±0.04	2.33	2.32	-0.22	50	Late[g]
S2-38	···	12.93±0.09	2.12	2.04	0.58	44	Late[f]
S2-31	GEN+2.91-0.20	13.06±0.10	2.84	2.83	-0.15	42	Late[g]
S1-34	···	13.20±0.14	1.29	0.86	-0.96	50	···
S2-5	GEN+1.91-0.86	13.32±0.05	2.05	1.89	-0.80	50	Early[f]
S1-68	···	13.38±0.06	1.97	1.89	-0.55	50	···
S2-21	GEN-1.70-1.65	13.47±0.10	2.36	-1.70	-1.65	12	Early[f]
S0-13	GEN+0.59-0.47	13.49±0.04	0.69	0.54	-0.42	50	Late[g]
S1-25	GEN+1.69-0.66	13.54±0.05	1.76	1.65	-0.60	50	Late[e]
S2-26	···	13.60±0.13	2.56	0.69	2.47	20	Late[e]
S0-15	E16:W5	13.70±0.07	0.98	-0.93	0.29	48	O9-9.5 V[c]
S0-14	E14:W9	13.72±0.08	0.83	-0.78	-0.27	50	O9.5-B2 V[c]
S1-19	GEN+0.38-1.58	13.82±0.12	1.62	0.36	-1.58	46	Early[f]
S2-2	GEN-0.54+2.00	14.07±0.11	2.12	-0.59	2.03	41	Late[f]
S0-2	E1:S2	14.16±0.08	0.12	-0.07	0.10	33	B0-2 V[b]
S1-8	E18:W11	14.19±0.11	1.08	-0.67	-0.85	49	OB[c]
S1-15	W4	14.21±0.10	1.46	-1.37	0.52	47	Late[f]
S0-6	S10	14.26±0.09	0.39	0.07	-0.38	49	Late[f]
S1-49	···	14.26±0.13	1.66	-1.65	0.15	23	···
S1-13	W12	14.27±0.12	1.42	-1.10	-0.90	46	Early[f]
S2-47	···	14.29±0.08	2.26	2.20	-0.49	48	Early[f]
S0-9	S11	14.31±0.08	0.55	0.14	-0.53	49	Early[f]
S0-12	W6	14.38±0.06	0.68	-0.57	0.37	49	Late[f]
S2-3	W15	14.48±0.09	2.09	-1.54	-1.41	23	Late[f]
S0-4	E10:S8	14.49±0.11	0.37	0.32	-0.19	49	B0-2 V[b]
S0-3	E6:S4	14.50±0.14	0.25	0.22	0.13	19	B0-2 V[b]
S2-75	···	14.52±0.12	2.78	2.65	-0.85	40	···
S2-69	···	14.57±0.14	2.64	-0.91	2.48	13	Early[f]
S3-4	···	14.61±0.20	3.14	3.10	-0.47	20	Early[f]
S0-1	E4:S1	14.67±0.11	0.14	-0.11	-0.09	49	B0-2 V[b]
S2-23	···	14.72±0.13	2.43	1.64	1.80	39	Late[f]
S1-55	···	14.80±0.39	1.69	1.58	0.59	41	···
S1-50	···	14.82±0.37	1.67	1.51	0.72	41	···
S1-52	···	14.83±0.29	1.66	-0.02	1.66	42	···

Table C.10—Continued

Star ID	Other ID	K (mag)	p (arcsec)	ΔR.A. (arcsec)	ΔDec. (arcsec)	Nights (days)	Type
S1-10	W8	14.88±0.12	1.15	-1.15	-0.04	42	···
S1-2	E17:GEN-0.06-1.01	14.90±0.12	1.00	-0.05	-1.00	45	Early[f]
S1-33	···	15.01±0.10	1.25	-1.24	-0.07	40	···
S1-58	···	15.04±0.35	1.77	-1.48	0.98	37	···
S1-51	···	15.05±0.15	1.66	-1.65	-0.20	39	Early[f]
S2-86	···	15.05±0.23	2.99	2.68	-1.33	24	Early[f]
S3-3	···	15.06±0.33	3.12	3.06	-0.62	19	Early[f]
S2-30	···	15.13±0.19	2.88	2.88	0.00	23	···
S1-18	···	15.14±0.15	1.66	-0.73	1.49	39	Early[f]
S0-5	E9:S9	15.17±0.16	0.36	0.18	-0.31	43	B0-2 V[b]
S0-31	E13	15.20±0.23	0.66	0.49	0.45	40	B V[c]
S2-34	···	15.21±0.22	2.04	1.79	0.98	43	···
S0-26	E8:S5	15.27±0.22	0.39	0.36	0.16	40	B4-9 V[b]
S1-44	···	15.28±0.41	1.61	0.26	1.59	40	···
S3-16	···	15.30±0.20	3.15	3.02	-0.88	14	Late[f]
S2-82	···	15.30±0.29	2.88	2.87	0.08	27	Late[f]
S2-12	···	15.33±0.17	2.07	1.68	1.22	38	Late[f]
S1-32	···	15.33±0.13	1.13	-0.93	-0.64	42	···
S1-39	···	15.35±0.16	1.45	-0.53	-1.35	30	Early[f]
S0-11	E12:S7	15.36±0.13	0.53	0.53	-0.01	40	B V[c]
S0-18	S18	15.36±0.13	0.43	-0.09	-0.42	45	···
S1-35	···	15.36±0.19	1.27	-1.24	-0.25	38	···
S2-63	···	15.39±0.28	2.56	-0.69	2.47	16	Early[f]
S1-54	···	15.41±0.23	1.68	-1.53	0.70	36	···
S1-62	···	15.41±0.31	1.82	0.51	1.74	37	···
S1-53	···	15.44±0.15	1.68	1.68	-0.09	30	···
S2-61	···	15.46±0.17	2.54	2.46	-0.64	38	···
S2-46	···	15.47±0.30	2.18	2.08	-0.64	38	···
S2-73	···	15.50±0.32	2.72	2.21	-1.58	29	···
S1-6	···	15.54±0.13	1.15	-0.91	0.71	34	Early[f]
S1-48	···	15.54±0.23	1.62	-0.60	-1.50	22	···
S0-7	E11:S6	15.55±0.27	0.45	0.44	0.11	35	B V[c]
S0-19	E5	15.56±0.19	0.19	-0.09	0.17	28	B4-9 V[b]
S1-64	···	15.57±0.36	1.91	0.60	1.81	34	···
S2-80	···	15.57±0.27	2.86	2.22	1.80	20	Early[f]
S2-40	···	15.58±0.18	2.15	1.68	1.34	35	Early[f]
S2-42	···	15.61±0.28	2.11	0.41	2.07	26	···
S1-27	···	15.62±0.27	1.09	-1.07	0.24	39	···
S1-26	···	15.62±0.13	1.02	-0.95	0.38	40	···
S1-37	···	15.63±0.16	1.42	-1.34	0.47	36	···
S1-47	···	15.67±0.23	1.63	-1.57	0.45	34	···
S0-16	E2	15.68±0.19	0.08	0.05	0.06	18	B4-9 V[b]
S1-59	···	15.70±0.25	1.86	0.01	1.86	27	···
S1-31	GEN-0.91+0.44	15.70±0.18	1.14	-0.99	0.57	31	···
S0-29	···	15.72±0.50	0.54	0.25	-0.48	21	···
S2-83	···	15.74±0.19	2.94	2.87	-0.63	16	···
S0-27	···	15.74±0.18	0.54	0.13	0.52	32	···
S1-36	···	15.75±0.27	1.36	-0.67	-1.18	30	···
S2-37	···	15.77±0.31	2.11	0.04	2.11	29	···
S0-8	E7	15.79±0.14	0.47	-0.32	0.34	29	B4-9 V[b]
S1-7	···	15.81±0.14	1.12	-1.00	-0.50	34	···
S1-65	···	15.82±0.15	1.93	1.43	1.29	31	Early[f]
S0-28	S19	15.85±0.18	0.61	-0.18	-0.58	30	···
S2-64	···	15.85±0.59	2.56	2.54	0.31	16	···
S0-36	···	15.85±0.28	1.03	-0.60	-0.84	29	···

Table C.10—Continued

Star ID	Other ID	K (mag)	p (arcsec)	ΔR.A. (arcsec)	ΔDec. (arcsec)	Nights (days)	Type
S0-20	E3	15.86±0.20	0.21	-0.18	-0.10	33	B4-9 V[b]
S1-40	···	15.95±0.23	1.50	-1.36	-0.64	26	···
S1-61	···	15.99±0.38	1.76	-1.43	-1.03	21	···
S2-52	···	16.02±0.20	2.37	2.37	-0.07	21	···
S1-42	···	16.13±0.22	1.60	0.94	1.29	19	···

Note. — See notes from Table 5.3.